Synthesis and AFM-based single-molecule force spectroscopy of helical aromatic oligoamide foldamers

Floriane Devaux

THÈSE EN COTUTELLE PRÉSENTÉE

POUR OBTENIR LE GRADE DE

DOCTEUR DE

L'UNIVERSITÉ DE BORDEAUX

ET DE L'UNIVERSITÉ DE LIÈGE

ÉCOLE DOCTORALE UBX

ÉCOLE DOCTORALE DE SCIENCES ULiège

SPÉCIALITÉ: CHIMIE

Par Floriane DEVAUX

Synthesis and AFM-based Single-Molecule Force Spectroscopy of Helical Aromatic Oligoamide Foldamers

Sous la direction de:
Anne-Sophie Duwez et Ivan Huc

Soutenue le 14 décembre 2018

Membres du jury :

M. QUINTON, Loïc	Professeur, Université de Liège	Président
M. JONAS, Alain	Professeur, Université Catholique de Louvain	Rapporteur
M. WILLET, Nicolas	Docteur, PhysIOL	Rapporteur
M. MAURIZOT, Victor	Chargé de recherche CNRS, Université de Bordeaux	Examinateur
Mme DUWEZ, Anne-Sophie	Professeur, Université de Liège	Directrice de thèse
M. HUC, Ivan	Directeur de recherche CNRS, Université de Bordeaux	Directeur de thèse

Titre : Synthèse et Spectroscopie de Force sur Molécule Unique par AFM de Foldamères Hélicoïdaux d'Oligoamides Aromatiques

Résumé : Ce travail décrit la synthèse de foldamères, conçus spécifiquement pour des mesures de spectroscopie de force sur molécule unique par AFM, ainsi que la caractérisation détaillée de leurs propriétés mécaniques par cette technique. L'objectif général de cette thèse est d'obtenir des informations sur les forces qui gouvernent le repliement ainsi que la compréhension des propriétés mécano-chimiques de molécule synthétiques repliées.

Nous avons conçu et étudié trois types de foldamères hélicoïdaux afin de comprendre l'influence de la taille du foldamère et l'influence de l'architecture chimique sur les propriétés mécaniques à l'échelle de la molécule unique en solution. Les expériences d'étirement sur des foldamères de quinoléines de quatre longueurs différentes ont révélé des motifs de dépliement caractéristiques. Le dépliement a pu être décrit par des ruptures séquentielles des groupements d'interactions impliquées dans le repliement hélicoïdal. La longueur des motifs est directement proportionnelle au nombre d'unités quinoléines constituant les foldamères. Toutefois, les forces du dépliement ne présentent pas cette même dépendance linéaire. Ces résultats ont démontré l'effet de la coopérativité des interactions chimiques le long du foldamère replié. A partir de mesures d'étirement-relaxation, nous avons évalué l'énergie libre de dépliement et avons mis en évidence la capacité des molécules dépliées à se replier rapidement contre la charge mécanique. Ces résultats, ainsi que les expériences dans différents solvants, démontrent la grande robustesse de cette classe de foldamères. Les expériences d'étirement de molécules uniques, sur un autre type de foldamère contenant une séquence de naphthyridines ont permis de confirmer la structure hélicoïdale en solution. Les unités naphthyridines induisent un angle plus grand entre les unités adjacentes. Les forces de dépliement mesurées suggèrent que les forces gouvernant le repliement d'une hélice de plus grand diamètre sont plus faibles. L'insertion d'un chainon aliphatique, tel qu'un groupement méthylène, a permis de constater une perturbation majeure des propriétés mécaniques. Sous tension le groupement méthylène interrompt la continuité des interactions dans l'hélice formée d'unités quinoléines.

Les résultats des caractérisations au niveau moléculaire de ces foldamères, qui sont complémentaires aux résultats de techniques d'ensemble, sont convaincants pour imaginer cette classe de foldamères comme futurs constituants de machines moléculaires avec des propriétés mécaniques spécifiques.

Mots clés : Microscopie à force atomique (AFM), spectroscopie de force sur molécule unique, mécano-chimie, foldamères, quinoléine, naphthyridine, structure repliée, hélice

Title : Synthesis and AFM-based Single-Molecule Force Spectroscopy of Helical Aromatic Oligoamide Foldamers

Abstract : In this work, we describe the synthesis of aromatic oligoamide foldamers designed for AFM-based single-molecule force spectroscopy (SMFS) and the detailed investigation of their mechanical properties by this technique. The aim of the thesis was to gain insights into the forces governing the folding and the mechanochemical properties of synthetic folded molecules.

We designed and studied three different kinds of helical foldamers to investigate the influence of the size of the foldamer and of the chemical architecture on the mechanical properties at the level of the single molecule in organic solvents. Pulling experiments on quinoline-based foldamers of four different sizes revealed a characteristic unfolding pattern, consistent with the sequential opening of the same groups of interactions involved in the helical conformation. The length of the unfolding patterns is proportional to the foldamer size, while the average unfolding forces show non-linear force dependence. This result highlighted the cooperativity of the interactions originating from the chemical sequence in the folding. From pulling-relaxing SMFS experiments, we evaluated the unfolding free energies and evidenced the capacity of the unfolded molecules to rapidly refold under the mechanical load. Together with experiments in different solvents, these results demonstrate the high robustness of this class of foldamers. SMFS experiments on the naphthyridine-constituted foldamer confirmed its helical structure and suggested that the strength of the interactions along the foldamer are weaker for a wider helix. The insertion of a methylene bridge in the aromatic oligoamide sequence showed a substantial effect on the mechanical properties. The aliphatic junction indeed disrupts the interaction continuum in the helical conformation under load.

Providing detailed characterizations down to the single-molecule level, which are complementary to the traditional ensemble experiments, we also showed that helically folded aromatic oligoamides are a genuine class of foldamers with very promising properties as building blocks for mechanized nanomachines

Keywords : Atomic force microscopy (AFM), single-molecule force spectroscopy, mechanochemistry, foldamers, quinoline, naphthyridine, folded structure, helix

---

Nanochemistry and Molecular Systems - Department of Chemistry
University of Liège
Allee du six aout, 13
4000 Liege - BELGIUM

Institut Européen de Chimie et Biologie (IECB)
University de Bordeaux
Rue Robert Escarpit, 2
33607 Pessac Cedex - FRANCE

Acknowledgments

Merci

I did not do this thesis alone, but thanks to the support, help and collaboration of many people, to whom I want to express my profound gratitude.

I gratefully acknowledge the funding sources of my thesis. This work would not have been feasible without the financial support from the FRIA (FRS-FNRS), which offered me great conditions to complete my project and to attend many international conferences. I acknowledge the Patrimoine de l'Université de Liège and the AcLg which also supported me financially for attending conferences and for accomplishing my research stay in Bordeaux.

I would like to express my sincere gratitude to my supervisors Professor Anne-Sophie Duwez and Professor Ivan Huc for welcoming me in their laboratories, in Liège in the "NanoChemsitry and Molecular Systems" and in Bordeaux in "the Ivan Huc group" respectively. They gave me the opportunity to carry out this fascinating research project. Thank you very much for the time you took to discuss our strategies, issues and results and for your guidance and your encouragements all along this journey. I also thank you for giving me the opportunity to work in two laboratories, to attend many conferences, to share my research and to meet so many interesting people.

I would like to express my gratefulness to my jury members, especially Professor Loïc Quinton for accepting to be the president of the jury and Professor Alain Jonas, Doctor Nicolas Willet and Doctor Victor Maurizot for having accepted to be part of my jury and for devoting their valuable time to read my manuscript and for giving me feedback and their viewpoints.

I want to express my gratitude to the members of my thesis committee, Doctor Antoine Debuigne and Doctor Nicolas Willet, for their trust and their encouragements.

I also thank Professor Francesco Zerbetto and Doctor Evangelos Bakalis from the University of Bologna for our collaboration. I also would like to thank Doctor Jéremy Brisbois for his attempts of helping our signal analysis. I want to acknowledge the CERM laboratory from the University of Liège for your supply in dry solvents and VaCo for your great availability for SEM analyses. I extend my gratitude to Professor Charles-André Fustin and to Doctor Roland Duchène for their technical expertise in manipulating small amounts of our precious compounds at the beginning of my thesis.

I would like to extend my gratefulness for the technical assistance of many people throughout my research. Without the synthesis of the foldamers, I would not have been able to perform many of the force spectroscopy experiments, so thank you Doctor Xuesong Li for the immense work you endeavored. Now I realize the tremendous work it represents! I hope I could honor your work with my results! It was also a great pleasure meeting you in Liège and in Bordeaux. For the synthesis part in Bordeaux, I would like to dedicate special thanks to Jinhua Wang and Doctor Subrata Saha for their inexhaustible help during the synthesis of my new foldamers. Thank you so much for your time and all your advice which allowed me to learn the foldamer chemistry and to create (or almost) sophisticated and exciting folded structures. The 'almost' is meant to also acknowledge all the help and work of Doctor Victor Maurizot, without whom I would not have been able to achieve the synthesis. Indeed, in addition of supporting and advising me along the synthesis, I owe Victor many thanks for having completed the molecular edifices.

I would like to thank all the members of the group in Bordeaux for their extraordinary professional encouragements and friendships. I also want to express my gratitude to Doctor Yann Ferrand for his useful comments and advice during the group meetings to optimize the syntheses and to Eric Merlet for supplying with generosity the monomers and for his technical tips and tricks for large-scale syntheses. I also want to specifically and sincerely thank Bappa for his support and particularly for staying with me in the lab when I needed more time to finish, which led to a great friendship. I thank SaiReddy for sharing his hood with me for a period of time, Daniella and Valentina for the nice neighbourship and all the other lab-colleagues from Bordeaux, Alabno, Antoine J, Antoine M, Arthur, Dragos, Jason, Joan, Lucile Fisher, Pedro, Sunbun and Xiabo for all your help or the fun we had during my stay. I would also like to thank the colleagues from neighbouring laboratories in particular Camille, Diane and Léonie for the nice coffee breaks and for our outside-the-lab friendships. Before finishing the acknowledgments for my colleagues from Bordeaux, I finally would also want to thank the on-site collaborators who rendered my research project possible: Doctor Valérie Gabelica and Doctor Frédéric Rosu for the mass spectrometry analyses and Estelle Morvan for the NMR training.

My deep and sincere gratefulness goes to the NanoChem members who had to endure me most! Doing a thesis is a truly life-changing experience and it would not have been possible without your solidarity and your guidance. Thank you so much for supporting me and for sharing your expertise with me in the lab. I would never have imagined that I could be able to manipulate individual molecules! Thank you very much for always pushing the limit of our understandings. It was really exciting to try unraveling together the questions arising from the recorded pulling traces! I particularly want to extend my gratitude to Damien and Sandrine for our brainteaser cogitations and for the joy of working with you. I would like to extend my gratefulness to Nicolas who also

particularly shared his experience, helped and guided me even after he left the lab. I appreciate and cherish as well the great friendship we have built all together over the years and also with all the former lab members! Thank you Andrea, Anastasia, Arnaud, Arpita, Coralie, Damien, Nicolas, Perrine and Sandrine for all the fun we had inside and outside the laboratory

I would like to sincerely express my warmest and deepest gratitude to my family, including in particular my parents, my sister, my brother and my grandparents, who have always been supporting me! Even if I really enjoyed my PhD thesis, it was not always easy, but your support and mostly our great understanding were highly valuable and allowed me to easily overcome any difficulties. Special thanks are dedicated to Jean, who has been accompanying me daily through this adventure. He continuously encouraged me, even when we were 1000 km apart during my stay in Bordeaux. Thank you for your calmness when necessary and for your great enthusiasm for our next adventures.

Thank you very much to all. I wish you a nice reading.

Merci beaucoup à tous,

Floriane

List of abbreviations

3D	Three-dimensional	**1,2,3…**
A	Acceptor (in case of hydrogen bonding)	**A**
A	Adenine (in case of DNA)	
AA	Amino Acids	
AFM	Atomic Force Microscopy or Atomic Force Microscope	
AFM-SMFS	AFM-based Single Molecule Force Spectroscopy	
B-DNA	Right-handed double helix	**B**
Boc	tert-butyloxycarbonyl	
bp	Base pair (in DNA)	
C	Cytosine (in case of DNA)	**C**
CD	Circular Dichroism	
DBU	1,8-Diazabicyclo(5.4.0)undec-7-ene	**D**
DCM	Dichloromethane	
DDS	Dodecyl sulfide	
D-H	Donor of proton	
DIEA/ DIPEA	Diisopropylethylamine	
DMB	2,4-dimethoxybenzaldehyde	
DMF	Dimethylformamide	
DMSO	Dimethylsulfoxide	
DNA	Desoxyribose Nucleic Acid	
eq.	Equation	**E**
	Equivalent	
ESI	Electrospray ionization	
EtOH	Ethanol	
FC	Force-Clamp	**F**
FD	Force-Distance	
FJC	Freely Jointed Chain	
Fmoc	Fluorenylmethyloxycarbonyl	
G	Guanine (in case of DNA)	**G**
Ghosez's reagent	1-chloro-N,N-2-trimethyl- 1-propenylamine	
GPC	Gel Permeation Chromatography	
H-bond	Hydrogen bond	**H**
iBu	Isobuthoxyl-group	**I**
IM	Ion Mobility	
IM-MS	Ion Mobility-Mass Spectrometry	
IMS	Ion Mobility Spectrometry	
InvOLS	Inverse Optical Lever Sensitivity	
IR	Infrared	

J	Joule	**J**
k_B	Boltzmann constant	**K**
k or kc	Spring constant of the AFM-cantilever	
Lc	Contour length	**L**
LC	Liquid Chromatography	
lp	Persistence length	
Lr	Loading rate	
MALDI	Matrix-assisted laser desorption ionization	**M**
Me	Methyl	
MeCN	Acetonitrile	
MS	Mass-Spectrometry	
MT	Magnetic Tweezers	
Mw	Molecular Weight	
N	2-amino-5-isobutoxy-1,8-naphthyridine-7-carboxylic acid	**N**
N_n	Naphthyridine oligomer with n units	
$NaBH(OAc)_3$	Sodium triacetoxyborohydride	
NMR	Nuclear Magnetic Resonance	
OT	Optical Tweezers	**O**
PEG	Polyethylene glycol same as PEO	**P**
PEO	Polyethylene oxide same as PEG	
ppm	Part per million	
PyBOP	Benzotriazol-1-yl-oxytripyrrolidinophosphonium hexafluorophosphate	
Q	8-amino-4-isobutoxy-2-quinolinecarboxylic acid	**Q**
Q_n	Quinoline oligomer containing n quinoline units	
^mQ	8-aminomethyl-4-isobutoxy-2-quinolinecarboxylic acid	
rt	Room temperature	**R**
S-DNA	Overstretched DNA conformation	**S**
SEM	Scanning electron microscopy	
SMFS	Single-Molecule Force Spectroscopy	
STM	Scanning Tunnelling Microscope	
T	Thymine (in case of DNA)	**T**
	Temperature in formula	
TCE	1,1,2,2, tetrachloroethane	
TFA	Trifluoroacetic acid	
THF	Tetrahydrofuran	
TLC	Thin layer chromatography	
UV-Vis	Ultraviolet-visible	**U**
v	Velocity	**V**
WLC	Worm-Like Chain	**W**
XRD	X-ray diffraction	**X**

Table of contents

Introduction, Objectives & Strategies

Why are we interested in folded structures?

Nature has marvellously shaped molecular machineries and tuned folding structures to make efficient and complex processes and functions. Most of the fundamental biological processes emerge from DNA written in a four-letter genetic code and from its transcription into proteins built from 21 amino-acids. The variety of structures and functions created and fulfilled by nature using only a limited number of building blocks has been teasing the scientist's curiosity and our understanding for a long time.

Understanding the roadmap that determines how a simple linear sequence predisposes the molecules to adopt a precise folding and yield functional molecules would represent a major progress in the field of biophysics as well as in nanotechnology.

Indeed, nowadays, a strong correlation has been established between diseases and misfolding of DNA[1] or proteins.[2,3] Further insights into the folding mechanisms would hence help tackling these issues. In addition to the development of cures or preventive care, nature's molecular machineries are highly inspiring. For example, to unzip one base pair, the RNA polymerase exerts a force of typically 15 pN over a 12 Å-long distance, which is equivalent to an energy use of 4.4 k_BT. It accomplishes this task with 40% efficiency whereas macroscopic man-made machines work only at maximum 20% efficiency in average (*e.g.* motors in cars).[4] Seeing the scale and performances of nature's molecular machineries, many scientists dream of reproducing and achieving similar or rivalling tasks. Being able to create tiny molecular machines would constitute a breakthrough in many different fields, be it in medicine, information technology, catalysis, or for example in self-healing materials.

For many years, chemists have therefore endeavoured to mimic nature. Recently, they have made phenomenal progress by achieving the synthesis of all kinds of secondary structures found in nature (*e.g.* helices[5–7], sheets[8], knots, double helix DNA[9], G-quadruplex DNA[10,11],...) and of molecular architectures even beyond natural structures such as rotaxanes[12], herringbone helices[13], helices of varying diameter.[14] However, after being able to recreate such secondary structures, the challenge of conferring controlled dynamical properties[15,16] and functionalities still lies ahead.

In this context, this thesis aims at contributing to this goal by investigating the dynamical and mechanical properties of synthetic folded structures. Mechanical properties have always been recognized in biological processes as playing fundamental roles in providing for example, elasticity and extensibility in muscle or displacement for molecular cargos and mechanical strength for the helicase to open the double DNA strands before replication....[17–20] Inspired by these latter, mechanical performances, including bond strength and stability also appear as crucially important for synthetic molecular machines.[16,21–23]

How can we contribute?

In this thesis we investigated the relationship between chemical sequence and both the mechanical and dynamical properties of synthetic helical structures by Atomic Force Microscopy based Single-Molecule Force Spectroscopy (AFM-based SMFS).

Since more than a decade, single-molecule force spectroscopy based on AFM has been increasingly recognized for its capabilities to investigate molecular processes by probing both intermolecular and intramolecular interactions, as well as conformational transitions.[24] This technique presents the defining advantage over ensemble techniques of not averaging temporal and spatial behaviours.[25–28] AFM-based SMFS is able to capture discrete behaviours and properties of molecules that are only displayed by molecular subpopulations. AFM-based SMFS is also able to probe multiple steps in molecular processes. Furthermore, it allows applying a force in a controllable manner onto a molecule, which thus better mimics biological perturbations than chemical denaturation when investigating proteins undergoing mechanical force in their natural environment.[18,29] For example, the molecular mechanism of the muscle machinery was deciphered thanks to the measurements of the mechanical properties of titin and myosin at the single molecule scale.[30,31]

This **thesis aims at probing helical synthetic systems** mimicking the local folded building blocks which initiate the folding of sophisticate biomolecules (by analogy with studying in depth the secondary structures of proteins). Helical molecules are indeed ubiquitous in biological processes and account for the most observed secondary structure in proteins (30% of the Protein Data Bank).[32] This approach concurs with a rational investigation for elucidating folding ingenuities and is in a perfect synergy with developing bottom-up approaches in molecular machines**.**[6,7] For such bottom-up approaches, all building blocks of the molecular machines should then be understood separately in order to build and assemble multiple different secondary structures into one complex molecular machine, which could then accomplish a large-scale task.

However, performing single-molecule force spectroscopy on small molecules (secondary structures) is currently still a major challenge. Initially, such experiments were performed on large macromolecular systems such as proteins as a whole, natural polysaccharides or long DNA chains, and synthetic polymers. Owing to recent technological and molecular AFM-design improvements, smaller molecular systems are becoming accessible, such as isolated secondary structures of proteins or small synthetic systems.[23,33–35]

Moreover, probing properties at the scale of the single molecule may lead to unexpected results. The thermodynamic laws explaining the macroscopic world are not always valid to describe the behaviours observed in the nanoscopic world.[4,36,37] Indeed, molecules can take advantage of thermal energy to overcome energetic reaction barriers and to carry out tasks out of equilibrium.

Owing to the challenges of studying small systems at the single molecule level, we focused our research on **synthetic helical molecular architectures, called foldamers**. The foldamer family regroups artificial (synthetic) folded molecules.[3,35–38] Their folded conformations are created to reproduce the properties of biomolecules but also to extend structures and functions beyond the reach of biomolecules. We selected the class of aromatic oligoamide foldamers. A great merit of these aromatic foldamers lies in their controlled syntheses and their predictable folding.[38] At the molecular scale, helically folded conformations have attracted considerable attention. However, there is still little knowledge about their dynamical behaviours in solution and their potential and promising mechanical properties are still completely unexplored.

Objectives and strategies: a synergy between synthesis and AFM-based SMFS

The objectives of this thesis are to investigate artificial, stable and predictable helical aromatic foldamers to provide detailed descriptions of their dynamical behaviours and their mechanical properties in solution at the single molecule scale. These properties are then interpreted in terms of conformational stability and mechanochemical properties.

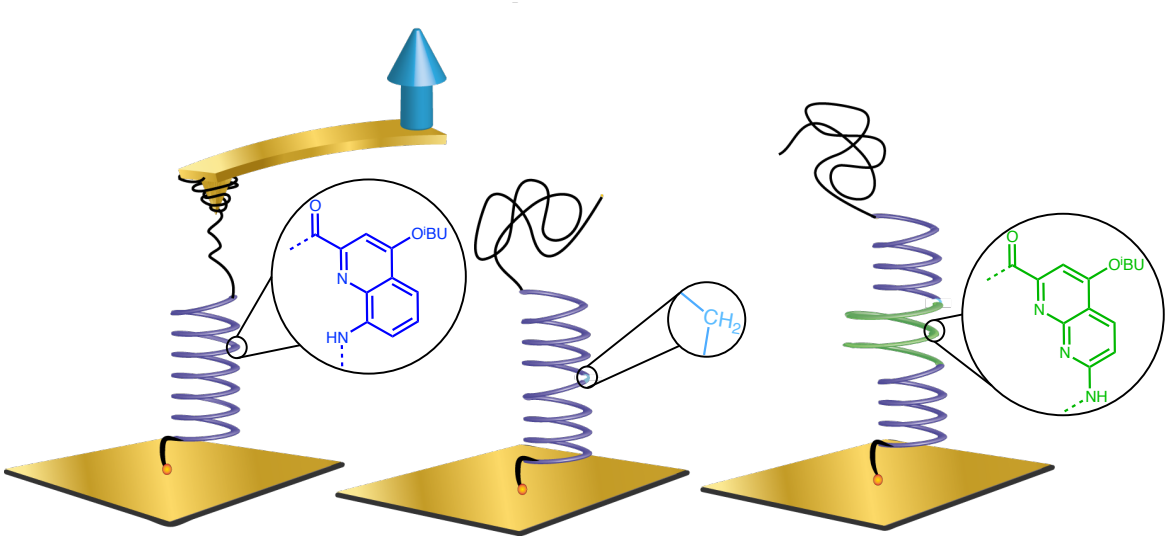

Figure 1 Schematic illustration of Single-Molecule Force Spectroscopy experimental set up with the studied aromatic oligoamide foldamers. From left to right pure quinoline-based foldamer, quinoline-based diblock foldamer, quinoline- and naphthyridine-based triblock.

We start our investigation with **pure quinoline-based oligomers of several sizes**, displaying a stable helical structure (Figure **1** left).[39] This type of foldamers has been thoroughly characterized using traditional ensemble experiments, since the beginning of the 2000s, but a detailed description of the dynamical and mechanical properties at the molecular scale is still missing. Knowledge gained from prior studies was considered to support the investigations of the intramolecular forces.[5,40–44] The quinoline-based foldamers were specifically tuned to suit SMFS experiments. A small spacer ending by thiol group was covalently attached to one extremity of the foldamer to ensure sustainable attachment to gold substrates and the other extremity was functionalized with a poly(ethylene glycol) (PEG) chain to link reversibly the AFM tip.

In this work, we perform standard single-molecule force spectroscopy on these specifically designed quinoline-based foldamers in order to determine their **unfolding force-distance patterns**. We aim at understanding the detailed **unfolding mechanism under load** and at investigating the **length-dependency** on the behaviours in solution. The unfolding patterns and the unfolding forces are then interpreted for relating their mechanical strength to their chemical structure (chapter 2).

In order to complete the detailed investigation of the pure quinoline-based foldamers and explore their **dynamical properties**, we also focus our efforts on a dynamical force spectroscopy study. Furthermore, we carry out pulling-relaxing SMFS experiments to probe the capabilities of the quinoline foldamers to refold after the forced unfolding. We thereby test the **elastic properties** of the foldamers (chapter 3).

Moreover, we also perform SMFS experiments in different solvents in order to **modulate the different types of potential interactions** present in the foldamers. Our objective here is to identify and measure the different contributions of electrostatic and π-stacking interactions (chapter 4).

On the one hand, all of these results complement knowledge of quinoline-based foldamers. On the other hand, they provide key elements, which could shed light on the **mechanical forces involved in molecular interactions and folding propensity/mechanisms**. These results would pave the way for the molecular-level understanding of mechanochemical properties, as well as for the rational development of artificial molecular machineries. Last, but not least, the experiments contribute to the development of AFM-based SMFS for the investigation of small molecules.

Following up the detailed investigation and understanding of the dynamical processes and mechanical properties of pure quinoline-based foldamers, **two other foldamers** are **rationally designed and synthesized**. The newly synthesized foldamers comprise chemically-different parts embedded in the quinoline-based foldamer. The stepwise segment doubling synthesis strategy is used to obtain precisely the desired molecules. The first foldamer consists in a **diblock** quinoline-based foldamer with a small aliphatic junction, which consists in a single CH_2 group between two quinoline blocks (Figure **1** center), whereas the second foldamer consists of a **triblock** foldamer where a **naphthyridine-based block** is inserted between two quinoline blocks (Figure **1** right). The naphthyridine-based foldamer has a quite similar chemical backbone, also exhibiting a helical folding but possessing a **wider helix diameter**[45] than quinoline based foldamer (chapter 5).

Using these two new foldamers, we aim at comparing the **differences in unfolding force-distance patterns and mechanical properties originating from the chemical and structural differences**. We therefore perform standard single-molecule force spectroscopy on these new AFM-designed systems to yield complementing mechanochemical insights (chapter 6).

More generally, this thesis aims at overcoming major challenges in both SMFS and in supramolecular synthesis. The first challenge relates to implementing SMFS for small molecules. The second one relates to the synthesis design strategy where spontaneous self-assembly of the naphthyridine-based foldamers has to be avoided. Finally, by studying small model architectures related to secondary structure building blocks, this work aims at yielding further understandings for complex (biological) systems and molecular machines.

References

1. London, T. B. C. *et al.* FANCJ is a structure-specific DNA helicase associated with the maintenance of genomic G/C tracts. *J. Biol. Chem.* **283,** 36132–36139 (2008).
2. Soto, C. Protein misfolding and disease; protein refolding and therapy. *FEBS Lett.* **498,** 204–207 (2001).
3. Dill, K. A. & MacCallum, J. L. The Protein-Folding Problem, 50 Years On. *Science (80-.).* **338,** 1042 LP-1046 (2012).
4. Ritort, F. The nonequilibrium thermodynamics of small systems. *Comptes Rendus Phys.* **8,** 528–539 (2007).
5. Jiang, H., Léger, J. M., Dolain, C., Guionneau, P. & Huc, I. Aromatic δ-peptides: Design, synthesis and structural studies of helical, quinoline-derived oligoamide foldamers. *Tetrahedron* **59,** 8365–8374 (2003).
6. Yashima, E., Maeda, K., Iida, H., Furusho, Y. & Nagai, K. Helical Polymers: Synthesis, Structures, and Functions. *Chem. Rev.* **109,** 6102–6211 (2009).
7. Yashima, E. *et al.* Supramolecular Helical Systems: Helical Assemblies of Small Molecules, Foldamers, and Polymers with Chiral Amplification and Their Functions. *Chem. Rev.* **116,** 13752–13990 (2016).
8. Sebaoun, L., Maurizot, V., Granier, T., Kauffmann, B. & Huc, I. Aromatic oligoamide β-sheet foldamers. *J. Am. Chem. Soc.* **136,** 2168–2174 (2014).
9. Ziach, K. *et al.* Single helically folded aromatic oligoamides that mimic the charge surface of double-stranded B-DNA. *Nat. Chem.* **10,** 511–518 (2018).
10. Bonnat, L. *et al.* Templated Formation of Discrete RNA and DNA:RNA Hybrid G-Quadruplexes and Their Interactions with Targeting Ligands. *Chem. - A Eur. J.* **22,** 3139–3147 (2016).
11. Flack, T. *et al.* Prefolded Synthetic G-Quartets Display Enhanced Bioinspired Properties. *Chem. - A Eur. J.* **22,** 1760–1767 (2016).
12. Kay, E. R. & Leigh, D. A. Hydrogen bond-assembled synthetic molecular motors and machines. *Top. Curr. Chem* **262,** 133–177 (2005).
13. Delsuc, N., Godde, F., Kauffmann, B., Léger, J. M. & Huc, I. The herringbone helix: A noncanonical folding in aromatic-aliphatic peptides. *J. Am. Chem. Soc.* **129,** 11348–11349 (2007).
14. Singleton, M. L., Pirotte, G., Kauffmann, B., Ferrand, Y. & Huc, I. Increasing the Size of an Aromatic Helical Foldamer Cavity by Strand Intercalation. *Angew. Chemie Int. Ed.* **53,** 13140–13144 (2014).
15. Feringa, B. L. The Art of Building Small: From Molecular Switches to Motors (Nobel Lecture). *Angew. Chemie - Int. Ed.* **56,** 11060–11078 (2017).
16. Le Bailly, B. A. F. & Clayden, J. Dynamic foldamer chemistry. *Chem. Commun.* **2,** 303 (2016).
17. Evans, E. & Ritchie, K. Dynamic strength of molecular adhesion bonds. *Biophys. J.* **72,** 1541–55 (1997).
18. Schönfelder, J., De Sancho, D. & Perez-Jimenez, R. The power of force: Insights into the protein folding process using single-molecule force spectroscopy. *J. Mol. Biol.* **428,** 4245–4257 (2016).
19. Dudko, O. K. Decoding the mechanical fingerprints of biomolecules. *Q. Rev. Biophys.* 1–14 (2015). doi:10.1017/S0033583515000220
20. Noy, A. & Friddle, R. W. Practical single molecule force spectroscopy: how to determine fundamental thermodynamic parameters of intermolecular bonds with an atomic force microscope. *Methods* **60,** 142–50 (2013).
21. Browne, W. R. & Feringa, B. L. Making molecular machines work. *Nat. Nanotechnol.* **1,** 25–35 (2006).
22. Ha, T. Probing Nature's Nanomachines One Molecule at a Time. *Biophys. J.* **110,** 1004–1007 (2016).

23. Schröder, T. *et al.* Single-molecule force spectroscopy of supramolecular heterodimeric capsules. *Phys. Chem. Chem. Phys.* **12,** 10981 (2010).
24. Binnig, G., Quate, C. F. & Gerber, C. Atomic Force Microscope. *Phys. Rev. Lett.* **56,** 930–933 (1986).
25. Getfert, S., Evstigneev, M. & Reimann, P. Single-molecule force spectroscopy: Practical limitations beyond Bell's model. *Phys. A Stat. Mech. its Appl.* **388,** 1120–1132 (2009).
26. Evans, E. Probing the Relation Between Force—Lifetime—and Chemistry in Single Molecular Bonds. *Annu. Rev. Biophys. Biomol. Struct.* **30,** 105–128 (2001).
27. Zhang, W. & Zhang, X. Single molecule mechanochemistry of macromolecules. *Prog. Polym. Sci.* **28,** 1271–1295 (2003).
28. Dougan, M. L. H. and L. The physics of pulling polyproteins: a review of single molecule force spectroscopy using the AFM to study protein unfolding. *Reports Prog. Phys.* **79,** 76601 (2016).
29. Stirnemann, G., Kang, S., Zhou, R. & Berne, B. J. How force unfolding differs from chemical denaturation. *Proc. Natl. Acad. Sci. U. S. A.* **111,** 3413–8 (2014).
30. Rief, M., Gautel, M., Oesterhelt, F., Fernandez, J. M. & Gaub, H. E. Reversible Unfolgind of Individual Titin Immunoglobulin Domains by AFM. *Science (80-.).* **276,** 1109–1112 (1997).
31. Evans, E. & Ritchie, K. Strength of a Weak Bond Connecting Flexible Polymer Chains. *Biophys. J.* **76,** 2439–2447 (1999).
32. Qin, Z., Fabre, A. & Buehler, M. J. Structure and mechanism of maximum stability of isolated alpha-helical protein domains at a critical length scale. *Eur. Phys. J. E* **36,** (2013).
33. Lussis, P. *et al.* A single synthetic small molecule that generates force against a load. *Nat. Nanotechnol.* **6,** 553–557 (2011).
34. Sluysmans, D. *et al.* Synthetic oligorotaxanes exert high forces when folding under mechanical load. *Nat. Nanotechnol.* **13,** 209–213 (2018).
35. Berkemeier, F. *et al.* Fast-folding -helices as reversible strain absorbers in the muscle protein myomesin. *Proc. Natl. Acad. Sci.* **108,** 14139–14144 (2011).
36. Jarzynski, C. Nonequilibrium equality for free energy differences. *Phys. Rev. Lett.* **78,** 2690–2693 (1997).
37. Collin, D. *et al.* Verification of the Crooks fluctuation theorem and recovery of RNA folding free energies. *Nature* **437,** 231–234 (2005).
38. Huc, I. & Hecht, S. in *Foldamers* I–XXII (Wiley-VCH Verlag GmbH & Co. KGaA, 2007). doi:10.1002/9783527611478.fmatter
39. Huc, I. Aromatic Oligoamide Foldamers. *European J. Org. Chem.* **2004,** 17–29 (2004).
40. Qi, T., Deschrijver, T. & Huc, I. Large-scale and chromatography-free synthesis of an octameric quinoline-based aromatic amide helical foldamer. *Nat. Protoc.* **8,** 693–708 (2013).
41. Delsuc, N. *et al.* Kinetics of helix-handedness inversion: Folding and unfolding in aromatic amide oligomers. *ChemPhysChem* **9,** 1882–1890 (2008).
42. Qi, T. *et al.* Solvent dependence of helix stability in aromatic oligoamide foldamers. *Chem. Commun. (Camb).* **48,** 48–51 (2012).
43. Uribe, L., Gauss, J. & Diezemann, G. Determining Factors for the Unfolding Pathway of Peptides, Peptoids, and Peptidic Foldamers. *J. Phys. Chem. B* **120,** 10433–10441 (2016).
44. Abramyan, A. M., Liu, Z. & Pophristic, V. Helix handedness inversion in arylamide foldamers: elucidation and free energy profile of a hopping mechanism. *Chem. Commun.* **52,** 669–672 (2016).
45. Ferrand, Y., Kendhale, A. M., Garric, J., Kauffmann, B. & Huc, I. Parallel and antiparallel triple helices of naphthyridine oligoamides. *Angew. Chemie - Int. Ed.* **49,** 1778–1781 (2010).

Chapter 1

Background and related work

TABLE OF CONTENTS

Chapter 1
Background and related work

This chapter is dedicated to cover the background information and a broad introduction of the related fields of this research. It is not exhaustive but it summarizes briefly the current knowledge and curiosities driving the accomplishment of this multidisciplinary thesis.

The first part sums up the universal molecular interactions and their subtle interplay entailing the folding of either natural or synthetic molecules. These forces become more and more understood in the extent of giving a 3D molecular structure but still arise incomprehension on their capabilities to induce particular dynamic properties.

The second part is devoted to retrace briefly the birth of supramolecular chemistry and particularly of the foldamer chemistry, as well as to discuss the performances of organic chemists to achieve predictable folded structures. An important part of this section is devoted to the man-ingenuity to create helical structures and particularly to the development of helical aromatic oligoamides foldamers.

The last part introduces and explains the most common molecular characterization techniques used to investigate molecular systems. It rises on the fundaments, the advantages and performances of single-molecule force spectroscopy investigation. Particular emphases are placed on the Atomic Force Microscopy (AFM) instrument and techniques to perform single-molecule force spectroscopy (SMFS) experiments. The literature of AFM-based SMFS experiments on biological molecules undergoing helical conformations is also summarized in this section. State-of-the-art examples of investigations on synthetic supramolecular systems are closing this introducing chapter.

1.1 Molecular properties and Folding

Molecules can adopt specific and controlled conformations and undergo conformational transitions. These conformations and transitions empower the molecules with roles and functions to life.

These conformations result from covalent bonds, providing the molecular backbone and from many non-covalent interactions, which interplay to give rise to sophisticate spatial arrangements and dynamical properties. The process to evolve in particular and dynamical conformations is known as folding. The promoting factors of folding are the backbone rigidity and the repulsive or attractive non-covalent interactions between chemical groups remote in the molecular backbone (intramolecular interactions), or between molecules (intermolecular interactions) or with solvent molecules (hydrophobic effect & solvation). Fundamentally, all non-covalent interactions are electrostatic in nature but they are commonly classified into different types including mainly hydrogen bonds, ion/metal coordination, hydrophobic forces, van der Waals forces, π-π interactions/stacking and electrostatic effects.

Individually these non-covalent bonds are weak (0-40 kcal.mol^{-1}). Cumulatively, the non-covalent interactions are significantly strong and allow giving rise to a wide range of stable folded conformations. The enthalpies of formation of some individual non-covalent interactions are on the order of thermal agitation due to Brownian motion (k_BT = 0,6 kcal.mol^{-1}). In nature, molecules harness this thermal energy to perform chemical and mechanical tasks.[1,2]

Without this perfect mastery of nature, life would not be the same; DNA transcription, protein expression, skin elasticity, molecular recognition would not be feasible. Usually, a folded state is highly sensitive to the backbone sequence and its environment.[3,4] Indeed a single defect in the primary structure of a protein or a change of pH can lead to a complete disorder. For many decades, scientists try to deeply understand these interactions and strive to establish a roadmap, which explains the reasons how the interactions interplay and the consequences of such modulation.

As the most impressive biological processes comprise complex 3D structures and folding propensity of proteins or of DNA, a high focus is dedicated to their understanding. Proteins and DNA constitute nowadays the prime source of inspiration for chemists challenged by the creation of molecular machineries.

This chapter will not be exhaustive but presents the most frequent contributions to folding in nature and the ones chemists mobilize to build synthetic counterparts.

1.1.1 Molecular and solvent interactions

Molecular interactions are universal and are involved in any level of molecular and supramolecular structures. Molecular structures are hold by a fine balance of many countervailing contributions, which are difficult to disentangle. Entropic and enthalpic driving effects often describe folding.

1.1.1.1 Backbone rigidity

The entropic contribution of the molecule is determined to a great extent by the backbone rigidity, as the formation of bonds restricts the motion and hence forces a defined spatial arrangement. The more the local conformation of the folded structure is restricted or sterically hindered, the lower the entropy cost of adopting a folded conformation is.

Proteins are constituted of 21 α-amino acids (AA) and their linear coupling leads spontaneously, or assisted by chaperones to 3D-complex folded conformations.[5] All the information to achieve this organization is encrypted in the α-amino acids properties and their order in the sequence, the primary structure. As represented in Figure 1.1.A and as the name indicates, the protein building blocks are made of a carboxylic acid, an amine and a side chain (R) attached to the same α-carbon. The coupling of 2 AA forms an amide bond, also called peptidic bond, which fixes the ω angle to 180°. The flexibility of the protein backbone is thus limited to rotate only around 2 bonds between *N*-Cα (called Phi, φ) and Cα-*C* (called Psi, ψ). Those angles are called torsion or dihedral angles.

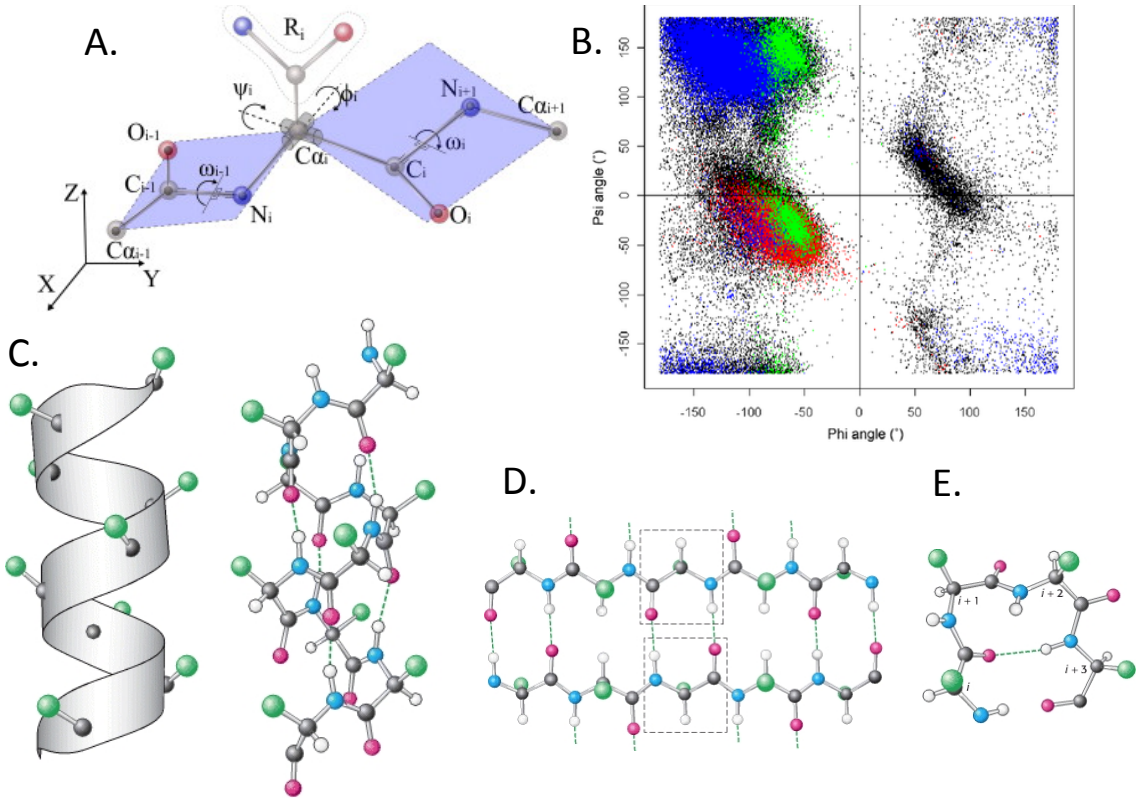

Figure 1.1 (A) Structural conformation of 2 coupled amino acids. Dihedral angles and degrees of freedom of the protein.[6] (B) The Ramachandran plot: plot of the dihedral angles, φ and ψ, of the amino acids contained in proteins. The AA involved in an α-helix, beta-strand, proline and coil structure are represented by red, blue, green and black dots, respectively.[7] (C) Illustration of the most common secondary structure of proteins[8]:Right handed α-helix. The planes of the rigid peptidic bonds are fused in the grey ribbon and the intramolecular H-bonds are shown by the green discontinued lines and are parallel to the long axis of the helix. (D) Antiparallel β Sheet, H-bonds connect amino acids of adjacent strands. (E) Turn, H-bonds connect the i and *i* + 3 amino acids. Adapted from references 6–8.

The side chain of the AA is also a determining entropic folding factor. Indeed, some side chains bring steric hindrance, others bring hydrophobic or hydrophilic groups (enthalpic effects will be discussed in a next section) and the proline, specifically, further decreases the allowed degrees of rotation of φ and ψ due to the ring formation. As a result, some AA favour or disfavour some secondary structures.[9] This is highlighted by the Ramanchandran plot[10], where each type of secondary structure elements prevails within characteristic range of φ and ψ angles and blank areas are not accessible angles due to steric hindrance (Figure 1.1.B). The Ramachandran plot of the proline indicates that proline is mainly comprised in α-helix, whereas glycine is found in each secondary structure and in random coil.[11]

In deoxyribonucleic acids (DNA), the assembly of four different nucleotides made of a 5-carbon ring sugar, a phosphate group and a varying nucleobase (guanine (G), cytosine (C), adenine (A) and thymine (T)), leads to the restricted variety of structural conformations that have been discovered until now (Figure 1.2.B&C).[12,13] As shown in Figure 1.2.A&B, the 5-carbon ring sugar, even if it is proved to twist, favours a perpendicular orientation of the nucleobases regarding the strand. Besides, as aromatic molecules, the nucleobases represent bulky component. These steric constrains bring some rigidity and thus favour some particular structures.

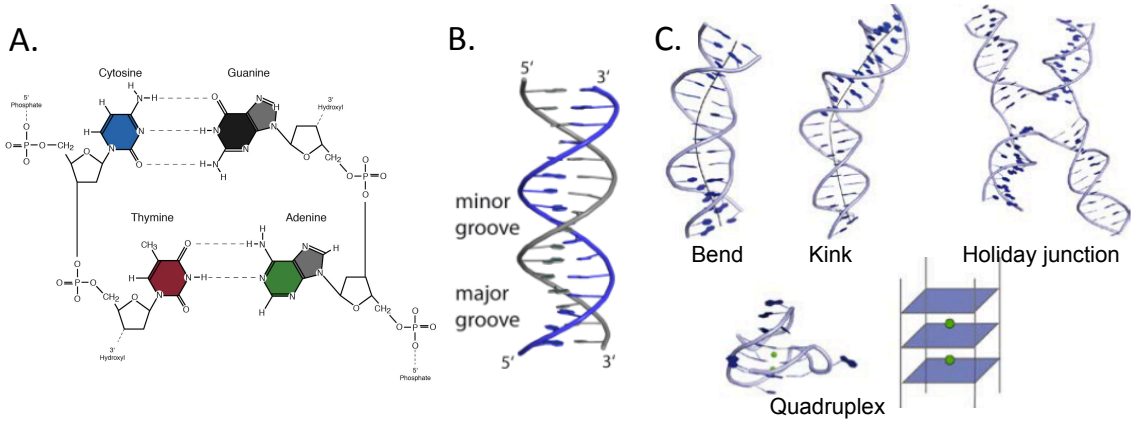

Figure 1.2 (A) Molecular structures of the 4 existing nucleotides in DNA and pairing: guanine (G) with cytosine (C) and adenine (A) with thymine (T). The planar pairing of G & C and A & T, through hydrogen bonds (dashed lines). (B) Structural conformation of the double-stranded helix of B-DNA. The pairing of the nucleobases are perpendicular to the long axis of the helix. (C) Less frequent secondary structures of DNA (not exhaustive). Adapted from reference 12.

In opposition, in the standard synthetic polymer field, a lot of different building blocks exist and provide different properties. Most polymers are known to be quite flexible because of the unrestricted free rotations brought by the monomers. Flexible polymers do not adopt particular folded states but a random coil conformation in solution. Due to Brownian motions, their conformations fluctuate between a mean equilibrium value.

1.1.1.2 Mechanical bonds

By nature, a mechanical bond has direct steric effects on the structure and the dynamics of the molecule as it confers a locked topology and restricts some motions. Resulting from a sharing of molecular entities, the mechanical bond is an emergent type of bond differing

from the more known chemical bonds. Its definition has been recently clarified by Carson J. Bruns and Sir J. Fraser Stoddart as *" An entanglement in space between two or more molecular entities (component parts) such that they cannot be separated without breaking or distorting chemicals bonds between atoms"*. The molecules containing such mechanical bonds are referred as **mechanomolecules (**Figure 1.3**)**. Either the mechanical bond owes to sterically impassable bulky groups (rotaxane), to closed ring-shaped interlocking (catenane), or to closed interlocked chain (knot). Intuitionally a mechanical bond should be as strong as a covalent bond since mechanical components cannot be separated without breaking a covalent bond. However, it has been demonstrated that the constrained nature of this architecture may destabilize some covalent bonds involved in the topology[14,15].

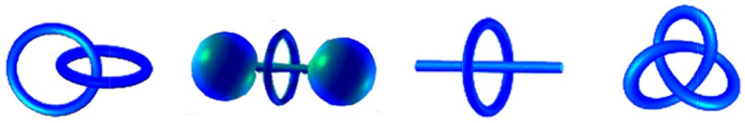

Figure 1.3 from left to right: [2]catenane, [2]rotaxane, pseudorotaxane, trefoil knot. Reproduced from reference 16.

1.1.1.3 Electrostatic interactions, H-bonding & ion pairing

The enthalpic contribution to folding arises with electrostatic interactions.

As declared by Hunter[17], electrostatics explains at the greatest extent intermolecular interactions. Numerous intermolecular interactions, apart from aromatic-stacking, can be described by the simple following equation and can be assimilated to H-bonding:

$$logK = c_1 \alpha_2^H \beta_2^H + c_2 \qquad \text{Eq. 1}$$

Eq. 1 K is the association constant of the interaction, c_1 and c_2 are constants that depend on the solvent and α_2^H and β_2^H are functional group constants which are directly related to the hydrogen-bond donor and hydrogen-bond receptor properties.

Electrostatic interactions can be repulsive. Two atoms are submitted to **short range repulsion** when they are brought in close vicinity. Surface electrons cause electrostatic repulsion when their orbitals overlap. This repulsive force takes place only at a very short range but is intense.

Hydrogen bonds are favourable attractive interactions between a hydrogen atom that is covalently bound to an electron withdrawing atom (proton donor, D-H) *i.e.* nitrogen, oxygen *etc*. and an atom with a basic lone pair of electrons (acceptor, A). The energy of a hydrogen bond can range from 0 to 40 kcal.mol^{-1} depending on the hydrogen-bond donor and hydrogen-bond receptor properties of the pair, the geometry, and its local environment. The common distance between the acceptor and the donor ranges from 2.2 Å to 4 Å.

As shown in Figure 1.1 and Figure 1.2, H-bonds are essential in the structures of proteins and nucleic acid molecules.

For the secondary structures of proteins, H-bonding is the driving factor of folding. For instance, α-helices are built up owing to H-bonds created between the amino hydrogens (N-H donor) of one amino acid *i* and carboxyl oxygens (C=O) of the amino acid *i+4* in the peptide backbone.

In DNA, H-bonds are responsible for the specific Watson-Crick pairing of the nucleobases leading to the double helix and assuring the storage and transcription of the genetic code.[18] Three H-bonds are formed between C and G, while only two between A and T. This implies C-G pairing to be stronger. Even if Watson-Crick base pairing is the most popular and most stable in energy, alternative base pairing interactions can be found in nucleic acids, such as Hoogsteen base pairing (Figure 1.4. A).[19–21] They are probably less frequent, to our knowledge up to now, and they likely lead to disrupted double helix or others conformations, such as G-quadruplexes, i-motifs and triplexes (Figure 1.4. B-D).[22] Although the H-bonds involved in these structures are weaker, the folding does take place; other factors are contributing to their occurrences and their stabilization. For example, G-quadruplexes are likely formed along guanine-rich sequence and in presence of coordinating cations.

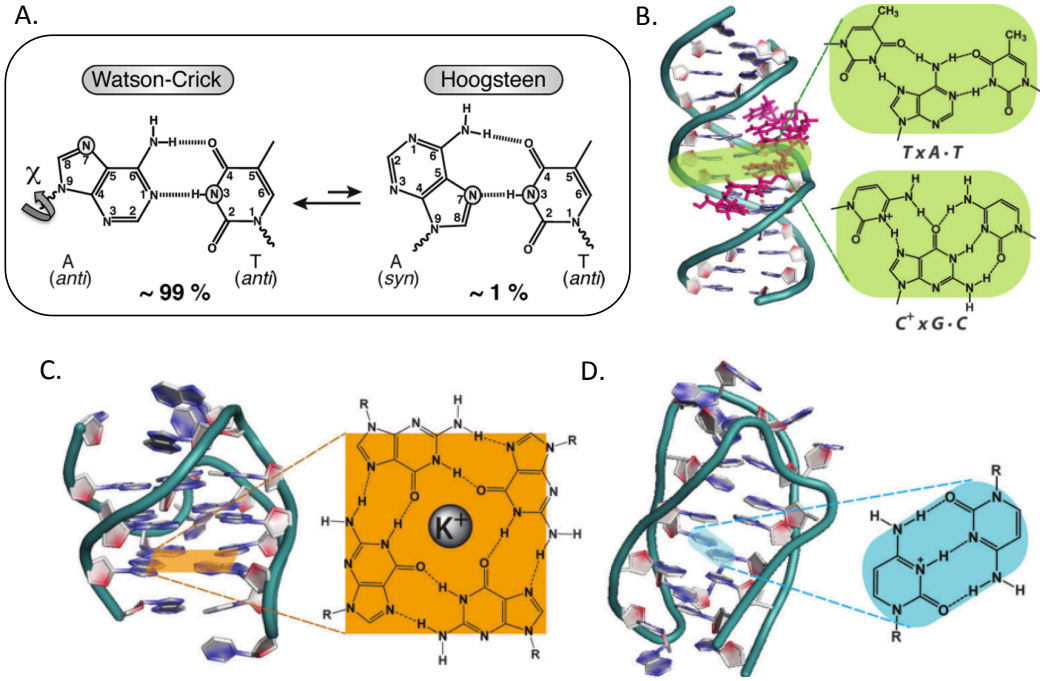

Figure 1.4 (A) Equilibrium between (ground state) Watson-Crick and (transient) Hoogsteen H-bonds between A and T in B-DNA (leading to disrupted double helix)[20]. Examples[22] of structures in which Hoogsteen H-bonds are involved: (B). Parallel triplex.(C) G-quadruplex. (D) i-motifs. Adapted from references 20,22.

Ion interactions or metal coordination is also another important stabilizing factor involved in numerous structures, as already mentioned. Ion interactions can refer to pairing of cationic and anionic functional groups within a molecule. In proteins, such interactions are likely when cationic AA (*i.e.* lysine or arginine) and anionic AA (e. aspartate or glutamate) are within 5 Å proximity. These interactions can be called salt bridges and can bring 1-4 kcal.mol^{-1} of stabilization. Ion interactions include as well the presence of mono- or divalent atomic/molecular cations (Na^+, Li^+, K^+, Mg^{2+}) or anions (Cl^-, SO_4^{2-}) in coordination with the molecule. This is a charge-dipole interaction. These interaction are present for manifold roles, including structural[23] and can account for 5-120 kcal.mol^{-1} of stabilization.

Ions have also an important role in the structural integrity of nucleic acids.[24] As visible in Figure 1.2.C., K^+ is taking part to the formation of G-quadruplexes. The strand of DNA is negatively charged owing to the phosphate groups (Figure 1.4.C). Without counterions such as Na^+, K^+ and Mg^{2+}, the double helix would not survive in this conformation.

The interactions presented in this section are particularly sensitive to their environment (ionic strength, pH, cation/anion concentrations, *etc*). As discussed in a following section, folding is able to create some solvent-excluded zones. Interactions comprised inside these zones or, in opposition, exposed to solvent differ largely as electrostatics is strongly attenuated in aqueous compared to apolar solvent or no-solvent environments.

1.1.1.4 π-Stacking

π-Stacking, commonly termed even if probably not appropriate[25], refers to the interactions between stacked aromatic rings. Since aromatic rings contain π-bonds, they have π-electron density on each face. This π-electron density creates a quadrupole moment with partial negative charge above and below the ring and partial positive charge in and around the ring as illustrated in Figure 1.5 (top left).[26] Quadrupole/quadrupole repulsive interactions destabilize the sandwich configuration but favour the edge-to-face and parallel-displaced stacking as predicted by Hunter and Sanders.[27] The situation is opposite for aromatic rings bearing strong electron-withdrawing atoms.

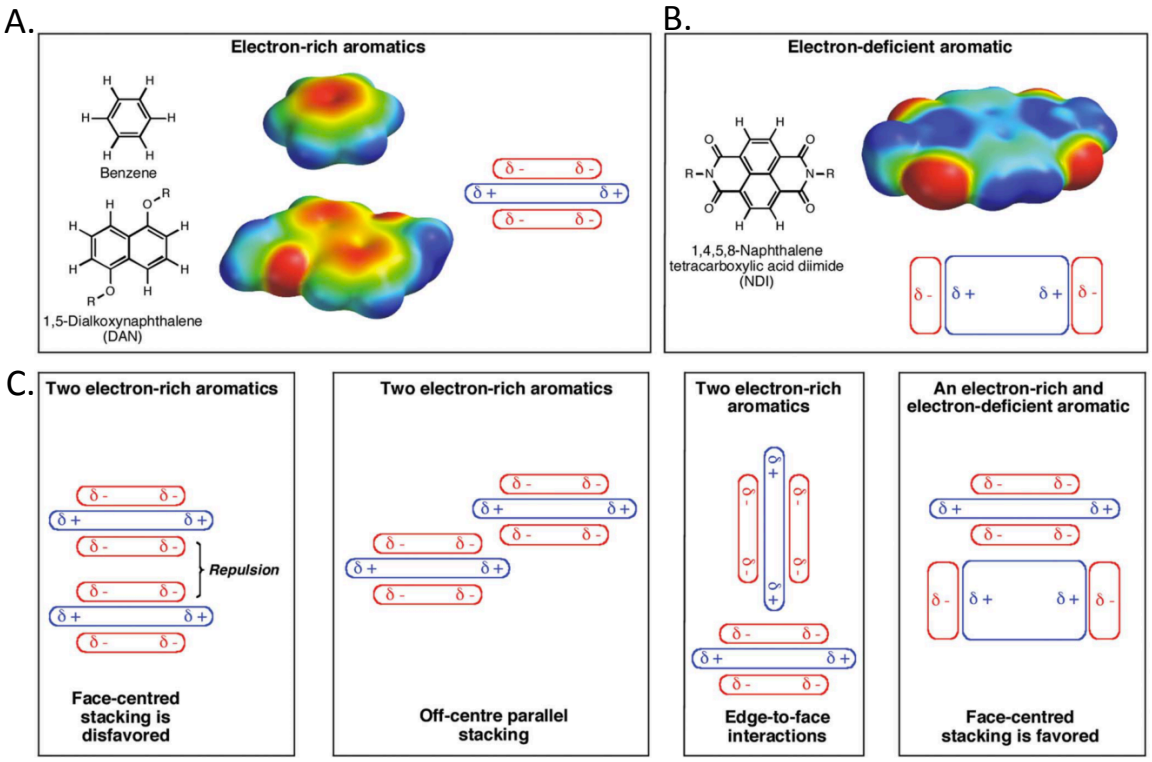

Figure 1.5 Illustrations of quadrupole moments and electrostatic potential surfaces of the π-electron density of aromatic rings with (A) electron-donating atoms and with (B) electron-withdrawing atoms. (C) "Stacked" configurations: left, the sandwich configuration is disfavoured because of repulsive interaction. The 3 configurations at the right are stabilized "stacking" configurations. Reproduced from reference 25.

The distance between 2 parallel-displaced benzene rings is 3.4 Å and this corresponds to the sum of twice the van der Waals radius of carbon; it is thus limited by short-range repulsion. Huber *et al*[28] show that the centroid-centroid distance varies from 3.6 to 3.9 Å within heterocycle-benzene in parallel-displaced configuration. According to calculations of the same authors, the energies of interaction are around 3-5 kcal.mol^{-1}. Some heterocycles interact more favourably with the benzene ring than the benzene with itself (Figure 1.6.B). They also observed that an unfavourable configuration between benzene-benzene costs up to 2 kcal.mol^{-1} (Figure 1.6.A left) and that *N*-heterocycles tend to rotate in order to remote the nitrogen atom as far as possible from the ring centre of benzene (Figure 1.6.B right).

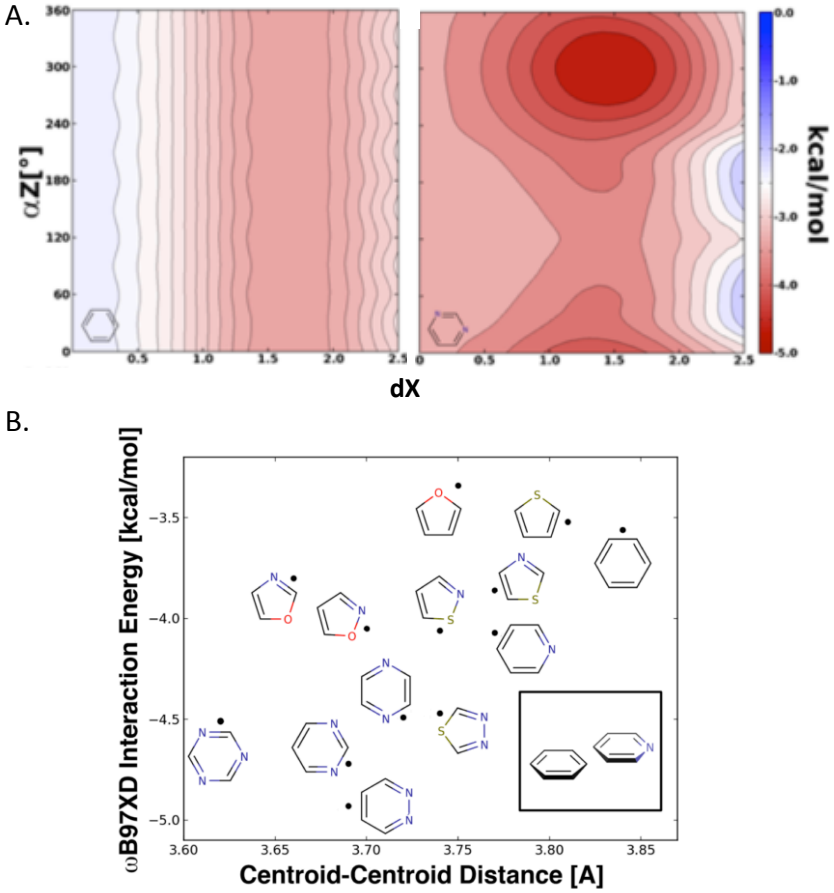

Figure 1.6 (A) Potential energy surfaces for parallel-displaced geometries of benzene-benzene (left), and pyrimidine-benzene (right). Lateral displacement is denoted by dX, rotation angle by αZ. (B) Interaction energies at the parallel-displaced minimum: The x-axis corresponds to the centroid distance at the energy minimum. Reproduced from reference 28.

Unexpectedly, stabilization in B-DNA results more significantly from the nucleobases stacking than from their H-bonds.[29] Besides, stacked nucleobases are not perfectly perpendicular to the helical axis. Thus the distance between two nucleobases along the axis is slightly less than 3.4 Å.

1.1.1.5 Solvent contribution

In solution, the molecules are directly interacting with the solvent. The surfaces of the molecules are fully coated with solvent molecules.[30] Thus the nature and the area of the surface of both the solute and the solvent play a crucial role in the folding. Indeed, organic solvents are known to usually denature the protein structures, or to keep the structure intact but to perturb the dynamic properties of the proteins.[31] In addition, hydrophobic/solvophobic interactions have also demonstrated their major contribution in the initiating step of folding of proteins.[32] Another example arises from the oxygen atoms of PEG which undergo H-bonds with water molecules, yielding a helical conformation in aqueous solutions[33,34], while PEG exhibits a coil conformation in organic solvents.

According to Hunter *et al.* solvent effects should be analysed as a competition between solute-solute, solvent-solvent and solute-solvent interactions[17,35] (Figure 1.7.A). Depending on the H-bond donor and acceptor (β_s) properties of the solvent (α_s and β_s respectively) and those of the interacting chemical groups (solute) in the folded molecule (α and β respectively), the intramolecular interactions between chemical groups in the folded structures are favourable or unfavourable in solution leading to the conservation or the unfolding of the folded structure respectively. Figure 1.7 B indicates the (un)favouring conditions to (un)promote intramolecular interactions within the folded molecule. Values of α_s, β_s, α and β can be found in the article of C.A. Hunter.[17]

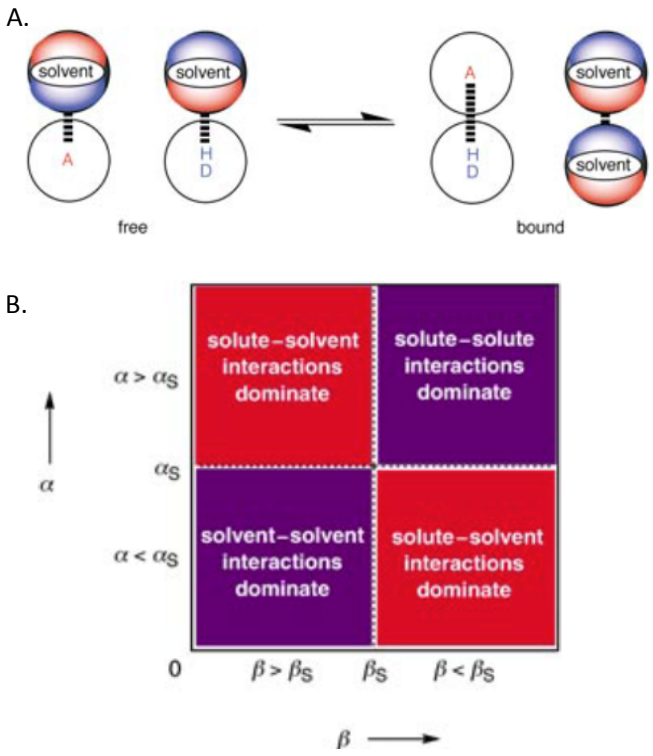

Figure 1.7 (A) Schematic representation of the competition of intermolecular interactions between solute-solvent in the free (unfolded) state with solute-solute and solvent-solvent interactions in the bound (folded) state. (B) Generalized plot of α and β (H-bond donor and H-bond acceptor constants for the solute molecules) and according to α_s and β_s (the H-bond donor and H-bond acceptor constants for the solvent) to assess more favourable intermolecular interactions (purple quadrants) or more favourable intramolecular solvent-solute interactions (red quadrants). Being in the bottom left quadrant would cause solvophobic interactions. Reproduced from reference 17.

For example, α-helices tend to bend in order to maximize the exposure of the carbonyl groups. They are good hydrogen-bond acceptors and favourably form H-bonds with water.

In biomacromolecules, it is not an easy task to evaluate the sum of all chemical interactions. Some simplifications are necessary and often the solvophobic effect can efficiently count the major effect of the solvent for the folded state. Solvophobic interactions define a local organization of the molecule chain in order to minimized unfavourable contact with the solvent molecules. As shown in Figure 1.8.A, insertion of a solute in a network of solvent molecules interacting more strongly with each other than with the inserted solute is energetically unfavourable. It disrupts the network and yields to destabilized interactions.

Therefore, non-polar molecular parts of a complex molecule (*e.g.* a protein) form a cage to bury hydrophobic side chains. This local organization creates a zone where the solvent is excluded. The interactions buried in this zone are further reinforced, as they are not submitted to the dielectric constant of water anymore, which has a dampening effect.

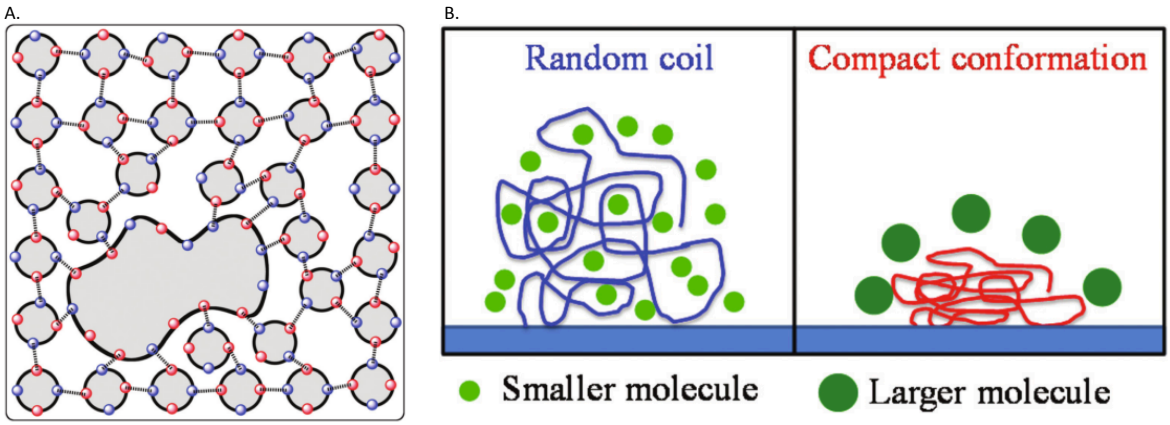

Figure 1.8 (A) Representation of the insertion of a solute in a solvent and the solute-solute and solvent-solute competitive interactions. If the solvent –solute interactions are weaker than solvent–solvent and solute–solute, the solute rearranges to minimized the surface contact with the solvent and forms a cage[30] (B) Illustrations of the excluded volume effect on the conformation of a polymer (blue and red) in small size- (light green) and large size- (dark green) molecule solvent.[34] Adapted from references 30,34.

Cui *et al*[34], demonstrated that the size of the solvent can be linked to different conformations as well (Figure 1.8.B.). They observed that PEG chains exhibit a more compact conformation in larger-molecule solvents.

1.1.2 Cooperativity

Cooperativity is not a kind of weak non-covalent interaction but is the process involving collective weak interactions acting together to synergistically reinforce each other along the folding.

As illustrated in Figure 1.9, cooperativity is achieved when the subsequent interaction formation is easier than the preceding one. For the non-cooperative folding (Figure 1.9.A top), the enthalpy (ε) and entropy (ω) changes remain the same for each step. In the cooperative folding (Figure 1.9.A bottom), the first interaction requires higher entropic cost (3ω) than the following interaction (ω) for an equivalent enthalpy gain (ε); *i.e.* the gain in energy along the folding propagation is increasing.

In the context of synthetic cooperative folding systems, Hill *et al* propose that cooperative systems should be only considered if the non-covalent interactions involved in the folding arise from non adjacent units.[36]

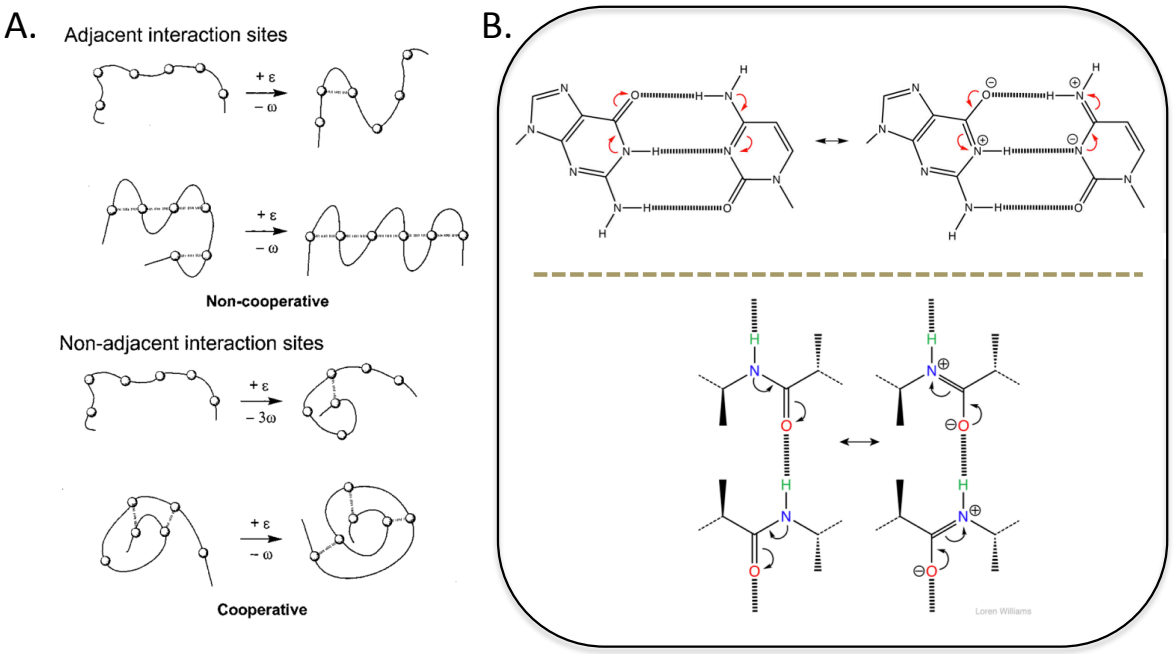

Figure 1.9 (A) Folding mechanism implicating no cooperativity (top) or promoted by cooperativity (bottom). ε and ω designate enthalpy and entropy changes respectively.[36] (B) Cooperativity occurrences in nucleobases pairing and proteins. Resonance strengthens H-bonds in G-C pairing and in antiparallel β-sheets. (Schematics made by Prof. Loren Williams, ww2.chemistry.gatech.edu).

Cooperativity is important in biological processes. It allows achieving uniqueness for folded structure as well as to undergo valuable conformation transitions. *"The folding of small proteins has been assumed to be an all-or-none process that involves high cooperativity within the structure*"[37]. Resonance is a benchmark of cooperativity by stabilizing H-bonds in nucleobases pairing and secondary structures of proteins (Figure 1.9.B).

1.2 "The art of building small"

1.2.1 Chemist's journey into the synthetic molecular world: achievements and limitations

As entitled by Nobel Laureate Ben Feringa the "Art of Building small" is a discipline in which many chemists endeavour to synthetically create functional and well-defined supramolecular conformations. Nature has been a great source of inspiration. However, motivated by different reasons, chemists have been also trying to create unprecedented molecular structures. Some of them assume that the mastery of nature would never be attainable, so they seek new tracks to achieve functional molecules and others think that the unlimited variety of synthetic building blocks, compared to the restricted limited set for *e.g.* proteins (21 amino acids) or for DNA/RNA (5 nucleobases), could surpass the existing molecular structures with structures having no natural counterpart leading to emergent properties.

The journey of supramolecular and synthetic folding chemistry started in the 1960's with the development of crown ethers by Charles J. Pedersen. It immensely burgeoned in the early 1980's, with the breakthrough of "host-guest" complexes. It continued with the development of mechanical interlocked systems, which ultimately paved the way to molecular machines.[38] In the 1990's, more sophisticated inter- and intra- self-assembled molecular systems arose, including foldamers and complex molecular systems with functionalities such as sensor or controlled motions.[39] Since these advancements, many systems have further evolved and have become increasingly impressive, with many more synthetic well-defined supra-molecular conformations flourishing in laboratories.

The tremendous advancements in this field have been acknowledged twice with the highest scientific honours, the Nobel Prize in Chemistry. In 1987, Charles J. Pedersen, Donald J. Cram, and Jean-Marie Lehn received the award for their fundamental research in organic chemistry as founders of “supramolecular chemistry” and recently in 2016, Jean-Pierre Sauvage, Sir Fraser Stoddart and Ben Feringa were recognized as Pioneers in the field of artificial nanomachines.

This research has been particularly driven by curiosity and the fascination of the beauty of the natural molecular world, to understand and to recreate it. Moreover, scientists have been also encouraged by Richard Feynman's lecture "there's plenty of room at the bottom" in 1959 on the large potential of exploring the molecular world to *e.g.* tackle the future storage depletion. Even though much progress has been made since this conference, applications are still in the stage of development in laboratories.

During the Nobel Prize award ceremony in 2016, the Royal Swedish Academy of Sciences greatly described the struggles and the stake at play:

"In terms of development, the molecular motor is at the same stage as the electric motor was in the 1830s, when scientists displayed various spinning cranks and wheels, unaware that they would lead to electric trains, washing machines, fans and food processors".

Building fully synthetic analogues of proteins or biological molecular machines is probably not an unrealistic dream. Nature took millions of years to perfect its machineries while chemists have only had half a century of experience but progress seems already very promising.

1.2.2 Foldamers

The term *foldamers*, coupling the terms *folding* and *polymer*, was firstly defined by Gellman as ‘‘*polymers with a strong tendency to adopt a specific compact conformation*’’[40] and then revised by Moore as ‘‘*oligomers that fold into a conformationally ordered state in solution, the structures of which are stabilized by a collection of noncovalent interactions between nonadjacent monomer units*’’[36] and finally simplified by Huc and Hecht as "*artificial folded molecular architectures*".[39] However, the term foldamer arose to institute and target synthetic oligomers made of non-natural monomers and exhibiting folded molecular architecture inspired by the biomolecules whilst artificial reproductions of biomolecules, using natural monomers, were already developed. Foldamers are designed from human-ingenuity of interplay of covalent and non-covalent chemistry (Figure 1.10).

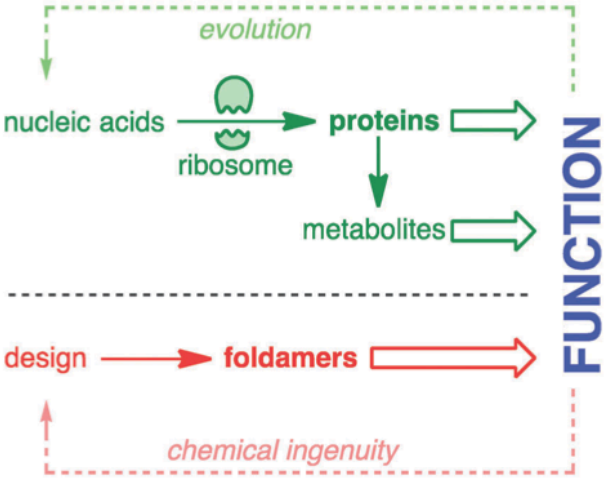

Figure 1.10 Natural and Man-made chemical functions. In nature the ribosome leads the assembly of amino acids from a nucleic acids sequence. For Man-made functional molecular machines, chemists have to design and predict molecular structures of secondary building blocks (*e.g.* foldamers) and of their subsequent supramolecular assembly. Reproduced from reference 41.

Compared to the building blocks used by nature (20 amino acids and 5 nucleobases), chemists have access to an unlimited set of building blocks and combinations.

"*Therefore, realization of the potential of folding polymers may be limited more by the human imagination than by physical barriers.*"[40]

Nowadays, chemists can mimic all the secondary structures occurring in nature (single strand helices, sheets, multi-helices, like DNA)[39,42–44] and even beyond, such as helices with varying diameter along the sequence[45], helices with inversion centers[46], or herringbone helices[47] (Figure 1.11).

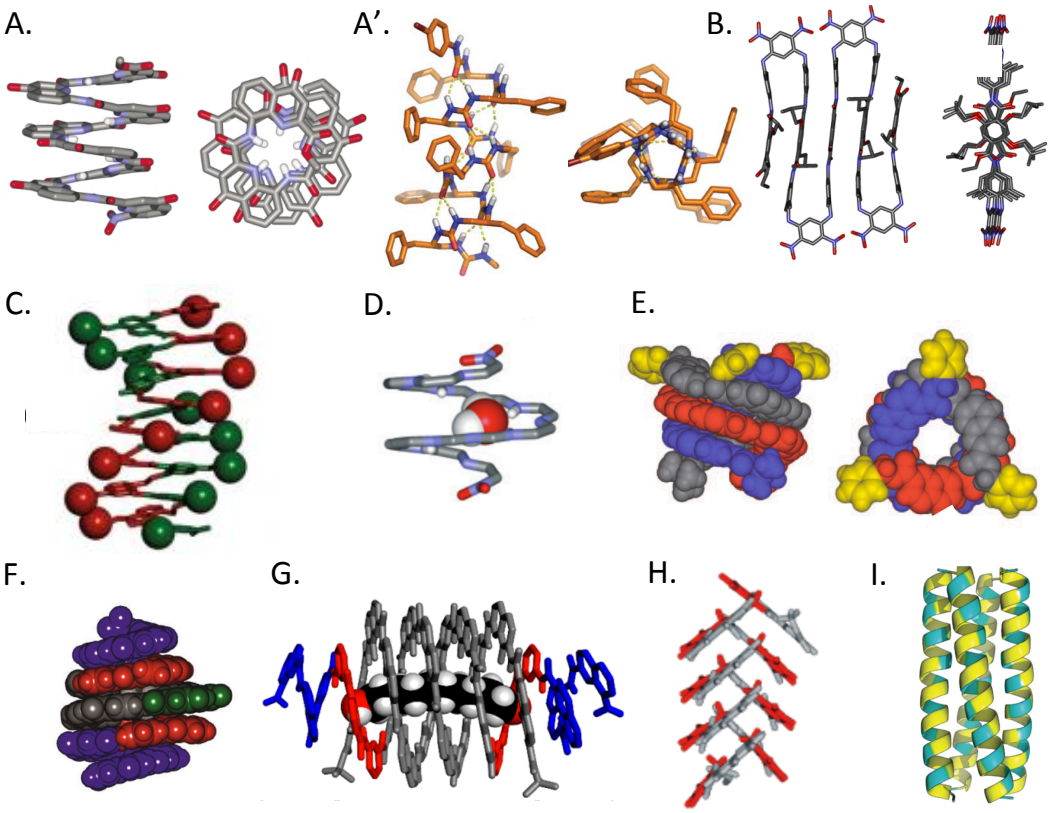

Figure 1.11 Synthetic folded molecules mimicking natural molecules: (A & A') helix[48,49], (B) sheet[50], (C) B-DNA[43], (D) capsule 'host-guest'[51]. (E) triple helix[52]. Synthetic molecules with any natural analogues: (F) Helix/Capsule with varying diameter along the sequence[53],(G) Tube-capsule complex[54], (H) Herringbone helix[47], (I) helix bundle[55]. Reproduced from references 43,47–55.

The main motivation and endeavour behind developing the foldamer chemistry comes from the possibility of being able to design predictable and well-defined folded structures. They lead towards fulfilling the challenge of the bottom-up molecular machinery design approach, where more complex and functional molecular systems can match and rival the chemical functions found in nature, without being based on miniaturized macroscopic machine designs.

To fulfil the challenge of controlling and create functional molecular systems, chemists have been exploring different interactions and factors (see previous section 1.1) which favour and entail molecule folding. These interactions can be denoted as folding factors. The folding factors which are currently the main focus in foldamer chemistry are (i) local rotational restrictions, (ii) specifically-designed interactions between sites which are remote in the sequence, (iii) solvophobic effects and assembly/hybridization with a high pre-eminence of the first one, as suggested by Huc and Hecht.[39] Indeed, to date, the most efficient way of achieving well-defined conformations is based on introducing backbone rigidity through local conformational preferences or on reducing the number of possible conformations of unfolded states.

To create novel folded structures with emergent properties, new folding rules have been also developed and are regrouped in the so-called 'abiotic' foldamers, in opposition to 'biotic' foldamers, which fold with the same folding rules as in natural polymers.

1.2.2.1 Aromatic oligoamide foldamers

For synthesizing functional molecular structures, the key elements to success lie in the ability of making well-defined folded structures obtained with high degrees of predictability and ease of synthesis.[39,40,53] These objectives can be attained for example using aromatic oligoamides. Their impressive potential in building abiotic foldamers is highlighted by their higher stabilities and their high modularity and tunablility.[56] This allows creating many different secondary structures or capsules,[54] with an ease of design and synthesis. Therefore this kind of foldamer is studied in this thesis.

The origin of the performances of aromatic oligoamides as foldamer is presumably stemming from the rigidity of the aryl-amide backbone. The rigidity both limits the entropic cost of the desired folded structure and allows positioning interacting groups in specifically anticipated relevant position in the sequence to favour a folded conformation. The coupling of aryl units through amide bonds constitutes π-conjugated systems, which are connected by single bonds (aryl–NHCO linkage & aryl–CONH linkage;). This results in adjacent units being almost coplanar due to the π-orbitals overlapping stabilization. To keep this planar stabilization, only a 180° rotation of a single bond would be acceptable. At this state, it is eventually easy to add asymmetrically some substituents on the aryls to degenerate the conformers and prefer the *syn* or *anti* conformations as illustrated in Figure 1.12. It is worth noting that the contribution of repulsive interactions (arrows) is probably as important as the attractive interactions of H-bonds (dashed lines), for example.

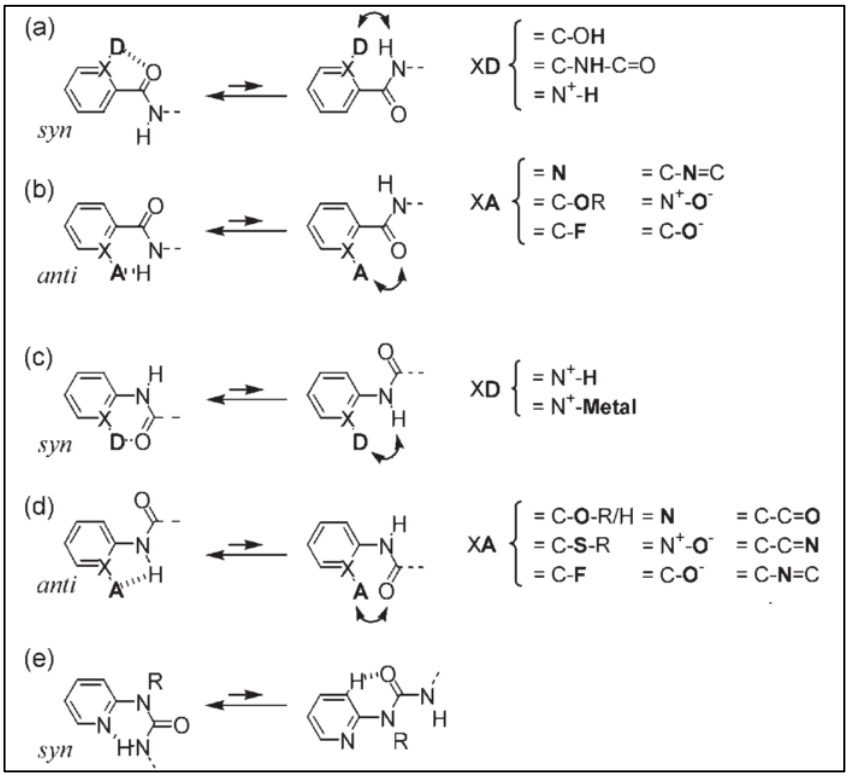

Figure 1.12 *Syn* and *anti* equilibrium of aryl-amide rotamers. Preferred stabilization of one conformation through local attractive (dashed lines) and repulsive (double headed arrows) interactions from H-bond donors "X-D" and acceptors "X-A". (a)–(b) aryl–CONH linkages; (c)–(e) aryl–NHCO linkages. Reproduced from reference 39.

The aromatic oligoamide foldamers belong to the group of *abiotic* foldamers owing to their folding rules, which differ from those in biotic aliphatic foldamers. Their resulting folded structures is attributed to

- Planar nature of the units, the linkages and the relative positions of the amine and acid substituents in the unit
- Conjugation or pseudo-conjugation between sp^2 conjugated systems: consecutive planar groups prefer to be coplanar
- Intramolecular electrostatic interaction (perpendicular to the helix axis)
- Steric hindrance
- π- π Stacking

The understanding of these interactions and the combination of several aryl-amide units offer a plethora of potential 3D structures. Some structures may be simple, like helices, crescent shapes, macrocycles, with major bending propensity (Figure 1.13(right)), single strands, sheets or ribbons with major linear orientation (Figure 1.13 (left)) whereas they may be as sophisticate as for example, capsules, helix bundles, helix-sheet-helix assemblies, enzymes active mimicry.[54,57–59]

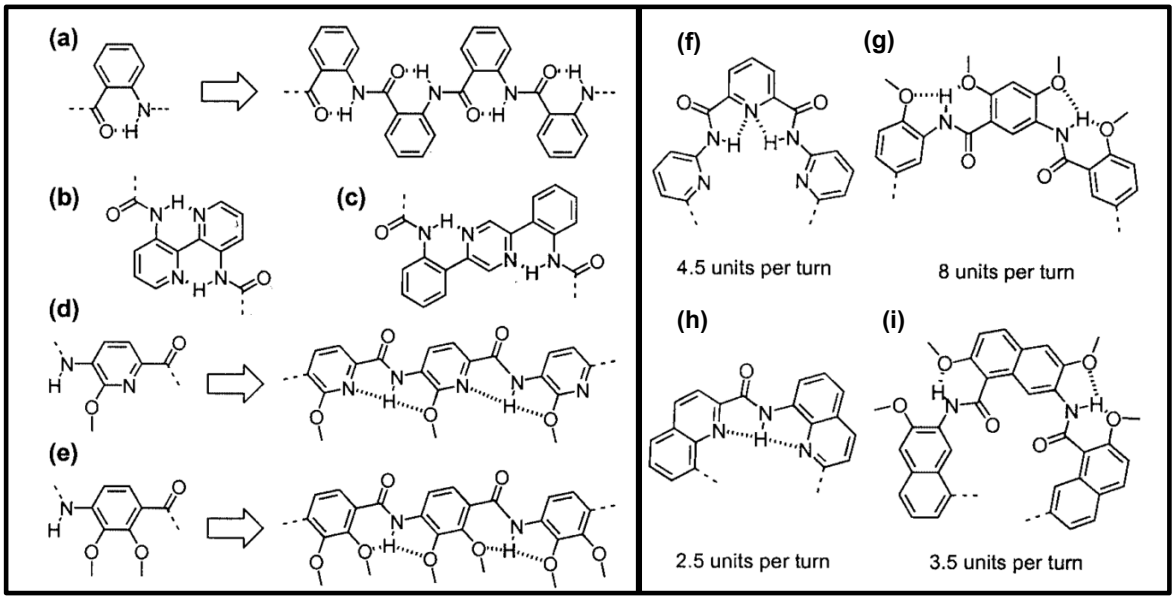

Figure 1.13 (Left) Examples of aromatic oligoamides adopting linear conformations (dashed lines display attractive interactions).[56] (Right) Examples of aromatic oligoamides adopting bended conformations. Reproduced from reference 56.

1.2.2.2 Helical Aromatic oligoamides

To date, the helix is by far the most studied architecture, in a single stranded state[42] or supramolecular assemblies[60]. Helical structures are ubiquitous in nature and are inherently chiral, rendering it very intriguing. Nature uses helices at the macromolecular (*e.g.* alpha-helix) and supramolecular (*e.g.* coiled-coil helix bundle) levels to carry out inspiring vital functions and to control its machineries, such as recognition, catalysis, ion transport, genetic information storage, and tissue strengths. Besides, its inherent chirality is attractive for optical properties.

In aromatic oligoamides, helical conformations are created by the succession of units in a curved/crescent local conformation preference, owing to mainly electrostatic interactions and the orientation of the amine and acid substituents. Until a given number of units, the short oligomer is bent and planar. As units are added, a deviation from planarity is forced by steric hindrance between the overlapping units, giving rise to the pilling up of remote units and eventually to the 3-D helical conformation. Each aryl-amide bond encounters a slight rotation of the torsional angle. Worth noting, independently of the nature of the aromatic unit, the pitch is always, except rare exceptions,[52] identical and corresponds to the minimum acceptable distance between two aromatic rings (3.4 Å).[39] Therefore, the more units are comprised in a turn, the smaller is the torsion, because the same global angle is distributed over more rotatable bonds.

Given the variety of aromatic compounds (Figure 1.14), it is possible to tune *inter alia* the diameter of the helix and the number of units per turn. The modification of these parameters opens the door to many different functions and applications. For example, it has been shown that helices with a large diameter can be used as a ion-channel, for recognition[61–64], catalysis[65] or they can extend like a spring and hybridize together[52,66].

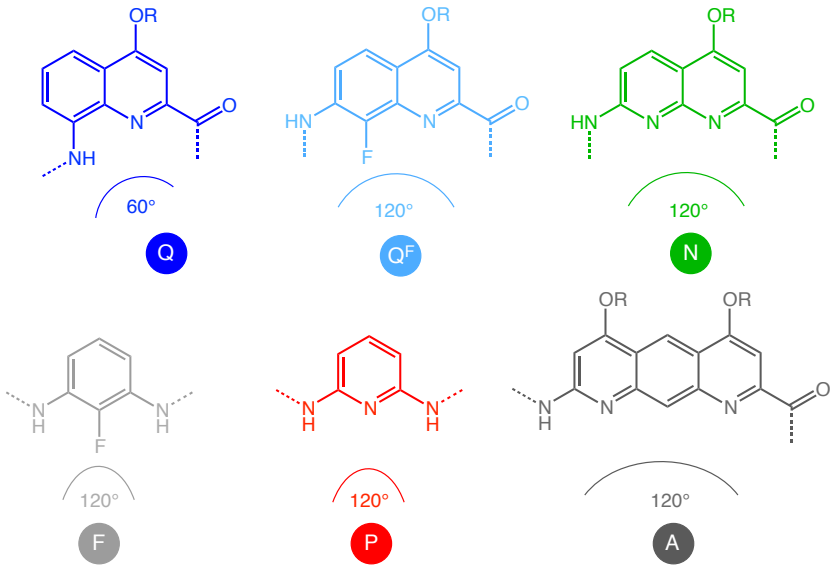

Figure 1.14 Chemical structures of some units used in aromatic oligoamide foldamers: Q (8-amino-2-quinolinecarboxylic acid), Q^F (7-amino-8-fluoro-2-quinolinecarboxylic acid), N (7-amino-8-naphtyridinecarboxylic acid), F (2,6-fluorobenzene-diamine), P (2,6-pyridine-diamine), A (1,8-diazaanthracene). The lateral chain R can be replaced by hydrophobic or hydrophilic chemical function to change the solubility.

There are 3 parameters for varying the helix diameter.

(1) The relative position of amine and acid substituents within the unit. In order to illustrate the impact of the relative positions of the amine and acid substituents, we can focus on a foldamer constituted by Q or Q^F units. In the Q unit foldamer, the angle between the amine and the acid functions, as represented in Figure 1.14, is 60°. This gives rise to highly curved helices. On the other hand in the Q^F unit foldamer, a 120° angle makes a wider helix. Besides, as shown in Figure 1.13 (right, *i.e.* (f) vs. (h)), molecules with smaller angle formed by the amine and acid substituents have fewer units per turn.

(2) The size of the unit. Larger units induce larger diameters but do not influence the numbers of units per turn.

(3) The hydrogen bonding location. Usually H-bonds formed in the inner rim pinch the curvature of the helix, while outer rim H-bonds tend to straighten the turns (in Figure 1.12 (right, *i.e.* (a) vs. (b))[56]. Additionally inner H-bonds reinforce the curvature. By consequence, an angle of 60° between the amine and the acid functions does not lead to three units per turn but to only 2.5 units per turn (Figure 1.13 (h)).

1.3 Tools to characterize folded structures

Nowadays, a full arsenal of techniques exists and helps scientists to characterize molecules and properties in the field of foldamer chemistry. Each technique has its advantages and limitations. The most crucial factor for this field and for determining dynamical properties is the ability to characterize bulk behaviours or single-molecule behaviours.

Ensemble techniques, such as Nuclear Magnetic Resonance spectroscopy (NMR), UV-Visible spectroscopy (UV-Vis), Infra-red spectroscopy (IR), circular dichroism (CD), mass spectroscopy (MS) and X-rays crystallography, are really powerful characterization techniques commonly used in chemistry specifically for studying chemical structures. However, these tools present the important limitation of averaging time-dependent motions in the structures over all existing molecular conformations. This limitation originates from random thermal fluctuations causing unsynchronized activities of the molecules over time. With the development of these tools and subterfuges, synchronization can nowadays be induced but only during very limited period of time. Nevertheless, many processes, such as protein folding, exceed these timescales. Therefore, ensemble techniques tend to smear out the dynamics and fluctuations of conformational transitions and, in addition miss rare events. These inherent limitations can either challenge the characterization or misguide the molecular description.

In order to overcome these limitations, complementary single-molecule approaches have been developed. They enable us to follow time-dependent behaviours of individual molecules and to distinguish subpopulations. The greatest challenge of those approaches is the magnitude of the signal, as it can be considered as proportional to the number of probed molecule. It is consequently time-consuming to explore individual molecules, as repetition is required for obtaining a statistically significant data analysis.

1.3.1 Ensemble techniques

NMR spectroscopy is routinely used for the characterization of foldamers. ^{1}H NMR provides chemical shifts of protons, ubiquitous atom in organic molecules. The chemical shift is associated to the resonant frequency and relates to the local magnetic field around the nucleus (^{1}H). This field is affected by electron shielding and thus by chemical function and the chemical environment such as aromatic ring current and bond strain. As a result, the chemical shift provides information on the environment of each distinguishable proton.

In Figure 1.15.A. ^{1}H NMR spectra of helical foldamers of 2 to 16 identical residues are represented. Although all residues are identical, the chemical shift of a given proton is spread and all signals are up-fielded upon the addition of residues. This highlights the influence of the helical environment (ring current, stacking or/and increase helical stability effects). 2D NMR techniques are also commonly used and help investigating the three-dimensional structure organizations and identifying exchange of conformations. The 2D-ROESY experiment of Figure 1.15.B. confirmed the exchange of the H_5 and H_3 of the macrocycle and thus proves the co-existence of two conformers. In 2D NMR, the

excitations of two different nuclei, *e.g.* bound ^{1}H and ^{13}C atoms, can be coupled for helping the atom identification.

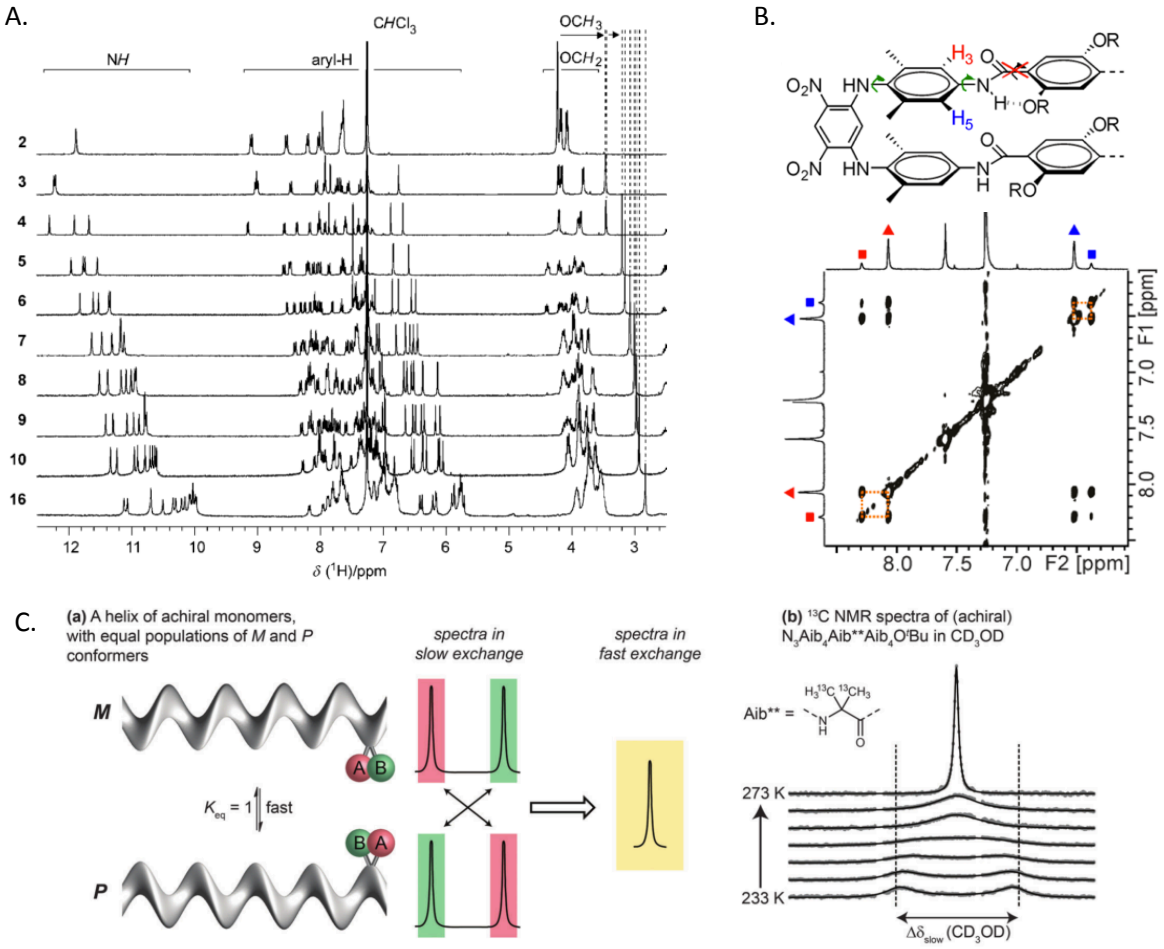

Figure 1.15 (A) ^{1}H NMR spectra of quinoline-based foldamer of increasing length. The number of quinoline units comprised in the foldamer is annotated at the left of each spectrum [67](B) Excerpt of the 2D ROESY plot (τm = 300 ms) taken at 223 K showing the chemical exchange between protons of the two conformers of macrocycle above.[50] (C) Detection of helical handedness preference by NMR in the fast exchange regime. Coalescence between signals in an equally populated pair of enantiomeric conformers[41]. Adapted from references 41,50,67.

When the investigated process is slow compared to the NMR timescale, dynamical information can be extracted[41]. As shown in Figure 1.15.C. at low temperature, the inversion of the handedness of the helix is slow compared to the NMR measurement timescale. This hence allows the observation of one peak for each conformer. On the contrary, when the inversion is fast compared to the NMR timescale (typically rates of 0.1–1x 10^{3} Hz) only one coalesced signal is visible.

X-ray Crystallography is another characterization technique often used for establishing the structures of foldamers. The asset of this technique comes from the precise and detailed structural information. The drawback is that this information reveals a solid-state structure which may differ from the solution conformation.

UV/Vis spectroscopy is especially valuable for aromatic-rich foldamers. The π-stacking of the aromatic functional groups tends to induce bathochromic shifts of the UV-Vis absorption and thus can evidence the folding and the influence of the number of monomer units in the foldamer.

Circular dichroism (CD) spectroscopy is used as a powerful tool to estimate the secondary structure of proteins.[68,69] As foldamers are meant to mimic these structures, CD has also been used to characterize them, as long as they are chiral[60].

Mass spectrometry (MS) is also a relevant technique for organic chemists. Besides identifying and validating the composition of molecular systems, MS also provides insights into complexation with guest molecule and allows the identification of the numbers of components in interlocked or self-assembled structures (Figure 1.16.B).[70,71] Hyphenated techniques such as ion mobility spectrometry coupled to mass spectrometry can also be used to investigate the global shape of molecules and thus the conformations of supramolecular structures (Figure 1.16.A).[72,73]

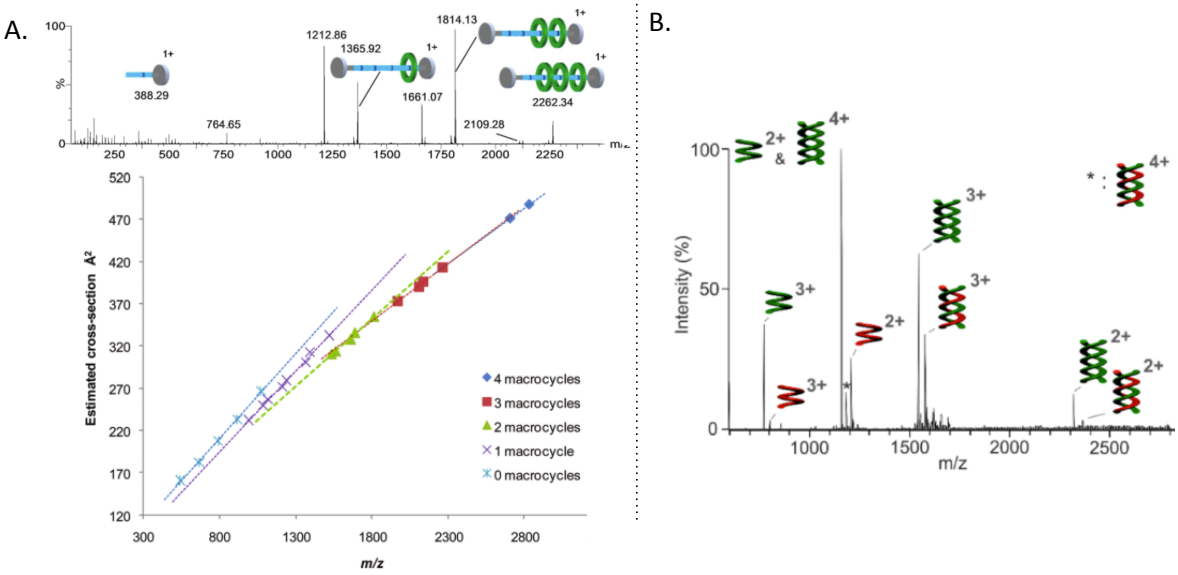

Figure 1.16 (A.top) MS ion spectra of polyrotaxane species made of an axle and containing varying number of rings (macrocycles). (A.bottom) Graph of estimated collision cross sections for polyrotaxane species and fragment ions with different numbers of associated macrocycles.[70] (B) MS ion spectra proving the formation of homoduplexes and heteroduplexes of aromatic oligoamides $Q_3^FQ_6$ (green) and $Q_3^FQ_6$-$COCF_3$ (red).[71] Adapted from references 70,71.

1.3.2 Single-molecule techniques

To overcome the limitation of averaged measurements provided by ensemble techniques and to potentially resolve rare, different and sequential behaviours encountered in molecular subpopulations, three approaches have been developed. They allow following individual molecules: manipulation methods, detection/visualization methods and theoretical calculations[74,75].

In order to investigate the origin of folding and ultimately the chemistry of functional molecular systems, single-molecule force spectroscopy has rapidly emerged since the late 1980s and opened the doors to directly probing molecular mechanochemical properties, intermolecular and intramolecular interactions, conformational transition and thus folding processes[76].

1.3.3 Single-molecule force spectroscopy

Mechanical force has always been recognized to play a fundamental role in biological processes; all motions, for example, operate through mechanical forces.[77]

The description of intermolecular and intramolecular interactions by entropy and enthalpy would hence be useful for understanding their dynamics and stability of the interactions, however the interpretation of experimental values of ΔH and ΔS is extremely ambiguous in complex systems. Direct measurements of forces may tackle these limitations.

In addition, given the growing interest in bottom-up molecular nanotechnologies, investigations of bond strengths, molecular stabilities and mechanical properties from the single-molecule point of view face an ever-increasing demand.

The most common single-molecule force spectroscopy techniques are optical tweezers (OT), magnetic tweezers (MT) and atomic force microscopy (AFM).[78] These techniques, illustrated in the Table 1, are complementary to each other and owing to the technical progress during the past 20 years, the current force and length detection capabilities span 7 (fN to few nN) and 6 (tenth of nm to few μm) orders of magnitude respectively.[78] The following table compares the capabilities, limitations and layouts of these three techniques.

The following of this chapter focuses on atomic force microscopy (AFM)-base single-molecule force spectroscopy. The performances of the technique fit better the requirement for the molecular system studied for this thesis. For readers interested in to OT and MT, we advise to check these articles [78–80] for more detailed information.

Table 1 Comparison of the most commonly used single-molecule force spectroscopy techniques: optical tweezers, magnetic tweezers and atomic force microscopy. Adapted from reference [78].

	Optical Tweezers	(Electro)Magnetic Tweezers	Atomic Force Microscopy
Spatial resolution (nm)	0.1-2	5-10 (2-10)	0.5-1
Temporal resolution (s)	10^{-4}	10^{-1}-10^{-2} (10^{-4})	10^{-3}
Stiffness (pN.nm^{-1})	0.005-1	10^{-3}-10^{-6}(10^{-4})	10-10^{5}
Force range (pN)	0.1-100	10^{-3}-10^{2} (0.01-10^{4})	10-10^{4}
Displacement range (nm)	0.1-10^{5}	5-10^{4} (5-10^{5})	0.5-10^{4}
Probe size (µm)	0.25-5	0.5-5	100-250
Typical applications	3D manipulation Tethered assay Interaction assay	Tethered assay DNA topology (3D manipulation)	High force pulling and interaction assays
Features	Low noise and drift dumbell geometry	Force Clamp Bead rotation Specific interactions	High resolution imaging
Limitations	Photodamage Sample heating Non specific	No manipulation (force hysteresis)	Large high-stiffness probe Large minimal force Non specific
Device	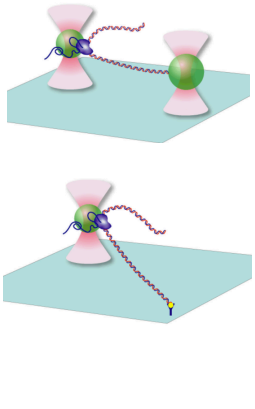	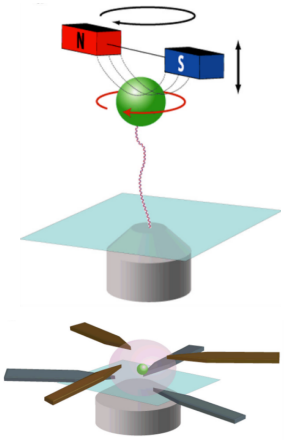	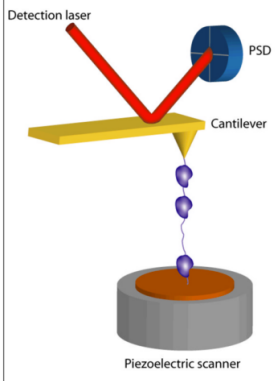

These performances make the full molecular force spectrum accessible, from entropic restoring forces to the rupture of covalent bonds, and allow the manipulation from cells to nucleobases pairing for example.

In Figure 1.17 force and extension scales of hierarchic levels of molecular stretching are represented. Worth noting are the frontiers of accessible mechanical information. Mechanical information can be revealed in the white area of the Figure 1.17. The lower frontier originates from the thermal stability of molecular structures. No mechanical detail corresponding to energies lower than k_BT can be observed. The upper limit is given by the rupture of the covalent bonds.[2,81]

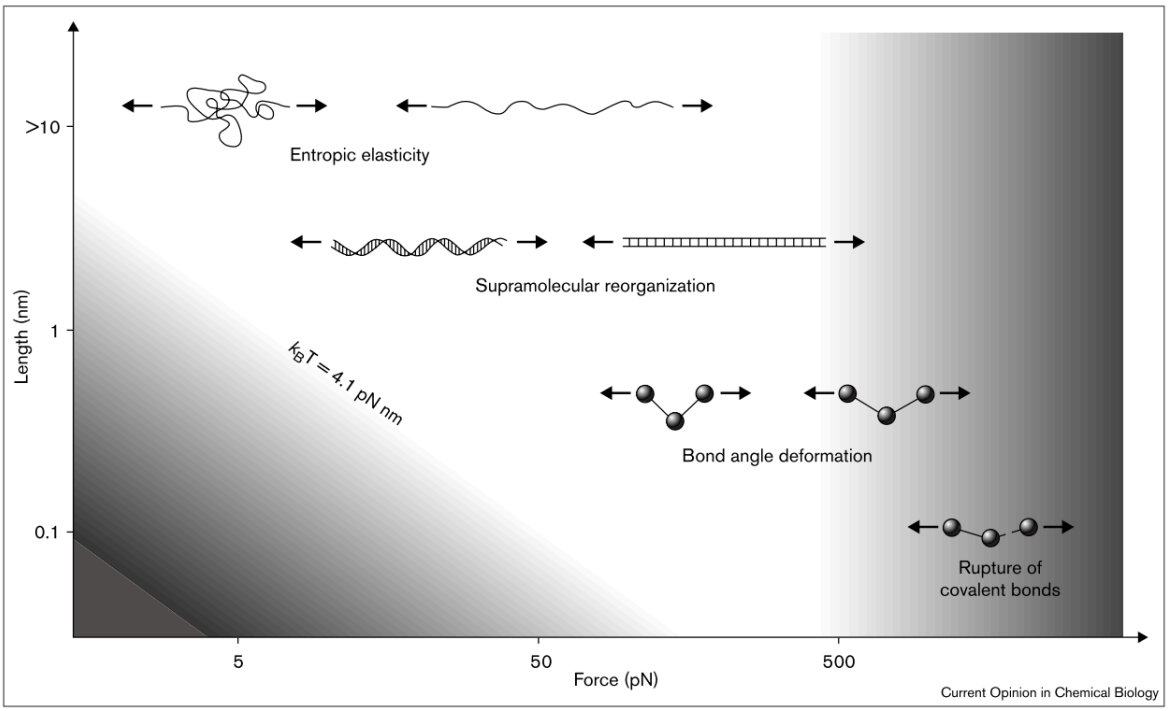

Figure 1.17 The force-scales and associated length-scales corresponding to different intermolecular interactions and bonds. The accessible and inaccessible regions by SMFS are limited to the white and grey area, respectively. Reproduced from reference 81.

1.3.4 AFM-based single-molecule force spectroscopy

In this thesis we used single-molecule force spectroscopy by atomic force microscopy (AFM) because it is the most appropriate technique to investigate synthetic folded molecules since they present rigid structures and thus high forces should be accessible.[82–84]

The AFM was invented in 1986 by Binnig, Quate and Gerber[85] and was inspired by the Scanning Tunnelling Microscope (STM), invented a few years earlier by Binnig and Röhrer.

The basic principle of these microscopies is *« the measurement of the interaction between atoms of a surface and atoms of a probe tip »*. (see Figure 1.18.A)

The first use of the AFM was as a high-resolution imaging tool (Figure 1.18.B). Later on, the AFM was used to probe and manipulate atoms and molecules with a sub-nanometre resolution, a sensibility at the piconewton level and a timescale resolution in the sub-millisecond range.[86]

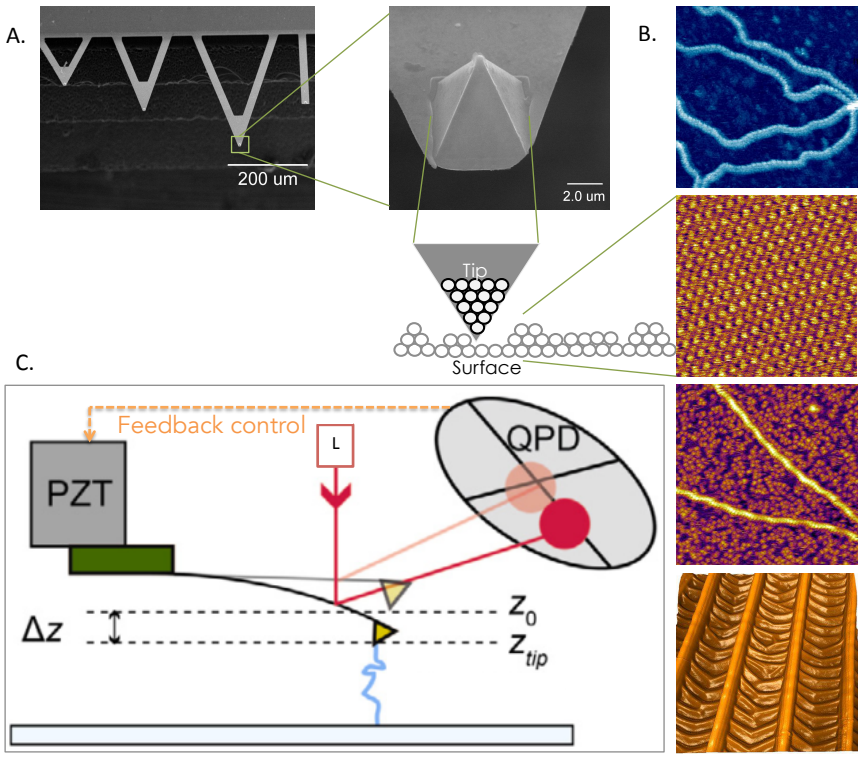

Figure 1.18 Principle of scanning probe microscopies: (A) zoom on AFM cantilevers and on a probe tip, together with a schematic representation of the interaction between the atoms of the tip and the atoms of the surface. (B) Illustrations of AFM imaging from top to bottom: DNA double helix, C8-BTBT thin film, actin filaments and a moth wing (from Asylum Research gallery). (C) Schematics of a AFM-based force spectroscopy experiment (PZT: piezo electric actuator, L, laser, QPD, quadrant photodetector). Adapted from reference 87 and from Asylum Research gallery.

1.3.4.1 Principles of AFM-SMFS experiments

An AFM-SMFS experiment consists in trapping a molecule between the nanoscopic tip of a flexible cantilever and the substrate (Table 1 and Figure 1.18.C) and subsequently pulling on it to observe its resulting stretching profile. This profile is monitored thanks to the deflection of the cantilever, which can be converted into force values.

1.3.4.1.1 AFM-SMFS modes

There are two main modes for performing AFM-SMFS experiments, which differ in the way of pulling: **force-distance and force-clamp mode**.

For both modes, the molecules of interest are typically sparsely grafted or simply deposited on a gold-coated surface, a silicon surface, or on a glass cover slide, *etc.* In some cases, the molecules can also be grafted on the tip, or even on both for molecular recognition or self-assembly experiments. Then, the tip and the substrate are brought in contact and withdrew in approach-retraction cycles. During these cycles, one molecule can adsorb on the tip at any point (steps 1 to 3 in Figure 1.19 and Figure 1.20), then is stretched (steps 4 to 5 in Figure 1.19 and 4 to 10 Figure 1.20) and finally detaches from the tip (step 6 in Figure 1.19 and 8 in Figure 1.20). The experiment can be performed in any liquid environment, aqueous or organic.

Here, the molecular design of the molecule becomes important. Linker molecules, covalently attached to the molecule of interest, are often used to catch the molecule on one extremity with the tip and to promote the full stretching of the molecule of interest.

In the force-distance mode (FD) or also called force-extension (FE) (Figure 1.19**)**, a z-piezo-electric actuator separates the tip from the substrate **at a constant velocity** and induces the stretching, unravelling or unfolding (steps 4 to 5) of the molecule or the detachment of the molecule (step 6), in line with the fundamental principle of SMFS 'the weakest interaction breaks first' and geometrical factors.[88]

Special care should therefore be taken in the experiment design to ensure that the interactions of interest are probed before the detachment of the molecule.

The molecule resisting to the stretching generates a restoring force that provokes the bending of the flexible cantilever until the detachment of the molecule from the tip and the recovery of the equilibrium deflection of the cantilever. The deflection of the cantilever is monitored using a laser beam that is reflected off the back of the cantilever and directed onto a photodetector (Figure 1.18.C). The specific stretching pattern can thus be recorded as a voltage (V) as a function of the piezo-electric displacement (z_0) or the time and then can be converted into force-extension curves (see Figure 1.19 and grey frame for signal transformation).

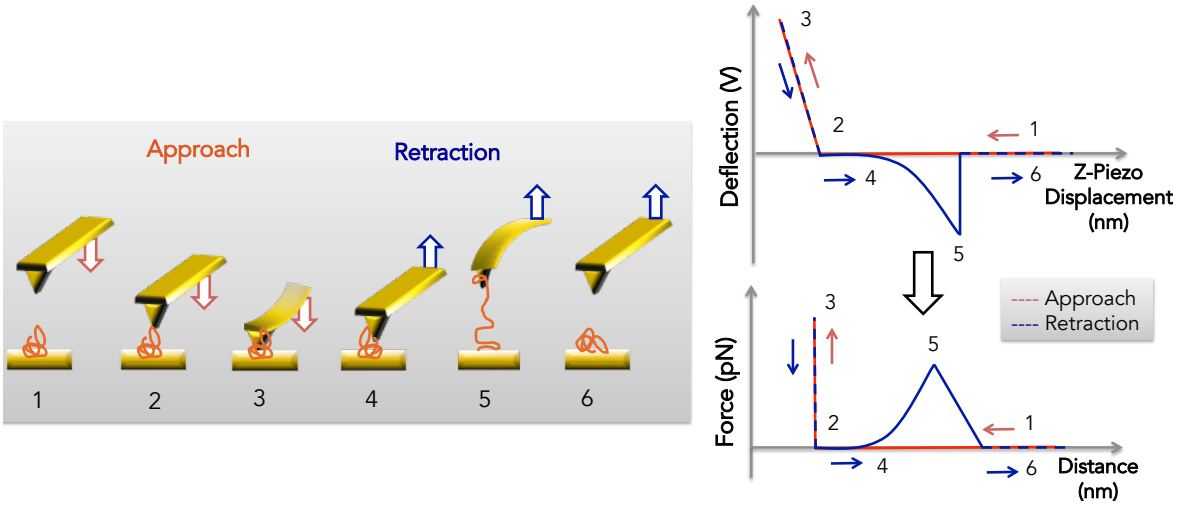

Figure 1.19 Schematic of a single-molecule force spectroscopy experiment in the force-distance mode (left). The corresponding plots of raw measurements (deflection vs. piezo-electric displacement) and the converted force-distance curve (right). Each step of the experiment is numbered and referred to on the measurement plots. The red curves and numbering (1→3) represent the approach of the tip to the surface where a molecule attaches to the tip (3) and the blue curves and numbering (4→6) represent the retraction of the tip from the surface where the molecule detaches from the tip (6) at the end of the experiment.

In the force-clamp mode (FC) (Figure 1.20**)**, the piezo-electric actuator is used to stretch the molecule up to a set force (or voltage) (step 4) and then the piezo-electric displacement **held to maintain this set force constant**, allowing to monitor the unfolding steps/processes at a constant force and over time (step 5 to 8).[89] This set up relies on an electronic feedback loop which controls the position of the cantilever in order to keep the stretching force constant (Figure 1.18. and Figure 1.20).

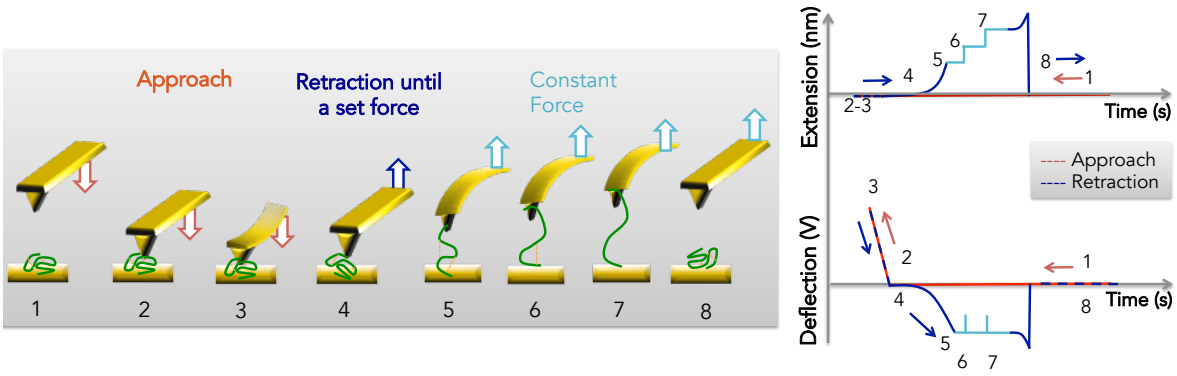

Figure 1.20 Schematic of a single-molecule force spectroscopy experiment in the force-clamp mode (left). The corresponding plots of extension or deflection plotted as a function of time (right). From point 5, the set force is reached and maintained. At 6 and 7, interactions (orange) break and reveal some length, measurable with the extension vs. time trace. On the deflection vs. time trace, immediate adjustments to recovered to set force can be observe at this breakings/openings.

The calibration of the cantilever is a crucial requirement in this technique. To measure the forces accurately, the spring constant (k) of the cantilever, the force transducer, has to be exactly determined. Many techniques have been developed for calibrating; currently, there are three prominent methods, being the thermal-noise method, the Sader method and the Cleveland methods. These methods are based on dynamic deflection theory, where the spring constant is measured from the cantilever's resonance behaviours. For further details, we refer the readers to some papers and reviews.[90–93]

THE SIGNAL TRANSFORMATION PROCEDURE:

In order to describe and interpret the stretching pattern in terms of force and extension, the raw signal is transformed into a force-extension curve using the deflection sensitivity (nm.V^{-1}) and the spring constant of the cantilever (pN.nm^{-1}) (see appendix C for calibration method).

The deflection sensitivity, also called InvOLS for Inverse Optical Lever Sensitivity, is the measurement of the cantilever deflection in nanometres for a given displacement of the laser beam on the photodetector. This value is instrument- (pathway) dependent and is determined along the repulsive contact curve of the tip on a hard surface.

1) The conversion of the laser beam displacement on the photodetector (V) into cantilever deflection *in nanometres* (*d*) is described by eq. 2. It consists in multiplying the laser displacement in volt (V) by its deflection sensitivity (S).

$$d = V \cdot S \qquad \text{Eq. 2}$$

2) The effective tip-sample distance or 'extension' (z) is then calculated using eq. 3, where z_0 is the piezo displacement and *d* is the cantilever deflection obtained using eq. 2.

$$z = z_0 - d \qquad \text{Eq. 3}$$

3) Finally, the force (F) is calculated using Hooke's law (eq. 4) where the cantilever deflection (d) is multiplied by the spring constant of the cantilever (k). The negative sign in the equation transforms the negative cantilever deflection (d) into a positive signal.

$$F = - k \cdot d \qquad \text{Eq. 4}$$

As mentioned in a previous section, AFM-SMFS performances allow probing several ranges of force and thus exposing several levels of "structural deformations and transitions" (Figure 1.17). The following sections are focused on the descriptions of the different intramolecular interactions that can be probed under load.

1.3.4.1.2 Molecular elasticity

Pulling on a molecule that can be assimilated to a semi-flexible polymer in a random coil conformation causes two kinds of restoring forces (Figure 1.17). At low stretching forces, the restoring force originates from the continuous reduction of the number of possible conformations adopted by the molecule. It is often referred to as the **entropic elasticity** of the molecule.[33,82,94] At higher stretching forces, the stretching acts on the molecular backbone which modifies the bonds angles and lengths. This stage is assigned to the **enthalpic elasticity**. Stretching a semi-flexible polymer within its entropic elasticity regime is usually reversible, whereas affecting the enthalpic elasticity may lead to irreversible changes. The behaviour of a random coil molecule stretched by an AFM tip can be described using elasticity models derived from statistical mechanics. Two main models are currently used to describe the entropic elasticity of those systems: the freely jointed chain (FJC)[95–97] and the worm-like chain (WLC)[97–100] models. Both models link the restoring force F of a semi-flexible polymer chain to its end-to-end extension x (corresponding to the tip-surface distance in SMFS force-extension curves) and allow deducing mechanical properties such as the overall length of the unravelled chain (called contour length or L_c in the WLC model) and its flexibility (persistence length or l_p in the WLC model). Some extended versions of those models have been developed to take into account supplementary contributions such as bond and angle deformation and the segment stiffness.[101]

1.3.4.1.3 Rupture of an interaction

Complex structures, including folded structures, supramolecular structures, or self-assemblies deviate from this entropic elastic behaviour as soon as a "structural feature" is submitted to tension. To represent the rupture of an (intra- or intermolecular) interaction during an AFM-SMFS experiment, we can describe the interaction by a single-well potential and the external force as a parabolic potential of a Hookean spring for the cantilever (inset in Figure 1.21). As the z-piezo actuator is retracted away from the surface, the interaction is put under tension and a secondary minimum emerges on the sum of the two potentials. Under increasing load, the energy landscape becomes more and more tilted at larger reaction coordinate and at some point (from the 3rd graph in Figure 1.21), thermal energy overcomes the barrier and induces the rupture transition from the bound state to the unbound state[102–104] (Figure 1.21).

This theory is the key to determine fundamental thermodynamic parameters of intermolecular bonds. Consequently, this implies that force values obtained from SMFS experiments are only valid for a given loading rate.[104–106] Further explanations on this subject will be discussed in chapter 3.

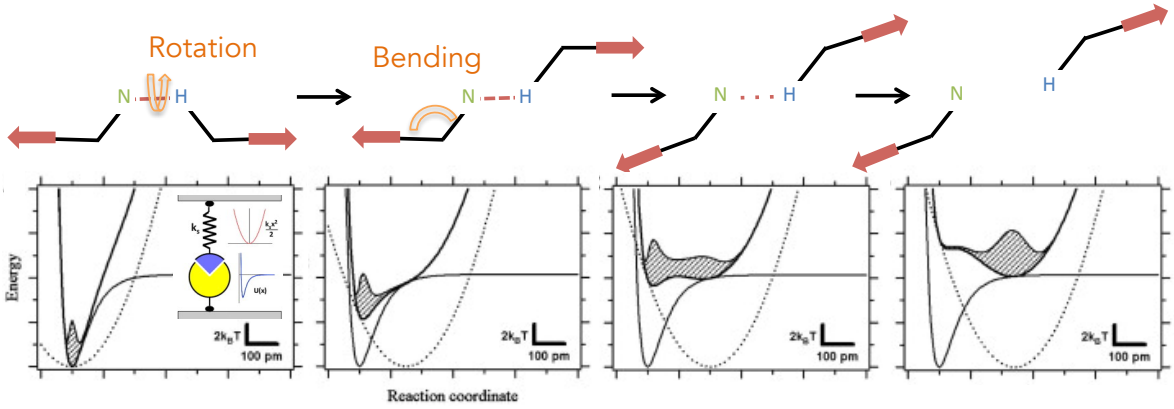

Figure 1.21 The top illustrations represent the corresponding bond deformations stages of the molecule during the SMFS experiment (*i.e.* pulling on molecule with an embedded interaction) (inspired from[15]). The bottom graphs show the corresponding energy potential according to the reaction coordinate (thick solid line), the populated density of states (shading), the bond potential (thin solid line) and the displacement of Hookean spring for the cantilever (dashed line) at the different stages of a single-molecule force spectroscopy experiment. In the first graph, the inset representing the bond, its potential (blue) and Hookean spring potential (red). Adapted from reference 104.

1.3.4.1.4 Hidden length

In the case of an embedded structural feature, the rupture may suddenly leave slack to the effective length of the molecule and releases the tension on the cantilever. This can be compared to a macroscopic untightening of a knot in a string, freeing abruptly a 'hidden length' of string. At this moment on the molecular scale, the force signal abruptly falls until a given further extension at which the molecule exerts again a force on the cantilever. The force-extension curve therefore shows a **peak**. For example, a polyprotein, protein made of several domains, exhibits a so-called **'saw-tooth' pattern**, where each peak corresponds to the unfolding of a domain of this protein (Figure 1.22). The distance between two peaks is denoted as **hidden length.**[88]

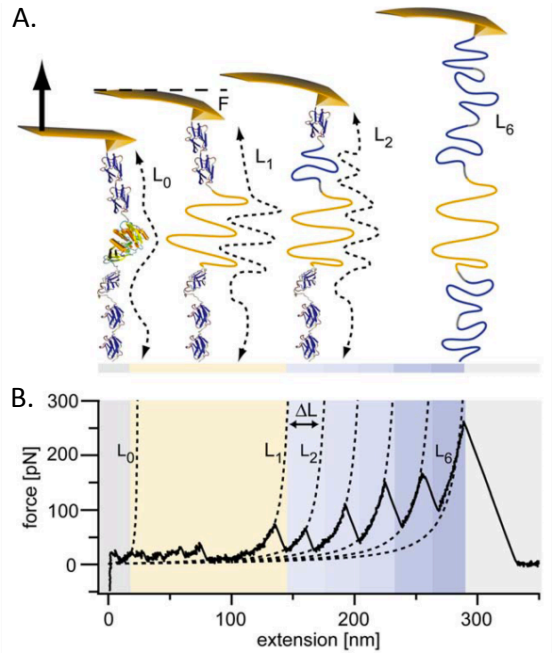

Figure 1.22 (A) Schematic of an AFM-SMFS experiment on a polyprotein (titin kinase flanked by Ig/Fn domains), which exhibits stepwise unfolding events of domains and (B) the corresponding force-extension curve. The dashed lines are WLC fits; they measure the contour length L_c after each domain unfolding. ΔL_c between 2 peaks reveal the contour length of the previously unfolded domain. Adapted from reference 107.

This hidden length is essential to understand the unfolding mechanism and properties of the molecular systems. Firstly, it indicates the unconstrained length of each unfolding event (see ΔL_c in Figure 1.22.B). Secondly, it sheds light on the mechanical strength of some structural features. Indeed, a large amount of energy may be required to stretch this hidden length. Therefore, it can be interpreted as a molecular mechanism which prevents subsequent unfolding events and toughens the structure. The bond which liberates such a hidden length is called the 'sacrificial bond' (Figure 1.23).

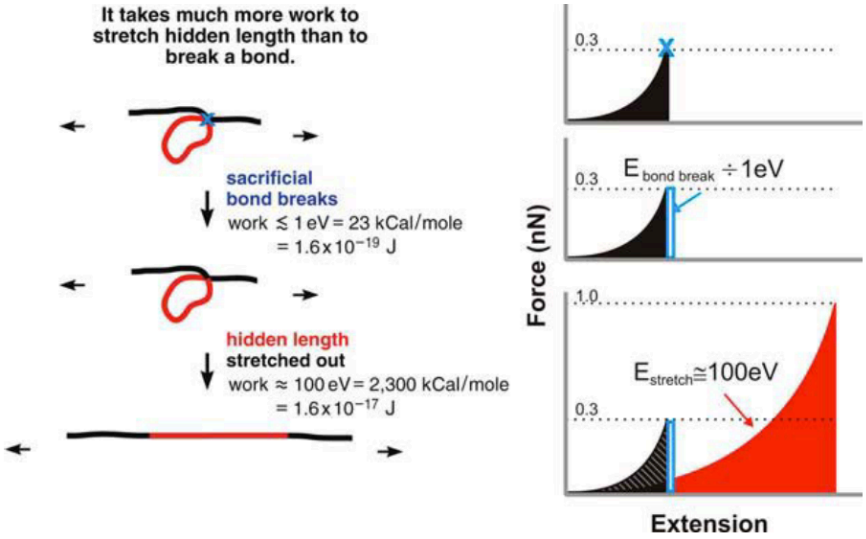

Figure 1.23 Illustrations of the 'sacrificial bond' and the 'hidden length'. The red portion of the molecule is not stretchable until the blue bond is broken. It is thus called respectively hidden length and sacrificial bond. A high amount of energy may be required to unravel a hidden length, making it a contributor to the mechanical strength of the molecule. Reproduced from reference 88.

1.3.4.2 Empirical criteria for single chain stretching

SMFS experiments are based on probing only one molecule at a time.

From a practical point of view, efforts are undertaken upstream the SMFS experiments to favour single molecule events. The molecules are sparsely grafted onto the surface aiming for the best balance between catching only single molecules at a time instead of multiple molecules, and still having statistically sufficient single-molecule events per experiment. Nevertheless, the probability of catching multiple molecules with the tip of the cantilever still exists.

During the data treatment, different criteria can then be used to select only single-molecule signals compared to multiple-molecule signals. [82,94,108] These criteria are:

1) The first criterion is the reproducibility of the unfolding profiles. With an optimized surface functionalization, profiles resulting from pulling on one individual molecule should be reproducible. Discrepancies from the observed profile may witness multiple-molecule attachments to the tip.

2) The second criterion is the experimental entropic elasticity which should match the theoretical one. Often, the molecule is made up of or covalently attached to a semi-flexible polymer used as linker. Given the nature of this chain, the force-distance profile exhibits an entropic elastic behaviour. This behaviour can be fitted with a WLC model. The value of the persistence length (l_p) is then a good indicator for evaluating the number of attached molecule to the tip during the experiment[69,89].

1.4 State-of-the-art AFM-SMFS examples

Although AFM-SMFS is still a quite young technique, less than 40 years old, it has already become a versatile tool for the structural and functional investigation of single natural, artificial and synthetic molecules. Particularly used to investigate natural systems, it has achieved great progress to understand complex and dynamic interactions underlying many biological processes that could not otherwise have been directly detected.[3,74,77] More over SMFS is a relevant alternative to chemical and temperature denaturing experiments. Mechanical force is involved in many biological processes and therefore performing SMFS on natural structures mimic such a biological perturbation. For example, protein folding-unfolding mechanisms[109–112] (Figure 1.22), elasticities of biomacromolecules[95,113–115], DNA mechanics[116,117], biomolecules conformational transitions[22,81,118] or binding potentials of host-guest pairs[119–121] were investigated.

The current challenges deal with the investigation of small systems, the identification of short-distance conformation changes, the tracking and measurement of molecular machines in real time while executing specific molecular tasks. [41,122–124]

This first section develops a selection of state-of-the-art examples which encounter and resolve these challenges. The second section summarizes the studies on natural molecules presenting helical structures.

1.4.1 AFM-SMFS studies on small (synthetic) systems

1.4.1.1 Cis-trans photoisomerization yield a reversible nanoscale contraction-extension

In 2002, H. Gaub and co-workers were the first to observe, at the single-molecule level, a reversible photo-mechanical actuator (Figure 1.24.A&B).[125,126] Single-molecule force spectroscopy experiments were performed with a modified AFM-instrument equipped with an optical excitation module in total internal reflection geometry. A polyazopeptide, a polymer containing azobenzene groups along the backbone, was attached covalently the polymer end groups to both the AFM tip and a glass slide by heterobifunctional chemistry. First, the polymer (initial configurationally mixed state) was irradiated at 420 nm to yield the polymer into the trans state. Then the polymer was pulled and the red trace of Figure 1.24.C was measured. After stretching, the polymer is irradiated at 365 nm to convert the polymer into the saturated *cis*-state. When the polymer was relaxed, it exhibited marked shortening (blue trace) compared to the red trace. This highlighted that the polymer made of azobenzene groups could contract and extend by switching between *trans*- and *cis*-azo configurations when ultraviolet light with specific wavelengths were switched on and off (Figure 1.24.C&D). This was the first demonstration of work produced by a supramolecular polymer.

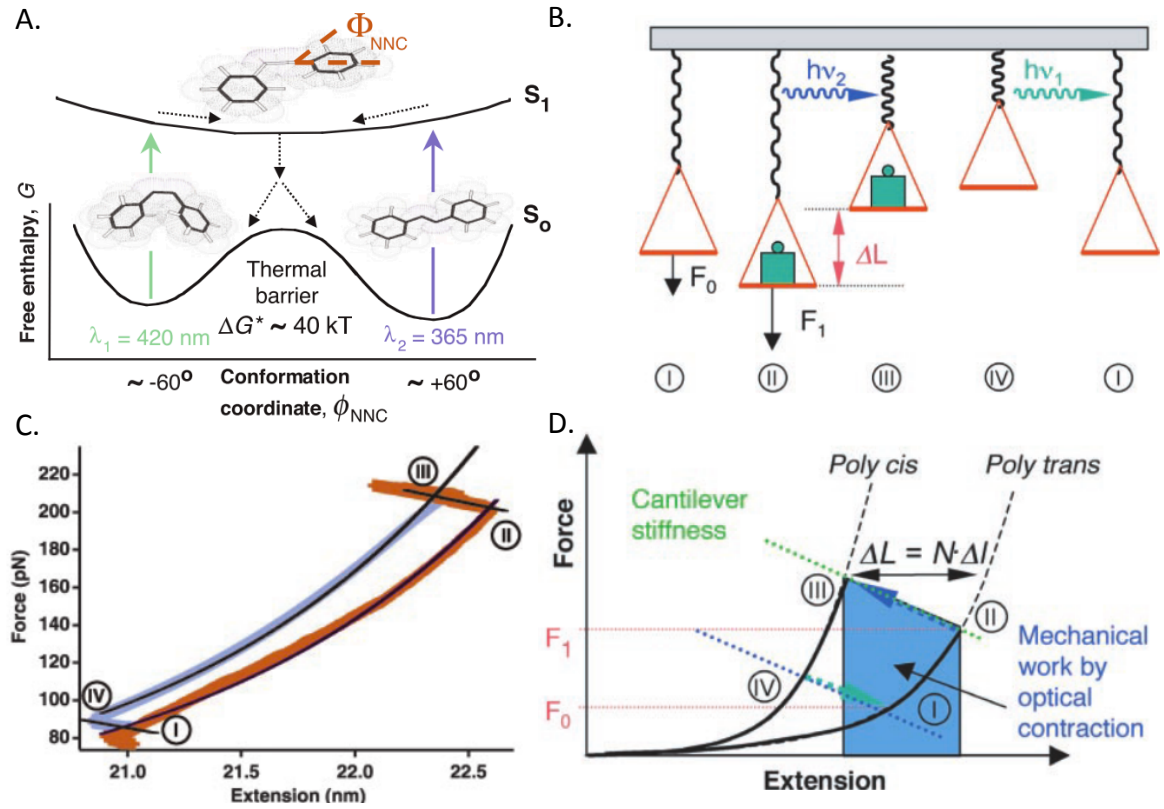

Figure 1.24 (A) Schematics of the potential energy landscape of the reversible azobenzene cis-trans transition along the inversion reaction pathway. The transition is induced by near ultra-violet wavelength. (B) Cartoon of the SMFS experiment with light transition activation. (C) Experimental force-distance curve (D) Schematic force-distance curve. From I to II, an external load is applied and thus the polymer stretches and exhibits an entropic elastic behaviour. At II, 365-nm pulses are applied and the polymer contracts as the azobenzenes take the *cis* configuration. The force increases during the contraction to the shortened state, point III. Upon release of the mechanical load, the polymer relaxes to point IV, from which a new cycle can be started by switching the shortened conformation to the extended state with 420-nm flashes. Adapted from reference 126.

1.4.1.2 Supramolecular interactions

In 2009, A. Janshoff and co-workers developed calix[4]arene catenane polymers –a sophisticated sequence of interlocked supramolecular architectures– to probe the 16 hydrogen bridges holding together a calix[4]arene capsule (Figure 1.25. A& B).[127] They added interlocked loops to restrain the dimers partners to irreversibly separate. As shown in Figure 1.25 they observed a sawtooth profile, indicating the subsequently breaking of capsules. Additionally, the rupture force was shown to be dependent on the loading rate. In the quasi-equilibrium condition, the rupture force is around 50 pN, thus resulting from a 3-4 pN force per H-bond. The force-distance profile also revealed two distinct length increments, one at 1.2 nm and a second one at 2.05 nm. This observation was confirmed using molecular dynamics simulations. This result implied the existence of intermediate states but such a detailed interpretation of the unfolding pattern could not be solved.

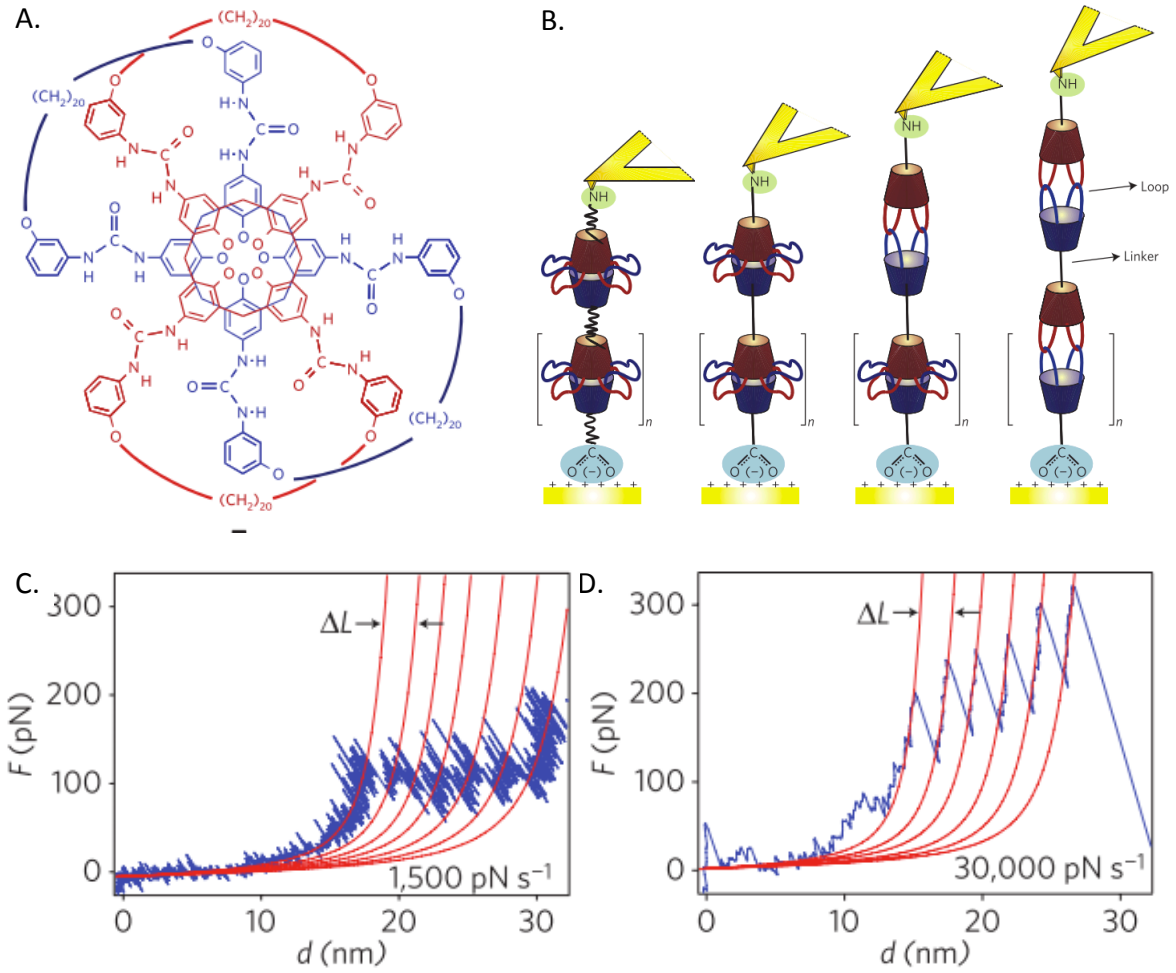

Figure 1.25 (A) Chemical structure of a bis-loop calix[4]arene catenane; the capsules are connected by 16 hydrogen bonds formed by the four urea groups at the upper rim of each calixarene. Eight hydrogen bonds can be considered to be strong and the other eight to be weaker. (B) Cartoon of the AFM-SMFS experiment with the subsequent capsule rupture and the loop-restricted stretching of the calix[4]arene catenane. (C. & D) Force-distance profiles at two loading rate, with both exhibiting a sawtooth profile, where each peak corresponds hypothetically to the rupture of one capsule. Adapted from reference 127.

1.4.1.3 Structural ion coordination

In 2011, the group of H. Li demonstrated that the ferric(III)-thiolate [128] and zinc(II)-thiolate bonds [129] play structural roles in rubredoxin. They measured the Fe(III)-thiolate and Zn(II)-thiolate bond rupture at ± 200 pN and ±170 pN respectively (Figure 1.26). The Fe(III)-thiolate bond was more labile than expected, as it is known to resemble a covalent bond. This suggested that covalence was not the determining factor in the mechanical stability of these Fe(III)-thiolate bonds. This highlighted the significant role of the environment of such bonds. The presence of competing H-bonds with the sulphur was hypothesized to destabilize the Fe-S interaction and, as already mentioned, the constrained structure (in this case tetrahedral) brings an entropic penalty and increases the probability of immediate bond reformation. It is also worth noting that their engineered polyproteins enabled them to specifically reveal the hidden length of this coordination. As expected they were similar in both Zn and Fe cases, as both cations are involved in the tetrahedral scaffold.

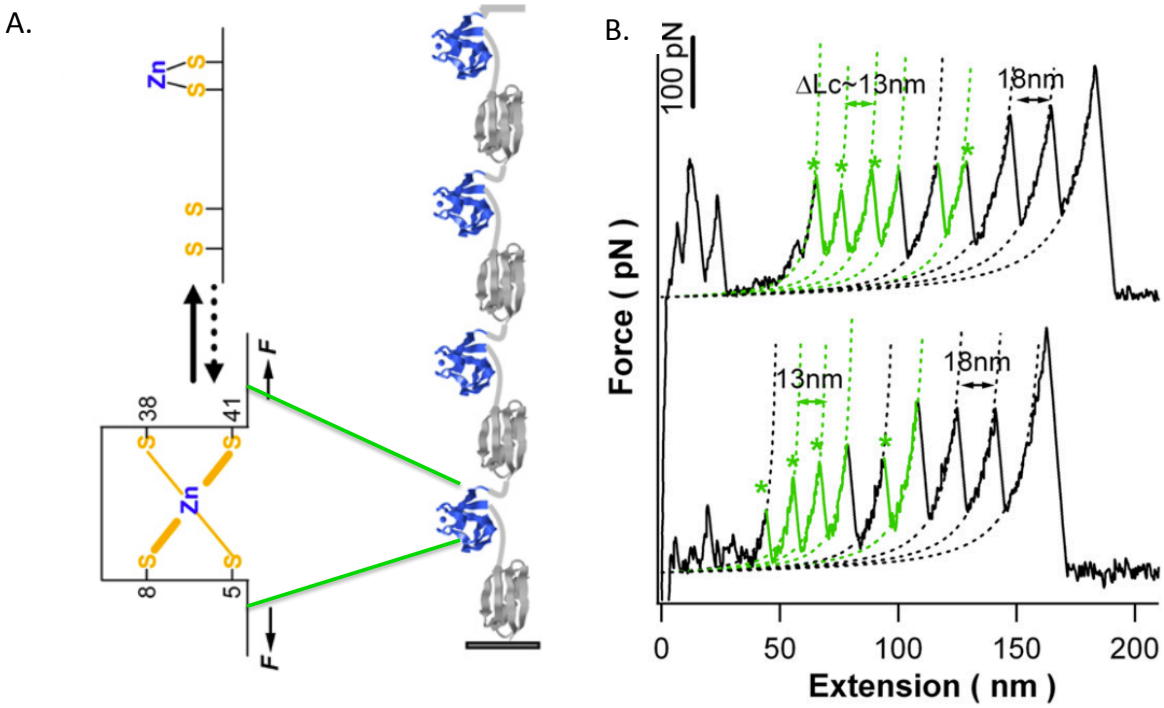

Figure 1.26 (A) Schematics of the mechanical rupture of Zn-thiolate bonds in Zn-pfRD, which is intercalated between two GB1 domains of the polyprotein: $(Zn\text{-}pfRD\text{-}GB1)_n$. The force is applied to Zn-pfRD through the N- and C-termini of the protein. (B) Typical force-extension curves of the unfolding of the polyprotein $(Zn\text{-}pfRD\text{-}GB1)_n$ show ΔL_c of ~18 nm corresponding to the unfolding GB1 domains (black parts of the curves) and ΔL_c ~13 nm (green parts of the curves and indicated by * in green) can be attributed to the unfolding of Zn-RD. Adapted from reference 129.

1.4.1.4 Interlocked intercomponent interaction

In 2011, A.-S. Duwez and co-workers investigated the mechanical stability of a molecular ring threaded onto a molecular axle with two non equivalent stations – a hydrogen-bonded [2]-rotaxane – not longer than 5 nm, synthesized by the group of D. Leigh (Figure 1.27.A).[130] They measured the force required to break the H-bonding of the molecular ring with the favoured station (25-50 pN) of the rotaxane. Moreover, they observed that an individual rotaxane can perform directional forces of similar magnitude than those generated by natural molecular machines (Figure 1.27.B&C).[131]

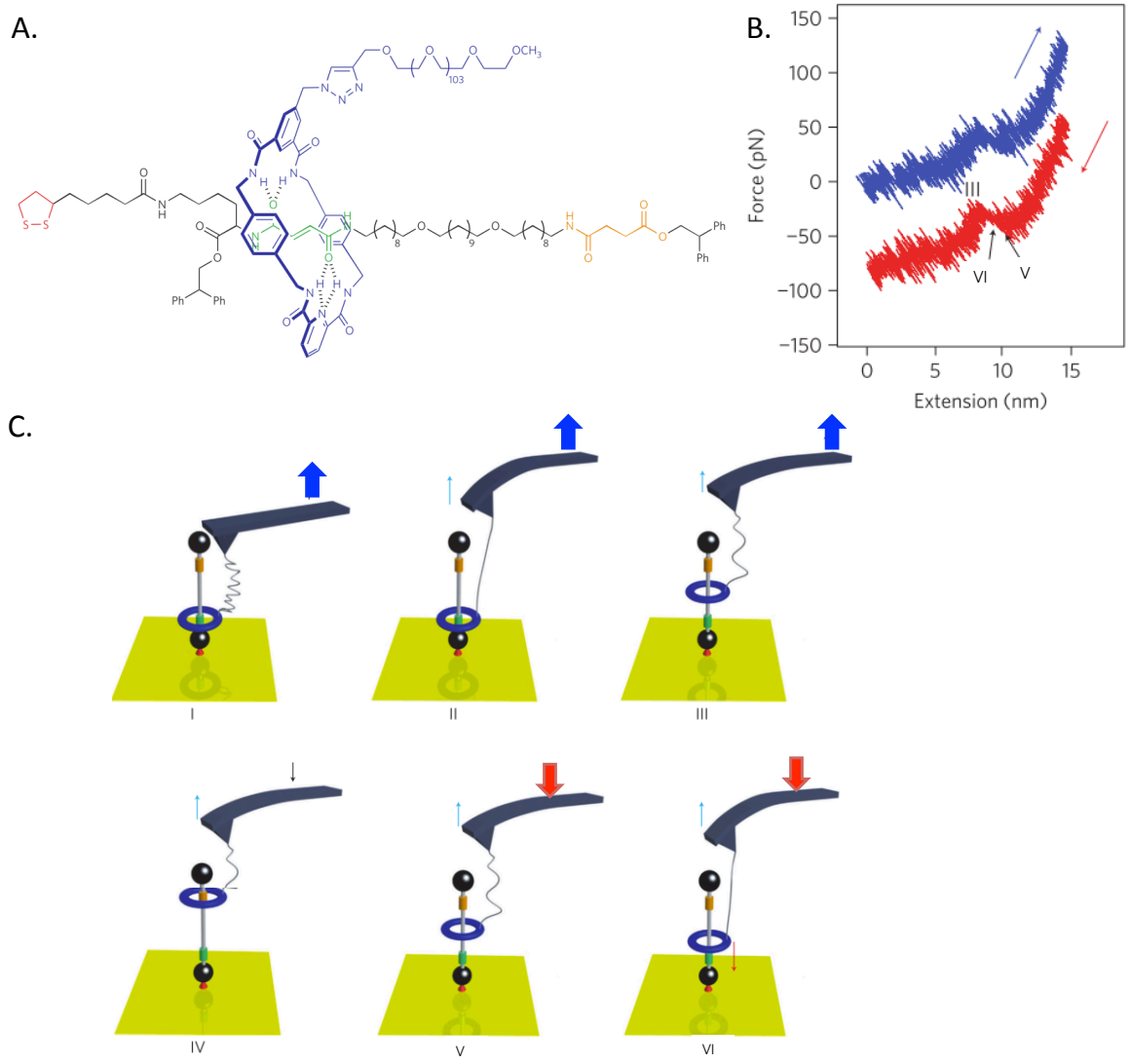

Figure 1.27 (A) Chemical structure of the hydrogen-bonded [2]-rotaxane. (B) Force-extension traces of pulling (blue) and relaxing (red) steps. (C) Cartoon of the SMFS experiment: tick arrows show the direction of cantilever displacement (blue for retraction, red for approach). Thin sky-blue arrows show the direction of the force exerted on the molecular ring. (I) Stretching of the PEO tether. (II) breaking of the H-bonds holding the ring at the fumaramide station (favoured), when the applied force on the tether exceeds the one of the H-bonds. (III) After rupture, the ring has some freedom to move along the thread, the tension in the PEO backbone is partly released, and the force decreases until the displacement of the cantilever stretches again the PEO tether (IV). (V) Relaxing of the tension in the PEO tether. (VI)The force suddenly increases as a result of the ring shuttling in the opposite direction (red arrow)-the ring rebounds to the fumaramide site. Adapted from reference 131.

In 2017, A.-S. Duwez and co-workers worked on supramolecular interlocked structures driven by aromatic-aromatic interactions: oligorotaxanes from F. Stoddart's group.[132] They consist in electron-poor cyclobis(paraquat-*p*-phenylene) rings commonly referred to 'the blue box' and which are interlocked in a dumbbell chain made of poly(ethylene oxide) oligomers comprising electron-donor dioxynaphthalene units. It was suggested that the aromatic interactions lead to a serpentine-like folding (Figure 1.28.A). They highlighted the stepwise breaking of one or two aromatic acceptor-donor partners implied between the 'blue box' and the dumbbell chain (100-150 pN), which confirmed the serpentine-like folded structure of the oligorotaxane. The rupture of one and two interactions revealed 1.2 nm and 2.3 nm, respectively, in a good agreement with the theoretical expected values (Figure 1.28.B&C). This study demonstrated that nanometric structural interactions can indeed be probed using AFM-SMFS. The performances of this system rivals the ones of natural folding proteins.[133] Later, they showed that the rupture force of the acceptor-donor partners was not loading rate-dependent over a wide range of loading rates. This result could be explained by a much faster bond reformation compared to the loading rate. This was hypothesized to be due to the permanent close proximity of both partners.[134] Therefore, this novel 3D structure, which has no natural counterpart, could have emergent properties.

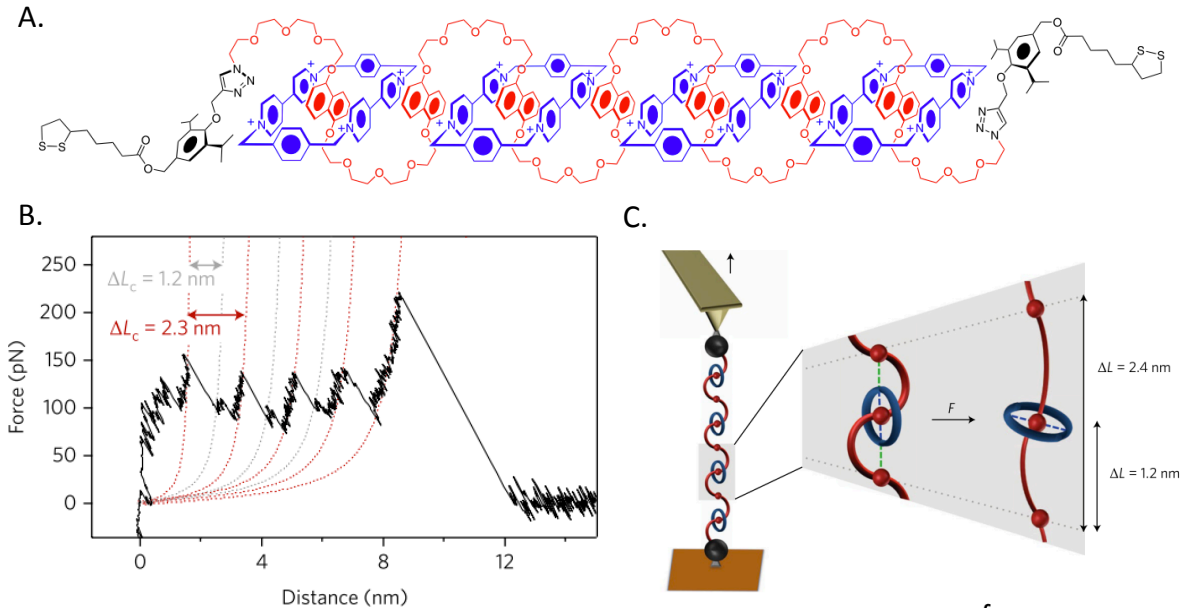

Figure 1.28 (A) Chemical structure of the [5]rotaxane of the [0.5(n–1)+2] family. The rotaxane is composed of cyclobis(paraquat-p-phenylene) rings called 'blue box' (blue) and dumbbell chain made of covalently attached poly(ethylene oxide) oligomers and dioxynaphthalene units (red). (B) Force-extension curve showing sawtooth profile overlaid by WLC fits to each peak (dashed red). The ΔL_c is either equal to 1.2 nm or 2.3 nm, which corresponds to the rupture of respectively 1 and 2 interactions between the 'blue box' and the dumbbell chain as illustrated in (C). Adapted from reference 133.

1.4.2 AFM-SMFS studies on natural helical systems

1.4.2.1 Proteins

Proteins are numerous and exhibit a wide panel of roles, comprising mechanical functions such as elastic properties or mechanical strength for muscle and cytoskeletal proteins respectively. Proteins are sophisticated structures; they are made of several structural motifs and sometimes several domains. Many proteins are composed almost exclusively of helical motifs. α-helices within a protein can either stand alone (*e.g.* calmodulin), or assemble and form rigid coiled-coil structure (*e.g.* myosin), or alternate with loops to form loop-repeats (*e.g.* ankyrin), or be in repeat of coiled-coil bundles (*e.g.* spectrin). This variety of structures leads to diverse force-distance patterns and demonstrates particular mechanical properties under load (for a review[2]).

Single α-helices are found in **calmodulin** (148 amino acids (aa)), a calcium-dependent signal transducer. The dumbbell shaped 3D-structure of calmodulin consists in 7 α-helices distributed in a helical central region capped by two globular regions, each containing two helix-loop-helix (Figure 1.29.A). The first attempt of stretching did not reveal any significant deviation form an entropic elastic stretching. The authors assumed that the unfolding forces were below the experimental noise (20 pN).[135] Later with more sensitive technical approaches, a different and richer unfolding pattern was probed, characteristic of a stepwise breaking of 2 domains between 5 and 15 pN, as shown in Figure 1.29.A.[136] Another example of force spectroscopy on α-helices was performed by Berkemeier *et al.* They worked on a homooctameric construct made of a series of eight identical immunoglobulin My12 domains linked to each other with an α-helical linker of **myomesin (**Figure 1.29.B). The repetitive pattern allowed observing a distinguishable plateau out of the typical peaks of Ig domains unfolding. The plateau occurs at 24 pN and is reversible if the Ig domains are intact.[137]

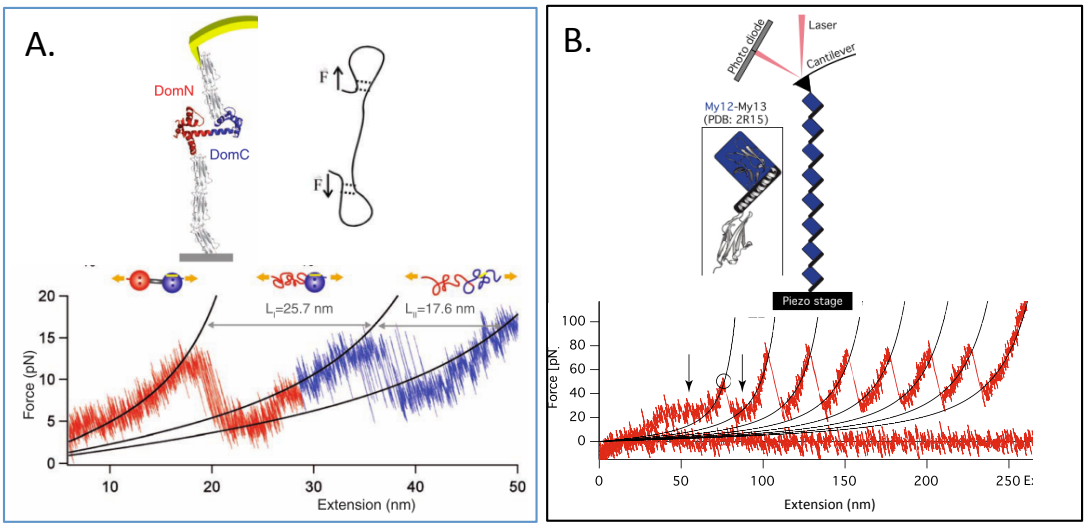

Figure 1.29 Cartoon of proteins and their corresponding force-extension curves (A) Calmodulin[136], with the 2 domains differently coloured (B) Ig domains and α-helical linker of myomesin.[137] The plateau, of the α-helices unfolding is shown by the arrow; the peaks correspond to the typical Ig unfoldings. The blue frame is one of the examples used in Figure 1.31. Reproduced from references 136,137.

A levelled-up coiled-coil structure is a component of **myosin**, a protein involved in the elasticity of muscles. Myosin II consists in 2 parts: the motors and the tail. The tail is made of two heavy chains, which hybridize into a 150 nm-long parallel coiled-coil structure. Its unfolding displays a long and reversible plateau at 25 pN, which is interpreted to be the total unfolding yielding a stretched peptidic sequence (Figure 1.30.D). This assumption is corroborated by the matching contour length gain between a folded coiled-coil and a completely unfolded polypeptide (1.4 Å ➔ 3.6 Å/aa).

Another step beyond in the structural dimension leads to proteins made of repeats of coiled-coil. For example, **ankyrin** protein (Figure 1.30.A) is a cytoskeletal protein made of 33-aa repeats composed of 2 antiparallel α-helices stacked on top of each other and linked by a short loop. Firstly, in opposition to the two-state unfolding process, this small protein reveals sequential unfolding steps at ~25 pN and spaced by about 11 nm from its *C*-terminus to the *N*-terminus.[112,138,139] Secondly, ankyrin repeats have shown their capacity to refold sequentially. The refolding peaks coincide with the unfolding peaks, giving evidence of no energy dissipation. Finally, mechanical effect of mutation was investigated thanks to protein engineering. Four histidines (H) were substituted with arginine (R) and the H/R mutant displays unfolding at lower forces and less robustness along refolding, suggesting a destabilization of the helical structure and responsibility for hereditary spherocytosis.[140] **Spectrin** is another repeat protein, each repeat is made of ~106 aa triple-helical antiparallel coiled-coil. Similarly to ankyrin, each repeat unfolds cooperatively and sequential between 25-35 pN and displays an increase in contour length of 31.7 nm in agreement with the contour length of one repeat (Figure 1.30.C).[141]

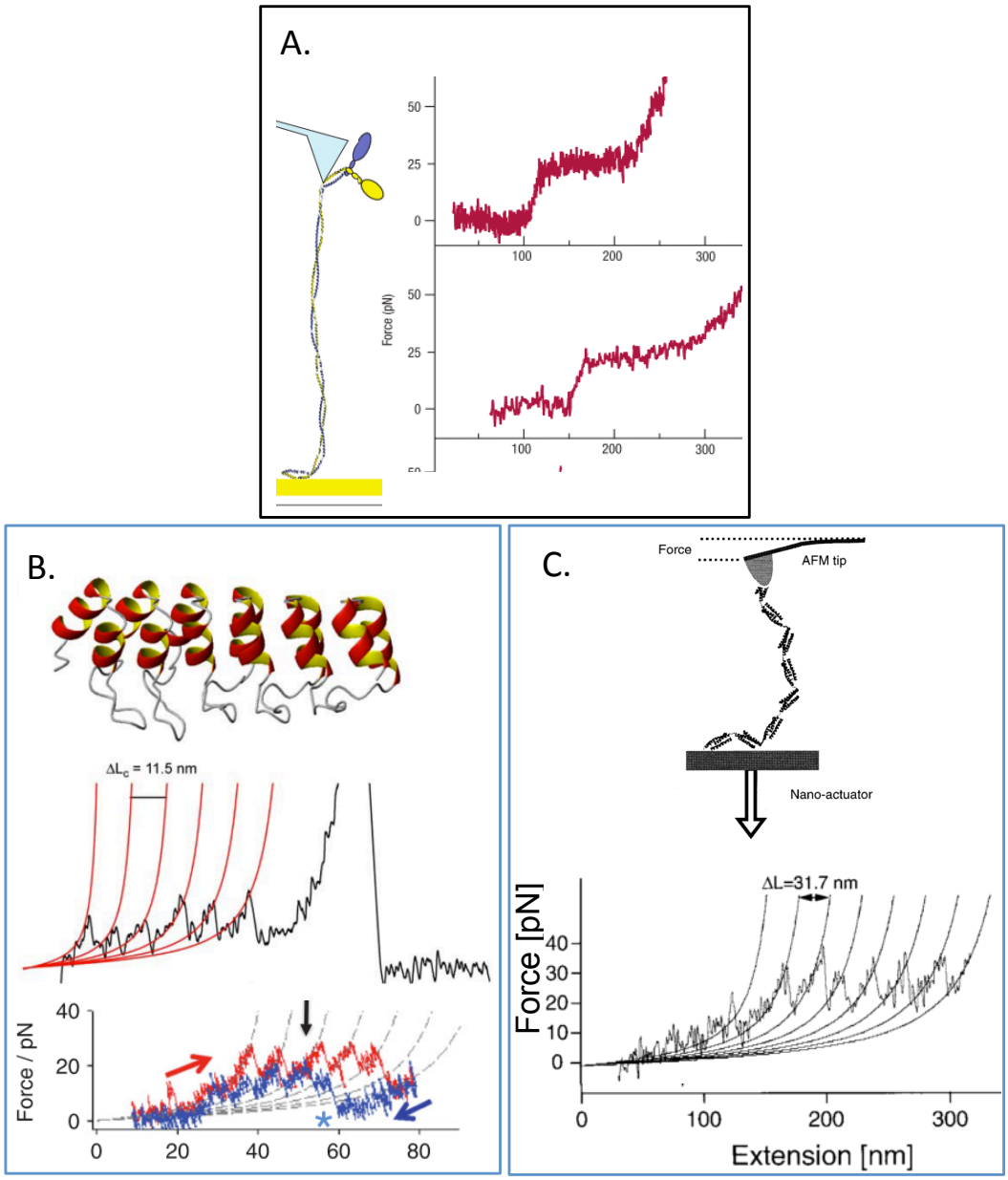

Figure 1.30 Cartoon of the protein and their corresponding force-extension curves (A) Myosin (coiled coil) with three force-extension curves for three myosin II from different origin.[115] (B) Ankyrin[3,139], the bottom plot display a pulling-relaxing experiment with the pulling in red and the relaxing in blue. (C) Spectrin repeats (helix bundle).[141] The panels with a blue frame are examples used in Figure 1.31. Reproduced from references 3, 115, 139, 141.

Furthermore, it has been confirmed that these helix-rich proteins sustain less mechanical force than the proteins containing mostly β-sheets or mixtures of both secondary structures (up to 500 pN) as shown in Figure 1.31. This strength is associated to the multiplicity and sheered topology of the H-bonds.[2] Conversely, α-helix rich proteins refold in average faster than the β-sheet-rich counterparts.[115,142,143] The sheets rather dissipate a large amount of energy. As sheets are not the scope of this thesis, we shall not develop further. However, it is interesting to note that these different performances between helices and sheets lead to associate rich-sheet proteins with shock absorber properties and rich-helix protein with strain absorber/elastic properties.

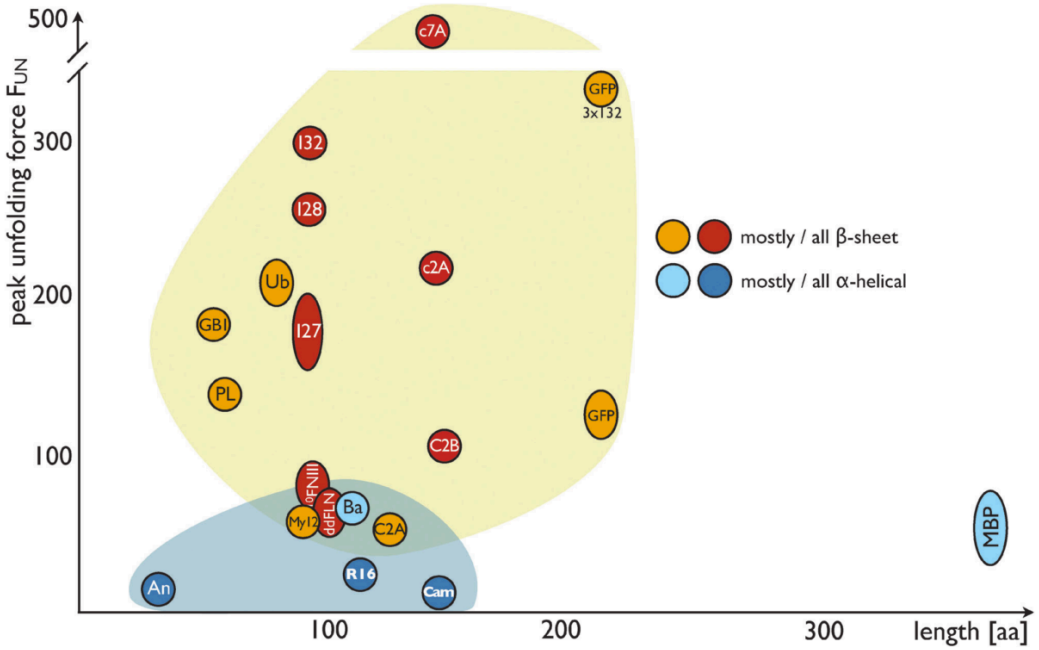

Figure 1.31 Graph of the unfolding force as a function of unfolding length for a large panel of proteins. In the blue and yellow area, rich α-helix and β-sheets protein are respectively found and likely to unfold. 'An' stands for ankyrin, 'R16' for spectrin and 'Cam' for calmodulin. Reproduced from reference 2.

1.4.2.2 DNA double helix

To accomplish its roles, DNA is endowed with several elastic properties. DNA molecules are capable of wrapping around histones as well as separating their strands during cell multiplication. Stretching of long double-stranded DNA (ds-DNA) (> 1000 bp) was widely investigated in the 90s[144,145] and revealed an entropic elasticity at low forces until the normal contour length is reached. Under higher forces, the ds-DNA, in its B-DNA conformation (right-handed double helix with an effective diameter of ~ 2 nm and pitch of 3.4 nm or 10.5 bp) is abruptly but reversibly overstretched to 1.7 times its contour length at 65 pN. Above 150 pN, the melting of the double helix into 2 single strands (Figure 1.32.A) was observed. The first conformational transition, known as B-S transition, is marked by a flat plateau (force range over 2 pN). This narrow force range is considered as a proof of cooperativity, as it reveals that the propagation of the conformation transition is easier than the creation of a new opening.[145] This conformational transition is reversible but may show some hysteresis (Figure 1.32.B). On the contrary, the second conformation transition shows a high hysteresis upon relaxing, indicating a significant topological change and a non-equilibrium transition within the time scale of the experiment.[117] However, when both strands of a ds-DNA are attached to both the tip and the substrate, no hysteresis is observed for none of the two transitions. Nevertheless the forces for both occurrences are upshifted to around 105 pN for the B-S transition and over 250 pN for the melting one.[117,146] These mechanical properties are also salt concentration dependent, temperature dependent and loading rate dependent.[117] The sequence dependency was also investigated and could highlight an important discrepancy in mechanical stability and base pairing forces. Synthetic double stranded poly(dG-dC) and poly(dA-dT) exhibit different

force-distance curves (Figure 1.32 C & D respectively). Whereas, poly(dG-dC) exhibit similar force-distance pattern than classical ds-DNA with a melting force shift to 300 pN, poly(dA-dT) shows a combination of the B-S transition and the melting at only 35 pN. These results are consistent with the base-paring free energy of poly(dA-dT) and poly(dG-dC)[147] and with the value of the base-pairing force of unzipping: 20 ± 3 pN for G-T and 9 ± 3 pN for A-T, previously measured.[116]

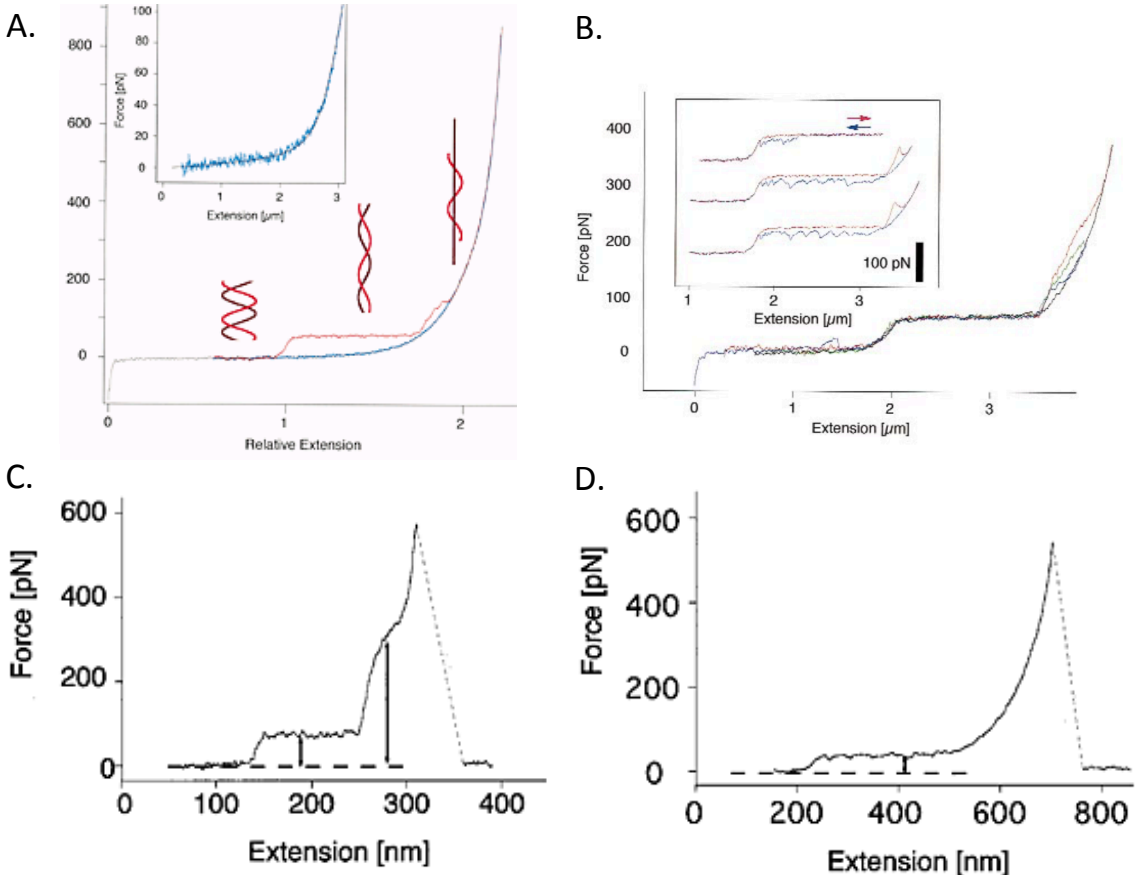

Figure 1.32 (A) Force-extension curve of pulling experiment on a ds-DNA molecule and cartoon of the corresponding conformations. The first plateau is associated to the B-S transition and takes place in equilibrium at 65 pN, the melting into single strand occurs around 150 pN. Inset: relaxation curve of λ-DNA previously split in the melting transition.[116] (B) Force-extension curve of pulling experiment on a ds-DNA molecule at different loading rates (red, 3 µm.s^{-1}; green, 1.5 µm.s^{-1}; blue, 0.7 µm.s^{-1} ; black, 0.15 µm.s^{-1}). In the inset: pulling-relaxing curves on the same molecule, some non-equilibrium melting effects can be seen in the relaxing curves. (C) Force-extension curve of pulling experiment on poly(dC-dG). (D) Force-extension curve of pulling experiment on poly(dA-dT), no melting step can be distinguished from B-S transition. Adapted from reference 116.

In the late 90s, Strunz *et al.* investigated the unbinding forces of short DNA duplexes (30 - 20 - 10 base pairs).[148] For all the duplex sizes, they did not observe the force-constant plateau associated to the B-S transition, but only a single peak rupture at a force lower than 65 pN, in most cases (Figure 1.33.C). In some cases, the 30-bp duplex DNA could dissociate at higher force than 65 pN, but no typical B-S transition could be unambiguously identified due to experimental noise. With the continuous development of the instrument and optimized molecular engineering, in 2007 Morfill *et al.* could evidence the occurrence (30 %) of the B-S transition in a ds-DNA duplex made of 30 bp at 64 pN.

This transition took place along a slightly shorter length than expected (Figure 1.33.A).[149] In 10% of these events, the force further increased to display a complete rupture at 78 pN (Figure 1.33.B). For the other events, the ds-DNA dissociated during the B-S transition. As demonstrated by Strunz, Morfill confirmed that a 20-bp DNA duplex shows only a single rupture. The dissociation force is loading-rate dependent but is always lower than 65 pN.

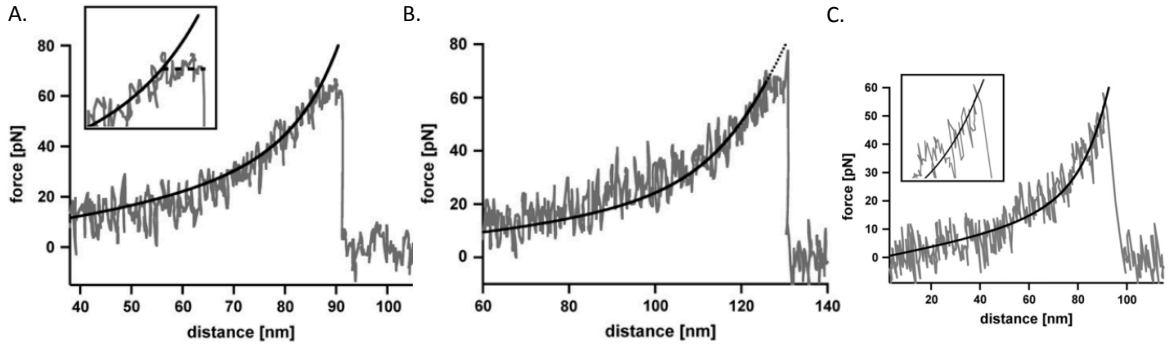

Figure 1.33 Typical force-distance curve of (A) the 30-bp DNA duplex displaying a B-S plateau transition combined with its dissociation, (B) the 30-bp DNA duplex displaying a B-S plateau transition followed by a further increase in force before rupture, (C) the 20-bp DNA duplex displaying a single peak dissociation. Adapted from reference 149.

In 2008, Hatch published sequence length-dependent shear force in DNA duplexes.[150] With magnetic tweezers, they measured the shearing force of DNA duplexes of 12, 16, 18, 24, 28, 32 and 50 base pairs. As shown in Figure 1.34 the shearing force increases linearly for 12- to 20-bp DNA duplexes than increases more slowly to finally reaching "saturation" around 61.5 pN with 50-bp DNA duplex. He concluded that the shear force is only exerted on a few base pairs (~7 bp) at the extremities of the sequence. We can conclude that the shearing force exerted on the strands during the beginning of pulling experiment is enough to dissociate short DNA oligomers. In others words, a force of 60 pN can, skipping the B-S transition, dissociate a 30-bp DNA duplex.

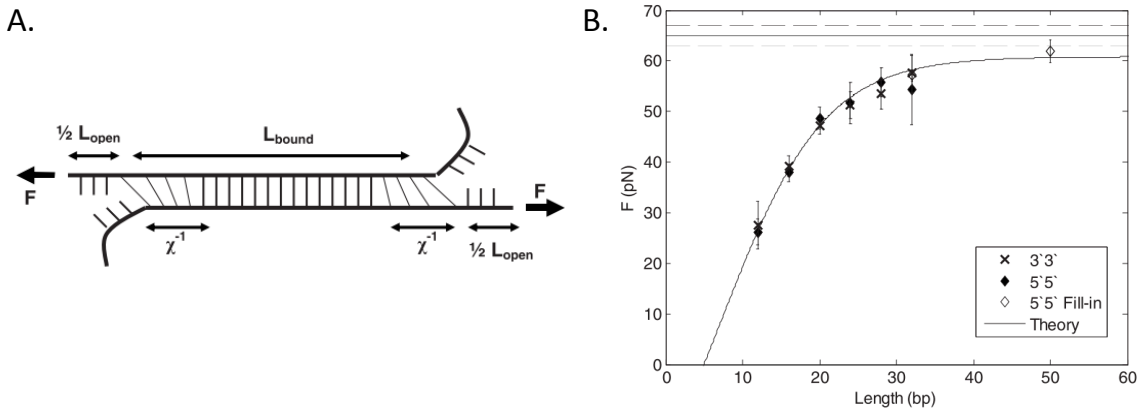

Figure 1.34 (A) Schematic of a 3'3' pulling experiment and localization of the bp (X^{-1}) affected by the shear force. (B) Plot of the shear force as a function of the bp number. Adapted from reference 150.

1.4.2.3 Polysaccharides

Polysaccharides (sugars) are found in plants and other organisms and they are known to play important structural roles and biochemical functions. They are also involved in multicomponent biomolecules such as glycoproteins and peptidoglycans, which act in cell wall structure, molecular recognition and energy storage. The first SMFS experiments on polysaccharide chains highlighted either only entropic elasticity behaviours (Figure 1.37.C) or a plateau at high forces (>300 pN). This plateau was associated to conformational switch of the sugar rings, constituting the polysaccharide chain, from the lower energy chairlike conformation to the higher energy boatlike conformation. This behaviour can be observed for polysaccharide presenting C-O bond in axial position (perpendicular to the ring), which induce a significant increase in distance when it flips to the equatorial position in the boatlike conformation. Among others, the amylose, made of α(1,4)-D-glucopyranose present a such behaviour in water (Figure 1.35.A grey).[3,151] Later it was identified that some polysaccharides can also underpin sophisticate complex supramolecular structures, which present essential role in their biofunctions. The polysaccharides can exist in single- and multi-helical structures. For example, whereas amylose exhibits a random coil conformation in water, it crystallizes in left-handed single-stranded helical structures, called V-amylose, from aqueous iodine solutions, butanol, or pentanol. The X-ray diffraction analysis allowed characterizing the V-amylose and determining that the helix contains six glucose residues per turn. SMFS experiments have also demonstrated this structure at the single molecule scale in butanol. Indeed a characteristic and reproducible plateau could be measured around 50 pN (Figure 1.35). Supported by theoretical simulation this plateau has been proven to correspond to the unwinding of the helix.

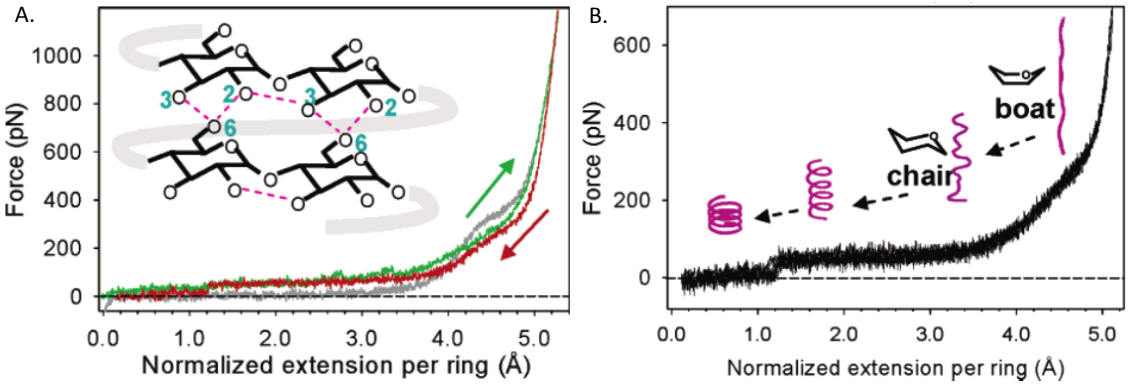

Figure 1.35 (A) Normalized consecutive stretching (green) and relaxing force-extension curves (red) of single amylose chains in butanol. The curve depicted in grey is a representative stretching curve of amylose in water. (Inset) Schematic structure of amylose helix showing inter-glucose hydrogen bonds and the inter-turn (n & n+6) hydrogen bonds. (B) Normalized relaxing curves in superimposition. (Inset) Schematic of the conformation transition. Adapted from reference 151.

On the contrary, in iodine solution, even if it is also known to crystalize into the same helical structure, the plateau was not visible on the force-distance curves. Nevertheless pulling curves exhibit higher force than the pulling curves in water (Figure 1.36.A black vs. green), which may stem from enthalpic contributions. Besides, the pulling-relaxing curves highlighted a particular hysteresis, which give evidence of the initial helical

structure (Figure 1.36.B). This result demonstrates that in aqueous environment the interactions are weaker and that the reformation of the helix is much slower. The reformation of the helix is not instantaneous under load.

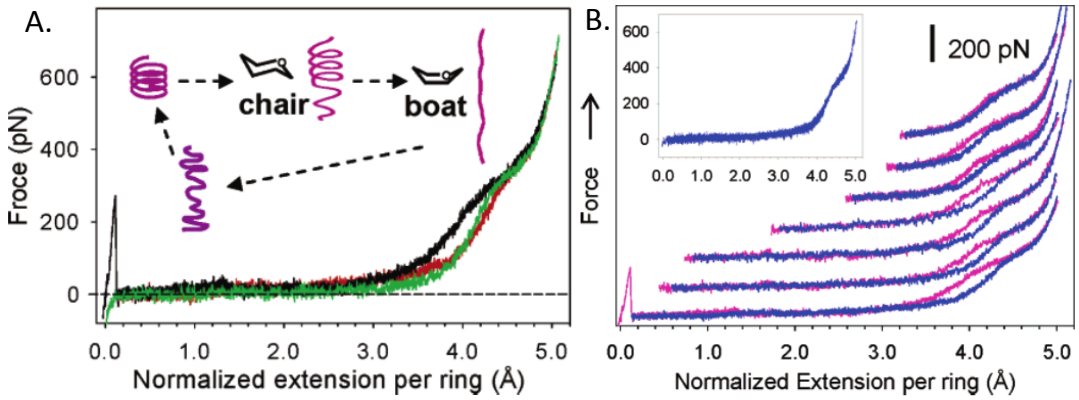

Figure 1.36 (A) Normalized consecutive stretching (black) and relaxing (red) force-extension curves of amylose in aqueous iodine solution and a stretching force curve of amylose in water (green). (B) A series of stretch (pink)-relax (blue) force curves of single amylose molecules in iodine solution obtained after relaxing these molecules to different starting extensions. (Inset) The relaxing force curves for this series are normalized and superimposed. Adapted from reference 151.

Concerning a multi-stranded helical structure of polysaccharides, a good example is the unwinding of the triple helix of the curdlan, a polysaccharide composed of β-(1,3)-linked D-glucose) by SMFS that has been demonstrated to exhibit a force-constant plateau. In adequate conditions to form the triple helix (low NaOH concentration), a plateau was observed at 60 pN (Figure 1.37 A&B.).

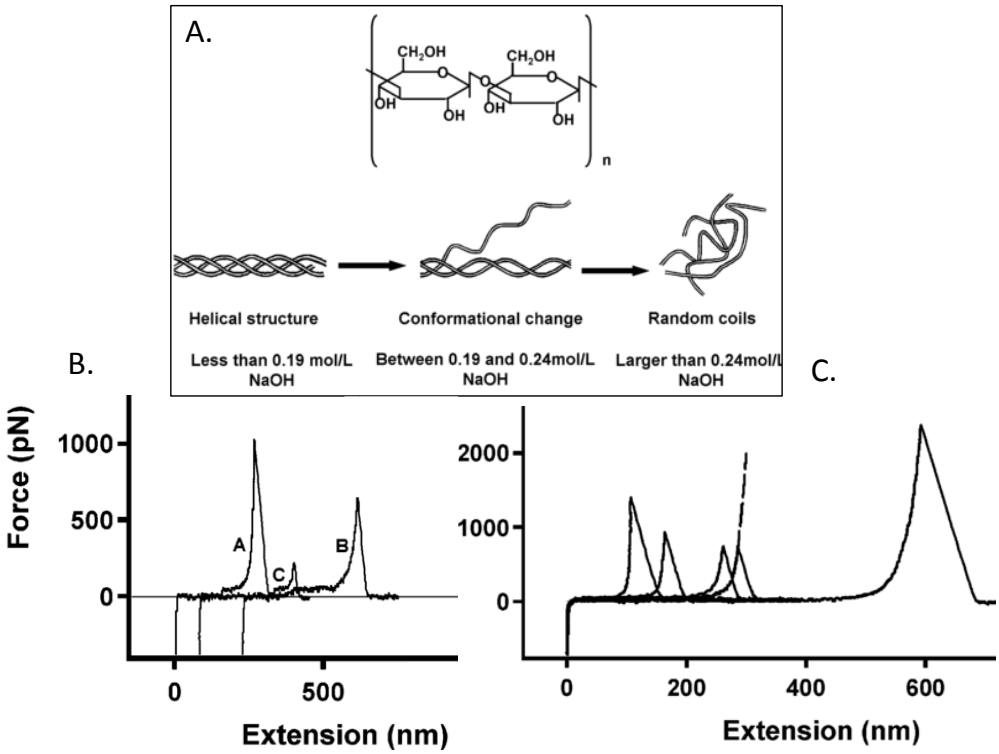

Figure 1.37 (A) Chemical Structure and conformations of curdlan in different concentrations of NaOH(aq). (B) Several typical force-extension curves of curdlan in 0.10 M NaOH(aq), which show a plateau of about 60 pN. (C) Several typical force-extension curves of curdlan in 0.50 M NaOH(aq). Adapted from reference 152.

In summary, some polysaccharides can present two plateaus on a pulling curve, which should not be confounded as that are not stemming from the same origin. Up to now in all the tested polysaccharide, the plateaus are quite distinguishable by the force value. The lower-force plateau corresponds to the unwinding of a helical structures and the high-force plateau to the flipping of the chairlike to boatlike conformations.

Worth noting is the relevancy of the SMFS experiments, many of these 'in solution' behaviours/properties could not be probed with others techniques. Force spectroscopy measurements allowed probing mechanical properties, which can be linked to molecular conformation information in a variety of environments, including poor solvents. For example we could analyse the V-amylose 'in solution' behaviour in butanol, while it crystalizes in this environment so other characterization provide 'solid-phase' behaviours.[151]

1.5 References

1. Ritort, F. The nonequilibrium thermodynamics of small systems. *Comptes Rendus Phys.* **8,** 528–539 (2007).
2. Hughes, M. L. & Dougan, L. The physics of pulling polyproteins: a review of single molecule force spectroscopy using the AFM to study protein unfolding. *Reports Prog. Phys.* **79,** 76601 (2016).
3. Scholl, Z. N., Li, Q. & Marszalek, P. E. Single molecule mechanical manipulation for studying biological properties of proteins, DNA, and sugars. *Wiley Interdiscip. Rev. Nanomedicine Nanobiotechnology* **6,** 211–229 (2014).
4. Soto, C. Protein misfolding and disease; protein refolding and therapy. *FEBS Lett.* **498,** 204–207 (2001).
5. Martin, J. & Hartl, F. Molecular Chaperones in Cellular Protein Folding. *BioEssays* **16,** 689–692 (1994).
6. Diez, M., Petuya, V., Martínez-Cruz, L. A. & Hernández, A. Biokinematic protein simulation by an adaptive dihedral angle approach. *Mech. Mach. Theory* **69,** 105–114 (2013).
7. Song, J., Tan, H., Wang, M., Webb, G. I. & Akutsu, T. TANGLE: Two-Level Support Vector Regression Approach for Protein Backbone Torsion Angle Prediction from Primary Sequences. *PLoS One* **7,** e30361 (2012).
8. Berg, J., M Tymoczko, J. L. & Stryer, L. *Biochemistry, 5th edition*. (2002).
9. Chakrabarti, P. & Pal, D. The interrelationships of side-chain and main-chain conformations in proteins. *Prog. Biophys. Mol. Biol.* **76,** 1–102 (2001).
10. Ramachandran, G. N., Ramakrishnan, C. & Sasisekharan, V. Stereochemistry of polypeptide chain configurations. *J. Mol. Biol.* **7,** 95–99 (1963).
11. Hovmöller, S., Zhou, T. & Ohlson, T. Conformations of amino acids in proteins. *Acta Crystallogr. Sect. D Biol. Crystallogr.* **58,** 768–776 (2002).
12. Harteis, S. & Schneider, S. Making the bend: DNA tertiary structure and protein-DNA interactions. *Int. J. Mol. Sci.* **15,** 12335–12363 (2014).
13. Rich, A. DNA comes in many forms. *Gene* **135,** 99–109 (1993).
14. Saitta, A. M. & Klein, M. L. First-Principles Study of Bond Rupture of Entangled Polymer Chains. *J. Phys. Chem. B* **104,** 2197–2200 (2000).
15. De Bo, G. Mechanochemistry of the mechanical bond. *Chem. Sci.* **0,** 1–7 (2018).
16. He, W. W. *et al.* Entangled structures in polyoxometalate-based coordination polymers. *Coord. Chem. Rev.* **279,** 141–160 (2014).
17. Hunter, C. Quantifying intermolecular interactions: Guidelines for the molecular recognition toolbox. *Angew. Chemie - Int. Ed.* **43,** 5310–5324 (2004).
18. WATSON, J. D. & CRICK, F. H. C. Molecular Structure of Nucleic Acids: A Structure for Deoxyribose Nucleic Acid. *Nature* **171,** 737–738 (1953).
19. Bochman, M. L., Paeschke, K. & Zakian, V. A. DNA secondary structures: Stability and function of G-quadruplex structures. *Nat. Rev. Genet.* **13,** 770–780 (2012).
20. Nikolova, E. N., Gottardo, F. L. & Al-Hashimi, H. M. Probing transient Hoogsteen hydrogen bonds in canonical duplex DNA using NMR relaxation dispersion and single-atom substitution. *J. Am. Chem. Soc.* **134,** 3667–3670 (2012).
21. Gilbert, D. E. & Feigon, J. Multistranded DNA structures Dara E Gilbert and Juli Feigon*. *Curr. Opin. Struct. Biol.* **9,** 305–314 (1999).
22. Choi, J. & Majima, T. Conformational changes of non-B DNA. *Chem. Soc. Rev.* **40,** 5893 (2011).
23. Sippel, K. H. & Quiocho, F. A. Ion-dipole interactions and their functions in proteins.

Protein Sci. **24,** 1040–1046 (2015).

24. Müller, J. Functional metal ions in nucleic acids. *Metallomics* **2,** 318 (2010).
25. Martinez, C. R. & Iverson, B. L. Rethinking the term 'pi-stacking'. *Chem. Sci.* **3,** 2191 (2012).
26. Cozzi, F., Ponzini, F., Annunziata, R., Cinquini, M. & Siegel, J. S. Polar Interactions between Stackedπ Systems in Fluorinated 1,8-Diarylnaphthalenes: Importance of Quadrupole Moments in Molecular Recognition. *Angew. Chemie Int. Ed. English* **34,** 1019–1020 (1995).
27. Hunter, C. A. & Sanders, J. K. M. The Nature of π-π Interactions. *J. Am. Chem. Soc.* **112,** 5525–5534 (1990).
28. Huber, R. G. *et al.* Heteroaromatic π-Stacking Energy Landscapes. *J. Chem. Inf. Model.* **54,** 1371–1379 (2014).
29. Yakovchuk, P., Protozanova, E. & Frank-Kamenetskii, M. D. Base-stacking and base-pairing contributions into thermal stability of the DNA double helix. *Nucleic Acids Res.* **34,** 564–574 (2006).
30. Calero, C. S. *et al.* Footprinting molecular electrostatic potential surfaces for calculation of solvation energies. *Phys. Chem. Chem. Phys.* **15,** 18262–73 (2013).
31. Mattos, C. & Ringe, D. Proteins in Organic Solvents. *Curr. Opin. Struct. Biol.* **11,** 761–764 (2001).
32. Agashe, V. R., Shastry, M. C. R. & Udgaonkar, J. B. Initial hydrophobic collapse in the folding of barstar. *Nature* **377,** 754–757 (1995).
33. Oesterhelt, F., Rief, M. & Gaub, H. E. Single molecule force spectroscopy by AFM indicates helical structure of poly(ethylene glycol) in water. *New J. Phys.* **1,** 6.1-6.11 (1999).
34. Luo, Z., Zhang, B., Qian, H., Lu, Z. & Cui, S. Effect of the size of solvent molecules on the single-chain mechanics of poly(ethylene glycol): implications on a novel design of a molecular motor. *Nanoscale* **8,** 17820–17827 (2016).
35. Amenta, V. *et al.* Interplay of self-association and solvation in polar liquids. *J. Am. Chem. Soc.* **135,** 12091–12100 (2013).
36. Hill, D. J., Mio, M. J., Prince, R. B., Hughes, T. S. & Moore, J. S. A Field Guide to Foldamers. *Chem. Rev.* **101,** 3893–4012 (2001).
37. Zhou, Z. & Bai, Y. Analysis of protein-folding cooperativity. *Nature* **445,** E16 (2007).
38. Durot, S., Reviriego, F. & Sauvage, J.-P. Copper-complexed catenanes and rotaxanes in motion: 15 years of molecular machines. *Dalt. Trans.* **39,** 10557–10570 (2010).
39. Huc, I. & Hecht, S. in *Foldamers* I–XXII (Wiley-VCH Verlag GmbH & Co. KGaA, 2007). doi:10.1002/9783527611478.fmatter
40. Gellman, S. H. Foldamers: A Manifesto. *Acc. Chem. Res.* **31,** 173–180 (1998).
41. Le Bailly, B. A. F. & Clayden, J. Dynamic foldamer chemistry. *Chem. Commun.* **2,** 303 (2016).
42. Yashima, E., Maeda, K., Iida, H., Furusho, Y. & Nagai, K. Helical Polymers: Synthesis, Structures, and Functions. *Chem. Rev.* **109,** 6102–6211 (2009).
43. Ziach, K. *et al.* Single helically folded aromatic oligoamides that mimic the charge surface of double-stranded B-DNA. *Nat. Chem.* **10,** 511–518 (2018).
44. Flack, T. *et al.* Prefolded Synthetic G-Quartets Display Enhanced Bioinspired Properties. *Chem. - A Eur. J.* **22,** 1760–1767 (2016).
45. Garric, J., Léger, J. M. & Huc, I. Molecular apple peels. *Angew. Chemie - Int. Ed.* **44,** 1954–1958 (2005).
46. Maurizot, V. *et al.* Design of an Inversion Center between Two Helical Segments. *J. Am. Chem. Soc.* **126,** 10049–10052 (2004).

47. Delsuc, N., Godde, F., Kauffmann, B., Léger, J.-M. & Huc, I. The Herringbone Helix: A Noncanonical Folding in Aromatic−Aliphatic Peptides. *J. Am. Chem. Soc.* **129,** 11348–11349 (2007).
48. Jiang, H., Léger, J. M., Dolain, C., Guionneau, P. & Huc, I. Aromatic δ-peptides: Design, synthesis and structural studies of helical, quinoline-derived oligoamide foldamers. *Tetrahedron* **59,** 8365–8374 (2003).
49. Fischer, L. & Guichard, G. Folding and self-assembly of aromatic and aliphatic urea oligomers: Towards connecting structure and function. *Org. Biomol. Chem.* **8,** 3102–3117 (2010).
50. Sebaoun, L., Maurizot, V., Granier, T., Kauffmann, B. & Huc, I. Aromatic oligoamide β-sheet foldamers. *J. Am. Chem. Soc.* **136,** 2168–2174 (2014).
51. Garric, J., Léger, J.-M. & Huc, I. Molecular apple peels. *Angew. Chem. Int. Ed. Engl.* **44,** 1954–8 (2005).
52. Ferrand, Y., Kendhale, A. M., Garric, J., Kauffmann, B. & Huc, I. Parallel and Antiparallel Triple Helices of Naphthyridine Oligoamides. *Angew. Chemie Int. Ed.* **49,** 1778–1781 (2010).
53. Guichard, G. & Huc, I. Synthetic foldamers. *Chem. Commun. (Camb).* **47,** 5933–5941 (2011).
54. Ferrand, Y. & Huc, I. Designing Helical Molecular Capsules Based on Folded Aromatic Amide Oligomers. *Acc. Chem. Res.* **51,** 970–977 (2018).
55. Price, J. L., Horne, W. S. & Gellman, S. H. Structural consequences of β-amino acid preorganization in a self-assembling α/β-peptide: Fundamental studies of foldameric helix bundles. *J. Am. Chem. Soc.* **132,** 12378–12387 (2010).
56. Huc, I. Aromatic Oligoamide Foldamers. *European J. Org. Chem.* **2004,** 17–29 (2004).
57. Singleton, M. L., Pirotte, G., Kauffmann, B., Ferrand, Y. & Huc, I. Increasing the Size of an Aromatic Helical Foldamer Cavity by Strand Intercalation. *Angew. Chemie Int. Ed.* **53,** 13140–13144 (2014).
58. Delsuc, N., Massip, S., Léger, J.-M., Kauffmann, B. & Huc, I. Relative Helix−Helix Conformations in Branched Aromatic Oligoamide Foldamers. *J. Am. Chem. Soc.* **133,** 3165–3172 (2011).
59. Delsuc, N., Léger, J.-M., Massip, S. & Huc, I. Proteomorphous objects from abiotic backbones. *Angew. Chem. Int. Ed. Engl.* **46,** 214–7 (2007).
60. Yashima, E. *et al.* Supramolecular Helical Systems: Helical Assemblies of Small Molecules, Foldamers, and Polymers with Chiral Amplification and Their Functions. *Chem. Rev.* **116,** 13752–13990 (2016).
61. Prince, R. B., Barnes, S. A. & Moore, J. S. Foldamer-based molecular recognition. *J. Am. Chem. Soc.* **122,** 2758–2762 (2000).
62. Jacquet, A. Capsules hélicoïdales d'oligoamides aromatiques : détecteurs moléculaires pour le dosage d'acides organiques du vin. (UNIVERSITÉ DE BORDEAUX, 2018). at <https://tel.archives-ouvertes.fr/tel-01714965>
63. Vallade, M. Reconnaissance de surfaces de protéines par les foldamères d'oligoamides aromatiques. (Université de Bordeaux, 2017). at <https://tel.archives-ouvertes.fr/tel-01452513>
64. Mateus, P., Wicher, B., Ferrand, Y. & Huc, I. Alkali and alkaline earth metal ion binding by a foldamer capsule: Selective recognition of magnesium hydrate. *Chem. Commun.* **53,** 9300–9303 (2017).
65. Meunier, A. Les foldamères comme mimes de la seconde sphère de coordination des hydrogénases [Fe-Fe]. (UNIVERSITÉ DE BORDEAUX, 2018). at <https://tel.archives-ouvertes.fr/tel-01690667>
66. Berni, E. *et al.* Assessing the mechanical properties of a molecular spring. *Chemistry* **13,**

8463–9 (2007).

67. Delsuc, N. *et al.* Kinetics of helix-handedness inversion: Folding and unfolding in aromatic amide oligomers. *ChemPhysChem* **9,** 1882–1890 (2008).
68. Greenfield, N. J. Using circular dichroism spectra to estimate protein secondary structure. *Nat. Protoc.* **1,** 2876 (2007).
69. Holzwarth, G. & Doty, P. The Ultraviolet Circular Dichroism of Polypeptides1. *J. Am. Chem. Soc.* **87,** 218–228 (1965).
70. Scarff, C. A., Snelling, J. R., Knust, M. M., Wilkins, C. L. & Scrivens, J. H. New structural insights into mechanically interlocked polymers revealed by ion mobility mass spectrometry. *J. Am. Chem. Soc.* **134,** 9193–9198 (2012).
71. Shang, J. *et al.* Self-association of aromatic oligoamide foldamers into double helices in water. *Org. Lett.* **16,** 4992–4995 (2014).
72. Haler, J. R. N. *et al.* Predicting Ion Mobility-Mass Spectrometry trends of polymers using the concept of apparent densities. *Methods* **144,** 125–133 (2018).
73. Palenčár, P. & Bleha, T. Gas-phase compaction of helical polymers. *Polym. (United Kingdom)* **54,** 4955–4962 (2013).
74. Bustamante, C. In singulo biochemistry: when less is more. *Annu. Rev. Biochem.* **77,** 45–50 (2008).
75. Ritort, F. Single-molecule experiments in biological physics: Methods and applications. *J. Phys. Condens. Matter* **18,** 531–583 (2006).
76. Best, R. B. Folding and Binding: When the Force is Against You. *Biophys. J.* **105,** 2611–2612 (2013).
77. Bustamante, C., Chemla, Y. R., Forde, N. R. & Izhaky, D. Mechanical processes in biochemistry. *Annu. Rev. Biochem.* **73,** 705–748 (2004).
78. Neuman, K. C. & Nagy, A. Single Molecule Force Spectroscopy: Optical Tweezers, Magnetic Tweezers and Atomic Force Microscopy. *Nat. Methods* **5,** 491–505 (2008).
79. Conroy, R. Force Spectroscopy with Optical and Magnetic Tweezers.
80. Moffitt, J. R., Chemla, Y. R., Smith, S. B. & Bustamante, C. Recent Advances in Optical Tweezers. *Annu. Rev. Biochem.* **77,** 205–228 (2008).
81. Clausen-Schaumann, H., Seitz, M., Krautbauer, R. & Gaub, H. E. Force spectroscopy with single bio-molecules. *Curr. Opin. Chem. Biol.* **4,** 524–530 (2000).
82. Hugel, T. & Seitz, M. The study of molecular interactions by AFM force spectroscopy. *Macromol. Rapid Commun.* **22,** 989–1016 (2001).
83. Zou, S., Schönherr, H. & Vancso, G. J. Stretching and rupturing individual supramolecular polymer chains by AFM. *Angew. Chem. Int. Ed. Engl.* **44,** 956–9 (2005).
84. Schröder, T. *et al.* Single-molecule force spectroscopy of supramolecular heterodimeric capsules. *Phys. Chem. Chem. Phys.* **12,** 10981 (2010).
85. Binnig, G., Quate, C. F. & Gerber, C. Atomic Force Microscope. *Phys. Rev. Lett.* **56,** 930–933 (1986).
86. Dougan, M. L. H. and L. The physics of pulling polyproteins: a review of single molecule force spectroscopy using the AFM to study protein unfolding. *Reports Prog. Phys.* **79,** 76601 (2016).
87. Sullan, R. M. A., Churnside, A. B., Nguyen, D. M., Bull, M. S. & Perkins, T. T. Atomic force microscopy with sub-picoNewton force stability for biological applications. *Methods* **60,** 131–41 (2013).
88. Fantner, G. E. *et al.* Sacrificial bonds and hidden length: unraveling molecular mesostructures in tough materials. *Biophys. J.* **90,** 1411–8 (2006).
89. Schlierf, M., Li, H. & Fernandez, J. M. The unfolding kinetics of ubiquitin captured with single-molecule force-clamp techniques. *Proc. Natl. Acad. Sci. U. S. A.* **101,** 7299–7304

(2004).

90. te Riet, J. *et al.* Interlaboratory round robin on cantilever calibration for AFM force spectroscopy. *Ultramicroscopy* **111,** 1659–1669 (2011).
91. Sader, J. E. *et al.* Spring constant calibration of atomic force microscope cantilevers of arbitrary shape. *Rev. Sci. Instrum.* **83,** (2012).
92. Kennedy, S. J., Cole, D. G. & Clark, R. L. A method for atomic force microscopy cantilever stiffness calibration under heavy fluid loading. *Rev. Sci. Instrum.* **80,** (2009).
93. Gibson, C. T., Smith, D. A. & Roberts, C. J. Calibration of silicon atomic force microscope cantilevers. *Nanotechnology* **16,** 234–238 (2005).
94. Giannotti, M. I. & Vancso, G. J. Interrogation of Single Synthetic Polymer Chains and Polysaccharides by AFM-Based Force Spectroscopy. *ChemPhysChem* **8,** 2290–2307 (2007).
95. Smith, S., Finzi, L. & Bustamante, C. Direct mechanical measurements of the elasticity of single DNA molecules by using magnetic beads. *Science (80-.).* **258,** 1122–1126 (1992).
96. Marszalek, P. E., Li, H. & Fernandez, J. M. Fingerprinting polysaccharides with single-molecule AFM. *Nat. Biotechnol.* **19,** 258–262 (2001).
97. Petrosyan, R. Improved approximations for some polymer extension models. *Rheol. Acta* **56,** 21–26 (2017).
98. Gordon, M. Statistical mechanics of chain molecules. P. J. Flory, pp. xix + 432, 1969. New York: Interscience. 164s. *Br. Polym. J.* **2,** 302–303 (1970).
99. Rivetti, C., Walker, C. & Bustamante, C. Polymer chain statistics and conformational analysis of DNA molecules with bends or sections of different flexibility. *J. Mol. Biol.* **280,** 41–59 (1998).
100. Marko, J. F. & Siggia, E. D. Stretching DNA. *Macromolecules* **28,** 8759–8770 (1995).
101. Janshoff, A., Neitzert, M., Oberdörfer, Y. & Fuchs, H. Force Spectroscopy of Molecular Systems-Single Molecule Spectroscopy of Polymers and Biomolecules. *Angew. Chem. Int. Ed. Engl.* **39,** 3212–3237 (2000).
102. Bell, G. I. Models for the specific adhesion of cells to cells. *Science (80-.).* **200,** 618 LP-627 (1978).
103. Evans, E. & Ritchie, K. Dynamic strength of molecular adhesion bonds. *Biophys. J.* **72,** 1541–55 (1997).
104. Noy, A. & Friddle, R. W. Practical single molecule force spectroscopy: how to determine fundamental thermodynamic parameters of intermolecular bonds with an atomic force microscope. *Methods* **60,** 142–50 (2013).
105. Evans, E. Probing the relation between force--lifetime--and chemistry in single molecular bonds. *Annu. Rev. Biophys. Biomol. Struct.* **30,** 105–28 (2001).
106. Porter-Peden, L., Kamper, S. G., Wal, M. Vander, Blankespoor, R. & Sinniah, K. Estimating kinetic and thermodynamic parameters from single molecule enzyme-inhibitor interactions. *Langmuir* **24,** 11556–11561 (2008).
107. Puchner, E. M. & Gaub, H. E. Force and function: probing proteins with AFM-based force spectroscopy. *Curr. Opin. Struct. Biol.* **19,** 605–14 (2009).
108. Zhang, W. & Zhang, X. Single molecule mechanochemistry of macromolecules. *Prog. Polym. Sci.* **28,** 1271–1295 (2003).
109. Rief, M., Pascual, J., Saraste, M. & Gaub, H. E. Single molecule force spectroscopy of spectrin repeats: Low unfolding forces in helix bundles. *J. Mol. Biol.* **286,** 553–561 (1999).
110. Ludwig, M. *et al.* AFM, a tool for single-molecule experiments. *Appl. Phys. A Mater. Sci. Process.* **68,** 173–176 (1999).
111. Puchner, E. M. & Gaub, H. E. Force and function: probing proteins with AFM-based force spectroscopy. *Curr. Opin. Struct. Biol.* **19,** 605–614 (2009).

112. Li, Q., Scholl, Z. N. & Marszalek, P. E. Capturing the mechanical unfolding pathway of a large protein with coiled-coil probes. *Angew. Chem. Int. Ed. Engl.* **53,** 13429–13433 (2014).

113. Marko, J. F., Siggia, E. D. & Smith, S. Entropic Elasticity of X-Phage DNA Explicit and Implicit Learning and Maps of Cortical Motor Output. *Science (80-.).* **265,** 1599–1600 (1994).

114. Strick, T. R., Allemand, J. F., Bensimon, D., Bensimon, A. & Croquette, V. The elasticity of a single supercoiled DNA molecule. *Science (80-.).* **271,** 1835–1837 (1996).

115. Schwaiger, I., Sattler, C., Hostetter, D. R. & Rief, M. The myosin coiled-coil is a truly elastic protein structure. *Nat. Mater.* **1,** 232–235 (2002).

116. Rief, M., Clausen-Schaumann, H. & Gaub, H. E. Sequence-dependent mechanics of single DNA molecules. *Nat. Struct. Biol.* **6,** 346–349 (1999).

117. Clausen-schaumann, H., Rief, M., Tolksdorf, C. & Gaub, H. E. Mechanical Stability of Single DNA Molecules. *Biophys. J.* **78,** 1997–2007 (2000).

118. Rief, M., Oesterhelt, F., Heymann, B. & Gaub, H. Single Molecule Force Spectroscopy on Polysaccharides by Atomic Force Microscopy. *Science* **275,** 1295–7 (1997).

119. Rief, M. & Grubmüller, H. Force spectroscopy of single biomolecules. *ChemPhysChem* **3,** 255–261 (2002).

120. Velez-Vega, C. & Gilson, M. K. Force and stress along simulated dissociation pathways of cucurbituril-guest systems. *J. Chem. Theory Comput.* **8,** 966–976 (2012).

121. Schönherr, H. *et al.* Individual Supramolecular Host−Guest Interactions Studied by Dynamic Single Molecule Force Spectroscopy. *J. Am. Chem. Soc.* **122,** 4963–4967 (2000).

122. Barnes, J. C. & Mirkin, C. A. Profile of Jean-Pierre Sauvage, Sir J. Fraser Stoddart, and Bernard L. Feringa, 2016 Nobel Laureates in Chemistry. *Proc. Natl. Acad. Sci.* **114,** 620–625 (2017).

123. Browne, W. R. & Feringa, B. L. Making molecular machines work. *Nat. Nanotechnol.* **1,** 25–35 (2006).

124. Kay, E. R., Leigh, D. A. & Zerbetto, F. *Synthetic molecular motors and mechanical machines*. *Angewandte Chemie - International Edition* **46,** (2007).

125. Holland, N. B. *et al.* Single molecule force spectroscopy of azobenzene polymers: Switching elasticity of single photochromic macromolecules. *Macromolecules* **36,** 2015–2023 (2003).

126. Hugel, T. *et al.* Single-Molecule Optomechanical Cycle. *Science (80-.).* **296,** 1103–1106 (2002).

127. Janke, M. *et al.* Mechanically interlocked calix[4]arene dimers display reversible bond breakage under force. *Nat. Nanotechnol.* **4,** 225–229 (2009).

128. Zheng, P. & Li, H. Highly covalent ferric-thiolate bonds exhibit surprisingly low mechanical stability. *J. Am. Chem. Soc.* **133,** 6791–6798 (2011).

129. Zheng, P. & Li, H. Direct measurements of the mechanical stability of zinc-thiolate bonds in rubredoxin by single-molecule atomic force microscopy. *Biophys. J.* **101,** 1467–1473 (2011).

130. Kay, E. R. & Leigh, D. A. Hydrogen bond-assembled synthetic molecular motors and machines. *Top. Curr. Chem* **262,** 133–177 (2005).

131. Lussis, P. *et al.* A single synthetic small molecule that generates force against a load. *Nat. Nanotechnol.* **6,** 553–557 (2011).

132. Zhu, Z. *et al.* Oligomeric Pseudorotaxanes Adopting Infinite-Chain Lattice Superstructures. *Angew. Chemie Int. Ed.* **51,** 7231–7235 (2012).

133. Sluysmans, D. *et al.* Synthetic oligorotaxanes exert high forces when folding under mechanical load. *Nat. Nanotechnol.* **13,** 209–213 (2018).

134. Sluysmans, D., Devaux, F., Bruns, C. J., Stoddart, J. F. & Duwez, A.-S. Dynamic force

spectroscopy of synthetic oligorotaxane foldamers. *Proc. Natl. Acad. Sci.* **115,** 9362–9366 (2018).

135. CarrionVazquez, M. *et al.* Mechanical design of proteins-studied by single-molecule force spectroscopy and protein engineering. *Prog Biophys Mol Biol* **74,** 63–91 (2000).
136. Junker, J. P., Ziegler, F. & Rief, M. Ligand-dependent equilibrium fluctuations of single calmodulin molecules. *Science (80-.).* **323,** 633–637 (2009).
137. Berkemeier, F. *et al.* Fast-folding -helices as reversible strain absorbers in the muscle protein myomesin. *Proc. Natl. Acad. Sci.* **108,** 14139–14144 (2011).
138. Lee, W. *et al.* Full reconstruction of a vectorial protein folding pathway by atomic force microscopy and molecular dynamics simulations. *J. Biol. Chem.* **285,** 38167–72 (2010).
139. Li, L., Wetzel, S., Plückthun, A. & Fernandez, J. M. Stepwise Unfolding of Ankyrin Repeats in a Single Protein Revealed by Atomic Force Microscopy. *Biophys. J.* **90,** L30–L32 (2006).
140. Lee, W., Strümpfer, J., Bennett, V., Schulten, K. & Marszalek, P. E. Mutation of conserved histidines alters tertiary structure and nanomechanics of consensus ankyrin repeats. *J. Biol. Chem.* **287,** 19115–19121 (2012).
141. Rief, M., Pascual, J., Saraste, M. & Gaub, H. E. Single molecule force spectroscopy of spectrin repeats: low unfolding forces in helix bundles. *J. Mol. Biol.* **286,** 553–561 (1999).
142. Bornschlögl, T. & Rief, M. Single-Molecule Dynamics of Mechanical Coiled-Coil Unzipping †. *Langmuir* **24,** 1338–1342 (2008).
143. Carrion-Vazquez, M. *et al.* Mechanical and chemical unfolding of a single protein: A comparison. *Biophysics (Oxf).* **96,** 3694–3699 (1999).
144. Cluzel, P. *et al.* DNA : An Extensible Molecule. *Science (80-.).* **271,** 792–794 (1996).
145. Smith, S. B., Cui, Y. & Bustamante, C. Overstretching B-DNA: the elastic response of individual double-stranded and single-stranded DNA molecules. *Science* **271,** 795–9 (1996).
146. van Mameren, J. *et al.* Unraveling the structure of DNA during overstretching by using multicolor, single-molecule fluorescence imaging. *Proc. Natl. Acad. Sci. U. S. A.* **106,** 18231–6 (2009).
147. Breslauert, K. J., Franks, R., Blockers, H. & Markyt, L. A. Predicting DNA duplex stability from the base sequence. *Proc. Natl. Acad. Sci. U. S. A.* **83,** 3746–3750 (1986).
148. Strunz, T., Oroszlan, K., Schäfer, R. & Güntherodt, H. J. Dynamic force spectroscopy of single DNA molecules. *Proc. Natl. Acad. Sci. U. S. A.* **96,** 11277–11282 (1999).
149. Morfill, J. *et al.* B-S transition in short oligonucleotides. *Biophys. J.* **93,** 2400–2409 (2007).
150. Hatch, K., Danilowicz, C., Coljee, V. & Prentiss, M. Demonstration that the shear force required to separate short double-stranded DNA does not increase significantly with sequence length for sequences longer than 25 base pairs. *Phys. Rev. E - Stat. Nonlinear, Soft Matter Phys.* **78,** 1–4 (2008).
151. Zhang, Q. & Marszalek, P. E. Identification of sugar isomers by single-molecule force spectroscopy. *J. Am. Chem. Soc.* **128,** 5596–5597 (2006).
152. Zhang, L., Wang, C., Cui, S., Wang, Z. & Zhang, X. Single-molecule force spectroscopy on curdlan: Unwinding helical structures and random coils. *Nano Lett.* **3,** 1119–1124 (2003).

Chapter 2

Pulling experiments on
Quinoline-based Foldamers
of different sizes

TABLE OF CONTENTS

Chapter 2
Pulling experiments on Quinoline-based Foldamers of different sizes

The second chapter starts by presenting the well-controlled and predictable helical quinoline-based foldamers, which were selected as starting helical model systems for the mechanochemical properties investigation by single-molecule force spectroscopy (SMFS). The specific design of the molecular system to suit such experiments is described and discussed.

Then, the results of the standard pulling experiments on quinoline-based foldamers of different sizes are presented. Unfolding patterns are in-depth scrutinized to unveil the mechanical and dynamical properties. Qualitative, quantitative and complementary signal analyses are carried out. The performances of these systems are compared to their natural counterparts and other synthetic structured molecules which, when put together, allows suggesting further interpretations in terms of mechanochemical properties.

2.1 Introduction

To investigate the mechanochemical properties of helical secondary structures, quinoline-based foldamers were relevantly selected as starting molecular systems. For more than 15 years, this structure has caught the attention of the I. Huc group and colleagues. Many characterizations have been already performed. Nevertheless, questions on their dynamical behaviour, conformational stability in solution are still pending and their mechanochemical properties are unknown.

2.1.1 Quinoline based-foldamers: background and synthesis

Quinoline− 8-amino-4-isobutoxy-2-quinolinecarboxylic acid − coded Q

In 2003, Jiang from Huc's group published[1] the synthesis, the solid state (single crystal X-ray diffraction) and in solution (^{1}H NMR) characterization of a series of convergent oligomers: dimer, tetramer, hexamer, octamer and decamer made of 8-amino-4-isobutoxy-2-quinolinecarboxylic acid units, with isobutoxy-group as lateral chain (Figure 2.1.A). They showed, thanks to X-ray structures, that the dimer is curved and planar and that the steric hindrance occurs from the addition of a third unit and yields consequently a tightly curved helix (Figure 2.1.B&C). This structure was expected according to their design predictions, as described in section 1.2.2.2. One turn is made of 2.5 quinoline units (equivalent to 15 atoms of the inner rim). The pitch is 3.4 Å high, as found in the other helical aromatic oligoamides.

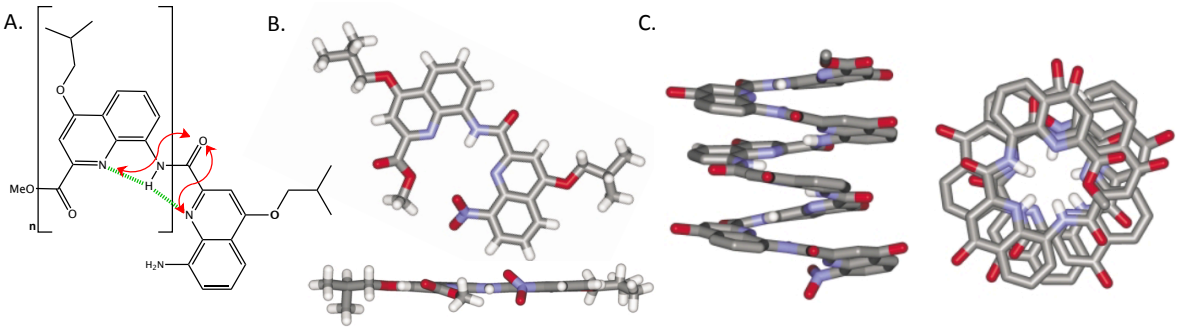

Figure 2.1 (A) Chemical structure of foldamer made of 8-amino-4-isobutoxy-2-quinolinecarboxylic acid and intramolecular interactions leading to the helical folding. The H-bond interactions are highlighted in green and the electrostatic repulsions are shown using red arrows. (B) Crystal structure obtained from X-ray diffraction of the dimer, front & side view (to show the high planarity). (C) Crystal structure of the octamer (solvent molecules and isobutyl chains have been omitted for clarity). The measurements obtained from X-ray diffraction of the helical structure indicate a pitch of 3.5Å and 2.5 quinoline units per turn. Atoms are colour coded as carbon in grey, hydrogen in white, oxygen in red and nitrogen in blue. Adapted from reference 1.

The amide protons, involved in two H-bonds with the adjacent units, fill the inside of helix and completely prevent penetration of solvent molecules. While the core of the helix exhibits a strictly regular structure, the lateral chains (isobutoxy) encompass different conformations. As represented in Figure 2.1.A, the helical structure holds owing to mainly intramolecular H-bonds (green lines), electrostatic restricted rotation (red arrows) and π-stacking. Even if the examination of the structure does not unambiguously display intramolecular aromatic stacking, the π-stacking effect was discerned in UV–Vis absorption spectra and in NMR (Figure 2.2).

As already mentioned in the previous chapter, despite the identical nature of some protons owing to the repetition of the same unit, in a ^{1}H NMR spectrum, separated peaks can be observed for a given proton of each unit due to the helical environment. Worth noting is the general upfield shift (to smaller chemical shift) of all peaks when the number of units increases in the foldamers (Figure 2.2).[2] The origin of this overall shift is still unclear but an important hypothesis links it to the progressive increase in helix stability. Stabilization results from a decrease in the local molecular motions, which enhances short-range ring current effects and consequently shifting upfield the peaks. This length-dependent stabilization hypothesis is further confirmed by narrowing or the increased diastereotopic aspect of the peaks, which corroborate slower conformation transition.[2]

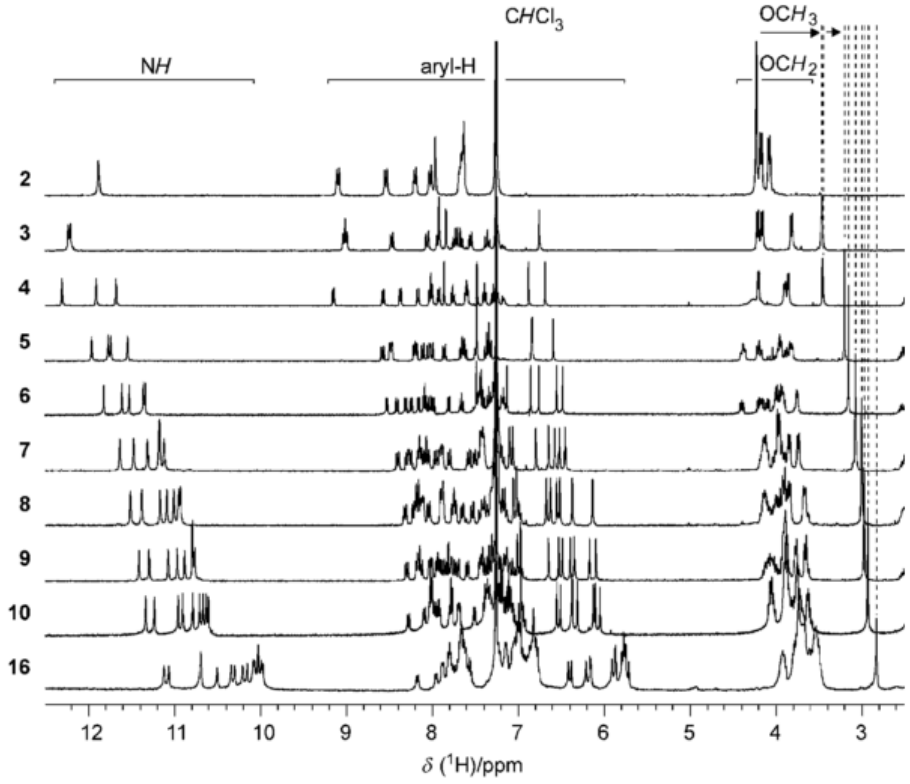

Figure 2.2 ^{1}H NMR spectra in $CDCl_3$ of a series of quinoline-based foldamers constituted of increasing number of quinoline units from top to bottom. Compound numbering is defined on the left of each spectrum. Reproduced from reference 2.

Hence NMR analysis clearly suggests that π-π stacking between aromatic units provides additional conformational stabilization; however this stabilization does not influence the curvature of the oligomers. Indeed, it was demonstrated that crystal structures of short crescent oligomers and of their longer helical analogues have identical curvature (see the superimposition of 2 adjacent units of the dimer and the octamer in Figure 2.3). Therefore we can believe that the curvature of the strands relies essentially on the hydrogen bonds. This suggests that either the H-bonds imply genuinely the optimized overlapping/stabilization or that the gain of energy from an optimized overlapping does not outweigh the cost of H-bonds deformation and the curvature change.[1]

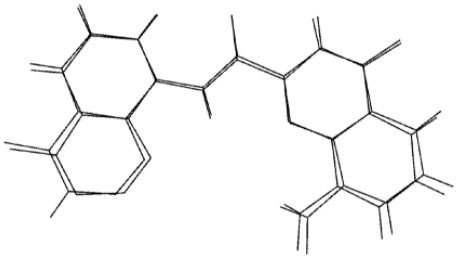

Figure 2.3 Superposition of part of the structure of the quinoline dimer in the crystal and the *N*-terminal fragment of the structure of quinoline octamer in the crystal. Reproduced from reference 1.

Since 2003, many investigations have been carried out and allowed much advancement with this family of foldamers.[3–5] The chromatography-free large-scale synthesis of octamers[6] was published in 2013 and more recently, the gram-scale preparation of nanosized/protein-sized up to 64-mers (15.6 kDa)[7]and the synthesis of quinoline-based foldamer of more than 10 nm (96 units-25.7kDa).[8] For clarity reasons, quinoline unit is coded Q and quinoline-based foldamers are Q_n, with n for the number of units. Further literature results on this subject will be developed later in the manuscript and will be put in the context of our results and interpretations.

2.1.2 Design of the molecular systems for SMFS experiments

To properly and efficiently perform single-molecule force spectroscopy (SMFS), particular set-ups are required. Careful experiment design has to be addressed (i) to ensure the exclusivity and the well-defined conformation of the desired molecule, (ii) to create strong bonds at the interfaces (substrate and tip) in order to be able to observe the entire stretching/unfolding of the molecule of interest before any detachment and (iii) to spatially isolate the molecule of interest from the probe or surface to avoid nonspecific interactions and to allow a free orientation of the tethered molecules.

2.1.2.1 Synthesis of the molecular system

With this recommendations and the capabilities of organic synthesis, Dr. Xuesong Li synthetized quinoline-based foldamers of different sizes (4-mer, 8-mer, 16-mer and 32-mer), during his thesis, following the established Q_8 protocols[6] and segment doubling strategy, as illustrated in Figure 2.4. He elongated these foldamers with an amino-methyl-quinoline unit, coded ^{m}Q, to increase the reactivity of the amine-terminus and to generate a 90° angle between the N-terminus of the molecule and the helical structure, promoting perpendicular position of the helical structure on the anchored surface. This allows the end-functionalization of the foldamers with a 11-mercaptoundecanoic acid providing a flexible thiol which is known to anchor strongly to a gold surface[9,10] and to provide some spatial spacing between the foldamer and the surface (aliphatic chain of 11 carbons, coded R). On the acid-terminus, he further covalently attached an amine-terminated long poly(ethylene glycol) chain (PEG) for several reasons that are explained later (see 2.1.2.2).[7] Final compounds are fully named SH-R-$^{m}QQ_n$-PEG with n=4,8,16,32 and are abbreviated to Q5, Q9, Q17, Q33 later in the manuscript.

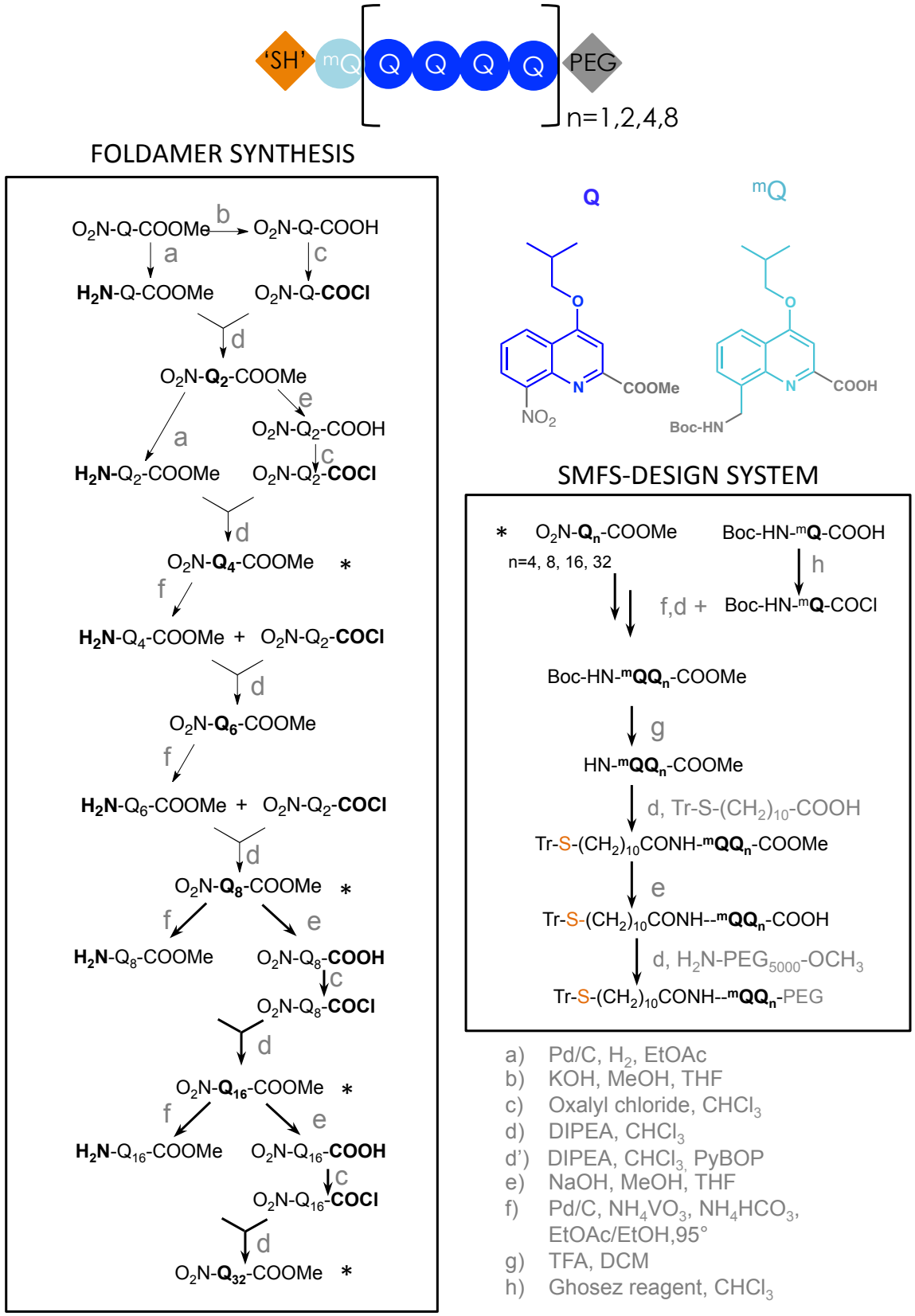

Figure 2.4 Synthesis pathway of the SMFS-designed quinoline-based foldamers through the segment doubling strategy[6]. Functionalization of both extremities of the foldamer to optimize the SMFS experiments.[7] The light blue ^{m}Q represents an aminomethyl-quinoline unit, the blue Q represents a quinoline unit.

2.1.2.2 PEG as a tether and a reference

The use of a long poly(ethylene glycol) (PEG) linker has several advantages. Covalently connecting a PEG molecule to a molecular system of interest is known to allow probing mechanical behaviors[11], intramolecular interactions[12], submolecular movements[9] and intermolecular interactions in recognition processes,[13–15] *etc*. The PEG chain is soluble in a large variety of solvents and is a flexible and distensible linker that can attach strongly and reversibly to the tip by multiple non-covalent interactions. PEG can thus act as a tether, which provides degrees of freedom in order to increase the probability of catching a molecule. A second advantage is that the PEG isolates the foldamer from the unspecific tip interactions. Consequently, it enables probing the full stretching/unfolding of the foldamers. If the tether is much longer than its persistence length, it behaves as truly flexible and ensures freedom to all freed-conformations.[11] In addition, the PEG can be used to distinguish pulling experiment on a single molecule from multiple attachments. Indeed the behaviour of the PEG under load is nowadays well-known and can be described by models of statistical mechanics. In organic solvents, the PEG adopts a random coil conformation. When it is stretched, it produces an entropic restoring force on the cantilever, which is predictable by the worm-like chain model (WLC). The WLC model, based on the polymer theory of Kratky and Porod, links the restoring force F of a semi-flexible polymer, as a homogenous chain of constant bending elasticity ('wormlike'), with its end-to-end extension x (Figure 2.5).[16]

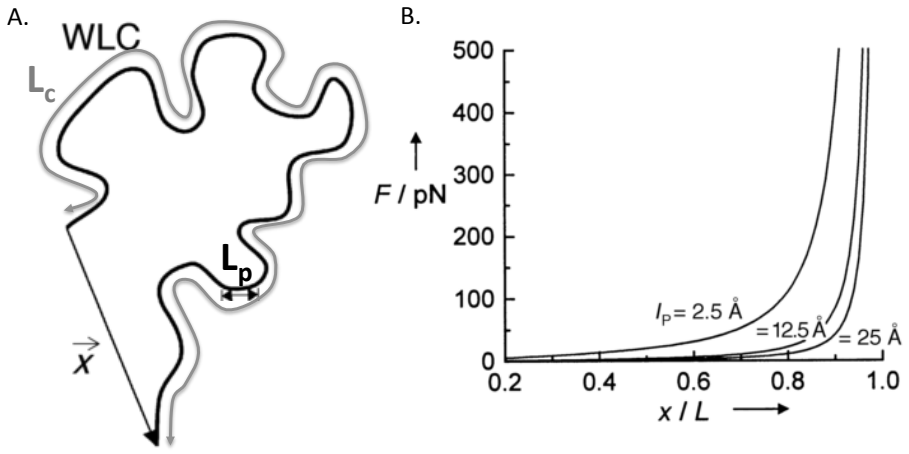

Figure 2.5 (A) Schematic representation of the worm-like chain model and its mechanical parameters. (B) Force-distance curves of the WLC model with different persistence length. reproduced from reference 17.

The extension of the molecule is limited by the contour length (L_c) and the flexibility is measured by the persistence length (l_p). The persistence length dictates the orientation of the chain. Under this length, the polymer is considered as linear.[17] The relationship between force and extension cannot be solved analytically but a good approximation is commonly used (Eq. 1)

$$F = \frac{k_B T}{l_p} \times \left[\frac{1}{4} \times \left(1 - \frac{x}{L_c} \right)^2 + \frac{x}{L_c} - \frac{1}{4} \right] \quad \text{Eq. 1}$$

Eq. 1 WLC model: where l_p is the persistence length, x the extension and L_c the contour length.

By comparing the l_p and L_c values obtained by fitting the experimental force-distance curves with the WLC model to the PEG theoretical values, we can validate or invalidate the well-controlled pulling on a single tethered molecule of interest. The l_p value is directly related to the flexibility, so that the value would change in case of pulling on several chains. For a single PEG chain, l_p is around 0.35 nm. The L_c value gives the maximum theoretical extension of the pulled system without deformation. In case of covalent binding between tip and tether, the L_c value is highly relevant to determine if we pull on the molecule of interest. In case of physisorption attachment method, the L_c value varies for each experiment, as the polymer chain attaches on a random location along the backbone. Nevertheless, the maximum value can still be used to discard the long profiles.

Moreover, given the known force-distance pattern of the PEG, any deviation from it can be considered as the unfolding pattern of the tethered molecule. It is particularly profitable when dealing with small molecules, as in this thesis.

An arguable aspect of the use of a tether arises for dynamic force spectroscopy experiment. While A. Noy[11] notes the relevant advantage of the linker which suppresses the interaction rebinding probability, as well as the drag effect of the cantilever, H. Gaub[18] does not neglect the impact of the non-linear spring behaviour of a soft linker on the effective loading rate, especially when the linker is a soft polymer exhibiting a broad dispersity. This subject will be particularly discussed in chapter 3.

2.2 Results and discussion

The investigation of mechanochemical properties at the single-molecule scale was started by performing standard pulling experiments on 33-, 17-, 9- and 5-mers of quinoline-based foldamers in *N,N*-dimethylformamide (DMF) and at the loading rate of 166 $nm.s^{-1}$.

2.2.1 How to ensure the pulling of a single molecule?

The first step of the force spectroscopy investigation is the identification of the specific force-distance unfolding pattern(s) of the foldamer, molecule of interest, at the single-molecule scale.

To attain this first challenge we relied on a three-step method.

The first step consists in optimizing the experimental functionalization conditions to sparsely graft the molecules of interest on the substrate so that the tip of the cantilever can ideally interact with only one molecule at a time during its approach-retraction cycles (section 1.3.3). For this step we dipped a freshly cleaned gold-coated surface in a dilute co-solution of the thiol-activated foldamers and a much higher amount of passivating molecules (details in Appendix B.). The passivating molecules are much smaller molecules that promote the foldamers to spread over the surface and to adopt a vertical position, and also prevent strong adhesion between the AFM tip and the bare gold surface, which otherwise could mask the unfolding signal. A schematic representation of the ideal set-up is given in Figure 2.6.

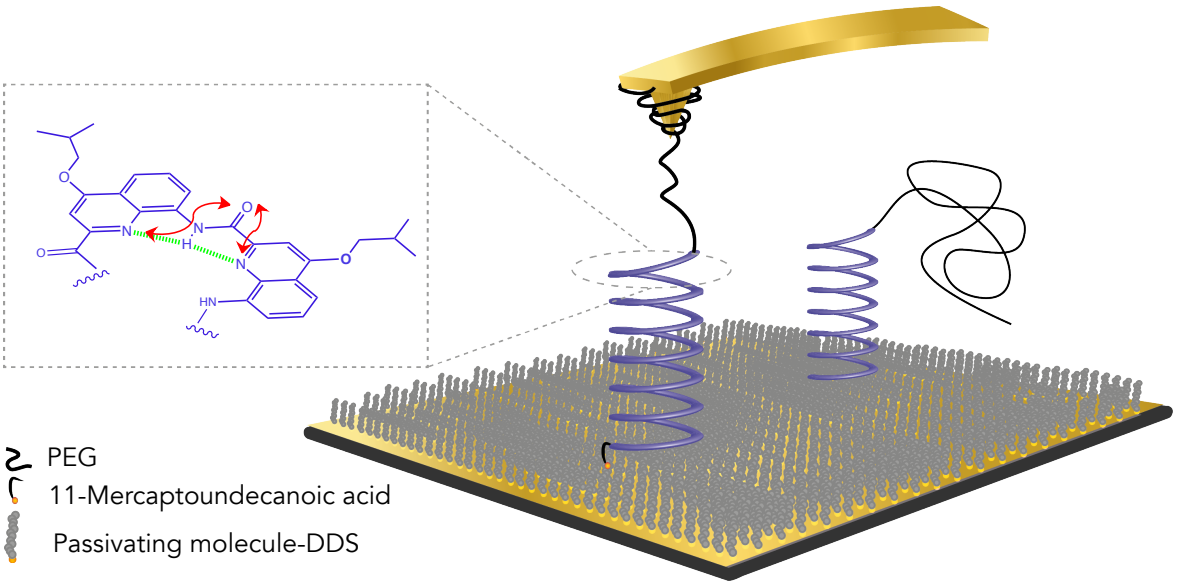

Figure 2.6 Illustration of the functionalized AFM set-up/substrate with the molecules of interest (SH-R-$^{m}QQ_{n}$-PEG), interacting with the AFM tip, and the passivating molecules layer. (Not at scale)

The second step lies in finding highly reproducible force-distance patterns, which match the theoretical features and expectations. Reproducibility of the pattern is a reliable parameter to prove that single molecules are stretched. The chance of pulling several times on 2 or 3 molecules with exactly the same geometry of attachment to the tip is significantly lower than having only one molecule. In our case the tethering with a PEG linker helped also a lot, as its stretching pattern is known and can be fitted with a WLC model at low-force regime. As explained in the previous section, the experimental PEG signal can be compared to a fit calculated with the l_p value (~ 0,3 nm) corresponding to one single PEG chain and be exploited as a reliable selection rule. The exact L_c value is meaningless in our case, as we coped with random physisorption of the PEG, which can take place at any position.

The third step applies a statistical analysis of the outlier values of the measurements. During the repeating experiments, some undesired phenomena can take place and have random effects on the force-distance curves. These irregularities may escape the experimenter's eye control. By plotting 2D graph of two related parameters (force and length) or plotting distribution of parameters, some outliers can be identified and discarded if they are statistically irrelevant.

2.2.2 Identification of the unfolding patterns of quinoline-based foldamers

Under these precautions, a reproducible force-distance profile could be identified for each size of the studied quinoline-based foldamers. As foreseen, the unravelling pattern of the PEG random coil helped us to identify the specific unfolding pattern of each foldamer. Represented here below (Figure 2.7), the representative force-distance profile of each foldamer displays a particular unfolding pattern embedded in the unravelling pattern of the PEG.[19] Although we recorded some premature-ended profiles due to too weak PEG-tip interactions (Figure 2.8.B), it is worth noting that the design enables to observe the full unfolding of the foldamers. We observed that the PEG-tip interactions can reach up to 800 pN. A force-distance curve where the tip did not catch any foldamer is represented in Figure 2.8.A.

Confirmed below by statistical and quantitative analysis, a unique pattern is observed for each foldamer. As illustrated in Figure 2.7, the force-distance curves are similar for all sizes and can be divided in 4 parts for the longer foldamers (Q33, Q17 and Q9) and 3 parts for Q5, highlighting different mechanical behaviours in each part.

Moreover, to tackle some calibration limitation of the cantilevers, we validated the comparison between foldamers of different sizes by performing some pulling experiments on substrates co-functionalized with foldamers of two different sizes.

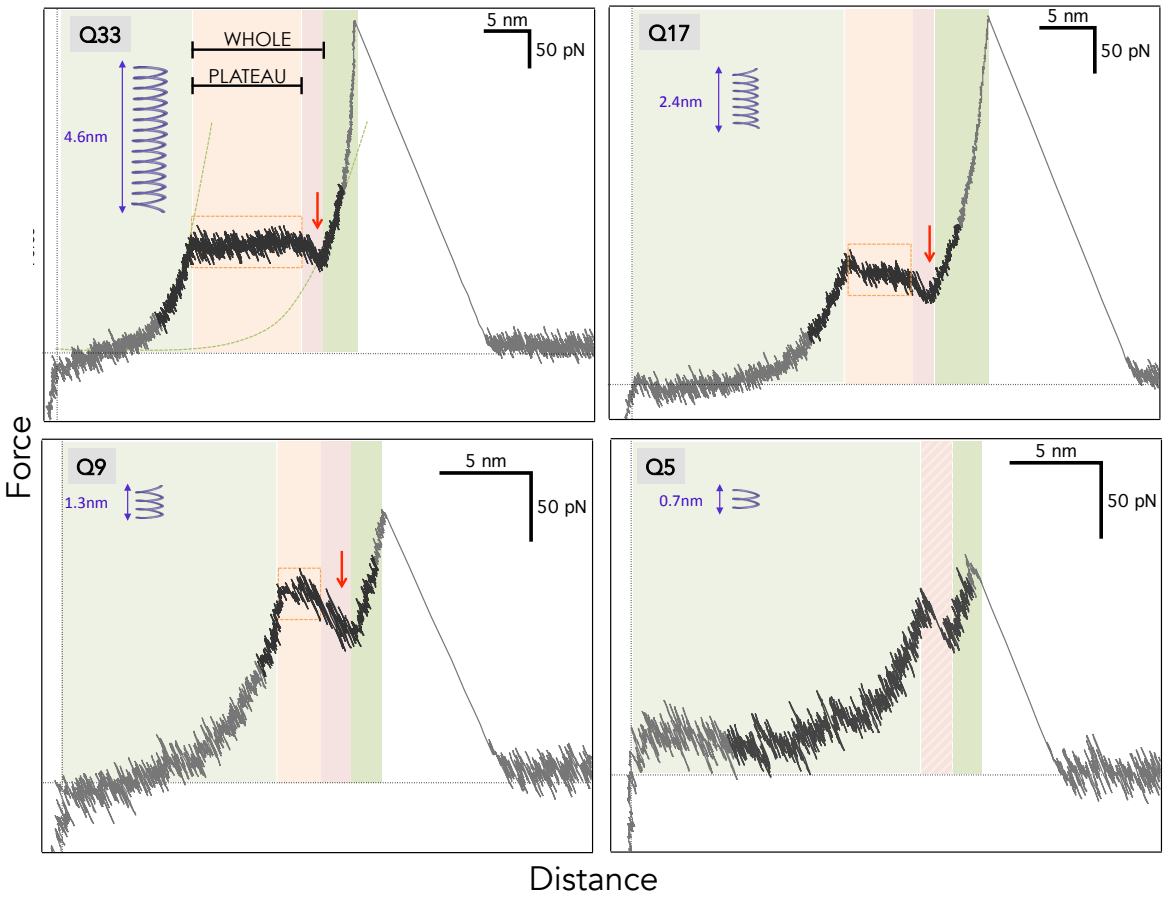

Figure 2.7 Representative force-distance curves of pulling experiments on foldamers made of n= 33 (Q33), 17 (Q17), 9 (Q9), 5 (Q5) units (including an aminomethyl quinoline (^{m}Q) at the amino terminus of a n-1 oligomers made of quinoline−8-amino-4-isobutoxy-2-quinolinecarboxylic acid (Q)) (for clarity the approach curve was omitted). The plateau is highlighted in a frame and a red arrow shows the decreasing-force feature. On the curves of Q33, the green dashed lines are WLC fits. They help to identify the unfolding pattern of the foldamer, as guiding lines. The coloured zones display the different mechanical behaviours.

In Figure 2.7, at low force regime (light green zone), the **entropic elastic profile** of the PEG can be observed up to a certain force value (green WLC fit). From this force value, the force-distance signal abruptly changes to exhibit a **force-constant plateau,** for foldamers made of 33, 17, and 9 quinoline units (orange zone). The plateau is followed by a **force-decreasing and oscillating feature** (red zone). In the case of the 5-mer, these 2 last patterns are not separately distinguishable and will be discussed further later in the manuscript. Finally, for all foldamers, the force rises again non-linearly as the unfolded molecule **stretching** continues until the PEG detaches from the tip (green zone). The signal deviating from the entropic elastic behaviours can be clearly attributed to the foldamers and suggests a significant conformation transition.[19]

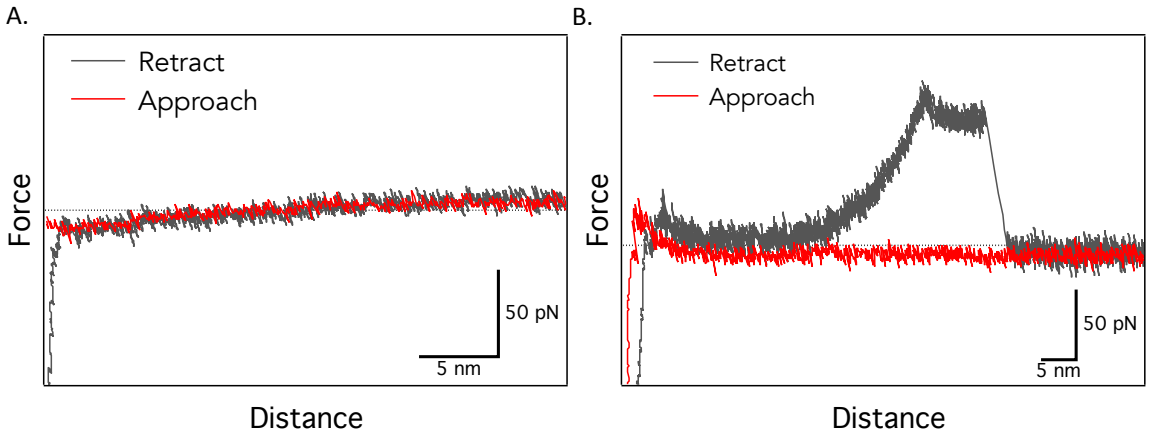

Figure 2.8 Force-distance curves of an approach-retraction cycle where (A) no foldamer was caught; (B) the foldamer detaches prematurely.

2.2.2.1 Qualitative interpretation of the plateau

In pulling experiments on 33-, 17-, and 9-mers, reproducible unfolding patterns of the foldamer comprise the force-constant plateau and the force-decreasing and oscillating feature at the end of the plateau. A plateau pattern has already been observed in the unfolding pattern of biomolecules, whereas the force-decreasing and oscillating feature is uncommon to our knowledge.

The force-constant plateau can be interpreted as subsequent ruptures of identical and sub-nanometric groups of interactions. It means in other words that the molecular helices mainly unfold by stepwise opening of parts of the helix and not uniformly like a macroscopic spring.

Theoretically, the turn-by-turn opening was proven to be the most energetically favourable mechanism for the unfolding of an α-helix made of 20 alanine residues.[20] Recently, force-probe molecular dynamics simulations (FPMD) on highly similar systems (isopentyl-groups instead of isobutoxy-groups as side chain, (see Figure 2.9.A&B) in chloroform are in agreement with a stepwise opening mechanism.[21] Although the significant loading rate difference hampers the comparison, we can mention that L.Uribe *et al.* theoretically identified precisely the unfolding mechanism. They measured in average the opening of the two H-bonds from the extremities to the centre (Figure 2.9.C& D).

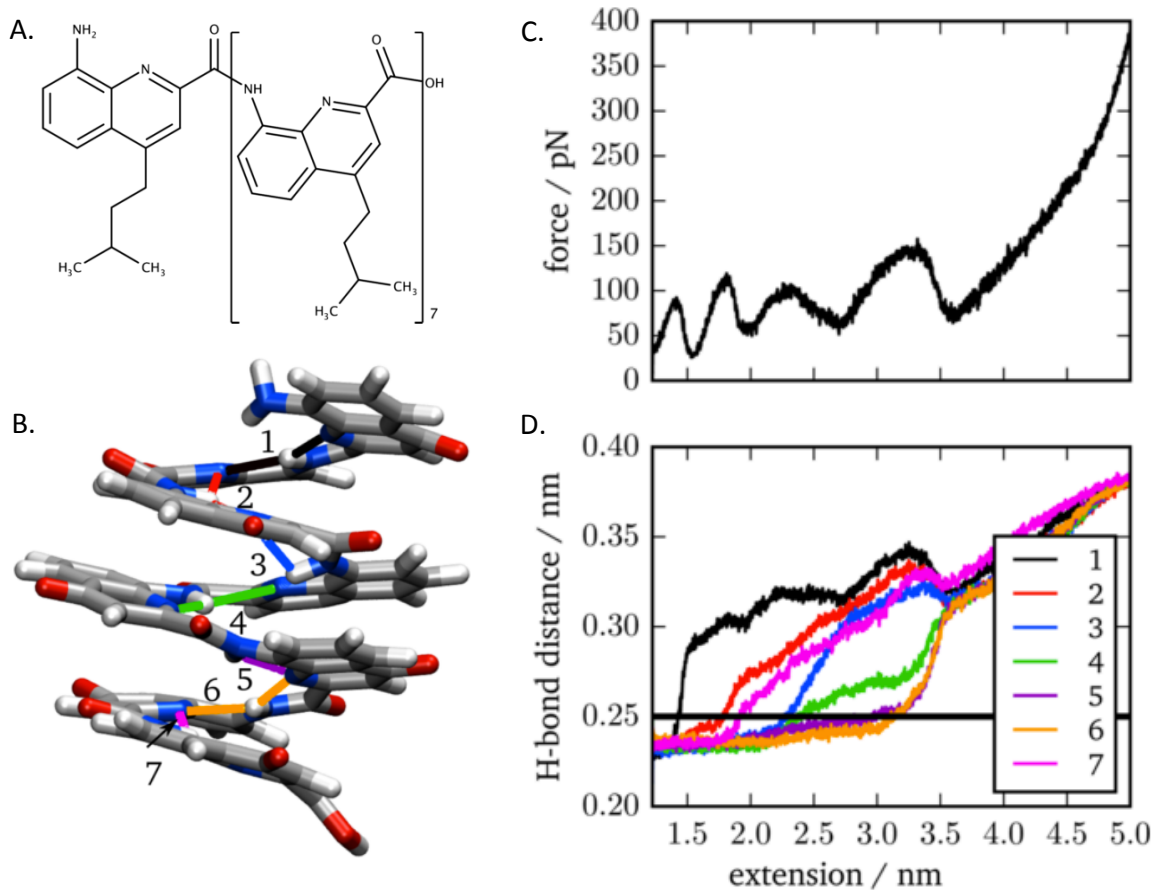

Figure 2.9 Force-probe molecular dynamics. (A) Chemical structure of the octamer of 8-amino-4-isopentyl-2-quinoline-carboxylic acid. (B) Schematics of the helical conformation adopted by the octamer with the different H-bonds highlighted in colours. (C) Typical Dynamic strength curve (average of 100 force-extension curves) of force-probe molecular dynamics simulation (FPMD) on the octamer with k= 100 pN.nm^{-1} and v= 0.1 m.s^{-1} at T= 200K and (D) its corresponding native contacts vs. extension curve with each coloured H-bonds from B. Adapted from the reference 21.

The fact that distinguishable peaks, associated to each subsequent rupture, are not observable in the experimental plateau can be explained either by a too low signal-to-noise ratio or by dynamical reasons.

The main noise contribution stems from thermal excitation of the cantilever motion.[22] In general we can consider the resolution of the measurement in force to be limited to $\Delta f \approx \sqrt{(k_B T.k)} \approx 10$ pN and in extension to $\Delta x \approx \sqrt{(k_B T/k)} \approx 0.4$ nm, with k= 30pN.nm^{-1} and at room temperature.[23] Therefore, we can imagine that the fluctuations of the cantilever due to Brownian motion can be comparable to or larger than the hidden length of each group of interactions. However, under tension, the thermal noise is damped, as we can see on the force-extension curve just before the plateau starts. In our case, on the contrary, enhanced fluctuations can be observed in the plateau. Thus, this indicates, on one hand, that the traces display specific unfolding features and on the other hand, that the invisibility of the peaks has another origin.

Another explanation comes from the dynamics of the systems and from the fundamentally kinetic view of an unbinding process.[24,25] If the on-off dynamic of unbinding and rebinding of the interactions is much faster than the pulling rate, the consecutive unbinding events occur in equilibrium and consequently the heights of the peaks decrease. As a result the unbinding signal may be dissimulated in the noise and results in a flat plateau.[19,26]

An example that illustrates this effect is the pulling experiments at several loading rate on mechanically interlocked oligo calix[4]arene[27]. As we can see in Figure 2.10, the heights of peaks recorded at the (a) slowest speed are low and almost masked compared to those measured at the (b) higher loading rate, indicating near equilibrium regime for the first experiment and far from equilibrium for the second. The identification of the peaks is still manageable thanks to a long enough slack (1.5-2 nm) given by the entangled loops of the interlocked oligo calix[4]arene system.

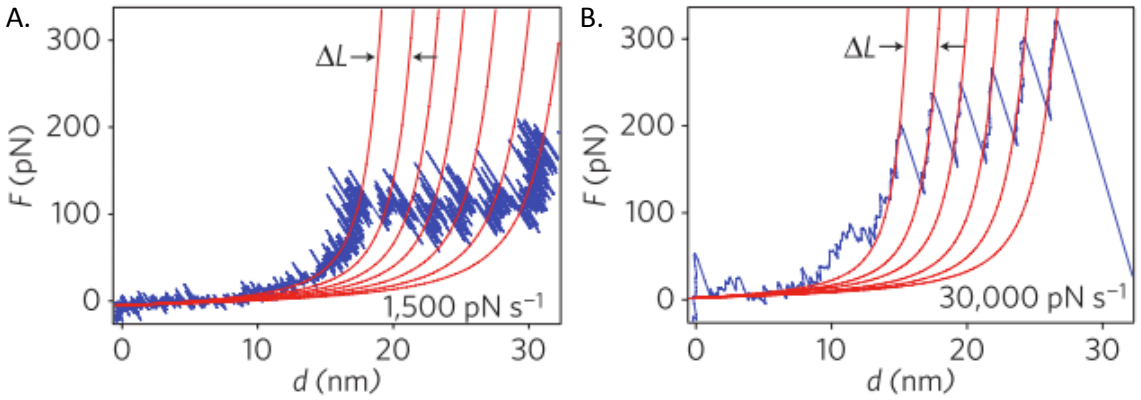

Figure 2.10 Force-distance curves of pulling experiments on oligo calix[4]arene at two different loading rates (a) 1500 pN.s^{-1} and (b) 30000 pN.s^{-1}. Adapted from reference 27.

We can thus already suggest by this observation that the longer foldamers exhibit fast dynamics of the intramolecular interactions responsible for the folding of the helical structure. This can be explained by the permanent close proximity of both interacting partners. In-depth discussion on dynamics is given in chapter 3.

2.2.2.2 Qualitative interpretation of the force-decreasing and oscillating feature

To our knowledge, this force-decreasing and oscillating feature (red zone) has not been observed in any system studied by SMFS. At the end of the plateau, the force decreases along a detectable distance. Since the basis of SMFS suggests that, when a molecule is stretched,[28,29] the first interactions to break are the weakest ones, this observation implies that some interactions have lost some strength upon unfolding. This weakening reveals at the same time longer hidden lengths. This observation exposes a cooperative process of folding, as it becomes easier to unravel the foldamer at the end of the unfolding process.

When we thoroughly scrutinize this feature in the 33-, 17-, 9-mers unfolding patterns, we observe 3 different patterns: either a progressive decrease in force (left curve of each graph on Figure 2.11) or large fluctuations between folded and unfolded states (centre curves on Figure 2.11), also called hopping events, or a single peak of rupture (right curves on Figure 2.11). These differences indicate some instability in this step of the unfolding, emphasizing the cooperativity. This will be discussed in depth in the next section (2.2.3). In parallel, the large back-and-forth fluctuations, *i.e.* the hopping events, give also direct evidence that the foldamer is able to exert a force against the pulling load to recreate the interactions that have been broken beforehand, as the signal is coming to its previous extension. Besides, it supports a really fast refolding dynamics as we can see several hops for a short period of time. This behaviour has been rarely mentioned in the literature[12,30–32]. Analysis of these real-time unfolding-refolding fluctuations contains kinetics information of folding and unfolding process, which will be examined in the chapter 3.

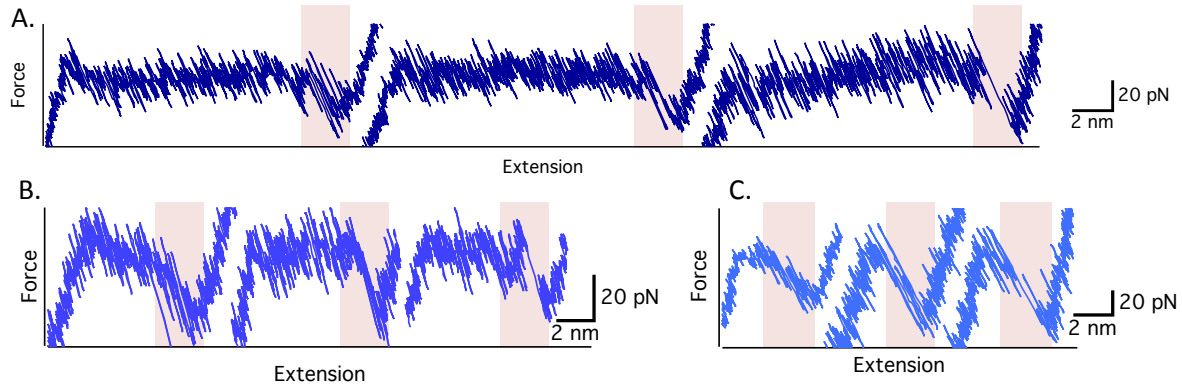

Figure 2.11 Zoom in the unfolding patterns of foldamers made of (A) 33, (B) 17 and (C) 9 units with different ending force-decreasing and oscillating features (highlighted in red). Left curves of A, B, C: a progressive decreasing in force; middle curves: hopping between a folded and an unfolded state; right curves: single peak of rupture.

2.2.3 Quantitative analyses and interpretations

In order to identify the mechanical properties of the foldamers under load and to compare between the different sizes we analysed the average forces and lengths of the whole unfolding pattern (orange + red zones of Figure 2.7) and only of the plateau (orange zone of Figure 2.7) of the 33-, 17- and 9-mers (details in Appendix E.). For a brief reminder, the PEG chain adsorbs unspecifically to the AFM tip, consequently the extension before the unfolding of the foldamer varies randomly, there is hence no point for measuring the absolute length.

We plotted all these data in histograms and we analysed their shapes, their mean values and the widths of the distributions.

2.2.3.1 Analysis of the lengths

Concerning the length of the whole unfolding pattern for each foldamer, we observed monomodal Gaussian distributions with the mean values increasing proportionally with the number of units comprised in the foldamer (Figure 2.12).

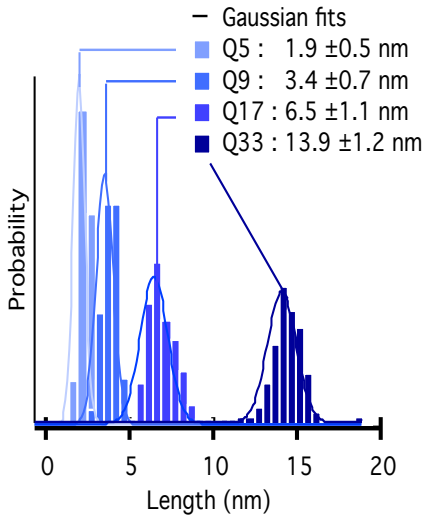

	Folded structure length (X-ray data)	Unfolded experimental structure length	Increase contour length per unit	Percentage of its original length
Q5	0.7 nm	1.9 nm	0.38 nm	370
Q9	1.26 nm	3.4 nm	0.38 nm	370
Q17	2.38 nm	6.5 nm	0.38 nm	370
Q33	4.62 nn	13.9 nm	0.42 nm	400

Figure 2.12 Histograms of the lengths of the whole unfolding of the foldamers of different sizes (foldamers made of respectively 33, 17, 9 and 5 units are coded Q33; Q17, Q9, Q5). In the table: 'folded structure lengths' were obtained from X-ray diffraction analysis and correspond to 3.5 Å per turn and 2,5 quinoline units per turn; 'Unfolded experimental structure lengths' are the mean values of experimental lengths. 'Increase in contour lengths per unit' are the gains for each quinoline unit calculated by dividing unfolded experimental lengths by the number of units; 'percentage of its original length' are obtained as such: (folded length + unfolded length)/folded length.

This analysis confirms the unique existence of the totally folded conformation in solution in opposition to the occurrence of intermediate folded structures. Indeed, the obtained length values are in very good agreement with the calculated length differences (0.39 nm/unit) between a totally folded foldamer (0.14 nm/unit from X-ray structure data)

and the most probable fully unfolded structure (0.535 nm/unit), obtained by the rotation (1) of the C-C(O) bond (Figure 2.13). In a quinoline-based foldamer, 3 bonds can undergo rotation; each rotation and every combination have been tested and are shown in Figure 2.13 (details in Appendix E.2.3). The structure resulting from the rotation (1) of the C-C(O) bond is a candidate to explain the experimental unfolded structure. Besides, it is in a really good agreement with calculations of torsion energies of the C-C(O) and C(O)-N bonds by Delsuc *et al*[2], as well as with the already mentioned force-probe molecular dynamics simulation[21] and with another meta dynamics study[33]. This latter meta dynamic investigation identified the rotation of the C-C(O) bonds as the handedness inversion driving factor for 4- to 6-mers.

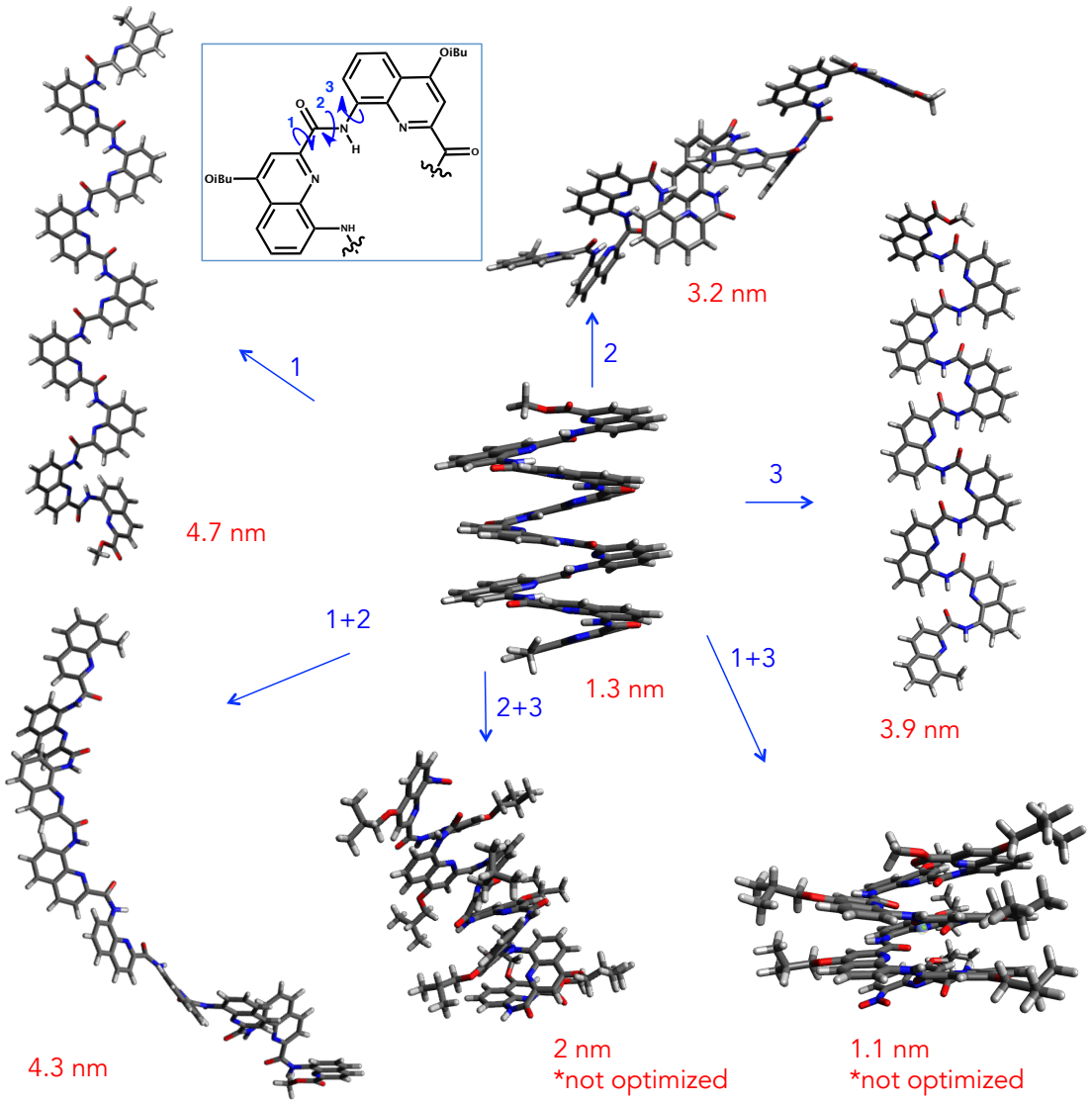

Figure 2.13 Schematics of structures obtained after rotations of rotable bonds in quinoline-based nonamer and energy minimization. In the inlet, the allowed rotations are displayed and numbered. For each unfolding attempt, the rotation in play is mentioned on the arrow. Lengths between the extremities of the oligomer are written in red below the rotated (stretched) structures. Atoms are colour-coded as carbon in grey, hydrogen in white, oxygen in red and nitrogen in blue.

This rotation of each C-C(O) bond between each quinoline unit yields an extension of around 380 % times its original folded state. In the folded state, one unit accounts for 0.14 nm in translation along the helical axis (X-ray data), in the extended states, they gain ~ 0.4 nm.

In parallel, we measured separately the length of the force-constant plateau for the 9-, 17- and 33-mers (orange zones of Figure 2.7). In Figure 2.14, we calculated a similar length difference of ~2 nm between the whole unfolding (orange plus red) and the plateau (orange) length for each foldamer, which corresponds to the length of the decreasing-force feature (red). This observation is interesting for two reasons. First, given that the length of the decreasing-force feature is independent of the number of units in the foldamer, it indicates that this ending feature of the unfolding pattern does not correspond to a subsequent conformational change from an intermediate unfolded conformation to the final one, as this would be length-dependent. It thus also suggests that the unfolding takes place directly through the suggested rotation above. Secondly it suggests a common unfolding segment for each foldamer, which can also be associated to the length of the unfolding pattern of Q5 (1.9 nm, Figure 2.12) and to a helix nucleation segment, as it will be largely discussed below, supported by the force analysis. The nucleation segment is the minimum number of units, which is required to create an energetically favoured folding (see details in 2.2.4).

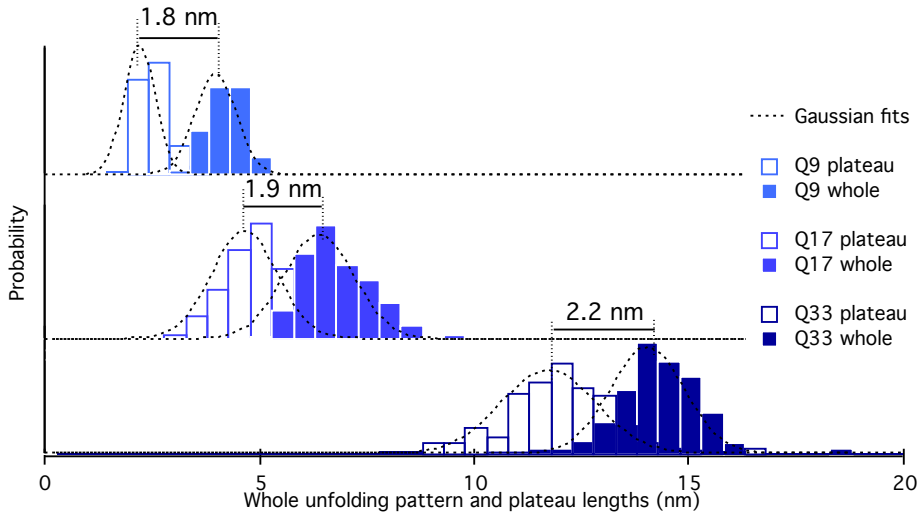

Figure 2.14 Histograms of the whole pattern (orange plus red zones in Figure 2.7) and of the plateau (orange zones in Figure 2.7) lengths for the Q33, Q17 and Q9.

In summary, the length values of the whole unfolding pattern, which is directly proportional to the number of units, enabled us to identify the fully folded state in solution. It also highlighted the great extensibility of these helical structures and suggested the rotation of the C-C(O) bond as the unfolding pathway, which is reinforced by theoretical studies and which leads directly to the most possible extended conformation. At this point,

it is difficult to say if the unfoldings take place through a single or two rotations and through an end-to-centre mechanism, as suggested by Uribe at al.[21] Finally, we identified that the particular decreasing-force feature is size-independent, likely revealing a nucleation segment and cooperativity.

2.2.3.2 Analysis of the forces

The second parameter that we investigated is the value of the **forces** required to unfold the foldamers. In order to compare all foldamers together, we averaged, in a first phase, force data value from the beginning to the end of the unfolding of the foldamer, *i.e.* the points comprised in the plateau and in the decreasing-force feature (orange + red zones in Figure 2.7). In a second phase, we measured the average force of the isolated plateau (orange zone in Figure 2.7) for the Q9, Q17 and Q33.

The histograms of average forces of the whole unfolding patterns can be fitted with mono-modal Gaussian distributions centred on a value, which do not evolve linearly with the number of units in the foldamer. From shorter to longer foldamers, the average force increases from ~ 70 pN until it reaches a maximum value of ~ 100 pN between 9 and 17 units (Figure 2.15.A).

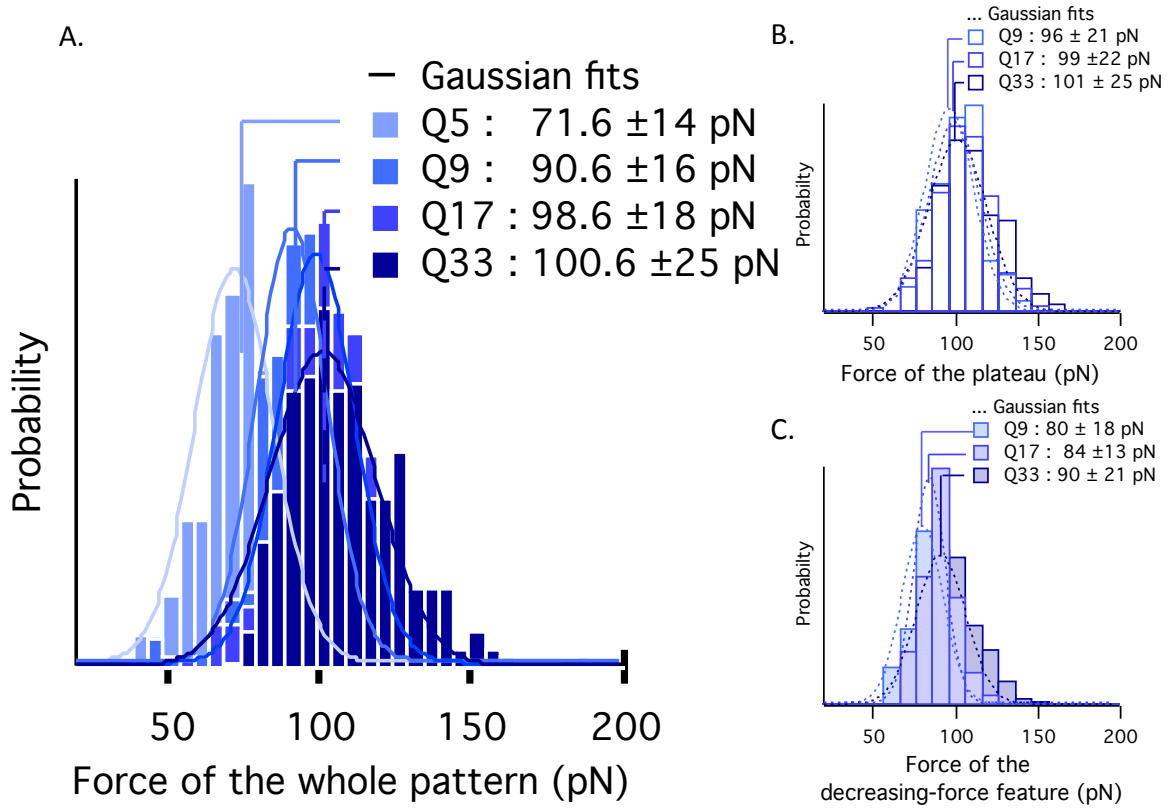

Figure 2.15 Histograms of (A) the average forces of the whole unfolding pattern of each foldamer. (B) the average forces of the plateau of each foldamer except Q5*. (C) the average forces of the decreasing/oscillating-force feature at the end of the unfolding of each foldamer except Q5*. (*as plateau and decreasing-force feature are not distinguishable). Foldamer made of respectively 33, 17, 9 and 5 units are coded Q33, Q17, Q9, Q5.

Firstly, the force values are higher than natural analogues of the foldamers (section 1.4 and details discussion in section 2.3). Secondly the particular evolution of the force values as a function of the number of units in the foldamer indicates that the addition of units reinforces the structure up to a given limit (Figure 2.16). This confirms the cooperativity effect within the structure. In parallel, looking at the average force values of the plateau, their differences can be considered as negligible (96-101 pN, see (Figure 2.15.B)). Nevertheless, a slight decreasing slope is observed in the plateau in the 33-mer (ΔF~10 pN), which corroborates the cooperativity propagation and the low differences in the evolution of force of the plateau. We could thus conclude that the force evolution in the whole pattern comes mainly from the ending feature that counts for an increasing statistical weight from long to short foldamers. In Q33, this feature accounts for 15 % whereas in Q17 for 30 % and Q9 for ~60 %.

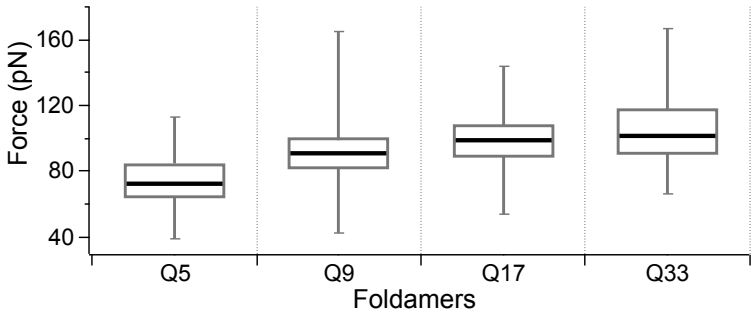

Figure 2.16 Box-plot of the the average forces of the whole unfolding pattern of each foldamer

In addition, investigating scrupulously Q5, we observed several patterns which all resemble the ending features of the longer foldamers (Figure 2.11). They have a similar length but the amplitude of the signal of Q5 is lower than in the others (Figure 2.17) and the average value of the force is also lower (71.6 pN) than those for this ending feature in the longer foldamers (80 to 90 pN, Figure 2.15.C).

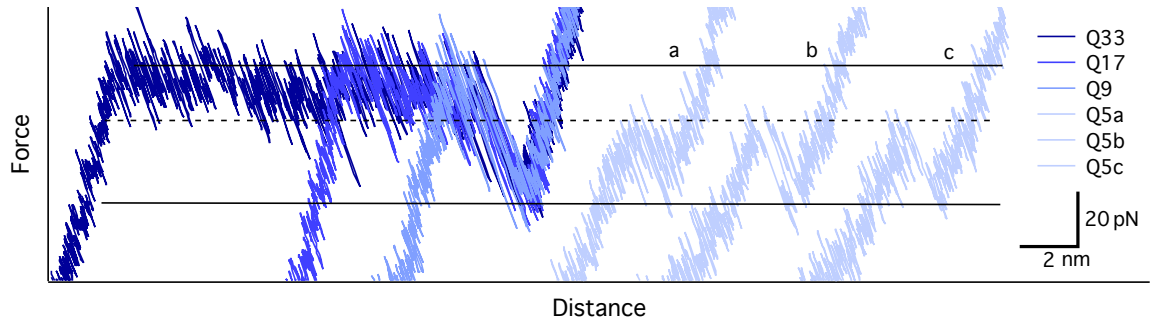

Figure 2.17 Force-distance curves of Q33, Q17, Q9 and Q5. Q5 curves exhibit overall smaller amplitude than the amplitude of the decreasing/oscillating-force features of Q33, Q17 and Q9.

The measurements on Q5 strongly suggest that the cooperativity is limited for 5-mer. Hand in hand with the observations from the other foldamers, the existence of a cooperative helix nucleation segment could be detected and suggested to be constituted of a little more than 5 units. Moreover given the results of the Q5 (lower force and smaller

signal amplitude) we can not exclude a non-negligible probability of pre-unfolded conformations in solution, which would consequently required a lower force. This is also supported by the handedness inversion analysis evidence of fast dynamics for Q5.[2]

In conclusion, the average force to unfold quinoline-based foldamers of different sizes increases with the length of the foldamer up to a limit. This observation highlights the cooperativity upon folding and the existence of a minimum number of units to reach a cooperative reinforced structure: the nucleation segment. It has not been clearly evidenced in previous studies. The average force measured can be considered as high, due to the nature of the intramolecular interactions involved in the probed helical structure. The high forces and stabilities arise jointly from a strong disfavoured bond rotation owing to a loss of aromatic conjugation and local electrostatic attractions and repulsions.

2.2.4 Origin and insights into the nucleation segment and cooperativity

As explained by Moore[34], assuming a helix with N_i unit per turn, as illustrated in Figure 2.18, the first coil-helix transition step consists in constraining the units to undergo a random coil-helix conformation change, which is a total loss of entropy and constitutes the nucleation phase. From the coil-helix conversion of N_{i+1} unit, the gain of enthalpy starts compensating the entropy loss. From this point cooperativity effect should be considered. Eventually the gain of enthalpy overcomes the loss of entropy, which leads to a negative free energy, resulting in the energetically favourable helical folding.

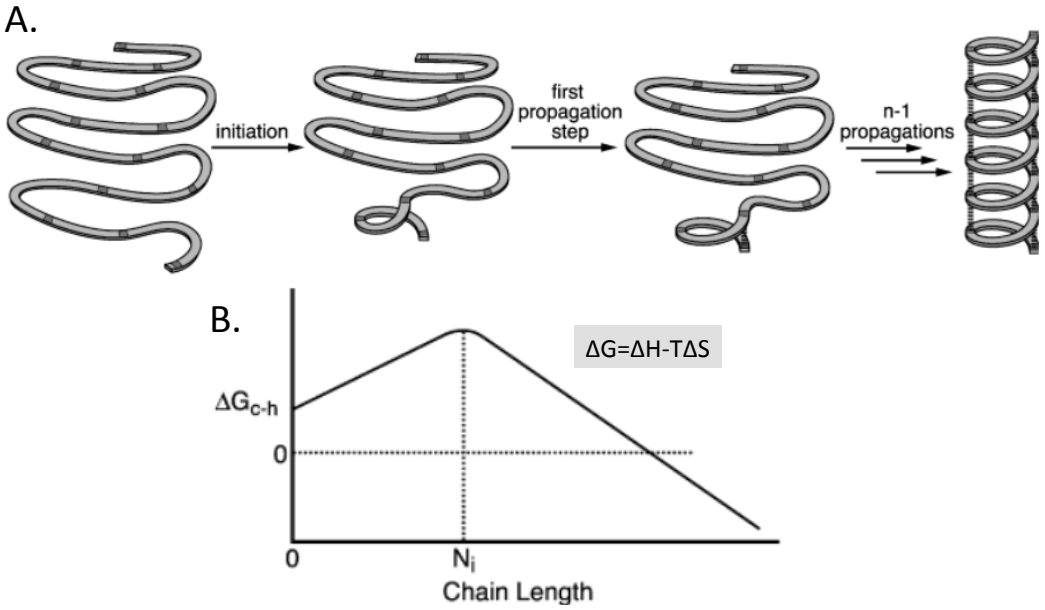

Figure 2.18 (A) Schematic representation of the nucleation and propagation steps in the coil-helix transition. (B) Graph of the free energy for the transition coil-helix $\Delta G_{c\text{-}h}$ as a function of the number of units (Ni) in the sequence. ΔG is positive during the nucleation phase and then becomes negative when enthalpic gain owing to favourable intramolecular interactions counterbalances the entropic loss of constraining the chain in the folded conformation. Adapted from reference 34.

Concerning the pulling experiments, opposite helix-coil conversion can be examined. At the end of the unfolding of the foldamers, the force to unfold decreases and the unfolding takes place either in a single step or progressively with intermediates states, *i.e.* the remaining helical structure is mechanically weaker. This instability can thus be explained by a loss of favourable enthalpic interactions to compensate the entropic cost of helical folding for the last remaining folded units. Given that the hidden length liberated in the force-decreasing feature is around ~2 nm, it corresponds to the elongation of 5-6 units. This elongation can be associated to a minimum of 2 turns (2.5 unit/turn) and hence concurs with the stabilizing network of π-stacking. This corroborates perfectly with the characteristic of cooperativity given by Moore as well[34]:

"*Cooperativity cannot be achieved for systems that fold exclusively from noncovalent interactions between repeat units held adjacent by covalent bonds or more specifically interacting sites held adjacent by covalent bonds"*.

To sum up, the helical structure is still stable for sequence even smaller than the helix nucleation number owing to its intrinsic stability (backbone rigidity) and to the H-bonds while it is significantly reinforced when the sequence is longer than 5-6 units, owing to the π-stacking. We could measure that to observe a plateau characteristic of a reinforced structure, a minimum of 6-7 units is required.

2.2.5 Confirmation of the cooperativity with literature results

The cooperativity was already suggested when investigating handedness inversion experimentally and through meta-dynamic simulation. Experimentally, the half-lives of racemization of handedness inversion were measured for quinoline foldamers of several sizes and these measurements clearly highlighted that the longer the foldamer is, the slower the inversion process is.[2] This indicated an increase in mechanical stability for longer foldamers. From the half-life values of racemization at various temperatures, using the Eyring equation, Gibbs energy barriers of activation between right-handed (P) or left-handed (M) helices could be measured. These energy barriers provide the energy difference between the folded helix and the most energetic transition state (limiting step) where the oligomer is partially unfolded to undergo helical handedness inversion. These values are represented in Figure 2.19 as a function of the number of units and as observed with the unfolding forces obtained in this thesis, the energy increases non-linearly with the addition of units until reaching a limit (Figure 2.16). A clear stabilization can thus be deduced as units are added to the sequence. Although, the mechanism of handedness inversion probably does not involve a total unfolding conformation (undergone in SMFS), we can draw similar conclusion.[2]

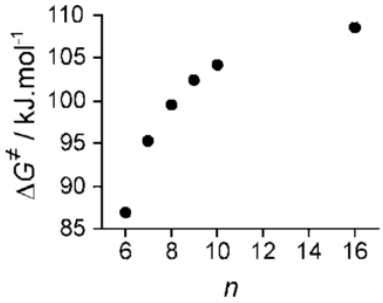

Figure 2.19 Trend of the Gibbs energy of helix-handedness inversion as a function of the number of quinoline units in the oligomer. Reproduced from reference 2.

Finally, the meta-dynamics study carried out by V. Pophristic[33] proposed an atomistic level mechanism for the handedness inversion and they calculated the free energy profiles for side-chainless quinoline tetramer to hexamer. Their inversion takes place firstly by the rotation of the second C-C(O) bond, then propagates by simultaneous further rotation of this latter bond to the opposite handedness and the rotation of the next C-C(O) bond (Figure 2.20 A). The barrier to overcome each rotation is written in the following table.

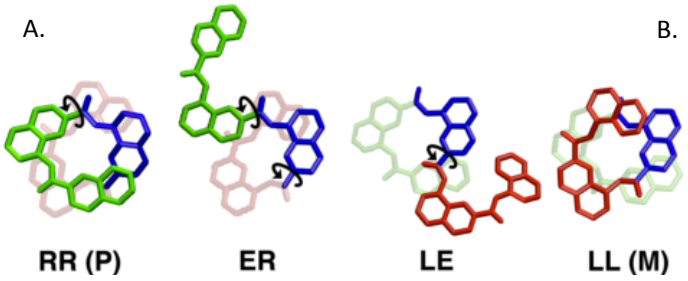

B.

Barrier energy (kcal/mol)	C-C(O) rotation number			
	2	3	4	5
Tetramer	9.5			
Pentamer	11-12	15-16	12	
Hexamer	11-12	16-17	16-17	12-13

Figure 2.20 (A) Snapshots from metadynamics simulation of pentamer, showing the handedness inversion mechanism and characteristic conformers on the RR↔ER↔LE↔LL (P: right-handed helix; M: left-handed helix, E stands for extended, L for left and R for right). path. Quinoline units are coloured differently for clarity; #1 and #2 are green, #3 is blue, #4 and #5 are red. Black arrows indicate 180°rotation of the C(O) bonds, leading to the subsequent conformer along the pathway. (B) Table of the barrier energies (in kcal.mol^{-1}) to overcome each intermediate step along the handedness inversion of quinoline-tetramer, pentamer and hexamer. Adapted from reference 33.

A slight increase in energy can be observed with the increasing length of the foldamer. This evolution is again in good agreement with the results obtained in this thesis. We can then conclude that the more the probed interactions are enclosed by other quinoline units, the higher is the energy/force to overcome them.

2.2.6 Force-distance signal analysis: insight into intermediate unfolding steps

Before the foldamer starts to unfold (green zone, in Figure 2.7), the amplitude of the fluctuation is damped as the tension increases. When the plateau starts, the amplitude abruptly increases (orange zone). This enhanced amplitude of the traces in the unfolding pattern of the foldamer reflects the occurrence of unfolding/folding transitions. We tried to decipher this information by several signal treatments. Our attempts to smooth, to Fourier-transform or to filter the signal, as well as to superimpose several force-distance curves were unsuccessful. Only the conversion of force spectroscopy data into the contour length space, *i.e.* a molecular coordinate, sheds some light on the unfolding mechanism.

Suggested by Puchner *et al*,[35] the analysis of the contour length (L_c) evolution over unfolding allows us to reveal directly the intermediate (un)folding states and the energy barriers occurring between the fully folded and unfolded states. As presented in the introduction (section 2.1.2.2), the contour length is a variable of the worm-like chain (WLC) model, a model of statistical mechanics describing the entropic elasticity of a single polymer chain. The L_c value corresponds to the extended length of a molecular system (see L_1 and L_2 in Figure 2.21, they represent the contour length of two different folded states of the molecule (referred to as 'folding state' in the Figure 2.21)). This variable is therefore a more appropriate variable than extension owing to its independency on thermal fluctuations and external experimental parameters: "It directly reflects the folding state of the molecule".[36]

The force-extension data were converted into contour length space, using the WLC equation. Histograms of the calculated L_c value are drawn to directly display the intermediate unfolding states (Figure 2.21).

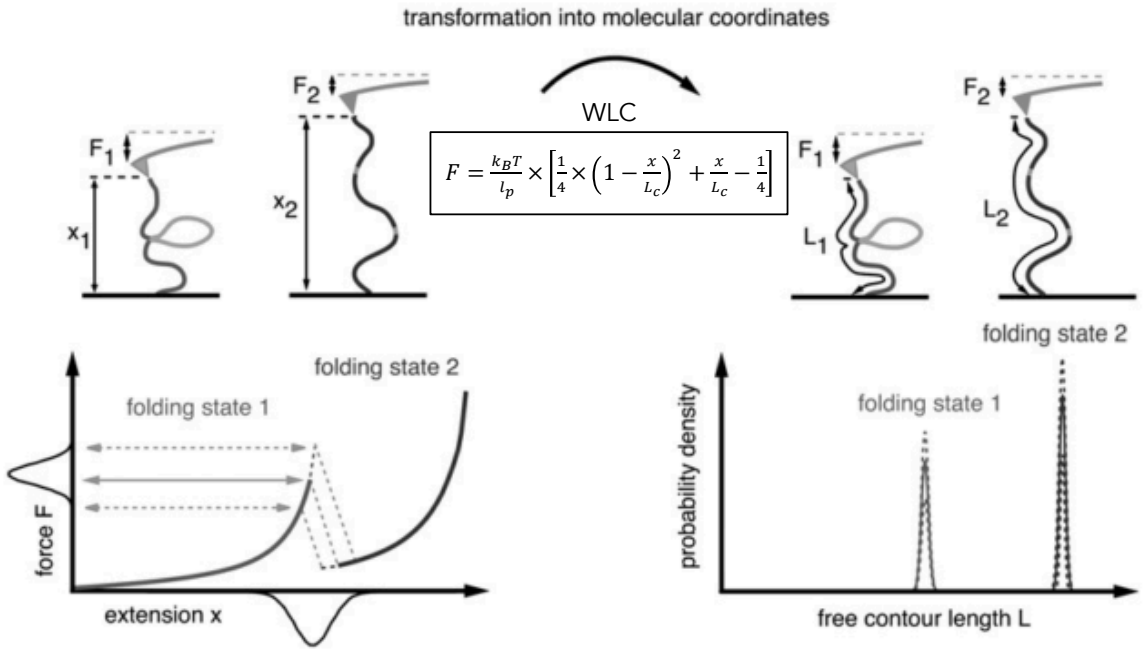

Figure 2.21 Transformation of force spectroscopy data from extension space into contour length space. The left side illustrates an AFM experiment. During the retraction of the cantilever, the force and the extension are recorded. In the beginning, the unfolded part of the molecule is stretched and the force increases until the energy barrier is overcome by thermal fluctuations. Further stretching results again in a rise of force. The rupture force and position differs from trace to trace due to fluctuations and may change on altered experimental conditions (dashed lines). On the right side, the transformation of each data point from extension to contour length space and the accumulation in a histogram are shown. Adapted from reference 36.

The force-extension data points of the foldamers unfolding pattern and some surrounding data points (top graph of each panel in Figure 2.22) were converted in contour length space by solving the WLC equation (eq.1 or Figure 2.21) with the persistence length value of 0.4 (several values of l_p have been tested to 0.3, 0.5 and 1, no significant difference was observed) (details in Appendix E.2.5.). In the contour length traces (bottom graph of each panel in Figure 2.22), we observed steady states before and after the foldamers unfolding, whereas, the L_c values increase incrementally along the plateau (each state is highlighted by a dotted line). The two steady states correspond to the fully folded and the fully unfolded states and confirm the continuous stretching behaviours. The incremented L_c value can be associated to each subsequent state having undergone a conformation transition, *i.e*. the intermediate folded states of the foldamers.

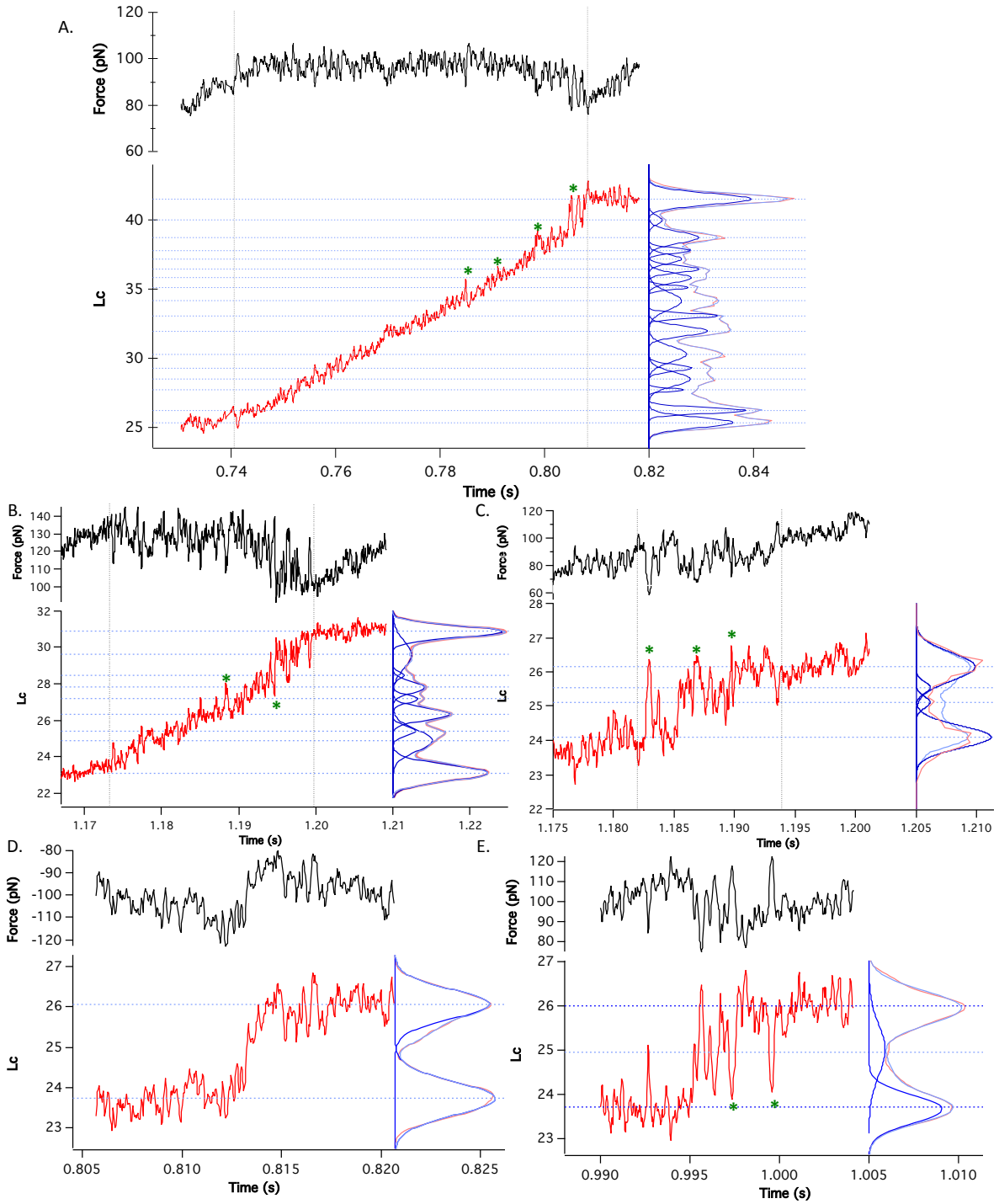

Figure 2.22 Conversion of force-extension curves in contour length (L_c,in nm) space of foldamers made of 33 units (A), 17 units (B), 9 units (C) and 5 units (D, single rupture & E, fluctuations). For each: Top: force as a function of time curve of the raw unfolding pattern (black); Bottom: L_c evolution as a function of time (red) and corresponding histogram of L_c (light red), the multi-Gaussian peaks fitting the histogram (blue) and the overall fit trace (light blue). The dotted blue lines are the mean L_c values of the intermediate folding states and the grey vertical lines mark the foldamer unfolding pattern of the elastic behaviour. Green stars indicate unwinding by simultaneous rotation of 4 units.

The distribution of contour length values (red trace, right part of the bottom graph of Figure 2.22) can be fitted with multiple Gaussian distributions (blue traces on the right of Figure 2.22). As a given value of L_c can be associated to one folded state, we can associate in average 17.3 ± 2 states for the 33-mer, 8.8 ± 1 for the 17-mer, 4 ± 0.5 for the 9-mer and 2 or 3 for 5-mer. These results suggest that each state is likely to be different from each other by the opening/unwinding of 2 quinoline units. They are supported by theoretical observations of Uribe *et al*[21] and in some extent of Abramyan *et al.*[33] Therefore we can suggest that the conformation transition occurs by the simultaneous rotation of 2 C−C(O) bonds. However, 4 units can also unwind simultaneously, as some vertical transitions between 2 non-successive states are sometimes observed (highlighted by a green star). This latter transition takes particularly place for the 9- and 5-mers, and at the end of the unfolding patterns of the longer foldamers, which is in good agreement with our previous conclusion that the cooperative stabilization disappears as interactions weaken progressively when adjacent interactions disappear along the extension. These transitions are often reversible, concurring with the *hopping* behaviour discussed above. A detailed analysis of the unfolding behaviour of the 5-mer corroborates also this interpretation. Two types of signatures (Figure 2.22 D&E) can be observed in the force-distance curves of the 5-mer: either a single rupture peak (D), or a small plateau or fluctuations (E). When a single rupture peak is detected, we observe only the two extreme states (fully folded and fully unfolded) in the contour length trace, whereas a third intermediate state is visible in the contour length trace when fluctuations are detected in the force-distance curve.

The contour length increase for each step is around 0.9 nm. This represents a very small transition and the energy barrier that can be associated is likely to be overcome by thermal energy (k_BT). Therefore, we can presume that, the proposed unfolding steps, *i.e.* simultaneous rotation of two units, is probably driven and thus upper-limited by thermal agitation. This has the consequence of probably eluding the rotation of a single bond. The distribution of the number of intermediate states (17.3 ± 2 states for Q33, 8.8 ± 1 for Q17, 4 ± 0.5 for Q9) concurs with this possibility; the unfolding is not strictly limited to two-rotation steps. In addition, the intermediate states are not perfectly always equidistant (Figure 2.22), suggesting again that a transition step can deviate from two rotations. Indeed, in equilibrium, it is conceivable that thermal energy fluctuations induce molecules to undergo slight variations in their unfolding processes. These differences can be detectable by such SMFS measurements.

When the contour length traces of two unfolding patterns are cross-superimposed, insights into unfolding mechanisms can be obtained[35]. The reproducibility or variations of the unfolding pathway can be analysed.

To analyse the 2D-cross patterns, the first step consists in determining the matching contour length increments of the two unfolding traces, which lies necessarily on the diagonal of the 2D-plot (Figure 2.23). The second step links the matching L_c values with the nearest next one and draws squares with these intersections. Then, several cases can be observed: (i) if in one square there is a L_c value having no match, it means that there is a missing step in one of the two unfolding trace (example in Figure 2.23.B. missing peak is shown by an arrow). (ii) if in one square there is an extra L_c value for each trace but having no match on the diagonal, it means that both unfoldings underwent a different intermediate step. The order of the step is inversed (example in Figure 2.23.B. displayed with horizontal brace). (iii) if no precedent case is encountered, it indicates that the unfoldings follow the same pathway in both traces (example in Figure 2.23.A). Furthermore, given the tiny transition step (~0.9nm), some L_c values (taken into account a 70% confidence interval) superimpose each other, which prevents us to clearly identify the step. Indeed, a broad-distributed L_c value of a given trace can match with two L_c values of the other trace. These uncertainties are encircled in Figure 2.23 B.

The cross-superposition of contour length traces of the unfolding patterns of 33-mers confirms that the unwinding occurs most of the time by the same pathway, *i.e.* subsequent rotation of 2 units (Figure 2.23.A). However, we can occasionally observe partially different pathways (Figure 2.23.B highlighted by the arrows and braces). Therefore, although unfolding by the rotation of 2 units appears to be the most probable pathway, it may also occur by the rotation of a single C−C(O) bond or by more than two bonds, and refolding happens as well. For short foldamers, the fewer intermediate states reduce the number of possible pathways(Figure S4 and S5).

Unfortunately, owing to the repeating nature of the units, the values of the ΔL_c between two subsequent steps are equivalent (except occasional variations) all along the unfolding. Therefore, we have no clue to detect where the opening occurs on the sequence along the process. Indeed, the rotation of two units in the beginning of the helix yields the same increase in length, *i.e.* equivalent ΔL_c value, as the rotation of two units somewhere else in the helix.

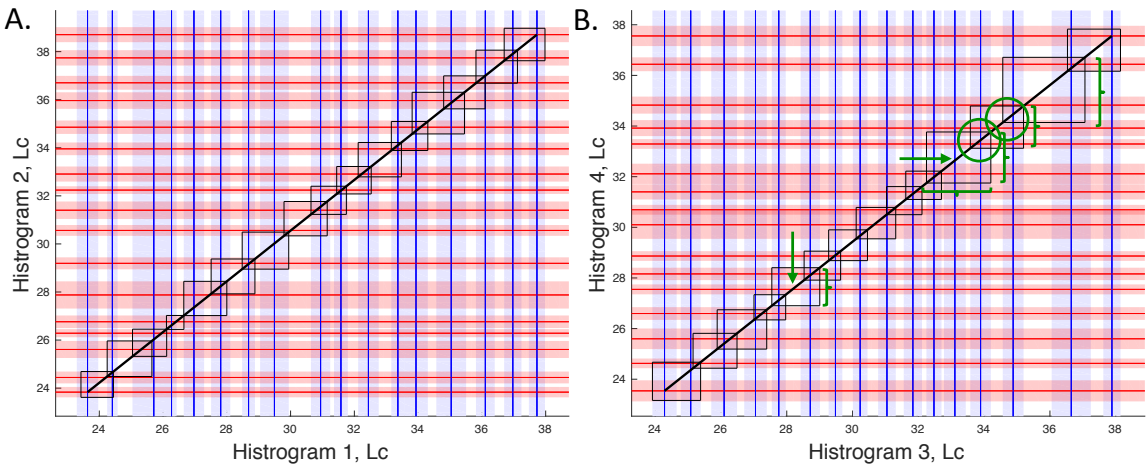

Figure 2.23 Cross-superimpositions of 4 L_c evolution histograms (2x2). Red and blue lines represent the mean L_c values of the Gaussian fits of the histograms. Transparent red and blue zones represent 70% of confidence interval (CI) of the position of the intermediate state (not negligible at this scale). Unfolding steps are determined by drawing rectangles between intersecting L_c value increments. If these intersections occur on the diagonal (black line) it implies that the same unfolding step occurs for both unfoldings. Since we need to take into account the CI, drawn rectangles comprise every potential step along unfolding. In A, diagonal rectangular are always between 2 intermediate states, while in B, we observed missing peaks (arrows), steps between 3 intermediate states (braces) and uncertainties (circles).

In conclusion, the conversion of the force-extension data point into contour length space allowed us to propose an unfolding pathway of the quinoline-based foldamers. We identified that most of the time, the foldamer unfolds by the simultaneous rotation of 2 C-C(O) bonds. Nevertheless, some evidences show the possibility of only one rotation or more than two rotations per step. This unfolding pathway seems to be driven by thermal fluctuations and occurs in equilibrium conditions, which is consistent with all the previous results.

2.3 Comparison with natural helical counterparts

As presented in the introductive chapter (section 1.4.2), several biological molecules presenting helical structures have already been explored by SMFS. With the aim of evidencing important characteristic to achieve molecular functions and properties or to understanding the chemical origins of dynamical functions, this section deals with comparing the performances, of the synthetic helical quinoline-based foldamers with natural helical structures discussed in the literature.

However, we should acknowledge significant differences for the comparison. Firstly, natural systems are mostly investigated in aqueous solution, whereas the foldamers were investigated in organic solvents (principally in N,N-dimethylformamide). Compared to aqueous solution, organic solvents intrinsically reinforce electrostatic interactions, as they have lower dielectric constants than water. Secondly folding factors and structures are not directly comparable, quinoline-based foldamers are abiotic foldamers (Figure 2.24.D). For instance, in α-helix (A), H-bonds are parallel to the helical axis while in the foldamer they are perpendicular. The helical coiled-coil structure (B) in protein involves two or more strands, which interweave owing to mainly hydrophobic interactions. In the double helix B-DNA (C), two strands intertwined together to build up the structure.

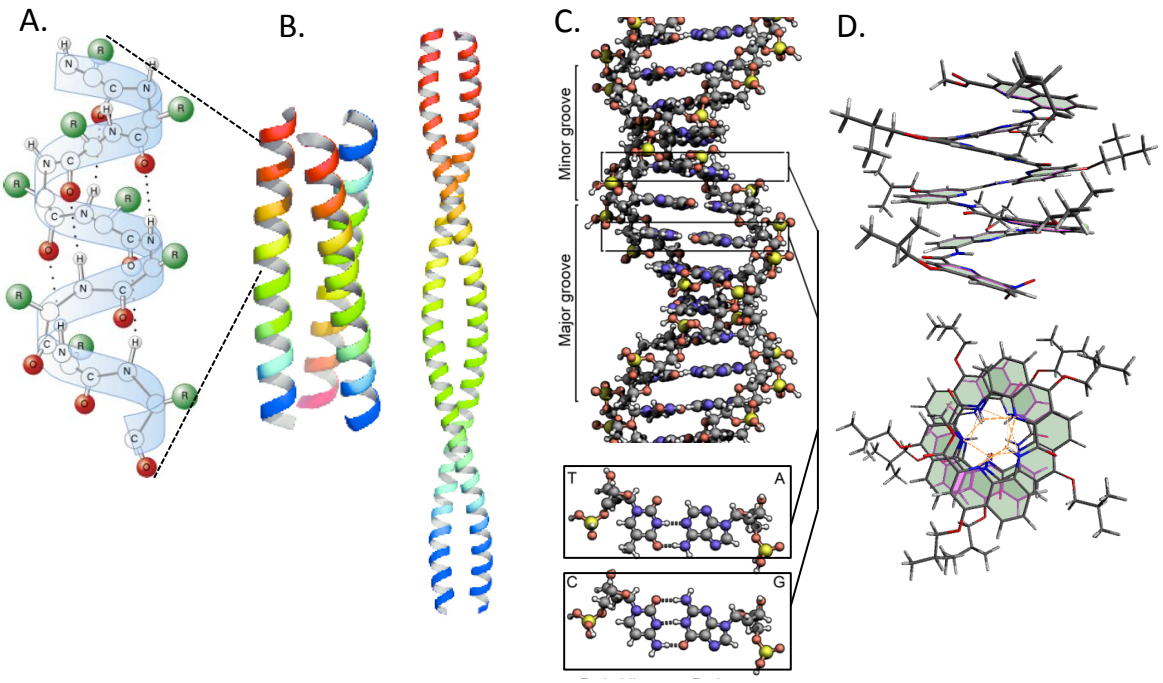

Figure 2.24 Illustration of natural helical counterparts of the quinoline based foldamer. (A) the α-helix, with the H-bonds represented with dashed lines between *i* and *i+4*. (B) triple (left) and double (right) coiled-coil structure. (C) Double helix B-DNA. Illustrations were uploaded from websites: respectively Chegg.com, google.com/site/chrismacdermaid and wikipedia.org. (D) Quinoline octamer side and top view.

2.3.1 Comparison with proteins

In the proteins world, several helical structures can be found with hierarchical degree of complexity. Several structures have been investigated in aqueous environment and their unfoldings require forces up to 40 pN. We can suggest that the increase of hierarchical helical assembly slightly reinforces the structure (single helix: 5-15 pN or 24 pN if surrounded by intact domains), coiled-coil: 20-25 pN, repeat of coiled-coil 25-35 pN). However, for any level, their unfolding force values are far below the performances of the quinoline-based helix (70-100 pN). Different force-distance patterns were observed. The double coiled-coil of the myosin and α-helical linker of myomesin unfold via a plateau, similar to what we observe in quinoline-based foldamers. For the other larger investigated proteins, a sawtooth pattern is observed where each peak corresponds to the unravelling of a domain. However, we may wonder if the lack of spatial resolution does not limit the detection of plateau for the unfolding of α-helix out of a domain. For example, in ankyrin, when we have a closer look at the unfolding pattern in Figure 1.30 B, we could suggest the occurrence of a tiny plateau in each peak[37,38]. In one repeat, 18 aa are involved in a helical conformation. The stretching of it would elongate along only 4 nm, possibly unnoticed. In calmodulin (Figure 1.29.A), with increased resolution[32], hopping events are observable for each domain and extent along non-negligible distances akin to a short and a longer plateau (~ 4 and 10 nm). Despite their weak interactions, the helical structure is yet robust as almost all unfolding is reversible.

2.3.2 Comparison with nucleic acids

Comparison of the quinoline-based foldamer behaviours with the double-stranded DNA cannot either be direct, as the foldamer only comprises one strand. However as the conformational transition for both molecules consists in unfolding the (double) helix to a straight (ladder) structure with overstretched backbone, DNA and quinoline foldamers can be compared to some extent.

Firstly, the patterns of the unfoldings under load are similar: for both systems plateaus are observed and can be interpreted as a progressive propagation of the unwinding the helix.
Secondly, although B-DNA is made of two intertwined strands, the helical structure of B-DNA is less strong than the one building the quinoline-based foldamers (for the helix-stretched backbone transition). The unfolding force is lower for the long B-DNA (65 pN)[39,40] than for long foldamers (100 pN). In addition, the reversibility of the helical structure in foldamers seems to be bounded by the covalent bond breaking, whereas the double helix DNA structure may undergo an irreversible melting from intermolecular interactions breaking. Finally, an interesting similarity between DNA and quinoline

foldamers comes with the similar force and unfolding feature evolution with the number of building units. Indeed, for both the plateau feature is observable only above a given number of building units. This supports a cooperative folding process for both structures. Interestingly, whereas the quinoline-based foldamer displays energetically instability in the formation of the helix below 6 units, the double helix DNA displays it below 28 bp[41], which in both cases corresponds to a little bit more than 2 pitches. This can be interesting information for designing molecular systems with tailored and controlled properties.

2.3.3 Comparison with polysaccharides

It has be shown that some polysaccharides can underpin single (amylose)[42] and multi-stranded (curdlan)[43] helical structures in given environment. These helical structures can also unfold with a plateau-like pattern in pulling experiments by AFM. The difference in unfolding forces between a single or a mutli-stranded structure does not seem to be significant (50 to 60 pN), as it was observed in protein and does not outweigh the force values obtained in the quinoline-based foldamers. Interestingly, a significant difference has been detected for pulling experiment in different environments. Indeed amylose polysaccharides are expected to present similar helical structure in butanol and in iodine solution as in both environments they crystalize in the same manner. However SMFS experiments recorded highly different patterns, as no plateau was observed in aqueous iodine. This allowed highlighting the stronger robustness of the helix in butanol, probably because of the reinforcement of H-bonds. As far it concerns the foldamers, this environment influence will be discussed in the chapter 4.

2.3.4 Closing discussion

As general conclusion, with the acknowledgment of some impeding factors to compare the natural and synthetic systems, the synthetic quinoline-based helix seems to clearly outperform the natural counterparts. Comparing all together, we can highlight the significant contribution of the π-stacking and of the hydrogen bonds in the helical structure. We can conclude that the more different kinds of interactions are interplaying, the higher is the force to unfold the helical structure. In proteins, the α-helix structure holds mostly by hydrogen bonds and is unfolded with forces lower than 25 pN. Coiled-coil structures, which interweave α-helices through hydrophobic interaction, also sustain only 25-40 pN. During the B-S transition in the unfolding DNA, a force of 65 pN is required to disrupt the base-π-stacking while we assume that most base pairings (H-bonds) remain in the S-DNA conformation.[44] Finally, the unfolding of the helical quinoline-based foldamers involves the ruptures of π-stacking and hydrogen bonds and it is characterised by significantly higher forces (around 100 pN). Nevertheless, given the difference of

unfolding forces for the curdlan in butanol (50 pN) and aqueous iodine (<20pN, undistinguishable from thermal noise), we can expect that these high forces are explained because organic solvents reinforce the electrostatic interactions in the quinoline-based foldamers.

Moreover, some similar behaviours could be identified leading to potentially universal behaviours of helices under load. Indeed, the plateau pattern seems to be a trademark in helical structure at several levels. Like for the synthetic foldamers, from a given length, a plateau is observed in DNA, as well as in some conformations of proteins and polysaccharides. Although the plateau is clearly observed for the unfolding of the coiled-coil myosin and the α-helix of myomesin, it is not yet always obvious for α-helix comprised of other structural parts (loops). It may just have gone unnoticed yet because of the lack of resolution when pulling on long molecules.

Besides, in many natural cases, the reversibility of the unfolding has been demonstrated, and it is also observed in the quinoline-based foldamers (see chapter 3). This advocates that permanent high proximity of interacting partners induces such performances.

From a biological point of view, it may be interesting to know that a helical structure may reversibly exert and/or generate a constant force under its elongation/retraction. From a nanomaterial point of view, it is beneficial to observe that an helical conformation could lead to behaviours such as cooperativity from more than 2 turns, stepwise unfolding, and that it is possible to tune the force values by varying the chemical backbone.

2.4 Conclusion

Pulling experiments and their analyses on quinoline-based foldamers of 4 different sizes (5-, 9-, 17-, 33-mer) in N,N-dimethylformamide showed so far a reproducible and characteristic unfolding profile for each size and allowed us to highlight some mechanical properties.

We identified 2 major parts in the forced-unfolding profiles: The longest foldamers exhibit a constant-force plateau ending by a force-decreasing feature. The smallest foldamer, 5-mers, is either made of this last part only, *i.e.* the force-decreasing feature, or of a single peak. The length of the constant-force plateau is linearly dependent on the number of units, whereas the force-decreasing feature is independent on the number of units and extends over around 2 nm.

The occurrence of a plateau suggests a stepwise unfolding of a highly dynamic system on the time scale of the experiment. The average force of the plateau is similar for all the foldamers and is around 95 pN. These combined results indicate that the foldamers constitute highly robust molecular helices. This mechanical property could be associated to the permanent proximity of the interacting chemical groups and to the rigidity of the backbone. Thorough analysis of the unfolding signal allows suggesting the unfolding to mostly take place by the simultaneous rotation of 2 quinoline units. This unfolding is probably driven by thermal fluctuations and occurs in equilibrium. Unfortunately, given the repetitive nature of the sequence, it is impossible to unveil the order of the unfolding, as each step is similar.

The decrease in force at the end of the plateau indicates a weakening in the interaction strength along unfolding, which is a clear demonstration of a cooperative folding. The measurement of the average force of the whole unfolding of the foldamer, taking from the beginning of the unfolding of the foldamer until the beginning of the overstretching of the molecule, jointly validated the cooperative process since as the forces increase non-linearly with the size to reach a limit. Further measurements on the force-distance traces allowed determining the nucleation segment of a reinforced structure, which had not been identified in previous investigations. Indeed, whatever the size of the foldamer, a helically folded structure exists in solution, owing to the backbone rigidity, H-bonds and electrostatic interactions. However, beyond 5-6 units of quinolines, which correspond to ~2 turns, the foldamers exhibit a mechanically reinforced helical conformation, owing presumably to the network of aromatic stacking.

The revealed extensions over the unfolding of each foldamer correspond perfectly to the theoretical difference between the totally folded and unfolded conformations, which is

obtained through the rotation of the each C-C(O) bond. It is the most extended conformation reachable before bond angle deformation. This endows the foldamers with an extensibility of 380 % their original length.

Finally, using the quinoline-based foldamer as an isolated helical model system, we identified some specific behaviours and patterns, which may exist in natural analogues but have so far been unnoticed because less apparent. Helices held by weak non-covalent interactions are ubiquitous in nature and some are really delicate. Now that we have associated some behaviours with our model helix, we could look after them. They may help to elucidate the (dis)functions of proteins for example.

2.5 References

1. Jiang, H., Léger, J. M., Dolain, C., Guionneau, P. & Huc, I. Aromatic δ-peptides: Design, synthesis and structural studies of helical, quinoline-derived oligoamide foldamers. *Tetrahedron* **59,** 8365–8374 (2003).
2. Delsuc, N. *et al.* Kinetics of helix-handedness inversion: Folding and unfolding in aromatic amide oligomers. *ChemPhysChem* **9,** 1882–1890 (2008).
3. Shang, J. *et al.* Self-association of aromatic oligoamide foldamers into double helices in water. *Org. Lett.* **16,** 4992–4995 (2014).
4. Dolain, C., Léger, J.-M., Delsuc, N., Gornitzka, H. & Huc, I. Probing helix propensity of monomers within a helical oligomer. *Proc. Natl. Acad. Sci. U. S. A.* **102,** 16146–51 (2005).
5. Delsuc, N., Godde, F., Kauffmann, B., Léger, J. M. & Huc, I. The herringbone helix: A noncanonical folding in aromatic-aliphatic peptides. *J. Am. Chem. Soc.* **129,** 11348–11349 (2007).
6. Qi, T., Deschrijver, T. & Huc, I. Large-scale and chromatography-free synthesis of an octameric quinoline-based aromatic amide helical foldamer. *Nat. Protoc.* **8,** 693–708 (2013).
7. Li, X. Synthesis and physical properties of helical nanosized quinoline-based foldamers : structure , dynamics and photoinduced electron transport. (University of Bordeaux and University of Liege, 2016).
8. Li, X. *et al.* Synthesis and Multibromination of Nanosized Helical Aromatic Amide Foldamers via Segment-Doubling Condensation. *Org. Lett.* **18,** 1044–1047 (2016).
9. Lussis, P. *et al.* A single synthetic small molecule that generates force against a load. *Nat. Nanotechnol.* **6,** 553–557 (2011).
10. Beyer, M. K. & Clausen-Schaumann, H. Mechanochemistry: the mechanical activation of colvalent bonds. *Chem. Rev.* **105,** 2921–2948 (2005).
11. Sulchek, T. A., Friddle, R. W. & Noy, A. Dynamic force spectroscopy in tethered single molecule systems. *Handb. Mol. Force Spectrosc.* (2007).
12. Sluysmans, D. *et al.* Synthetic oligorotaxanes exert high forces when folding under mechanical load. *Nat. Nanotechnol.* **13,** 209–213 (2018).
13. Bacharouche, J. *et al.* Multivalency: influence of the residence time and the retraction rate on rupture forces measured by AFM. *J. Mater. Chem. B* **3,** 1801–1812 (2015).
14. Kudera, M., Eschbaumer, C., Gaub, H. E. & Schubert, U. S. Analysis of Metallo-Supramolecular Systems Using Single-Molecule Force Spectroscopy. *Adv. Funct. Mater.* **13,** 615–620 (2003).
15. Hinterdorfer, P. & Dufrêne, Y. F. Detection and localization of single molecular recognition events using atomic force microscopy. *Nat. Methods* **3,** 347–55 (2006).
16. Rivetti, C., Walker, C. & Bustamante, C. Polymer chain statistics and conformational analysis of DNA molecules with bends or sections of different flexibility. *J. Mol. Biol.* **280,** 41–59 (1998).
17. Janshoff, A., Neitzert, M., Oberdörfer, Y. & Fuchs, H. Force Spectroscopy of Molecular Systems-Single Molecule Spectroscopy of Polymers and Biomolecules. *Angew. Chem. Int. Ed. Engl.* **39,** 3212–3237 (2000).
18. Friedsam, C., Wehle, A. K., K hner, F. & Gaub, H. E. Dynamic single-molecule force spectroscopy: bond rupture analysis with variable spacer length. *J. Phys. Condens. Matter* **15,** S1709–S1723 (2003).
19. Hugel, T. & Seitz, M. The study of molecular interactions by AFM force spectroscopy. *Macromol. Rapid Commun.* **22,** 989–1016 (2001).
20. Rohs, R., Etchebest, C. & Lavery, R. Unraveling Proteins : A Molecular Mechanics Study. *Biophys. J.* **76,** 2760–2768 (1999).

21. Uribe, L., Gauss, J. & Diezemann, G. Determining Factors for the Unfolding Pathway of Peptides, Peptoids, and Peptidic Foldamers. *J. Phys. Chem. B* **120,** 10433–10441 (2016).
22. Zlatanova, J., Lindsay, S. M. & Leuba, S. H. Single molecule force spectroscopy in biology using the atomic force microscope. *Prog. Biophys. Mol. Biol.* **74,** 37–61 (2000).
23. Ritort, F. The nonequilibrium thermodynamics of small systems. *Comptes Rendus Phys.* **8,** 528–539 (2007).
24. Bell, G. I. Models for the specific adhesion of cells to cells. *Science (80-.).* **200,** 618 LP-627 (1978).
25. Evans, E. & Ritchie, K. Dynamic strength of molecular adhesion bonds. *Biophys. J.* **72,** 1541–55 (1997).
26. Noy, A. & Friddle, R. W. Practical single molecule force spectroscopy: how to determine fundamental thermodynamic parameters of intermolecular bonds with an atomic force microscope. *Methods* **60,** 142–50 (2013).
27. Janke, M. *et al.* Mechanically interlocked calix[4]arene dimers display reversible bond breakage under force. *Nat. Nanotechnol.* **4,** 225–229 (2009).
28. Fantner, G. E. *et al.* Sacrificial bonds and hidden length: unraveling molecular mesostructures in tough materials. *Biophys. J.* **90,** 1411–8 (2006).
29. Li, H., Oberhauser, A. F., Fowler, S. B., Clarke, J. & Fernandez, J. M. Atomic force microscopy reveals the mechanical design of a modular protein. *Proc. Natl. Acad. Sci. U. S. A.* **97,** 6527–31 (2000).
30. Liphardt, J., Bibiana, O., Smith, S. B., Tinoco, I. J. & Bustamante, C. J. Reversible Unfolding of Single RNA Molecules by Mechanical Force. *Science (80-.).* **292,** 733–737 (2001).
31. Berkemeier, F. *et al.* Fast-folding -helices as reversible strain absorbers in the muscle protein myomesin. *Proc. Natl. Acad. Sci.* **108,** 14139–14144 (2011).
32. Junker, J. P., Ziegler, F. & Rief, M. Ligand-dependent equilibrium fluctuations of single calmodulin molecules. *Science (80-.).* **323,** 633–637 (2009).
33. Abramyan, A. M., Liu, Z. & Pophristic, V. Helix handedness inversion in arylamide foldamers: elucidation and free energy profile of a hopping mechanism. *Chem. Commun.* **52,** 669–672 (2016).
34. Hill, D. J., Mio, M. J., Prince, R. B., Hughes, T. S. & Moore, J. S. A Field Guide to Foldamers. *Chem. Rev.* **101,** 3893–4012 (2001).
35. Puchner, E. M., Franzen, G., Gautel, M. & Gaub, H. E. Comparing proteins by their unfolding pattern. *Biophys. J.* **95,** 426–34 (2008).
36. Puchner, E. M., Franzen, G., Gautel, M. & Gaub, H. E. Comparing proteins by their unfolding pattern. *Biophys J* **109,** 426–434 (2008).
37. Li, L., Wetzel, S., Plückthun, A. & Fernandez, J. M. Stepwise Unfolding of Ankyrin Repeats in a Single Protein Revealed by Atomic Force Microscopy. *Biophys. J.* **90,** L30–L32 (2006).
38. Scholl, Z. N., Li, Q. & Marszalek, P. E. Single molecule mechanical manipulation for studying biological properties of proteins, DNA, and sugars. *Wiley Interdiscip. Rev. Nanomedicine Nanobiotechnology* **6,** 211–229 (2014).
39. Smith, S. B., Cui, Y. & Bustamante, C. Overstretching B-DNA: the elastic response of individual double-stranded and single-stranded DNA molecules. *Science* **271,** 795–9 (1996).
40. Rief, M., Clausen-Schaumann, H. & Gaub, H. E. Sequence-dependent mechanics of single DNA molecules. *Nat. Struct. Biol.* **6,** 346–349 (1999).
41. Morfill, J. *et al.* B-S transition in short oligonucleotides. *Biophys. J.* **93,** 2400–2409 (2007).
42. Zhang, Q. & Marszalek, P. E. Identification of sugar isomers by single-molecule force spectroscopy. *J. Am. Chem. Soc.* **128,** 5596–5597 (2006).

43. Zhang, L., Wang, C., Cui, S., Wang, Z. & Zhang, X. Single-molecule force spectroscopy on curdlan: Unwinding helical structures and random coils. *Nano Lett.* **3,** 1119–1124 (2003).

44. Marko, J. F. & Siggia, E. D. Stretching DNA. *Macromolecules* **28,** 8759–8770 (1995).

Chapter 3

Dynamics & Energetics of Quinoline-based Foldamers

TABLE OF CONTENTS

Chapter 3
Dynamics & Energetics of Quinoline-based Foldamers

In this chapter, we tackle the thermodynamic parameters of the helical quinoline-based foldamers at the single molecule scale. Theoretically, investigating one molecule at a time allows us to probe the dynamics of molecular processes since the obtained signal is not an average of signals from several molecules undergoing different process steps at the time of the measurement.

We highlight the information obtained on dynamics and energy, as well as the technical limitations that we have encountered to obtain a detailed description of the dynamics of the molecular processes.

Practically, we investigated the effect of the pulling speed during the stretching of single foldamers of different sizes in DMF. We probed and traced the relaxing patterns in the force-distance curves after the foldamers were completely stretched. Finally we exploited the visible back and forth fluctuations at the end of the foldamer unfolding.

3.1 Introduction

In order to understand the underlying interactions and processes giving rise to the molecular folding, it is essential to determine their thermodynamics and kinetics down to the molecular scale.[1–3] Owing to the stochastic nature of the interaction dissociation and formation, Single-Molecule Force Spectroscopy (SMFS) is a versatile technique able to explore these parameters, whereas ensemble techniques usually fail as they average out discrete dynamical events (section 1.3).

In the context of quinoline-based foldamers, such information is particularly missing. So far, their high stability has prevented the detection of measurable amounts of unfolded conformers. Indirect measurements were obtained by monitoring the handedness inversion over time. They provided the energy barrier associated to the highest transition state.[4] Theoretical simulations have also been performed.[5,6] However simulations also have some limitations stemming from the choice of the calculation model or the implementation of the solvent. Complementary experimental analyses are more than welcome to complete this investigation.

Dynamical force spectroscopy experiments (DFS), by pulling molecules away from the equilibrium regime, make it possible to probe the underlying energy landscape of molecular interactions or folding and to extract kinetic constants of various interactions (section 3.2).[7,8] Pulling-relaxing experiments, by consecutively monitoring the unfolding of a molecule and its relaxing trace, allow us to compare the folding and unfolding pathways as well as to probe the performances at refolding under load.[9,10] This latter observation can shed light on both elasticity and dynamical properties. By combining dynamical force spectroscopy and pulling-relaxing experiments it is possible to approach more precisely equilibrium (un)folding free energy;[11–13] using the Crooks fluctuation theorem, which is based on the intrinsic behaviour of a molecule to deviate from an average behaviour owing to thermal energy (section 3.3).[14] Finally, it has also been proven that direct analysis of real-time fluctuations (hopping events) can provide kinetic information of the molecular system without extrapolating models, as these hops evidence unfolding and folding events at the equilibrium regime (section 3.4).

3.2 Dynamical force spectroscopy

3.2.1 The simple bond theory and extrapolation models

In the first approximation, the strength of a simple bond can be evaluated by the maximum force that the bond can withstand before it breaks. However, Eyring and Zhurkov predicted that the bond strength depends on the equilibrium energy but also on the temperature and the time scale of the measurement. This assumption was eventually described by Arrhenius and its model of thermal activation over energy barriers. It demonstrated that the bond has a finite probability to acquire sufficient thermal energy to overcome spontaneously the activation barrier and thus to dissociate after a given time. This observation leads to the natural lifetime (τ_0) definition of the bond (Eq. 1).[15,16] The simple bond model can be applied to any non-covalent interaction or conformational change.

$$\tau_0 = \tau_{osc} \,.\, exp\left(\frac{E_a}{k_B T}\right) \qquad \text{Eq. 1}$$

Eq. 1 Natural life time of a bond; where τ_{osc} is the inverse of the natural vibration frequency, E_a the activation energy for the bond dissociation, k_B the Boltzmann constant and T the temperature.

As explained in the introductive chapter, during a pulling experiment, the application of a continuously increasing force (force ramp) tilts the energy landscape of a bond progressively down to lower energy until the energy barrier can be overcome (by thermal energy) and the bond breaks (Figure 3.1). In addition to the applied force, the bond is submitted to thermal energy, which also activates the bond with time. Therefore, the faster is the pulling experiment, the lesser the thermal forces (10^{-12}s) have time to destabilize the bond and by consequence the higher the force is required to dissociate the bond.

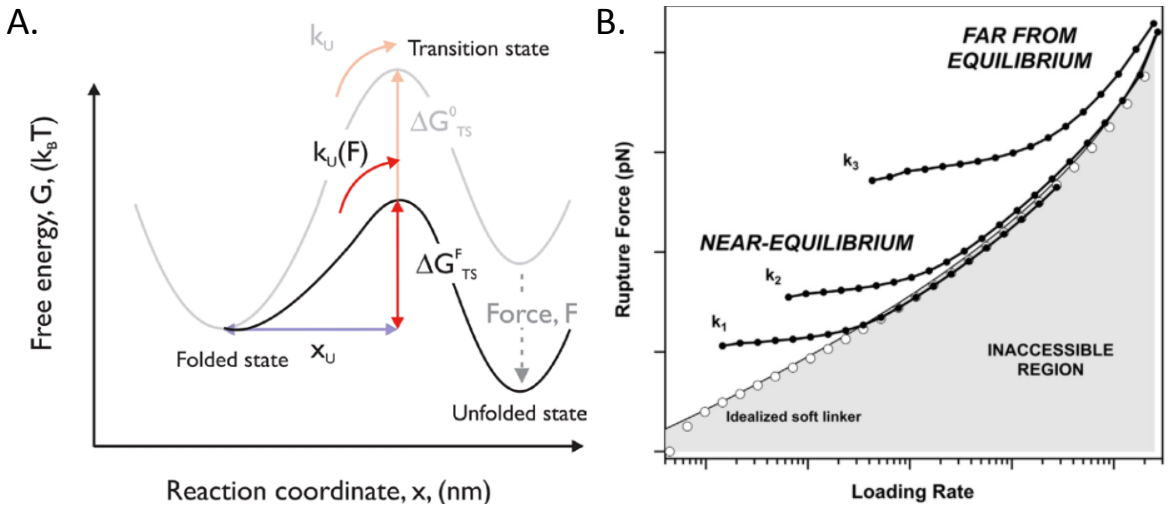

Figure 3.1 (A) Schematic diagram showing the effect of mechanical force on the energy landscape of a bond/folded system (two-state transition): the application of an external force tilts the energy landscape and lowers the energy barrier to achieve the unfolded state.[17] (B) A dynamic force spectrum of an ideal non-covalent bond showing the different pulling regimes: filled circles represent the force spectrum resulting from loading of a Morse potential using harmonic cantilevers of different stiffness ($k_1<k_2<k_3$); open circles are associated to a system containing an idealized soft linker between the probe and the bond; shaded region indicates an inaccessible region of binding force and loading rate combinations.[2] Reproduced from references 2,17.

Depending on the relative natural dissociation constant of the system compared to the pulling speed, the system can face 2 different regimes (Figure 3.1.B): (i) When the external force is applied much faster (higher loading rate) than the natural off-rate of the molecular system, the system is pulled *'far from equilibrium'* or *'out-of equilibrium'* and exhibits a rate dependence on the rupture force. (ii) When the loading rate is similar or smaller than the dissociation constant, the system encounters a *'near-equilibrium regime'* pulling experiment and the measured force is independent on the loading rate and can be directly related to the free energy between the bound and unbound states. This force is referred to as equilibrium force, F_{eq} (see Eq. 5).

Typically pulling speeds used in SMFS experiments vary in the range of a few ~ $nm.s^{-1}$ to ~ 10 $\mu m.s^{-1}$. The lower limit is due to thermal drift and the upper limit comes from hydrodynamic drag force acting on a cantilever. The *apparent* loading rate (l_r) is calculated, in the first approximation, by multiplying the velocity (v) by the spring constant of the cantilever (k) (Eq. 2). In some cases, the *effective* loading rate is different from the *apparent* loading rate as discussed later. It is experimentally measured on each curve from the slope of the force-time traces just before rupture (Eq. 3).

$$lr_{apparent} = k \times v \qquad \text{Eq. 2}$$

Eq. 2 *Apparent* loading rate, where k is the spring constant of the cantilever and v the velocity.

$$lr_{effective} = \left[\frac{dF}{dt}\right]_{rupture} \quad \text{Eq. 3}$$

Eq. 3 *Effective* loading rate.

Given the activation of a bond over time, several models have been developed to relate the rupture forces with the loading rates at the scale of the single-molecule pulling. From these models, thermodynamic parameters of the probed interaction, such as the position (Δx), the free energy of the barrier (ΔG) and the natural dissociation constant (k_{off}) can be extracted.

Bell[18] and then Evans[19] developed the first model and it has been the most extensively used to determine the free energy landscape of proteins to date. Using Kramer's theory[20] to suit experiments in solution and assuming the loading rate (l_r) is independent of the force (linear spring), they found a dependence of the rupture force (F) on the logarithm of the loading rate (Figure 3.2.A). This model provides the dissociation constant and the barrier coordinate.

$$F(lr) = \frac{k_B T}{\Delta x} \ln\left(\frac{lr}{\Delta x\, k_{off}} \frac{\Delta x}{k_B T}\right) \quad \text{Eq. 4}$$

Eq. 4 Bell Evans equation, where k_{off} is the natural off rate and Δx the potential width.

A second developed and commonly used model is the Friddle-Noy-De Yoreo model (Figure 3.2.C).[21] It integrates the potential reversibility of the bond. Therefore, the bond being pulled apart can undergo two regimes: at lower pulling speeds, the bond can rebind, it is in equilibrium regime, the rupture force (F_{eq}) is independent of the loading rate. At higher loading rates, the bond unbinds irreversibly and reaches a kinetic phase (out of equilibrium), where the rupture forces evolve with the loading rates. An approximation can provide the rupture force.

$$F(lr) = F_{eq} + \frac{k_B T}{\Delta x} \ln\left(1 + \frac{lr\, e^{-\gamma}}{\Delta x\, k_{off}(F_{eq})} \frac{\Delta x}{k_B T}\right) \text{ and } F_{eq} = \sqrt{2\, k_c \Delta G} \quad \text{Eq. 5}$$

Eq. 5 Friddle-Noy-De Yoreo model, where $k_{off}(F_{eq})$ is the natural off rate, γ is Euler's constant, Δx the potential width, k_c the spring constant of the cantilever and ΔG free energy of unfolding.

Another more sophisticate model, the Dudko–Hummer–Szabo model attempts to generalize the shape of the force transducer, unlike to the Bell-Evans model which considers a linear evolution with the logarithm of the loading rate (Figure 3.2.B).[22] An arbitrary parameter $\boldsymbol{\nu}$ gives access to different shapes of the energy landscape. Interestingly it could help to consider more exactly the influence of a linker.[23]

It consists in transforming the rupture-force histograms obtained at different loading rates into the force-dependent life times (Eq. 6) and consequently extract kinetic information.

$$\tau(F) = \tau_0 \left(1 - \frac{v\,F\,\Delta x}{\Delta G}\right)^{1-1/v} exp\left(-\beta\Delta G\left[1 - \left(1 - \frac{v\,F\,\Delta x}{\Delta G}\right)^{1/v}\right]\right) \qquad \text{Eq. 6}$$

Eq. 6 Dudko–Hummer–Szabo equation, where Δx is the potential width, τ0 is the lifetime and ΔG is the apparent free-energy of activation in the absence of an external force. ν specifies the nature of the underlying free-energy profile: ν = 1/2 corresponds to a harmonic well with a cusp-like barrier, or equivalently a harmonic barrier with a cusp-like well; ν = 2/3 corresponds to a potential that contains linear and cubic terms; for ν = 1 Bell's formula is recovered.

This model is quite recent and only a few examples were described. It does not take into account a potential reversibility of the bond. The Figure 3.2 summarizes the three most common models used to extract dynamical information from SMFS experiment on molecular systems.

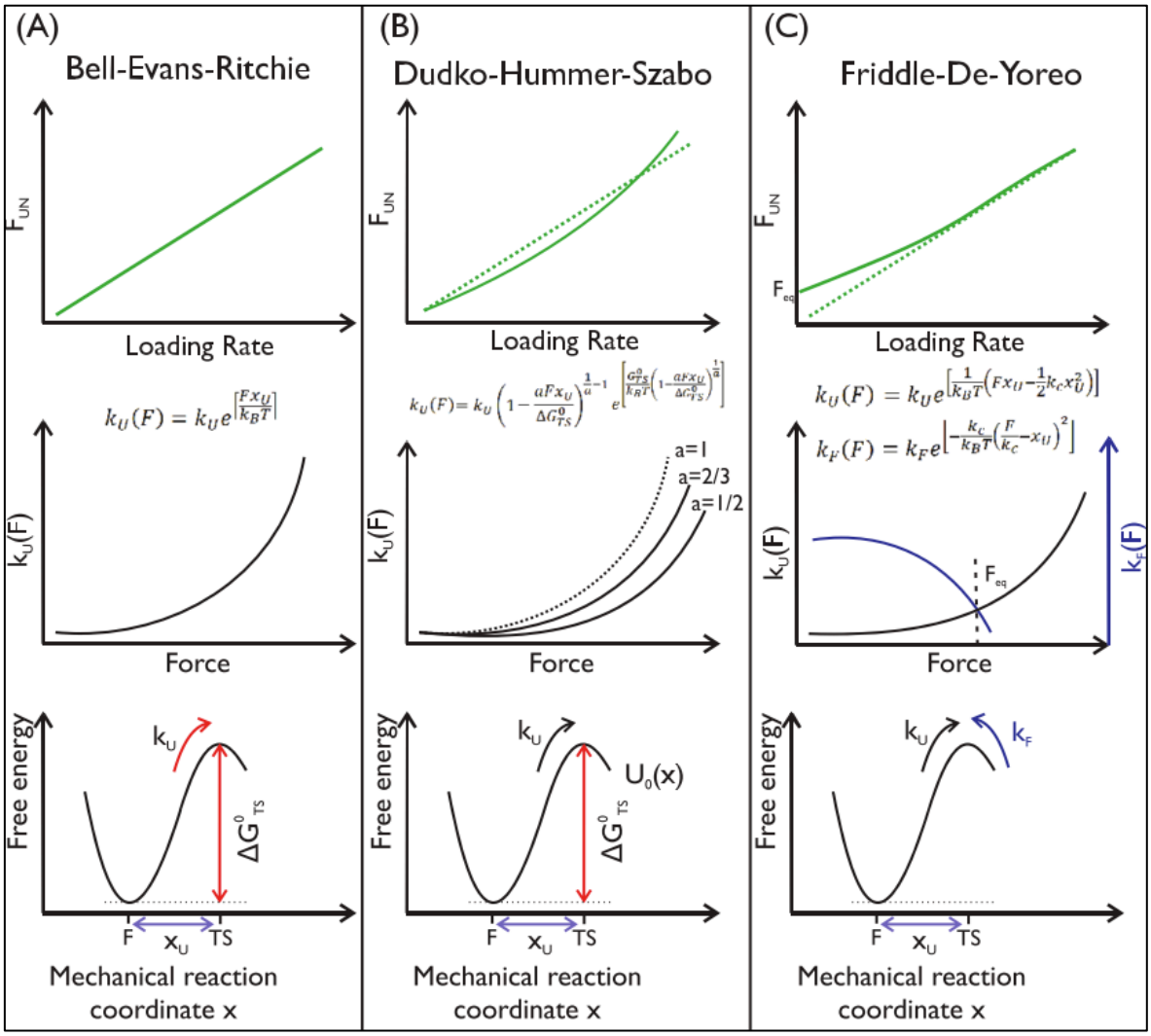

Figure 3.2 Schematic diagrams of the different models describing dependence of the unfolding forces on the loading rates. (A) Bell–Evans–Ritchie (B) Dudko–Hummer–Szabo and (C) Friddle–Noy-De Yoreo models. Reproduced from reference 17.

3.2.2 The impact of a flexible linker: the concession

As addressed by the Dudko–Hummer–Szabo model, a recent question deals with the influence of a compliant linkage or a tether between the cantilever and the interaction(s) of interest in comparison to a direct link with a linear-flexible cantilever.[23]

Tethering a molecule or an interaction has many indispensable advantages for single-molecule force spectroscopy. For example, it increases the probability of catching a single molecule. It allows us to distinguish the full specific unfolding or interactions involved in the molecule of interest from the nonspecific interactions of the probe tip and sample. It also provides a reliable pattern, which can be used as an internal reference to validate the single molecule condition and to efficiently identify small rupture or unfolding events of the molecule of interest. For molecular recognition applications, it also presents advantages as it provides conformational freedom to dock and dissociate the partners in similar conditions as in their natural environment. Finally, as described by Noy[24], a tethered system forms a nearly-ideal experimental system as the elasticity of the tether prevents the rebinding event.

However, all these advantages may have a significant cost as a linker or tether may render the dynamic force spectroscopy analysis much more complex than without. The addition of a compliant linker provokes a non-trivial loading process. Although the cantilever moves at a constant rate, the applied load to the molecule/interaction does not rise linearly but according to a combination of the tether/linker compliance and the cantilever spring. As described in the introduction, a flexible polymer exhibits a non-linear entropic restoring force when it is stretched (Figure 3.3). Nonlinear loading introduces substantial complications in the force analysis.

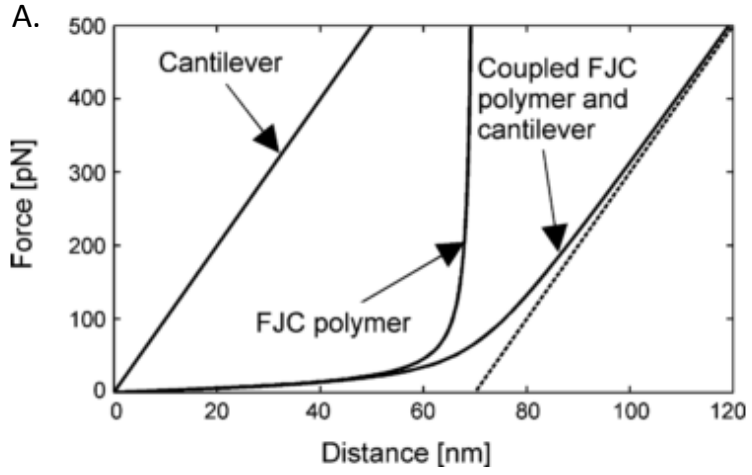

Figure 3.3 The calculated force–distance relation for a cantilever, a freely jointed chain (FJC) polymer and a coupled polymer–cantilever system. Reproduced from reference 25.

Zlatanova also noticed that "the longer molecules generate a force that increases more slowly with time for the same overall pulling speed".[26]

Evans and Ritchie found that the bond linked by a polymer breaks at lower force than linked by a stiff connection, because it remains longer at lower force.[27] They also showed that only when the internal (effective) loading rate is considered, the unfolding forces of short and long titins (from nano- to micrometres) fall on a universal line derived from the Bell-Evans model; while considering the apparent speed, the unfolding forces do not match to common energy landscape.[27] They concluded that to determine correctly bond rupture or unfolding forces, both the effective loading rate and the sample size should be considered.

Moreover, the inclusion of a compliant linker with large dispersity may lead to distortion in the force distribution (Figure 3.4), as highlighted by Friedsam *et al.* They demonstrated that short linkers have a marginal effect, whereas long flexible linkers induce significant perturbations of the measured force values.[15]

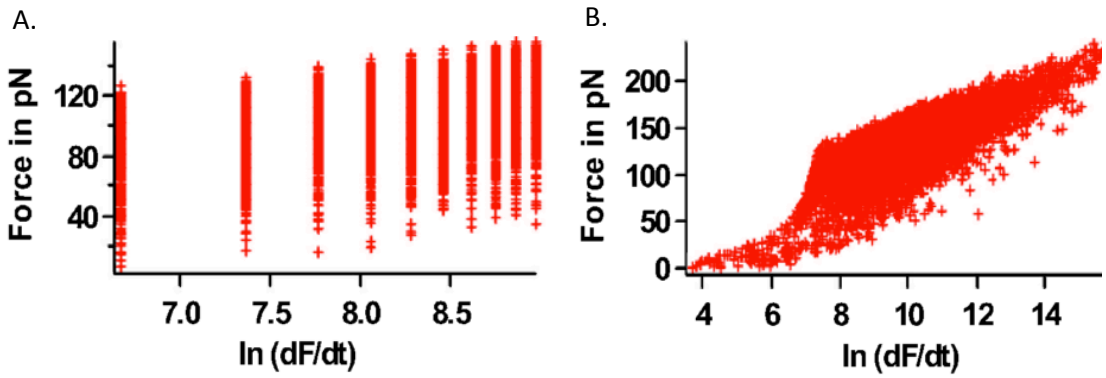

Figure 3.4 Distributions of the Monte Carlo data in Force over ln(*lr*) diagrams of 2 types of simulations. The input values of the simulations were k_{off} = 0.05 s^{-1} and Δx = 3 Å. (A) The linear force ramp (no linker) (B) with poly(ethylene glycol) linker with a large dispersity from one to 150 monomers. Adapted from reference 15.

To take this influence into consideration and to be able to probe more accurately the thermodynamic parameters, some authors have prescribed to measure the effective loading rates at each rupture, to recalculate the forces depending on the effective spring constant and to use these obtained values in the models.[15]

3.2.3 Results and discussion

The dynamics of the foldamers was investigated by studying the effect of the loading rate on the unfolding forces during standard pulling experiments, as described in the previous chapter 2, except that the pulling speed varied. Five pulling velocities (33, 167, 833, 1667 and 4167 $nm.s^{-1}$) were tested. The lowest and fastest speeds are respectively restricted by the drift time and from a technical limitation of data saving. This range of velocity allowed covering three orders of magnitude in terms of apparent loading rates. The apparent loading rate (in $pN.s^{-1}$) is a constant parameter calculated with pulling velocity v (in $nm.s^{-1}$) and the spring constant of the cantilever (k) (Eq. 2). The cantilevers we used have a spring constant around 28 $pN.nm^{-1}$. To overcome the limitation of calibration and validate the influence of the loading rate, dynamic force spectroscopy experiments were carried out using the same cantilever for several velocities and the analyses were reproduced with several cantilevers.

We observed similar pulling profiles over the whole range of tested velocities (see Figure 3.5 for 33-mers and Figure 3.9 for 5-mers). Therefore, we could measure and compare the average unfolding force, as explained in the previous chapter, for each force-distance curve at each velocity. We made histograms out of these average force values and observed monomodal Gaussian distributions for each condition. Then, we plotted the most probable values of the average unfolding forces as a function of the apparent loading rates.

We started the investigation on the longest foldamer, *i.e.* the 33-mers, in N,N-dimethylformamide (DMF). Typical traces are shown in Figure 3.5 and the dynamical force spectrum results are shown in Figure 3.6. In general, within the replica, we cannot observe any relevant influence of the loading rates on the unfolding pattern and forces of the foldamers. The unfolding forces oscillate between 85 and 120 pN without clear tendency that could fall on a previous presented model, which relates the rupture forces of out-of-equilibrium pulling experiments to thermodynamic parameters.

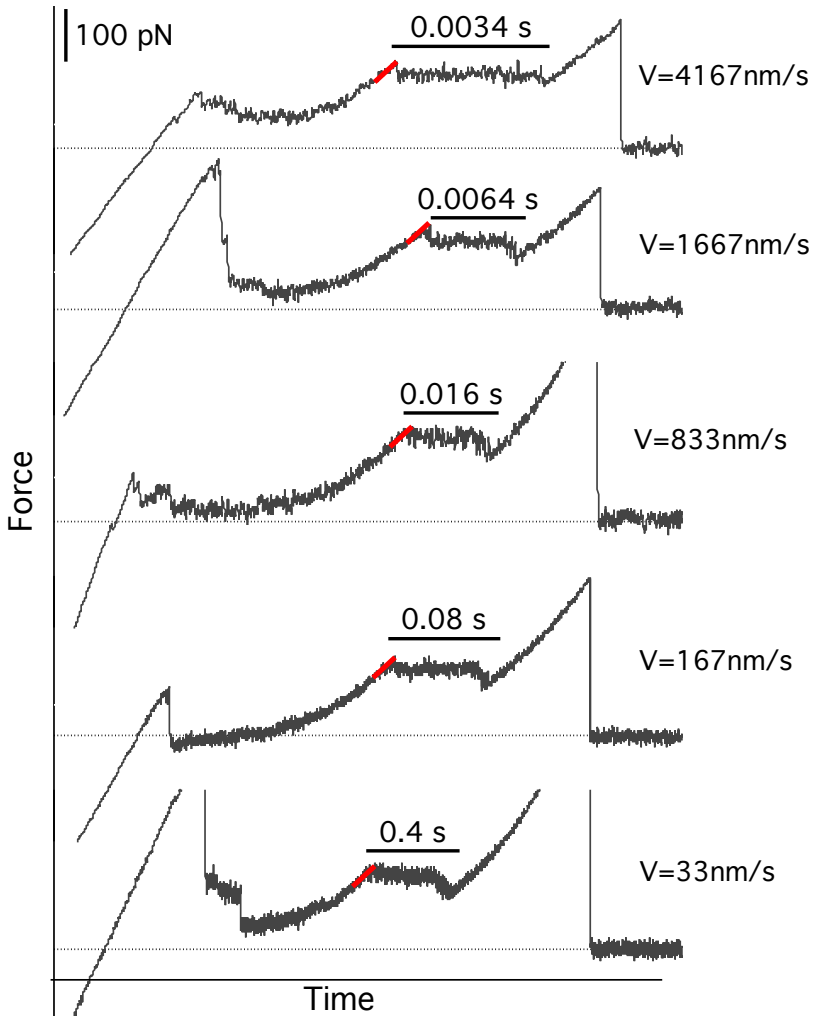

Figure 3.5 Typical force-time traces of pulling experiments on Q33 at several pulling velocities (written on the right of each curve). The red lines show the slopes at the rupture, given the effective loading rate.

This loading-rate independency of the unfolding forces highly suggests the equilibrium regime, proposed by Friddle-Noy-De Yoreo model.[21] They integrated the possibility of rapid refolding/rebounding on the time scale of the experiment.

This indicates that the foldamer is capable of refolding, to recreate the interactions with a rate much higher than the pulling rate. This outcome is in perfect agreement with the hopping events observed particularly at the end of the unfolding (see section 3.4 for details) and with the occurrence of a flat plateau (section 2.2.1.1).[28] The occurrence of a flat plateau can be associated to consecutive dissociations and formations of interactions characterized by natural dynamics faster than the loading rate.

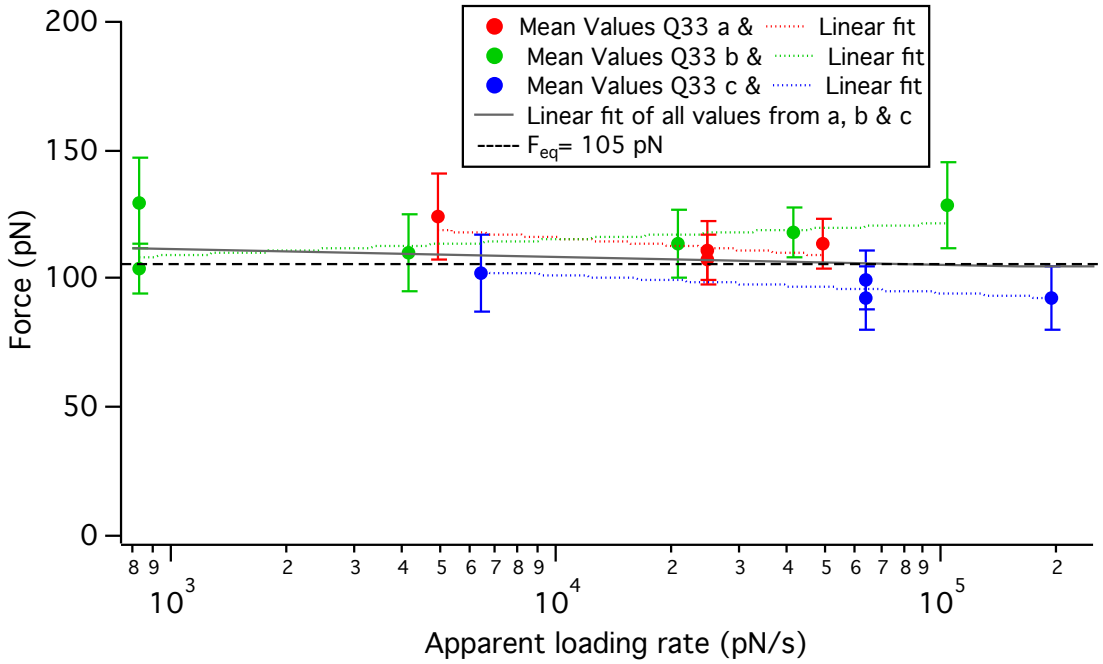

Figure 3.6 Dynamic force spectrum (average unfolding forces as a function of logarithm of the apparent loading rate) of the 33-mers in DMF. Each colour corresponds to a different cantilever, constituting replica. The dots correspond to the most probable unfolding force for each velocity/loading rate and the error bars to the 70% confidence interval. The thin dashed lines are linear fits on non-logarithmic scale for each cantilever. The bold grey dash line is the overall linear extrapolation.

Given that the foldamer seems to unfold under equilibrium regime over this wide range of loading rates, we cannot extract kinetic parameters of the probed interactions. Nevertheless, using the Friddle-Noy-De Yoreo model, we can estimate the free energy difference of the interactions from the 'equilibrium force' (Figure 3.2.B & Eq. 5: $\Delta G = {F_{eq}}^2 / 2\,k_c$). As far as it concerns the unfolding of the foldamer and given the fact that it exhibits a plateau as unfolding pattern, the estimated free energy from the equilibrium force (F_{eq}) corresponds to free energy of the unfolding transition step (opening of a group of intramolecular interactions) underlying the full unfolding process. Indeed the plateau can be seen as consecutive rupture peaks for the opening of a group of interactions with the same force for each unfolding step. It is thus not the total free energy of the unfolding process of the foldamer.

The equilibrium force, F_{eq}, was simply extracted from the dynamic force spectrum by a linear fit of the most probable averaged forces at each loading rate (dashed thick line, Figure 3.6). The free energy was calculated using the mean value of the spring constants of the 3 cantilevers used and we found:

$$\Delta G \approx 193\,pN.nm\,/\,step \approx 47\,k_BT/step \approx 2\times10^{-19}\,J/step$$

$$\cong 116\,kJ.mol^{-1} \approx 28\,kcal.mol^{-1}$$

Unfortunately, without any additional information about the energy landscape of the system pulled by AFM-based SMFS (and the confirmation of a two-wells potential, essential for the use of Eq. 5), we cannot validate the accuracy of these free energy values. Nevertheless, this free energy value of the transition step is in good agreement with the value obtained by Delsuc *et al* (see figure 2.19).[4] Moreover, this energy can certainly correspond to the sum of multiple interaction energies including cooperatively reinforced 2 hydrogen bonds (3-12 kcal.mol^{-1} per H-bonds), π-stacking (3-5 kcal.mol^{-1}), conformational entropy.

Up to date, examples of such rate-independent behaviours are not frequent in the literature. Only few examples of molecular systems show equivalent results.[12,29,30] As pointed above, some scientists associated this behaviour to the presence of long and compliant linkers, having potentially profound effects on the effective loading rates and thus unfolding forces. In order to test if this loading rate independency is due to the PEG linker, we investigated the influence of the linker by taking into consideration the potential compliance effect of the PEG linker. We measured the effective loading rate (lr_{eff}) from the slope of the elastic stretching of the PEG linker before the plateau starts unfolding the foldamer (Figure 3.5, red lines). Firstly, in Figure 3.7.A, we can see that the effective loading rates display a linear relationship with the corresponding apparent loading rates, which indicates that even in the presence of the PEG linker, in our case, the load rises steadily, yet with a constant shift to lower effective loading rate values. The steady increase may be due to the high force (100 pN) at which the unfolding steps occur. Indeed, as shown in Figure 3.3, the elasticity of the combined system (cantilever with linker) behaves linearly akin to the cantilever from a given force.

With these effective loading rates we calculated the effective spring constants k_{eff} (combination of the cantilever and PEG chain compliance) for each pulling curve and we adjusted the force values. The dynamic force spectrum taking into account the effective loading rates (Figure 3.7.B) and the effective forces shows an overall decrease in the equilibrium force down to 70 pN but as foreseen still no evolution of the unfolding force with the loading rate. As the shape of the dynamical force spectrum did not change, it confirms the fast dynamics of (unfolding) of the foldamers compared to the experimental time scale.

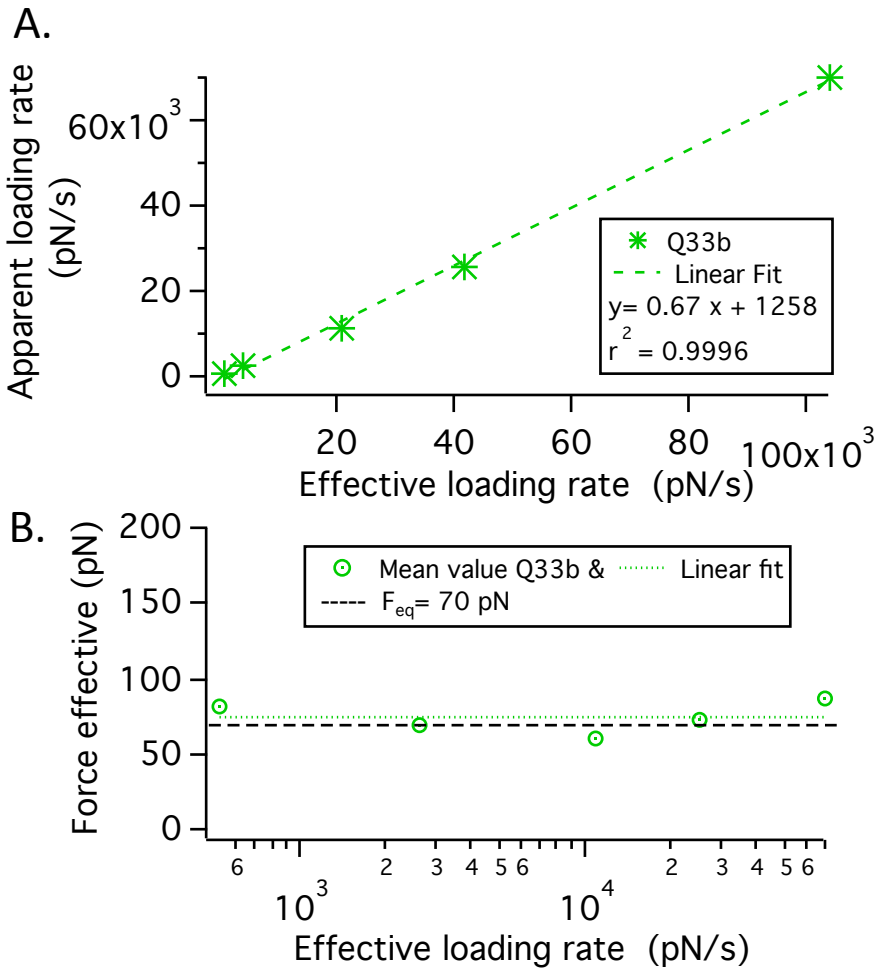

Figure 3.7 (A) Plot of the apparent loading rates as a function of the effective loading rates. The apparent loading rate is $lr_{apparen} = v.k$ and is valid for the whole experiment whereas the effective loading rate is calculated from each curve by measuring the slope before the plateau $lr_{effective} = (dF/dt)$. (B) Dynamic force spectrum, with the measured effective forces and loading rates, of the 33-mers in DMF. The data corresponds to the Q33b of Figure 3.6.

For further analysis, we decided to no longer consider the effective loading rate to draw the dynamic force spectra. However, we cannot ensure that this approach is free of error. Indeed, this analysis is in fact not yet very common, and even less for tethered molecule exhibiting high elasticity differences between the tether (PEG) and the molecule of interest (foldamers). In our case, the signal from the elastic stretching of the linker changes abruptly when the foldamer starts to be under tension and to unfold. Moreover, we are not looking at only a single interaction but successive interactions, for which the effective loading spring might continuously vary. In addition, in our group, other systems comprising also a PEG tether have already been studied.[9] The presence of the tether did not prevent the observation of a rate-dependent force evolution as a function of the loading rate. Finally, as noticed by Evans, Ritchie and Zlatanova, the influence of a compliant force transducer increases with its own length.[26] Therefore, in our set ups, as we

deal with PEG_{5000} (~ 30 nm), which is small compared to studied biological samples, its effect may be actually negligible.

In brief, the effect of the PEG tether should be kept in mind but more investigations and comparison on similar molecular systems should be investigated, before validating this method.

We reproduced the same classic dynamic force spectroscopy experiments on the 17-mer. As expected this smaller foldamer exhibits the same apparent loading rate-independent behaviour (Figure 3.8). No significant evolution could be observed over the probed loading rates, indicating an equilibrium regime as well. Due to a similar equilibrium force (≈ 102 pN), the free energy ($\approx 45\ k_BT \approx 112$ kJ.mol^{-1}) is obviously similar to the one of the 33-mer. These results are consistent with the observations of Chapter 2.

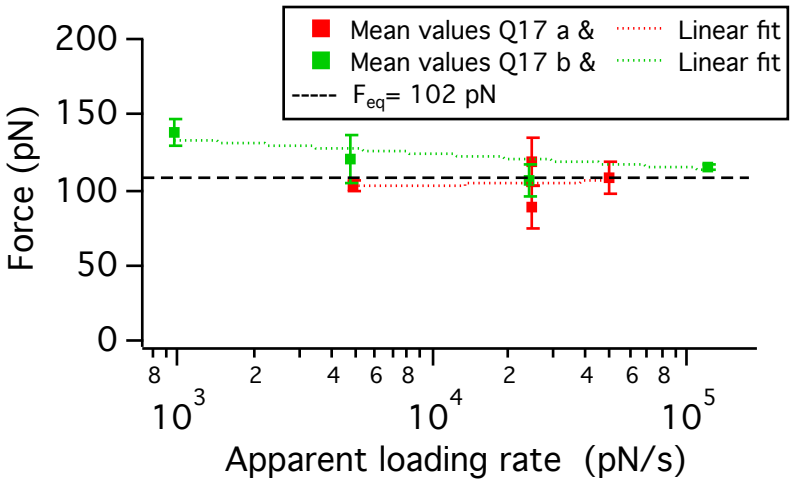

Figure 3.8 Dynamic force spectrum (average unfolding force as a function of logarithm of the loading rate) of the 17-mers. Each colour corresponds to a different cantilever and constituted replica. The dots correspond to the most probable unfolding forces at each velocity/loading rate and the error bars to the 70% confidence interval. The fine dashed lines are linear fits for each cantilever. The bold dash line is the overall linear extrapolation.

Given the appearance of instabilities in the unfolding pattern of the 5-mer, we could expect ultimately a different behaviour for this smallest foldamer according to the loading rate. Therefore we performed also this analysis and we observed the similar variety of unfolding patterns (progressive decreasing force feature, hopping events or single rupture; section 2.2.1.2) on the pulling traces for each tested velocity (Figure 3.9).

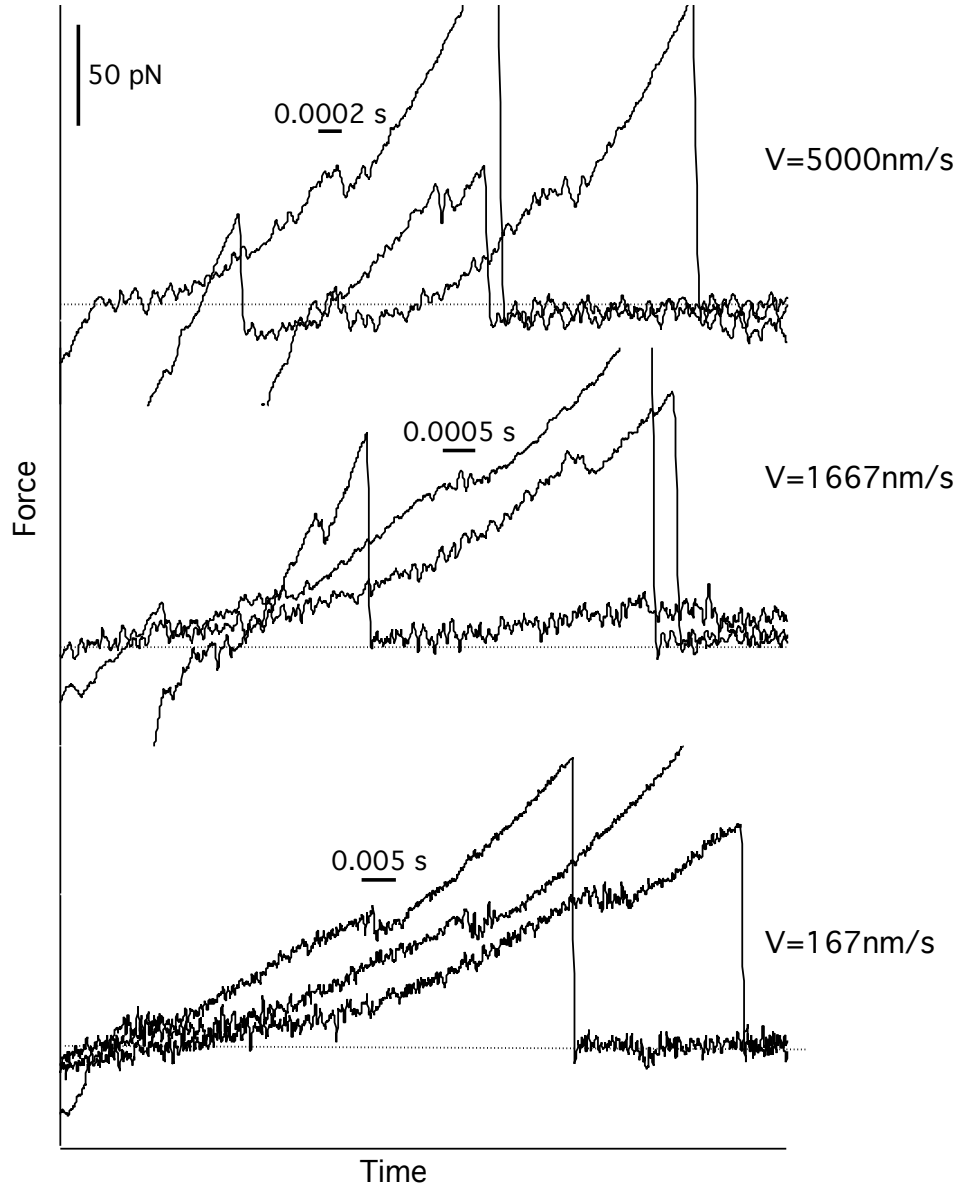

Figure 3.9 Force-time traces of pulling experiments at several pulling velocities on Q5 (provided on the right of each curve). We can distinguish the unfolding features observed previously, *i.e.* progressive decreasing force, back and forth hops and single rupture.

The dynamical force spectrum (Figure 3.10) shows the same evolution as for the longer foldamers, *i.e.* the unfolding forces are not dependent on the apparent loading rates. This observation confirms the high mechanical stability and fast dynamics of the helical structure, even for species as small as 2 turns. This underlines the strength provided by the backbone rigidity and the H-bonds.

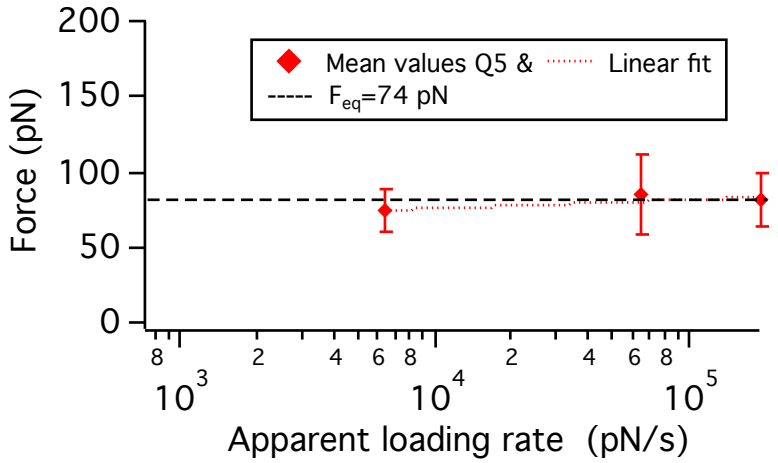

Figure 3.10 Dynamic force spectrum (average unfolding force as a function of logarithm of the loading rate) of the 5-mer in DMF. The dots correspond to the most probable unfolding force at each velocity/loading rate and the error bars to the 70% confidence interval. The fine dashed line is a linear fit. The bold dash line is the overall average extrapolation.

The equilibrium force is on the contrary as already measured about 70 pN, which results in lower free energy value. Under the validity of the use of the Friddle-Noy-De Yoreo model (Eq. 5), the free energy of an unfolding step of a 5-mer is equal to:

$$\Delta G \approx 24\, k_B T/\, step \cong 59\, kJ.mol^{-1} = 14\, kcal.mol^{-1}$$

This value of free energy is again in very good agreement with Delsuc *et al*[4] results on the energy barriers to inverse handedness and metadynamic simulation for Free Energy Profile of handedness inversion as well (14-16 kcal.mol^{-1} for 5-mer).[5]

The obtained value of free energy are presented in Figure 3.11 as a function of the number of units and the evolution is similar to results of Delsuc *et al*[4] (see Figure 2.19).

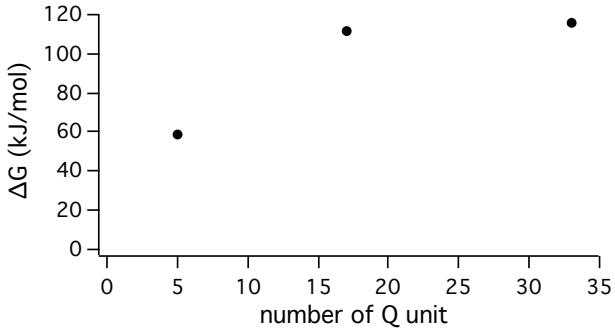

Figure 3.11 Graphic of the free energies measured from the equilibrium force from the DFS as a function of the number of quinoline units comprised in the foldamer.

In order to validate or better estimate the free energy of the unfolding process, pulling-relaxing experiments combined with the use of Crooks fluctuation theorem is usually envisaged. This approach allows taking into account the contribution of the linkers. In our case, it does not provide exactly the same information, as we probe several consecutive interactions. This method based on Crooks fluctuation theorem calculates the total free energy of the full unfolding process. It will be discussed in the next section.

3.2.4 Summary

We depicted the dynamical force spectra (DFS) using the apparent and effective loading rates and spring constant, the foldamer being tethered with a PEG chain, which induces a non-linear elastic response. We observed that the effective loading rate increases linearly as the apparent loading rate. Therefore, we could conclude that in our case, the consideration of an effective loading rate only affects the value of the force and not its behaviour as a function of the loading rate range. To our knowledge, it is the first studied system, for which a large difference in the elastic properties can be observed between the tether (flexible PEG chain) and the molecule of interested (robust aromatic helix). Therefore, for comparing the dynamical properties with other systems, we concluded on the results of standard DFS, but we should keep in mind a potential impact on the force, which goes along with the prediction of Mouritsen.[25] They indeed proposed a general decrease of the forces because the system spends more time at low forces owing to the non-linear force ramp induced by flexible linkers.

The standard dynamic force spectroscopy experiments performed on the 33-, 17- and 5-mers have demonstrated that the force is not loading rate-dependent. The measured unfolding forces at each loading rate are equivalent, which indicates that the quinoline-based foldamers undergo an unfolding forced process at equilibrium over the 3-orders of magnitude loading rate range (from 9×10^2 to 1.3×10^5 pN.nm^{-1}). In other words, the foldamers possess really fast (un)folding kinetics.

This DFS analysis led us to also estimate the free energy of the group of interactions, which is broken during an unfolding step. The obtained energy value (47 k_BT and 27 k_BT for respectively Q33 and Q5) are consistent with the hypothesis of interplay of non-covalent interactions and the cooperative reinforcement for longer foldamers. They are also in good agreement with the supposed interactions involved in the unfolding transition step as well as with literature results of the potentially akin transition steps.[4,5]

The wide range of apparent loading rates used for the experiment did not drive the foldamers to the 'out of equilibrium' regime. Therefore we did not have access to kinetics parameters. In comparison, over this loading rate range, bio-molecules have reached their kinetic ('out of equilibrium') regime and exhibit loading rate dependent rupture forces that can be fitted with the Bell-Evans model in most cases.

This loading-rate independent behaviour under this range of loading rates reflects a very fast dynamics and remarkable rebinding capabilities of the intramolecular interactions. These performances highlight the strength of the designed backbone and intramolecular interactions, which do not allow much conformational freedom. The imparted rigidity of

the quinoline oligomers construct and the high proximity of the interacting partners suggest a near locked system from the smallest oligomer. These results concur with the interpretation of a flat plateau as unfolding pattern.

3.3 Pulling-relaxing, work and free energy measurements

The free energy values obtained by the dynamical force spectrum rely upon models using assumptions and approximations of the underlying energy landscape. Methods using the theories of Jarzynski and Crooks enable to more accurately determine the free energy differences from force-extension curves of (non-equilibrium) SMFS experiments. This method is based on intrinsic properties of small (molecular) systems and uses fluctuations theorems. When the dimensions of a system decrease to the molecular scale, energy fluctuations begin to dominate and induce significant deviations from the equilibrium behaviours.[8]

3.3.1 Fluctuations theorems

To measure the free energy between an initial and a final conformations, the external parameter used to do the measurement has to change infinitely slowly along the path from the initial conformation to the final one. Only under this condition the total work W performed on the system is equal to the free energy difference ΔG. In practice, experiments are performed at a finite rate, leading to the second law of thermodynamics:

$$\langle W \rangle \geq \Delta G \qquad \text{Eq. 7}$$

Eq. 7 Transformed second law of thermodynamics: "total entropy of an isolated system can never decrease over time".

This second law of thermodynamics indicates that for an irreversible process, the average work performed on the system is always larger than the free energy. For a reversible process, the mechanical work equals the Gibbs free-energy change of the process, but in small systems the distribution of work trajectories typically results in hysteresis because of the fluctuations. In other words, repeating the same experiment many times provides different values of the work W because of the thermal fluctuations. However, these values are described by a probability distribution, P(W), which has a mean value always larger than the reversible work.

The difference between the measured work and the reversible work is the dissipated work, $W_{diss} = W - \Delta G$

Given the inequality nature of the Eq. 7 Transformed second law of thermodynamics: "total entropy of an isolated system can never decrease over time".

the free energy cannot be directly obtained from the measurements of the work.

In 1997, Christopher Jarzynski reported a non-equilibrium work relation. He transformed the inequality to an solvable equality, now called the Jarzynski equality (JE).[31] The JE relates the equilibrium free energy difference, ΔG, between two states to an exponential

average of the work, *W*, performed on the system and measured an infinite number of repeated non-equilibrium experiments (equation IV.2).

$$exp\left(\frac{\Delta G}{k_B T}\right) = \langle exp\left(\frac{W}{k_B T}\right)\rangle \qquad \text{Eq. 8}$$

Eq. 8 The Jarzynski equality where ΔG is the equilibrium free-energy difference, k_B is the Boltzmann constant, *T* the temperature and *W* the work done by the system. The brackets note the average.

The implementation of the Jarzynski equation is not particularly trivial and is only valid for systems performing near from equilibrium.

In 1999, Gavin Crooks developed a more robust and more rapid method to obtain equilibrium free energies from non-equilibrium processes in solution, using unfolding and refolding trajectories.[14] The Crooks fluctuation theorem (CFT) predicts symmetry of the work fluctuations associated with the forward and reverse cycles of a system driven far from equilibrium by the action of an external perturbation. Both *forward (*unfolding*)* and *reverse (*refolding*)* processes are related to a work probability $P_U(W)$ and $P_R(-W)$ respectively and quantify respectively the amount of hysteresis of the irreversible work done to unfold and refold a molecule. Given the predicted symmetry in these probabilities, it is possible to extract the free-energy difference between both equilibrium and out-of-equilibrium states with the relation:

$$\frac{P_U(W)}{P_R(-W)} = exp\left(\frac{W - \Delta G}{k_B T}\right) \qquad \text{Eq. 9}$$

Eq. 9 Crooks fluctuation theorem equation, where $P_U(W)$ and $P_R(-W)$ are the work probability to respectively unfold and refold the system, ΔG is the equilibrium free-energy difference, k_B is the Boltzmann constant, *T* the temperature and *W* the work done by the system.

When $P_U(W)$ and $P_R(-W)$ are equal, the value of the work corresponds to the free energy.

Jarzynski and Bustamante shown that this theorem can be applicable to single-molecule force spectroscopy experiments and can determine free energies for folding and unfolding processes occurring in weak as well as strong non-equilibrium regimes.[13] Pulling-relaxing experiments can be performed and associated to the forward and reverse processes.

3.3.2 Pulling-relaxing experiments

Using an AFM setup, we can precisely control the movement of the cantilever as a function of the distance or the time, but also as a function of the relative voltage or force. Therefore, it is possible to pull a single molecule, to stop its stretching before it detaches from the tip and to re-approach towards the surface to allow the monitoring of the refolding of the molecule. The molecule is thus trapped between the AFM tip and the

surface and 'pulling-relaxing' cycles are performed continuously to monitor the unfolding and relaxing traces of a molecule, as long as it stays attached to the tip (Figure 3.12).

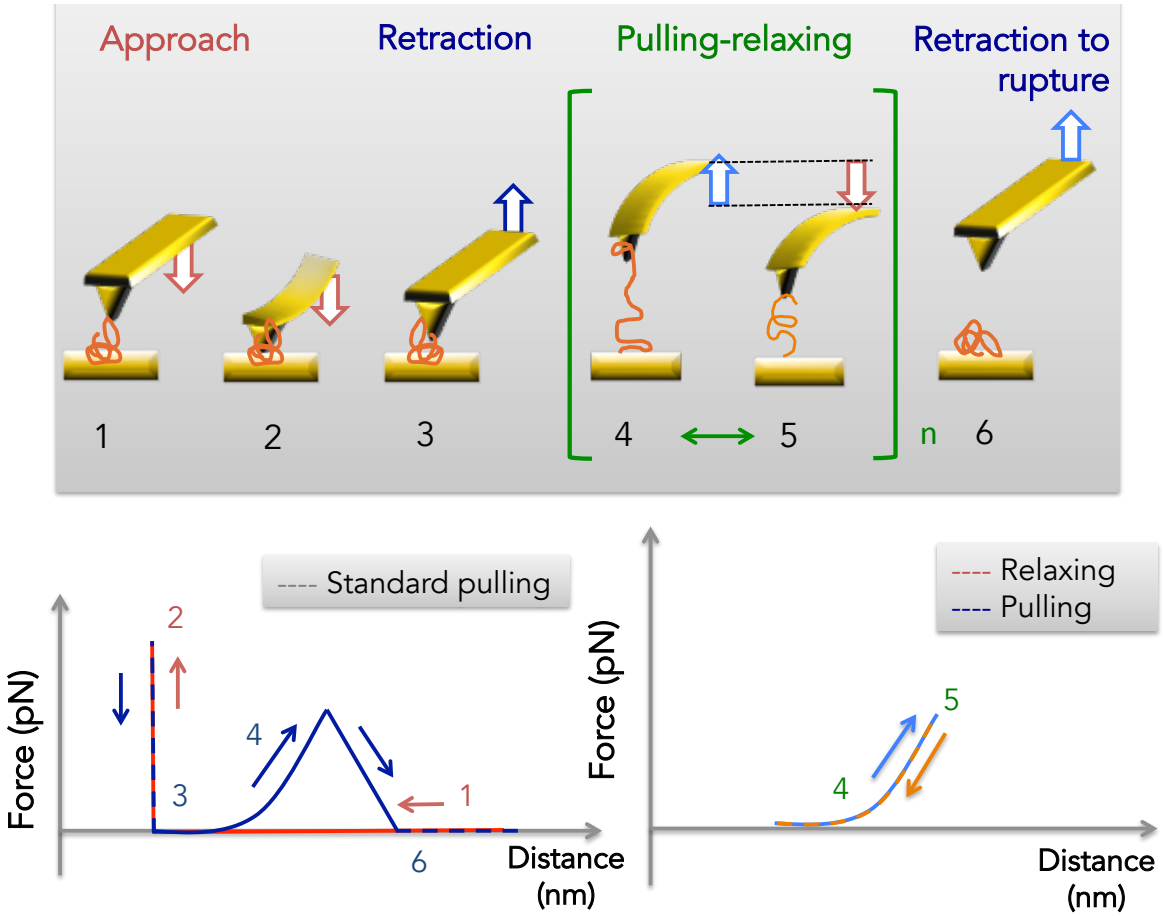

Figure 3.12 Illustration of the pulling-relaxing experiment and the associated force-distance curves. (1) At the beginning of a pulling-relaxing cycle, the tip is approached to the substrate and (2) gently put in contact to adsorb a molecule (similar as standard pulling experiment). (3) Then the tip is retracted from the substrate to monitor the pulling curve. (4) We control the pulling of the molecule until the stretching force reaches a limit value (relative threshold), which likely preserves the molecule attached to the tip. (5) Reaching this threshold, the tension is released by approaching again the tip towards the substrate. (4-5) Once a molecule is trapped between the tip and the substrate, the ideal pulling-relaxing experiment consists in performing numerous cycles (*N*) in order to successively detect the characteristic unfolding and refolding of the molecule over time, until the molecule eventually detaches (6).

Comparing both traces provides essential information about the mechanical behaviour such as reversibility, fatigue properties, refolding dynamics and refolding pathway.[32] In the literature, examples are quite rare but are very valuable for the characterization of the molecule's mechanical behaviour.[10,13,33–35] Several cases have been observed:[36] (i) When the force-extension profile of relaxation follows exactly the same trace as during pulling, the stretching is a fully reversible process (Figure 3.13.A: almost fully reversible). (ii) When the relaxation trace does not follow exactly the puling curve, the small hysteresis observed indicates a partial reversible process on the time scale of the experiment (Figure

3.13.B). (iii) Sometimes, a large hysteresis can be observed; no characteristic peak from the pulling is recovered along the relaxing. This may indicate an irreversible unfolding process. However, if the next pulling curve exhibits the previous pattern, it means that the unfolding is reversible if sufficient time is given (Figure 3.13.C). Successive pulling-relaxing cycles on the same molecule can evidence the robustness or the fatigue properties (Figure 3.13.B: fatigue).

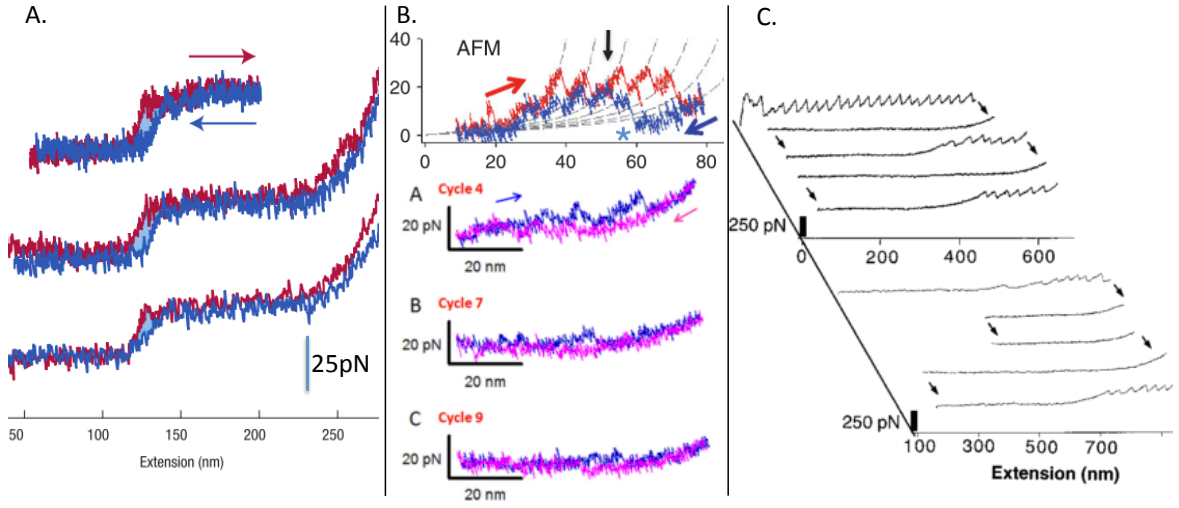

Figure 3.13 Force-distance curves of pulling-relaxing cycle experiments on (A) myosin. The unfolding process is almost fully reversible. Only a small hysteresis can be observed (highlighted in light blue area).[10] (B) On ankyrin, partial refolding can be observed. Reformation of peaks appears after some relaxing time. The bottom graphs capture mechanical fatigue. On cycle 9, the refolding pattern almost disappered.[34] (C) On titin: the refolding curves show high hysteresis, the unfolding pattern is not recovered directly during the refolding but the specific unfolding pattern reappeared on the following pulling curve[32]. Adapted from references 10,32,34.

Under the force-distance traces, the area represents the work performed on (or by) the molecule to break (or reform) the intramolecular interactions and to stretch the hidden length that is released after the breaking (see chapter 1).[37]

By varying the pulling and relaxing speeds, we can pull the system out of equilibrium and measure deviations from the reversible process. According to the Crooks theorem, the symmetry on the relaxing is expected.

3.3.3 The validity of the Crook fluctuation theorem for SMFS

The first validation of the Crooks fluctuation theorem (CFT) in SMFS was performed with small RNA hairpins.[13] Bustamante's group and collaborators used optical tweezers to measure repeatedly the mechanical works associated with the unfolding during the pulling experiment and refolding during the relaxing experiments on small RNA hairpins occurring near equilibrium.

The work can be measured by the integral of force over the extension (*i.e.* $W = \int_a^b F\,dx = \sum_a^b F_i\,\Delta x_i$F) (Figure 3.14.A). $P_U(W)$ and $P_R(-W)$ can be associated to the probability distributions of the work performed on, and by, the stretched molecule during the mechanical unfolding and refolding processes, respectively (Figure 3.14.B).[13,17,38] When both (pulling and relaxing) movements are performed at the same velocity at near or out of equilibrium regimes, the value of ΔG can be determined at the crossing of both forward and reverse work distributions. For the 3 tested velocities, they observed 2 distinct work distributions for each velocity. By increasing the pulling velocity, the hysteresis is increased and the overlapping region between both work distributions became smaller but still sufficient to measure the crossing which always appear near 110 k_BT. These observations validated the applicability of the Crooks theorem for SMFS experiments on molecular systems driven out of equilibrium.

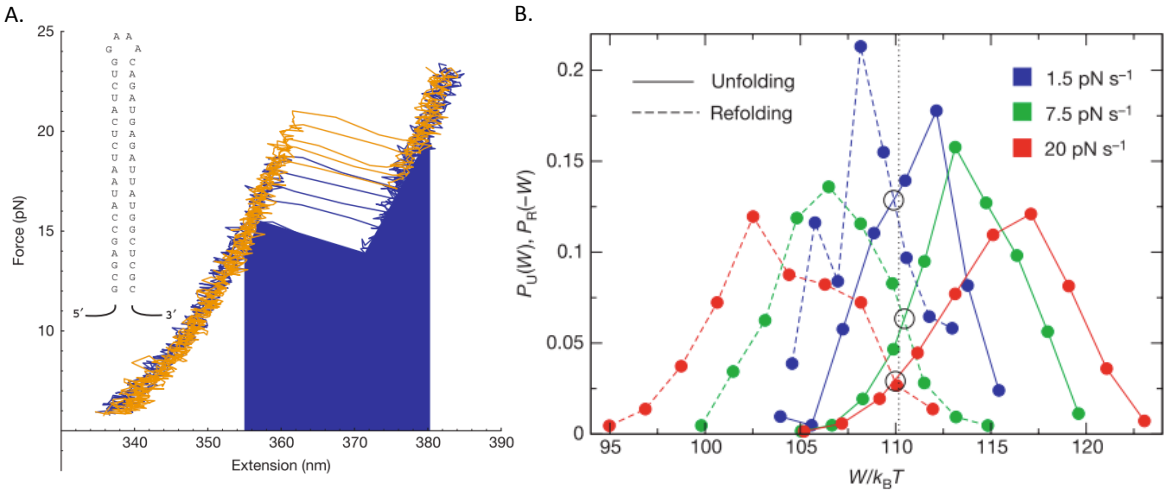

Figure 3.14 (A) Pulling (blue) and relaxing (orange) force curves of the RNA hairpin. The blue area corresponds to the work measurement ($W=F.d$). The RNA sequence is shown as an inset. (B) Work distributions for RNA unfolding (P_U-continuous lines) and refolding (P_R-dashed lines) at three loading rates. The distributions of the different loading rates cross at the similar work value of 110 k_BT. Reproduced from reference 13.

The limit of the Crooks fluctuation theorem stands in the detection of the crossing between both distributions, in a very-far-from-equilibrium regime. This study shows that this method is applicable as long as the amount of dissipated work, is equal or less than ~ 100 k_BT. For large values of the dissipated work the experimental unfolding and refolding work distributions hardly cross, thereby limiting the direct applicability of the CFT. When the experimental speed is approaching the equilibrium regime, both distributions completely overlap and ΔG is given by the most probable work value.

3.3.4 Results and discussion

Pulling-relaxing experiments were performed on the longest foldamer (33-mer) in DMF at identical velocity for the pulling and relaxing curve of 100 $nm.s^{-1}$, 167 $nm.s^{-1}$ and 1667 $nm.s^{-1}$. As illustrated in Figure 3.15, the relaxing curves follow exactly the pulling curves. Thanks to a relative deflection threshold we could monitor the whole foldamer unfolding and refolding many consecutive times (See appendix D. for details).

The force-constant plateau as well as the decreasing and oscillating force feature are observed for both traces. This highlights the full reversibility of the unfolding process. Moreover, it demonstrates the strong elastic properties of the foldamer. During its forced unfolding, the foldamer has not dissipated any amount of energy but stored it (in the chemical structure) to be able to pull back on the cantilever and refold back without hysteresis. It means that the unfolded foldamer has the energy to change its conformation and recreate interactions that have been broken. This unfolding and refolding can take place more than hundred times consecutively, exhibiting no evidence of fatigue. Nevertheless we cannot ensure that the mechanisms are exactly inverse to each other. These results are consistent with the fast kinetics of un(folding).

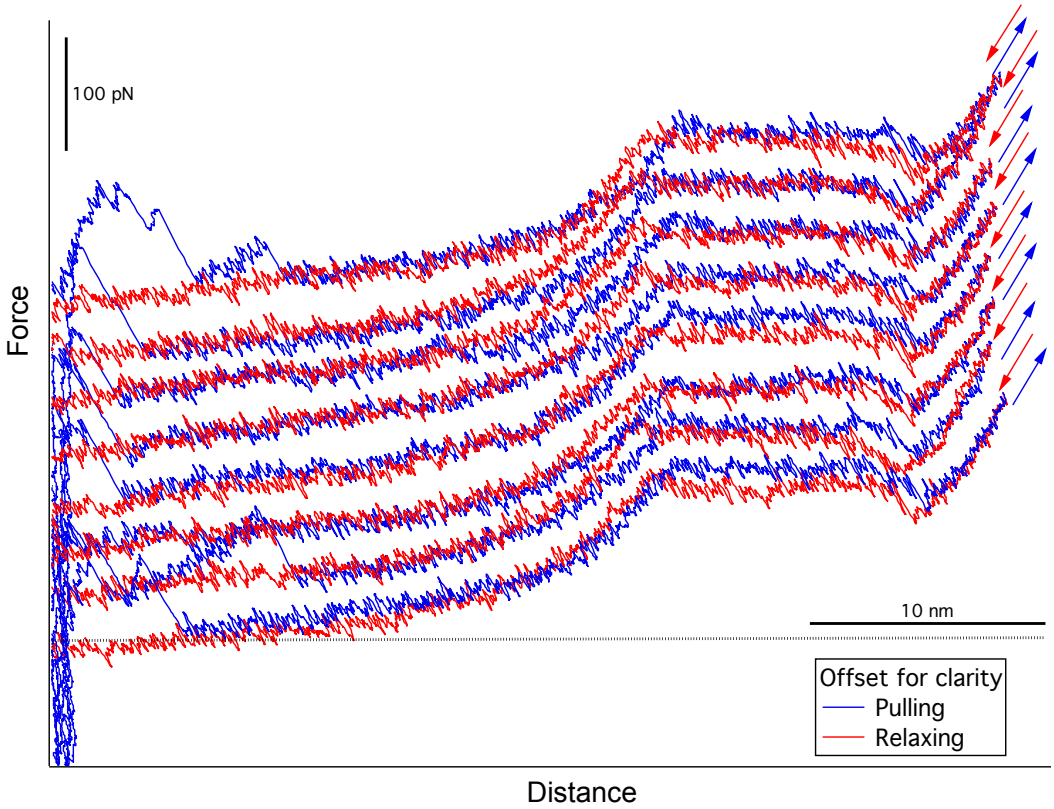

Figure 3.15 Typical consecutive pulling relaxing cycles on Q33 foldamer in DMF at 166 $nm.s^{-1}$. For clarity each cycle is offset on the graph. The arrows on the left show the displacement of the cantilever regarding the substrate.

Our observations demonstrated that a single synthetic helix could be extended up to 3.5 times its original length (Figure 2.12). This transition is fully and rapidly reversible, making these synthetic foldamers truly elastic helices. The molecules are able to refold against considerable forces of 150 pN and can store energy to exert a force against a load of at least 100 pN. Our results show that these foldamers have the potential to surpass the mechanical performance of natural helices.[10,39]

Interestingly, Marden and Allen classified the maximum net forces produced by a broad variety of animal- and human-made motors.[40] The productions of net forces follow two general trend lines (Figure 3.16). The synthetic molecular motors deviate from these trends, presumably because of the multiaxial stress dimensions compared to the single axial, often translational, motion in the other systems. It is interesting to see, that the foldamers also seem to present greater performances making it deviates also from a common trend line. This highlights the broad potential of the molecular world and shows promising properties for building nanomachines.

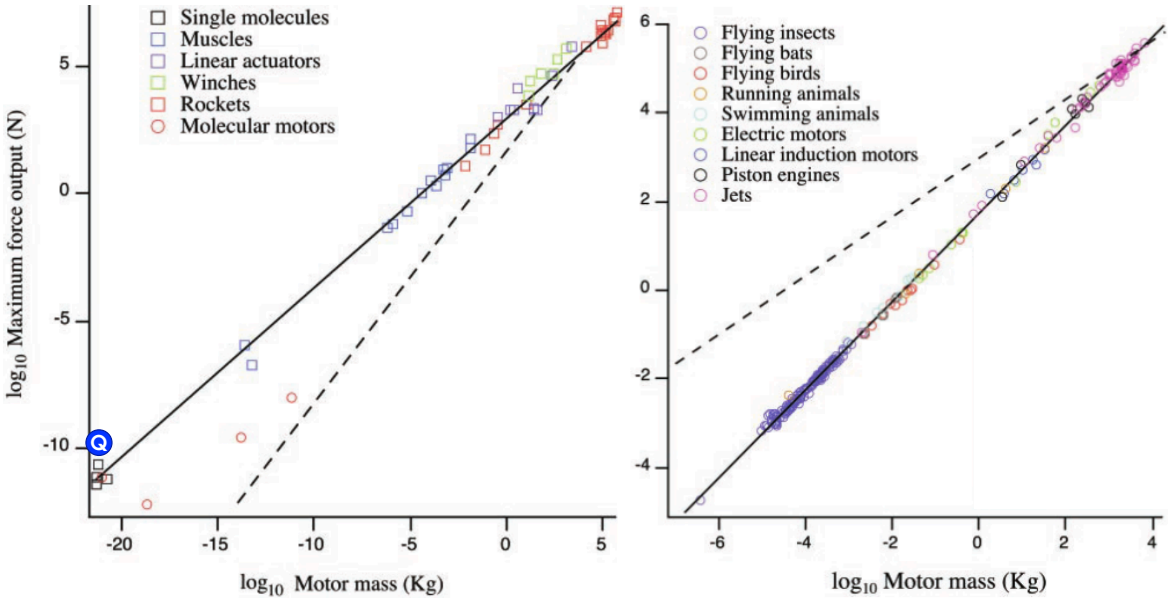

Figure 3.16 Graphs of the maximum net force output as a function of motor mass for translational motors. In the left graph, the solid line represent the Group 1 motors and the dashed line is the isometric scaling equation for the Group 2 motors shown in the left graph as the solid line. Molecular motors (circular symbols) are excluded from the regression fits. A blue sphere with Q inside shows the force performance of the 33-mer quinoline-based foldamer. Reproduced from reference 40.

To measure the work required to unfold the foldamer and the work applied by the foldamer to pull back on the cantilever during refolding, we integrated the area beneath the pattern of the foldamer unfolding (delimited in the previous chapter) during the pulling and the relaxing respectively, as illustrated by the dotted vertical lines in Figure 3.17. From this area we subtracted the entropic elastic contribution from the PEG tether

stretching by adjusting a WLC fit on the last part of the force-distance trace and considering the area beneath.[37] The obtained work values are plotted into histograms. We performed this analysis at three loading rates.

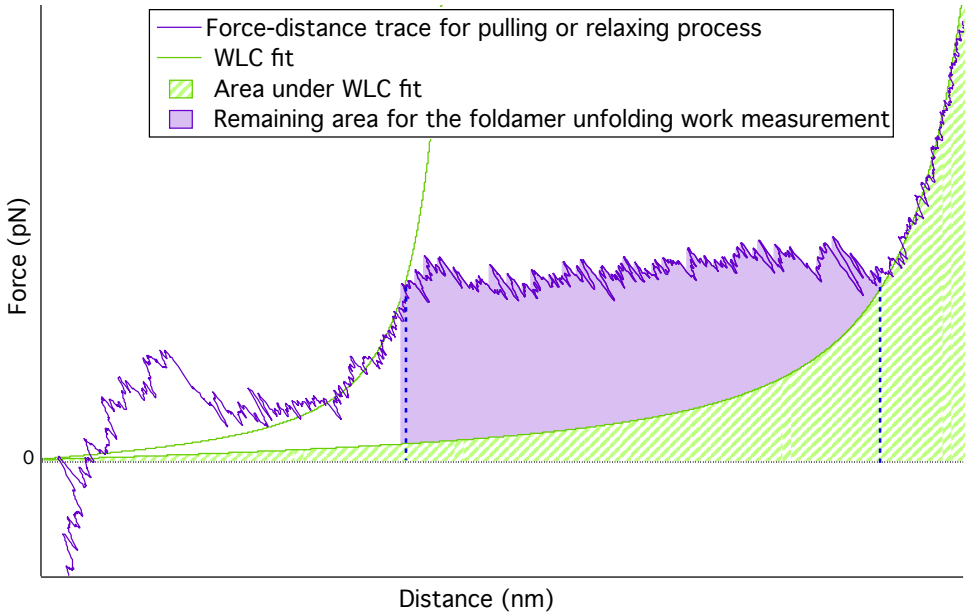

Figure 3.17 Illustration of the measurement of the work for each curve of the pulling-relaxing experiment. Typical force-distance curve observed during a pulling or relaxing experiment and WLC fits to guide the elastic contribution of the PEG linker. The area, which corresponds to the work for the unfolding or the refolding process, is the purple shaded area. It is measured by integrating the area under the pulling/relaxing curve and the WLC fit between the beginning and the end of the foldamer's whole un/re-folding pattern.

In Figure 3.18, we can observe that the distribution of the work probabilities for unfolding and refolding superimpose almost perfectly and can be fitted with Gaussian functions. We measured almost the same work values for the pulling and the relaxing process for all the three loading rates. A slight difference of 10-20 pN.nm can be measured between the unfolding and refolding works. This may be related to a slight hysteresis, although it is not significant given the experimental and analysis errors. In addition, as described by the non-equilibrium theory, this hysteresis value should have increased as we increased the loading rate.[13,14] Therefore considering this difference as not significant, it clearly suggests a (quasi-)fully reversible process.

Comparing the values from experiments carried out at different loading rates, no significant difference could be observed, as expected with the DFS analysis. Slight differences come from technical artefacts (*e.g.* a difference in resolution). Indeed, a global small shift of each distribution to higher work value is physically meaningless. If an influence of the loading rate should have had been observed, it should also have gone hand in hand with an increasing separation between pulling and relaxing works as we increase the loading rate.

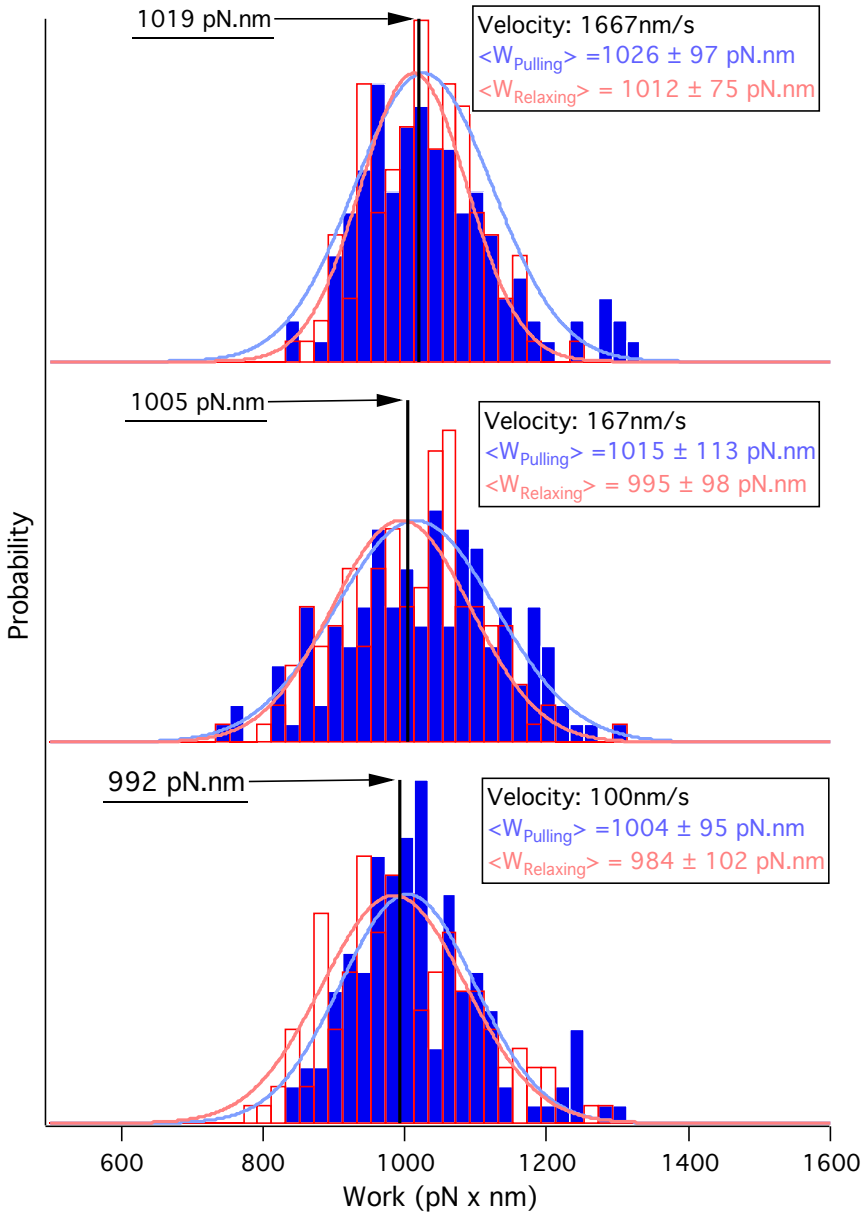

Figure 3.18 Histograms and Gaussian fits of the unfolding work (blue) applied by the cantilever and the refolding work applied by the foldamer (red) at different loading rates. The loading rates are indicated on the right. The crossings of the distribution are shown by a black line and estimate the free energy of the complete unfolding of the foldamer (Crooks fluctuation theorem).

These results are in good agreement with the dynamical force spectroscopy study: over the accessible loading rate range of our system, the 33-foldamer unfolds and refolds in an equilibrium regime. The Crooks fluctuation theorem could be successfully applied on our results to determine the free energy of the full foldamer unfolding and refolding. We averaged the three results, as all are in equilibrium and we obtained:

$$P_U(W) = P_R(-W) \rightarrow W = \Delta G = 244 \pm 24\, k_B T = 144 \pm 14\, kcal.mol^{-1}$$
$$= 10 \pm 1\, kcal.(mol.nm)^{-1}$$

This proves the extreme mechanical stability of the folded structures and their elastic properties. Compared to the same extension for a protein, they store around 4 times more energy than the helical proteins.[10,41]

3.3.5 Summary

Whereas the DFS coupled to the Friddle-Noy-De Yoreo model allowed us to estimate (under validity condition) the free energy of the interactions at each unfolding step (28 kcal.mol^{-1}), the pulling-relaxing experiments coupled to the Crooks fluctuation theorem provided us, with less approximation and more accuracy (we take into account the entropic contribution of the linker), the total free energy between the fully folded state and the fully unfolded state (144 kcal.mol^{-1}). These last experiments clearly proved the total reversibility of the mechanical unfolding, the huge mechanical stability, robustness and the remarkable elastic properties of the helical quinoline-based foldamers. No significant hysteresis has been identified between the unfolding and refolding trace, which indicates that no energy was dissipated during the unfolding process. The foldamer is thus able to store energy and to use it to exert a force against a load higher than 100 pN to reform its initial helical conformation. The performances surpass the ones of the natural counterparts[10,42] and can be explained by the numerous interactions taking place in the quinoline-based foldamers and the fact that they are in close vicinity. These interactions constrain enthalpically and entropically the conformation in the folded state.

3.4 Insights into the dynamics from the hopping

3.4.1 Hopping: real-time unfolding-folding transitions

Hopping events refer to folding-unfolding transitions in real-time.[43] They are the hallmark of thermodynamic equilibrium. Kinetic information can be directly extracted from these fluctuations.[44,45] In force-distance experiments, hopping events occur when the molecular system being unfolded refolds much faster than the time required to increase the load to apply a sufficient force to maintain the system in its unfolded state. The molecule is experiencing a *(near)-equilibrium* unfolding process.

In the literature, examples of such observations are very rare. However with the development of low drift atomic force microscopes (AFM), such observations become technically accessible. Slow pulling velocities with a good force resolution are nowadays achievable and enable to observe refolding process in proteins in real-time.[46]

Such observations of refolding events are clearly dependent on the natural folding rate of the interaction/molecule and are limited by the experimental rate. To observe real-time unfolding-refolding transitions, the molecular system needs to be able to fold in a shorter time than the time given by the experimental pulling load. Therefore, the accessibility to relatively low experimental pulling velocities is crucial to be able to observe hopping events in the molecular systems of interest. Figure 3.19 sheds light on the relevant ranges of timescales associated to the different hierarchy of structure formations in protein folding. Whereas the nucleation of secondary structures can occur within a few microseconds, local domains are formed in rather millisecond and full quaternary structures of proteins may require a few seconds to fold.[47,48]

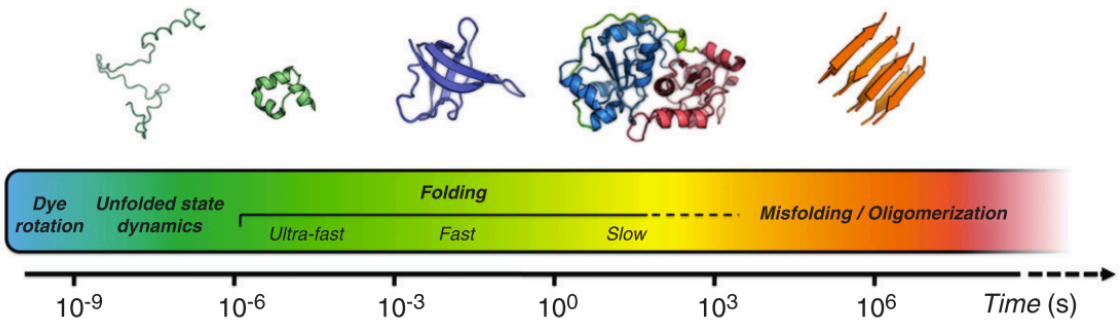

Figure 3.19 Timescales of protein folding. Reproduced from reference 48.

The group of C. Bustamante observed hopping events for the first time in RNA hairpins unfolded by optical tweezers in 2001 (Figure 3.20.A-B).[49] They observed the back and forth fluctuations on force-distance curves at several loading rates. When the loading rate was increased up to 10 pN.s^{-1}, hysteresis appeared between pulling and relaxing traces and

hopping eventually disappeared (Figure 3.20.C). They performed additionally force-clamp experiments to unfold the hairpins at different constant forces. They determined the range of critical forces in which the hairpins are bi-stable and hop between 2 states and they calculated the force-dependent equilibrium constants of these transitions (Figure 3.20.D).

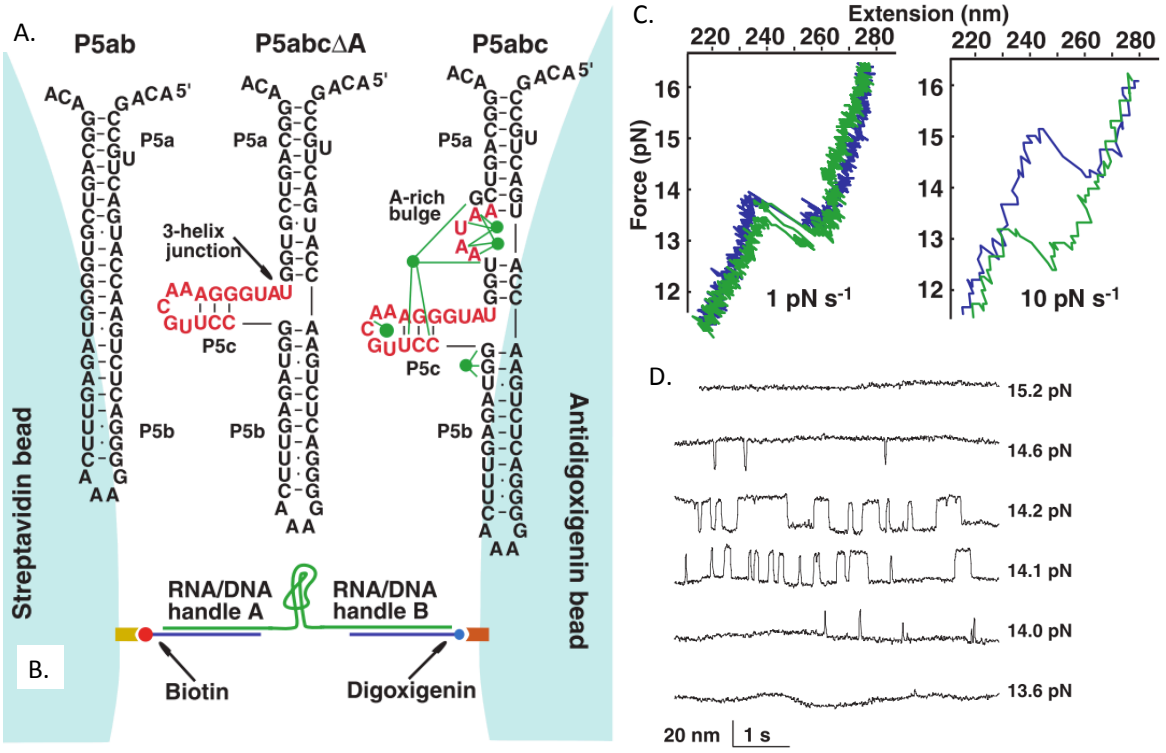

Figure 3.20 (A) Sequence and secondary structure of the RNA hairpins. (B) Illustration of the optical tweezers set-up on the RNA hairpins attached between 2 beads with DNA handles. (C) Force-extension pulling (blue) and relaxing (green) curves at lower and higher loading rates. Hopping can be observed on the left graph. (D) Extension-time traces of the RNA hairpin at various constant forces. Reproduced from reference 49.

The group of M. Rief used low drift AFM to observe hopping events during the unfolding of the helices of calmodulin (Figure 3.21).[46] Extremely slow pulling was required to observe the fluctuations (1 nm.s^{-1}). With previous knowledge of the transition state from the folded state ($\Delta x_{N\text{-}TS}$ = 2 nm), they reconstructed the full energy landscape and they calculated the folding rate under equilibrium regime to be of ~2×10^5 s^{-1} using Monte-Carlo simulations. They identified the helix-containing calmodulin to be one of the fastest folding proteins known to date.

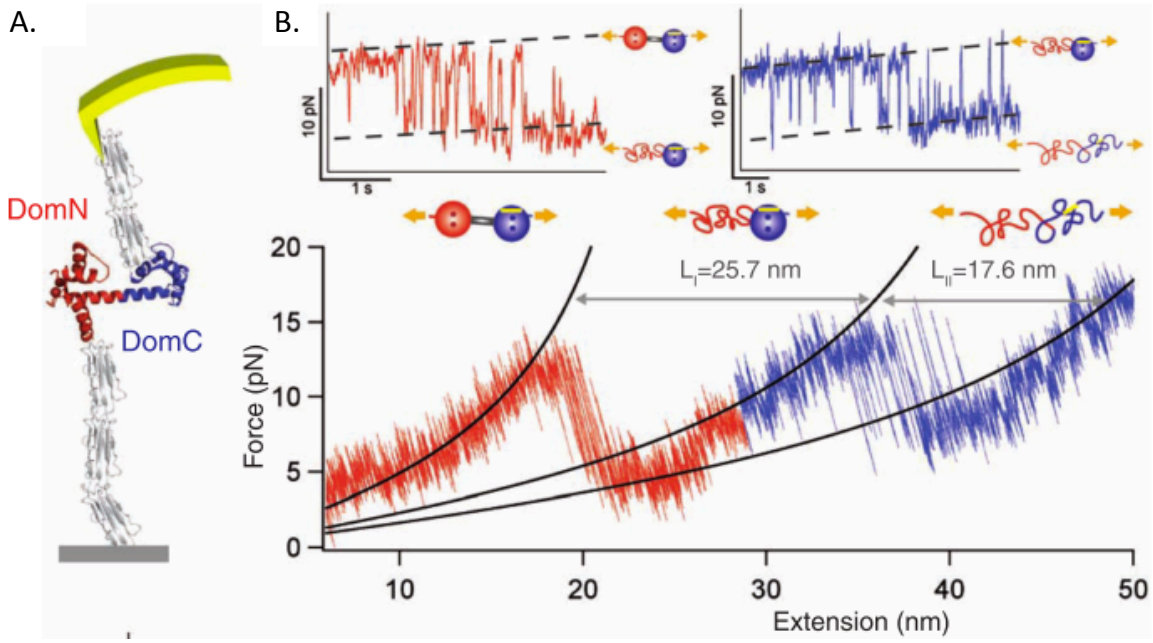

Figure 3.21 (A) Illustration of the AFM-setup, with calmodulin attached to AFM cantilever tip and surface by means of filamin domains that serve as handles and force reference. (B) Force-distance curve of the unfolding process and force-time traces of zoom on the hopping events. Reproduced from reference 46.

3.4.2 Results and discussion

In the standard (Figure 2.7) and pulling-relaxing (Figure 3.15) force-distance traces previously measured, we could often observe out of noise unfolding-refolding fluctuations at the end of the unfolding process of the foldamer. In the previous chapters, we associated these fluctuations to the unfolding and refolding of the nucleation segment of the foldamers, which corresponds to the breaking of 6-7 quinoline units and their reformation to recreate a helical segment. We cannot refute the probability of creating a helical segment with other quinoline units of the foldamer. On the contrary, already stretched units are highly likely to contract.

We observed these fluctuations at a wide range of velocities from 33 $nm.s^{-1}$ to the very high velocity of 3333 $nm.s^{-1}$ (Figure 3.22). We could observe hopping events for all the loading rates and we counted the number of fluctuations and thereby measured the fluctuation frequency, as well as the average refolding time for the different velocities.

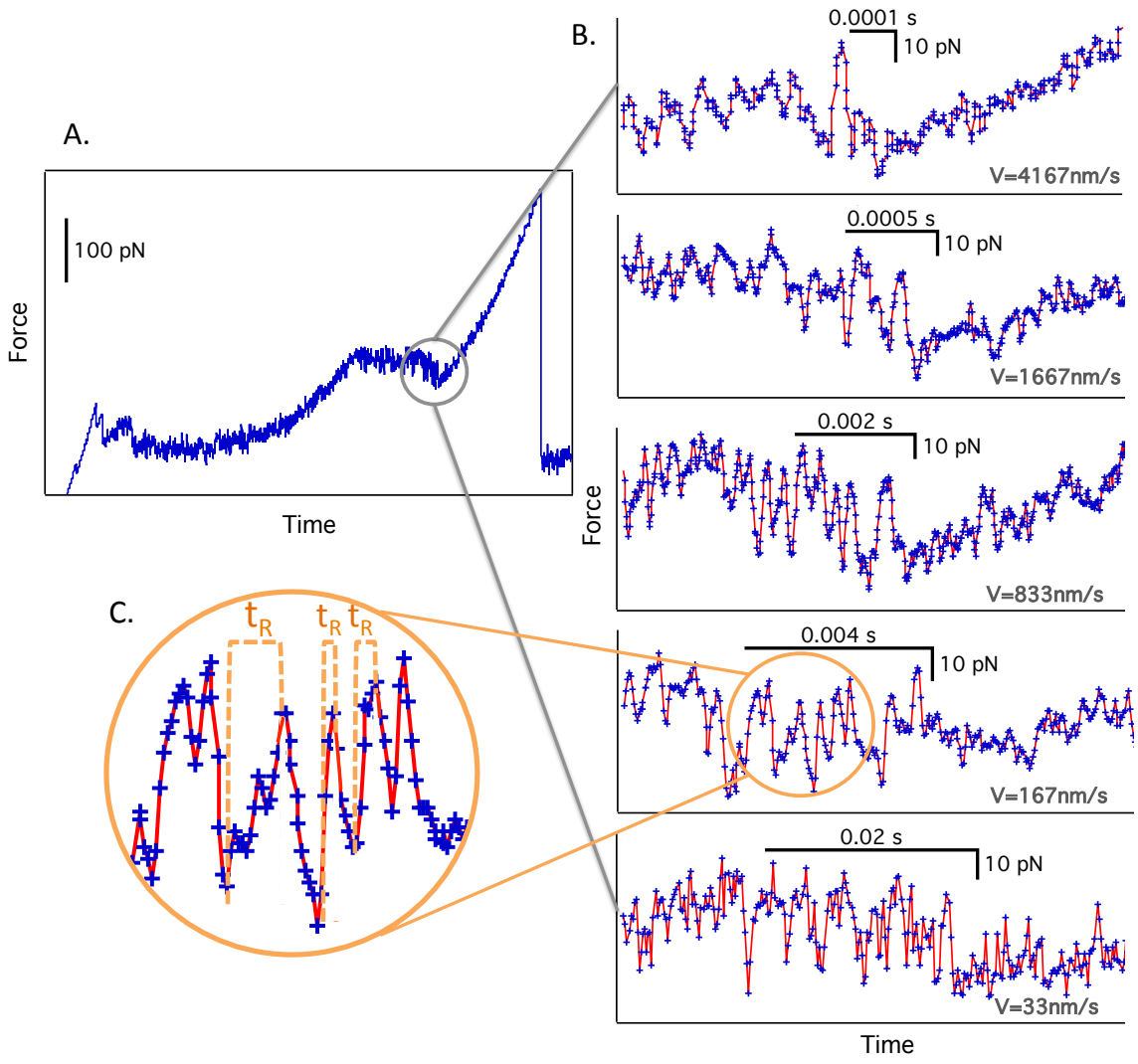

Figure 3.22 (A) Full force-time trace and (B) zooms on the hopping events at the end of the foldamer unfolding at several pulling velocities (given in the right of each graph). The blue crosses represent the recorded data points. (C) Zoom to show the refolding time measurements.

As given in Table 1, we calculated that the frequencies of fluctuation increase with the velocity and loading rate. It was expected as this frequency includes the unfolding step, which is driven by the pulling force-ramp. The higher is the velocity, the faster the foldamer is forced to unfold. Therefore, we cannot directly extract kinetic information. To have access to this information force-clamp experiments are necessary, as discussed above. Nevertheless, given this evolution, we can suggest that the refolding is not a time-consuming step compared to the unfolding time. It means that the refolding takes place much faster than the unfolding, in good agreement with the stability of the folded conformation in solution.

Table 1 Analysed parameters for the investigation of the hopping events.

'K' is the spring constant of the cantilever; 'velocity' is the speed of the pulling motion; 'time step' is the duration between two data points in the pulling trace (Picoview software records at regular time steps initially calculated by dividing the duration of the trace by the number of points for the trace (18000 pints for pulling; 2000 for approach)); 'loading rate' is obtained by multiplying the velocity by the spring constant; 'sampling frequency' is the number of data points per second; 'number of hops' is the number of hopping events (back and forth oscillation) (averaged over ~ 100 curves); 'hopping frequency' is the number of hopping event over one second (averaged over around hundred curves); 'total time of hopping' is the duration during which hopping event are observed (averaged over ~ 100 curves); 'refolding average time' is the duration of the back trace of each hops (averaged over ~ 100 curves); 'force increment over total hopping' is the theoretical force applied by the cantilever over the time of the hopping; 'force difference of the hops' is the measured force difference between the beginning and the end of the hops (averaged over ~ 100 curves).

	K (pN/nm)	Velocity (nm/s)	Time step (s)	Loading rate (pN/s)	Sampling frequency (Hz)	Number of hops	Hopping frequency (Hz)	Total time of hopping (s)	Refolding average time (s)	Force increment over total hopping (pN)	Force difference of the hops (pN)
1	40	167	$3{,}3.10^{-5}$	6667	30000	3,3	543,9	-	-	35,2	-
2	40	1667	$8{,}3.10^{-6}$	66667	120000	1,5	2169,5	-	-	49,4	-
3	28,9	33	$1{,}67.10^{-4}$	963	6000	8	338,5	0,01732	0,001338	30,2	31
4	28,9	167	$3{,}3.10^{-5}$	4817	30000	4,4	706,3	0,00430	0,000695	32,8	27
5	28,9	833	$1{,}67.10^{-5}$	24083	60000	2	1531,7	0,001080	0,000253	25,9	26
6	28,9	1667	$6{,}67.10^{-6}$	48167	150000	2,3	3692,2	0,000437	0,000176	35,2	28
7	28,9	4167	$3{,}3.10^{-6}$	120417	300000	1,6	7737,8	0,00007	0,00004	31,1	28

In addition, by monitoring the number of fluctuations for each velocity, we observed that the number decreases with the increasing loading rate. This result is expected when the system is perturbed under (near-)equilibrium regime. The slower the system is pulled, the slower the load increases. The system is thus submitted to a lower force increment after the unfolding step, which allows easier refolding than when it is submitted to a large force increment from faster loading rates. When we pull very fast, the applied force on the molecule is already very high shortly after the unfolding, which decreases the probability of refolding. These observations confirm again the equilibrium regime under a wide range of loading rates, including much higher loading rates than previously observed for biological molecules. Consequently, it underlines the remarkable fast dynamics of the system.

This very fast dynamics of the foldamer hampers the extraction of quantitative information. We observed that the fluctuation frequencies are governed by the velocities but also by the sampling frequency. As prescribed by the Nyquist theorem, the sampling frequency needs to be at least twice higher than the signal frequency to be able to record the real signal frequency. In general, at slower sampling frequency than the unfolding-refolding frequency we cannot record the real unfolding-refolding frequency.

Technically the sampling frequencies are given by the number of data points for a trace (18000 points) divided by the total time of the recording of this trace, which is dependent on the velocity. In other words, the resolution of time (or increment of time between two points) is lower (larger) for slow velocity, *i.e.* slow loading rate. We indeed clearly observed at the slowest velocity (33 $nm.s^{-1}$ - line 3 of Table 1), the ratio between hopping frequency and sampling frequency is not following the same trend as the others and in Figure 3.22, we can see that the hops are made by the minimum points (3) required to draw a fluctuation. At slower velocity, we were obviously not able to probe the real number of fluctuations. At higher velocity, it was not clearly observable.

Then we estimated the refolding time (t_R) by measuring the time lapse between the last point of unfolded state and the first point of the subsequent refolded state (Figure 3.22.C). We again found values that depend on the loading rate and the sampling rate (Figure 3.23). This means that we do not have access to the intrinsic refolding time of the foldamer but an upper limit. Given the evolution of the average refolding time, with the higher sampling speed (300 kHz), we tend to approach the intrinsic refolding time. Therefore, we can suggest that the nucleation sequence should refold in less than 40 µs. This value is in good agreement with theoretical folding dynamics of α-helix in proteins.[48,50] Nevertheless, to our best knowledge, there is no evidence of hopping events in α-helices pulling experiments at such high velocities (up to 4166 $nm.s^{-1}$). For the calmodulin case[51], hops were observed up to 500 $nm.s^{-1}$.

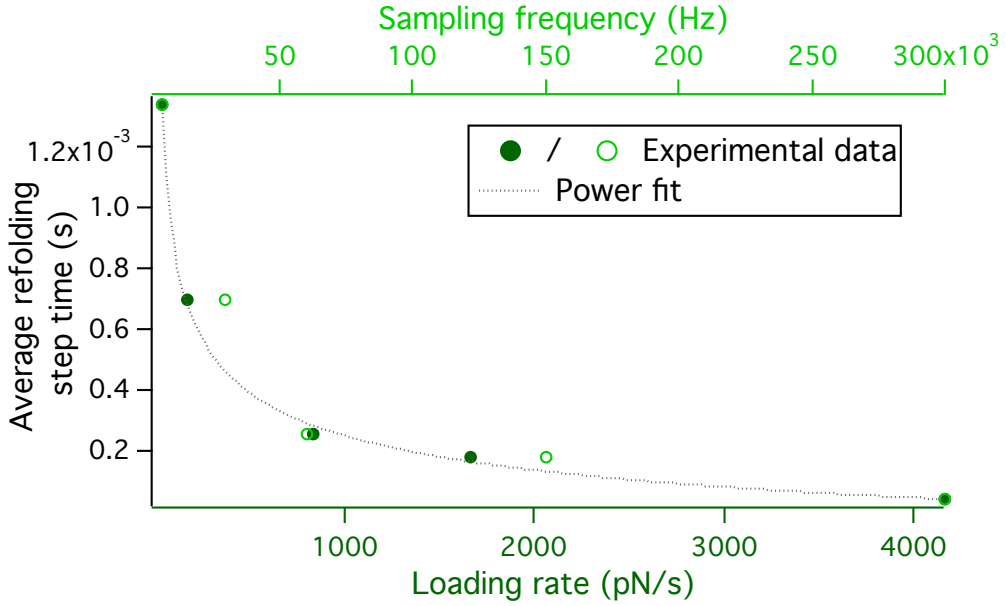

Figure 3.23 Plot of the average refolding time measured along the *back process* of the hopping events as a function of the loading rate or the sampling frequency.

The analysis of the total time, along which hopping can be observed, provides also interesting information. For all velocities, the increment of the mechanical load during this pulling time converges to a similar value of around 30 pN. This confirms the explanation on the decrease in the number of fluctuations as the velocity is increased and particularly it indicates that the nucleation segment can refold up to an extra force of 30 pN is applied. This force value corresponds also to the force difference between the folded state before the hopping events start and the unfolded state at the end of the hopping events. This is a proof of the full reversibility and also a proof that no energy is dissipated along the unfolding, since the foldamer can exert an equivalent force to the energy gain from the previous unfolding step.

3.4.3 Summary

The occurrence of hopping events is a direct proof of the ability of the foldamer to refold under mechanical load, or in other words to recreate interactions that have been broken, in a shorter time than the time needed by the external pulling to reach a load high enough to prevent the refolding. Indeed, back and forth observable fluctuations are the hallmark of thermodynamic equilibrium. In the case of the 33-quinoline-based foldamers, the analysis of these hops allow us to determine that the unfolded foldamer can exert a force of up to 30 pN against a force of 100 pN to locally refold the nucleation segment in less than 40 µs. As cooperativity promotes the folding, we can expect even shorter time for the following folding step. While the mechanical performances of the quinoline-based helix overcome unambiguously those of the peptidic helices, the technical limitations to measure the dynamics prevent us from obtaining an accurate value. We could only determine an upper limit of 40 µs, which is in the same range as the theoretical value.[47,48] No experiment is available on peptidic helices.

3.5 Conclusion

The analyses allowed us to determine some thermodynamic parameters. Nevertheless, the robust quinoline-based foldamers have also confronted the single-molecule force spectroscopy with its limitations. Indeed, very fast dynamics of unfolding and refolding of these helices hampered to access to out-of equilibrium regime, which prevents us to quantify kinetics parameters like the off-rate of the interactions. In solution, even the 2-turns Q5 does not exhibit thermal destabilization on the time scale of fast SMFS experiments.

Dynamic force spectroscopy experiments exhibit only the equilibrium regime over the 3-order of magnitude of loading rates. The measured force did not depend on the loading rate. This underlines the very fast dynamics of unfolding and refolding of all the foldamers (from 5-mer to 33-mer). We could determine the free energies of the group of interactions that opens along an unfolding step (under the condition of validity of the Friddle-Noy-De Yoreo model). The free energy for the consecutive transition in the foldamers of different sizes indicated the cooperative reinforcement with the addition of quinoline units; $\Delta G = 47\ k_BT$ and $45\ k_BT$ were calculated for 33- and 17-mers, respectively and $\Delta G = 27\ k_BT$ was found for the 5-mer. These values are in good agreement with the energy barriers calculated for handedness inversion.[4,5]

Complementary, the pulling-relaxing analysis confirmed the fast dynamics of unfolding and refolding, as the full reversibility of the helical 33-mer was demonstrated. The relaxing traces superimpose to the pulling curves without significant hysteresis, over the wide range of loading rates and during more than hundred consecutive cycles. These observations indicate the remarkable elastic properties without any fatigue evidence. This can be associated to high proximity of the interacting partners and low motion freedom. Another argument, which would contribute to the fast dynamics, is given by the probability that other units may refold when some units are being unfolded. In combination with the Crooks fluctuation theorem, we could measure the total free energy of the unfolding process. For the 33-mer, the total free energy is equal to $244 \pm 24\ k_BT$ or 10 ± 1 kcal.(mol.nm)$^{-1}$. This high energy difference explains why a totally unfolded quinoline-based foldamer is unlikely to exist in solution. For a same length, the synthetic helix is able to store 4 times more energy than a peptidic helix.[10]

Finally, the hopping events clearly proved the thermodynamic equilibrium and allowed us to estimate the time of the helix nucleation folding under mechanical load to less than 40 µs and to assume that the propagation is even faster. Unfortunately, we do not have access to kinetic constants, as the time resolution of the experiment was not sufficient. We

evidenced that the unfolded foldamer can exert a force of up to 30 pN against a force of 100 pN to locally refold the nucleation segment.

In order to obtain more information about thermodynamics, force-clamp experiments should be performed to have access to unfolding and refolding kinetics.

To conclude, the high values of the equilibrium forces, and the free energies, as well as the fast dynamics evidence the particular robustness and interesting mechanical properties of the quinoline-based foldamers. These results could enable such foldamers to evolve as building blocks for synthetic predictable functional systems.

3.6 References

1. Schönfelder, J., De Sancho, D. & Perez-Jimenez, R. The power of force: Insights into the protein folding process using single-molecule force spectroscopy. *J. Mol. Biol.* **428,** 4245–4257 (2016).
2. Noy, A. & Friddle, R. W. Practical single molecule force spectroscopy: how to determine fundamental thermodynamic parameters of intermolecular bonds with an atomic force microscope. *Methods* **60,** 142–50 (2013).
3. Morfill, J. *et al.* Force-based analysis of multidimensional energy landscapes: application of dynamic force spectroscopy and steered molecular dynamics simulations to an antibody fragment-peptide complex. *J. Mol. Biol.* **381,** 1253–66 (2008).
4. Delsuc, N. *et al.* Kinetics of helix-handedness inversion: Folding and unfolding in aromatic amide oligomers. *ChemPhysChem* **9,** 1882–1890 (2008).
5. Abramyan, A. M., Liu, Z. & Pophristic, V. Helix handedness inversion in arylamide foldamers: elucidation and free energy profile of a hopping mechanism. *Chem. Commun.* **52,** 669–672 (2016).
6. Uribe, L., Gauss, J. & Diezemann, G. Determining Factors for the Unfolding Pathway of Peptides, Peptoids, and Peptidic Foldamers. *J. Phys. Chem. B* **120,** 10433–10441 (2016).
7. Sturm, S., Bullerjahn, J. T. & Kroy, K. Intramolecular relaxation in dynamic force spectroscopy. *Eur. Phys. J. Spec. Top.* **223,** 3129–3144 (2014).
8. Ritort, F. The nonequilibrium thermodynamics of small systems. *Comptes Rendus Phys.* **8,** 528–539 (2007).
9. Lussis, P. *et al.* A single synthetic small molecule that generates force against a load. *Nat. Nanotechnol.* **6,** 553–557 (2011).
10. Schwaiger, I., Sattler, C., Hostetter, D. R. & Rief, M. The myosin coiled-coil is a truly elastic protein structure. *Nat. Mater.* **1,** 232–235 (2002).
11. Holland, N. B. *et al.* Single molecule force spectroscopy of azobenzene polymers: Switching elasticity of single photochromic macromolecules. *Macromolecules* **36,** 2015–2023 (2003).
12. Sluysmans, D., Devaux, F., Bruns, C. J., Stoddart, J. F. & Duwez, A.-S. Dynamic force spectroscopy of synthetic oligorotaxane foldamers. *Proc. Natl. Acad. Sci.* **115,** 9362–9366 (2018).
13. Collin, D. *et al.* Verification of the Crooks fluctuation theorem and recovery of RNA folding free energies. *Nature* **437,** 231–234 (2005).
14. Crooks, G. E. Entropy production fluctuation theorem and the nonequilibrium work relation for free energy differences. *Phys. Rev. E - Stat. Physics, Plasmas, Fluids, Relat. Interdiscip. Top.* **60,** 2721–2726 (1999).
15. Friedsam, C., Wehle, A. K., K hner, F. & Gaub, H. E. Dynamic single-molecule force spectroscopy: bond rupture analysis with variable spacer length. *J. Phys. Condens. Matter* **15,** S1709–S1723 (2003).
16. Noy, A. & Friddle, R. W. Practical single molecule force spectroscopy: how to determine fundamental thermodynamic parameters of intermolecular bonds with an atomic force microscope. *Methods* **60,** 142–50 (2013).
17. Hughes, M. L. & Dougan, L. The physics of pulling polyproteins: a review of single molecule force spectroscopy using the AFM to study protein unfolding. *Reports Prog. Phys.* **79,** 76601 (2016).
18. Bell, G. I. Models for the specific adhesion of cells to cells. *Science (80-.).* **200,** 618 LP-627 (1978).
19. Evans, E. & Ritchie, K. Dynamic strength of molecular adhesion bonds. *Biophys. J.* **72,** 1541–55 (1997).

20. Freshman Chemistry. Kramers ' Theory of Reaction Kinetics. *Cl. notes*
21. Friddle, R. W., Noy, A. & De Yoreo, J. J. Interpreting the widespread nonlinear force spectra of intermolecular bonds. *Proc. Natl. Acad. Sci.* **109,** 13573–13578 (2012).
22. Hummer, G. & Szabo, A. Kinetics from Nonequilibrium Single-Molecule Pulling Experiments. *Biophys. J.* **85,** 5–15 (2003).
23. Dudko, O. K., Hummer, G. & Szabo, A. Theory, analysis, and interpretation of single-molecule force spectroscopy experiments. *Proc. Natl. Acad. Sci.* **105,** 15755–15760 (2008).
24. Sulchek, T. A., Friddle, R. W. & Noy, A. Dynamic force spectroscopy in tethered single molecule systems. *Handb. Mol. Force Spectrosc.* (2007).
25. Thormann, E., Hansen, P. L., Simonsen, A. C. & Mouritsen, O. G. Dynamic force spectroscopy on soft molecular systems: Improved analysis of unbinding spectra with varying linker compliance. *Colloids Surfaces B Biointerfaces* **53,** 149–156 (2006).
26. Zlatanova, J., Lindsay, S. M. & Leuba, S. H. Single molecule force spectroscopy in biology using the atomic force microscope. *Prog. Biophys. Mol. Biol.* **74,** 37–61 (2000).
27. Evans, E. & Ritchie, K. Strength of a Weak Bond Connecting Flexible Polymer Chains. *Biophys. J.* **76,** 2439–2447 (1999).
28. Hugel, T., Rief, M., Seitz, M., Gaub, H. & Netz, R. Highly Stretched Single Polymers: Atomic-Force-Microscope Experiments Versus Ab-Initio Theory. *Phys. Rev. Lett.* **94,** 48301 (2005).
29. Schönherr, H. *et al.* Individual Supramolecular Host−Guest Interactions Studied by Dynamic Single Molecule Force Spectroscopy. *J. Am. Chem. Soc.* **122,** 4963–4967 (2000).
30. Zou, S., Schönherr, H. & Vancso, G. J. Stretching and rupturing individual supramolecular polymer chains by AFM. *Angew. Chem. Int. Ed. Engl.* **44,** 956–9 (2005).
31. Jarzynski, C. Nonequilibrium equality for free energy differences. *Phys. Rev. Lett.* **78,** 2690–2693 (1997).
32. Rief, M., Gautel, M., Oesterhelt, F., Fernandez, J. M. & Gaub, H. E. Reversible Unfolgind of Individual Titin Immunoglobulin Domains by AFM. *Science (80-.).* **276,** 1109–1112 (1997).
33. Camunas-Soler, J., Ribezzi-Crivellari, M. & Ritort, F. Elastic Properties of Nucleic Acids by Single-Molecule Force Spectroscopy. *Annu. Rev. Biophys.* **45,** 65–84 (2016).
34. Lee, W. *et al.* Full reconstruction of a vectorial protein folding pathway by atomic force microscopy and molecular dynamics simulations. *J. Biol. Chem.* **285,** 38167–72 (2010).
35. Diezemann, G. & Janshoff, A. Dynamic force spectroscopy: Analysis of reversible bond-breaking dynamics. *J. Chem. Phys.* **129,** (2008).
36. Janshoff, A., Neitzert, M., Oberdörfer, Y. & Fuchs, H. Force Spectroscopy of Molecular Systems-Single Molecule Spectroscopy of Polymers and Biomolecules. *Angew. Chem. Int. Ed. Engl.* **39,** 3212–3237 (2000).
37. Fantner, G. E. *et al.* Sacrificial bonds and hidden length: unraveling molecular mesostructures in tough materials. *Biophys. J.* **90,** 1411–8 (2006).
38. Liphardt, J., Dumont, S., Smith, S. B., Tinoco Jr, I. & Bustamante, C. Equilibrium information from nonequilibrium measurements in an experimental test of Jarzynski's equality. *Science (80-.).* **296,** 1832–1835 (2002).
39. Bustamante, C., Chemla, Y. R., Forde, N. R. & Izhaky, D. Mechanical processes in biochemistry. *Annu. Rev. Biochem.* **73,** 705–748 (2004).
40. Marden, J. H. & Allen, L. R. Molecules, muscles, and machines: universal performance characteristics of motors. *Proc. Natl. Acad. Sci. U. S. A.* **99,** 4161–4166 (2002).
41. Carrion-Vazquez, M. *et al.* Mechanical and chemical unfolding of a single protein: A comparison. *Biophysics (Oxf).* **96,** 3694–3699 (1999).
42. Žoldák, G., Stigler, J., Pelz, B., Li, H. & Rief, M. Ultrafast folding kinetics and

cooperativity of villin headpiece in single molecule autocorrelation force spectroscopy. *Proc. Natl. Acad. Sci. U. S. A.* **110,** 18156–61 (2013).

43. Dudko, O. K., Graham, T. G. W. & Best, R. B. Locating the barrier for folding of single molecules under an external force. *Phys. Rev. Lett.* **107,** 3–6 (2011).
44. Neupane, K., Wang, F. & Woodside, M. T. Direct measurement of sequence-dependent transition path times and conformational diffusion in DNA duplex formation. *Proc. Natl. Acad. Sci.* **114,** 1329–1334 (2017).
45. Neupane, K. *et al.* in **352,** 5521–5532 (2016).
46. Junker, J. P., Ziegler, F. & Rief, M. Ligand-dependent equilibrium fluctuations of single calmodulin molecules. *Science (80-.).* **323,** 633–637 (2009).
47. Muñoz, V. Conformational Dynamics and Ensembles in Protein Folding. *Annu. Rev. Biophys. Biomol. Struct.* **36,** 395–412 (2007).
48. Schuler, B. & Hofmann, H. Single-molecule spectroscopy of protein folding dynamics-expanding scope and timescales. *Curr. Opin. Struct. Biol.* **23,** 36–47 (2013).
49. Liphardt, J., Bibiana, O., Smith, S. B., Tinoco, I. J. & Bustamante, C. J. Reversible Unfolding of Single RNA Molecules by Mechanical Force. *Science (80-.).* **292,** 733–737 (2001).
50. Berkemeier, F. *et al.* Fast-folding -helices as reversible strain absorbers in the muscle protein myomesin. *Proc. Natl. Acad. Sci.* **108,** 14139–14144 (2011).
51. Stigler, J. & Rief, M. Calcium-dependent folding of single calmodulin molecules. *Proc. Natl. Acad. Sci.* **109,** 17814–17819 (2012).

Chapter 4

Modulation of the molecular interactions in Quinoline-based Foldamers

TABLE OF CONTENTS

Chapter 4
Modulation of the molecular interactions in Quinoline-based Foldamers

In order to fundamentally investigate in details the molecular interactions involved in the foldamers, to estimate the different contributions of the interplay of non-covalent interactions (H-bonds, hydrophobic effect, electrostatic interactions, π-stacking) and to probe or modulate the different behaviours and stabilities of these helices in different solvents, we performed pulling SMFS-experiments in a large variety of solvents.

Previous NMR and circular dichroism characterizations indicated that the helical structure is preserved in a large variety of solvent.[1–3] In this chapter, we can suggest the same tendency at the scale of the single molecule. The force-distance curves of each size of foldamer exhibit a pattern of the unfolding a helical folded conformation in all solvents. Nevertheless, the different solvents modulate the strength of the interactions and we were able to assess the contribution of the different kinds of molecular interactions by analysing the unfolding forces. We evidenced a contribution of both the H-bonds and the π-stacking. We also demonstrated some small but relevant mechanical behaviour differences between polar and apolar solvents.

4.1 Introduction

A molecular architecture, its stability and its properties, may critically differ in the gas-phase, in the solid state, in solution-phase and even depend on the nature of the solvent. Although the non-covalent interactions are universal, the different behaviours stem exclusively from the modulation and the ranking of the intensities of these intra- & inter-molecular interactions depending on the environment. As presented in chapter 1, folding propensity and properties are controlled by the molecular interactions.

Given that the potential of supramolecular chemistry and the foldamers is likely to operate in solution and that the relationship between solute and solvent has been demonstrated to play a role in chemical processes[4], it is essential to investigate the correlation between the nature of the solvents and the quinoline-based foldamer architectures and their mechanical properties.

4.1.1 SMFS-Pulling experiments in different solvents

Probing the strength of the interactions and studying the folded states by single-molecule force spectroscopy experiments is quite common for proteins or DNA. The salt concentration, buffers, pH are parameters often investigated to highlight the role of the repulsive electrostatic interactions or to investigate the biomolecules in their own environement.[5–8] The few examples of artificial molecular systems already described in the literature have evidenced interesting mechanochemical behaviours depending on the environment.

In our case, the studied foldamers are known to be insoluble in aqueous solvent.

By varying the organic solvents, it is still possible to modulate the intensity of the interactions and thus, the stability and potentially the folding propensity and the properties of molecules. In apolar solvents, presenting low dielectric constants, electrostatic interactions are reinforced, whereas in polar solvent, hydrophobic interactions are favoured. From some solvents, competing interactions such as H-donor or acceptor and π-intercalating properties should be considered.

The measurement of the mechanical unfolding behaviours in several solvents, by SMFS-pulling experiments, can evidence different mechanochemical properties. Firstly, by analysing the pulling traces, the conformational changes can be detected. Secondly, the measured mechanical forces to unfold the molecule would reflect the strength of the interactions controlling the structure, which would enable to obtain a better picture of the contribution of each kind of interaction. Finally, hand in hand, it provides knowledge for predicting folding and functions.

The following examples highlight the interpretations that can be proposed from the stretching force-distance traces of artificial molecular systems to provide information on folding and conformation understanding.

In 1999, P. Oesterhelt *et al.* evidenced the different conformations of PEG chain in organic solvents and water from their force-distance curves. The pulling traces of the stretching of PEG chain differed in two tested solvents. Whereas the trace of the stretching in hexadecane followed the theoretical trace of an ideal entropic string, it highly deviated in aqueous environment. As shown in Figure 4.1.A, this last force-distance curve could not be fitted with the freely jointed chain model (FJC - an elasticity model derived from statistical mechanics). They thus highlighted different elastic behaviours of PEG and particularly an enthalpic contribution to the unfolding of PEG chain in aqueous environement.[9] These observations allowed suggesting a particular supra-structure of PEG chain in water. They identified the enthalpic elasticity as the conformation transition from trans-trans-gauche conformation, held by water bridges, to a trans-trans-trans conformation (Figure 4.1.B).

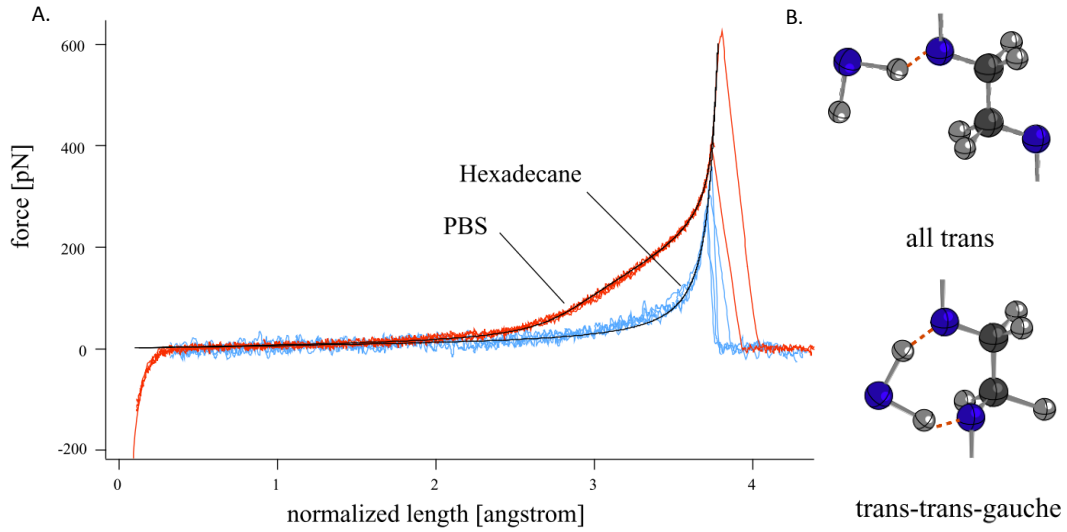

Figure 4.1 (A) Superposition of the force-distance traces in (blue) phosphate-buffered saline (PBS) and in (red) hexane after normalization of their contour length. The solid line shows the best fit to the models: Elastically coupled two-level system for PEG chain in hexadecane and freely jointed chain (FJC) in PBS. (B) Observable conformations of PEG chain; trans-trans-gauche in aqueous environment and all trans in hexane or when tension is applied in aqueous solvent. Reproduced from reference 9.

Another group investigated the folding propensity of flexible donor (dialkoxynaphthalene)−acceptor (pyromellitic dianhydride) foldamers by performing SMFS experiments in different conditions.[10] They measured a specific pulling curve in KSCN saturated methanol/chloroform solution, which suggest a folded architecture of the foldamer, while in DMSO the force-distance curve could be fitted with a WLC model, which indicates that the foldamer presents mainly a coiled state with a minimum folding

(Figure 4.2). They concluded that DMSO was a too poor solvent to stabilize the required charge-transfer between the donor and acceptor moieties. On the contrary, they identified that reinforcing the hydrophobic interactions and the complexation of the linker highly promote the folding and that these folding conditions can be provided by a mixture of methanol/chloroform/KSCN.

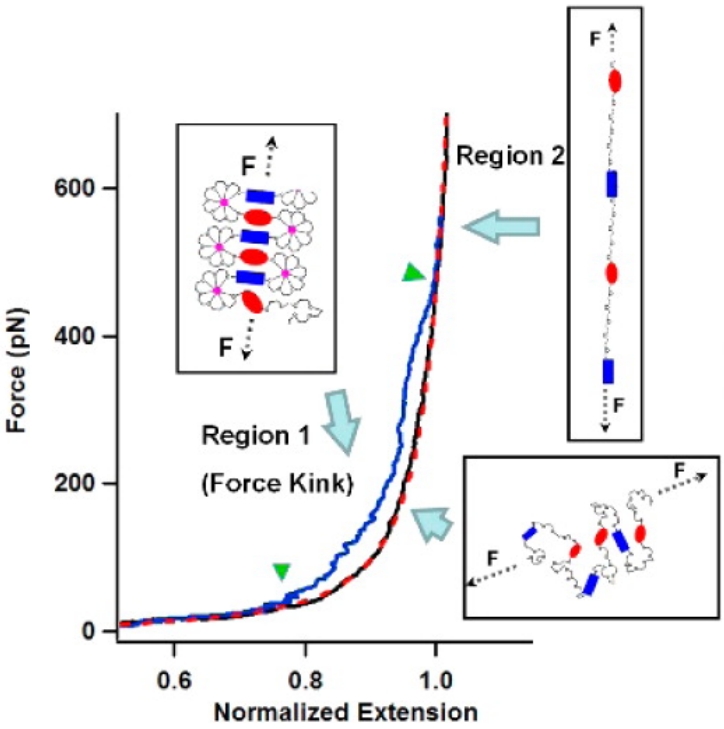

Figure 4.2 Normalized force-extension curves (normalization force: 500 pN) for the donor (dialkoxynaphthalene)−acceptor (pyromellitic dianhydride) foldamer (DA) in DMSO (black colour) and in KSCN saturated solution (solvent: methanol/chloroform = 1:1, v/v) (blue colour). The red dotted line is the fitting curve of the freely coiled chains, using the WLC model with a parameter of l_p = 3.6 Å and L_c = 1.08. In the frames, schematics of the conformation of the DA foldamer are illustrated for different steps of an unfolding experiment. Reproduced from reference 10.

Finally, the group of J. Vancso demonstrated that the self-assembly of long supra-polymers could be directly dependent on the solvent.[11] They performed SMFS experiments on self-complementary 2-ureido-4-pyrimidinone molecules (UPy), which are known to form supramolecular non-covalent polymers or "reversible polymers". In these experiments, Upy are respectively immobilized on the tip and on the substrate and bis-Upy (two UPy groups at the end of a small PEG chain) are provided in the solution to interact with the immobilized one and to form in-situ non-covalent UPy-linked supramolecular polymers (see Figure 4.3). They measured, in hexadecane and in DMSO/propanol, the stretching lengths, to which they associated a degree of polymerization. As shown in Figure 4.3.D&E, they observed a solvent dependency on the degree of polymerization of the Upy supra-polymer. In DMSO/propanol, stretching

lengths corresponding to the rupture of the Upy moieties immobilized on the tip and substrate (dimer) are almost exclusive, while in hexadecane, they could measure stretching lengths up to 150 nm, corresponding to an assembly of 15 bis-UPy molecules. This indicated that polar solvents (DMSO/propanol) disrupt the hydrogen bonds required to form supra-polymers.

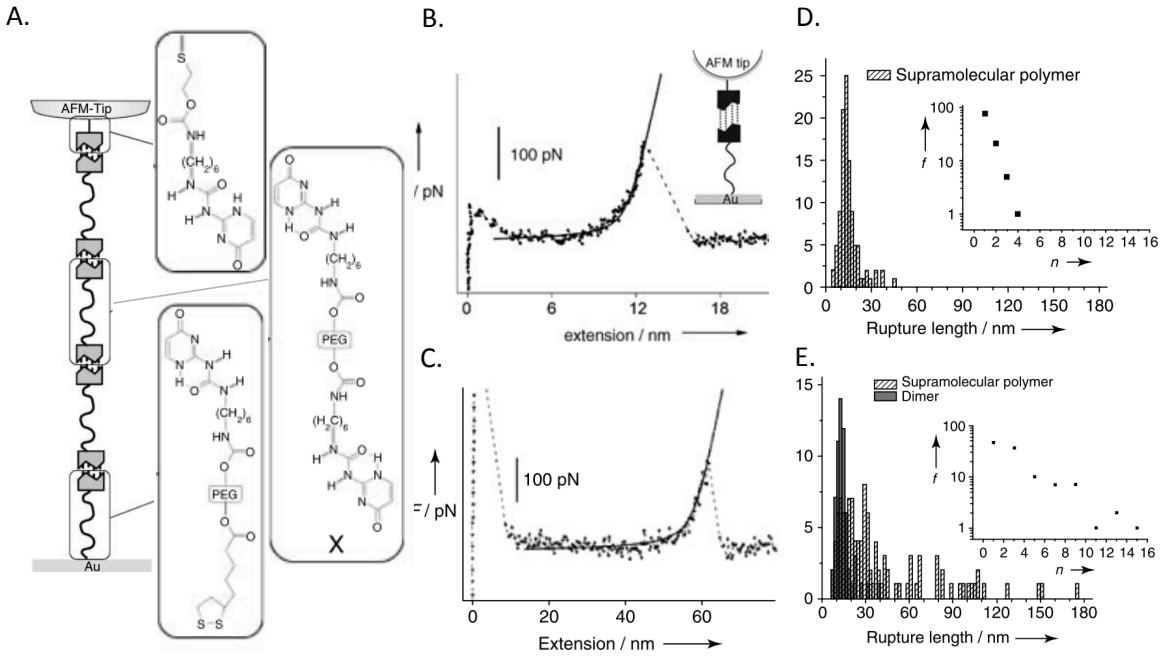

Figure 4.3 (A) Schematic representation of the single-molecule force spectroscopy experiment on non-covalently UPy-linked supramolecular polymers. (B) Representative force–extension curves measured in absence of bis-UPy, (C) in presence of bis-UPy. (D) Histogram of the rupture length observed in the presence of bis-UPy in hexadecane, (E) in 15% DMSO in 2-propanol. Inset: Frequency of extension events versus the number of repeat units *n* in stretched supramolecular polymers. Reproduced from reference 11.

These examples prove that AFM-SMFS can distinctively shed light on the role of the environment and can highlight different mechanical behaviours of molecular system when they are in different kinds of solvent.

4.1.2 Previous knowledge on quinoline-oligomers in solvents

Concerning the solubility, helical aromatic oligoamide foldamers have been recognized to show a poor dependence on solvents. They appear to fold in a large variety of solvents, from highly apolar solvents, such as chloroform, to highly polar solvents, such as methanol or water, with chemical composition adjustment (side chains).

Nevertheless, even if the foldamers are soluble and take a helical conformation in many solvents, their stability may greatly depend on the nature of the solvent. Indeed, a study, conducted by Huc's group, investigated the helical stability of an octamer of 2-

quinolinecarboxylic acid bearing tri-ethylene glycol as side chains (Figure 4.4.A).[12] They followed the handedness inversion in different solvents by circular dichroism and they measured inversion kinetics spanning about 4 orders of magnitude for the different solvents (Figure 4.4.B). These results demonstrated a strong and unexpected solvent-dependent stability. They suggested that the helical stability of this foldamer is weaker in apolar solvent and considerable stronger in polar solvents. This suggests that, although polar solvents are expected to destabilize electrostatic interactions, such as H-bonds, in this case, the hydrophobic effects of polar solvents play a dominant role. From NMR analysis, no aggregation could be observed in any of the solvents and thus the aggregation effect can be rejected as a cause of stability.

A.

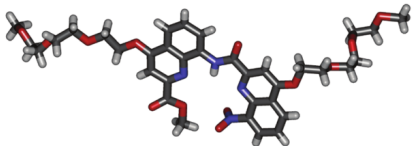

B.

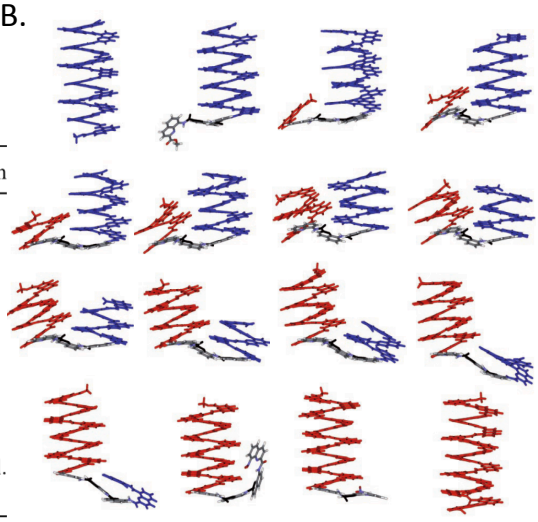

C.

Solvent	K^a/min^{-1}	$t_{1/2}{}^a$/min
$CHCl_3$	1.2×10^{-1}	6
THF	4.4×10^{-2}	16
Toluene	2.5×10^{-2}	28
DMF	1.7×10^{-2}	40
Et_2O	9.0×10^{-3}	77
2-Propanol	2.0×10^{-3}	350
MeOH	7.7×10^{-4}	900
95 : 5 MeOH/H_2O^b	4.8×10^{-4}	1445
80 : 20 MeOH/H_2O^b	1.7×10^{-4}	4080
50 : 50 MeOH/H_2O^b	ND[c]	ND[c]

[a] Determined by monitoring the decay of CD intensity of *P*-**1**. [b] vol/vol. [c] Too slow to be determined.

Figure 4.4 (A) Representation of the chemical structure of a dimer of 2-quinolinecarboxylic acid bearing tri-ethylene glycol. (B) Representation of a hypothetic handedness inversion of a hexadecamer mechanism and the intermediate energy-minimized conformations. (C.) Table of first order kinetic constant and half-life of helix handedness inversion of dimer shown in (A.) in various solvents. Adapted from reference 13.

These results should not be directly compared to the ones obtained in our study without taking some considerations. Firstly, the chemical structure slightly differs by the nature of the side chains, which may have non-negligible impact. Indeed, for this published study, the conditions needed to be adjusted to separate the P and M conformers, this foldamer bearing tri-ethylene glycol side chain, regarding to the previously known separating conditions for oligomers bearing isobutoxy side chains. Secondly, the intermediates and final conformations are not the same. For the handedness inversion, a hypothetic mechanism is proposed in Figure 4.4.B and shows that intermediates are only locally unfolded, most of the foldamer is steadily undergoing a helical conformation. Therefore, its surface area exposed to the solvent is equal (only at the beginning) or smaller than the surface areas of the progressively unfolded conformations in our SMFS experiments.

Finally, the concentration and configuration should be considered. Those experiments were performed in diluted solution, while our pulling experiments are performed at the scale of the single molecule and anchored to a surface, limiting to a certain extend the total free motion.

4.1.3 Quantifying interactions according to Hunter's theory

Efficiently summarised by C.A. Hunter, the complex interplay of many different molecular interactions in solution can be analysed as a competition between solute–solute, solvent–solvent, and solute–solvent interactions.[14] He suggested that the dominant role of the electrostatic interactions, compared to minor contributions of the induction or dispersion, could exclusively explain the molecular interaction competitions between solute and solvent molecules. Based on this simplistic viewpoint, he established an equation to evaluate the free energy of the interactions of a molecular system in any solvent. He assimilated to each chemical functional group and solvents both hydrogen-bonding donor and acceptor constants and formulated the following equation:

$$\Delta\Delta G_{H-bond} = -(\alpha - \alpha_s)\,(\beta - \beta_s)$$

Eq. 1 Prediction of the free energy of interaction ($\Delta\Delta G_{H-bond}$) based on the H-bond scale, where α and β are H-bond donor and H-bond acceptor constants for the solute molecules, and α_s and β_s are the corresponding constants for the solvent.

Additionally to the equation, the H-bonding donor and H-bond acceptor constants allow directly determining, in any solvent, which is the dominant interaction between solute–solute, solvent–solvent, and solute–solvent interactions (Figure 4.5.A). Depending on the solvent, on the one hand, the interactions between functional groups of a solute with themselves can be more favourable than with the solvent molecules (blue). This leads to intra- or supra-molecular interactions within solute molecules. On the other hand, these intramolecular interactions can be unfavourable (red), which leads to intermolecular interactions with the solvent molecules. For example, on Figure 4.5 C. vs. D., same functional groups from the solute, *e.g.* nitrogen of a nitrile and hydrogen of an amide, would favourably interact together in chloroform (C), whereas they would preferably interact with the solvent molecules in dimethylsulfoxide (D).

Although the fact that this approach presents some limitations, which should be kept in mind, many significant successes in the prediction of molecular complexes can approve the potential of this simplistic approach. The two main limitations of this approach are related to the lack of the implementation of the aromatic stacking and of the cooperative effects.

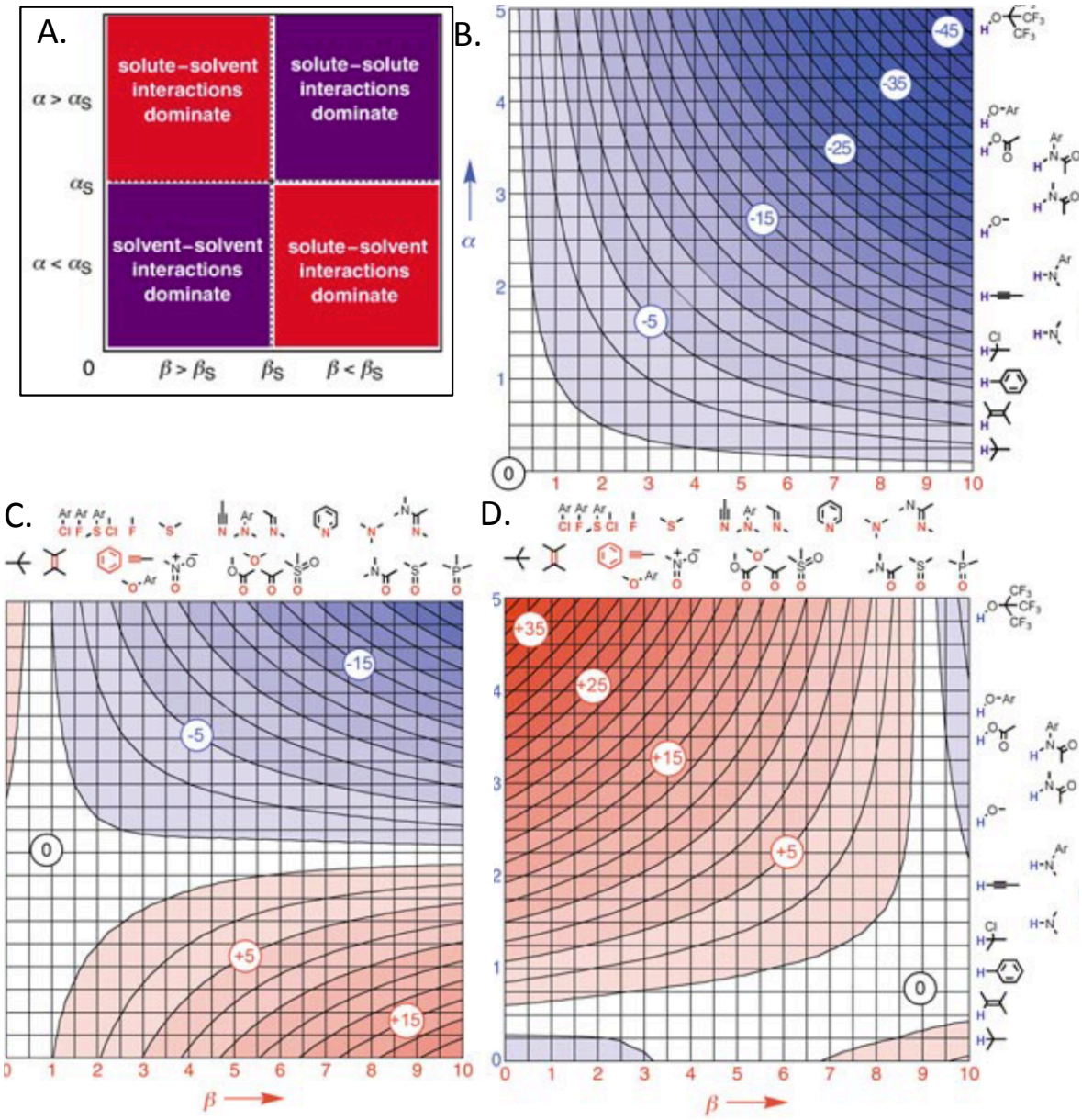

Figure 4.5 (A) The generalized profile for H-bond-like interactions between functional groups in solution (Eq. 1) The H-bond constants are denoted α and β for the solute molecules and α_s and β_s for the solvent. For a given solvent, the functional group interaction space is partitioned into four quadrants. In the two red quadrants, $\Delta\Delta G_{H-bond}$ is positive, and the functional group interactions are unfavourable. In the two blue quadrants, $\Delta\Delta G_{H-bond}$ is negative, and the functional group interactions are favourable. The values of α_s and β_s set the boundaries between these quadrants and define how the space is partitioned. (B-C-D) Functional group interaction profiles (B) in the solid state or a noble gas ($\alpha_s = \beta_s = 0$), (C) in chloroform, (D) in DMSO. The structures of a set of functional groups are illustrated on the α and β scale. Blue represents a favourable interaction ($\Delta\Delta G_{H-bond} < 0$), and red an unfavourable interaction ($\Delta\Delta G_{H-bond} > 0$). The zero point on each plot corresponds to ($\alpha = \alpha_s$, $\beta = \beta_s$) where desolvation perfectly balances the solute–solute interactions. Reproduced from reference 14.

4.2 Results and discussion

To modulate the intramolecular interactions involved in the helical scaffold of the quinoline-based foldamers bearing isobutoxy-groups as side chains, we tested several solvents with different physico-chemical properties. In Table 1, dielectric constant, dipolar moment, H-donor and H-acceptor properties (from Hunter's theory) are given for several solvents.

To probe the electrostatic interactions, we performed experiments in apolar solvents such as toluene, *1,1,2,2*-tetrachloroethane (TCE) and in polar solvents such as ethanol (EtOH), *N,N*-dimethylformamide (DMF), dimethylsulfoxide (DMSO) and acetonitrile (MeCN). Concerning the polar solvents, we selected particularly good H-donors (DMF, EtOH) or good H-acceptors (DMF, DMSO) to try to directly compete with the intramolecular interactions. To investigate the π-stacking, we analysed the results obtained in the toluene. Thermal noise prevents the use of organic solvents with a low boiling point, as we need high environmental stability. Therefore, molecular forces cannot be probed in the widely used chloroform or dichloromethane at room temperature. We functionalized the surface as previously described (see appendix B.) and we worked in a closed and solvent saturated chamber.

Table 1 Physicochemical parameters of some solvents. The H-donor and H-acceptor properties α_s and β_s come from C.A. Hunter solvation theory. The values with * indicate value from a similar chemical function. The DMF values are from an amide, the EtOH values are from an alcohol average and toluene values are from benzene.[14,15]

Solvent	MW	Boiling point (°C)	Density	Dielectric constant	Dipolar moment	H-acceptor α_s	H-donor β_s
Acetonitrile (MeCN)	41.05	81.6	0.88	36.64	3.92	5.1	1.7
Chloroform	119.4	61.2	1.5	4.81	1.04	0.8	2.2
Dimethylformamide (DMF)	73.09	153	0.9445	38.25	3.82	~ 8.3*	~ 2.9*
Dimethylsulfoxide (DMSO)	78.13	189	1.092	47.2	3.96	8.9	0.8
Ethanol (EtOH)	46.07	78.5	0.789	24.6	1.69	~ 5.8*	~2.7*
1,1,2,2-tetrachloroethane (TCE)	167.8	146	1.6	8.42	1.32	1.3	2
Toluene	92.14	110.6	0.867	2.38	0.375	~ 2.2*	~1*
Water	18.02	100	1	78.54	1.85	4.5	2.8

4.2.1 Qualitative analysis on the longer foldamers

We started the solvent investigation with the longest foldamers Q33, made of 33 quinoline units. As illustrated in Figure 4.6 in each tested solvent, similar unfolding patterns as in the previous study in DMF were exclusively obtained. This indicates unambiguously the totally folded and helical conformation of the foldamers in every organic solvent tested. The distributions of the length of the foldamer unfolding patterns, which deviates from the entropic elastic behaviour of PEG chain (green zones), are monomodal and correspond to the hidden length between the totally unfolded and totally folded foldamer. The specific unfolding pattern is also in good agreement with conformational transition of such helical molecules as explained in chapter 2.

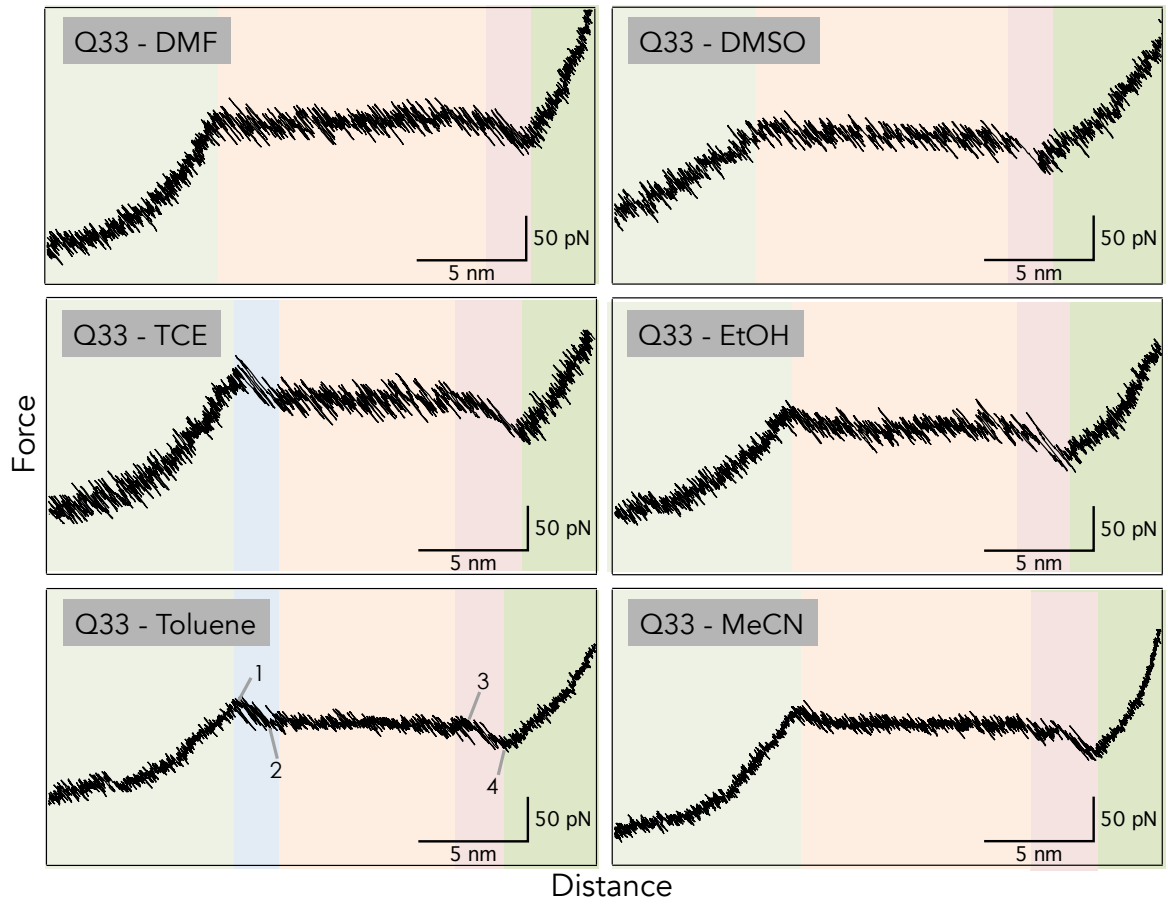

Figure 4.6 Force-distance curves of pulling experiments on Q33 in several organic solvents. Each solvent and foldamer are written in the top-left corner of the curve. The colour zones indicate the different mechanical behaviours of the foldamers.

Similar variety of ending features (red zone: large hopping, progressive decreasing force and single rupture) as in DMF was also observed. These observations have indicated the cooperative folding propensity and the existence of a reinforcement in the helical structure with the number of units in all the solvent conditions, as observed in DMF. The hopping is reported and is a direct evidence of reversibility in the unfolding and refolding process in each solvent.

Interestingly, we observed a difference in the unfolding pattern in TCE and toluene, compared to the other solvents. In these two apolar solvents, the unfolding of the foldamer starts mostly with significant hopping events fluctuating between a higher force than the plateau force and the plateau (blue zone). In the other solvents, this feature is almost negligible. We interpreted this as a trigger force before the stepwise opening of the foldamer. In other words, it means that it is more difficult to break the first cooperative interactions than the following ones in these 2 solvents. This feature is also observable in the smaller foldamers Q17 and Q9 (Figure 4.11& Figure 4.12) when they are pulled in both these apolar solvents. These starting hopping events extend over slightly less than 2 nm, which can be associated to the simultaneous opening of 4-5 quinoline units (see appendix E.2.1). Curiously, it is almost the symmetry of the ending decreasing force feature. Further discussions will follow based on the forces at play.

4.2.2 Quantitative force modulation on the longer foldamers

To compare all the data, we performed experiment at the same speed (166 $nm.s^{-1}$) in each solvent and we analysed the data considering the in-air-calibrated spring constants. Worth noting, we always calibrated the cantilevers with the Sader method in air, which is one of the most common calibration methods and which enables us to obtain a common reference for the different conditions.[16–18] Indeed, studies in different organic solvents are quite rare to date. Therefore, the influence of the solvent on the cantilever has never been clearly investigated and direct calibration in the liquid phase has not been optimized. Compared to air, measurements in viscous liquid environment are highly challenging due to damping effects or surface stresses from the viscous solvents on the cantilevers. Nevertheless, to date, the spring constant has been demonstrated to be an intrinsic parameter of the object and to be independent or negligibly influenced by the environment. Therefore calibration in air is the most reliable method to obtain the spring constant.[17–22]

From the force-distance curves of Figure 4.6, we measured the average forces of the whole unfolding pattern (composed of blue, orange and red zones) and of the plateau (orange zone), the force differences between the beginning of the unfolding of the foldamer and the plateau (blue zone and referred to as $\Delta F_{\text{starting trigger}}$), and the force differences between the end of the plateau and the end of the foldamer unfolding (red zone and referred to as $\Delta F_{\text{ending rupture}}$). We represented the data and their distributions by histograms in Figure 4.7 and Figure 4.8.

Analysing the average forces of the whole foldamer unfolding and the plateau (Figure 4.7), we observed that they follow Gaussian distributions and that the most probable forces range between 100 and 130 pN according to the solvent. This non-negligible range

highlights some mechanical stability differences depending on the solvent. The average forces of the whole pattern and the plateau are almost equal. The starting and ending features have negligible influence on the average force (blue and red zones). These parts are either counterbalancing themselves (in TCE and toluene) or are not contributing in the averaging as the involved number of points is low compared to the rest of the unfolding pattern. In the following lines, we discuss the average force of the plateau, as it is attributed to a single and specific mechanical behaviour (stepwise unfolding of identical groups of interactions). We could order the most probable forces such as $F_{plateau\text{-TCE}} > F_{plateau\text{-MeCN}} > F_{plateau\text{-EtOH}} \approx F_{plateau\text{-DMF}} \approx F_{plateau\text{-DMSO}} > F_{plateau\text{-Toluene}}$. We observed that the highest mechanical force required to unfold the foldamer is in TCE and acetonitrile, with 128 ± 20 pN and 122 ± 25 pN respectively. Then in DMF, DMSO and EtOH, the unfolding forces are equivalent and are around 20 pN weaker than in TCE and MeCN, with ~110 ± 15 pN. Finally, the weakest unfolding force is found in toluene with 96 ± 16 pN.

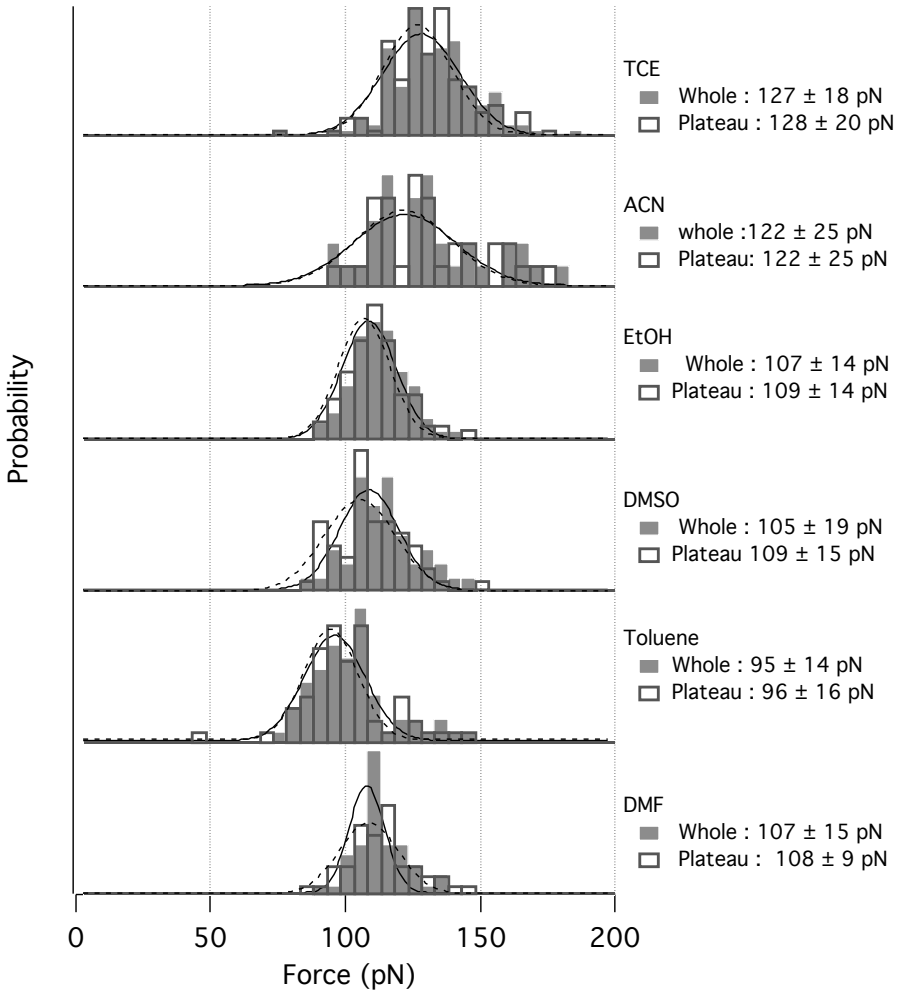

Figure 4.7 Histograms of the average forces of the whole unfolding pattern (from #1 to #4 of Figure 4.6) and of the plateau (from # 2 to #3 of Figure 4.6) of pulling experiments on Q33 in different solvents (indicated in the right of the graphs).

In parallel, we measured the starting forces of the unfolding, called the trigger forces. For MeCN, DMSO, DMF and EtOH, we could not measure any significant difference of the plateau force (<5 pN), while substantial differences were measured in toluene and TCE compared to the plateau force. Increases of 30 pN and 40 pN were measured on toluene and TCE, respectively (see Figure 4.8 and Figure S3). The order of the mechanical stability changes slightly owing to the higher trigger force in toluene, which exceeds this time the trigger forces of the more polar solvents (MeCN, EtOH, DMSO and DMF). We obtained: $F_{trigger\text{-}TCE} > F_{trigger\text{-}Toluene} > F_{trigger\text{-}MeCN} > F_{trigger\text{-}EtOH} \approx F_{trigger\text{-}DMF} \approx F_{trigger\text{-}DMSO}$.

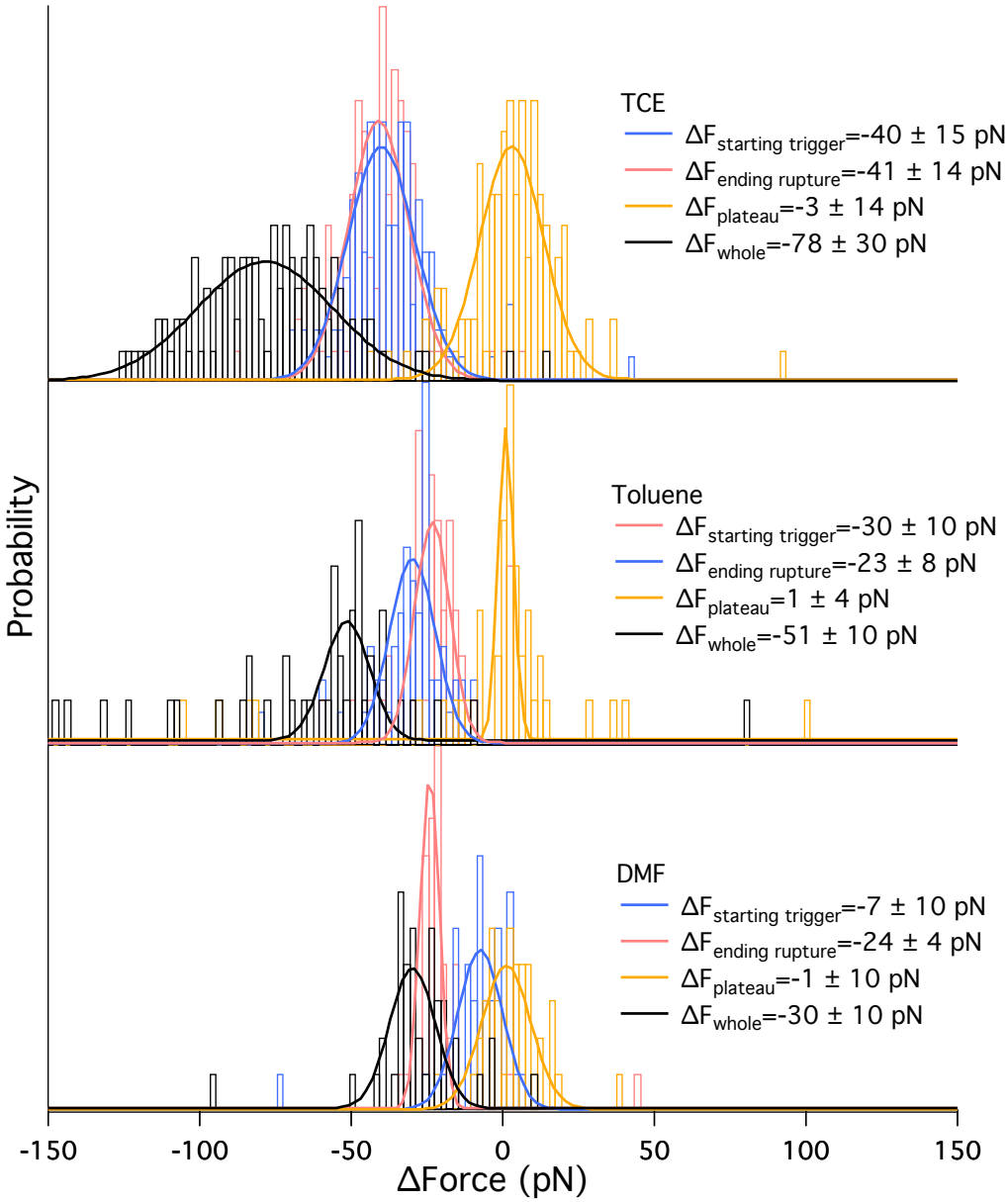

Figure 4.8 Histograms of the difference of forces of the different mechanical features along a pulling trace of Q33 in TCE, toluene and DMF. DMSO, MeCN and EtOH exhibit similar distributions than DMF. The colours of the distributions correspond to the different mechanical behaviours highlighted with the same colour in the force-distance curves (Figure 4.6) (starting trigger: difference in force between #1 to #2; ending rupture: difference in force between #3 to #4; plateau: difference in force between #2 to #3; whole: difference in force between #1 to #4).

With these results, we could link some mechanochemical properties to the solvent properties and the molecular interactions.

First, within non-aromatic solvents, we can suggest that the (plateau) force to unfold follows the Hunter-estimated interaction strengths between the hydrogen of the amide and the aromatic nitrogen of the quinoline unit. In Figure 4.9, we reproduced functional group interaction profiles in the different solvent conditions (Figure 4.5). The red point locates the interaction between the hydrogen of the amide and the nitrogen of the quinoline. The vertical and horizontal lines partition the space into the four quadrants delimiting the 'dominant solvent-solute interactions' (top left and bottom right) and the 'dominant solute-solute interactions' (bottom left) and the dominant 'solute-solute interactions' (top-right).

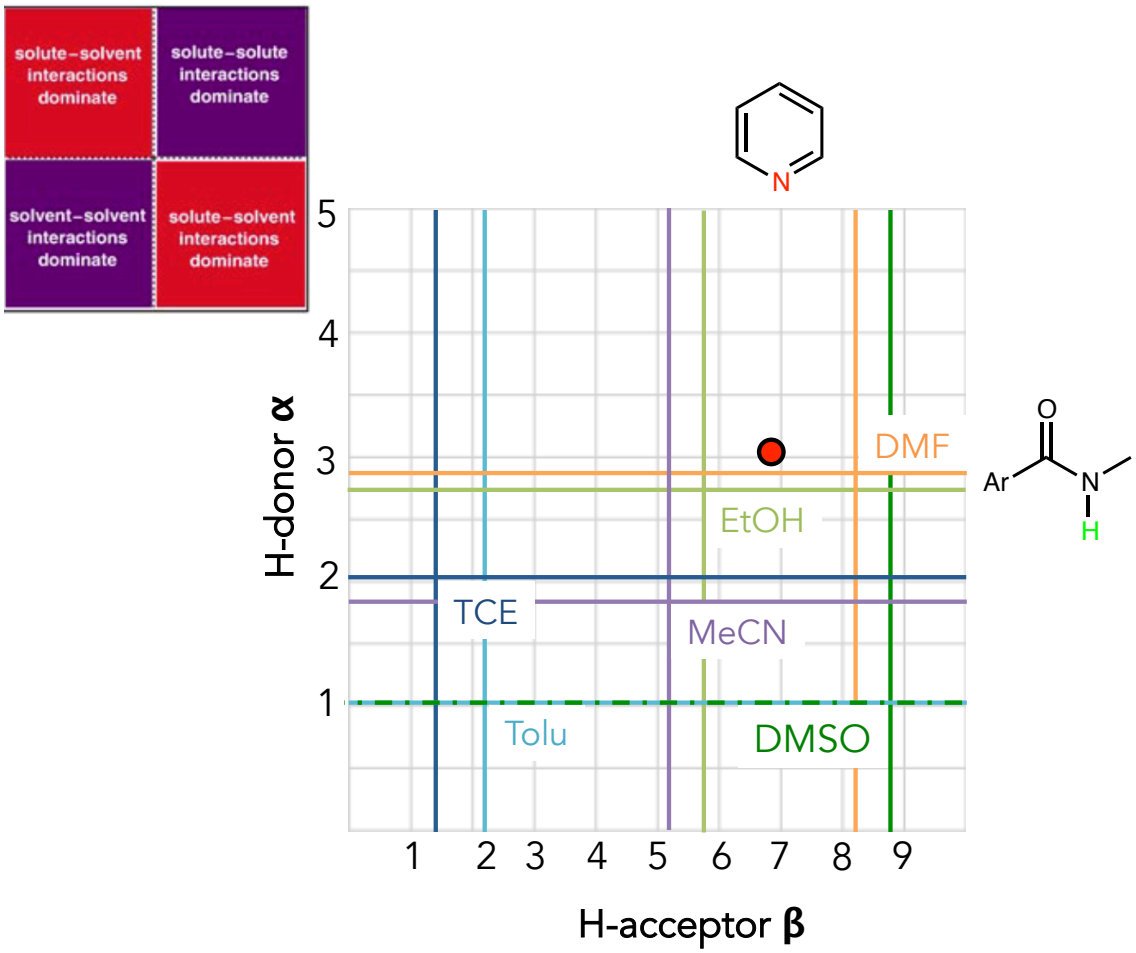

Figure 4.9 Reproduction of the functional group interaction space of Hunter's theory.[14] The interaction of interest is highlighted with the red point. The vertical and horizontal lines partition the space relatively into the four quadrants associated to the most dominant interaction: in the top-left: solute-solvent; in the top right: solute-solute; in the bottom left: solvent-solvent; in the bottom-right: solute solvent.

Looking at the relative position of the red point, the Hunter's theory suggests that the intramolecular interaction between the amide (H-donor) and the aromatic nitrogen (H-acceptor) is slightly unfavourable compared to intermolecular interactions with solvent molecules in DMF and DMSO and is increasingly favourable in EtOH, MeCN, TCE and toluene respectively. In our experimental results, the unfolding patterns indicate that the foldamer conserved its folded conformation in all the solvents, including DMF and DMSO. In others words, we did not observe critical unfavourable interactions and instead we confirmed the formation of intramolecular interactions rather than the intermolecular interactions with the solvent. As a result, with certain moderation, the Hunter's theory classifies the amide-quinoline interaction energies in this following order:
$\Delta G_{\text{H-bond}}(\text{DMSO}) \approx \Delta G_{\text{H-bond}}(\text{DMF}) \leq \Delta G_{\text{H-bond}}(\text{EtOH}) \leq \Delta G_{\text{H-bond}}(\text{MeCN})$
$< \Delta G_{\text{H-bond}}(\text{TCE}) < \Delta G_{\text{H-bond}}(\text{toluene})$, which is in quite good agreement with our results. This confirms the important contribution of these H-bonds.

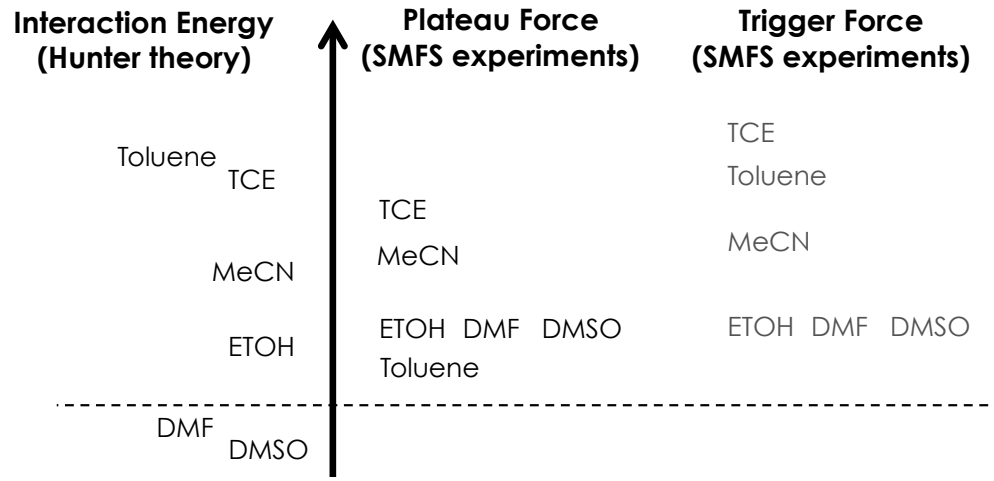

Figure 4.10 Graphical comparison of the intensities of the interactions in different solvents from the Hunter theory (interaction between nitrogen in an aromatic cycle and hydrogen of an amide) and the unfolding forces (plateau and trigger) obtained by SMFS.

Secondly, further comparisons between theory and experiments enabled to shed light on the other molecular interactions involved in the foldamers (hydrophobic effect, electrostatic interactions, π-stacking) and to relate them to mechanical behaviours and stability of the foldamers in different solvents. Indeed, according to the theory, the helical structure should not be preserved in DMF and DMSO. The variation between the theory and the experiment can be explained by the addition of the maybe minor but not negligible favourable contribution of other folding factors (than H-bond and analogues) such as the presumed π-stacking, backbone rigidity or the unfavourable electrostatic repulsion.
Moreover, according to our results we observed a serious discrepancy for toluene, when we deal with the plateau force. This leads us to our second deduction and highlights the important contribution of the π-stacking. Although the trigger force in toluene follows

Hunter's prediction, the most part of the helix unfolds under a weaker force than theoretically expected. As mentioned in the introduction of this chapter, Hunter's model does not take into account π-stacking contribution and therefore we can link the observed difference to the default. Hereby, we could deduce that toluene, with its aromatic ring, likely interacts with the aromatic rings of the quinoline oligomers and destabilizes some interactions by a direct competing interaction, leading to weaker intramolecular interactions and consequently to lower unfolding forces.

Thirdly, the results confirmed the interplay of different molecular interactions that can also counterbalance each other according to the environment. Although we tested solvents with different H-donor or H-acceptor properties (DMF, DMSO and EtOH), they exhibited the same impact on the helical stability. The foldamers can be perturbed and can respond back on different ways.

4.2.3 Trigger force in apolar solvents

Then, the remarkable decrease in the unfolding force of the foldamer in toluene ($\Delta F_{\text{starting trigger}}$= 30 pN) and in TCE ($\Delta F_{\text{starting trigger}}$= 40 pN) is intriguing (Figure 4.8) and resembles a cooperative effect. Their occurrences are though still unclear. We can only propose hypothesis.

One hypothesis is related to the theory of the perturbation of a structured solvent cage. As the foldamers do not show aggregation[3], we can imagine that the solvent molecules surround really well the helix. In its fully folded state, the outside of the helix is rather apolar owing to the isobutoxy-groups, allowing an ideal organization of TCE and toluene molecules around them. At the beginning of the unfolding, highly polar functions (amide) are revealed and thus introduced into this solvent cage. This step may require additional force to perturb the structure made by apolar solvent. It is totally energetically unfavourable as it decreases the entropy of the solvent and the molecule and decreases the favourable interactions.[23] Therefore the solvent molecules act as applying a pressure against the opening of the helix. For subsequent unfolding steps we could assume that the disorder solvent organization is more adapted to accept the following polar chemical functions and therefore the force to unfold is not as high as the first one. In polar solvents, as there is no electrostatic clash between the solvent molecule and the functional group of the foldamer, the first step is not more unfavourable than the following.

Another interpretation we could develop based on this solvent-dependent behaviour suggests a difference in the forced-unfolding mechanism. Given the hidden length liberated along the starting rupture, which indicates the opening of slightly less than 2 turns at once (hopping), we can suggest that the unfolding takes place through the opening

of the first turns at both extremities simultaneously in apolar solvent. On the contrary we could rather assume the opening of only one group of interactions from one side in polar solvents. This interpretation would need confirmation but could explain why the inversion occurs faster in apolar solvent than polar solvent (Huc previous results).[13] If the inversion takes place from both sides, it probably goes faster than from only one side.

In summary, with the measurements of the highest force in TCE and the progressively decreasing forces for the other solvents according to the Hunter-predicted order, we confirm the important contribution of the H-bond between the amide and the quinoline. With the results in toluene, we could also probe the important contribution of the π-stacking. Compared to another solvent (apolar or polar), in toluene, the major unfolding process take places at a weaker force. Although the electrostatic interactions are reinforced, the destabilization of π-stacking overbalances this electrostatic reinforcement and induces a lower mechanical stability along the intermediate unfolding step. We also highlighted a different mechanical behaviour in apolar solvents compared to polar solvents. In apolar solvents, a trigger force is required to start the unfolding of the foldamers.

4.2.4 Qualitative analysis on the shorter foldamers

Given the results of the longer foldamers, which allows us to identify some mechanical properties and to disentangle fairly the contribution of the intramolecular interaction, we only performed a qualitative solvent analysis on the shorter foldamers (less data).

As expected, the specific unfolding traces, found in DMF for each foldamer (chapter 2), are also obtained in the other tested solvents. With a qualitative eye, the pulling traces on these smaller foldamers seem also to confirm the same mechanical unfolding patterns as in DMF. In Q17, unambiguously the unique folded helical conformation is supported in all solvents (Figure 4.11). For Q9, it is sometimes more uncertain, particularly in EtOH (Figure 4.12). In this solvent, the plateau feature is not always present for Q9, which may evidence a more compliant folded structure.

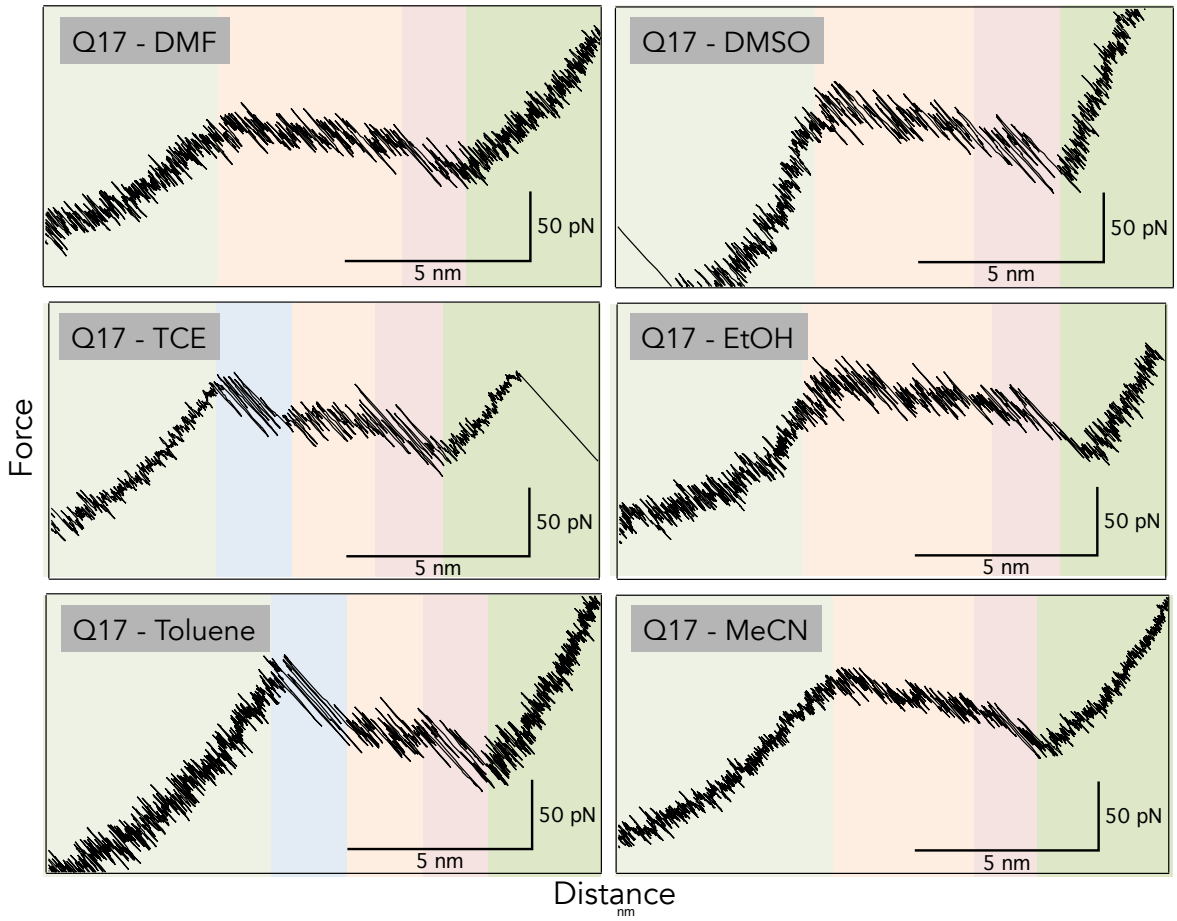

Figure 4.11 Force-distance curves of pulling experiments on Q17 in several organic solvents. Each solvent is written in the top-left corner of the curve. The colour zones indicate the different mechanical behaviours of the foldamers.

As already mentioned, the trigger force and the hopping events are also observed at the beginning of the unfolding patterns of Q17 and Q9 in TCE and toluene. Interestingly, the trigger inverses the mechanical behaviour of the Q9. For the more polar solvents (EtOH and DMF), the unfolding starts with a force-constant plateau and finishes with a decreasing-force behaviour, which has been previously associated to a destabilized nucleation segment. For the apolar solvents (TCE and Toluene), the unfolding on the contrary starts with a high force trigger and finishes at the small constant force of a plateau.

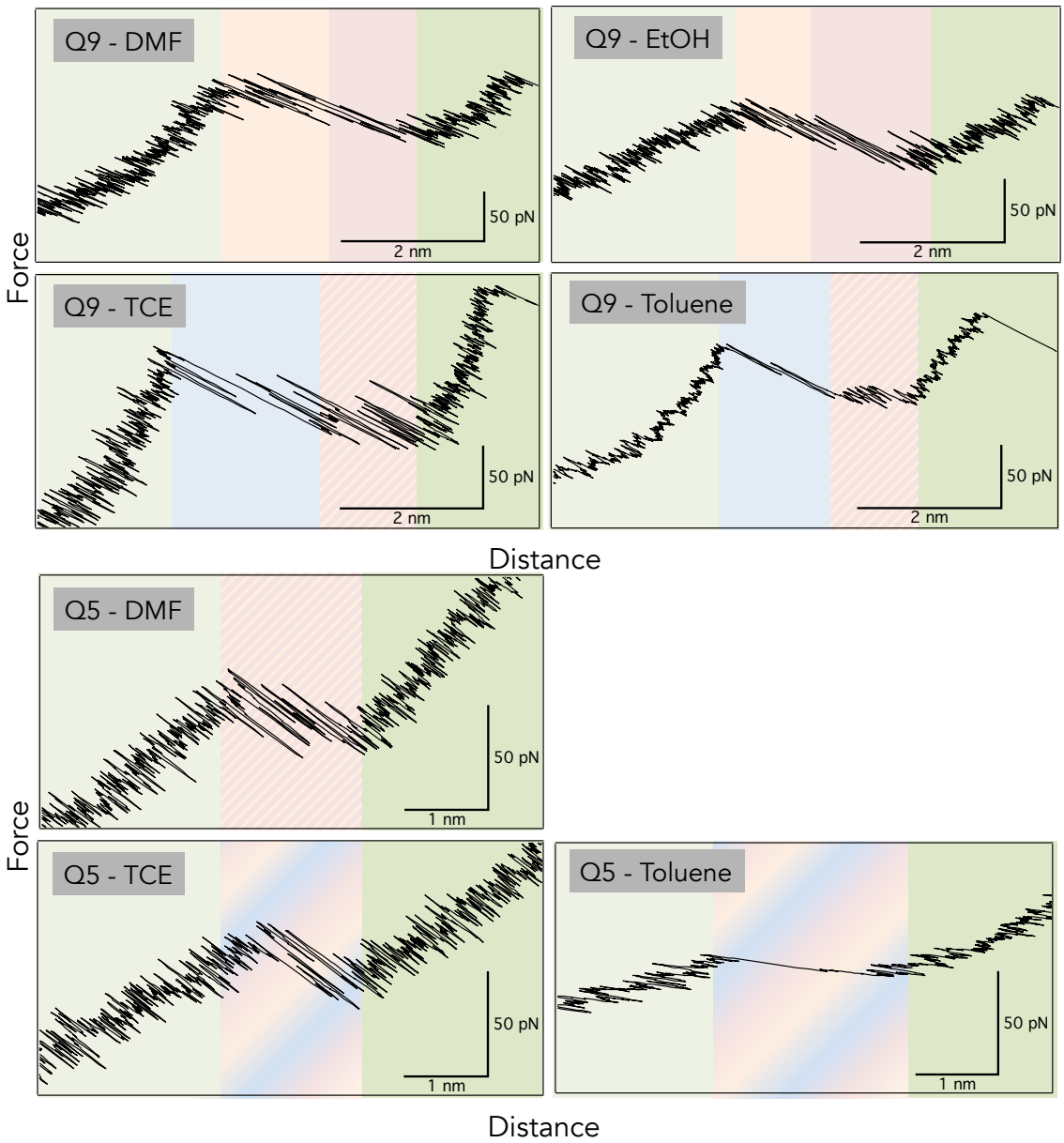

Figure 4.12 Force-distance curves of pulling experiments on Q9 (top) and Q5 (bottom) in several organic solvents. Each solvent is written in the top-left corner of the curve. The colour zones indicate the different mechanical behaviours of the foldamers, the bi- and tricolour zone indicate an uncertainty in the mechanical behaviours.

Q5, as already evidenced in DMF, are very short and their unfolding patterns do not exhibit distinguishable features (Figure 4.12). Therefore, it is highly difficult to demonstrate different mechanical behaviours depending on the solvent. Their unfolding patterns confound the trigger, the plateau and the nucleation features. Although sometimes we probed single rupture, some hopping can also be measured in each solvent. This concurs with the high stability of the helix as it proves that even a 2-turns helix fluctuates between the unfolded and the folded states under a load. This occurs even in toluene, in which we could imagine that refolding would not take place so rapidly as the toluene molecules could intercalate with the quinoline cycles and compete with the intramolecular interactions.

4.3 Conclusion

The analysis of pulling curves in several organic solvents covering a wide range of properties allowed obtaining some preliminary information about the contributions and possible modulations of the non-covalent interactions involved in the helical folding of the quinoline-based foldamers.

No solvent dismantles the helical structure. In general, we can admit that good H-donor and good H-acceptor ones would induce weaker forces and the poor H-donor and poor H-acceptor would reinforce the structure. Nevertheless, the toluene deviates from this rule owing to its non-negligible stacking ability and exhibits the weakest unfolding force among the others tested solvents. On one side, being apolar it reinforces the electrostatic interactions, but on the other side it is able to compete the π-staking with quinoline units. These results proved the important contributions of both H-bonds and π-stacking in the folding.

The hopping feature could be observed in each solvent at the end of the unfolding. As previously shown, this feature indicates the reversibility of the unfolding. Even when the chemical groups are revealed and exposed to the solvent molecules they do not interact strongly enough to prevent the refolding.

Intriguingly a new feature, highlighting a new mechanical behaviour, has been observed in toluene and TCE. It represents a strong (cooperative) interaction taking in 4-5 units at the beginning of the unfolding. We could not find an evident interpretation, either we can associate it to an unfavourable solvent disordering when polar function are revealed in apolar solvent or to a different unfolding mechanism.

From another point of view, we highlighted the capacity of tuning the mechanical properties by changing the solvent. Indeed, the force modulation by the solvent could be efficient. Depending on the solvent, we could measure unfolding forces ranging over a little bit more than 30 pN. It represents a possible modulation of 30 %.

Finally, it was one of the first studies, where the solvent has no dramatic effect on the architecture. The plateau-based unfolding has been conserved in all the conditions; only the strength of the interactions has been modulated by changing the solvent. It is thus an interesting study from a SMFS point of view, as well as for the foldamer field. Once again we could highlight the remarkable mechanical stability in these foldamers. As prospect, an interesting solvent that is probably worth exploring is hexafluoropropan-2-ol. It is considerably better H-donor than the amides according to Hunter's constants. It is known to solubilize a wide range of polymers, including polyamides, polyesters, which are

usually not soluble in the most common organic solvents. It is also used in biochemistry to solubilize peptides or to monomerize ß-sheet protein aggregates.

Thus it would be interesting to probe whether the foldamer resists or how it influences the unfolding force.

4.4 References

1. Li, X. *et al.* Synthesis and Multibromination of Nanosized Helical Aromatic Amide Foldamers via Segment-Doubling Condensation. *Org. Lett.* **18,** 1044–1047 (2016).
2. Qi, T., Deschrijver, T. & Huc, I. Large-scale and chromatography-free synthesis of an octameric quinoline-based aromatic amide helical foldamer. *Nat. Protoc.* **8,** 693–708 (2013).
3. Qi, T. *et al.* Solvent dependence of helix stability in aromatic oligoamide foldamers. *Chem. Commun. (Camb).* **48,** 48–51 (2012).
4. Amenta, V. *et al.* Interplay of self-association and solvation in polar liquids. *J. Am. Chem. Soc.* **135,** 12091–12100 (2013).
5. Stirnemann, G., Kang, S., Zhou, R. & Berne, B. J. How force unfolding differs from chemical denaturation. *Proc. Natl. Acad. Sci. U. S. A.* **111,** 3413–8 (2014).
6. Camunas-Soler, J., Ribezzi-Crivellari, M. & Ritort, F. Elastic Properties of Nucleic Acids by Single-Molecule Force Spectroscopy. *Annu. Rev. Biophys.* (2015). doi:10.1146/annurev-biophys-062215-011158
7. Ritort, F. Single-molecule experiments in biological physics: Methods and applications. *J. Phys. Condens. Matter* **18,** 531–583 (2006).
8. Abu-Lail, N. I. & Camesano, T. A. Polysaccharide properties probed with atomic force microscopy. *J. Microsc.* **212,** 217–238 (2003).
9. Oesterhelt, F., Rief, M. & Gaub, H. E. Single molecule force spectroscopy by AFM indicates helical structure of poly(ethylene glycol) in water. *New J. Phys.* **1,** 6.1-6.11 (1999).
10. Liu, K. *et al.* Stretching Single Polymer Chains of Donor–Acceptor Foldamers: Toward the Quantitative Study on the Extent of Folding. *Langmuir* **29,** 14438–14443 (2013).
11. Zou, S., Schönherr, H. & Vancso, G. J. Stretching and rupturing individual supramolecular polymer chains by AFM. *Angew. Chem. Int. Ed. Engl.* **44,** 956–9 (2005).
12. Qi, T. *et al.* Solvent dependence of helix stability in aromatic oligoamide foldamers. *Chem. Commun. (Camb).* **48,** 48–51 (2012).
13. Delsuc, N. *et al.* Kinetics of helix-handedness inversion: Folding and unfolding in aromatic amide oligomers. *ChemPhysChem* **9,** 1882–1890 (2008).
14. Hunter, C. Quantifying intermolecular interactions: Guidelines for the molecular recognition toolbox. *Angew. Chemie - Int. Ed.* **43,** 5310–5324 (2004).
15. Emenike, B. U., Bey, S. N., Bigelow, B. C. & Chakravartula, S. V. S. Quantitative model for rationalizing solvent effect in noncovalent CH-Aryl interactions. *Chem. Sci.* **7,** 1401–1407 (2016).
16. Sader, J. E. *et al.* Spring constant calibration of atomic force microscope cantilevers of arbitrary shape. *Rev. Sci. Instrum.* **83,** 103705 (2012).
17. Kennedy, S. J., Cole, D. G. & Clark, R. L. A method for atomic force microscopy cantilever stiffness calibration under heavy fluid loading. *Rev. Sci. Instrum.* **80,** (2009).
18. Burnham, N. A. *et al.* Comparison of calibration methods for atomic-force microscopy cantilevers. *Nanotechnology* **14,** 1–6 (2003).
19. te Riet, J. *et al.* Interlaboratory round robin on cantilever calibration for AFM force spectroscopy. *Ultramicroscopy* **111,** 1659–1669 (2011).
20. Sader, J. E. Frequency response of cantilever beams immersed in viscous fluids with applications to the atomic force microscope. *J. Appl. Phys.* **84,** 64–76 (1998).
21. McFarland, A. W., Poggi, M. A., Doyle, M. J., Bottomley, L. A. & Colton, J. S. Influence of surface stress on the resonance behavior of microcantilevers. *Appl. Phys. Lett.* **87,** 1–4 (2005).

22. Pirzer, T. & Hugel, T. Atomic force microscopy spring constant determination in viscous liquids. *Rev. Sci. Instrum.* **80,** (2009).

23. Calero, C. S. *et al.* Footprinting molecular electrostatic potential surfaces for calculation of solvation energies. *Phys. Chem. Chem. Phys.* **15,** 18262–73 (2013).

Chapter 5

Synthesis of Naphthyridine-constituted Foldamer and Quinoline-based Foldamer with an aliphatic junction

TABLE OF CONTENTS

Chapter 5
Synthesis of Naphthyridine-constituted Foldamer & Quinoline-based Foldamer with an aliphatic junction

In this chapter, we describe the synthesis design strategy and the reaction pathways of two new foldamers. In order to further develop the mechanochemical study, two other foldamers were rationally designed and synthesized. To suit for AFM-SMFS experiments and to benefit from the characterization of the pure quinoline-based foldamers, we designed foldamers comprising chemically different parts embedded in quinoline-based foldamer blocks.

The first foldamer consists in a triblock foldamer where a naphthyridine-based block is inserted into two quinoline blocks (Tr-S-R-$^{m}QQ_8$-N_8-$^{m}QQ_8$-PEG). The naphthyridine-based block has a similar chemical backbone than the quinoline one and also exhibits helical folding. Compared to quinoline foldamers, the naphthyridine foldamers have a wider helix diameter.

For the synthesis of the first foldamer, we undertook two changes in a basic quinoline foldamer. First, the naphthyridine block was inserted, and secondly, an aliphatic link (methylene bridge) was needed for coupling the quinoline and naphthyridine blocks. Therefore, conjointly synthetized with the first triblock foldamer, the second new foldamer consisted in the quinoline foldamer with only the small aliphatic link in the middle of its sequence (Tr-S-R-$^{m}QQ_8$-$^{m}QQ_8$-PEG). On the one hand, this foldamer was hence used as a reference for investigating the first new, triblock foldamer. On the other hand, the effect of the insertion of a methylene bridge, which breaks the aromatic conjugation, could be investigated. Such influences on the structure have not yet been studied in the literature. The methylene bridge could potentially add mechanical flexibility to the structure, which should be investigated independently of the triblock foldamer.

To obtain the desired precise and monodisperse distributions for both foldamers, the convergent segment doubling method was used. At the end of the syntheses, the foldamers were functionalized for AFM-SMFS studies. This means that the foldamer extremities were functionalized with a thiol group and with a poly(ethylene glycol) (PEG) chain, as it was the case for the previously studied quinoline-based foldamers.

5.1 Introduction

Aromatic oligoamides have the great potential of becoming building parts of nanomachines and molecular materials[1–3]. Their structures are predictable, which allows designing, prior to synthesis, molecules with a given shape. It also allows the investigation of the relationship between the chemical sequences, the structures and the mechanical properties of folded molecules. The complete understanding of their folding mechanism and their corresponding mechanical properties is promising to allow the design of foldamers adapted for specific applications.

After having evidenced the robust mechanical properties of quinoline-based foldamers we proceeded to compare their results to looser molecular helices. For this purpose, 1,8-naphthyridine units were selected[4] (Figure 5.1.B). These helices exhibit a wider diameter. Therefore, we will also probe if the diameter variable follows in molecular scale the Hooke's Law (Eq. 1) as in macroscopic scale.

$$k = G\,\frac{d^4}{8nD^3} \qquad \text{Eq.1}$$

Eq. 1 where k is the spring constant, D the spring diameter, G is the material shear modulus, n is the number of coils, and d the thickness of the coiled wire.[5]

1,8-Naphthyridine: 2-amino-5-isobutoxy-1,8-naphthyridine-7-carboxylic acid

Identically to quinoline unit, naphthyridine unit is a *N*-hetero-bicycle aromatic molecule. However, the relative positions of amine and (carboxylic) acid substituents at the 2 and 7 positions in naphthyridine induce a larger angle of 120° between adjacent units compared to the 60°-angle in quinoline oligomers due to their substituents at position 2 and 8 (Figure 5.1). Consequently, naphthyridine-based foldamers exhibit a wide helix diameter and jointly a cavity, while quinoline helices are considered not to exhibit a cavity. 1,8-naphthyridine units are valued for their propensity of creating H-bonds with recognized guest compounds[6] or in self-assemblies. They could also be used for creating capsules with an inside cavity.[7,8] Worth noting, the H-bonds (grey in Figure 5.1) between the heterocyclic amine and amide proton strengthen the curvature of the helix, they lead to helices of respectively 2.5 quinoline units and 4 naphthyridine units per turn.

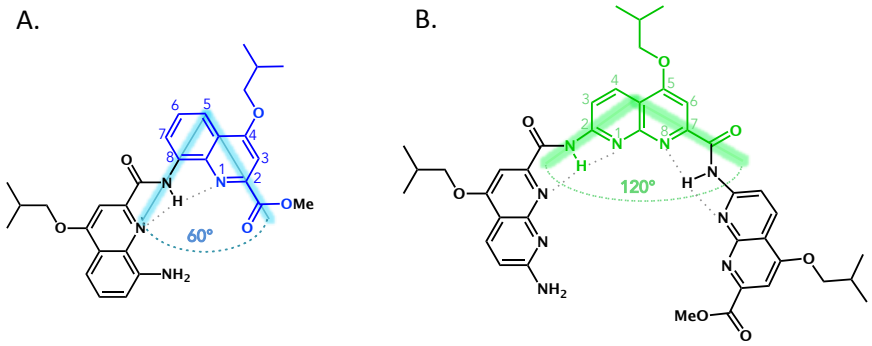

Figure 5.1 Chemical structure of (A) a quinoline dimer and (B) a naphthyridine trimer. The angle formed by the amine and acid substituents in quinoline is 60° and in naphthyridine is 120°C.

Naphthyridine units can be used in both homo-foldamers and in hetero-foldamers. Hetero-foldamers are made up of several kinds of aromatic units and homo-foldamers are made up of only one kind of aromatic unit. Although naphthyridine units are commonly used in hetero-foldamers, they are difficult to handle as long homo-foldamers. Nevertheless, Huc's group endeavoured to synthesize naphthyridine-homo-oligomers and, in 2010, they demonstrated that in many solvents, such as chloroform and acetonitrile, pure naphthyridine tetramers lead exclusively to the formation of a triple helix, which was not expected and is a rare synthetic molecular architecture[7]. This structure is based on similar interactions than those involved in quinoline-based helices (H-bonds, electrostatic repulsion; Figure 5.2.A), which seem to be also involved in inter-strand interactions. The naphthyridine tetramer, making one full turn, assembles as a triple helix, where each strand extends like a spring to adopt a pitch of 10.5 Å, *i.e.* triple the expected pitch of other aromatic helical oligoamides (3.5 Å), and a cavity diameter of 4.3 Å (Figure 5.2.C&D). The synthesis was limited to tetramers due to weak reactivity, caused partly by the triple helix hybridization. Exceptionally, in pyridine, the tetramer adopts a single-stranded helical conformation of one turn with a pitch of 3.5 Å and a helix cavity diameter of 5 Å (Figure 5.2.B). Here below, naphthyridine unit is coded N.

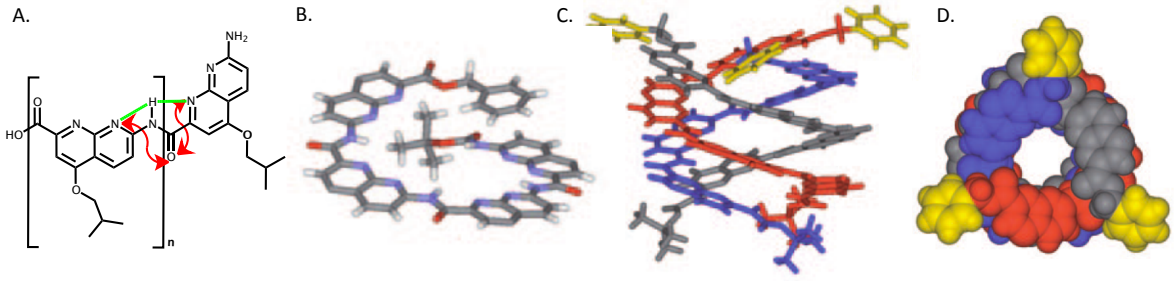

Figure 5.2 Representations of naphthyridine oligoamides. (A) Chemical structure and intramolecular interactions leading to the helical folding. The H-bond interactions are highlighted in green and the electrostatic repulsions are shown using red arrows. (B) Structure of a single strand helix obtained from X-ray diffraction of a single crystal grown from a pyridine/hexane mixture. The foldamer is constituted by a sequence of 4 units forming one helical turn. (C and D) Triple helix structures obtained from X-ray diffraction of a crystal grown from a chloroform/pyridine/hexane mixture (side and top view respectively). The three oligoamide strands forming the triple helix are represented in red, blue and grey (with terminal groups in yellow). Adapted from reference 7.

With these observations, one could imagine that a single-stranded naphthyridine is mechanically less robust than quinoline helix, as it can spontaneously extend to hybridize. In other words, it means that the energy cost of helix extension is lower in naphthyridine oligomers than in quinoline oligomers. This result can be explained by a smaller torsion required per naphthyridine unit than it would be for quinoline unit, as there are more units

(4 units) per turn than in quinoline oligomers (2.5 units per turn). This brings us to the question: how is this reflected in SMFS force measurements?

Moreover, our investigation is also motivated by the remarkable folding differences between quinoline and naphthyridine oligoamides. Indeed, an increase in torsional angle and pinching of the diameter is often observed in naphthyridine foldamers, when they assemble in triple helices or accommodate solvent molecules in their cavity.[7] Although the chemical structures are quite similar in both oligoamides, quinoline-oligomers appear not to be able to deform nor to accommodate any guest molecule. Besides, as a brief reminder, the relative positions of the quinoline units seems to remain the same in a dimer as in an octamer, indicating that no pinching occurs with the addition of stacking interactions (see chapter 3 and [9]).

Finally, it would be interesting to understand the driving forces leading to multi-stranded structures.

5.2 Design of the triblock naphthyridine-constituted foldamer and of the diblock quinoline-based foldamers for SMFS experiments

To date, it is premature to investigate a self-assembled triple helix by AFM-SMFS. Indeed given the challenge of interpreting force-distance signals, it is required to pull on a well-determined and well-controlled single complex molecule. Moreover, it is more rational to start with a simpler, *i.e.* single-stranded helix and to obtain comparable results with the previously characterized systems.

To ensure a controlled, efficient and well-determined system suited for SMFS analyses and particularly to avoid the formation of the triple helices we developed a specific design. We decided to covalently intercalate a sequence of naphthyridine oligomer (N_8) in between two quinoline-based foldamer blocks (Q_8), $\mathbf{^{m}QQ_8\text{-}N_8\text{-}^{m}QQ_8}$, as shown in Figure 5.3 (centre). Quinoline-based foldamers are used to prevent any extension of naphthyridine oligomer which could otherwise lead to their hybridization, as Q_8 are strongly compact and folded[10,11]. This subterfuge was also chosen because Q_8 has previously been studied in this thesis (Figure 5.3 (top)) and its unfolding pattern is hence already characterized. Therefore $Q_{(2x8)}$ will act as an internal reference to help the identification of the new unfolding pattern(s) of the naphthyridine-based helix.

Moreover, to achieve the synthesis of this triblock naphthyridine-constituted foldamer, an amino-methyl-quinoline unit had to be added at the amino end of the Q_8 to ensure the coupling with the naphthyridine acid sequence (poor nucleophilicity of aromatic amine). This insertion breaks the aromatic conjugation and its effect on the structure is still unknown. For this reason, we decided to additionally synthesize the diblock composed of only quinoline-based blocks, **$^{m}QQ_8$-$^{m}QQ_8$**, as represented in Figure 5.3 (bottom). The insertion of an aliphatic junction has never been investigated mechanically. Independently from its use as reference, it is therefore interesting to investigate its effect on mechanical properties.

Finally, as for the previously studied foldamers[12], we functionalized the foldamer ends with a thiol group on one side to strongly anchor the foldamer on a gold-coated substrate. In order to have the foldamer standing perpendicularly to the anchored surface as much as possible, an amino-methyl-quinoline unit was also added before the thiol linker. The flexibility induced by the presence of the methylene bridge is expected to allow a 90° angle between the *N*-terminus of the molecule and the helical structure. On the other side of the foldamer, a poly(ethylene glycol) (PEG) chain was covalently attached to be able to fully unfold the foldamer by catching it by a tether.[12–14]

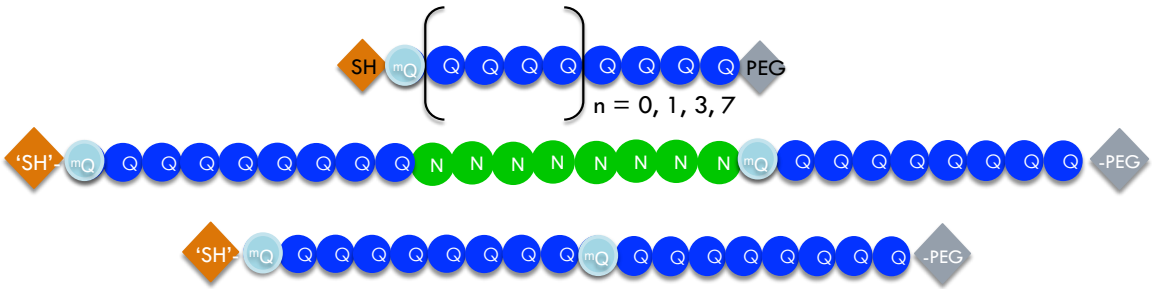

Figure 5.3: Schematic representation of (Top) Tr-S-$^{m}QQ_{4n}$-PEG previously studied foldamers, made up of quinoline units. (centre) Tr-S-R-$^{m}QQ_8$-N_8-$^{m}QQ_8$-PEG: new foldamer, made up of a triblock of quinoline-, naphthyridine-, quinoline-blocks; (bottom) Tr-S-R-$^{m}QQ_8$-$^{m}QQ_8$-PEG: new quinoline-based foldamer with the insertion of one amino-methyl quinoline unit in-between two Q_8. Each foldamer is designed specifically to be adapted to SMFS experiments: addition of a thiol group at one end and a PEG chain as tether at the other end. The light blue ^{m}Q represents an amino-methyl-quinoline unit, the blue Q represents a quinoline unit, the green N represents a naphthyridine unit.

5.3 Synthesis of the triblock naphthyridine-constituted foldamer: Trityl-S-R-$^{m}QQ_8$-N_8-$^{m}QQ_8$-PEG

5.3.1 Segment doubling synthesis strategy

Chemists have not yet mimicked the function of the marvellous ribosome. Even if state-of-the-art studies have been performed to use its machinery with other building blocks than amino acids or to create an artificial ribosome[15,16], it is still not a trivial pathway to obtain foldamers.

To attain the desired precise and monodisperse distribution for foldamers, the convergent segment doubling method was successfully implemented in the group of Ivan Huc[10]. This stepwise synthesis consists in coupling two monomers to make a dimer, then coupling two dimers to make a tetramer and so on, in order to converge on the desired molecule.[4] This synthesis strategy, in the case of oligoamides, is based on coupling amines with (carboxylic) acids to form amide bonds. It allows doubling the size at each step and therefore rapidly reaching high molecular weights. At the same time, the large size difference between reactants and products simplifies the product purification performed using gel permeation chromatography (GPC), as it is based on size exclusion. For this purpose, *i.e.* the ease of purification and the efficient increase in molecular weight, the whole synthesis scheme has been designed to be as symmetrical as possible. Even if we aimed at building a triblock '$^{m}QQ_8$-N_8-$^{m}QQ_8$', the synthesis did not involve three blocks, *i.e.* one '$^{m}QQ_8$', one 'N_8' and one '$^{m}QQ_8$' block, but rather two 'N_4' blocks of the central 'N_8' block which were coupled to each of the terminal '$^{m}QQ_8$' blocks. These half-foldamers were subsequently jointed together, as shown in Figure 5.4.

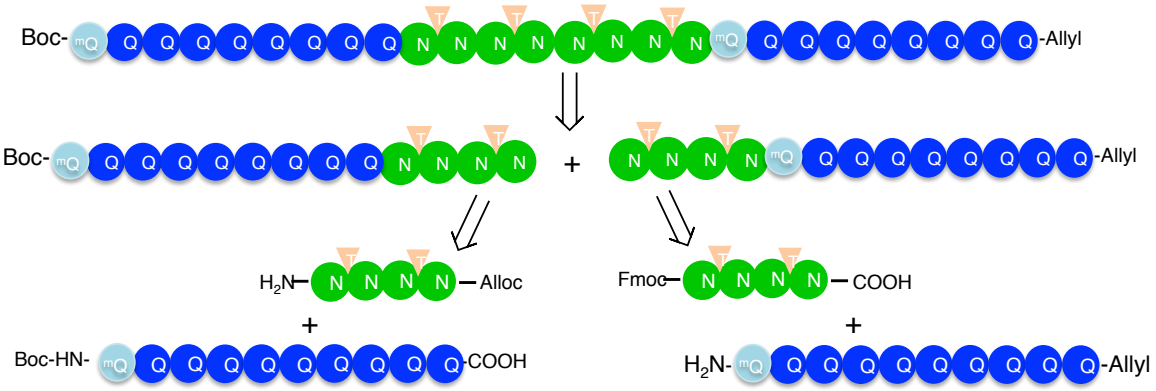

Figure 5.4 Schematic representation of the retrosynthesis strategy of a triblock '$^{m}QQ_8$-N_8-$^{m}QQ_8$'. The light blue ^{m}Q represents an aminomethyl-quinoline unit, the blue Q represents a quinoline unit, the green N represents a naphthyridine unit and the beige T represents the formation of a tertiary amide as folding-protecting group to prevent hybridization as triple helix. Fmoc, allyl and Boc represent protected terminal ends.

Schematic outline of the global reaction scheme followed for synthesizing the triblock Trityl-S-R- $^{m}QQ_8$-N_8-$^{m}QQ_8$-PEG is presented in Figure 5.5. The next sections of this chapter follow the described reaction scheme.

A. Synthesis of the quinoline blocks Q_8 and $^{m}QQ_8$ Described in section 5.3.2.
B. Synthesis of the naphthyridine monomers, dimers and tetramers N(DMB)N and $(N(DMB)N)_2$ .Described in section 5.3.3.
C. Couplings of $^{m}QQ_8$ + $(N(DMB)N)_2$: $^{m}QQ_8$-$(N(DMB)N)_2$ and $(N(DMB)N)_2$ + $^{m}QQ_8$: $(N(DMB)N)_2$-$^{m}QQ_8$. Described in section 5.3.4.
D. Coupling of $^{m}QQ_8$-$(N(DMB)N)_2$+$(N(DMB)N)_2$-$^{m}QQ_8$: $^{m}QQ_8$-$(N(DMB)N)_4$ $^{m}QQ8$ and the deprotection of tertiary amides to yield the $^{m}QQ_8$-N_8-$^{m}QQ_8$. Described in section 5.3.5.
E. Functionalization of the foldamer for SMFS experiments: Trityl-S-R-$^{m}QQ_8$-N_8-$^{m}QQ_8$-PEG. Described in section 5.3.6

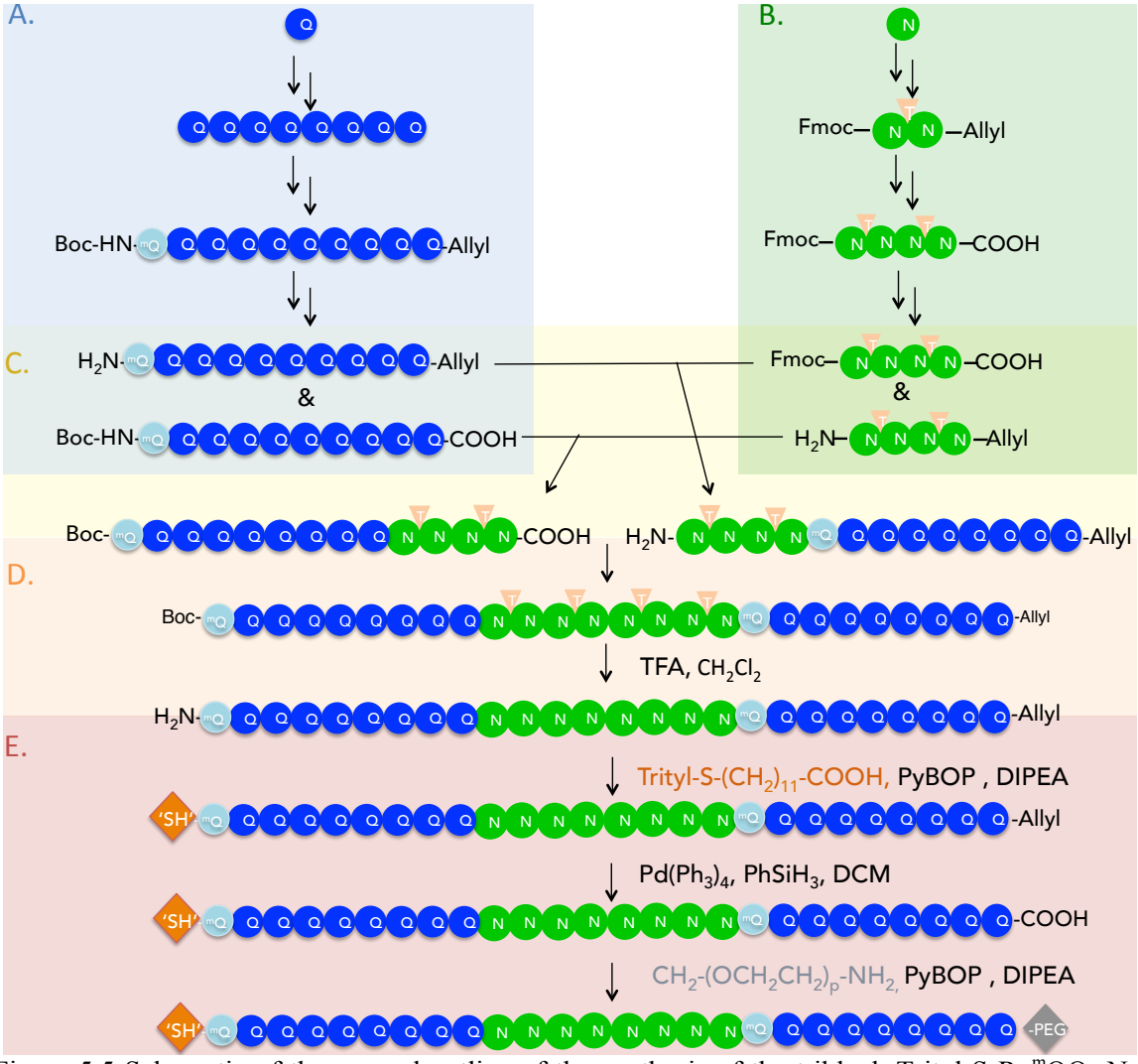

Figure 5.5 Schematic of the general outline of the synthesis of the triblock Trityl-S-R- $^{m}QQ_8$-N_8-$^{m}QQ_8$- PEG. The light blue ^{m}Q represents an aminomethyl-quinoline unit, the blue Q represents a quinoline unit, the green N represents a naphthyridine unit and the beige T represents the formation of a tertiary amide as folding-protecting group to prevent hybridization as triple helix. 'SH' represent the small linker bearing a trityl-protected-thiol and ' PEG' stand for a PEG of Mw~5000g/mol.

5.3.2 Synthesis of quinoline blocks

The synthesis of the first and last blocks $^{m}QQ_8$ of the targeted triblock foldamer are synthetized following the reaction pathway published in literature (Figure 5.5.A).[10] The reactions were adapted and optimized for the Q_8 system in close collaboration with Jinhua Wang. The synthesis was already presented in chapter 3. The starting material was provided by Eric Merlet, the technician engineer of the laboratory.

As already mentioned in the introduction of this chapter, the quinoline amine is a poor nucleophile, unable to be efficiently coupled with the carboxylic-naphthyridine acid (for foldamer block couplings) or to the aliphatic carboxylic acid (of the thiol linker). Because of this lack of reactivity we added an **8-aminomethyl-4-isobutoxy-2-quinolinecarboxylic acid (^{m}Q)** at the N-terminus of the Q_8. This addition is also used to assure an efficient positioning of the helices towards the SMFS set up.

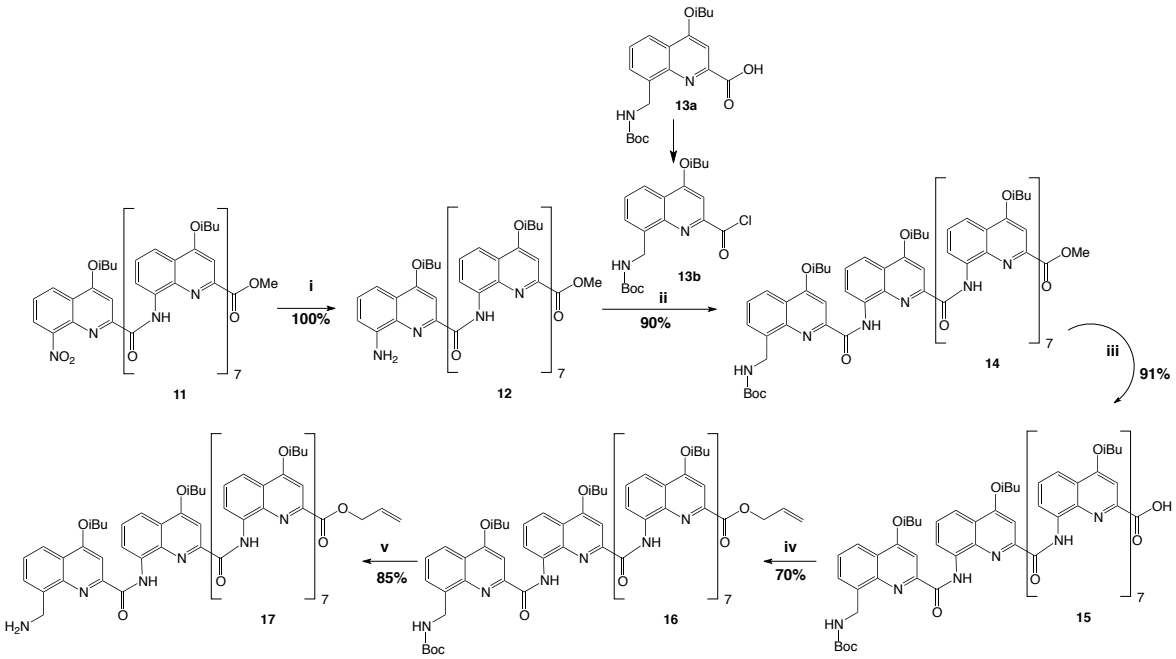

Scheme 1: Representation of the synthesis of $^{m}QQ_8$ acid **15** and $^{m}QQ_8$ amine **17** from Q_8 **11** with the following reaction conditions: i) Pd/C, ammonium metavanadate (cat), ammonium formate, EtOAc, EtOH, H_2O, RT; ii) **13b** Ghosez's reagent, $CHCl_3$, RT; DIEA, $CHCl_3$; iii) NaOH, MeOH, THF, RT; iv) HCl, H_2O; v) Allyl alcohol, DIEA, PyBOP, $CHCl_3$, RT; vi) TFA, CH_2Cl_2, RT. The reaction molar yields (in %) are provided under the reaction arrows.

The synthesis of the nonamer $^{m}QQ_8$ **15** is presented in **Scheme 1**. The octamer quinoline **11** is reduced using Pd/C, NH_4VO_3 and NH_4HCO_2 by refluxing in ethyl acetate and ethanol mixture. The 8-boc-aminomethyl-4-isobutoxy-2-quinolinecarboxylic acid (^{m}Q) **13a** was provided by Jinhua Wang and converted to its acid chloride with oxalyl chloride to be quantitatively added to **12**. The boc-protecting group is the appropriate protecting group choice as it can be removed using TFA treatment, which also removes

simultaneously the DMB ("steric"-protecting group) on the naphthyridine (see next section). On the contrary, the terminal methyl ester needed to be exchanged into an allyl ester group, in order to be able to selectively deprotect the carboxylic acid function before the final addition of the PEG linker at the very end of the synthesis. The allyl ester was chosen because its deprotection reaction is orthogonal with the others and particularly because it has been proven to be harmless to naphthyridine oligomers. The deprotection of allyl ester is performed using $Pd(PPh_3)_4$ with triisopropylsilane.

The methyl ester was saponified under strong base conditions (NaOH in a THF/MeOH mixture) to obtain **15** and the allyl ester was installed through a coupling with the allyl alcohol using PyBOP.

5.3.3 Synthesis of naphthyridine dimers & tetramers

As briefly discussed previously, the synthesis of naphthyridine oligomers is still challenging (Figure 5.5.B). Difficulties usually arise from the formation of reaction-inhibiting conformations and from the poor nucleophilicities of aromatic amines. Helical folding and hybridization occur even for short sequences, causing steric hindrance at terminal main chain reactive functions. Issues come also from the low stability of the naphthyridine units and oligomers, which on the one hand leads to side reactions and on the other hand prevents the use of some efficient activating steps (acid chloride reaction). All together, it causes low coupling yields and purification difficulties.

Dr. Subrata Saha optimized the synthesis of the naphthyridine tetramer (**Scheme 2**). To circumvent the low-yield issues, a "steric" protecting group is temporally added on the nitrogen of the amide, which disrupts locally the folding, avoiding hybridization into multi-stranded helices and thus alleviates steric hindrance **5**.[17] To have a good orthogonality over the protecting groups, meaning that the functional groups can be selectively deprotected, the 2,4-dimethoxy benzaldehylde (DMB) acid-labile was selected as unfolding group and added every other amide bond. This protecting group is kept all along the synthesis of the foldamer and is only removed at the end of the synthesis by an acidic treatment. Fmoc is employed to protect the amines and is deprotected under DBU treatment, while an allyl ester is used to protect the acids and is deprotected with $Pd(PPh_3)_4$ and triisopropylsilane.

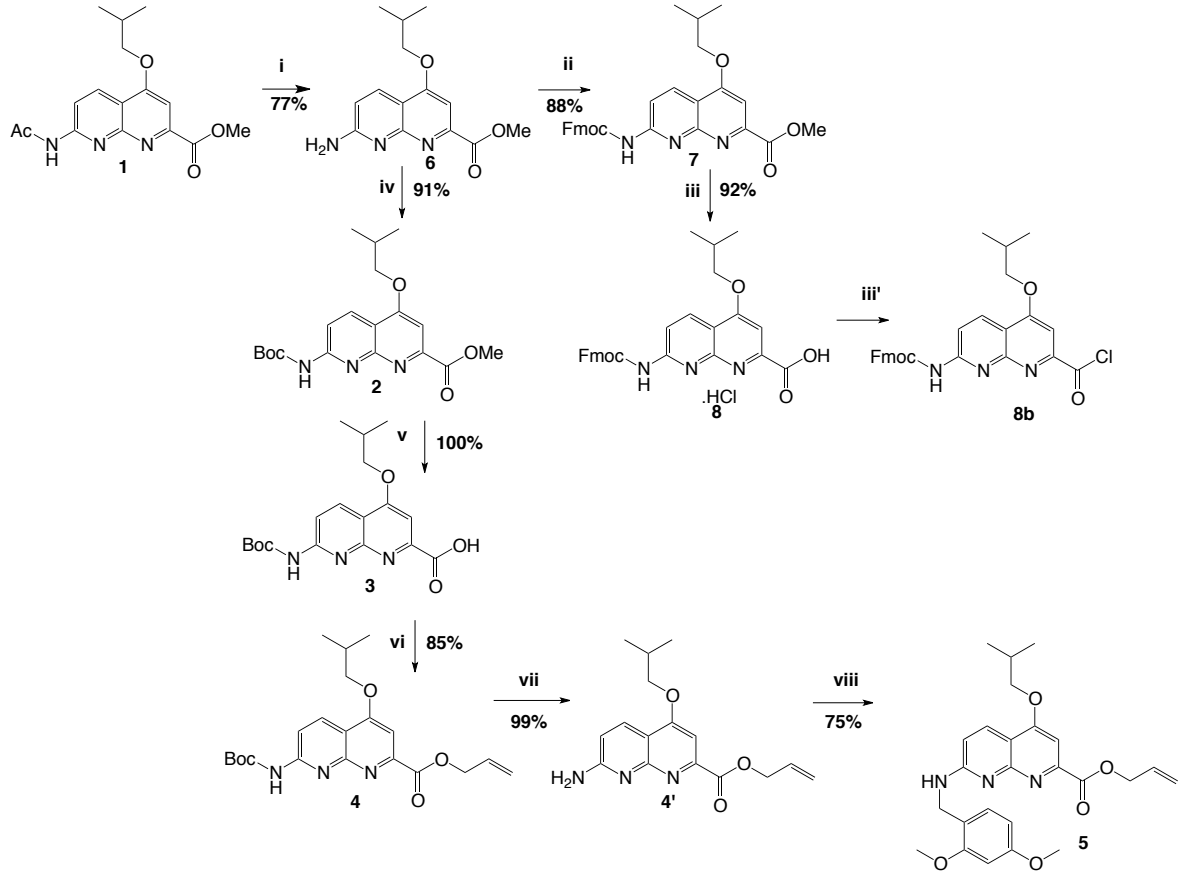

Scheme 2: Representation of the synthesis of N-acid 8 and N-amine-DMB protected **5** from **1** with the following reaction conditions: i) H_2SO_4, MeOH, 65°C, then RT. ii) Fmoc-OSu, dioxane, 90°C; iii) LiI, ethyl acetate, 78°C, 4h; HCl, THF, RT. iii') Oxalyl chloride, $CHCl_3$, DMF, 0°C then RT. iv) Boc_2O, Dioxane, 90°C; v) NaOH, dioxane, H_2O, room temperature; acetic acid. vi) Allyl alcohol, PyBOP, DIEA, $CHCl_3$, RT; vii) TFA, CH_2Cl_2, RT; viii) 2,4-Dimethoxybenzaldehyde, $NaBH(OAc)_3$, 1,2-dichloroethane, RT. The reaction molar yields (in percentage) are provided under the reaction arrows.

Eric Merlet provided the starting material **1** with acetyl and methyl ester protecting groups. Firstly the acetyl was removed by sulfuric acid and replaced by either Boc or Fmoc protecting groups. The methyl ester of the Boc-protected monomer was saponified under basic conditions, to convert it into an allyl ester **4**. The Boc was finally removed with TFA and the DMB was installed on **4'** by reductive amination on 2,4-Dimethoxybenzaldehyde in presence of the mild reducing agent, sodium triacetoxyborohydride to form the monomer amine **5**. The Fmoc-protected monomer **7** is then converted to carboxylic acid **8** by mild cleavage with lithium iodide of the methyl ester. The global yields for the preparation of the monomer amine **5** and for the monomer acid **8** are respectively 60% and 80%.

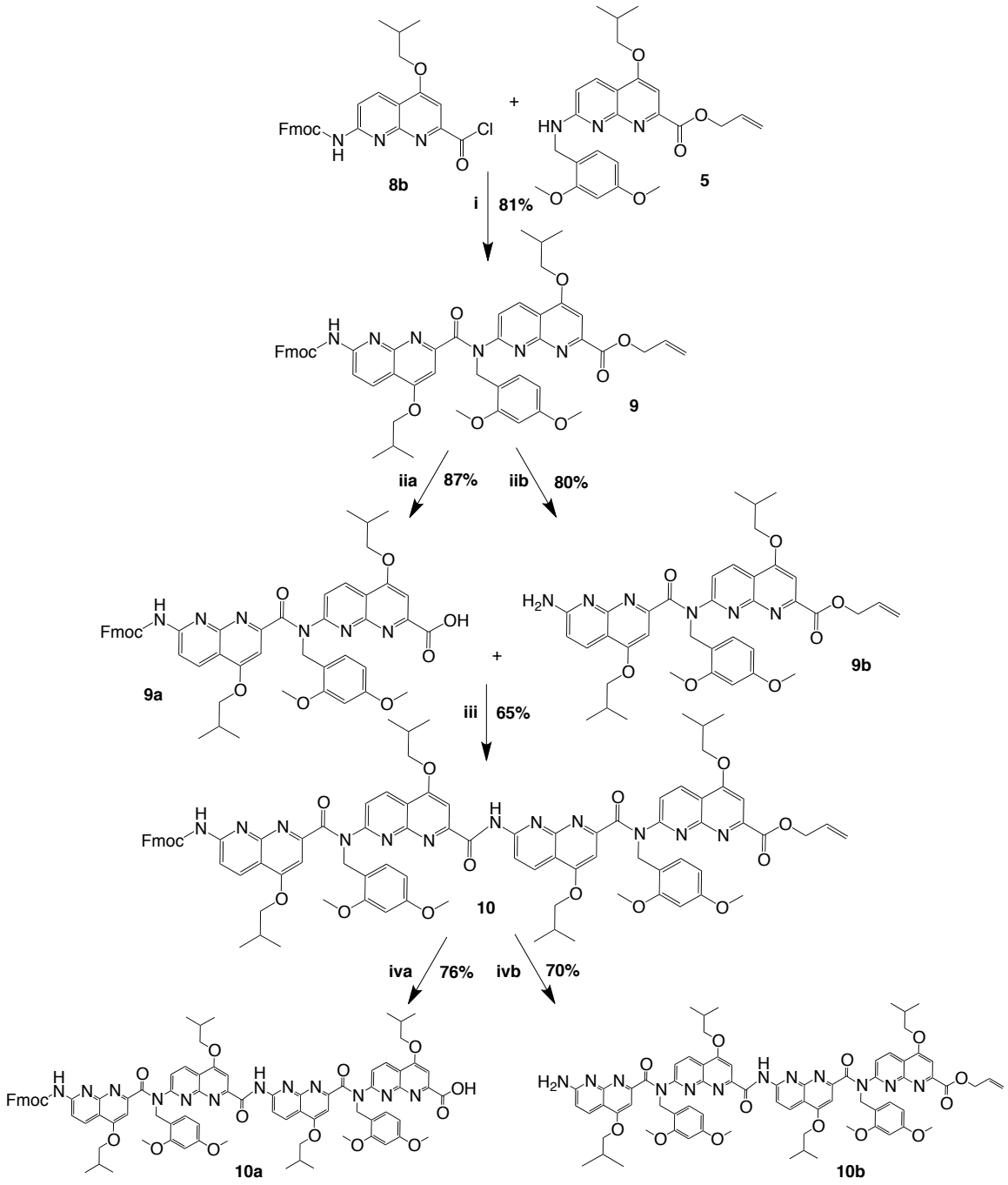

Scheme 3: Representation of the synthesis of tetramer $(N(DMB)N)_4$ amine **10b** and tetramer $(N(DMB)N)_4$ acid **10a** from monomer acid chloride **8** and amine **5**: i) $CHCl_3$, DIEA, 0°C then RT. iia) & iva) DBU, $CHCl_3$, RT. iib) & ivb) $Pd(PPh_3)_4$, $PhSiH_3$, CH_2Cl_2, RT. iii) PyBOP, DIEA, $CHCl_3$, RT. The reaction molar yields (in percentage) are provided at the reaction arrows.

The use of (base-labile) Fmoc allows activating of the carboxylic acid into an acid chloride **8b** and therefore yielding an efficient coupling reaction to obtain the dimer **9** as represented in **Scheme 3**. This acid chloride activation is conveniently used to increase the reactivity for the coupling

Nevertheless the protected tertiary amide also presents a drawback. It leads to the instability of the amide bond under harsh synthesis conditions, which prevents further acid chloride activation. The coupling agent PyBOP is further used for the next convergent coupling steps of synthesis, such as the formation of the tetramer **10**. Half of dimer **9** is Fmoc-deprotected to make the amine partner **9b** and half is allyl-ester-deprotected to obtain the acid partner **9a** as mentioned earlier. Then both are coupled together in the presence of DIEA and PyBOP.

Whereas all previous compounds could be purified by precipitation or on silica gel column, tetramers required re-cycling GPC purifications. Naphthyridine oligomers are polar and basic, therefore required highly polar solvents and tend to stick to the silica. GPC appeared to permit efficient separations. These GPC purification steps are unfortunately time-consuming, as only small amounts of products can be purified at a once (200 mg of crude reaction mixture/injection).

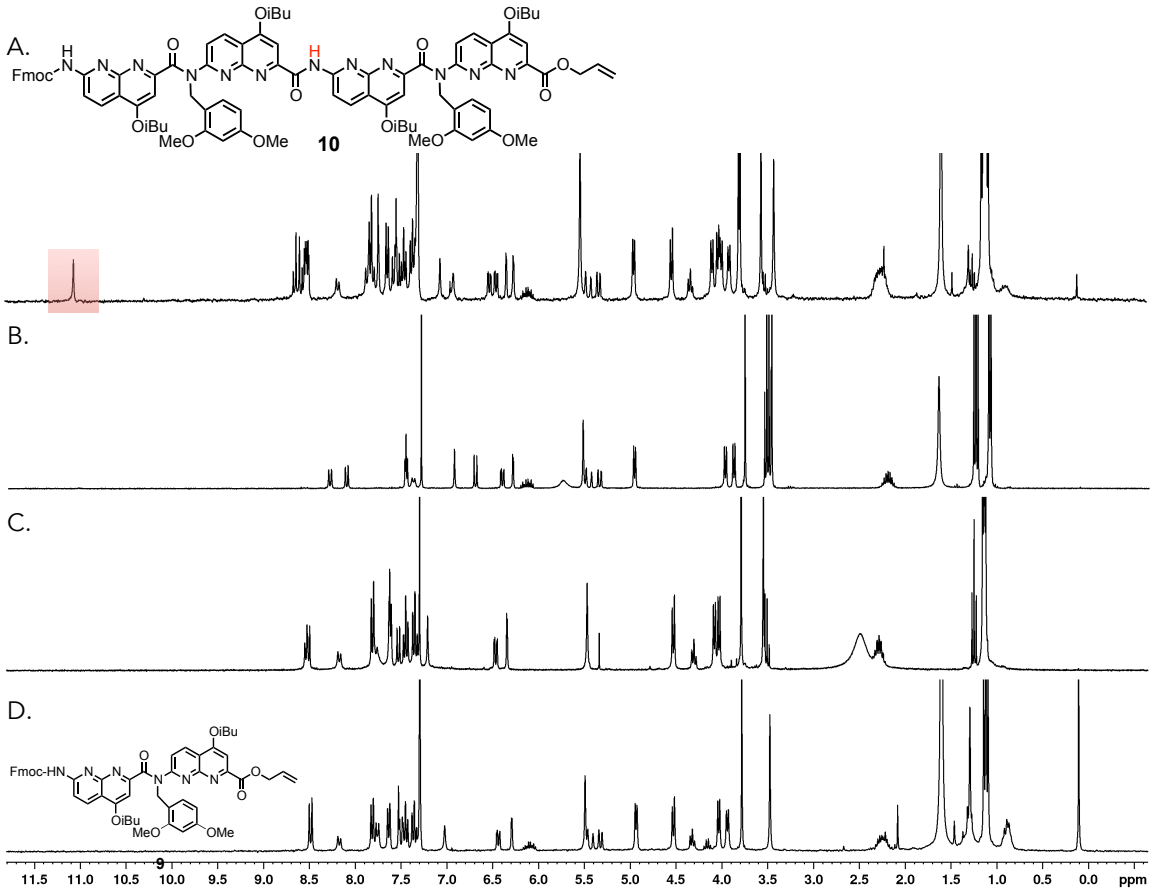

Figure 5.6 ^{1}H NMR spectra of (A) pure tetramer: Fmoc-[N(DMB)N]$_2$-Allyl **10**, (B) Fmoc-deprotected-N_2 acid: H_2N-N(DMB)N-Allyl **9a** , (C) Allyl-ester-deprotected N_2 amine: Fmoc-N(DMB)N-COOH **9b,** (D) dimer DMB-protected N_2: Fmoc-N(DMB)N-Allyl **9**. The characteristic aromatic amide proton is highlighted in red.

As shown by the ^{1}H NMR spectra of the tetramer (Figure 5.6), the amide proton, formed by the coupling of the DMB-protected dimers, appears as a sharp signal downfield shifted (~11.5ppm). These peaks are characteristic of the amide proton environment and represent a great help to monitor the coupling reaction (number of peak equals number of amide proton), as well as some influences of the chemical environment (internal[18] and external[19]). Despite the identical nature of (amide) proton in the units, one given proton on each unit exhibits a different chemical shift value according to its position in the helix. In quinoline oligomers, as shown previously (chapter 3), amide proton peaks are shifted upfield, *i.e.* towards lower ppm values when the number of unit increases. This shift is explained by an increase of ring current effects associated with aromatic stacking in the helical structure[9,10]. This effect was associated to an increase in stability.[18]

Fmoc is removed under DBU treatment for half of the tetramer to form the tetramer amine **10b**, while the allyl ester is deprotected under $Pd(PPh_3)_4$ and triisopropylsilane on the other half of the tetramer to obtain the tetramer acid **10b**.

5.3.4 Coupling of quinoline and naphthyridine oligomers

In order to facilitate the product purification, acid- **10a** and amine- **10b** naphthyridine tetramers (**Scheme 3**) were first coupled to **17** amine- and to **15** acid- $^{m}QQ_8$ blocks (**Scheme 1**) respectively with PyBOP. Then, these 2 compounds were similarly coupled to yield the triblock $^{m}QQ_8$-(N(DMB)N)$_4$-$^{m}QQ_8$.

The coupling of **15** with **10b,** yielding $^{m}QQ_8$-(N(DMB)N)$_2$ **18 (Scheme 4),** gives rise to a new amide proton sharp peak in ^{1}H NMR spectra (Figure 5.7), which is shifted upfield (~9.5ppm) compared to amide protons between two quinoline or two naphthyridine units (>10ppm). Nonetheless, this shift is commonly observed with coupling of naphthyridine and quinoline units. The reaction is not quantitative but the yield of the coupling was yet an acceptable 70%. The allyl ester of **18** was cleaved to obtain the reactive acid function of **19** for the next convergent coupling**.**

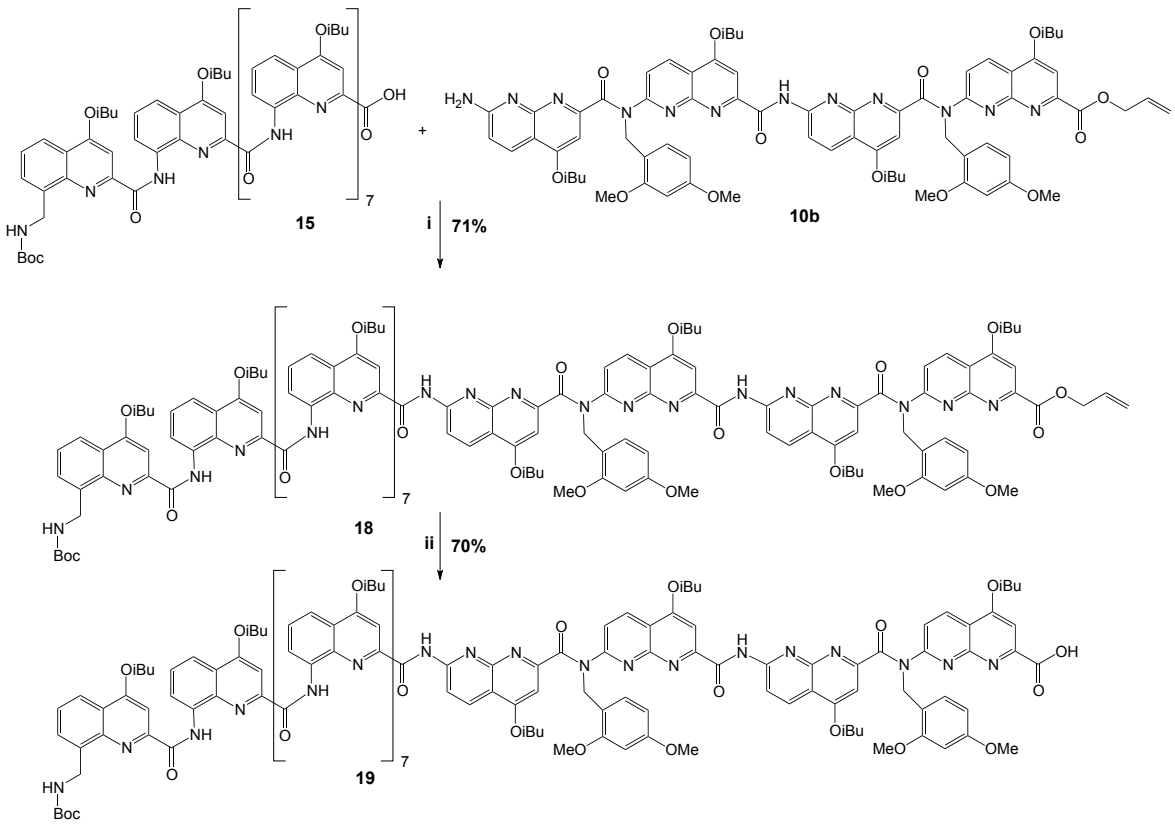

Scheme 4: Representation of the synthesis of **$^{m}QQ_8$ -(N(DMB)N)$_2$ acid 19** from **$^{m}QQ_8$ 15** and **(N(DMB)N)$_2$ amine 10b** i) DIEA, PyBOP, $CHCl_3$, RT; ii) $Pd(PPh_3)_4$, $PhSiH_3$, degased CH_2Cl_2, RT. The reaction molar yields (in percentage) are also provided under the reaction arrows.

The coupling of **17** and **10a** yields **20** (**Scheme 5**). The reaction does not form an aromatic amide proton, so no additional downfield signal appears on the NMR spectra (Figure 5.7); as the coupling takes place between an aliphatic amine and an aromatic acid. This coupling seemed to be quantitative but after purification, the yield was found to be 65%. **19** was treated with DBU to deprotect the amine reactive group **21** for continuing the convergent synthesis (**Scheme 5**).

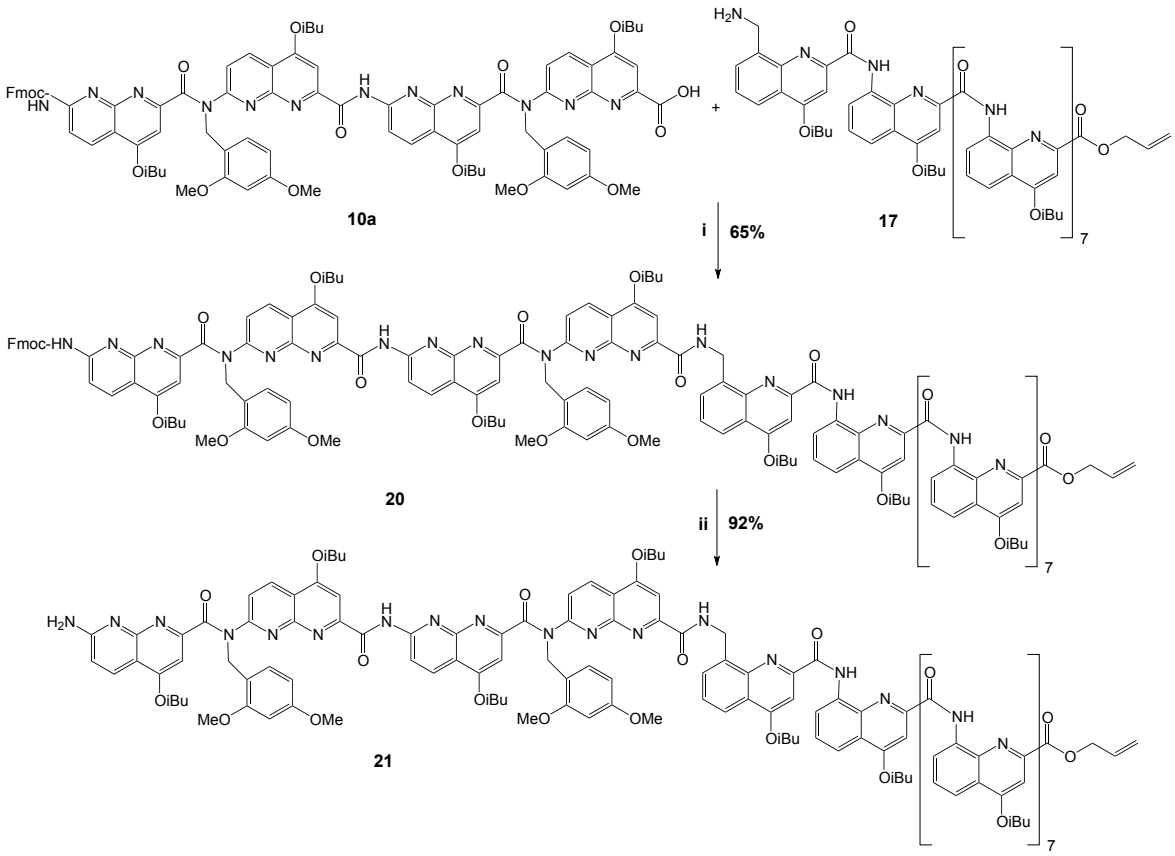

Scheme 5: Representation of the synthesis of **$(N(DMB)N)_2$-$^mQQ_8$** amine 21 from **$(N(DMB)N)_2$** acid **10a** and **$^mQQ_8$** amine **17** i) DIEA, PyBOP, $CHCl_3$, RT; ii) DBU, CH_2Cl_2, RT. The reaction molar yields (in percentage) are also provided under the reaction arrows.

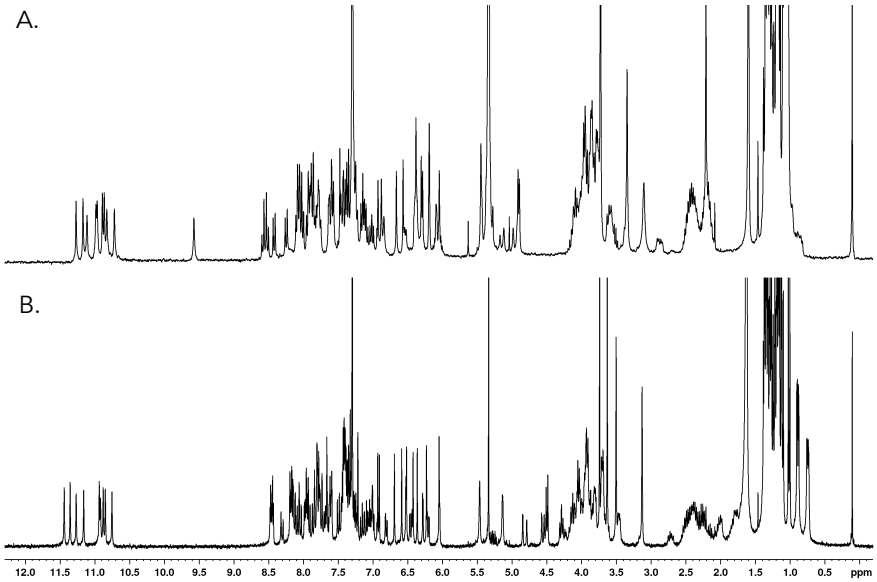

Figure 5.7 ^1H NMR spectra in $CDCl_3$ of (A) Boc-$^mQQ_8$-$[N(DMB)N]_2$-Allyl **18** and (B) Fmoc-$[N(DMB)N]_2$-$^mQQ_8$-Allyl **20**. In Boc-$^mQQ_8$-$[N(DMB)N]_2$-Allyl, we can observe an aromatic amide proton in the downfield region but yet slightly upfielded (~9.5ppm)

5.3.5 Coupling of precursor blocks of the final naphthyridine-constituted foldamer and DMB deprotection

After the coupling of the corresponding quinoline-based foldamer with the tetra-naphthyridine oligomers, we coupled these 2 compounds together with PyBOP to obtain the triblock of quinoline-naphthyridine-quinoline with a yield of around 40% after GPC purification ($^{m}QQ_8$-(N(DMB)N)$_4$-$^{m}QQ_8$) (**Scheme 6**).

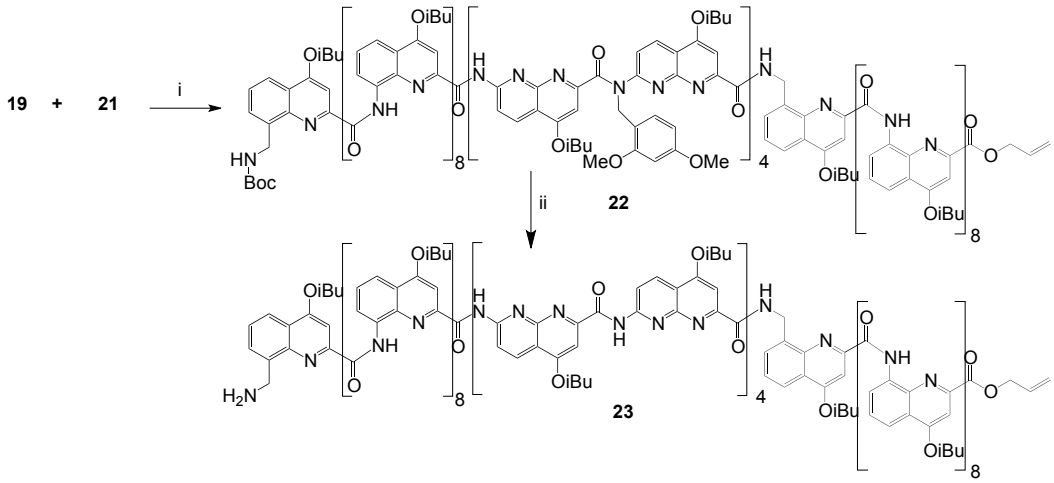

Scheme 6: Representation of the synthesis of **$^{m}QQ_8$-N$_8$-$^{m}QQ8$ amine 23** from **(N(DMB)N)$_2$-$^{m}QQ_8$ amine 21** and **(N(DMB)N)$_2$-$^{m}QQ_8$ acid 19.** The yield could not be calculated because of too small amounts.

We monitored the reaction over time, in this case, after 2h, 6h and overnight (Figure 5.8). It seems that the reaction occurred prior to the first measurement time-point (2h) and no major evolution occurred at longer reaction time. The reaction was not quantitative. The reaction mixture was purified using GPC and the impurity peak was composed of a mixture of the starting materials.

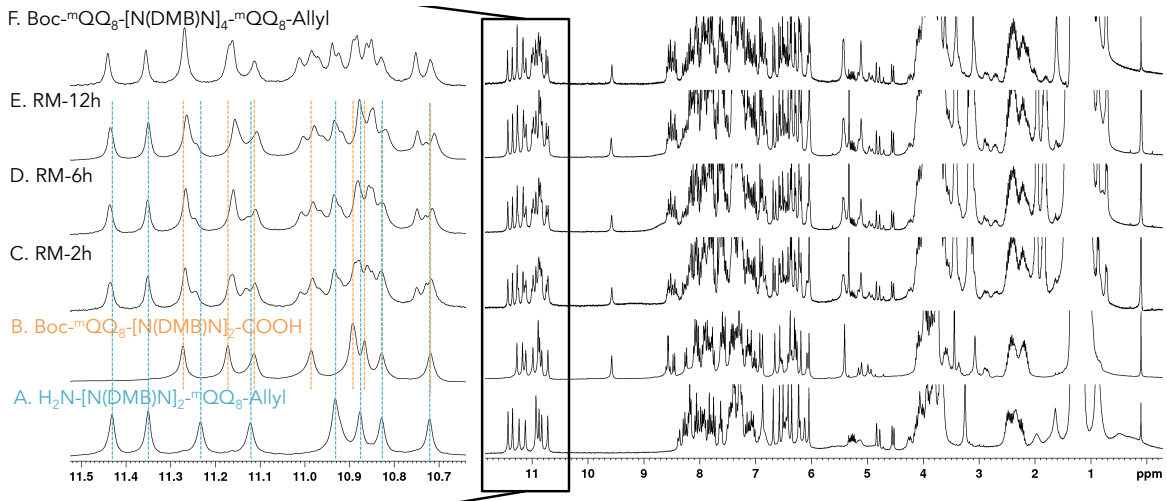

Figure 5.8 ^{1}H NMR spectra in $CDCl_3$ of starting reagents (A) H_2N-[N(DMB)N]$_2$-$^{m}QQ_8$-Allyl **21** & (B) Boc-$^{m}QQ_8$-[N(DMB)N]$_2$-COOH **19**; reaction mixture after (C) 2h, (D) 6h, (E) 12h and (F) purified coupling product Boc-$^{m}QQ_8$-[N(DMB)N]$_4$-$^{m}QQ_8$-Allyl **22**. The inlet represents the zoom of the aromatic amide protons; the orange and blue dashed lines indicate the reactants.

Interestingly, although the size of the foldamer was doubled, we did not observe an overall proton upfield shift, as it was observed with pure quinoline foldamers.[18] It was expected for the quinoline signals as the quinoline nonamers are not directly attached to each other and so cannot influence directly each other. As far as it concerns naphthyridine signals, this upfield shit is probably not observed because of the DMB protecting groups which prevent the folding.

Then we deprotected the terminus amine function (boc-protecting group) at the same time as all the tertiary amide functions from the DMB group using a TFA treatment. After this step, the ^{1}H NMR spectrum is complex, providing evidence of several conformations (Figure 5.9). We observed a slight narrowing and a decrease of the number of the peaks with time (days), but no variation with dilution. We suggested that several handednesses from the different helical blocks were coexisting and it took several days to reach the equilibrium conformation. Besides, an overall upfield shift compared to the protected analogue is eventually observed with time, suggesting the folding and stabilization over the whole foldamer or at least along the amine terminus $^{m}QQ_8$-N_8. For instance, amide protons chemical shifts extend from 11.42 to 10.72 ppm in the protected assembled triblock and shift to the range extending from 11.15 to 8.2 ppm and aromatic protons shift from 8.5-6ppm to 8.4-5.5ppm.

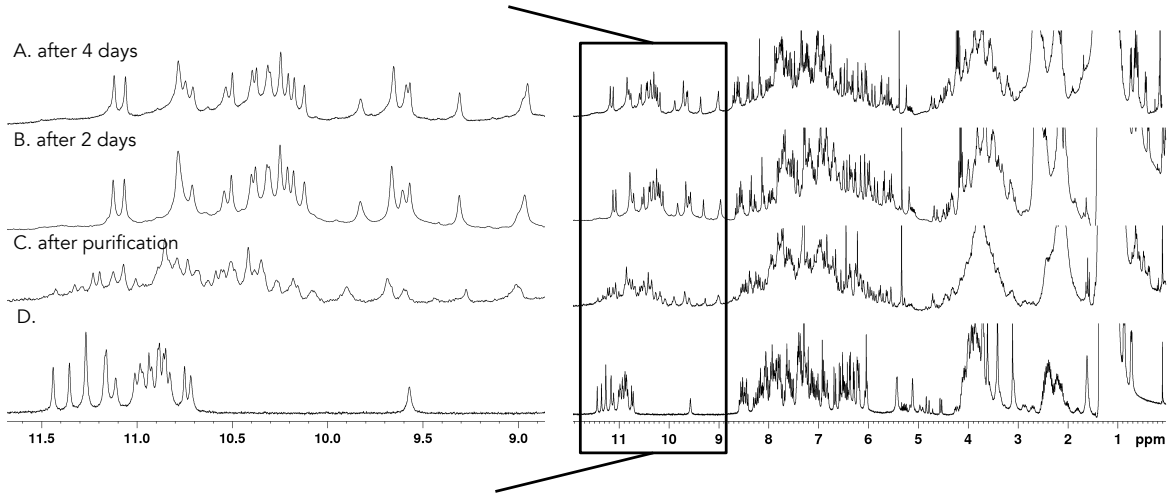

Figure 5.9 ^{1}H NMR in $CDCl_3$ of H_2N-$^{m}QQ_8$-N_8-$^{m}QQ_8$-Allyl **23** after purification (C), after 2 days in solution (B), after 2 days in solution and after 4 days in solution (A). (D) Starting material: Boc-$^{m}QQ_8$-[N(DMB)N]$_4$-$^{m}QQ_8$-Allyl **22.** (Left) zoom on the aromatic amide proton area. After reaction and purification, many peaks are present (more than 24) and peaks were broad. After some time, the peaks narrowed and their integration decreased to 24.

5.3.6 Functionalization of the triblock for SMFS experiments

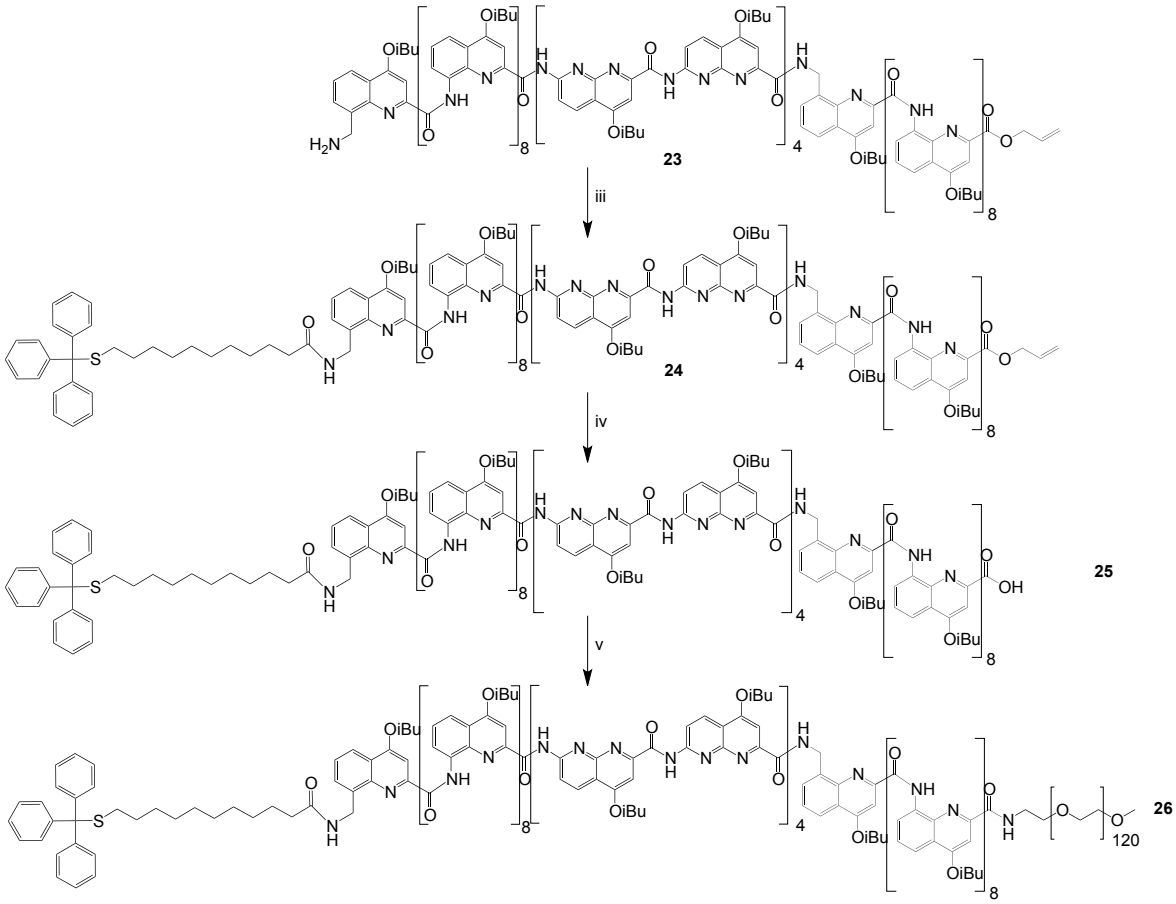

Scheme 7: Representation of the synthesis of the functionalization of the extremities of **Tr-S-^{m}QQ$_8$-N$_8$-^{m}QQ8-PEG** iii) Trityl-S-$(CH_2)_{10}$-COOH, DIEA, PyBOP,$CHCl_3$, RT; iv) $Pd(PPh_3)_4$, $PhSiH_3$, degased CH_2Cl_2, RT ; v) H_2N-PEG-OMe, DIEA, PyBOP, $CHCl_3$, RT. The reaction molar yields could not be measured.

High-resolution mass spectrometry (HRMS) analysis confirmed the synthesis of the fully deprotected compound. Finally the extremities of the foldamer were functionalized with specific chemical functions required for AFM-based SMFS experiments (**Scheme 7**). Following the same protocol proposed by Dr. Xuesong Li[12] and Dr. Victor Maurizot, we firstly added the trityl-protected-11-mercaptoundecanoic acid using PyBOP as coupling agent. Secondly, the allyl ester was deprotected before adding an amine terminated polyethylene glycol (PEG) 5000g/mol. Probably due to the hygroscopic character of PEG, the yield of the reaction is low. However, owing to the PEG dispersity and affinity for cations, HRMS or ion mobility-mass spectrometry (IMMS) could not certify the final compound, but we obtained MALDI spectra which shows a quite convincing broad peak around the expected mass of the final trityl-deprotected compound (see Figure S6). ^{1}H NMR spectra signals were not easily quantifiable as some peaks could not be integrated (Figure 5.10). Nevertheless, the stepwise reactions strategy together with the with the ^{1}H

NMR analyses after each reaction step, and the MS control analyses provided confidence in obtaining the expected compound after the foldamer-PEG coupling. The addition of the trityl-protecting thiol group could be identified, the deprotection of the allyl ester and the addition of PEG as well.

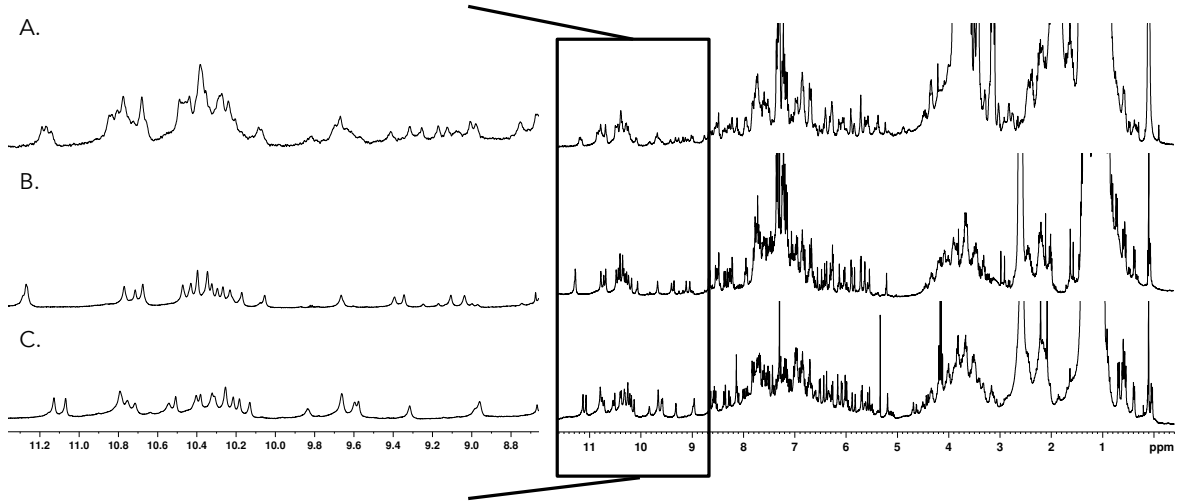

Figure 5.10 ^{1}H NMR in $CDCl_3$ of (A) Tr-S-R-$^{m}QQ_8$-N_8-$^{m}QQ_8$-PEG, (B) Tr-S-R-$^{m}QQ_8$-N_8-$^{m}QQ_8$-COOH and (C) Tr-S-R-$^{m}QQ_8$-N_8-$^{m}QQ_8$-Allyl. The downfield area of the NMR spectra is zoomed in the inset.

5.4 Synthesis of diblock quinoline-based foldamers: Trityl-S-R-$^{m}QQ_8$-$^{m}QQ_8$-PEG

Tr-S-R-$^{m}QQ_8$-$^{m}QQ_8$-PEG is a simplified version of the previously discussed foldamer. It is much easier to handle quinoline units and to synthetize quinoline oligomers. They exhibit a high chemical stability and do not tend to aggregate, facilitating also the characterization. We coupled quinoline-block amine **17** and quinoline-block amine **15** (**Scheme 1**) using PyBOP, to obtain the diblock **30** with a yield of 75% after GPC purification (**Scheme 8**). We then followed the same procedure to functionalize the extremities as in section 5.3.6. Each step of the synthesis was validated by NMR and MS.

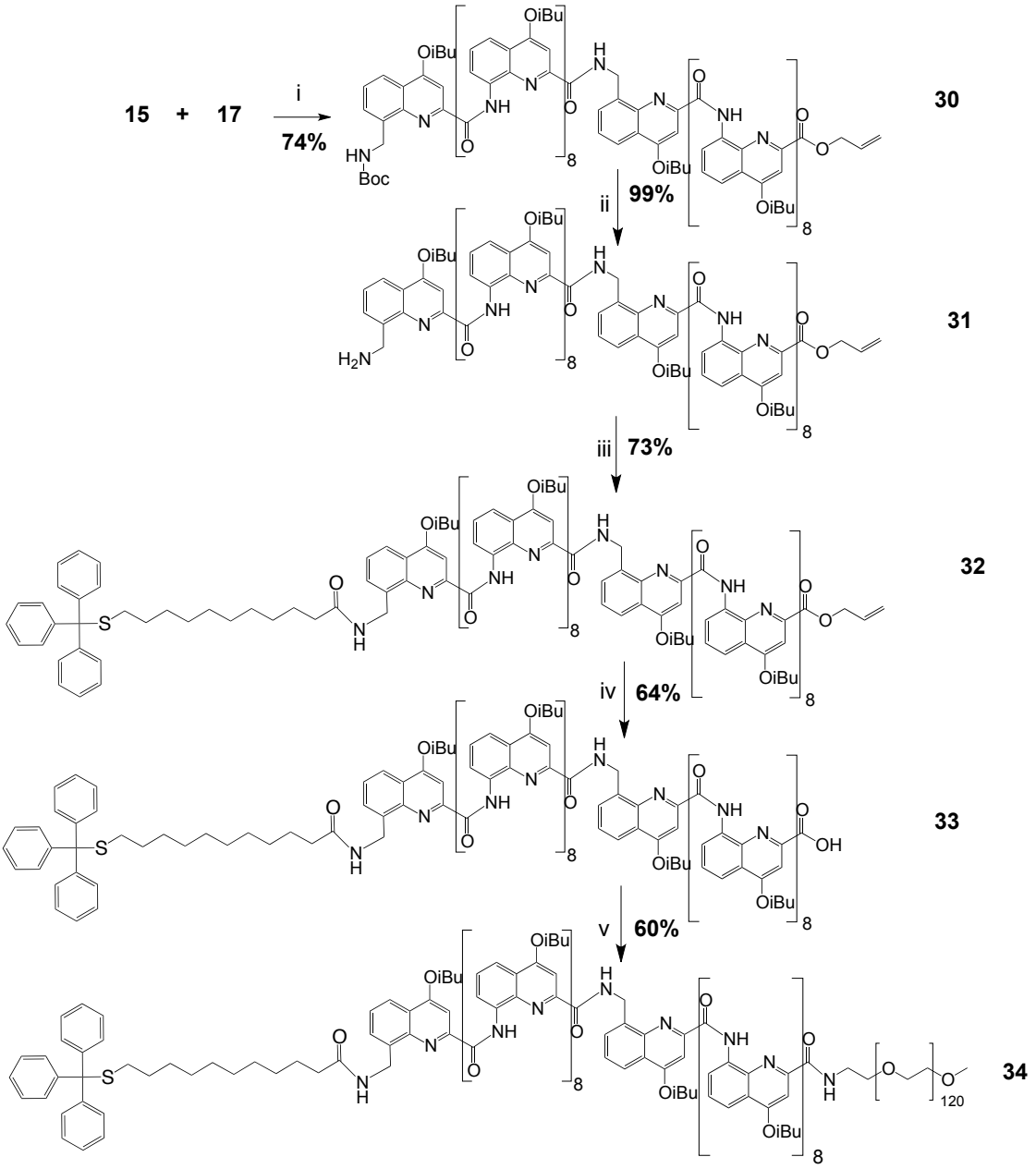

Scheme 8: Scheme of the synthesis for the functionalization of the extremities of Tr-S-$^{m}QQ_8$-QQ8-PEG **34** i) DIEA, PyBOP, $CHCl_3$, RT ii) TFA, CH_2Cl_2; RT ; iii) Trityl-S-$(CH_2)_{10}$-COOH, DIEA, PyBOP,$CHCl_3$, RT; iv) $Pd(PPh_3)_4$, $PhSiH_3$, degased CH_2Cl_2, RT ; v) H_2N-PEG-OMe, DIEA, PyBOP, $CHCl_3$, RT. The reaction molar yields are also provided under the reaction arrows.

The NMR spectrum of the coupling product Boc-$^{m}QQ_8$-$^{m}QQ_8$-Allyl displays 16 peaks in the downfield area associated to aromatic amide protons, *i.e.* no new aromatic amide proton appeared from the coupled amide. This means that the additional methylene bridge has a significant effect on the chemical shift of the directly attached amide proton. Besides, one of the amide proton peaks is significantly shifted to a lower value (9.55 ppm, Figure 5.11 C), indicating a change of chemical environment, probably in the nearest surrounding. Indeed in a homo-foldamer Q_{16}, all amide proton peaks are located between 11.2 and 10 ppm.[12] Nevertheless, an overall upfield shift can be unambiguously observed, as the oligomer doubles in length (Figure 5.11.C vs. D&E). This observation has been previously associated to an increase of the ring currents from the aromatic conjugation and intramolecular π-π stacking in the helical structure[9,10]. Eventually, these two observations suggest that the addition of the methylene bridge from the aminomethyl-quinoline in the middle of the foldamer perturbs the propagation of the aromaticity, but only to a certain extend. The cooperative stabilization stemming from the increase of the ring currents is not totally interrupted by the aliphatic junction.

Comparing the final product, Tr-S-R-$^{m}QQ_8$-$^{m}QQ_8$-PEG, with the spectrum of the chemically unperturbed tr-S-R-$^{m}QQ_{16}$-PEG, synthetized by Dr. Xuesong Li[12], confirms only a slight difference of the chemical shift of the amide protons (Figure 5.11. A vs. B).

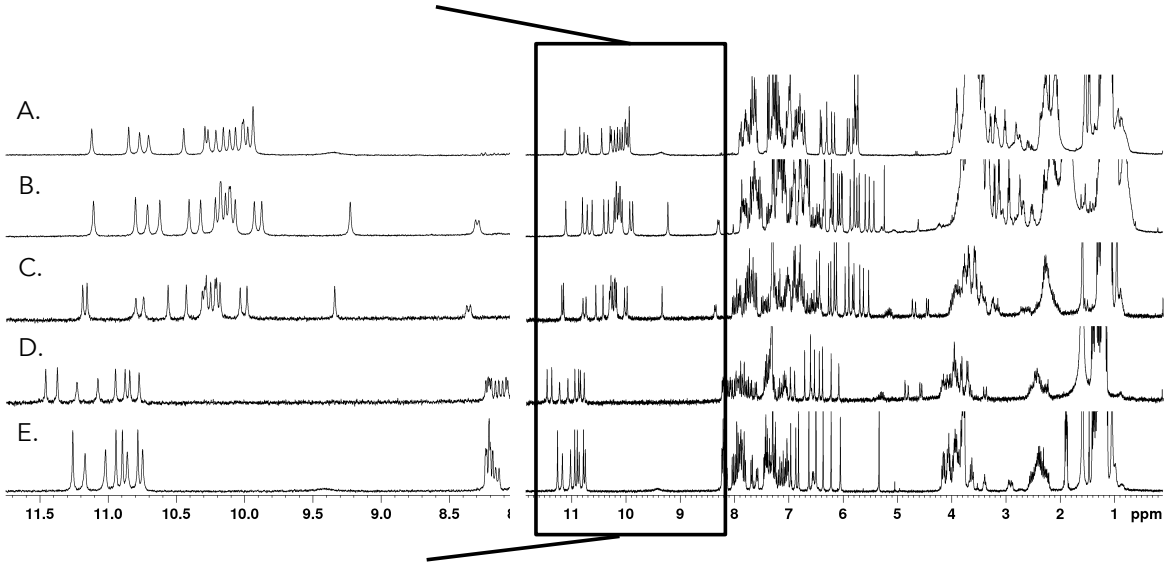

Figure 5.11 ^{1}H NMR in $CDCl_3$ of (A) Tr-S-R-$^{m}QQ_{16}$-PEG, synthetized by Dr. Xuesong Li for this thesis. (B) Tr-S-R-$^{m}QQ_8$-$^{m}QQ_8$-PEG **34**. (C) Boc-$^{m}QQ_8$-$^{m}QQ_8$-Allyl (D) NH_2-$^{m}QQ_8$-Allyl (E) Boc-$^{m}QQ_8$-COOH.

5.5 Conclusion

We successfully synthesized two sophisticate foldamers, a diblock and a triblock, through the doubling segment method, to further investigate the mechanochemical properties of foldamers possessing helical conformations.

Both are made of two quinoline-based blocks with an (amino)methyl at the *N*-terminus ($^{m}QQ_8$). For the triblock, a naphthyridine octamer was embedded in between the two quinoline blocks. For the triblock foldamer, the influence of the diameter of the helix will be investigated. For the diblock, nothing is inserted between the quinoline blocks and it was synthesised for two reasons. The insertion of a methylene bridge inside a fully aromatic sequence, which was a technical requirement for the previous synthesis, was unknown so far. Therefore, this diblock was synthesized to serve as a reference for the identification of the unfolding pattern of the naphthyridine helix. Then, it will also be used to specifically investigate the influence of a small aliphatic link inside a helical aromatic sequence.

Whereas the synthesis of the diblock was relatively easy, as it is constituted of optimized quinoline-oligomer synthesis, the synthesis of a long naphthyridine for the triblock, represented a challenge. Each step in the naphthyridine oligomer synthesis required special care and was relatively time consuming, as they required softer reaction conditions and long purification processes. The last coupling step between the two quinoline-naphthyridine 13-mer to form the triblock was also completely new. The coupling reaction, using PyBOP as coupling agent, took place quite rapidly with an acceptable yield for such coupling between long oligomers. The DMB-tertiary amide strategy has been demonstrated to be helpful to achieve a naphthyridine oligomer. Interestingly, the NMR spectra of the triblock, right after the DMB-deprotection, exhibited many peaks, which evidenced several conformations. Over time, a slight narrowing and a decrease in the peak numbers could be observed. This suggested that the triblock requires times to find the equilibrium folded conformation. Due to a lack of time, no further investigation (NMR, X-rays crystallography) could be conduct to characterize the structure.

The end-functionalizations of the foldamers with the trityl-protecting thiol and the PEG chain were successful for both foldamers.

5.6 Methods for NMR

NMR spectra were recorded on an Avance II NMR spectrometer (Bruker BioSpin) with a vertical 7,05T standard-bore/ultrashield magnet operating at 300 MHz for 1H observation. All chemical shifts are quoted in parts per million (ppm, d) relative to the 1H residual signal of the deuterated solvent used (CDCl3 at 7.26 ppm). 1H NMR splitting patterns with observed first-order coupling are designated as singlet (s), doublet (d), double doublet (dd), triplet (t), or quartet (q). Splitting patterns that could not be interpreted or easily visualized are designated as multiplet (m) or broad (br). Coupling constants (J) are reported in hertz. Samples were not degassed. Data processing was performed with Topspin 2.0 and Mestrenova software.

5.7 Methods of Chemical Synthesis

All reactions were carried out under a dry nitrogen atmosphere. Commercial reagents were purchased from Sigma-Aldrich, Alfa-Aesar or TCI and were used without further purification unless otherwise specified. Tetrahydrofurane (THF), dichloromethane (CH_2Cl_2) and toluene were dried over alumina columns; chloroform ($CHCl_3$), triethylamine (Et_3N) and diisopropylethylamine (DIEA) were distilled over calcium hydride (CaH_2) prior to use. Reactions were monitored by thin layer chromatography (TLC) on Merck silica gel 60-F254 plates and observed under UV light. Column chromatography purifications were carried out on Merck GEDURAN Si60 (40-63 µm). Gel permeation chromatography was performed at room temperature on an LC-9130G NEXT (Japan Analytical Industry Co., Ltd.) setup equipped with two preparative columns (Inner diameter of 20mm and length of 600mm): a JAIGEL 2.5H and a JAIGEL 3H. A mixture of chloroform (HPLC grade, ethanol stabilized) and trimethylamine (0.5% v/v) was used for the separations. The GPC collected fraction is directly washed with citric acid 5% and water, dried on Na_2S0_4 and solvents are evaporated. ESI mass spectra were obtained from the Mass Spectrometry Laboratory at the European Institute of Chemistry and Biology (UMS 3033 - IECB), Pessac, France.

5.8 Experimental procedures

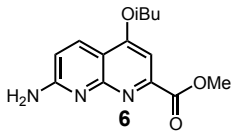

Monomer 6. Monomer **1**[1] (10 g, 31.5 mmol) is dissolved in MeOH (70 mL). On ice, with a dropping funnel solution of H_2SO_4 (2 mL) in 30 mL MeOH is added dropwise. 50 mL of MeOH were added rising funnel and flask. The reaction mixture was then heat up to 78°C and refluxed during 5h. The reaction mixture was neutralized by addition of saturated $NaHCO_3$ solution and was extracted with CH_2Cl_2 and washed with distilled water and then with brine. The organic phase was dried over Na_2SO_4 then evaporated to obtain a grey-brown solid (7.7 g ; 77%).

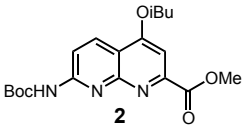

Monomer 2. Monomer 6 (5 g, 18.1 mmol) was dissolved in dioxane (30 mL) at 90°C under reflux. 7.9 g of Boc_2O were added to the solution and let stir overnight. The solvent is evaporated and the the reaction mixture was directly purified by flash chromatography (SiO_2) eluting with EtOAc:cyclohexane (10:90 vol/vol) , followed by a second flash chromatography with a gradient from 10 to 40 % of EtOAc with cyclohexane to obtain **2** (6.2 g, 91%).

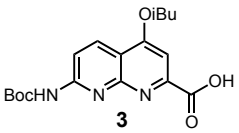

Monomer 3. Monomer **2** (6.2 g, 16.5mmol) is dissolved in dioxane (100 mL). A aqueous solution of NaOH (1.94 g in 25 mL H_2O) is progressively added in the reaction flask. The reaction is allowed to proceed during 45min, monitored by TLC. The reaction mixture is quenched with acetic acid. the solvents are evaporated and then the reaction mixture is washed with DCM and H_2O. The organic phase was dried over Na_2SO_4, filtered and evaporated and the compound **3** is obtained (5.96 g, 100%).

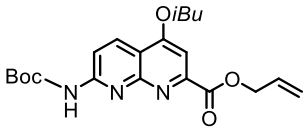

4

Monomer 4. Monomer **3**[1] (8.3 mmol, 3.0 g), PyBOP (16.6 mmol, 8.6 g) were dissolved in dry chloroform (18 mL). Then, allyl alcohol (24.9 mmol, 1.7 mL) was added followed by addition of DIEA (24.9 mmol, 4.3 mL) and was stirred at room temperature for 24 h. The organic phase was washed with 5% aqueous citric acid solution and with water, dried over Na_2SO_4, filtered and then concentrated. The residue was purified by flash chromatography (SiO_2) eluting with EtOAc:cyclohexane (30:70 vol/vol) to obtain **4** as a white solid (85 %, 2.835 g). ^{1}H NMR (300 MHz, $CDCl_3$) δ ppm = 8.52 (d, *J* = 9.1 Hz, 1H), 8.32 (d, *J* = 9.1 Hz, 1H), 7.54 (d, *J* = 13.2 Hz, 2H), 6.28 – 5.97 (m, 1H), 5.54 – 5.22 (m, 2H), 4.94 (m, 2H), 4.04 (d, *J* = 6.5 Hz, 2H), 2.28 (m, 1H), 1.56 (s, 9H), 1.13 (d, *J* = 6.7 Hz, 6H). ^{13}C NMR (75 MHz, $CDCl_3$) δ 165.5, 163.5, 155.6, 155.0, 152.2, 151.9, 133.8, 132.0, 119.3, 114.1, 114.0, 101.0, 82.0, 75.6, 67.0, 28.3, 28.2, 19.3 HRMS (ESI^+): *m/z* calcd for $C_{21}H_{27}N_3O_5[M+H]^+$: 402.2023 found 402.2037.

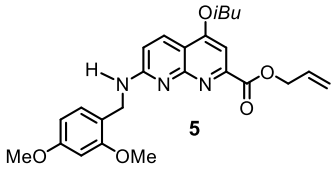

5

Monomer 5. Trifluoroacetic acid (4 mL) was added drop wise to a solution of monomer **4** (6.8 mmol, 2.7 g) in 12 mL of dry CH_2Cl_2 under nitrogen in an ice bath and was stirred for 3h at room temperature. The reaction mixture was neutralized by addition of saturated $NaHCO_3$ solution and was extracted with CH_2Cl_2 and washed with distilled water and then with brine. The organic phase was dried over Na_2SO_4 then the volatiles were removed under reduce pressure to give the amine derivative as off-white solid, which was used directly in subsequent reaction without further purification. The amine monomer (6.3 mmol, 1.9 g), 2,4-dimethoxybenzaldehyde (9.45 mmol, 1.57 g) and $NaBH(OAc)_3$ (12.6 mmol, 2.6 g), were suspended in 1,2-dichloroethane (6 mL), and then the reaction mixture was stirred at room temperature for 48 hours. The reaction mixture was dissolved in CH_2Cl_2, washed with saturated solution of $NaHCO_3$ and then water, dried over Na_2SO_4, filtered and then concentrated. The residue was purified by precipitation from minimum amount of CH_2Cl_2 with excess diethyl ether to obtain **5** as a yellow solid (91 %, 2.585 g). ^{1}H NMR (300 MHz, $CDCl_3$) δ ppm = 8.17 (d, *J* = 8.9 Hz, 1H), 7.38 (s, 1H), 7.30 (s, 1H), 6.65 (d, *J* = 9.0 Hz, 1H), 6.53 – 6.38 (m, 2H), 6.11 (m, 1H), 5.49 – 5.25 (m, 3H), 4.93 (m, *J* = 5.9, 1.4 Hz, 2H), 4.74 (d, *J* = 5.6 Hz, 2H), 3.98 (d, *J* = 6.5 Hz, 2H), 3.82 (d, *J* = 14.6 Hz, 6H), 2.22 (m, *J* = 13.6, 6.8 Hz, 1H), 1.09 (d, *J* = 6.7 Hz, 6H). ^{13}C NMR (75 MHz, $CDCl_3$) δ 166.1, 163.1, 160.5, 159.8, 158.8, 157.7, 150.9, 132.3, 131.6, 130.5, 119.3, 119.0, 110.9, 104.1, 99.8, 98.7, 75.1, 66.7, 55.5, 41.0, 28.3, 19.3 HRMS (ESI^+): *m/z* calcd for $C_{25}H_{29}N_3O_5$ $[M+H]^+$: 452.2180 found 452.2191.

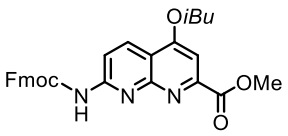

7

Monomer 7. Monomer **6**[20] (14.7 mmol, 4.04 g) and Fmoc-OSu (29.4 mmol, 9.9 g) were suspended in dioxane (70 mL) and the reaction mixture was heated at 75°C for 12h. Then, the solvents were removed under reduced pressure and the residue was purified by flash chromatography (SiO_2) eluting with ethyl acetate: cyclohexane (30:70 vol/vol) to obtain **7** as a white solid (90 %, 6.6 g). ^{1}H NMR (300 MHz, $CDCl_3$) δ ppm = 8.61 (d, *J* = 9.1 Hz, 1H), 8.33 (d, *J* = 9.0 Hz, 1H), 7.89 – 7.77 (m, 3H), 7.66 (d, *J* = 7.4 Hz, 2H), 7.58 (s, 1H), 7.52 – 7.32 (m, 4H), 4.57 (d, *J* = 7.2 Hz, 2H), 4.37 (t, *J* = 7.2 Hz, 1H), 4.09 (d, *J* = 7.9 Hz, 5H), 2.32 (dt, *J* = 13.3, 6.7 Hz, 1H), 1.17 (d, *J* = 6.7 Hz, 6H).

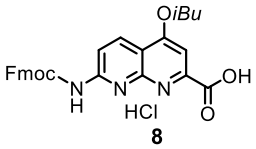

8

Monomer 8. Monomer **7** (10 mmol, 4.97 g) and LiI (15.0 mmol, 2.0 g) were dissolved in degassed EtOAc (50 mL) and the reaction mixture was heated at 78°C for 4h under an argon atmosphere. A yellow precipitate developed, which was filtered and washed with EtOAc then diethyl ether and dried in vacuum. Then, the precipitate was suspended in THF (40 mL) followed by addition of conc. HCl (4.2 mL) dropwise under stirring condition. The reaction mixture becomes clear reddish solution and after sonication for 10 minutes, precipitate developed immediately, which was filtered and washed with diethyl ether and dried in vacuum to obtain **8** as a yellow solid (88 %, 4.6 g). ^{1}H NMR (300 MHz, DMSO-d_6) δ ppm = 11.10 (s, 1H), 8.59 (d, *J* = 9.1 Hz, 1H), 8.17 (d, *J* = 9.2 Hz, 1H), 7.92 (d, *J* = 7.4 Hz, 2H), 7.86 (d, *J* = 7.4 Hz, 2H), 7.44 (t, *J* = 7.4 Hz, 2H), 7.36 (t, *J* = 7.4 Hz, 2H), 4.46 (d, *J* = 7.3 Hz, 2H), 4.35 (t, *J* = 7.3 Hz, 1H), 4.13 (d, *J* = 6.4 Hz, 2H), 2.23 – 2.14 (m, 1H), 1.08 (d, *J* = 6.7 Hz, 6H).

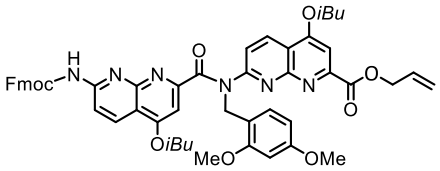

9

Dimer 9. Monomer **8** (2.7 mmol, 1.4 g) was suspended in dry $CHCl_3$ (25 mL). Then, oxalyl chloride (10.8 mmol, 0.92 mL) was added at 0 °C followed by addition of catalytic amount of dry DMF (2 drops) into the reaction mixture, then the reaction was stirred vigorously at room temperature for 2 hours. The volatiles were removed under high vacuum to give corresponding acid chloride as solid which was subsequently used for the next step without further purification. A solution containing **5** (2.5 mmol, 1.13 g) and DIEA (5.4 mmol, 0.94 mL) in dry $CHCl_3$ (15 mL) was transferred into the acid chloride flask at 0 °C under nitrogen atmosphere and stirred overnight at room temperature . The organic phase was washed with 5% aqueous citric acid solution and with water, dried over Na_2SO_4, filtered and then concentrated. The residue was purified by flash chromatography (SiO2) eluting with EtOAc:cyclohexane (30:70 vol/vol) to obtain **9** as a white solid (81 %, 1.850 g). ^{1}H NMR (300 MHz, $CDCl_3$) δ ppm = 8.45 (d, *J* = 8.3 Hz, 2H), 8.13 (d, *J* = 9.0 Hz, 1H), 7.79 – 7.66 (m, 4H), 7.59 (d, *J* = 7.4 Hz, 2H), 7.49 – 7.39 (m, 4H), 7.35 – 7.30 (m, 2H), 6.98 (s, 1H), 6.40 (dd, *J* = 8.4, 2.4 Hz, 1H), 6.25 (d, *J* = 2.4 Hz, 1H), 6.13 – 6.00 (m, 1H), 5.46 (s, 2H), 5.40 (dd, *J* = 17.3, 1.6 Hz, 2H), 5.29 (dd, *J* = 10.3, 1.4 Hz, 1H), 4.90 (d, *J* = 5.9 Hz, 2H), 4.49 (d, *J* = 7.1 Hz, 2H), 4.29 (t, *J* = 7.1 Hz, 1H), 4.00 (d, *J* = 6.5 Hz, 2H), 3.89 (d, *J* = 6.5 Hz, 2H), 3.75 (s, 3H), 3.43 (s, 3H), 2.28– 2.13 (m, 2H), 1.11– 1.05 (m, 12H). ^{13}C NMR (75 MHz, $CDCl_3$) δ ppm = 170.4, 165.3, 163.2, 162.8, 160.1, 158.9, 158.6, 158.0, 155.3, 154.6, 153.7, 152.8, 151.8, 143.4, 141.3, 134.1, 132.6, 131.9, 130.2, 127.9, 127.2, 125.0, 120.5, 120.1, 119.2, 118.1, 115.1, 113.1, 112.7, 104.2, 101.8, 101.1, 98.0, 75.5, 75.4, 67.6, 66.9, 55.3, 54.9, 46.8, 46.4, 28.1, 28.1, 27.0, 19.2, 19.2. HRMS (ESI^+): *m/z* calcd for $C_{53}H_{52}N_6O_9$ $[M+H]^+$: 917.3869 found 917.3896.

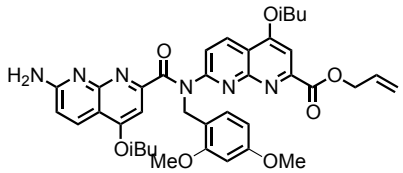

9b

Dimer 9b. Fmoc-deprotection of the dimer 9: Fmoc-protected oligomer **9** (1 g, 1 equiv.) dissolved in dry CH_2Cl_2 (7 mL, 0.1 M) was treated with 2,3,4,6,7,8,9,10-Octahydropyrimidol[1,2-*a*]azepine, DBU (462 µl, 3 equiv.) and was stirred at room temperature for 1h. The organic phase was washed with aqueous 5% citric acid solution, water, dried over Na_2SO_4 and filtered. The solvent was removed and the crude was suspended in minimum amount of diethyl ether, sonicated for 10 minutes and the

precipitate was filtered, washed with small amount of diethyl ether and dried under vacuum to give corresponding oligomer amine as a solid **9b**, which was used directly in subsequent reaction without further purification (yield: 80%). ^{1}H NMR (300 MHz, $CDCl_3$) δ ppm= 8.32 (d, *J* = 8.8 Hz, 1H), 8.11 (d, *J* = 8.9 Hz, 1H), 7.52 (d, *J* = 8.8 Hz, 1H), 7.45 (s, 1H), 7.41 (d, *J* = 8.3 Hz, 1H), 6.83 (s, 1H), 6.66 (d, *J* = 9.0 Hz, 1H), 6.36 (dd, *J* = 8.4, 2.4 Hz, 1H), 6.23 (d, *J* = 2.3 Hz, 1H), 6.18 – 5.99 (m, 1H), 5.51 – 5.35 (m, 3H), 5.33 – 5.26 (m, 1H), 4.91 (d, *J* = 6.0 Hz, 2H), 3.96 (d, *J* = 6.5 Hz, 2H), 3.81 (d, *J* = 6.5 Hz, 2H), 3.72 (s, 3H), 3.42 (s, 3H), 2.16 (s, 2H), 1.26 – 0.84 (m, 12H)

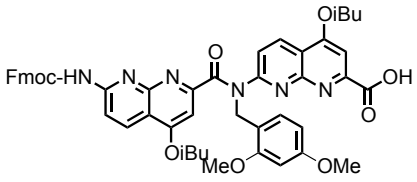

9a

Dimer 9a. Allyloxycarbonyl deprotection of the dimer 9: Alloc-protected oligomer **9** (1 g, 1 equiv.) dissolved in degassed CH_2Cl_2 (4.4 mL, 0.1M) was treated with $Pd(PPh_3)_4$ (118 mg, 0.1 equiv.) and $PhSiH_3$ (504 µl, 5 equiv.) under argon atmosphere and was stirred at room temperature for 1h in dark. The organic phase was washed with water, dried over Na_2SO_4 and filtered. The solvent was removed and the crude was suspended in diethyl ether, sonicated for 10 minutes and the precipitate was filtered, washed with diethyl ether and dried under vacuum to give corresponding oligomer acid as a solid **9a**, which was used directly in subsequent reaction without further purification..(yield: 85%) ^{1}H NMR (300 MHz, $CDCl_3$) δ ppm = 8.47 (d, *J* = 8.5 Hz, 2H), 8.14 (d, *J* = 8.9 Hz, 1H), 7.77 (d, *J* = 7.5 Hz, 4H), 7.58 (d, *J* = 5.5 Hz, 2H), 7.54 – 7.35 (m, 4H), 7.32 (d, *J* = 7.2 Hz, 2H), 7.17 (s, 1H), 6.43 (d, *J* = 8.3 Hz, 1H), 6.31 (s, 1H), 5.43 (s, 2H), 5.30 (s, 1H), 4.49 (d, *J* = 7.1 Hz, 2H), 4.28 (d, *J* = 6.7 Hz, 1H), 4.02 (dd, *J* = 14.5, 6.5 Hz, 4H), 3.78 (d, *J* = 14.9 Hz, 3H), 3.57 – 3.45 (m, 3H), 2.24 (s, 2H), 1.20 – 0.92 (m, 12H).

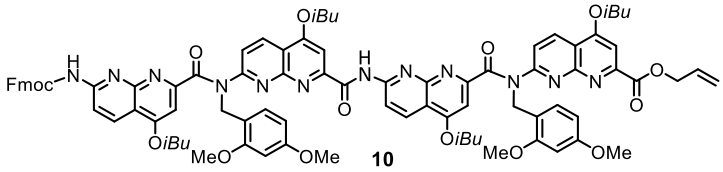

10

Tetramer 10. dimer acid 9a (250 mg, 1 equiv.), dimer amine 9b (177.3 mg, 1 equiv.) and PyBOP (300 mg, 3 equiv.) were dissolved in dry $CHCl_3$ (2.2 mL, 0.2 M) with DIEA (60 µl, 1.2 equiv.) and were stirred at room temperature for 12 h. Then, the reaction mixture was washed with 5% citric acid solution and with water. The solvents were

removed under reduced pressure and the crude was purified by GPC with 0.5 % NEt_3, 1 % EtOH in $CHCl_3$ as mobile phase. A brownish solid is obtained **10.** Yield: 355 mg (67 %). ^{1}H NMR (300 MHz, $CDCl_3$) δ ppm = 11.02 (s, 1H), 8.62 – 8.45 (m, 4H), 8.13 (d, *J* = 9.0 Hz, 1H), 7.83 – 7.73 (m, 4H), 7.69 (s, 2H), 7.59 (d, *J* = 7.4 Hz, 2H), 7.54 – 7.29 (m, 7H), 7.02 (s, 1H), 6.87 (s, 1H), 6.48 (dd, *J* = 8.4, 2.4 Hz, 1H), 6.41 (dd, *J* = 8.4, 2.4 Hz, 1H), 6.29 (d, *J* = 2.4 Hz, 1H), 6.22 (d, *J* = 2.4 Hz, 1H), 6.13– 6.00 (m, 1H), 5.49 (s, 4H), 5.43– 5.27 (m, 2H), 4.90 (d, *J* = 6.0 Hz, 2H), 4.49 (d, *J* = 7.1 Hz, 2H), 4.28 (t, *J* = 7.1 Hz, 1H), 4.06– 3.85 (m, 8H), 3.76– 3.74(m, 6H), 3.51 (s, 3H), 3.38 (s, 3H), 2.30 – 2.13 (m, 4H), 1.11– 1.04 (m, 24H). ^{13}C NMR (75 MHz, $CDCl_3$) δ ppm = 170.9, 170.4, 165.4, 164.0, 163.4, 163.0, 162.7, 160.2, 160.1, 159.1, 158.9, 158.7, 158.5, 158.1, 158.0, 155.4, 154.9, 154.7, 154.5, 153.7, 153.4, 152.9, 151.9, 143.5, 141.4, 134.3, 134.2, 132.9, 132.0, 130.3, 130.0, 129.8, 128.0, 127.3, 125.1, 120.6, 120.2, 119.3, 118.4, 118.1, 115.4, 115.2, 114.2, 113.7, 113.2, 112.7, 104.3, 104.2, 101.8, 101.1, 100.9, 99.3, 98.2, 98.0, 75.8, 75.6, 75.5, 75.4, 67.7, 67.0, 55.4, 55.4, 55.1, 54.9, 46.9, 46.2, 28.2, 28.1, 19.3, 19.3, 19.2. HRMS (ESI^+): *m/z* calcd for $C_{88}H_{88}N_{12}O_{15}$ $[M+H]^+$: 1553.6565 found 1553.6664.

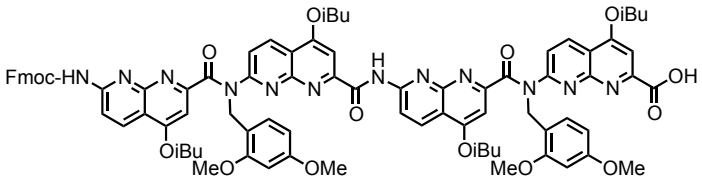

10a

Tetramer 10a. Allyloxycarbonyl deprotection of the tetramer 10: Allyl-protected oligomer **10** (280 mg, 1 equiv.) dissolved in degassed CH_2Cl_2 (2 mL, 0.1 M) was treated with $Pd(PPh_3)_4$ (20 mg, 0.1 equiv.) and $PhSiH_3$ (110 µl, 5 equiv.) under argon atmosphere and was stirred at room temperature for 1 h in dark. The organic phase was washed with water, dried over Na_2SO_4 and filtered. The solvent was removed and the crude was suspended in diethyl ether, sonicated for 10 minutes and the precipitate was filtered, washed with diethyl ether and dried under vacuum to give corresponding oligomer acid as a solid, which was used directly in subsequent reaction without further purification. (yield: 76 %)

^{1}H NMR (300 MHz, $CDCl_3$) δ ppm= 10.94 (s, 1H), 8.64 – 8.55 (m, 2H), 8.53 (d, *J* = 8.9 Hz, 1H), 8.46 (dd, *J* = 8.9, 2.1 Hz, 2H), 8.15 (d, *J* = 9.0 Hz, 1H), 7.78 (d, *J* = 7.4 Hz, 4H), 7.71 (d, *J* = 10.1 Hz, 2H), 7.60 (d, *J* = 9.2 Hz, 2H), 7.49 (dd, *J* = 8.4, 3.3 Hz, 2H), 7.45 – 7.37 (m, 2H), 7.33 (d, *J* = 7.4 Hz, 2H), 7.12 (s, 1H), 7.00 (s, 1H), 6.52 – 6.38 (m, 2H), 6.29 (d, *J* = 2.1 Hz, 2H), 5.48 (d, *J* = 12.6 Hz, 4H), 4.50 (d, *J* = 7.1 Hz, 2H), 4.29 (t, *J* = 7.0 Hz, 1H), 4.08 – 3.93 (m, 8H), 3.75 (d, *J* = 2.1 Hz, 6H), 3.49 (d, *J* = 3.3 Hz, 6H), 2.40 – 2.18 (m, 7H), 1.08 (ddd, *J* = 9.5, 6.5, 4.1 Hz, 24H).

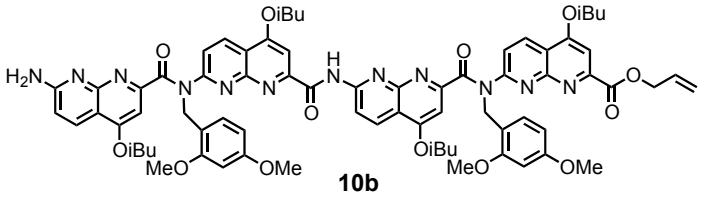

Tetramer 10b. Fmoc-deprotection of the tetramer 10: Fmoc-protected oligomer **10** (200 mg, 1 equiv.) dissolved in dry CH_2Cl_2 (800 µl, 0.1 M) was treated with 2,3,4,6,7,8,9,10-Octahydropyrimidol[1,2-*a*]azepine, DBU (54 µl, 3 equiv.) and was stirred at room temperature for 1h. The organic phase was washed with aqueous 5 % citric acid solution, water, dried over Na_2SO_4 and filtered. The solvent was removed and the crude was suspended in minimum amount of diethyl ether, sonicated for 10 minutes and the precipitate was filtered, washed with small amount of diethyl ether and dried under vacuum to give corresponding oligomer amine as a solid, which was used directly in subsequent reaction without further purification. (yield: 70 %). ^{1}H NMR (300 MHz, $CDCl_3$) δ ppm= 11.10 (s, 1H), 8.67 – 8.43 (m, 3H), 8.33 (d, *J* = 8.8 Hz, 1H), 7.85 (d, *J* = 8.8 Hz, 1H), 7.58 (s, 1H), 7.52 (dd, *J* = 8.4, 4.3 Hz, 2H), 7.37 (d, *J* = 8.9 Hz, 2H), 7.17 (s, 1H), 6.89 (s, 2H), 6.53 – 6.45 (m, 2H), 6.42 (dd, *J* = 8.4, 2.3 Hz, 1H), 6.36 (d, *J* = 2.2 Hz, 1H), 6.27 (d, *J* = 2.1 Hz, 1H), 6.07 (ddd, *J* = 16.4, 11.2, 6.0 Hz, 1H), 5.50 (s, 2H), 5.44 – 5.35 (m, 2H), 5.30 (t, *J* = 5.2 Hz, 1H), 4.85 (d, *J* = 6.0 Hz, 2H), 4.68 (s, 1H), 3.97 (dd, *J* = 11.5, 6.5 Hz, 4H), 3.73 (d, *J* = 9.2 Hz, 7H), 3.61 (s, 3H), 3.48 (d, *J* = 7.0 Hz, 6H), 2.34 – 1.88 (m, 4H), 1.24 – 0.85 (m, 24H).

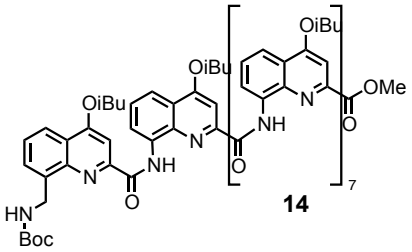

Nonamer 14. Boc^{m}Q monomer **13a**[10] (201 mg, 0.54 mmol, 1,7 equiv.) was suspended in anhydrous $CHCl_3$ (9 mL), then Ghosez's reagent (150 µl, 2 equiv.) was added and the reaction was allowed to stir at room temperature for 2 hours. The solvent and excess reagents were removed under vacuum and the residue was dried under vacuum for at least 4 hours to yield the corresponding acid chloride as a pink solid **13b**. To a solution of compound **12** (610 mg, 0.32 mmol, 1equiv.) and distilled DIEA (166 µl, 3 equiv.), freshly prepared solution of **13b** with anhydrous $CHCl_3$ was quantitatively transferred via a syringe. The reaction was allowed to proceed at room temperature overnight. Solvent was evaporated until precipitation. The crude product was purified by precipitation from a minimum amount of MeOH in highly concentrated DCM solution to obtain **14** as a light-

yellow solid which was collected by filtration (642 mg, 90 %). ^{1}H NMR (300 MHz, $CDCl_3$) δ in ppm 11.44 (s, 1H), 11.30 (s, 1H), 11.14 (s, 1H), 10.98 (s, 1H), 10.91 (s, 1H), 10.84 (s, 1H), 10.79 (s, 1H), 10.68 (d, *J* = 13.1 Hz, 1H), 8.17 (d, *J* = 7.7 Hz, 2H), 8.10 (d, *J* = 7.6 Hz, 1H), 8.02 (t, *J* = 8.1 Hz, 2H), 7.97 – 7.84 (m, 4H), 7.83 (d, *J* = 8.5 Hz, 1H), 7.77 (d, *J* = 8.3 Hz, 2H), 7.71 (d, *J* = 7.3 Hz, 1H), 7.65 (d, *J* = 6.6 Hz, 1H), 7.56 (d, *J* = 7.7 Hz, 1H), 7.45 – 7.29 (m, 5H), 7.22 (t, *J* = 7.9 Hz, 2H), 7.13 (t, *J* = 8.0 Hz, 1H), 7.09 – 6.95 (m, 3H), 6.93 (s, 1H), 6.84 (s, 1H), 6.66 (s, 1H), 6.51 (d, *J* = 11.7 Hz, 3H), 6.40 (s, 1H), 6.35 (s, 1H), 6.17 (s, 1H), 6.01 (s, 1H), 4.20 – 3.53 (m, 18H), 3.36 (s, 1H), 2.99 (s, 3H), 2.89 (s, 1H), 2.66 – 2.06 (m, 9H), 1.55 (s, 9H), 1.41 – 1.00 (m, 54H).

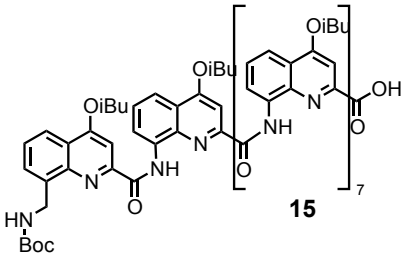

15

Nonamer 15. Nonamer **14** (800 mg, 0.35 mmol, 1 equiv.) is solubilized in THF (7.2 mL). Under a strong stirring, a solution of NaOH (30 mg, 20 equiv.) in MeOH (0.8 mL) is added. The reaction is monitor by TLC until no starting material is detected (1h). The solution mixture is then acidified to pH 6 with HCl 1 M. The solvents are evaporated until precipitation. The precipitate is dissolved in CH_2Cl_2 and washed with H_2O and brine, dried over Na_2SO_4 and filtered. The light-yellow compound **15** (720 mg, 91 %) was obtained after a filtration. ^{1}H NMR (300 MHz, DMSO) δ in ppm 11.22 (s, 1H), 11.13 (s, 1H), 10.98 (s, 1H), 10.91 (s, 1H), 10.86 (s, 1H), 10.82 (s, 1H), 10.75 (s, 1H), 10.71 (s, 1H), 8.26 – 8.06 (m, 4H), 7.88 (tdd, *J* = 24.9, 18.0, 7.1 Hz, 8H), 7.72 – 7.46 (m, 3H), 7.46 – 7.28 (m, 5H), 7.25 – 6.96 (m, 6H), 6.93 (s, 1H), 6.83 (s, 1H), 6.78 (s, 1H), 6.59 (s, 1H), 6.52 (d, *J* = 6.1 Hz, 1H), 6.46 (s, 2H), 6.33 (s, 1H), 6.18 (s, 1H), 6.01 (s, 1H), 4.13 – 3.71 (m, 18H), 3.35 (s, 1H), 2.89 (d, *J* = 15.8 Hz, 1H), 2.58 – 2.13 (m, 9H), 1.55 (s, 9H), 1.46 – 0.97 (m, 54H).

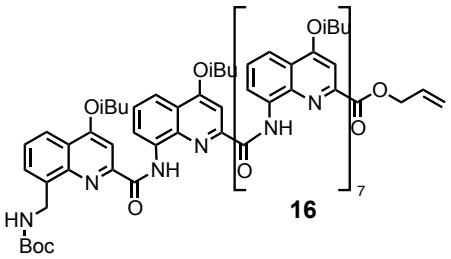

16

Nonamer 16. Nonamer **15** (500 mg, 0.21 mmol, 1 equiv.) and PyBOP (226 mg, 2 equiv.) were dissolved in dry chloroform (725 µL, 0.3 M). Then, allyl alcohol (30 µL, 2 equiv.) was added followed by addition of DIEA (114 µL, 3 equiv.) and was stirred at room temperature for 24 h. The reaction mixture was washed by citric acid, H_2O and then purified by chromatography (SiO_2) eluting with EtOAc/cyclohexane (25:75 vol/vol) to obtain **16** after evaporation (385 mg, 70 %). FTMS + p ESI Full MS: *m/z* calcd for $C_{135}H_{142}N_{18}O_{21}$ $[M+2H]^+$: (2352.06) 1177.03 found 1176.75. ^{1}H NMR (300 MHz, $CDCl_3$) d ppm 11.40 (s, 1H), 11.31 (s, 1H), 11.13 (s, 1H), 10.98 (s, 1H), 10.89 (s, 1H), 10.82 (s, 1H), 10.79 (s, 1H), 10.70 (s, 1H), 8.23 – 8.07 (m, 3H), 8.02 (dd, *J* = 12.3, 6.9 Hz, 2H), 7.97 – 7.82 (m, 4H), 7.85 – 7.73 (m, 3H), 7.70 (dd, *J* = 8.3, 1.1 Hz, 1H), 7.64 (d, *J* = 6.6 Hz, 1H), 7.55 (d, *J* = 7.5 Hz, 1H), 7.34 (dt, *J* = 21.9, 7.9 Hz, 5H), 7.22 (d, *J* = 4.0 Hz, 2H), 7.17 – 6.94 (m, 4H), 6.93 (s, 1H), 6.84 (s, 1H), 6.65 (s, 1H), 6.58 – 6.41 (m, 3H), 6.38 (s, 1H), 6.32 (s, 1H), 6.17 (s, 1H), 6.01 (s, 1H), 5.38 – 5.15 (m, 1H), 4.78 (dd, *J* = 17.2, 1.5 Hz, 1H), 4.52 (dd, *J* = 10.4, 1.3 Hz, 1H), 4.17 – 3.52 (m, 20H), 3.35 (s, 1H), 2.88 (dd, *J* = 15.5, 6.5 Hz, 1H), 2.61 – 2.07 (m, 9H), 1.58 (s, 9H), 1.43 – 1.00 (m, 54H).

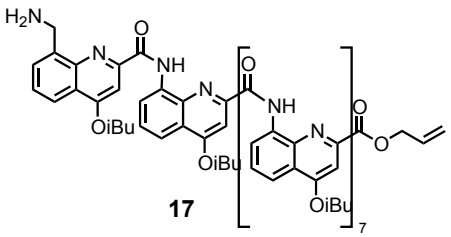

17

Nonamer 17. Trifluoroacetic acid (20 µL, excess) was added drop wise to a solution of nonamer **16** (72 mg, 0.03 mmol) in 150 µL of dry CH_2Cl_2 under nitrogen and was stirred for 2 h at room temperature. The reaction mixture was neutralized by addition of saturated $NaHCO_3$ solution and was extracted with CH_2Cl_2 and washed with H_2O. The organic phase was dried over Na_2SO_4 then the filtrate's solvents were removed under reduce pressure to give compound **17** (59 mg, 85 %). ^{1}H NMR (300 MHz, $CDCl_3$) d ppm = 11.44 (s, 1H), 11.35 (s, 1H), 11.21 (s, 1H), 11.05 (s, 1H), 10.93 (s, 1H), 10.86 (s, 1H), 10.82 (s, 1H), 10.75 (s, 1H), 8.25 – 7.56 (m, 15H), 7.47 – 7.32 (m, 5H), 7.29 – 7.20 (m, 2H), 7.15 (s, 1H), 7.08 (dd, *J* = 15.3, 7.7 Hz, 3H), 6.96 (s, 1H), 6.88 (s, 1H), 6.69 (s, 1H), 6.58 (s, 2H),

6.51 (s, 1H), 6.42 (s, 1H), 6.36 (s, 1H), 6.21 (s, 1H), 6.06 (s, 1H), 5.33 – 5.20 (m, 1H), 4.82 (d, *J* = 17.1 Hz, 2H), 4.55 (d, *J* = 10.3 Hz, 2H), 4.25 – 3.52 (m, 18H), 3.37 (d, *J* = 15.2 Hz, 2H), 2.42 (d, *J* = 7.5 Hz, 9H), 1.56 – 1.08 (m, 54H).

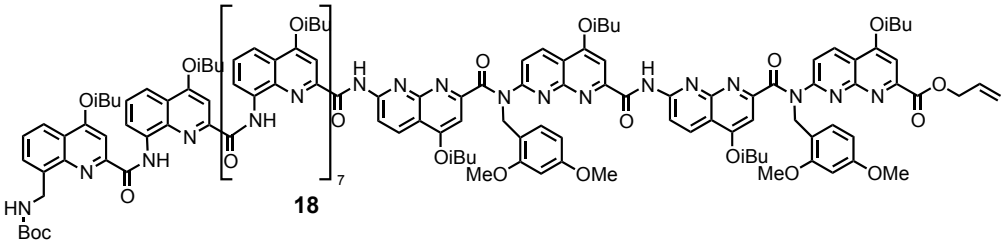

18

13-mer (Boc-^{m}QQ$_8$- (N(DMB)N)$_2$ -Allyl) 18. quinoline-based oligomer acid **15** (200 mg, 0.087 mmol, 1 equiv.), naphthyridine oligomer amine **10b** (104 mg, 0.087 mmol, 1 equiv.), DIEA (20 µL, 1.5 equiv.) and PyBOP (120 mg, 2 equiv.) in dry $CHCl_3$ (1000 µL) were stirred at room temperature for 12 h. Then, the reaction mixture was washed with 5% citric acid solution and with water. The solvents were removed under reduced pressure and the crude was purified by GPC with 0.5 % NEt_3, 1 % EtOH in $CHCl_3$ as mobile phase**.** The collected fraction is washed with citric acid 5 % and water, dried on Na_2S0_4 and solvents are evaporated to obtained **18** (160 mg, 68 %). ^{1}H NMR (300 MHz, $CDCl_3$) δ in ppm: 11.24 (s, 1H), 11.13 (s, 1H), 11.08 (s, 1H), 10.95 (s, 1H), 10.93 (s, 1H), 10.85 (s, 1H), 10.83 (s, 1H), 10.79 (s, 1H), 10.68 (s, 1H), 9.54 (s, 1H), 8.51 (dd, *J* = 18.6, 9.0 Hz, 2H), 8.39 (d, *J* = 8.9 Hz, 1H), 8.21 (d, *J* = 8.8 Hz, 1H), 8.13 – 7.93 (m, 5H), 7.94 – 7.64 (m, 9H), 7.64 – 7.48 (m, 4H), 7.48 – 7.26 (m, 7H), 7.26 – 7.17 (m, 3H), 7.10 (dd, *J* = 15.1, 7.0 Hz, 3H), 6.99 (dd, *J* = 15.6, 8.6 Hz, 2H), 6.86 (dd, *J* = 22.8, 8.3 Hz, 3H), 6.63 (s, 1H), 6.57 – 6.45 (m, 2H), 6.45 – 6.29 (m, 4H), 6.25 (d, *J* = 8.4 Hz, 2H), 6.15 (s, 2H), 6.12 – 5.90 (m, 3H), 5.40 (d, *J* = 3.1 Hz, 2H), 5.26 (d, *J* = 10.3 Hz, 1H), 5.17 – 4.89 (m, 2H), 4.87 (d, *J* = 6.0 Hz, 2H), 4.15 – 3.69 (m, 26H), 3.63 – 3.48 (m, 3H), 3.31 (s, 4H), 3.07 (s, 3H), 2.87 (s, 2H), 2.27 (dddd, *J* = 25.3, 21.2, 14.6, 7.3 Hz, 17H), 1.54 – 0.66 (m, 87H).

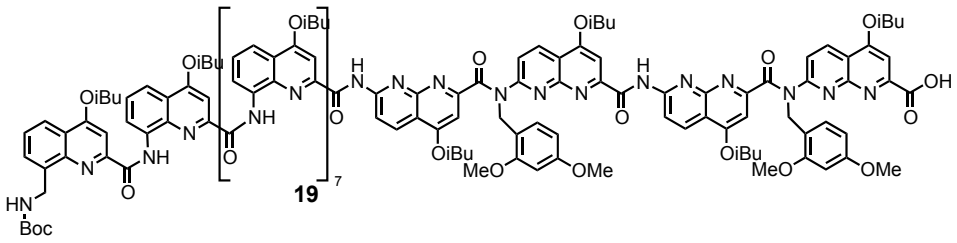

19

13-mer (Boc-^{m}QQ$_8$- (N(DMB)N)$_2$ -COOH) 19. Allyl-protected oligomer **18** (177 mg, 0.05 mmol, 1 equiv.) dissolved in degassed CH_2Cl_2 (1 mL) was treated with $Pd(PPh_3)_4$

(5.6 mg, 0.1 equiv.) and $PhSiH_3$ (30 µL, 5 equiv.) under argon atmosphere and was stirred at room temperature for 1h in dark. The reactive mixture was diluted with CH_2Cl_2 and washed with water. The organic phase was then dried over Na_2SO_4. The solvent was removed and the crude was purified by GPC with 0.5 % NEt_3, 1 % EtOH in $CHCl_3$ as mobile phase. The collected fraction is washed with citric acid 5% and water, dried on Na_2SO_4 and solvents are evaporated to obtained 19 (125 mg, 71%) ^{1}H NMR (300 MHz, $CDCl_3$) δ ppm: 11.27 (s, 1H), 11.17 (s, 1H), 11.11 (s, 1H), 10.99 (s, 1H), 10.88 (d, *J* = 7.9 Hz, 2H), 10.83 (s, 1H), 10.72 (s, 1H), 9.58 (s, 1H), 8.57 (q, *J* = 9.2 Hz, 2H), 8.46 (d, *J* = 8.9 Hz, 1H), 8.25 (d, *J* = 8.9 Hz, 2H), 8.21 – 7.98 (m, 6H), 7.98 – 7.69 (m, 9H), 7.58 (dd, *J* = 15.7, 8.0 Hz, 5H), 7.39 (ddd, *J* = 14.0, 10.9, 5.3 Hz, 7H), 7.28 – 7.20 (m, 3H), 7.20 – 7.06 (m, 4H), 7.06 – 6.97 (m, 1H), 6.90 (d, *J* = 14.6 Hz, 2H), 6.66 (s, 1H), 6.61 – 6.49 (m, 2H), 6.46 – 6.33 (m, 3H), 6.28 (dd, *J* = 11.1, 4.0 Hz, 3H), 6.19 (s, 1H), 6.06 (d, *J* = 11.4 Hz, 2H), 5.37 (d, *J* = 22.6 Hz, 2H), 5.05 (dd, *J* = 50.4, 16.3 Hz, 2H), 4.28 – 3.74 (m, 26H), 3.57 (dd, *J* = 24.9, 16.5 Hz, 4H), 3.44 (s, 2H), 3.33 (d, *J* = 20.2 Hz, 1H), 3.03 (d, *J* = 26.0 Hz, 3H), 2.91 (dd, *J* = 23.7, 16.9 Hz, 2H), 2.60 – 2.01 (m, 17H), 1.80 – 0.43 (m, 87H).

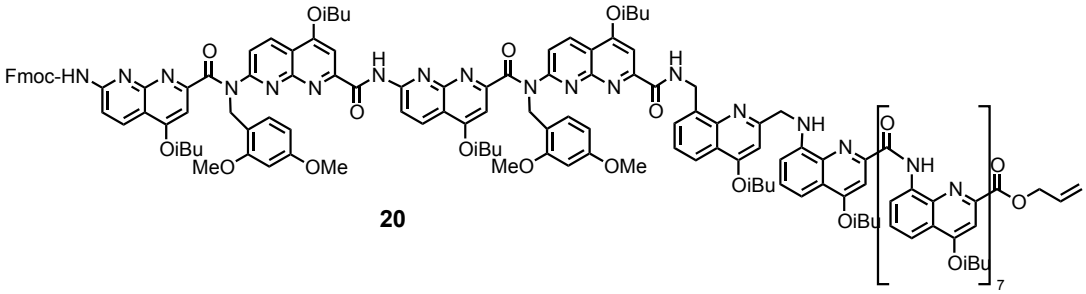

20

13-mer (Fmoc-(N(DMB)N)$_2$ -^{m}QQ$_8$-Allyl) 20. quinoline-based oligomer amine **17** (145 mg, 0.063 mmol, 1 equiv.), naphthyridine oligomer acid **10a** (106 mg, 0.069 …, 1 equiv.), DIEA (18 µL, 1.2 equiv.) and PyBOP (72 mg, 2 equiv.) in dry $CHCl_3$ (1000 µL) were stirred at room temperature for 12 h. Then, the reaction mixture was washed with 5 % citric acid solution and with water. The solvents were removed under reduced pressure and the crude was purified by flash chromatography (SiO2) eluting with EtOAc/cyclohexane (35:65 vol/vol)followed by GPC purification to obtain **20** as white solid (160 mg, 65%). ^{1}H NMR (300 MHz, $CDCl_3$) δ in ppm: 11.40 (s, 1H), 11.32 (s, 1H), 11.23 (s, 1H), 11.12 (s, 1H), 10.89 (d, *J* = 4.8 Hz, 2H), 10.84 (s, 1H), 10.81 (s, 1H), 10.71 (s, 1H), 8.50 – 8.35 (m, 3H), 8.27 (d, *J* = 9.1 Hz, 1H), 8.09 (ddd, *J* = 26.5, 12.0, 6.7 Hz, 7H), 7.98 – 7.86 (m, 4H), 7.85 – 7.67 (m, 7H), 7.68 – 7.52 (m, 5H), 7.46 (d, *J* = 8.4 Hz, 1H), 7.43 – 7.27 (m, 10H), 7.25 – 6.92 (m, 8H), 6.89 (t, *J* = 5.7 Hz, 2H), 6.77 (d, *J* = 6.0 Hz, 1H), 6.66 (s, 1H), 6.55 (s, 1H), 6.49 (d, *J* = 1.7 Hz, 2H), 6.46 – 6.36 (m, 2H), 6.33 (s,

1H), 6.28 – 6.11 (m, 3H), 6.01 (s, 2H), 5.43 (s, 2H), 5.29 – 5.14 (m, 1H), 5.11 (s, 2H), 4.85 – 4.51 (m, 2H), 4.53 – 4.42 (m, 2H), 4.35 – 3.24 (m, 29H), 3.70 (s, 3H), 3.58 (d, *J* = 6.6 Hz, 3H), 3.50 – 3.44 (m, 3H), 3.09 (s, 3H), 2.78 – 2.19 (m, 11H), 2.14 – 2.06 (m, 1H), 2.01 – 1.92 (m, 1H), 1.78 (d, *J* = 6.5 Hz, 2H), 1.34 – 0.68 (m, 78H).

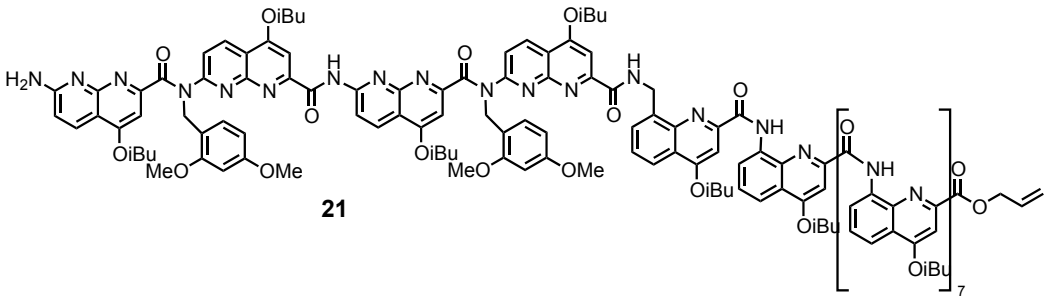

21

13-mer (H_2N-(N(DMB)N)$_2$ -^{m}QQ$_8$-Allyl) 21. Fmoc-protected oligomer **20** (138 mg, 0.04 mmol, 1 equiv.) dissolved in dry CH_2Cl_2 (250 µL) was treated with 2,3,4,6,7,8,9,10-Octahydropyrimidol[1,2-*a*]azepine, DBU (16.5 µL, 3 equiv.) and was stirred at room temperature for 1h. The organic phase was washed with aqueous 5 % citric acid solution, water, dried over Na_2SO_4 and filtered. The solvents were removed under reduced pressure and the crude was purified by GPC with 0.5 % NEt_3, 1 % EtOH in $CHCl_3$ as mobile phase to obtained 21 (120 mg, 92%). ^{1}H NMR (300 MHz, $CDCl_3$) δ in ppm: 11.39 (s, 1H), 11.31 (s, 1H), 11.20 (s, 1H), 11.09 (s, 1H), 10.97 – 10.73 (m, 4H), 10.68 (s, 1H), 8.34 (d, *J* = 8.9 Hz, 1H), 8.29 – 8.08 (m, 6H), 7.95 (ddd, *J* = 18.2, 14.7, 6.8 Hz, 7H), 7.84 – 7.52 (m, 7H), 7.38 (ddd, *J* = 19.6, 15.4, 8.8 Hz, 9H), 7.25 – 6.95 (m, 9H), 6.87 (d, *J* = 21.2 Hz, 4H), 6.65 (s, 1H), 6.54 (s, 1H), 6.49 – 6.36 (m, 4H), 6.32 (s, 1H), 6.18 (d, *J* = 6.5 Hz, 3H), 6.09 (s, 1H), 6.01 (s, 1H), 5.24 (ddd, *J* = 16.1, 9.4, 4.2 Hz, 2H), 5.09 (s, 1H), 4.77 (d, *J* = 17.2 Hz, 1H), 4.51 (d, *J* = 10.4 Hz, 1H), 4.31 – 3.03 (m, 42H), 2.30 (dddd, *J* = 71.0, 64.3, 31.9, 25.5 Hz, 13H), 1.94 (s, 2H), 1.38 – 0.80 (m, 78H).

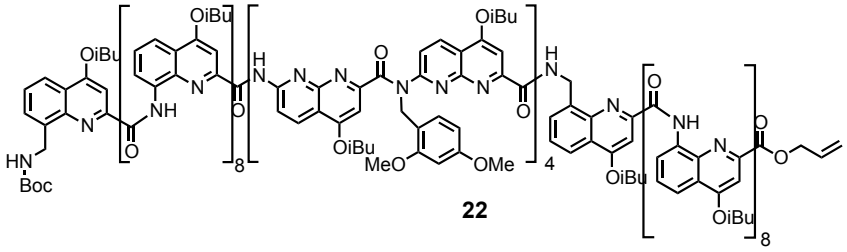

22

26-mer oligomer Boc-^{m}QQ$_8$-(N(DMB)N)$_4$-^{m}QQ$_8$-Allyl 22. 13-mer amine **21** (120 mg, 1 equiv.), 13-mer acid **19** (124 mg, 1 equiv.) and PyBOP (3 equiv.) in dry $CHCl_3$ (500 µL) was treated with DIEA (2 equiv.) and was stirred at room temperature for 12 h. Then, the reaction mixture was washed with 5% citric acid solution and with water. The solvents were removed under reduced pressure and the crude was purified by GPC with 0.5 % NEt_3, 1 % EtOH in $CHCl_3$ as mobile phase. The collected fraction is washed with citric acid 5% and water, dried on Na_2S0_4 and solvents are evaporated to obtained **22**. HRMS (ESI^+): *m/z* calcd for $C_{402}H_{414}N_{60}O_{63}$ $[M+4H]^{+4}$: 1774.28483 found 1774.29763; $[M+3H]^{+3}$: 2365.37977 found 2365.38939; $[M+2H]^{+2}$: 3547.56966 found 3547.58529. ^1H NMR (300 MHz, $CDCl_3$) δ 11.40 (s, 1H), 11.32 (s, 1H), 11.23 (s, 2H), 11.13 (s, 2H), 11.08 (s, 1H), 11.03 – 10.87 (m, 5H), 10.82 (dd, *J* = 9.8, 6.3 Hz, 5H), 10.72 (s, 1H), 10.68 (s, 1H), 9.53 (s, 1H), 8.61 – 8.35 (m, 6H), 8.31 – 7.68 (m, 33H), 7.56 (ddd, *J* = 24.4, 15.9, 9.4 Hz, 11H), 7.43 – 7.27 (m, 13H), 7.25 – 6.94 (m, 14H), 6.92 – 6.73 (m, 7H), 6.64 (d, *J* = 10.0 Hz, 2H), 6.59 – 6.30 (m, 11H), 6.26 (d, *J* = 5.6 Hz, 2H), 6.23 – 6.11 (m, 5H), 6.01 (t, *J* = 6.8 Hz, 4H), 5.40 (s, 4H), 5.29 – 5.17 (m, 1H), 5.17 – 4.83 (m, 3H), 4.83 – 4.46 (m, 1H), 4.20 (d, *J* = 8.5 Hz, 2H), 4.12 – 2.98 (m, 82H), 2.82 (s, 1H), 2.66 (s, 1H), 2.57 – 2.01 (m, 26H), 1.98 (d, *J* = 6.5 Hz, 1H), 1.77 (s, 1H), 1.35 – 0.93 (m, 165H), 0.82 – 0.53 (m, 9H).

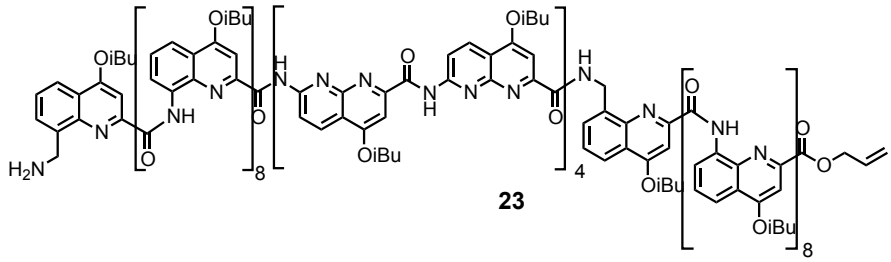

23

26-mer oligomer (H_2N-^{m}QQ$_8$-N$_8$ -^{m}QQ$_8$-Allyl 23. Boc and DMB protected 26-mer **22** is dissolved in 500 µL of CH_2Cl_2 and 500 µL of TFA are added dropwise and the reaction is allowed to proceed during 1h30. The reaction mixture was quenched by addition of saturated $NaHCO_3$ solution and was extracted with CH_2Cl_2 and washed with distilled water. The organic phase was dried over Na_2SO_4. The product is dry under reduced pressure and purified by EtOAc precipitation. (NMR quite broad) HRMS (ESI^+): *m/z*

calcd for $C_{361}H_{366}N_{60}O_{53}$ $[M+4H]^{+4}$: 1599.20361 found 1599.21976; $[M+3H]^{+3}$: 2131.93815 found 2131.95560; $[M+2H]^{+2}$: 3197.40722 found 3197.42530. ^{1}H NMR (300 MHz, $CDCl_3$) δ in ppm: 11.06 (d, *J* = 17.8 Hz, 2H), 10.90 – 10.64 (m, 4H), 10.49 (d, *J* = 10.1 Hz, 2H), 10.45 – 9.90 (m, 8H), 9.80 (s, 1H), 9.63 (s, 2H), 9.55 (d, *J* = 5.6 Hz, 2H), 9.28 (s, 1H), 8.92 (s, 2H), 8.82 – 7.26 (m, 42H), 7.25 – 5.31 (m, 53H), 5.15 (s, 1H), 5.12 – 5.01 (m, 1H), 4.73 – 4.55 (m, 2H), 4.54 – 4.39 (m, 2H), 4.18 – 4.10 (m, 4H), 4.08 – 2.83 (m, 52H), 2.34 – 1.96 (m, 26H), 1.51 – 0.84 (m, 156H).

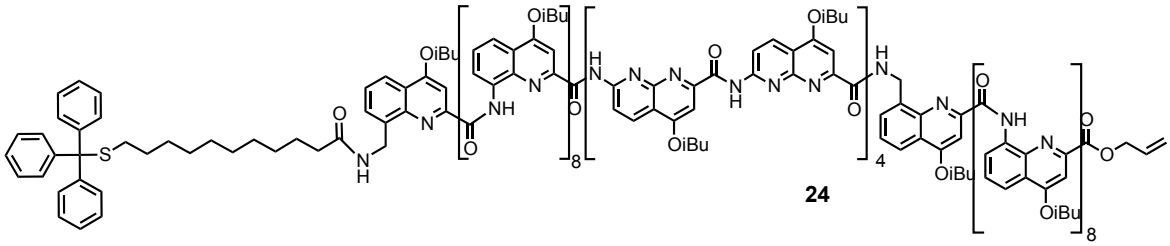

26-mer oligomer Trityl-(CH2)$_{10}$-^{m}QQ$_8$-N$_8$-^{m}QQ$_8$-Allyl 24. dried 26-mer amine 23(84 mg, 13 µmol) are mixed with trityl-S-$(CH_2)_{10}$-COOH (12 mg, 2 equiv.), PyBOP (14 mg, 2 equiv.) and are treated with DIEA (10 µL, 4 equiv.) in $CHCl_3$ (300 µL) overnight at room temperature. The reaction mixture was washed with citric acid 5% and H_2O. The crude was directly purified by recycling GPC (not pure). HRMS (ESI^+): *m/z* calcd for $C_{361}H_{366}N_{60}O_{53}$ $[M+4H]^{+4}$: 1709.763786 found 1709.77155; $[M+3H]^{+3}$2279.349105 found 2279.35839; ^{1}H NMR (300 MHz, $CDCl_3$) δ in ppm: broad peaks

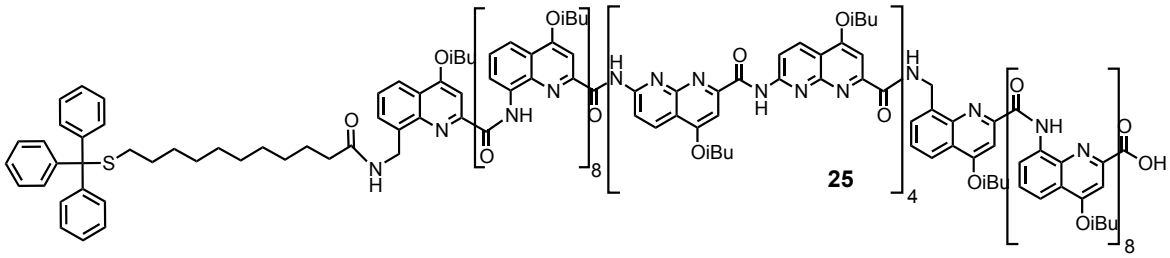

26-mer oligomer Trityl-S-(CH2)$_{10}$-^{m}QQ$_8$-N$_8$-^{m}QQ$_8$-COOH 25. Alloc-protected 26-mer **24** (40 mg, 6 µmol, 1 equiv.) dissolved in degassed CH_2Cl_2 (0.5 mL) was treated with $Pd(PPh_3)_4$ (0.14 mg, 0.12 µmol, 0.02 equiv.) and $PhSiH_3$ (2 µl, 3 equiv.) under argon atmosphere and was stirred at room temperature for 4h in dark. The organic phase was washed with water, dried over Na_2SO_4 and filtered. The solvent was removed and the

crude was purify by GPC and dried under vacuum to give corresponding oligomer acid as a solid **25** (15 mg, yield 40 %). ^{1}H NMR (300 MHz, $CDCl_3$) δ in ppm: 11.18 (s, 2H), 10.96 – 10.48 (m, 6H), 10.43 – 10.06 (m, 8H), 9.97 (s, 1H), 9.58 (s, 1H), 9.28 (d, *J* = 14.6 Hz, 2H), 9.05 (dd, *J* = 41.0, 22.2 Hz, 4H), 8.66 – 8.53 (m, 2H), 8.49 – 8.33 (m, 4H), 8.32 – 8.20 (m, 2H), 8.21 – 8.07 (m, 3H), 8.05 – 7.93 (m, 2H), 7.85 (dd, *J* = 9.5, 4.0 Hz, 3H), 7.79 – 7.21 (m, 37H), 7.17 – 6.65 (m, 32H), 6.65 – 6.08 (m, 14H), 5.75 (dddd, *J* = 52.6, 38.2, 26.9, 10.7 Hz, 12H), 4.36 – 3.17 (m, 52H), 2.79 (dd, *J* = 38.0, 14.2 Hz, 4H), 2.43 – 1.87 (m, 26H), 1.20 (d, *J* = 9.1 Hz, 24H), 1.04 – 0.90 (m, 156H).

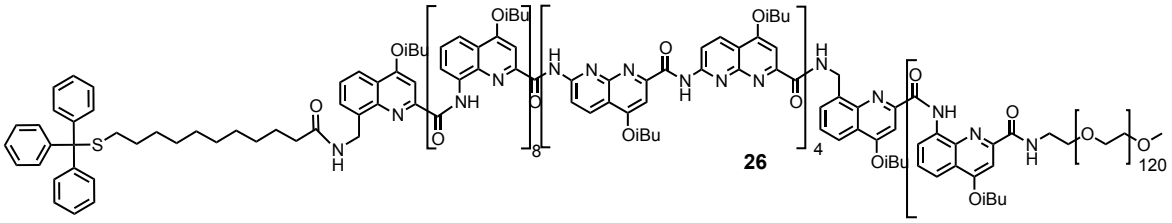

26

26-mer oligomer Trityl-S-$(CH_2)_{10}$-^{m}QQ$_8$-N$_8$-^{m}QQ$_8$-PEG 26. 26-mer acid (11.8 mg, 1.74 µmol, 1 equiv.) is dissolved with H_2N-PEG_{5000}-OMe (18 mg, 3.47 µmol, 2 equiv.), PyBOP (2.3 mg, 2.5 equiv.) in $CHCl_3$ (500 µL) and DIEA (1 drop) and allowed to react overnight at room temperature under argon atmosphere. The crude was washed with citric acid and water, dried over Na_2SO_4 and directly purified by recycling GPC. ^{1}H NMR (300 MHz, $CDCl_3$) δ in ppm: broad peaks

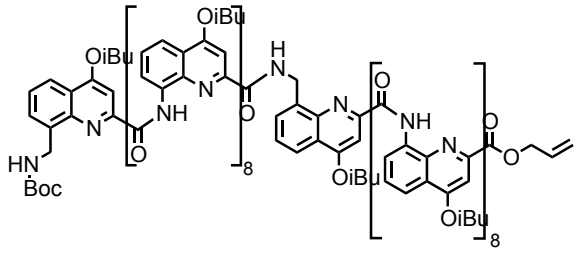

30

18-mer oligomer Boc-^{m}QQ$_8$-^{m}QQ$_8$-Allyl 30. Nonamer acid **15** (112 mg, 0.05 mmol), nonamer amine **17** (110 mg, 0.05 mmol) and PyBOP (38 mg, 1.5 equiv.) are dissolved in $CHCl_3$ and DIEA (42 µL, 5 equiv.) overnight at room temperature. Then, the reaction mixture was washed with 5% citric acid solution and with water. The solvents were removed under reduced pressure and the crude was purified by GPC with 0.5 % NEt_3, 1 % EtOH in $CHCl_3$ as mobile phase. The collected fraction is washed with citric acid 5% and water, dried on Na_2S0_4 and solvents are evaporated to obtained **30** (yield 74 %). 1H NMR

(300 MHz, $CDCl_3$) δ 11.13 (d, *J* = 9.7 Hz, 2H), 10.72 (d, *J* = 16.8 Hz, 2H), 10.52 (s, 1H), 10.38 (s, 1H), 10.18 (dd, *J* = 21.7, 8.5 Hz, 7H), 9.96 (d, *J* = 14.9 Hz, 2H), 9.30 (s, 1H), 8.30 (s, 1H), 8.00 – 7.83 (m, 5H), 7.82 – 7.53 (m, 13H), 7.48 – 7.32 (m, 4H), 7.22 – 6.34 (m, 37H), 6.21 (d, *J* = 12.5 Hz, 2H), 6.10 (d, *J* = 12.1 Hz, 4H), 5.92 (s, 1H), 5.85 (s, 2H), 5.77 (d, *J* = 7.8 Hz, 2H), 5.65 (s, 1H), 5.59 (s, 1H), 5.49 (s, 1H), 5.11 (s, 1H), 4.66 (d, *J* = 17.2 Hz, 2H), 4.40 (d, *J* = 10.4 Hz, 2H), 3.87 – 3.24 (m, 36H), 2.71 – 2.49 (m, 4H), 2.36 – 2.03 (m, 18H), 1.55 (s, 9H), 1.11 (dddd, *J* = 43.8, 36.8, 25.6, 15.1 Hz, 108H).

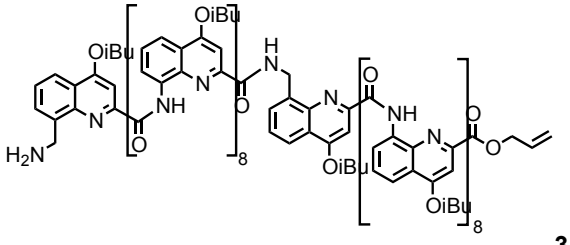

31

18-mer oligomer (H_2N-$^{m}QQ_8$-$^{m}QQ_8$-Allyl) 31. Boc protected 18-mer **30** is dissolved in 500 µL of CH_2Cl_2 and 500 µL of TFA are added dropwise and the reaction is allowed to proceed during 1h30. The reaction mixture was quenched by addition of saturated $NaHCO_3$ solution and was extracted with CH_2Cl_2 and washed with distilled water. The organic phase was dried over Na_2SO_4. Solvents are evaporated and the solid is dry under reduced pressure. (yield: 99 %) ^{1}H NMR (300 MHz, $CDCl_3$) δ in ppm: 11.13 (d, *J* = 9.6 Hz, 2H), 10.77 (d, *J* = 17.5 Hz, 2H), 10.52 (s, 1H), 10.38 (s, 1H), 10.35 – 10.09 (m, 7H), 9.96 (d, *J* = 15.0 Hz, 2H), 9.29 (s, 1H), 8.31 (d, *J* = 7.7 Hz, 1H), 8.06 – 7.81 (m, 6H), 7.82 – 7.52 (m, 13H), 7.40 (ddd, *J* = 16.7, 14.4, 8.3 Hz, 4H), 7.23 – 6.34 (m, 35H), 6.15 (dd, *J* = 31.3, 12.3 Hz, 6H), 5.92 (s, 1H), 5.86 (s, 2H), 5.78 (d, *J* = 13.5 Hz, 2H), 5.65 (s, 1H), 5.59 (s, 1H), 5.49 (s, 1H), 5.17 – 5.05 (m, 1H), 4.65 (dd, *J* = 17.2, 1.5 Hz, 2H), 4.41 (d, *J* = 10.5 Hz, 2H), 4.04 – 3.34 (m, 36H), 3.25 – 3.04 (m, 4H), 2.56 (d, *J* = 8.6 Hz, 2H), 2.38 – 2.02 (m, 18H), 1.49 – 1.00 (m, 108H).

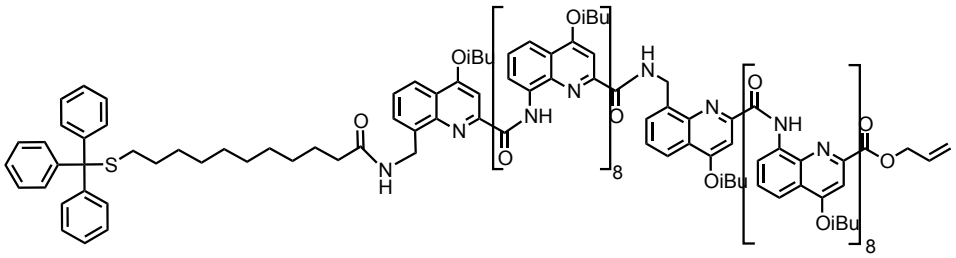

32

18-mer oligomer (Trityl-S-$(CH_2)_{10}$-^{m}QQ$_8$-^{m}QQ$_8$-Allyl) 32. 18-mer amine **23** (123 mg, 8.6 µmol) are mixed with trityl-S-$(CH_2)_{10}$-COOH (26 mg, 2 equiv.), PyBOP (30 mg, 2 equiv.) and DIEA (14.5 µL, 3 equiv.) in $CHCl_3$ (500 µL) overnight at room temperature. The reaction mixture was washed with citric acid 5% and H_2O. The product is dried under reduced pressure and purified by precipitation with minimum amount of MeOH in highly concentrated solution in CH_2Cl_2 to obtain yellowish product **31** (100 mg, 73%). HRMS (ESI^+): *m/z* calcd for $C_{287}H_{296}N_{36}O_{38}S$: $[M+3H]^{+3}$: 1630.74347 found 1630.74903; $[M+2H]^{+2}$: 2445.61520 found 2445.61677. ^1H NMR (300 MHz, $CDCl_3$) δ in ppm: 11.16 (d, *J* = 9.6 Hz, 2H), 10.81 (s, 1H), 10.72 (s, 1H), 10.55 (s, 1H), 10.42 (s, 1H), 10.35 – 10.12 (m, 7H), 10.00 (d, *J* = 15.1 Hz, 2H), 9.32 (s, 1H), 8.37 (s, 1H), 8.12 – 7.85 (m, 5H), 7.85 – 7.56 (m, 14H), 7.59 – 7.31 (m, 12H), 7.27 – 6.40 (m, 41H), 6.32 (d, *J* = 6.7 Hz, 1H), 6.24 (d, *J* = 12.7 Hz, 2H), 6.18 – 6.08 (m, 4H), 5.96 (s, 1H), 5.89 (s, 2H), 5.80 (t, *J* = 11.9 Hz, 2H), 5.67 (d, *J* = 9.7 Hz, 1H), 5.60 (d, *J* = 8.7 Hz, 1H), 5.51 (d, *J* = 11.4 Hz, 1H), 5.11 (d, *J* = 20.8 Hz, 1H), 4.68 (dd, *J* = 18.0, 8.0 Hz, 1H), 4.41 (t, *J* = 16.9 Hz, 1H), 3.93 – 3.49 (m, 36H), 3.16 (t, *J* = 21.3 Hz, 2H), 2.98 (d, *J* = 29.9 Hz, 1H), 2.55 (d, *J* = 19.4 Hz, 1H), 2.47 – 2.08 (m, 18H), 2.03 (s, 1H), 1.51 (d, *J* = 15.3 Hz, 22H), 1.24 – 1.00 (m, 108H).

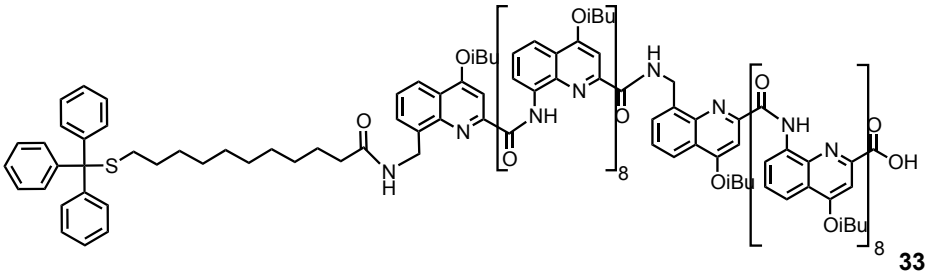

33

18-mer oligomer (Tr-S-$(CH_2)_{10}$-^{m}QQ$_8$-^{m}QQ$_8$-COOH) 33. Allyl-protected 18-mer **32** (31 mg, 6.4 µmol, 1 equiv.) dissolved in degassed CH_2Cl_2 (0.1 M) was treated with $Pd(PPh_3)_4$ (1 mg, ≈ 0.1 equiv.) and $PhSiH_3$ (1 drop, ≈5 equiv.) under argon atmosphere and was stirred at room temperature for 40 min in dark. The organic phase was washed with water, dried over Na_2SO_4 and filtered. The solvent was removed and the crude was purify by precipitation CH_2Cl_2/MeOH and dried under vacuum to give corresponding oligomer acid as a solid **33** (19.7 mg, yield: 64 %) HRMS (ESI^+): *m/z* calcd for $C_{284}H_{292}N_{36}O_{38}S$

$[M+3H]^{+3}$: 1617.402305 found 1617.40689 ; $[M+2H]^{+2}$: 2425.599545 found 2425.60310. ^{1}H NMR (300 MHz, $CDCl_3$) δ 10.96 (s, 1H), 10.77 (s, 1H), 10.68 (s, 1H), 10.54 (d, *J* = 2.9 Hz, 2H), 10.43 (s, 1H), 10.36 – 10.06 (m, 7H), 9.96 (d, *J* = 18.0 Hz, 2H), 9.30 (s, 1H), 8.31 (s, 1H), 8.10 – 7.82 (m, 5H), 7.68 (ddt, *J* = 16.6, 8.3, 5.2 Hz, 13H), 7.53 – 7.26 (m, 13H), 7.24 – 6.66 (m, 35H), 6.65 – 6.37 (m, 6H), 6.36 – 6.25 (m, 2H), 6.22 (s, 1H), 6.09 (t, *J* = 8.0 Hz, 4H), 5.93 (s, 1H), 5.85 (s, 2H), 5.81 (s, 1H), 5.77 (s, 1H), 5.67 (s, 1H), 5.59 (d, *J* = 1.6 Hz, 1H), 5.49 (s, 1H), 4.03 – 3.34 (m, 36H), 3.16 (d, *J* = 23.9 Hz, 2H), 3.00 (s, 1H), 2.53 (d, *J* = 27.3 Hz, 1H), 2.39 – 2.10 (m, 18H), 1.70 – 1.27 (m, 22H), 1.24 – 1.03 (m, 108H).

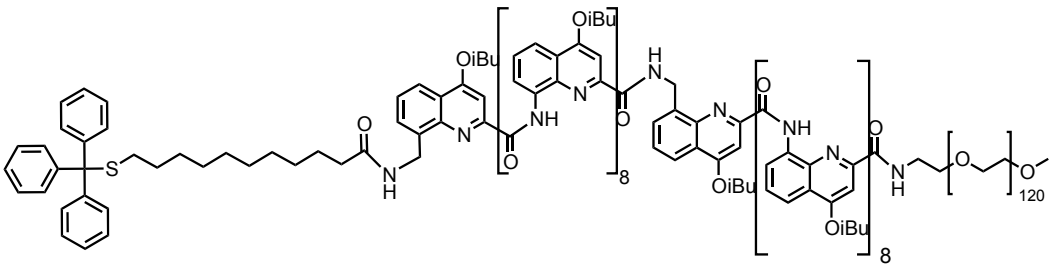

34

18-mer oligomer (Tr-S-$(CH_2)_{10}$-^{m}QQ$_8$-^{m}QQ$_8$-PEG$_{5000}$) 34. 18-mer acid (19.7 mg, 4.7 µmol, 1 equiv.) is dissolved with H_2N-PEG$_{5000}$-OMe (24,4mg, 1.2 equiv.), PyBOP (4.2 mg, 2 equiv.) in $CHCl_3$ (500 µL) and DIEA (3.5 µL, 5 equiv.) and allowed to react overnight at room temperature under argon atmosphere. The crude was washed with citric acid and water, dried over Na_2SO_4 and directly purified by recycling GPC. Yield: 60%. HRMS (ESI^+): *m/z* calcd for $C_{284}H_{292}N_{37}O_{37}S$-$(CH_2$-$CH_2$-$O)_{112}$-OMe $[M+6H]^{+6}$: 1637,66 found 1637,67 ^{1}H NMR (300 MHz, $CDCl_3$) δ 11.16 (s, 1H), 10.86 (s, 1H), 10.77 (s, 1H), 10.68 (s, 1H), 10.42 (d, *J* = 25.4 Hz, 2H), 10.29 – 10.10 (m, 7H), 9.96 (d, *J* = 16.2 Hz, 2H), 9.28 (s, 1H), 8.35 (d, *J* = 6.7 Hz, 1H), 7.95 – 7.55 (m, 19H), 7.46 – 7.32 (m, 9H), 7.11 (dddd, *J* = 37.4, 29.6, 14.3, 5.1 Hz, 24H), 6.89 – 6.38 (m, 22H), 6.25 (d, *J* = 10.4 Hz, 2H), 6.11 (dd, *J* = 18.9, 7.1 Hz, 4H), 5.92 (s, 1H), 5.85 (s, 2H), 5.80 (s, 1H), 5.76 (s, 1H), 5.65 (s, 1H), 5.57 (s, 1H), 5.49 (s, 1H), 3.68 – 3.50 (m, x H- PEG), 1.25 (s, 22H), 1.21 – 1.03 (m, 108H).

5.9 References

1. Guichard, G. & Huc, I. Synthetic foldamers. *Chem. Commun. (Camb).* **47,** 5933–41 (2011).
2. Gellman, S. H. Foldamers: A Manifesto. *Acc. Chem. Res.* **31,** 173–180 (1998).
3. Feringa, B. L. The Art of Building Small: From Molecular Switches to Motors (Nobel Lecture). *Angew. Chemie - Int. Ed.* **56,** 11060–11078 (2017).
4. Huc, I. Aromatic Oligoamide Foldamers. *European J. Org. Chem.* **2004,** 17–29 (2004).
5. Berni, E. *et al.* Assessing the mechanical properties of a molecular spring. *Chemistry* **13,** 8463–9 (2007).
6. Ferrand, Y. & Huc, I. Designing Helical Molecular Capsules Based on Folded Aromatic Amide Oligomers. *Acc. Chem. Res.* **51,** 970–977 (2018).
7. Ferrand, Y., Kendhale, A. M., Garric, J., Kauffmann, B. & Huc, I. Parallel and Antiparallel Triple Helices of Naphthyridine Oligoamides. *Angew. Chemie Int. Ed.* **49,** 1778–1781 (2010).
8. Yashima, E. *et al.* Supramolecular Helical Systems: Helical Assemblies of Small Molecules, Foldamers, and Polymers with Chiral Amplification and Their Functions. *Chem. Rev.* **116,** 13752–13990 (2016).
9. Jiang, H., Léger, J. M., Dolain, C., Guionneau, P. & Huc, I. Aromatic δ-peptides: Design, synthesis and structural studies of helical, quinoline-derived oligoamide foldamers. *Tetrahedron* **59,** 8365–8374 (2003).
10. Qi, T., Deschrijver, T. & Huc, I. Large-scale and chromatography-free synthesis of an octameric quinoline-based aromatic amide helical foldamer. *Nat. Protoc.* **8,** 693–708 (2013).
11. Li, X. *et al.* Synthesis and Multibromination of Nanosized Helical Aromatic Amide Foldamers via Segment-Doubling Condensation. *Org. Lett.* **18,** 1044–1047 (2016).
12. Li, X. Synthesis and physical properties of helical nanosized quinoline-based foldamers : structure , dynamics and photoinduced electron transport. (University of Bordeaux and University of Liege, 2016).
13. Lussis, P. *et al.* A single synthetic small molecule that generates force against a load. *Nat. Nanotechnol.* **6,** 553–557 (2011).
14. Schröder, T. *et al.* Single-molecule force spectroscopy of supramolecular heterodimeric capsules. *Phys. Chem. Chem. Phys.* **12,** 10981 (2010).
15. Lewandowski, B. *et al.* Sequence-Specific Peptide Synthesis by an Artificial Small-Molecule Machine. *Science (80-.).* **339,** 189–193 (2013).
16. De Bo, G. *et al.* An artificial molecular machine that builds an asymmetric catalyst. *Nat. Nanotechnol.* **13,** 381–385 (2018).
17. Zhang, A., Ferguson, J. S., Yamato, K., Zheng, C. & Gong, B. Improving foldamer synthesis through protecting group induced unfolding of aromatic oligoamides. *Org. Lett.* **8,** 5117–5120 (2006).
18. Delsuc, N. *et al.* Kinetics of helix-handedness inversion: Folding and unfolding in aromatic amide oligomers. *ChemPhysChem* **9,** 1882–1890 (2008).
19. Qi, T. *et al.* Solvent dependence of helix stability in aromatic oligoamide foldamers. *Chem. Commun. (Camb).* **48,** 48–51 (2012).
20. Ferrand, Y., Kendhale, A. M., Garric, J., Kauffmann, B. & Huc, I. Parallel and Antiparallel Triple Helices of Naphthyridine Oligoamides. *Angew. Chemie Int. Ed.* **49,** 1778–1781 (2010).

Chapter 6

Force Spectroscopy on
Diblock & Triblock
Foldamers

TABLE OF CONTENTS

Chapter 6
Force Spectroscopy on Diblock & Triblock Foldamers

Previously, the force spectroscopy investigation on the quinoline-based foldamers of different sizes has demonstrated particular unfolding profiles and a cooperative effect according to the foldamer size. We have identified two major parts in the unfolding profile: the longest foldamers exhibit mainly a constant-force plateau ending by a decreasing-in-force feature, which becomes dominant in the unfolding profile of the shortest foldamers. The total length of the unfolding profile is linearly dependent on the number of units. The ending feature is size-independent and has been associated to the nucleation segment of the π-stacking reinforced helical structure. The average force of the unfolding profile, taken from the beginning of the unfolding of the foldamer up to the beginning of the overstretching of the molecule, decreases with the increasing size of the foldamer and ranges between 100 pN to 70 pN. The revealed length along the unfolding of each foldamer corresponds to the difference between a totally estimated unfolded and the fully folded conformations. Some pulling-relaxing experiments have allowed observing the complete and reversible refolding capability under tension of a mechanically unfolded 33-mer. We determined that the foldamer possesses extremely fast folding dynamics. Even at the fastest pulling rate, the foldamers undergo transition under equilibrium. From the fact that these profiles are repetitive and unique and that the unfolding forces are higher than 80 pN, the foldamer can be considered as a really stable and robust molecular architecture.

In the preceding chapter, we synthetized two foldamers comprising different chemical structures to further understand the mechanochemical properties of the foldamers. One of them was designed to probe the mechanical properties of a wider molecular helix than the quinoline foldamers and the other one was synthetized as a reference for the first one and to investigate the influence of an aliphatic link embedded in the robust and cooperative quinoline foldamers.

In this chapter, we describe preliminary SMFS investigation and results on these two newly synthetized foldamers. We performed pulling experiments in DMF at the same velocity as the experiments on the quinoline-based foldamer in the first chapter. This allowed us to compare the mechanical behaviours of the three studied foldamers and to draw some conclusions on the mechanochemical properties.

We highlight significant impacts of the chemical changes introduced in the foldamers backbone.

6.1 Introduction

One of the big current challenges in the art of building small is to endow molecules and molecular systems with predictable functions. The first step to achieve this request is to develop techniques and methods able to probe the potential functions. Investigating movements or other functions at the molecular scale is not trivial. The first chapters of this thesis have proven the applicability of AFM-based single-molecule force spectroscopy to provide unprecedented insight into the mechanical properties of the helical quinoline-based foldamers.

In this chapter, we performed similar force experiments to investigate the mechanical properties of a wider molecular helical foldamer and to evaluate the mechanical impact of the insertion of a small aliphatic link in the aromatic oligoamide backbone.

The investigated foldamers are schematically represented in Figure 6.1. The illustrated structures are speculated from previous knowledge and 1D-NMR spectra, and not from thorough structural investigation or crystallography analysis.

As explained in details in chapter 5, the wider helix (green), made of eight naphthyridine units (N), is embedded into rigid quinoline (Q) helices ($^{m}QQ_8N_8{}^{m}QQ_8$). On the one hand, this insertion strategy prevents the formation of a highly favourable triplex and on the other hand, it includes the quinoline block as an internal reference.

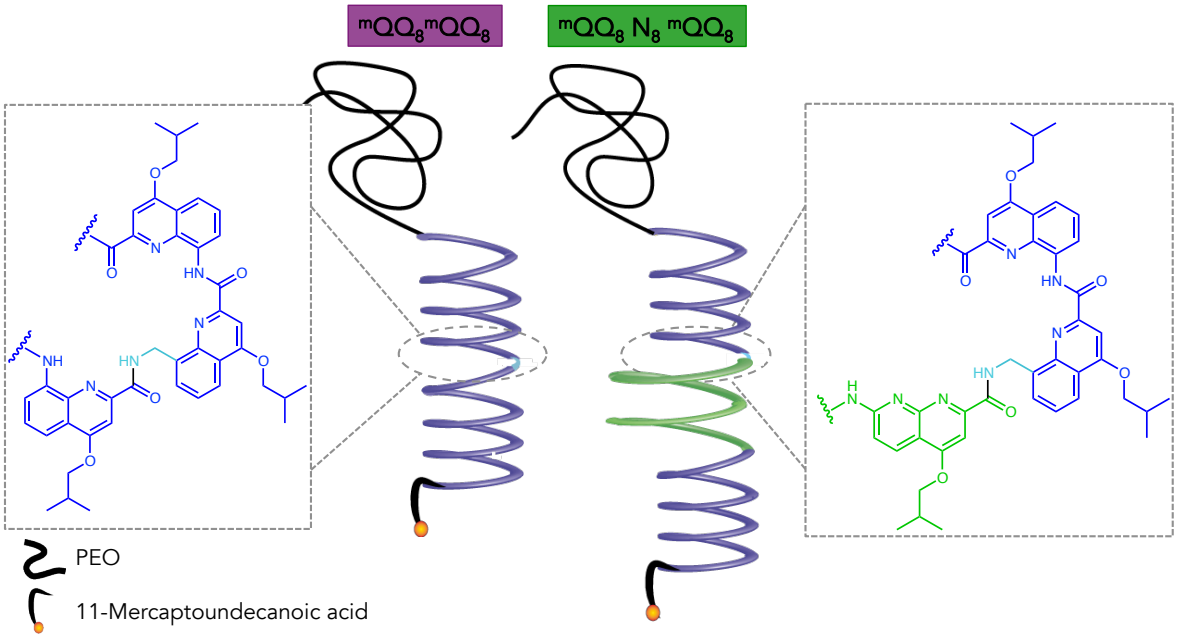

Figure 6.1 Schematic illustration of (left) the diblock quinoline-based foldamer incorporating one methylene bridge (light blue) between two quinoline 9-mers (dark blue) (SH-R-$^{m}QQ_8{}^{m}QQ_8$-PEG referred as to $^{m}QQ_8{}^{m}QQ_8$; (right) the triblock naphthyridine constituting foldamer, composed of a naphthyridine 8-mer (green) inserted between two quinoline 9-mers and including one methylene bridge between the N-block and the Q-block at the C-terminal side.

The variation of the diameter of a helix has not been identified as a natural approach to control its molecular machinery. However, the non-natural building blocks, developed by the chemists' ingenuity, give access to this potential field. It could enable to mimic natural properties and even go beyond. Demonstrated by the preliminary naphthyridine investigations[1] and among others examples, the enlargement of the diameter of aromatic oligoamides appears to increase the ability of the helix to hybridize in triple helix or double helix.[2] This propensity has been mainly explained owing to the capacity of undergoing a lower torsion angle for a same extension compared to a helix of a smaller diameter. This hypothesis stems from studies on energy differences between single helices and duplexes.[2] Probing the unfolding forces would adequately shed light on the mechanical properties, which have never been investigated.

The incorporation of an aliphatic link was a technical requirement for the synthesis, but we can also consider introducing it on purpose to achieve particular folding or spatial arrangement of functional groups. It has been shown that some aromatic structures and folding propensities may also not be affected by such insertion.[3–5] A few studies have already been conducted on *e.g.* the propensity of aliphatic units to transmit or to disrupt the helical conformation but the impact on the mechanical properties is totally unexplored.

This study paves the way of probing the mechanical properties of hybrid artificial folded molecules mimicking natural secondary structures. We aim at providing complementary information to the characterization of the naphthyridine-based foldamers, as well as, working hands in hands with organic chemists, giving clues in order to tune molecular structures and to yield different and probably emerging functional molecules.

6.2 Results and discussion

In this section, we need to start with some terminological precisions. Up to now the foldamers were abbreviated as Q5, Q9, Q17 and Q33, although more precisely they are SH-R-$^{m}QQ_4$-PEG, SH-R-$^{m}QQ_8$-PEG, SH-R-$^{m}QQ_{16}$-PEG and SH-R-$^{m}QQ_{32}$-PEG, respectively, with ^{m}Q standing for amino-methyl quinoline unit. Indeed, one of the external quinoline units is an amino-methyl quinoline unit (^{m}Q) in all the foldamers studied in this thesis (chapter 2). This modified quinoline unit was added at the *N*-terminus of the oligomers of pure aromatic quinoline (Q_8) synthesis to promote a vertical orientation of the foldamer regarding to the gold-substrate, as the methylene bridge, -CH_2-, is at the end of the foldamer; it can thus induce a 90° angle (appendix A.2.). For the new foldamers studied in this chapter, we will omit as well the terminal functionalizations in the terminology, but we keep the more precise annotation of the central part. The diblock comprising a methylene bridge in between two aromatic quinoline blocks is named **$^{m}QQ_8{}^{m}QQ_8$** instead of SH-R-$^{m}QQ_8{}^{m}QQ_8$-PEG and the triblock comprising the additional naphthyridine oligomer (N_8) is referred to as **$^{m}QQ_8N_8{}^{m}QQ_8$** instead of SH-R-$^{m}QQ_8N_8{}^{m}QQ_8$-PEG. This terminology is more appropriate to underline the symmetry of the synthesis as well as to indicate the incorporation of the methylene bridge (-CH_2-) in the fully aromatic sequences (Figure 5.3).

As a reminder, in quinoline-based oligomer one helical turn is made of 2.5 units, therefore each $^{m}QQ_8$ block makes 3.6 turns (section 1.2.2.2). In naphthyridine-based oligomers, one turns is made out of 4 units (section 5.1). Consequently, N_8 is expected to be a 2-turn helix.

We performed the functionalization on gold substrates and the SMFS experiments as described for the previous investigations (Chapter 2). We prepared some functionalized substrates with only one type of foldamers and others with two types of foldamers to confirm data comparison. We successfully mixed $^{m}QQ_8{}^{m}QQ_8$ with $^{m}QQ_8N_8{}^{m}QQ_8$ and $^{m}QQ_8{}^{m}QQ_8$ with Q17. We conducted standard pulling experiments in DMF at the fixed velocity of 166 nm.s^{-1} with cantilevers with a spring constant around 30 pN.nm^{-1}.

6.2.1 Identification of the unfolding pattern of the diblock quinoline-based foldamer

Starting pulling experiments on functionalized substrates with only the diblock $^{m}QQ_8{}^{m}QQ_8$, a highly reproducible force-distance profile could be identified (Figure 6.2). The specific unfolding pattern of the $^{m}QQ_8{}^{m}QQ_8$ is made of two peaks, which was not expected. At the beginning of the force-distance curve in Figure 6.2, the pulling profile indicates the unravelling of the PEG chain until it displays the two peaks. With a closer

look, each peak is actually composed of a short plateau followed by some large hopping events or a rupture peak, as we observed for the Q9 ($^{m}QQ_8$) in chapter 2. Both peaks are separated by a short entropic stretching pattern. The pulling curve continues with the overstretching of the foldamers until the detachment of the PEG chain from the AFM tip. Some small variations can be observed along the forced unfolding of $^{m}QQ_8{}^{m}QQ_8$ as shown in Figure 6.2 (right). The length of plateau varies and the way the force decreases after the plateau can be abrupt or progressive.

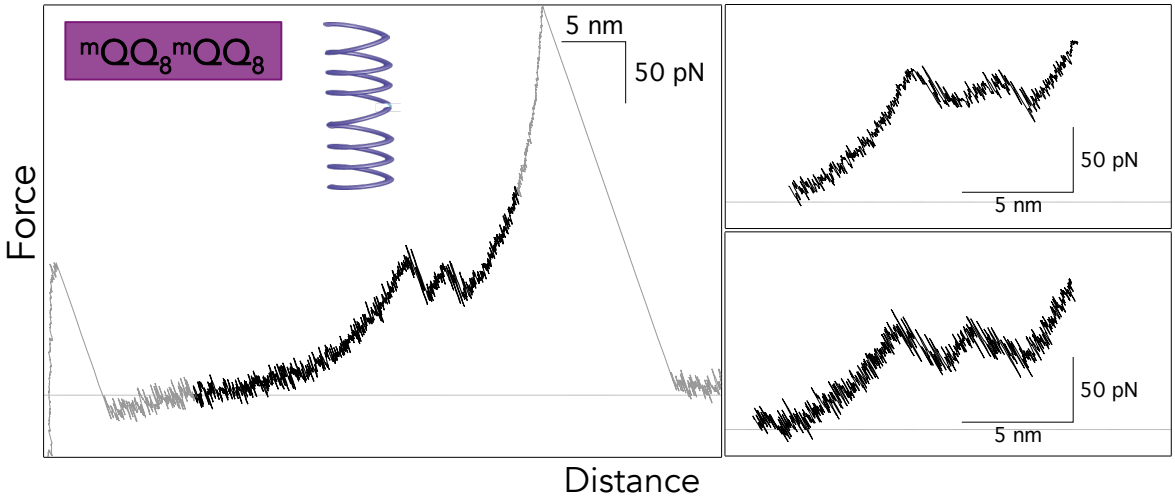

Figure 6.2 Representative force-distance curves of pulling experiments on diblock quinoline-based foldamers made of 2 blocks of 8 units of 8-amino-4-isobutoxy-2-quinolinecarboxylic acid (Q_8) and 1 unit of 8-aminomethyl-4-isobutoxy-2-quinolinecarboxylic acid (^{m}Q) at the amino-terminus. It consists in 2 quinoline blocks linked to each other with a methylene bridge. On the left, the full pulling curves (for clarity approach was omitted). On the right, zoom in on the unfolding pattern of the foldamer to show some variations (hopping events (top), progressive decreasing force (bottom)).

The force-distance curves of $^{m}QQ_8{}^{m}QQ_8$ highlight the substantial impact of the insertion of the methylene bridge (-CH_2-) within fully aromatic sequences. In chapter 2, the unfolding pattern of a Q17 shows a constant-force plateau along the whole foldamer unfolding without any break. Therefore, we can suggest that in presence of the -CH_2-, *i.e.* an aliphatic link, the quinoline oligomers, which are separated by only one additional CH_2, behave as two independent helices under mechanical load. Quantitative measurements on the unfolding lengths and forces are consistent with the sequential unfolding of one $^{m}QQ_8$ after the other. Details are discussed in a next section.

This is twofold intriguing. First, the insertion of the tiniest aliphatic link was not expected to have such a significant impact. Secondly, this effect was even not expected given the only small discrepancy in the NMR spectra of $^{m}QQ_8{}^{m}QQ_8$ and Q17 (Figure 5.11). The NMR spectrum of the $^{m}QQ_8{}^{m}QQ_8$ does not disclose a significant loss of mutual interaction along the foldamer elongation compared to Q17. In both cases, the amide proton peaks exhibit a different chemical shift value for each given proton, as well as a global upfield

shift, which have been attributed to chain-length dependence. Therefore, we could believe that the helical conformation and the cooperativity were efficiently transmitted through the methylene bridge.

Based on the SMFS experiments, we can propose that under mechanical load, the CH_2 offers more degrees of freedom, which therefore firstly extends. This extension moves off the stacked quinoline cycles too far away from each other to maintain π interactions. This cancels out the chain-length dependence cooperativity. Each $^{m}QQ_8$ block of the diblock appears as isolated and unfolds one after the other. This behaviour is similar to what is observed for the unfolding of domains of multi-domain proteins.[6] In multi-domain proteins, the domains are identical and unfold one after the other with similar unfolding force as illustrated in Figure 6.3. For the diblock, we can also observe the sequential unfolding of the two blocks, just like observed from proteins domains. The cooperativity of the interaction upon folding within a block renders the subsequent unfolding steps within this block easier and thus promotes the complete unfolding of one block before the other starts.

Another hypothesis to explain the sequential unfolding comes from geometrical effect. It has been demonstrated that the geometry of the bonds regarding the pulling direction may influence to unfolding/stretching pattern.[7] With the methylene bridge, we can imagine that the two quinoline blocks are not similarly aligned, which may imply a difference in how the force is transduced and therefore may cause sequential unfolding.

At the moment, it is impossible to conclude about the correct mechanism.

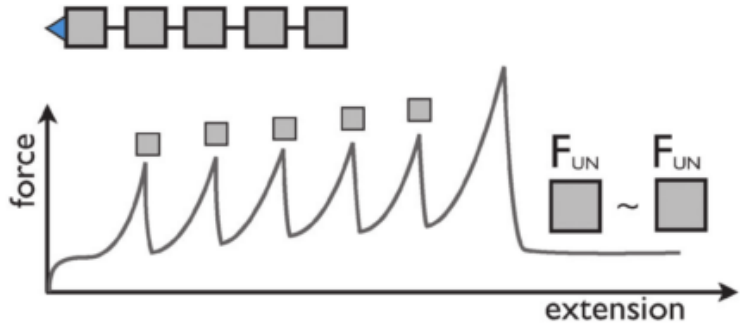

Figure 6.3 Schematic representation of the unfolding of a homopolyprotein. Reproduced from reference 6.

In conclusion of this section, we highlighted that the insertion of a methylene bridge in rigid aromatic sequences induces a breaking in the forced unfolding. It acts as a separator of the aromatic sequences and leads to sequential unfolding of the blocks delimited by the $-CH_2-$. With these results, we may also suggest the key role of the π-stacking.

6.2.2 Identification of the unfolding patterns of the triblock naphthyridine-constituting foldamer

Pulling experiments on $^{m}QQ_8N_8{}^{m}QQ_8$ provided reproducible force-distance curves shown in Figure 6.4. With the unfolding profile of $^{m}QQ_8{}^{m}QQ_8$ in mind, the specific unfolding pattern of the wider helix N_8 could unambiguously be identified. At lower forces, a force-constant plateau interrupts the elastic unravelling of the PEG. The PEG is further stretched to reach a force at which the two-peaks pattern, exactly as identified in the $^{m}QQ_8{}^{m}QQ_8$ profile, is observable. Therefore, the force-constant plateau at lower force can be associated to the unfolding of the N_8.

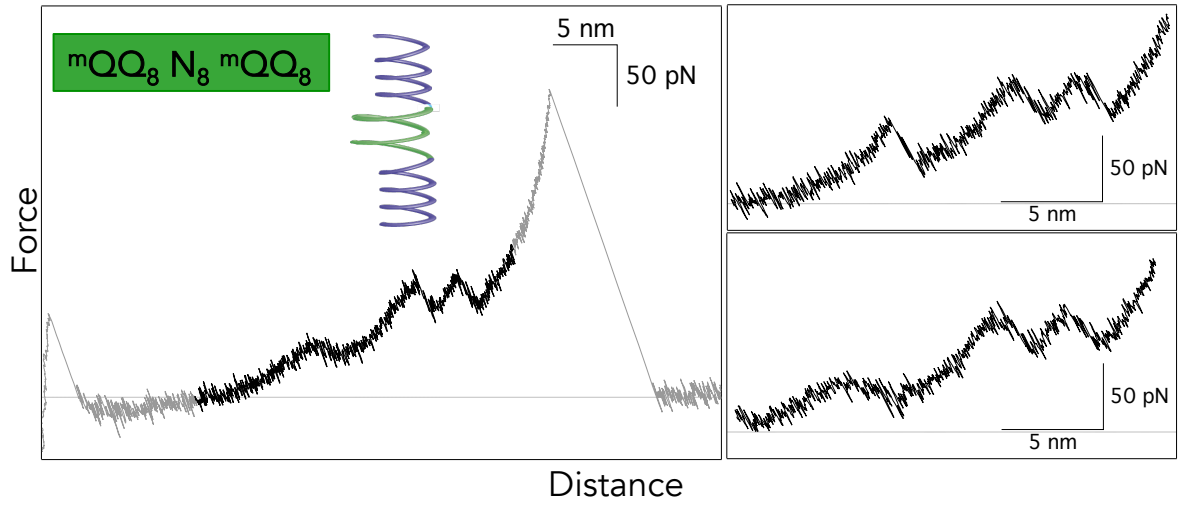

Figure 6.4 Representative force-distance curves of pulling experiments on triblock naphthyridine-constituting foldamer made of an octamer of 2-amino-5-isobutoxy-1,8-naphthyridine-7-carboxylic acid (N_8) embedded in two blocks of 8 units of 8-amino-4-isobutoxy-2-quinolinecarboxylic acid (Q_8) and one unit of 8-aminomethyl-4-isobutoxy-2-quinolinecarboxylic acid (^{m}Q) at the amino-terminus. On the left, the full pulling curves (for clarity approach was omitted). On the right, zoom on the unfolding pattern of the foldamer to show some variations (hopping events (top), progressive decreasing force (bottom)).

These force-distance curves highlight several interesting concepts:

First of all, the unfolding pattern of the naphthyridine oligomer is not a single peak in most cases, but a constant-force plateau. This confirms that the embedded naphthyridine oligomer is undergoing an unwinding process, presumably from a 2-turns helix which does not break at once. In rare cases, it may happen that a single rupture is recorded in the PEG chain stretching as the N_8 unfolding pattern (Figure 6.4 top inset), but most of the force-distance curves exhibit a constant-force plateau (Figure 6.4) or a slightly force-decreasing continuous extension (Figure 6.4 inset bottom). The plateau suggests that the helix unfolds through stepwise multiple conformational transitions, as it has been demonstrated in details for the quinoline oligomers in chapter 2.

Secondly, the unfolding of the naphthyridine helix prior to the quinoline unfolding indicates that the interactions maintaining the helical conformation are weaker in the N_8 oligomer. Besides, it is also interesting to analyse the unfolding sequence as it may shed light on the mechanics of the force transmission. Although the naphthyridine oligomer is in the middle of the foldamer, it unfolds first keeping the quinoline folded. This behaviours is consistent with the general concept of force spectroscopy: "The sacrificial bonds will break in the order of their lowest rupture force, regardless of their spatial order in the molecule"[8] and demonstrates the capability of creating molecular systems with several force levels.

Last but not least, it seems that the N_8 does not influence at all or is not involved in the quinoline folding. Indeed, exactly the same unfolding pattern of the quinoline blocks is recovered in presence of naphthyridine. Supported by quantitative measurements, the independence mechanics of the different helices is confirmed in a next section.

6.2.3 Quantitative analysis and comparison of the unfolding patterns of the diblock and the triblock

In order to support the previous qualitative interpretations of the force-distance curves and to characterize the mechanical properties of these foldamers, we performed quantitative length and force analyses of distinct unfolding patterns.

6.2.3.1 Quantitative mechanical properties of the diblock $^{m}QQ_8{}^{m}QQ_8$

As we already observed, the pattern of the diblock $^{m}QQ_8{}^{m}QQ_8$ is also identified in the triblock $^{m}QQ_8N_8{}^{m}QQ_8$ comprising the naphthyridine oligomer. In Figure 6.5, we firstly compared the lengths of the unfolding pattern of the quinoline blocks $^{m}QQ_8$ in both the diblock and the triblock.

In both foldamers, the length distributions of the first part and of the second part of the $^{m}QQ_8{}^{m}QQ_8$ unfolding profiles are highly similar, they are both centred on one single value of 2.4 nm and present same dispersity. As evidenced in the identification of the specific unfolding patterns of both foldamers, the exact correspondence of the lengths in both foldamers profiles confirms the complete mechanical independency of the naphthyridine and the quinoline oligomers in the composite triblock. Indeed, even the full length (dotted pattern in Figure 6.5) measured from the first unfolding step associated to the first $^{m}QQ_8$ to the last unfolding step of the second $^{m}QQ_8$ is unchanged in the composite triblock, compared to the referencing diblock. This also indicates on the one hand that once the N_8 is unfolded, the naphthyridine chain acts as a rigid and unstretchable linker at higher

forces. On the other hand, it demonstrates the usability of the $^{m}QQ_8$ as an appropriate reference, as it rendered the identification of the N_8 unfolding obvious.

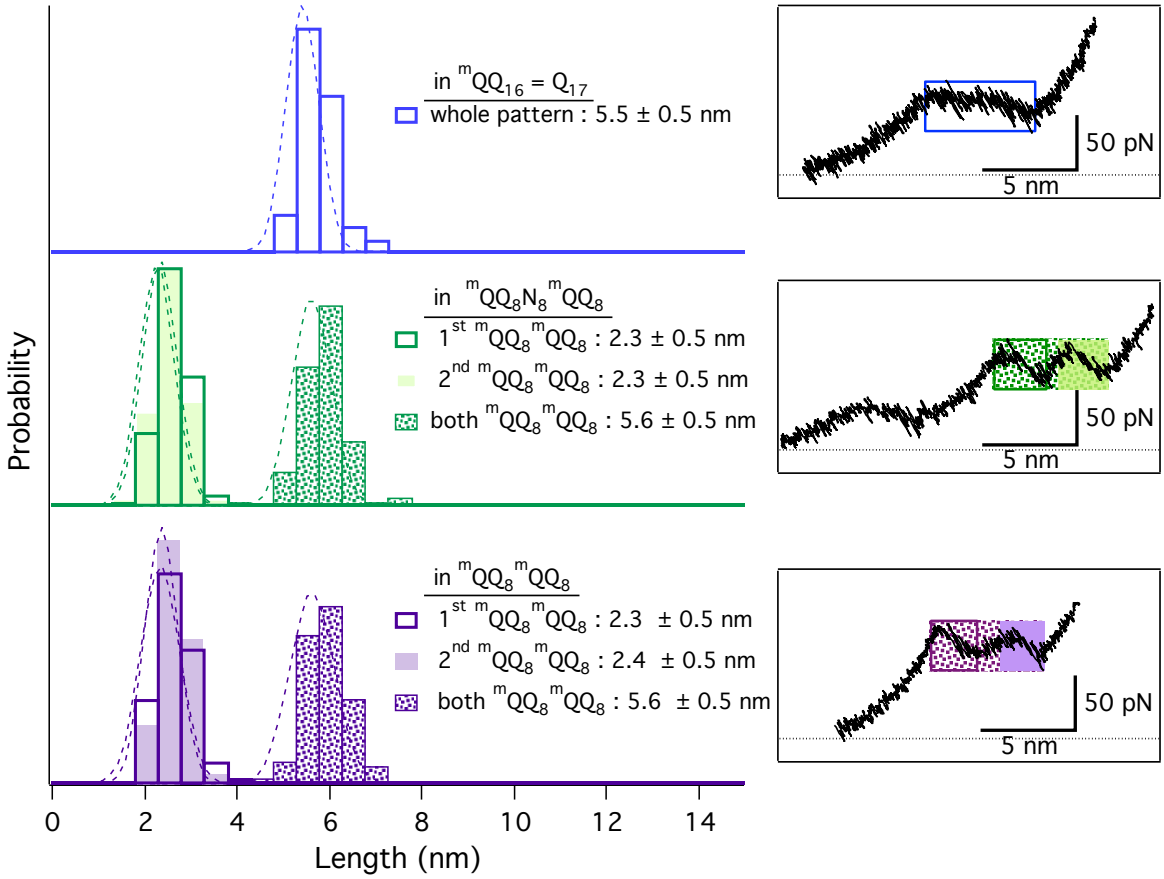

Figure 6.5 Histograms and Gaussian fits of the lengths of different parts of the specific unfolding pattern of the diblock $^{m}QQ_8{}^{m}QQ_8$, the triblock $^{m}QQ_8N_8{}^{m}QQ_8$ and the monoblock Q17 (measurement from hybrid surface). The different parts are explicitly shown on the force-distance curves on the right.

The identical length values of the 2 parts advocate the sequential unfolding of one quinoline block after the other. Nevertheless, the most probable lengths of these unfolding patterns are actually slightly smaller (2.4 nm) than the values for the measurements performed previously on Q9 (3.4 nm). To confirm the discrepancy in length with the previous results on Q9, we tried to perform control experiments with hybrid surfaces functionalized with a combination of $^{m}QQ_8{}^{m}QQ_8$ and Q17 or Q9, as internal references. The trials with Q9 were unsuccessful, whereas with Q17, we could obtain both unfolding patterns. We measured the corresponding length in each foldamer pattern and it appeared that the plateaus of the Q17 (5.5 nm) were also shorter than in the precedent results (6.5 nm). Therefore, we could believe that the differences between the $^{m}QQ_8$ and the Q9 probably come from statistical uncertainty. Nevertheless, we compared the length values of the $^{m}QQ_8$ unfolding (2.4 nm for 9 units: 0.27 nm/unit) with the controlled Q17 measurements (5.5 nm for 17 units: 0.32 nm /unit) and we still noticed a smaller unfolding length than expected from a presumable fully folded $^{m}QQ_8$ conformation.

The full length of the two $^{m}QQ_8$, highlighted in Figure 6.5 with dotted pattern, appeared to be a better match (5.6 nm/18 units: 0.31 nm/unit). This could highlight that part of the quinoline helices unfold like a spring. However, as seen in Figure 6.6, the length of the entropic spring-like pattern, separating the two peaks (marked as A) depends on the attachment point of the PEG with the AFM tip. Indeed, we can find a direct correlation between the length of this entropic pattern (A) and the extension at the end of the characteristic foldamer unfolding. This extension is directly linked to PEG chain length between the tip and the foldamer. This indicates the contribution of the PEG chain stretching in the length pattern. Furthermore, we found that we cannot fit this pattern with a WLC fit corresponding to the PEG chain and it suggests that both PEG chain stretching and quinoline-based block stretching may contribute to the length.

All of these results suggest that small parts of the $^{m}QQ_8$ $^{m}QQ_8$ are pre-unfolded or extend like a spring.

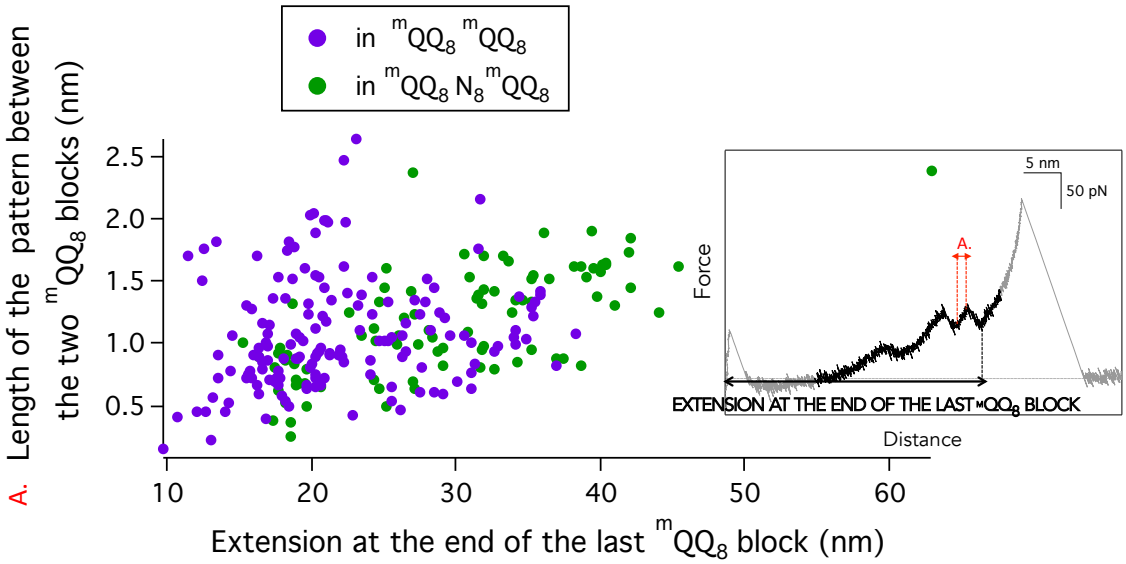

Figure 6.6 Graphic of the lengths of the entropic spring-like pattern between the two quinoline blocks as a function of the final extension value at the end of the last quinoline block unfolding in the diblock and the triblock.

Regarding the forces, in Figure 6.7, we can see that the most probable values of the unfolding forces are around 85 pN for both blocks in both foldamers; this means that the force values to unfold these blocks are identical and are slightly lower than the force to unfold Q17 (hybrid surface - 90 pN). They are thus in good agreement with the previous results and the unfolding force value of Q9 (Chapter 2).

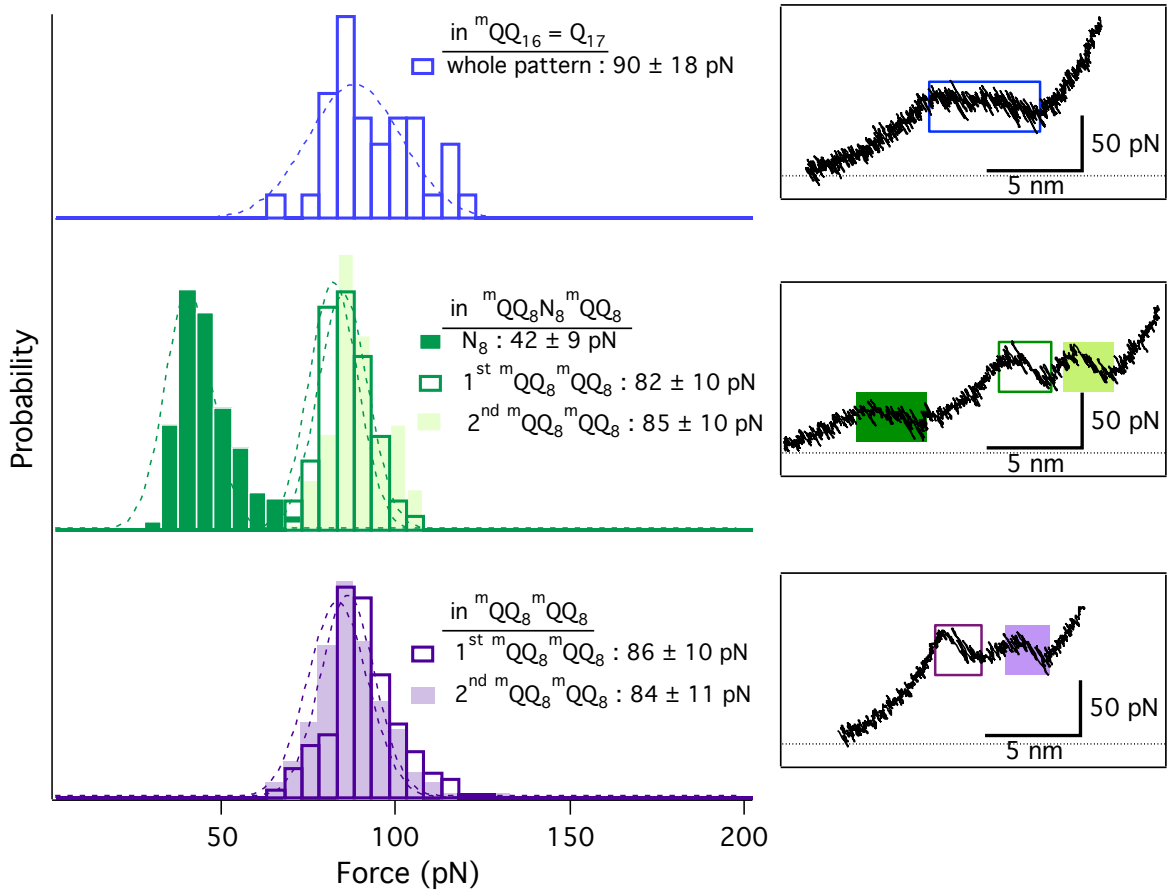

Figure 6.7 Histograms and Gaussian fits of the unfolding forces of different parts of the specific unfolding pattern of the diblock $^{m}QQ_8{}^{m}QQ_8$, the triblock $^{m}QQ_8N_8{}^{m}QQ_8$ and the monoblock Q17. The different parts are explicitly shown on the force-distance curves on the right.

In conclusion, the insertion of the methylene bridge causes the $^{m}QQ_8$ blocks unfold separately around the same force as the Q9 and appear to be partially extended or induces that a part of the quinoline block unfolding takes place through elastic-like stretching. The blocks of quinolines do not seem to be affected by the presence of the N_8, as identical unfolding pattern are identified in both foldamers profiles.

6.2.3.2 Quantitative mechanical properties of the triblock $^{m}QQ_8N_8{}^{m}QQ_8$

In Figure 6.8, we displayed the length distribution of the unfolding pattern of the naphthyridine helix as well as other length measurements constituting the complete pulling profile of the composite triblock.

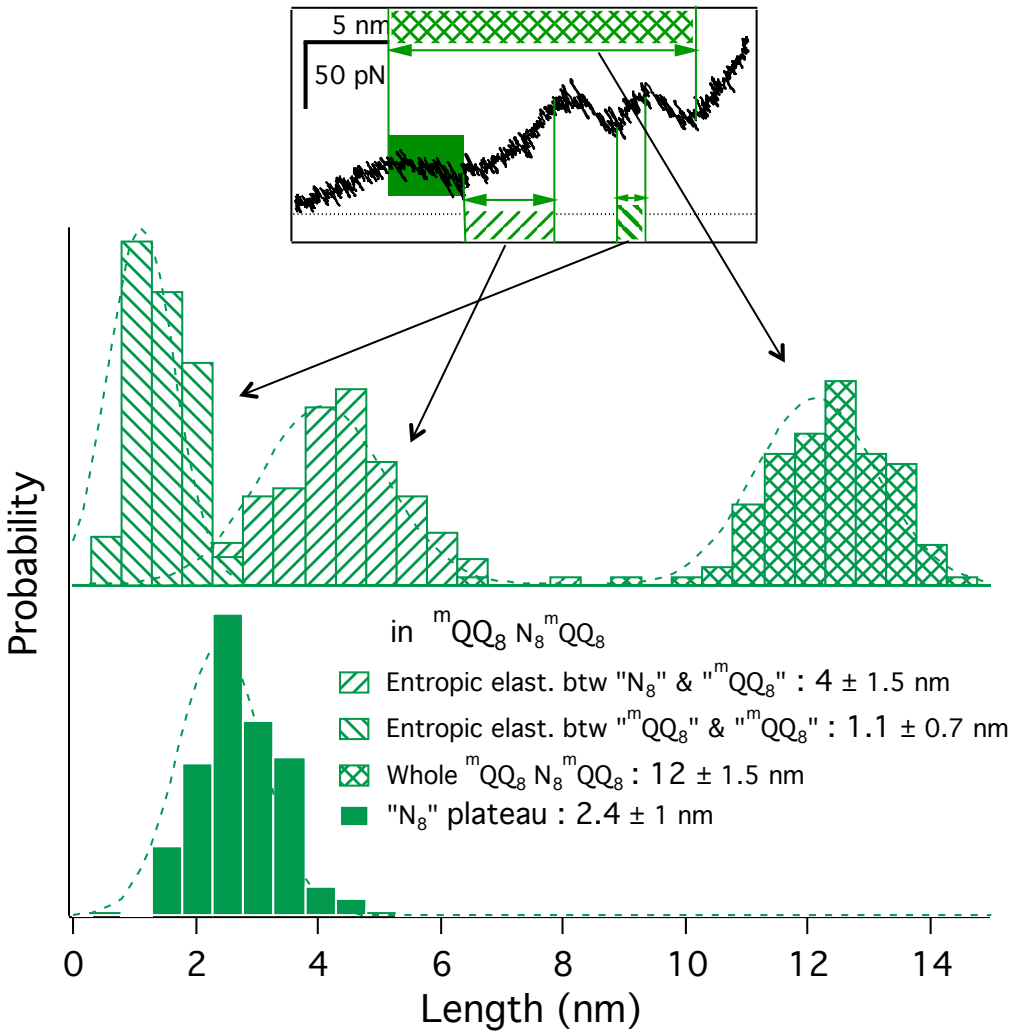

Figure 6.8 Histograms and Gaussian fits of the lengths of different part of the specific unfolding pattern of the triblock $^{m}QQ_8N_8{}^{m}QQ_8$. The different parts are explicitly shown on the force-distance curves on the top insert.

The length distribution of the N_8 unfolding (mostly plateau) is centred at 2.4 nm and presents a large distribution (SD ~50 %). This most probable value does not correspond to the theoretically length difference (5 nm) between the fully folded helical conformation (0.7 nm)[1] and the most extended structure obtained from mechanical simulations (~5.7 nm) shown in Figure 6.9 but is significantly shorter. Only a minority of the measurements reaches the minimum theoretical value. These results do not confirm that in solution the pitch of this helix is the predicted minimum accessible distance between 2 aromatic rings (3.4 Å).[9] Considering the spring-like extended conformation in the triplex (2.1 nm)[1], the length difference with the most extended structure would be 3.6 nm, which is still longer than the experimental measurements.

Analysing the unfolding forces, the measurements showed that the naphthyridine helix unfolds at around half the force (48 pN) required to unfold the long quinoline helices, which are about 90-100 pN (see Figure 6.7). However Q5 is more appropriate to compare

as it also underpins a 2-turns helix as N_8. The unfolding of Q5 is down to 72 pN; so we can expect that longer naphthyridine oligomers would require higher unfolding forces too but it still indicates that naphthyridine helices are less strong than quinoline ones. This weakness was expected from the previous understanding of the naphthyridine oligomers. The naphthyridine oligomers have demonstrated the ability to hybridize in triplexes, whereas the quinoline oligomers form exclusively single and compact helical conformations.[1] This hybridization was associated to a capacity of spontaneous extension, which could be allowed owing to smaller torsional energy for a given extension in wider-diameter helices than in smaller ones.

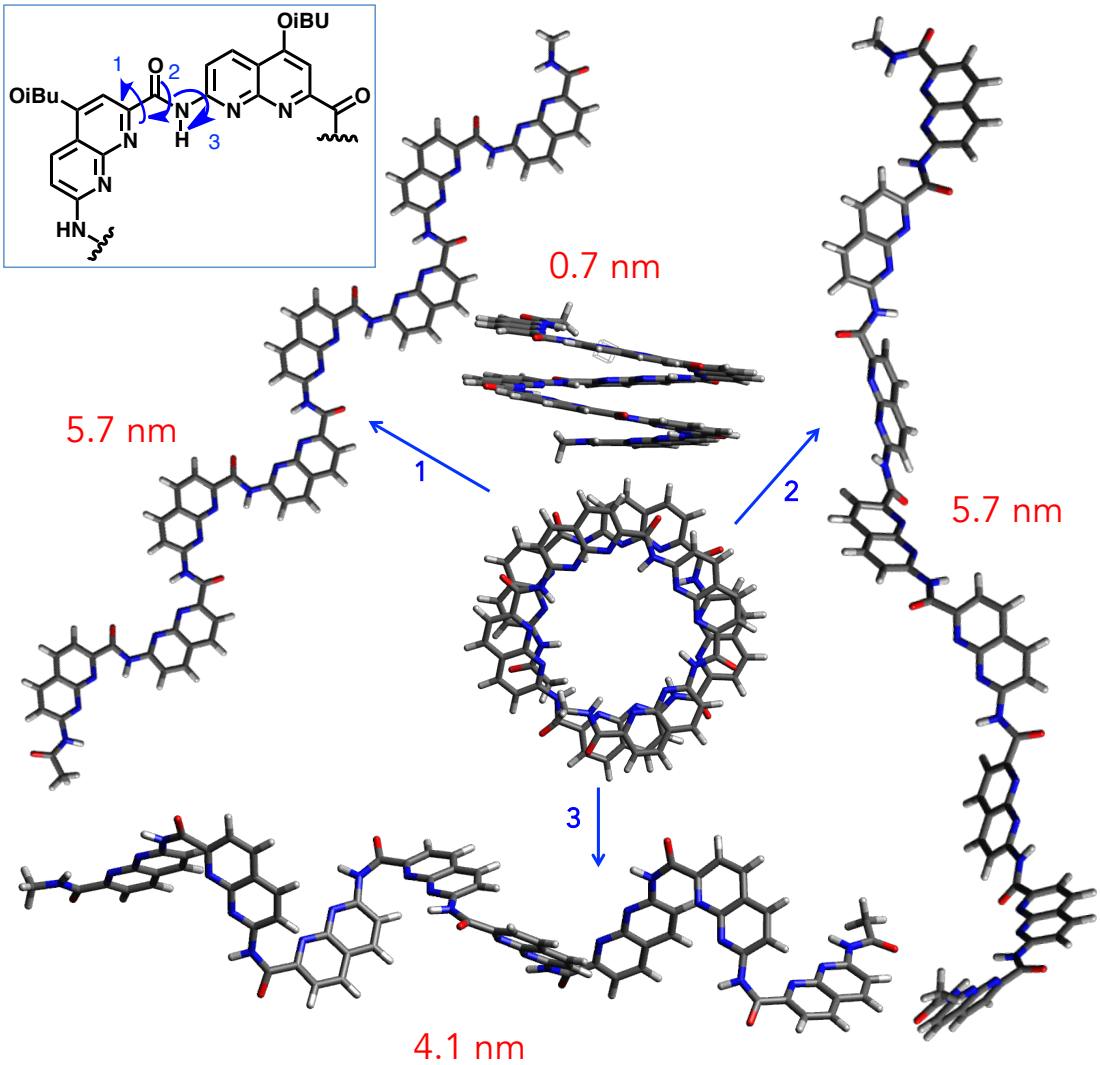

Figure 6.9 Schematic representation of structures obtained after 180°-rotations of rotable bonds in naphthyridine-based octamer and energy minimization (Appendix E.2.3). In the inset, the allowed rotations are displayed and numbered. For each unfolding attempt, the rotation in play is mentioned on the arrow. Lengths between the extremities of the oligomer are written in red below the rotated (stretched) structures. Atoms are colour-coded as carbon in grey, hydrogen in white, oxygen in red and nitrogen in blue.

The weaker unfolding forces and the broad unfolding length distribution shifted to smaller values than expected shed light on the mechanical behaviours of the naphthyridine oligomers in solution. We can indeed suggest that the naphthyridine oligomers present a weak tendency of being fully folded or highly compact in solution at room temperature even when they cannot interact with partners and form their most stable triple helix. This indicates that their structures are likely more flexible than the quinoline backbone. They can spontaneously extend in solution and therefore several partially unfolded/extended conformations may coexist. This behaviour is also in good agreement with the occasionally observed single-rupture unfolding pattern. From these results, we can also suppose that an important part of the unfolding process takes place like an entropic elastic extension, which would be confused with the PEG chain stretching or that there is a conformation transition at really low force, which we could not distinguish from noise. The detected unfolding of the N_8 would then only correspond to the final rotations of the bonds, *e.g.* of the C(O)-Aryl, to yield the longest unfolded conformations (Figure 6.9).

Finally, we could also expect a combination of these suggestions (partially pre-extended in solution, unfolding like an entropic spring, or prior conformation transition at low force) to describe the mechanical properties of the naphthyridine helix in solution.

In parallel, we measured the lengths of the parts exhibiting entropic elasticity behaviours (A in Figure 6.6 and B in Figure 6.10), as well as the full length of the entire foldamer extension (from the beginning of the N_8 to the end of last $^{m}QQ_8$). This latter states the length of the PEG chain between the tip and the foldamer. We drew histograms and it is worth noting that the obtained values present larger distributions (Figure 6.8). Moreover, Figure 6.6 and Figure 6.10 shows that these lengths depend on the attachment point of the PEG with the AFM tip. This highlights the contribution of the PEG in between the oligomer unfoldings. The longer is the PEG chain, the longer is the stretching to reach a given force.

Another point that needs to be mentioned is the good agreement of the full length of the entire foldamer unfolding (~ 12 nm - from the beginning of the N_8 to the end of last $^{m}QQ_8$) and the theoretical value (~ 11.8 nm). This result opposes to the contribution of PEG chain stretching. Given the non-negligible uncertainties of these SMFS-measurements, it may thus be possible that the entropic elastic-like patterns, between the characteristic unfolding patterns of the foldamers, originate from the foldamer unfolding without some PEG stretching contribution. Therefore, this suggests that a major part of the foldamer exhibits entropic elastic unfolding, or in other words that the foldamer extends like a spring.

Further analyses are required to confirm the mechanochemical behaviours of those foldamers.

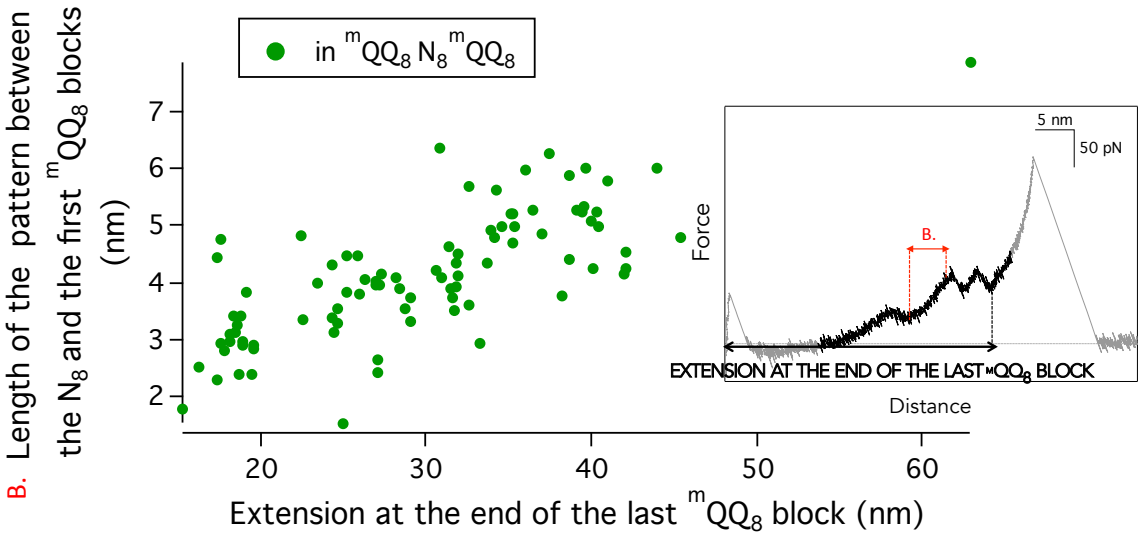

Figure 6.10 Graphic of the lengths of the entropic spring-like pattern between the two quinoline blocks as function of the final extension value at the end of the last quinoline block unfolding in the diblock and the triblock.

In conclusion of this section, we confirmed the weakness of the wider naphthyridine helix compared to the quinoline helices. We suggested that the naphthyridines exhibit partially extended helical conformations in solution even if they do no interact with other naphthyridine oligomers.

Considering the interest of being able to attribute the mechanical properties of a molecular helix according to the macroscopic Hooke's law (eq 1 chapter 5), we can conclude that the analogy seems to be realistic as far as it concerns the influence of the diameter. We indeed observed a decrease of the mechanical resistance with the increase of the helix diameter, which follows the Hooke's law. However, the unfolding mechanisms are unlikely akin.

6.2.4 Pulling-Relaxing experiments on the triblock

Preliminary pulling-relaxing curves could be obtained on $^{m}QQ_8N_8{}^{m}QQ_8$ (Figure 6.11).. In the first cycles, we could unambiguously recognize the pattern of the unfolding and refolding of the N_8 and of the first $^{m}QQ_8$ block. They prove the folding-unfolding reversibility and they demonstrate the ability of the naphthyridine to refold under mechanical load in the time scale of the SMFS experiments. Even if the naphthyridines are characterized by a lower strength than the quinolines, they are robust as they can exert a force on the cantilever against a mechanical load to recover a helical conformation from an extended conformation. On the left side of Figure 6.11, consecutive pulling-relaxing cycles highlight the performance over time. No trace of fatigue could be distinguished. On the right side, the traces are superimposed to confirm the reversibility with minimum hysteresis.

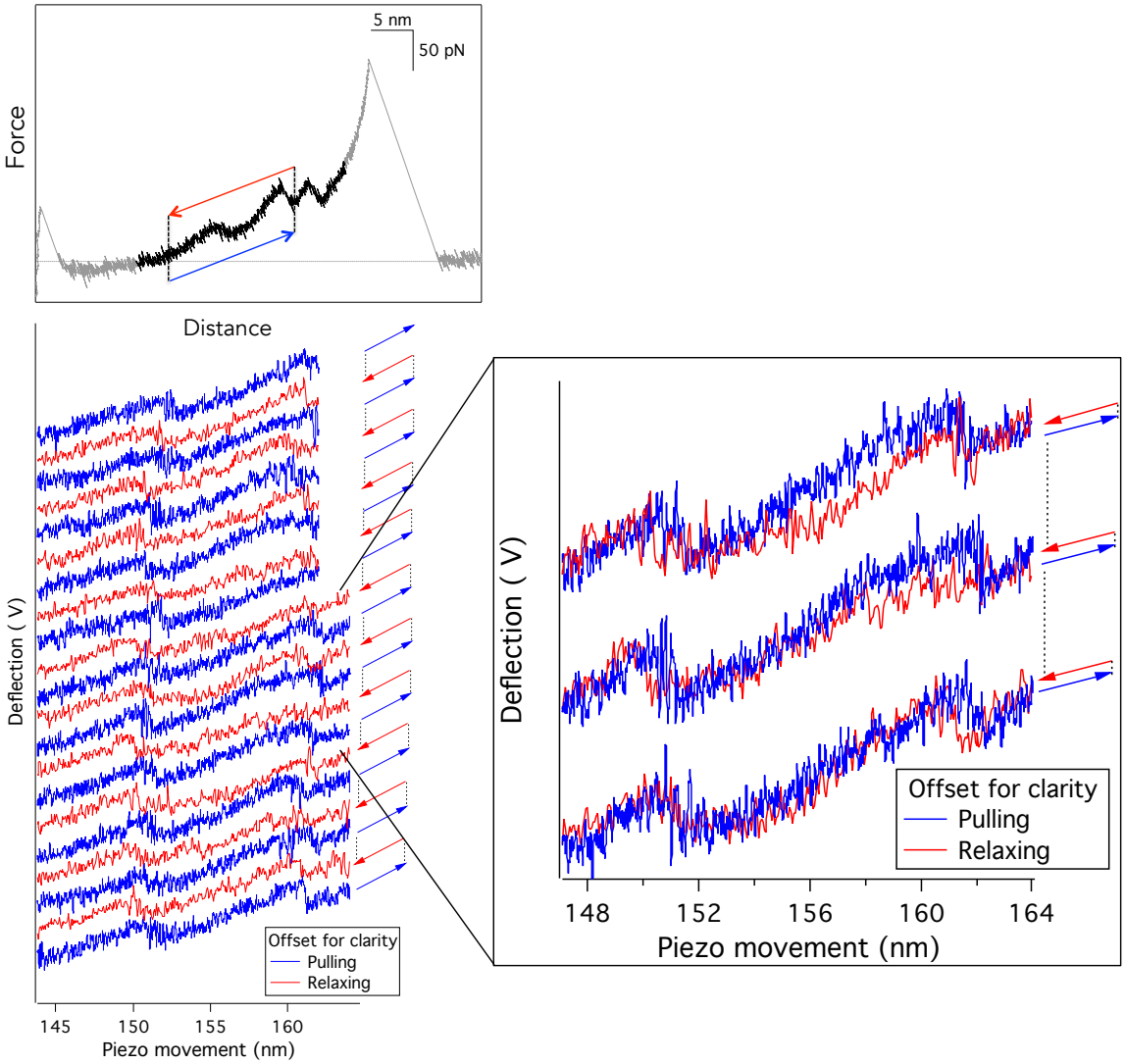

Figure 6.11 Pulling relaxing curves on SH-R-$^{m}QQ_8N_8{}^{m}QQ_8$-PEG in DMF at the pulling and relaxing velocity of 166 nm.s^{-1}.

6.3 Conclusion

The exploratory investigation described in this chapter allows us to identify new mechanical properties of foldamers and to conclude on unprecedented insights into the mechanochemical behaviour.

For SH-R-$^{m}QQ_8{}^{m}QQ_8$-PEG, we observed that the insertion of an aliphatic methylene bridge inside a fully aromatic sequence induces unexpected and substantial consequences. Mainly, this bridge acts as a separator. The aromatic foldamers delimited by this bridge appear mechanically independent and unfold sequentially, like different domains.

For SH-R-$^{m}QQ_8N_8{}^{m}QQ_8$-PEG, we could demonstrate that the molecular enlargement of the diameter of the helix leads to a significant weakening in the mechanical stability of the helical folded structure. The force required to unfold the wider naphthyridine helix is much lower than the unfolding force of the narrower quinoline helix. This difference is remarkable given the resemblance of the intramolecular interactions responsible for the folding. The lowering of the mechanical stability is in agreement with the study on hybridization energetics. We could emphasize the role of the torsional angle. Therefore, we can suggest that the more units are comprised in a turn, the less is the torsion, and the less strong is the helical structure. This proves the capacity of tuning the force by varying the diameter of the helix. Furthermore, the unfolding patterns are shorter than expected for a fully folded helix. This observation suggests a partially pre-unfolded or rather pre-extended conformation in solution, which is in agreement with a decrease in strength of the compact helical conformation. Nevertheless, the helical folding seems to be robust as relaxing curves demonstrated the ability of the oligomers to exert a force against the mechanical load to refold. It would be highly interesting to investigate longer naphthyridine oligomers to analyse the unfolding force evolution with additional naphthyridine units and determine a possible force limit as observed in quinoline helices. These results would also provide more insights into the cooperativity in these helical molecular systems.

Worth noting, we identified the independence of the different mechanophores in a linked molecular system. Despite the fact that the naphthyridine sequence was embedded into quinoline blocks, once it is unfolded, it does not influence the subsequent unfolding of the others parts.

Moreover, the roles of the stacking and of the torsional angle in the mechanical properties of the foldamers have been reinforced.

Altogether, these results provided highly interesting information for the single molecule mechanics field as well as for the bottom up design of molecular devices. Indeed, we identified some useful concepts for creating molecular systems with specific mechanical functions. We suggested that it is possible to provide controlled extension at different force levels. A foldamer with several blocks possessing different mechanical properties will unfold starting with the weakest blocks to the strongest blocks independently on the location in the molecule. It is not necessarily the nearest helix from the AFM tip which unfolds first.

This study was only preliminary and deserves further investigation and confirmations. It would be highly interesting to probe the effects of some guest-molecules, for instance pyridine or short naphthyridine oligomers, which are known to interact with the naphthyridines oligomers.

6.4 References

1. Ferrand, Y., Kendhale, A. M., Garric, J., Kauffmann, B. & Huc, I. Parallel and Antiparallel Triple Helices of Naphthyridine Oligoamides. *Angew. Chemie Int. Ed.* **49,** 1778–1781 (2010).
2. Berni, E. *et al.* Assessing the mechanical properties of a molecular spring. *Chemistry* **13,** 8463–9 (2007).
3. Delsuc, N., Poniman, L., Léger, J.-M. & Huc, I. Assessing the folding propensity of aliphatic units within helical aromatic oligoamide foldamers. *Tetrahedron* **68,** 4464–4469 (2012).
4. Delsuc, N., Godde, F., Kauffmann, B., Léger, J.-M. & Huc, I. The Herringbone Helix: A Noncanonical Folding in Aromatic−Aliphatic Peptides. *J. Am. Chem. Soc.* **129,** 11348–11349 (2007).
5. Hunter, C. a, Spitaleri, A. & Tomas, S. Tailbiter: a new amide foldamer. *Chem. Commun.* 3691 (2005). doi:10.1039/b506093a
6. Hoffmann, T. & Dougan, L. Single molecule force spectroscopy using polyproteins. *Chem. Soc. Rev.* **41,** 4781–4796 (2012).
7. Stevenson, R. & De Bo, G. Controlling Reactivity by Geometry in Retro-Diels-Alder Reactions under Tension. *J. Am. Chem. Soc.* **139,** 16768–16771 (2017).
8. Fantner, G. E. *et al.* Sacrificial bonds and hidden length: unraveling molecular mesostructures in tough materials. *Biophys. J.* **90,** 1411–8 (2006).
9. Huc, I. Aromatic Oligoamide Foldamers. *European J. Org. Chem.* **2004,** 17–29 (2004).

Conclusions
&
Prospects

Conclusions & Prospects

This thesis is the result of a synergistic approach to contribute to the challenge of designing molecular systems with predictable mechanical properties through the study of the influences of the chemical functions and secondary structure on the mechanical properties. We combined the synthesis of unconventional foldamers and their molecular mechanical characterization by AFM-based single-molecule force spectroscopy (SMFS). Using this technique we have investigated the mechanical and dynamical performances of several foldamers, and obtained detailed information on their mechanochemical behaviours.

Aromatic oligoamide foldamers are a novel class of folded oligomers belonging to the abiotic category. They extend the building block alphabet to tackle the challenge of bio-mimicry and the race for emergent molecular applications. Aromatic oligoamide foldamers were selected for this study because of their predictable three-dimensional structures making them promising candidates for predictable functional molecules. We worked on three different kinds of helical foldamers to investigate the influence of the chemical architecture on the mechanical properties at the level of the single molecule. We started our investigations with pure quinoline oligomers, which are known to create compact helices. Foldamers of different sizes were studied: 5-, 9-,17- & 33-mers. Based on the SMFS results obtained on these foldamers, we continued to design two other foldamers made up of two quinoline nonamers embedding in between either a central naphthyridine octamer or a methylene bridge. The naphthyridine octamer is presumed to yield a helix with a wider diameter, while the methylene bridge ruptures the conjugation of the two quinoline-based nonamers.

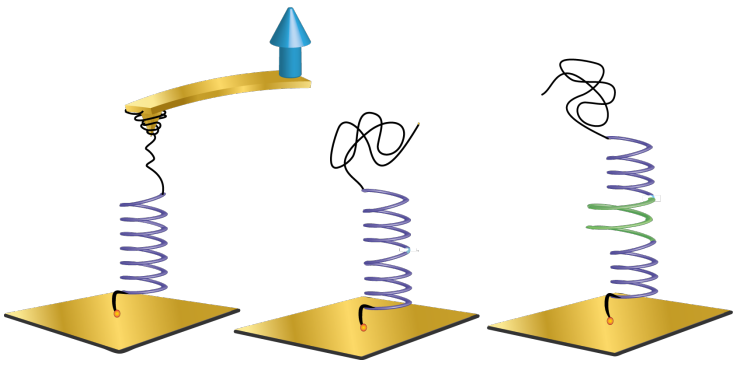

Owing to the specific design of these foldamers for AFM studies, *i.e.* with thiol and PEG functionalities at the ends of the foldamers, we successfully caught and stretched the foldamers between an AFM tip and the substrate. The stretching experiments revealed specific unfolding force-distance curves, which could be interpreted and which provided unprecedented structural, mechanical and dynamical insights at the scale of the single molecule.

The first study of pure quinoline-based foldamers of different sizes (5-, 9-, 17-, 33-mer) was performed in N,N-dimethylformamide. The force-distance profiles were measured for all the foldamers and revealed consistent behaviours. Their typical force-distance profile

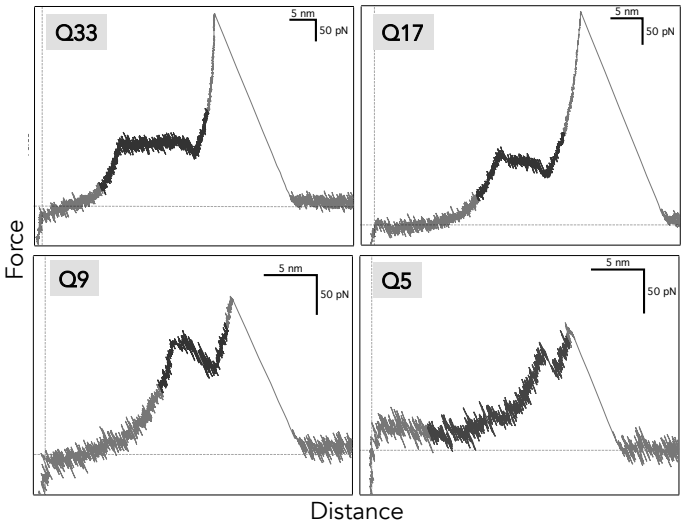

could be divided into four distinguishable steps, including the low-force unravelling of the PEG random coil, the quinoline oligomer unfolding and the overstretching of the whole foldamer. The unfolding of the quinoline oligomers could be easily identified. Deviating from the trace of the PEG random coil unravelling, a long constant-force plateau ending with a decreasing-force feature could be observed for the longest foldamers.

For the shortest foldamer, the decreasing-force feature became major while observing only a minor plateau. The total length of both these features is proportional to the number of quinoline units contained in the oligomers. Furthermore, the interpretations of these features are in good agreement with the unfolding of the helices. Consequently, these features could unambiguously be linked to the unfolding of the molecular helix. The plateau pattern was associated to the stepwise breakings of identical intramolecular interactions. This indicated that the helical quinoline-based foldamers do not elongate like a spring but by numerous and subsequent intermediate states with partial helical conformations. The decreasing-force feature at the end of the plateau being of the same length for all foldamer sizes, it evidenced a decrease in strength for the last 5-6 remaining folded units. These 5-6 units correspond to two turns of the helix. This shed light on the cooperativity in the helical folding and we associated the decreasing-force feature to the nucleation segment of a reinforced helical structure. Indeed, a quinoline oligomer smaller than 6 units still forms a helical, but likely weaker, structure. With the addition of units, π-stacking between stacked units probably reinforces the structure.

By investigating the total length of the unfolding of the oligomers, we could identify the final unfolded conformation. With the signal transformation into contour length evolutions, we were able to discuss the details of the unfolding mechanism. An unfolding step would consist in the rotation of two Cα-C(O) bonds simultaneously. Given the similar energy of the interactions along the foldamer helix and using only force-distance measurements, we could however not determine from which side(s) of the helix the unfolding takes place.

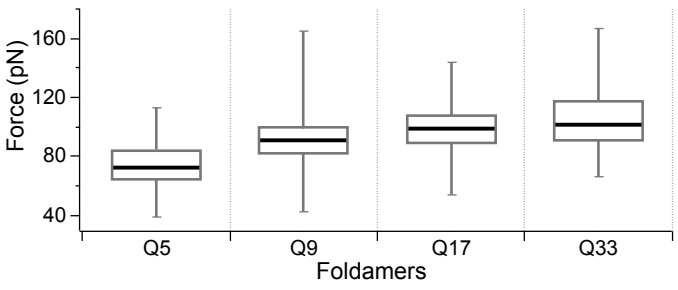

The analysis of the unfolding forces also highlighted the cooperativity of the interactions. From smallest to longest oligomers,

the unfolding force did not increase linearly. The unfolding force reached a limit for foldamers containing between 9 and 17 units. In other words it indicated that the addition of a unit reinforces the strength of the interaction until a given extent. The unfolding force values were found to be around 95 pN, which also highlights the strength of the system.

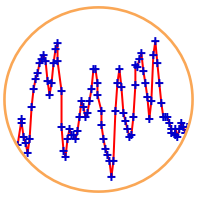

This strength was confirmed by three other remarkable observations. First, we observed hopping events on every force-distance curve independently of the loading rate and the solvent. These fluctuations between intermediate folded and unfolded states indicate that during the pulling, the oligoamide foldamer was able to pull on the AFM tip in the opposite direction to the pulling force to re-create broken interactions and to refold against the mechanical load.

Secondly, the unfolding force of the quinoline foldamer demonstrated loading rate-independence over more than three orders of magnitude. Jointly with the hopping observations, this indicated that the unfolding process occurs under equilibrium conditions up to the loading rate of at least 5.10^4 pN.s^{-1}. The fast refolding dynamics evidenced the robustness of the system. We measured that the helical nucleation segment can refold faster than 40 µs under load.

Last but not least, the quinoline oligomers exhibited full folding reversibility without hysteresis on the time scale of the experiment and without evidence of fatigue. This observation makes these synthetic foldamers truly elastic helices. The study of the influence of the loading rates, as well as the pulling-relaxing experiments also allowed us to estimate the free energy values, within the limitations and the validity conditions of the theories. On the one hand, the dynamical force spectroscopy experiments provided a measurement of the free energy of the groups of interactions which break during an unfolding step. The results evidenced the interplay of non-covalent interactions with the cooperative reinforcement for longer foldamers (14 to 28 kcal.mol^{-1}). They were in good agreement with previous measurements of the energy barriers of handedness inversions.[1] On the other hand, the pulling-relaxing experiments allowed us to measure the work (i) needed to unfold and (ii) performed by the molecule to refold. Both were found to be equal (144 kcal.mol^{-1} or 10 kcal (mol.nm)$^{-1}$), which indicated that no energy was dissipated during the unfolding process.

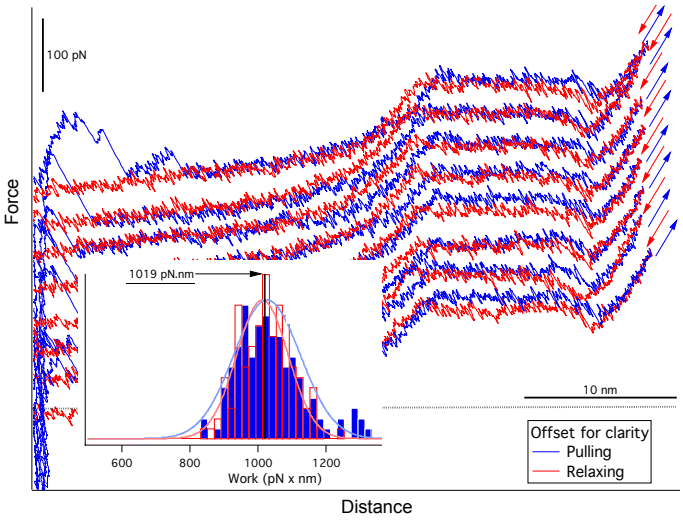

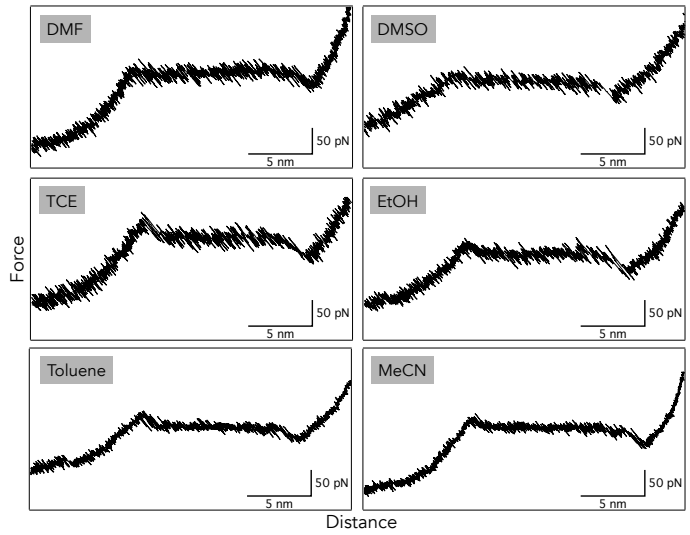

The solvent investigation allowed us to confirm the high strength of the helical structure in varied environments. No solvent was able to break the intramolecular interactions of the quinoline-based foldamers. Futhemore, we were able to highlight a modulation of the interaction strengths by solvents. We showed that solvents possessing strong H-donor or H-acceptor properties and π-stacking abilities weaken the interactions responsible of the mechanical properties of these foldamers. Moreover we observed, in apolar solvents, that a higher-force unfolding trigger is needed to start unfolding.

In summary, for quinoline-based foldamers, we were able to investigate the size dependency of the extension length (proportionally tunable) and of the unfolding force (selectable until a certain limit). We highlighted the great robustness of the quinoline-based foldamers. We attributed their remarkable mechanical and dynamical performances to the contribution of the many interactions comprised in the quinoline-based foldamers, which are in close vicinity. Indeed, we could suggest that, additionally to the π-stacking between stacked units, the interactions between adjacent units lock the conformation in the folded state enthalpically and entropically, which results in highly robust helices. This relationship represents an interesting mechanochemical insight for the prediction of functional molecular systems.

Given the properties of these foldamers, one could imagine applications such as mechanical switches, as energy storage systems or as strong building blocks for positioning persistently a chemical group with atomic precision into a complex molecular assembly (mimicking active site of proteins).

Upon modification of the quinoline-based foldamers with the insertion of a naphthyridine octamer, we observed adequately the influence of an increase of the diameter of the helix. The chemical modification of quinoline with naphthyridine units and the change in the relative positions of amine and acid substituents induced a significant weakening in the interaction strength. However, the helical structure was confirmed and its robustness was

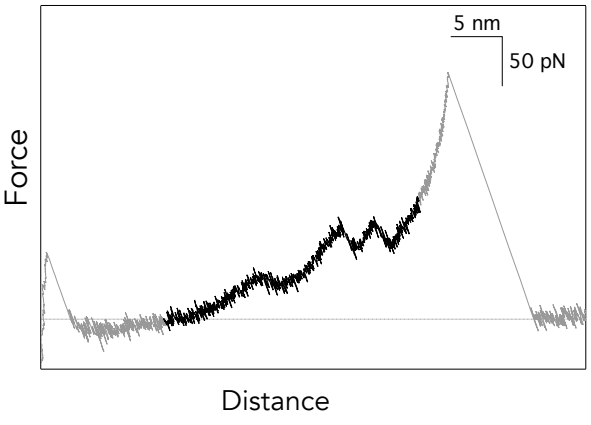

demonstrated. The lower strength of the helical structure, compared to the quinoline helix, could be interpreted from the significantly lower unfolding force (45 pN), as well as the apparently shorter plateaus than expected, which indicate less compact folded structures. Making the diameter wider provides more degrees of freedom than in a highly compact helix. A small rotation of each unit can induce a larger spring-like extension of the helix (entropy gain) in a helix containing more units per turn. Nevertheless, the naphthyridine helix is robust, as evidenced from the refolding traces in pulling-relaxing curves, which exhibit instantaneous refolding of the helix after stretching.

The insertion of a methylene bridge in between pure aromatic quinoline oligomers yielded an unexpected large modification in the mechanical behaviour. The pulling traces of the modified quinoline 18-mer exhibited a separate and sequential unfolding of the two blocks. The insertion of the methylene bridge seems to result in the interruption of the quinoline-blocks interactions. We proposed two hypotheses to explain that the foldamer behaves as two independent blocks under mechanical load: (i) the aliphatic methylene bridge spatially separate the two nonamers away from each other, which in turn prevents the mutual reinforcing interactions or (ii) geometrical effects, due to the methylene junction, modulate the transmission of the force.

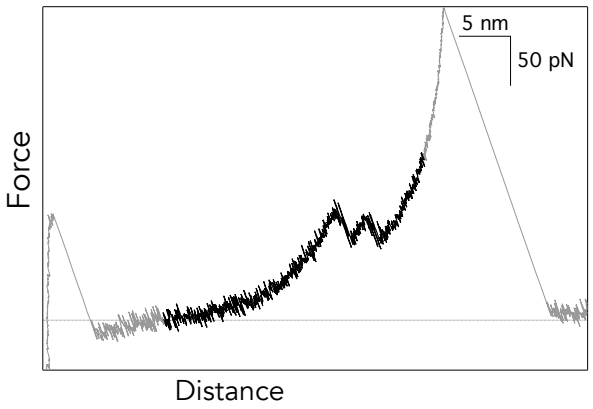

In summary, these exploratory investigations on the mechanochemical properties of foldamers by single-molecule force spectroscopy provided rich fingerprint-like unfolding and refolding traces, which allowed us to identify characteristic mechanical behaviours of very well-defined molecular systems in solution at the molecular scale. These results highlighted the adequacy of AFM-SMFS for deciphering information complementary to traditional ensemble techniques and for characterizing small folded molecular systems undergoing mechanical loading.

We also proved the great potential of this class of foldamers. We confirmed that the implementation of chemical modifications in the foldamer sequence is synthetically manageable and that these modifications clearly and efficiently induce mechanical variations. For example we identified that the limitation of degree of freedom increases the unfolding force and that conjugated aromatics are much less compliant than aliphatic linkages. Therefore their high tunability is interesting for applications with mechanical specifications. The complete understanding of the folding propensity and of the mechanical functions that arise from the secondary structure will allow designing, prior to synthesis, folded oligomers with shape and functions adapted for the desired applications.

With continuous collaborations between SMFS and supra-molecular synthesis, progress can be made to endow molecules with functions, allowing us to imagine creating libraries of functional molecules that can be assembled bottom-up to create molecular devices.

Moreover, we can also envisage the investigation of more complex molecular systems such as proteins. Indeed proteins are assemblies of several parts including specific structures such as α-helices or helical coils. In a few cases, plateaus were observed in the unfolding pattern of such helices, but in numerous other cases, this characteristic unfolding pattern could not be perceived in the large unfolding traces. Given the results on our model foldamer, one could now look for plateaus for the unfolding of α-helices or helical coils in natural biomolecules. They may indeed be limited to only subtle features as structures in nature are more delicate. In general, experiments on model systems, such as foldamers, could also help to gain more details and confident interpretations of AFM-SMFS data on large biomolecule systems.

Finally, the quinoline-based foldamers present great qualities as force-calibrating systems. Indeed, their performances under load were strong owing to the highly stable conformation, which were also reproducible in a large variety of solvents.

As prospects of this thesis, it would be incredibly interesting to perform the experiments with cantilevers of different spring constant and to conduct a round robin interlaboratory trial to establish the quinoline-based foldamers as internal force calibrating references. The quinoline oligomers could be covalently coupled to a molecule of interest or could be grafted on the substrate in parallel with the molecule of interest. The 17-mer seems to be the ideal calibrating molecule as it is the best compromise between an unmistakable unfolding fingerprint and the ease of synthesis. This approach has been already introduced for investigating small biological sample in aqueous environments.[2–6] The well-known globular I27 domains of titin have been used as internal force reference or fingerprint reference. Owing to the protein engineering, a series of I27 domains can be included in the protein sequence and their unfolding pattern can be recognized and used for direct comparison.

From this exploratory study, many other investigations could be performed to further understand new mechanochemical parameters and to further characterize this novel class of foldamers.

Force-clamp experiments on quinoline-based foldamers should be the next step to obtain information on the foldamers' kinetics. The extremely fast dynamics of these synthetic helices exceeded the current performances of the AFM-based SMFS techniques, which prevented us from being able to conclude on quantitative kinetic values. Here, force-clamp experiments could constitute an alternative.

Then it would be interesting to directly compare the results to natural analogues. For this purpose, experiments should be performed in water. Nevertheless special care has to be given to check the solubility. At the scale of the single molecule and anchored on substrate, aggregation of molecules does not necessarily occur as in batch solution. We can imagine that the molecules collapse or that a cage of solvent forms around the molecule. The impact of such phenomenon is unknown.
As already proposed in chapter 4, the strong H-donor hexafluoropropan-2-ol or perfluoro-tert-butanol could also be tested as they are known to compete with the H-bonds in biopolymers and solubilize *e.g.* polyamides.
Concerning the naphthyridine foldamers, it would also be interesting to test firstly the pyridine as it was highlighted to interact differently than the other solvents with the naphthyridine oligomers.[7] In pyridine, the single-stranded helix appeared to be favourable, while in other solvents, we observed exclusively the triple helices.[7] Secondly, it would also be interesting to investigate the formation of the triple helix. Many complementary parameters could be assessed with SMFS experiments. The influence in the unfolding force, in the spring properties, but also assembly formation constant and kinetics could be probed.

Finally, we highlighted the relationship between the helix diameter and the unfolding force. However, it is intriguing to verify the origin of this property. It would be interesting to synthetize a helix with 4 units per turn with a similar diameter than the quinoline-based foldamer or a helix with a wider diameter but with fewer units in order to compare the results and to explain the weakening in force with either the diameter or the number of bonds in a turn that can undergo torsion.

References

1. Delsuc, N. *et al.* Kinetics of helix-handedness inversion: Folding and unfolding in aromatic amide oligomers. *ChemPhysChem* **9,** 1882–1890 (2008).
2. Scholl, Z. N., Li, Q. & Marszalek, P. E. Single molecule mechanical manipulation for studying biological properties of proteins, DNA, and sugars. *Wiley Interdiscip. Rev. Nanomedicine Nanobiotechnology* **6,** 211–229 (2014).
3. CarrionVazquez, M. *et al.* Mechanical design of proteins-studied by single-molecule force spectroscopy and protein engineering. *Prog Biophys Mol Biol* **74,** 63–91 (2000).
4. Dougan, L. Rapid and Robust Polyprotein Production Facilitates Single-Molecule Mechanical Characterization of β - Barrel Assembly Machinery Polypeptide. (2015).
5. Ferreon, A. C. M., Moran, C. R., Gambin, Y. & Deniz, A. a. Single-molecule fluorescence studies of intrinsically disordered proteins. *Methods Enzymol.* **472,** 179–204 (2010).
6. Wolny, M. *et al.* Stable Single α-Helices Are Constant Force Springs in Proteins. *J. Biol. Chem.* **289,** 27825–35 (2014).
7. Ferrand, Y., Kendhale, A. M., Garric, J., Kauffmann, B. & Huc, I. Parallel and Antiparallel Triple Helices of Naphthyridine Oligoamides. *Angew. Chemie Int. Ed.* **49,** 1778–1781 (2010).

Résumé de la thèse en français

La nature a développé le repliement d'oligomères pour contrôler la conformation de sa machinerie moléculaire qui lui permet de réaliser des tâches essentielles à la vie telles que la catalyse enzymatique, le stockage d'information, la duplication des acides nucléiques, la génération de force, le transport de molécules,... Étant donné que les repliements des biomolécules régulent leurs conformations et leurs fonctions, nous pouvons imaginer qu'en synthétisant des molécules et macromolécules adoptant des structures repliées mimant celles de la nature, un vaste éventail de matériaux fonctionnels serait potentiellement accessible. Durant les vingt dernières années, la recherche sur les foldamères, des oligomères synthétiques capables d'adopter des conformations ressemblant aux motifs des biopolymères naturels, a été très active. Les recherches sur les foldamères visent à reproduire et à étendre les structures et les fonctions de ces bio-opolymères en utilisant de nouvelles briques élémentaires qu'elles soient aliphatiques ou aromatiques. La classe des foldamères d'oligoamides aromatiques présente un très grand potentiel dans ce domaine. Les progrès récents ont montré que la synthèse chimique par étape et le design moléculaire basé sur un squelette oligoamide aromatique permettaient de produire des architectures moléculaires repliées bien définies et prévisibles. L'assemblage de cette nouvelle sorte de briques permet de mimer toutes les structures secondaires de la nature ainsi que de nouvelles structures n'ayant pas de contrepartie naturelle. Le grand mérite des ces foldamères réside dans la modularité d'assemblage de différentes unités monomériques aromatiques et dans la prédictibilité de leur repliement avant la synthèse. Dès le début de ces recherches, un intérêt particulier s'est tourné vers les structures hélicoïdales dû à leur ubiquité dans la nature. Depuis lors, les structures de ces molécules hélicoïdales ont été abondamment caractérisées à l'état solide par cristallographie des rayons X. Par contre, leurs comportements dynamiques en solution, ainsi que leurs propriétés mécano-chimiques, sont très peu connus à ce jour.

C’est de cette problématique qu’a découlé le projet de cette thèse. Nous avons étudié des molécules synthétiques hélicoïdales basées sur un squelette oligoamide aromatique par spectroscopie de force sur molécule unique (SMFS) en se servant d'un microscopie à force atomique (AFM - atomic force microscopy), afin d'obtenir des informations détaillées sur leur dynamique en solution et sur leur propriétés mécano-chimiques.

La spectroscopie de force sur molécule unique à l'aide d'un AFM (AFM-SMFS) est une technique moderne qui a déjà prouvé son efficacité lors de plusieurs études de comportements dynamiques de molécules repliées. Durant ces 15 dernières années, la spectroscopie de force sur molécule unique (basée sur des pinces optiques ou l'AFM) est devenue incontournable pour obtenir des informations détaillées sur la manière dont les biomolécules naturelles se replient et opèrent à l'échelle de la molécule unique. Cette technique est reconnue pour sonder des forces mécaniques intramoléculaires de l'ordre du piconewton (pN) avec une résolution sous-nanométrique, permettant de comprendre les processus intramoléculaires.

Concrètement, la thèse s'est déroulée en trois grandes phases. Pour commencer nous avons réalisé des études détaillées de spectroscopie de force sur des foldamères de plusieurs

tailles constitués d'une répétition de quinoléines (8 aminoquinoléine-2-carboxylate). Ces foldamères se replient en hélice grâce à des interactions intramoléculaires électrostatiques et à la conjugaison des cycles aromatiques et des liaisons amides. Alors que la conjugaison des cycles aromatiques a tendance à maintenir la molécule plane, les ponts hydrogène (en vert, Figure 1) et les répulsions électrostatiques (en rouge, Figure 1) provoquent une courbure de la molécule, ce qui induit la formation d'hélices avec 2,5 unités quinoléines par tour. Ces foldamères avaient été préalablement synthétisés et préparés pour des mesures de spectroscopie de force par le Dr. Xuesong Li.[1] Ensuite, avec les résultats de spectroscopie de force obtenus pour ces foldamères, nous avons imaginé et synthétisé d'autres foldamères hélicoïdaux afin d'explorer les effets de certaines modifications chimiques de la séquence de quinoléines sur les propriétés mécaniques. Et enfin, nous avons fait une étude exploratrice de ces derniers foldamères modifiés.

Les expériences de spectroscopie de force par AFM consistent en des cycles d'approche–retrait verticaux d'un levier microscopique muni d'une pointe nanoscopique à différents endroits d'une surface où sont greffées des molécules d'intérêt. Les molécules sont dispersées sur la surface de façon à pouvoir attraper une seule molécule à la fois. L'étirement et le dépliement d'une molécule sont mesurés grâce à la déflection du levier, qui est suivie par un laser, en fonction du déplacement vertical du levier. Ce signal peut alors être transformé en 'force' en fonction de la 'distance entre le pointe et la surface' grâce à la constante de raideur du levier.
Afin de pouvoir réaliser des expériences de spectroscopie de force sur les foldamères, ceux-ci ont été fonctionnalisés en leurs extrémités par un groupement thiol à une extrémité et une chaine de polyéthylène glycol (PEG) à l'autre extrémité. Ces fonctionnalisations permettent d'un coté de greffer fermement des foldamères sur une surface dorée (mince couche d'or sur silicium), grâce à la forte interaction or-soufre et de l'autre coté d'accrocher réversiblement la chaine de PEG à la pointe du levier d'AFM et de déplier entièrement le foldamère. Un schéma représentatif du système est présenté à la Figure 1.

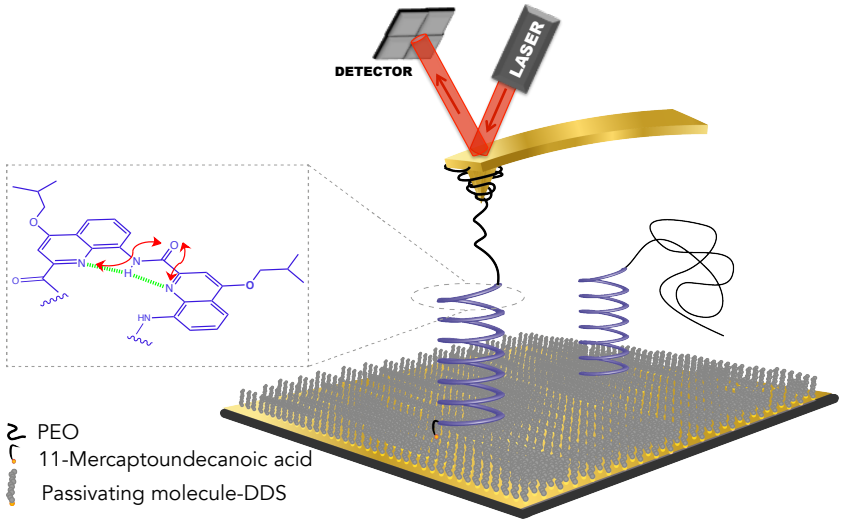

Figure 1 Schéma représentatif (hors échelle) d'une expérience de spectroscopie de force sur molécule unique avec un AFM. Sur une surface d'or sont greffés un foldamère de quinoléines (du synthon 8 aminoquinoline-2-carboxylate) et d'un agent de passivation (sulfure de didodécyle). La déflection du levier est suivie grâce à la réflexion d'un laser sur le levier vers une photodiode.

Mis en solution dans le diméthylformamide (DMF), les foldamères greffés et composés de 33, 17, 9 et 5 unités quinoléines, appelés respectivement Q33, Q17, Q9 et Q5, ont été étudiés séparément tout en gardant les mêmes paramètres expérimentaux (vitesse d'approche, vitesse de retrait, temps d'attente au contact, type de levier). Les courbes de force-distance de dépliement obtenues lors des expériences de spectroscopie de force standard sur ces foldamères de quinoléines de différentes tailles ont montré des motifs très reproductibles et cohérents en fonction de la taille du foldamère (Figure 2). On constate que chaque profil force-distance peut être divisé en quatre parties, excepté pour le pentamère (Q5) en uniquement trois parties. Le début du profil (plage vert pâle) consiste en un dépliement élastique contraint par la perte d'entropie conformationnelle de la chaine de PEG. A partir d'une certaine force, l'allure du profil change complètement et montre un plateau à force constante (plage orange). Après une certaine longueur de plateau qui varie en fonction de la taille du foldamère, on peut observer une diminution de la force, progressive ou soudaine, sur une faible distance (plage rouge). Finalement la molécule dépliée est à nouveau étirée jusqu'au détachement de celle-ci de la pointe (plage vert foncé). Le levier, n'étant plus sous tension, revient à sa position d'équilibre à la ligne de base (plage blanche).

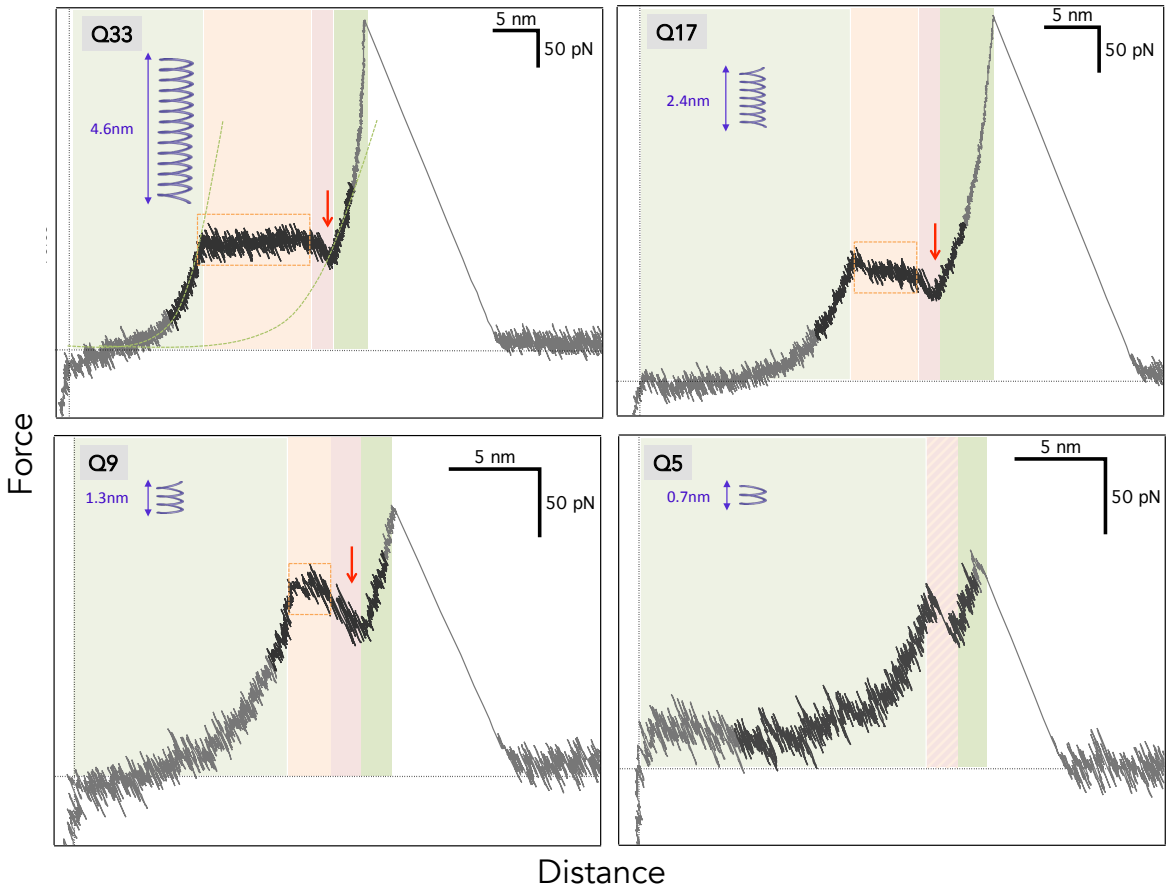

Figure 2 Courbe de force-distance caractéristique pour chaque taille de foldamère (représentée en haut à gauche de chaque graphique). Les différents comportements mécaniques sont mis en évidence avec les couleurs. Le plateau à force constante est entouré d'un rectangle et le segment présentant une diminution en force est marqué d'une flèche.

La partie centrale des profils force-distance, composée du plateau et de l'affaiblissement en force (plages orange et rouge), représente le motif caractéristique du dépliement des foldamères. Une analyse plus détaillée des motifs de dépliement des différents systèmes a permis de mettre en évidence la disparition progressive du plateau aux dépens de la partie témoignant une diminution de la force pour des tailles décroissantes de foldamères. Le plateau suggère un réarrangement conformationnel progressif par la rupture séquentielle de mêmes groupes d'interactions intramoléculaires le long de toute l'hélice du foldamère. Dans cette partie du profil, cette observation indique que l'hélice moléculaire ne se déplie pas comme un ressort mais par segment d'hélice. La partie du motif de dépliement après le plateau marque un affaiblissement de la force d'interaction au sein de l'hélice, révélant que le dépliement devient plus facile à la fin. Tout cela reflète une première évidence de la coopérativité des interactions intramoléculaires impliquées dans l'hélice. En effet, comme très bien expliqué par Hill, Moore et leur collègues[2], au début de la conversion d'une chaine sous forme de pelote statistique en forme d'hélice, il y a une grande perte d'énergie entropique, dû à la contrainte structurale des premiers monomères sous une conformation hélicoïdale. La nucléation de l'hélice n'est donc pas un processus énergétiquement favorable, en d'autres mots, la structure hélicoïdale n'est pas encore bien stabilisée au début de sa formation. La conversion ne devient énergétiquement favorable que lorsque le gain d'énergie enthalpique des interactions stabilisant la structure contrebalance et dépasse la perte entropique. Dans notre cas, ce phénomène semble se refléter à la fin du dépliement quand il ne reste plus que quelques unités quinoléine sous forme d'hélice. La force nécessaire pour déplier les dernières unités diminue car la conformation hélicoïdale est moins énergétiquement favorable. Cette observation est discutée plus loin, appuyée par les mesures quantitatives.

En ce qui concerne les mesures quantitatives des longueurs des motifs de dépliement des foldamères, l'analyse des histogrammes de longueurs du motif global du dépliement du foldamère (orange et rouge), représentée à la Figure 3 (droite), montre que chaque distribution est gaussienne et centrée autour d'une seule valeur. Les longueurs les plus probables obtenues sont cohérentes entre elles et directement proportionnelles au nombre d'unités quinoléines du foldamère étiré. Ces données dévoilent deux informations importantes. Premièrement une distribution normale indique que le foldamère est toujours étiré de la même manière, à partir du même état initial vers le même état final. Ceci implique qu'il n'y a principalement en solution qu'une seule conformation stable repliée. Deuxièmement, le fait que la longueur soit proportionnelle au nombre d'unités signifie que le mécanisme de dépliement est certainement identique pour chaque taille de foldamère. Par modélisation moléculaire, nous avons obtenu une structure dépliée dont la longueur coïncide avec la somme de l'extension mesurée par l'expérience et de la longueur de la conformation repliée obtenue par RX (Figure 4). Cette structure est obtenue en exerçant une rotation de 180° de la liaison aryle-C(O) de chaque unité quinoléine. Ceci suggère un hypothétique mécanisme de dépliement mécanique qui est en adéquation avec d'autres études théoriques.[3,4]

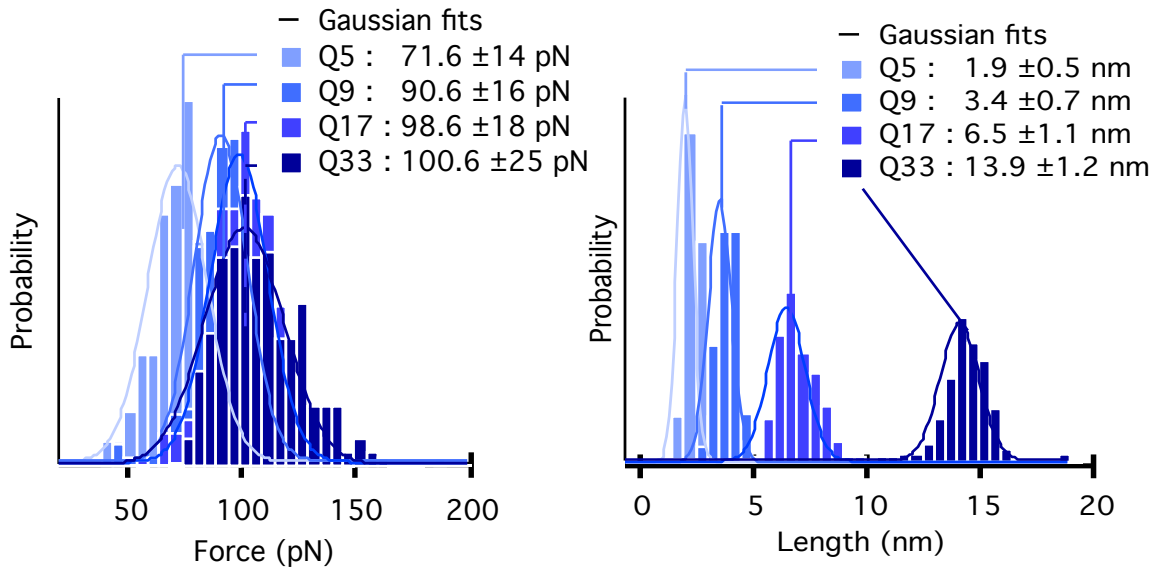

Figure 3 Histogrammes de forces (gauche) et de longueurs issus des mesures des courbes de force-distance des foldamères de différentes tailles.

Une transposition mathématique[5] des courbes de force-distance en une variable 'longueur de contour' (issu d'un modèle de mécanique statistique), nous a permis d'obtenir plus de détails sur les étapes de dépliement. Les résultats suggèrent qu'une étape de dépliement consiste en la rotation simultanée de deux rotations de 180° de la liaison aryle-C(O), mais étant donné la ressemblance de chaque interaction intramoléculaire, ces résultats de longueurs de contour ne permettent pas de discerner si ces deux rotations ont lieu sur des unités adjacentes ou non.

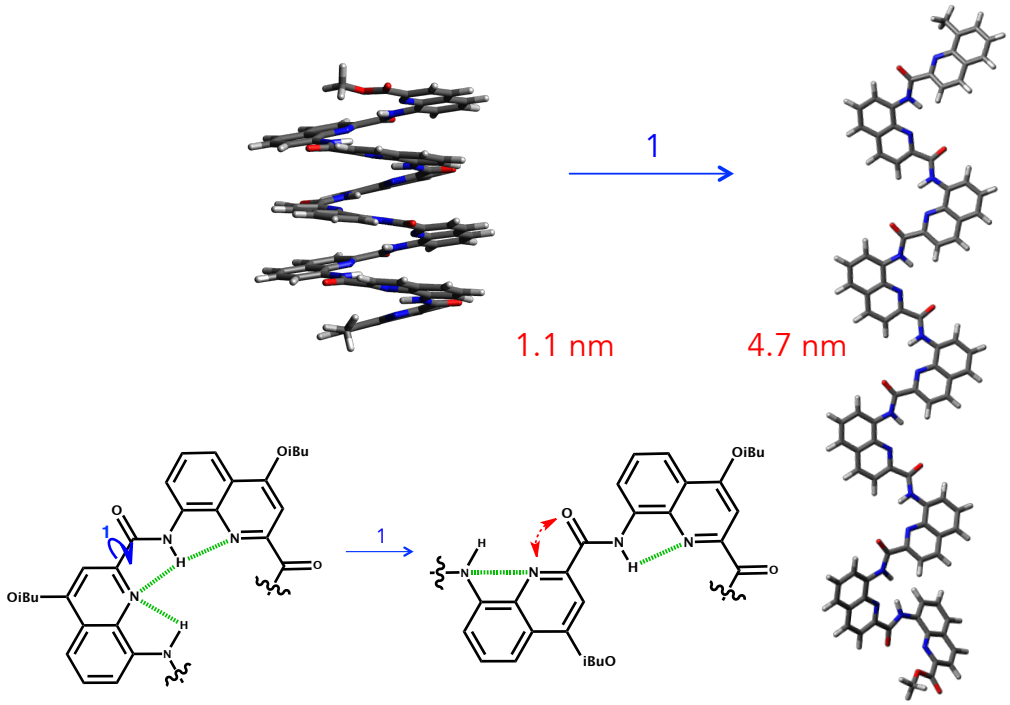

Figure 4 (En haut) Représentation figurative de la structure RX du foldamère replié et d'une structure dépliée obtenue par modélisation moléculaire. (En bas) Représentation schématique de changement de conformation lors du dépliement par rotation séquentielle des liaisons aryle-C(O).

Afin d'étudier l'influence de la taille sur les propriétés mécaniques, nous avons mesuré la force moyenne du motif de dépliement pour chaque taille de foldamère (Figure 3). Nous avons remarqué que la force la plus probable augmente partant de 70 pN pour arriver à 100 pN de façon non linéaire jusqu'à observer une valeur limite vers 17 unités de quinoléines. Ceci constitue une deuxième preuve de la coopérativité. L'addition d'unité quinoléines renforce la structure hélicoïdale jusqu'à une certaine limite.

Nous avons aussi identifié que la partie finale caractérisée par une diminution de force présente une extension identique pour chaque foldamère et mesure environ 2 nm, ce qui peut être associé à l'ouverture de 6-7 unités quinoléines ou un peu plus que 2 tours d'hélice. Cette similarité pour toutes les tailles de foldamères renforce la mise en évidence du segment de nucléation de l'hélice. De plus, l'apparence de cette partie peut être variable (saut ou fluctuations progressives) suggérant une instabilité structurale. Par ailleurs, les motifs de dépliement du Q5 sont très similaires à ces derniers, toutefois le dépliement du Q5 s'avère être plus court et moins ample (Figure 2). Ces observations renforcent l'hypothèse qu'une séquence repliée plus petite que 6 unités présente une plus faible stabilité, ce qui peut être associé au segment de nucléation de l'hélice. Ainsi, un minimum de 6-7 unités semble nécessaire pour obtenir un plateau, représentatif d'une structure hélicoïdale renforcée. Ces résultats suggèrent également que la coopérativité du repliement est associée au renforcement de l'empilement π.

En plus des mesures de forces de dépliement révélant des forces assez élevées, la robustesse de ces hélices a été confirmée par d'autres analyses. Des expériences à différentes vitesses sur trois ordres de grandeurs ont été réalisées et ne montrent aucun changement sur la force de dépliement. Selon la théorie du temps de vie d'une liaison[6–8], on aurait pu s'attendre à avoir une augmentation de la force pour des vitesses croissantes étant donné qu'on octroie aux liaisons intramoléculaires moins de temps pour accumuler suffisamment d'énergie pour se rompre spontanément. Cette observation démontre que les foldamères ont été étirés dans des conditions d'équilibre, c'est-à-dire que les vitesses expérimentales étaient bien plus faibles que la dynamique du foldamère. Ces expériences ont également permis de calculer les énergies libres de rupture de chaque groupe d'interactions au sein des hélices (Figure 5 gauche). La différentiation des valeurs d'énergie selon les tailles de foldamères est à nouveau une preuve de coopérativité et est en accord avec des mesures de cinétique pour l'inversion chirale de l'hélicité (Figure 5 droite). Ce résultat renforce les hypothèses de mécanisme de dépliement du changement d'hélicité, chacun proposant une rotation de la liaison aryle-C(O).[3,9]

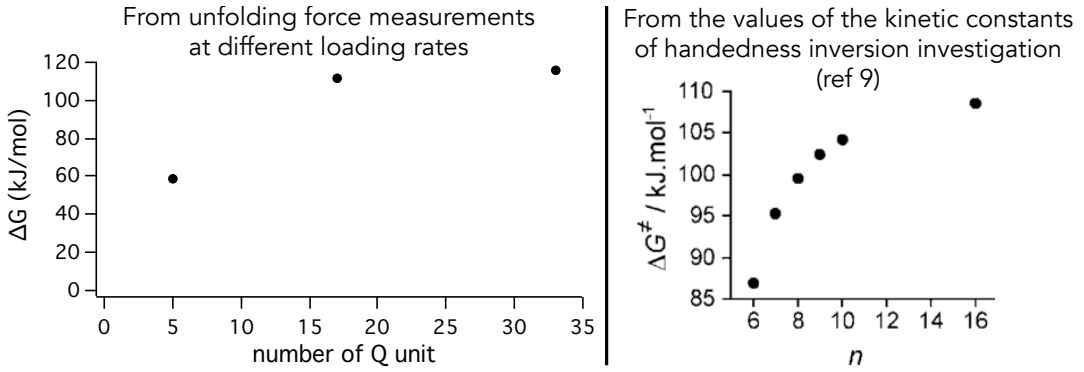

Figure 5 (A Gauche) Graphique de l'énergie libre d'une transition conformationnelle lors du dépliement forcé du foldamère, calculée à partir des forces de dépliement. (A Droite) Graphique de l'énergie libre calculées à partir des mesures cinétiques du changement du sens de l'hélicité (*n* étant le nombre d'unité Q). Reproduit de la référence 9.

Un autre résultat remarquable des propriétés mécaniques des foldamères a été observé lors des expériences "étirement–relaxation". Il s'agit d'expériences où la molécule est maintenue accroché entre la surface et la pointe du levier pendant plusieurs cycles d'approche-retrait successifs. Ces expériences nous permettent de déplier la molécule et ensuite de relâcher progressivement la tension afin d'observer le repliement éventuel. On a pu remarquer que les traces de l'étirement et de la relaxation, reproduites à la Figure 6, se superposaient parfaitement, preuve que le dépliement est entièrement réversible mais aussi que le foldamère est capable de générer une force pour se replier. Il n'y a eu aucune perte d'énergie lors du dépliement forcé. Les foldamères se comportement comme un élastique idéal. Les mesures d'aire sous les traces ont permis de calculer le travail nécessaire pour déplier le foldamère et le travail fourni par le foldamère pour se replier. Comme attendu, les valeurs d'énergie coïncident, et ce aussi à des vitesses différentes. Nous avons obtenu une valeur d'environ 600 kJ mol^{-1} pour le dépliement entier ou de 42 kJ mol^{-1} par nm étiré. Ainsi même à vitesse très élevée (1667 nm s^{-1}) et sous tension, le foldamère se replie.

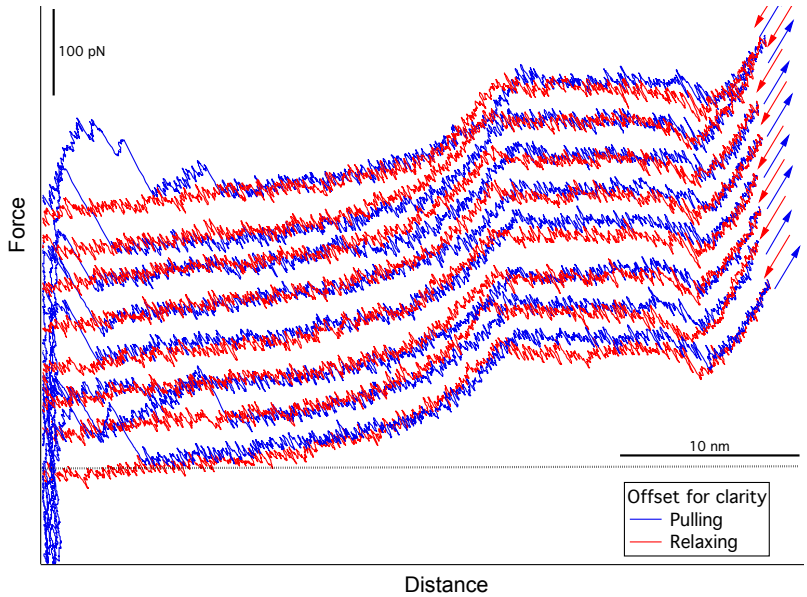

Figure 6 Série de courbes de force-distance consécutive d'expériences d'"étirement-relaxation". Les traces en bleu représentent le dépliement et les traces en rouge le signal de relaxation, chaque courbe étant décalée pour des raisons de clarté.

Finalement, des phénomènes particuliers de *hopping* ont également été observés à de nombreuses reprises à la fin du plateau. Il s'agit de fluctuations conformationnelles en temps réel entre un état (intermédiaire) déplié et un état (intermédiaire) replié qui reflètent la capacité du foldamère à reformer directement des interactions qui viennent d'être rompues. Ce motif n'a été que très rarement observé dans des expériences de spectroscopie de force sur des biomolécules. Dans notre cas, on a pu remarquer que les 6-7 dernières unités peuvent rompre simultanément mais ont également tendance à se reformer. Toutefois, étant donné la similitude de chaque groupe d'interactions au sein de l'hélice, on peut envisager la reformation de n'importe quel groupe d'interactions qui a rompu au sein de la séquence. L'analyse de ces évènements fournit des informations sur la cinétique de repliement. Nous avons pu constater que les foldamères de quinoléines défiaient la capacité de la spectroscopie de force par AFM. En effet, nous n'avons pas été capables de faire des mesures suffisamment rapides pour échantillonner de manière optimale les fluctuations conformationnelles. Nous n'avons pu déterminer qu'une valeur supérieure du temps de repliement local du segment de nucléation de 40 µs sous tension.

Au niveau chimique, l'influence de la nature des solvants sur les interactions impliquées dans la structure a été étudiée pour ces foldamères. Les objectifs de cette étude étaient d'identifier les motifs de dépliement dans les différents milieux (polaire, apolaire, donneur/accepteur de ponts hydrogène) et d'étudier les contributions des différentes natures d'interaction (pont-H, électrostatique, empilement π) en les modulant selon les solvants. Pour ce faire, nous avons comparé les courbes de dépliement des foldamères dans du diméthylforamide (DMF), du diméthylsulfoxide (DMSO), de l'acétonitrile (MeCN), du toluène (Tolu), de l'éthanol (EtOH), et du tétrachloréthane (TCE). Dans ces différents solvants, nous avons identifié des profils très similaires aux résultats préliminaires dans le DMF. Comme on peut le voir à la Figure 7 pour les longs foldamères Q33, chaque courbe dans chaque solvant est composée d'un motif en plateau. Ce qui indique que la structure secondaire hélicoïdale est maintenue indépendamment du solvant. Toutefois quelques différences ont été identifiées. Par exemple, dans le toluène et dans le TCE, un saut quantitativement plus important que dans les autres solvants a été identifié avant le plateau (plage bleu Figure 7). Il s'agit d'un motif intéressant car il pourrait s'agir d'une force "initiatrice" nécessaire pour déclencher le dépliement. Dans le DMF, ce saut présente une distribution en force autour de 6 pN, ce qui est négligeable vis à vis du bruit des mesures. Par contre dans le toluène, la valeur centrale se trouve à 30 pN et dans le TCE à 40 pN. Ces solvants sont apolaires par rapport aux autres, l'hypothèse principalement mise en avant pour expliquer ce phénomène provient d'un effet de perturbation du réseau des molécules de solvant autour du foldamère. De même, nous avons pu mettre en évidence que les interactions étaient renforcées en solution apolaire et non compétitive de l'empilement π. Les plus grandes forces de dépliement ont été mesurées dans le TCE (≈ 128 pN), ensuite les forces ont diminué selon l'ordre prévu par la théorie de Hunter[10] en fonction des capacités des solvants à être bon donneur ou accepteur de ponts hydrogènes (MeCN ≈ 122 pN et EtOH ≈ DMSO ≈ DMF ≈ 107 pN) et finalement la plus faible force a été mesurée dans le toluène (≈96 pN), un éventuel compétiteur d'empilement π. Ce résultat n'est pas encore évident à expliquer.

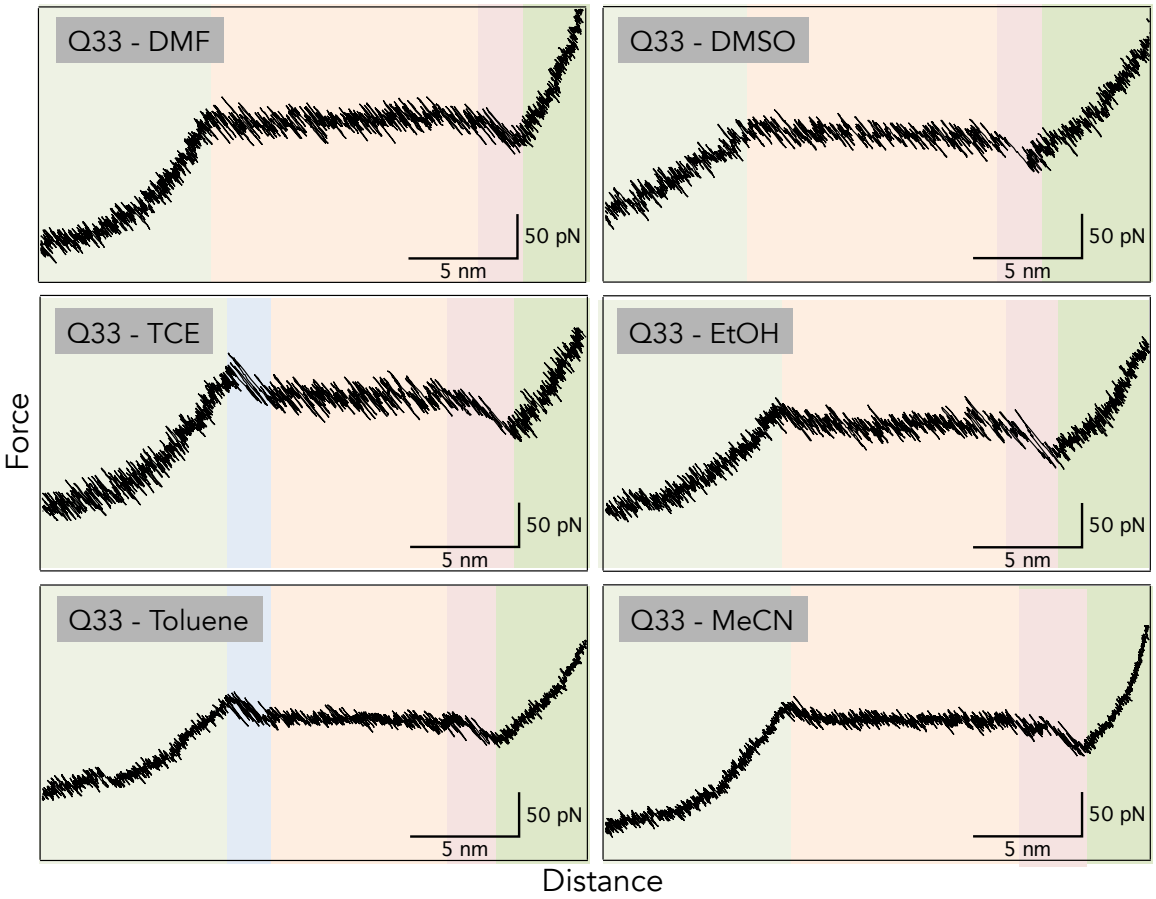

Figure 7 Courbes de force-distance caractéristiques du Q33 dans les différents solvants (nommés en haut à gauche de chaque graphique). Les parties caractéristiques des différents comportements mécaniques sont mises en évidence avec les plages de couleurs.

A partir des résultats obtenus sur les foldamères de quinoléines, nous avons conçu deux autres foldamères afin d'obtenir des résultats supplémentaires concernant les propriétés mécano-chimiques de molécules synthétiques présentant une structure secondaire hélicoïdale (Figure 9). Nous avons conçu un foldamère avec une hélice présentant un plus grand diamètre et un foldamère de quinoléines séparé au milieu par un maillon aliphatique ($-CH_2-$).

Pour répondre à la fois aux contraintes de de synthèse et des mesures SMFS, le choix a été d'insérer un octamère de naphthyridines entre 2 hélices composées de quinoléines ('SH'-$^{m}QQ_8$-N_8-$^{m}QQ_8$-PEG). Les monomères quinoléines et naphthyridines sont tous les deux des hétérocycliques avec respectivement 1 et 2 atomes d'azote dont leurs oligomères ont démontré la capacité de former des hélices.[11,12] L'angle entre 2 unités adjacentes de naphthyridine est de 120°, par contre pour ceux de quinoléines il est de 60° (Figure 8). En conséquence, une hélice du foldamère de naphthyridine est formée de 4 unités par tour et présente un plus grand diamètre, ce qui implique probablement des propriétés mécano-chimiques et dynamiques différentes.

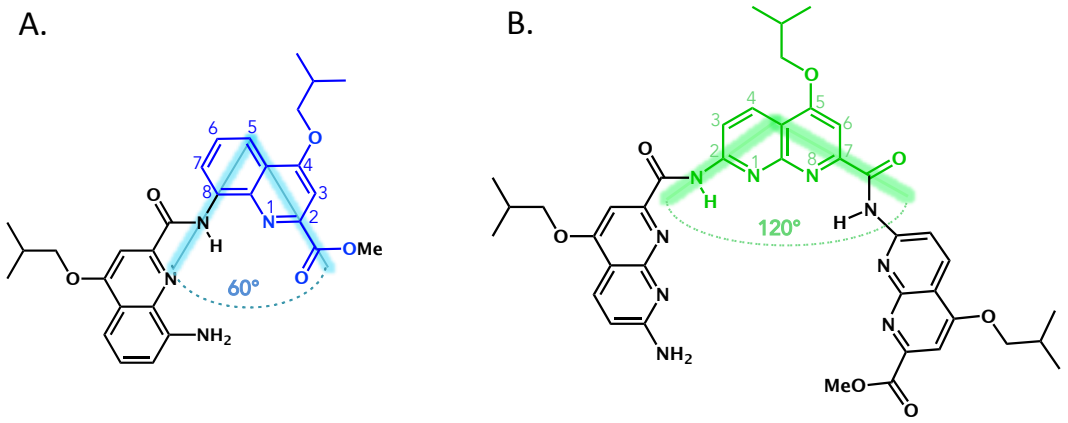

Figure 8 Structures chimiques d'un dimère de quinoléines (A) et d'un trimère de naphthyridines (B). Les angles entres les unités adjacentes sont respectivement de 60° et 120°.

Plusieurs arguments justifient la décision de construire un tel tribloc. Premièrement, alors que la synthèse de longs oligomères de quinoléines est de plus en plus maitrisée, celle de longs oligomères de naphthyridines nécessite encore des développements et des optimisations. Par exemple, la synthèse d'un octamère de naphthyridines est toujours un grand défi. Effectivement, les oligomères de naphthyridine ont tendance à s'hybrider en triple hélice, ce qui rend leur synthèse problématique et certains produits de réaction très sensibles ou difficiles à purifier. Deuxièmement, du point de vue spectroscopie de force, les manipulations de molécules si courtes représentent un réel défi. Troisièmement, la tendance à s'hybrider en double ou triple hélice peut s'avérer également problématique lors des expériences de spectroscopie de force sur molécule unique. Il est primordial de maitriser parfaitement l'entièreté du système sur lequel on conduit toute expérience afin de pouvoir interpréter les résultats. Dès lors nous avons décidé d'insérer l'hélice de naphthyridines entre des hélices de quinoléines pour agrandir le motif d'extension, faciliter l'identification du nouveau motif par comparaison avec le motif connu et empêcher la formation de triple hélices.

Lors de l'optimisation de la rétro-synthèse de ce tribloc, nous avons dû insérer des unités aminométhyle-quinoléines possédant une amine terminale aliphatique au lieu d'aromatique, plus réactionnelle que cette dernière. Ne connaissant pas l'effet de l'ajout d'un maillon aliphatique (-CH_2-), nous avons également décidé de synthétiser le foldamère cible dépourvu de l'oligomère de naphthyridines ('SH'-$^{m}QQ_8$-$^{m}QQ_8$-PEG), afin d'avoir une molécule de référence. Ce faisant, cela va permettre également d'étudier l'effet qu'apporte un chainon aliphatique au sein d'une séquence l'oligoamide aromatique.

Les synthèses de ces foldamères ont été réalisées suivant la méthode de doublement de segment.[13] Cette technique permet un contrôle parfait du nombre d'unités, grâce aux réactions de couplage contrôlées et des purifications optimisées.

A l'heure actuelle, la synthèse des oligomères de quinoléines est très bien maitrisée au sein du laboratoire,[13] alors que la synthèse de petits oligomères de naphthyridines est connue mais plus complexe.[14] Afin de pallier le phénomène d'hybridation pendant la synthèse d'oligomères de naphthyridines qui rend les amines terminales peu accessibles et peu

réactionnelles, une stratégie de protection a été développée au laboratoire. Un groupement encombrant est ajouté à l'amine terminale d'une unité naphthyridine sur deux. Ainsi, en formant un amide tertiaire après couplage, l'amide ne peut plus former de ponts hydrogène ce qui empêche son repliement et l'hybridation en triple hélice.

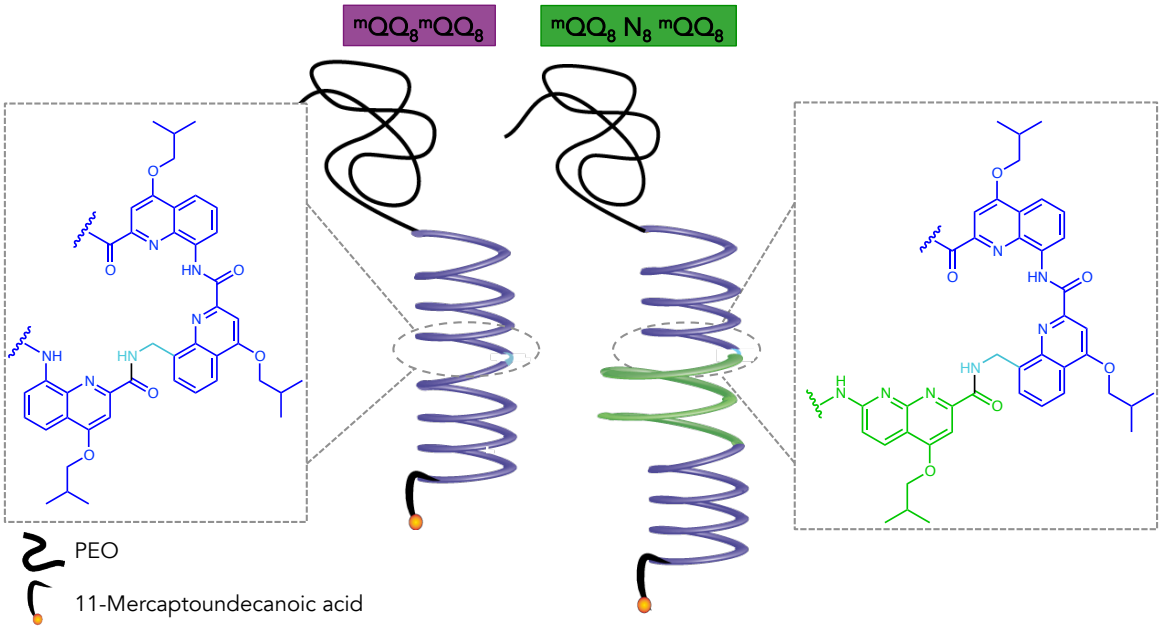

Figure 9 Schéma représentatif des nouveaux foldamères synthétisés. (A gauche) le dibloc constitué de quinoléines et séparés au milieu par un groupe méthylène. (A droite) tribloc comprenant un oligomère de naphthyridines entre deux blocs de quinoléines.

Pour la synthèse du tribloc contenant un octamère de naphthyridines, le groupement protecteur de l'amine choisi est le 2,4-dimethoxybenzyle (DMB). Sa déprotection est orthogonale par rapport aux autres groupements protecteurs impliqués dans la synthèse[15] et ne peut être retiré qu'en fin de synthèse par un traitement acide. Le schéma réactionnel de la synthèse de ce foldamère est représenté à la Figure 10. (A) Les blocs de quinoléines ($^{m}QQ_8$) et (B) des tétramères de naphthyridines ont d'abord été synthétisés. (C) Les blocs de quinoléines ont été ensuite couplés aux tétramères de naphthyridines. (D) Ces deux parties hybrides ont alors été couplées ensemble et les agent stériques DMB ont été déprotégés pour créer le tribloc contenant ainsi un octamère de naphthyridines. Ce mode de couplage a permis de garder une symétrie dans la synthèse ce qui a facilité la purification à chaque étape. (E) Finalement les foldamères a été fonctionnalisés en leurs extrémités avec le groupement thiol, nécessaire au greffage sur surfaces dorées, et avec le PEG pour l'accrochage à la pointe et le dépliement complet du foldamère.

L'analyse RMN a montré qu'il est nécessaire d'octroyer un certain temps pour que le repliement de l'hélice de naphthyridines ait lieu après déprotection des amines tertiaires des unités naphthyridines.

Concernant le dibloc, sa synthèse a été plus aisée, n'étant constitué que d'oligomères de quinoléines. Selon l'analyse RMN l'ajout d'un lien méthylène dans la séquence quinoléine ne perturbe pas significativement l'hélicité du foldamère.

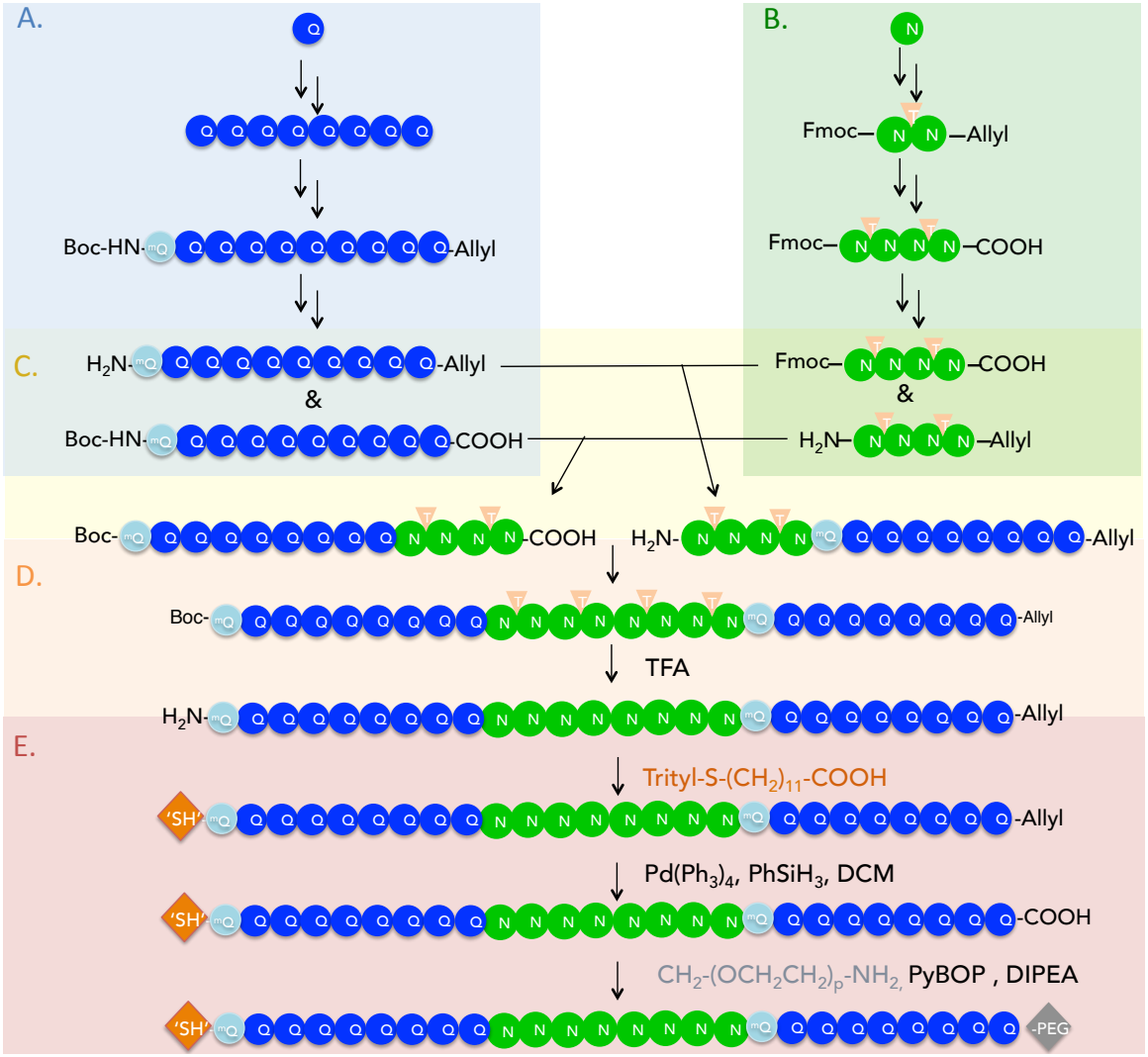

Figure 10 Schéma réactionnel de la synthèse de 'SH'-$^{m}QQ_8$-N_8-mQQ_8-PEG. Les billes bleu clair, bleu foncé et vertes représentent respectivement les unités quinoléines avec une amine aliphatique, les unités quinoléines purement aromatiques et les unités naphthyridines. Les triangles orange clair représentent les groupements de protection structurale (DMB). Les fonctionnalisations des extrémités du foldamère pour des expériences de spectroscopie de force sont représentées par un carré orange pour le groupement thiol et un carré gris pour le PEG.

Les analyses de spectroscopie de force sur ces foldamères dans le DMF présentent des résultats très intéressants et mettent bien en évidence l'influence de ces modifications chimiques sur les propriétés mécaniques lorsqu'ils sont soumis à une force.

Nous avons pu confirmer que l'oligomère de naphthyridines de 'SH'-$^{m}QQ_8$-N_8-$^{m}QQ_8$-PEG avait bien une structure repliée lorsqu'elle était coincée entre des oligomères de quinoléines. L'assignation des différents motifs de dépliement a été rendue évidente grâce au foldamère 'SH'-$^{m}QQ_8$-$^{m}QQ_8$-PEG servant de référence. Les motifs du dépliement des oligomères de naphthyridines et de quinoléines sont bien distincts (Figure 11 en haut).On a pu également montrer que l'hélice de naphthyridines se déplie en premier et à plus faible force (≈ 40 pN) autrement dit à la moitié de la force nécessaire pour déplier une hélice de quinoléines. Des études précédentes suggéraient que des hélices de plus grand diamètres pouvaient plus s'étendre comme une ressort que les hélices avec des plus petits diamètres.

Ceci peut être expliqué par le fait qu'il faut fournir moins d'énergie pour une même extension dans une hélice comprenant plus d'unités par tour.[16] Nos résultats sont en adéquation avec ces hypothèses.

L'analyse du motif de 'SH'-$^{m}QQ_8$-$^{m}QQ_8$-PEG nous montre que l'insertion du -CH_2- rompt la séquence aromatique (Figure 11 en bas). Nous avons observé le dépliement d'un bloc de quinoléines et puis de l'autre. En comparant les motifs de ces deux derniers foldamères nous pouvons affirmer qu'il ne s'agit pas d'un effet de géométrie mais d'un effet de force. En effet, nous n'observons aucune différence de dépliement des blocs de quinoléines qu'ils soient séparés d'un groupe méthylène ou d'un oligomère de naphthyridines. Le dépliement commence par rompre les interactions les plus faibles et puis les plus fortes. Une fois le processus de dépliement d'un bloc de quinoléines démarré, la coopérativité facilite sa poursuite, c'est certainement pourquoi nous pouvons observer le dépliement séquentiel de chaque bloc.

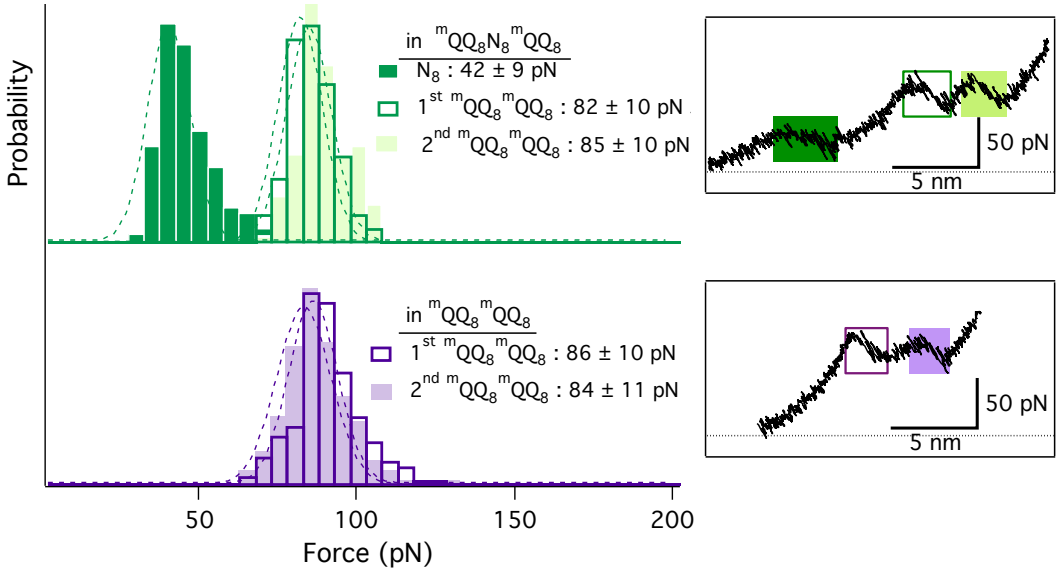

Figure 11 (A gauche) Histogrammes des mesures de forces des différents motifs identifiés dans les courbes de force–distance des dibloc 'SH'-$^{m}QQ_8$-$^{m}QQ_8$-PEG et tribloc 'SH'-$^{m}QQ_8$-N_8-$^{m}QQ_8$-PEG. (A droite) Représentation des courbes récurrentes de dépliement des dibloc et tribloc dans le DMF.

En résumé, les expériences de spectroscopie de force sur différents systèmes moléculaires synthétiques et hélicoïdaux ont permis de mettre en évidence des propriétés mécaniques au niveau moléculaire. Nous avons déterminé que les foldamères de quinoléines étaient extrêmement robustes et présentent une dynamique très rapide ce qui contribue à leur stabilité repliée. Cette robustesse peut être expliquée par la proximité des fonctions chimiques impliquées dans les interactions intramoléculaires et par la rigidité du squelette qui limite les degrés de liberté. Une hélice de plus grand diamètre semble montrer une résistance moindre, se dépliant sous l'effet d'une plus faible force. L'ajout d'un maillon aliphatique a des conséquences fondamentales sur le dépliement du foldamère.

Les résultats engrangés complètent la caractérisation complète des foldamères de quinoléines et offrent des pistes intéressantes pour la construction de systèmes moléculaires plus complexes avec des propriétés mécaniques bien déterminées.

Références

1. Li, X. Synthesis and physical properties of helical nanosized quinoline-based foldamers : structure , dynamics and photoinduced electron transport. (University of Bordeaux and University of Liege, 2016).
2. Hill, D. J., Mio, M. J., Prince, R. B., Hughes, T. S. & Moore, J. S. A Field Guide to Foldamers. *Chem. Rev.* **101,** 3893–4012 (2001).
3. Abramyan, A. M., Liu, Z. & Pophristic, V. Helix handedness inversion in arylamide foldamers: elucidation and free energy profile of a hopping mechanism. *Chem. Commun.* **52,** 669–672 (2016).
4. Uribe, L., Gauss, J. & Diezemann, G. Determining Factors for the Unfolding Pathway of Peptides, Peptoids, and Peptidic Foldamers. *J. Phys. Chem. B* **120,** 10433–10441 (2016).
5. Puchner, E. M., Franzen, G., Gautel, M. & Gaub, H. E. Comparing proteins by their unfolding pattern. *Biophys J* **109,** 426–434 (2008).
6. Noy, A. & Friddle, R. W. Practical single molecule force spectroscopy: how to determine fundamental thermodynamic parameters of intermolecular bonds with an atomic force microscope. *Methods* **60,** 142–50 (2013).
7. Friedsam, C., Wehle, A. K., K hner, F. & Gaub, H. E. Dynamic single-molecule force spectroscopy: bond rupture analysis with variable spacer length. *J. Phys. Condens. Matter* **15,** S1709–S1723 (2003).
8. Hoffmann, T. & Dougan, L. Single molecule force spectroscopy using polyproteins. *Chem. Soc. Rev.* **41,** 4781–4796 (2012).
9. Delsuc, N. *et al.* Kinetics of helix-handedness inversion: Folding and unfolding in aromatic amide oligomers. *ChemPhysChem* **9,** 1882–1890 (2008).
10. Hunter, C. Quantifying intermolecular interactions: Guidelines for the molecular recognition toolbox. *Angew. Chemie - Int. Ed.* **43,** 5310–5324 (2004).
11. Ferrand, Y., Kendhale, A. M., Garric, J., Kauffmann, B. & Huc, I. Parallel and Antiparallel Triple Helices of Naphthyridine Oligoamides. *Angew. Chemie Int. Ed.* **49,** 1778–1781 (2010).
12. Jiang, H., Léger, J. M., Dolain, C., Guionneau, P. & Huc, I. Aromatic δ-peptides: Design, synthesis and structural studies of helical, quinoline-derived oligoamide foldamers. *Tetrahedron* **59,** 8365–8374 (2003).
13. Qi, T., Deschrijver, T. & Huc, I. Large-scale and chromatography-free synthesis of an octameric quinoline-based aromatic amide helical foldamer. *Nat. Protoc.* **8,** 693–708 (2013).
14. Ferrand, Y., Kendhale, A. M., Garric, J., Kauffmann, B. & Huc, I. Parallel and Antiparallel Triple Helices of Naphthyridine Oligoamides. *Angew. Chemie Int. Ed.* **49,** 1778–1781 (2010).
15. Zhang, A., Ferguson, J. S., Yamato, K., Zheng, C. & Gong, B. Improving foldamer synthesis through protecting group induced unfolding of aromatic oligoamides. *Org. Lett.* **8,** 5117–5120 (2006).
16. Berni, E. *et al.* Assessing the mechanical properties of a molecular spring. *Chemistry* **13,** 8463–9 (2007).

Appendices

TABLE OF CONTENTS

Appendices

A. Synthesis of Quinoline-based Foldamers

The Trityl-S-R-$^{m}QQ_n$-PEG with n= 4, 8, 16, 32 were synthetized by Dr. Xuesong Li during his thesis. All details of the synthesis can be found in his thesis manuscript.[1]

In brief 4-, 8-, 16- and 32- mer of 8-amino-2-quinolinecarboxylic acid (quinoline unit) oligoamides were synthetized by the segment doubling strategy.[2] These foldamers were further elongated with an aminomethyl quinoline monomer (^{m}Q) at the N-terminal for synthetic and AFM-design reasons. Then they were functionalized with trityl-protected thiol group. At the C-terminal, one amine-terminated polyethylene glycol (PEG) was coupled in the presence of PyBOP.

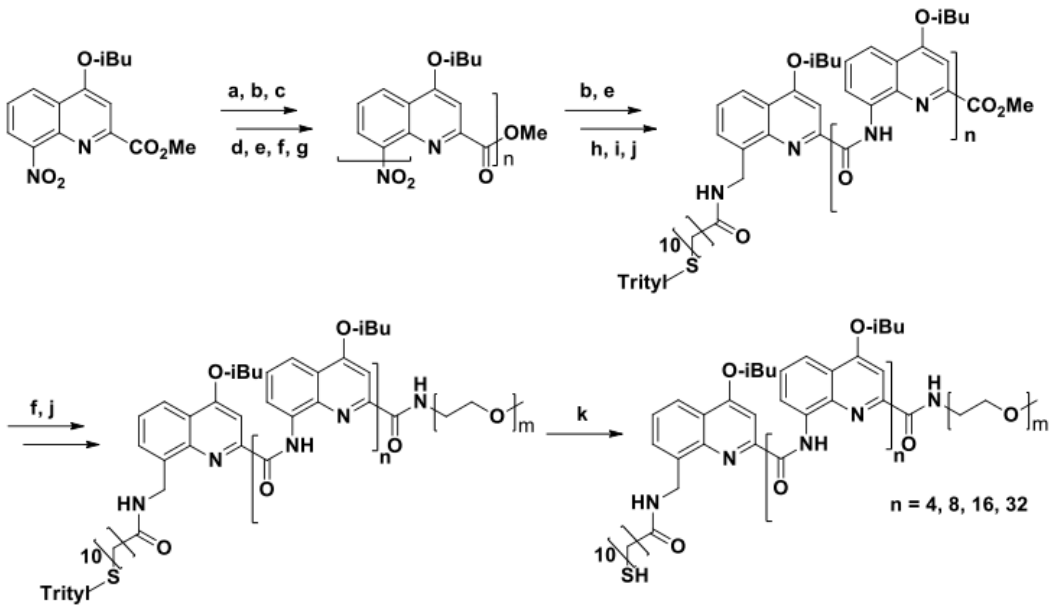

Scheme S 1: Scheme of the synthesis of HS-R-$^{m}QQ_n$-PEG with n= 4,8,16,32: a), Pd/C, H_2, r.t., overnight; b), KOH, THF/H_2O, r.t., overnight; c), oxalyl chloride, DCM, r.t., ~ 4 h; d), DIPEA, DCM or $CHCl_3$, 0 °C to r.t., overnight; e), Pd/C, NH_4VO_3, $_{NH4HCO2}$, EtOAc/EtOH, 95 °C, overnight; f), NaOH, THF/MeOH, r.t., 0.5 h to overnight; g), pyridine/H_2O, reflux, overnight; h), Ghosez reagent, CHCl3, r.t, approx. 3 h; i), TFA, DCM or $CHCl_3$, r.t. 4 to 6 h; j) PyBOP, DIPEA, $CHCl_3$, r.t., overnight; k) $CHCl_3$/H_2O, TFA, r.t., approx. 4 h.

A.1 NMR data

NMR spectra were recorded on an Avance II NMR spectrometer (Bruker BioSpin) with a vertical 7,05T standard-bore/ultrashield magnet operating at 300 MHz for 1H observation. All chemical shifts are quoted in parts per million (ppm, d) relative to the 1H residual signal of the deuterated solvent used (CDCl3 at 7.26 ppm). 1H NMR splitting patterns with observed first-order coupling are designated as singlet (s), doublet (d), double doublet (dd), triplet (t), or quartet (q). Splitting patterns that could not be interpreted or easily visualized are designated as multiplet (m). Coupling constants (J) are reported in hertz. Samples were not degassed. Data processing was performed with Topspin 2.0.

A.1.1 Trityl-S-$^{m}QQ_4$-PEG:

1H NMR (300 MHz, CDCl3): δ 11.90 (s, 1H), 11.75 (s, 1H), 11.56 (s, 1H), 11.54 (s, 1H), 8.51 (t, J = 9.0 Hz, 2H), 8.12 (d, J = 33 Hz, 1H), 8.15 (s, 1H), 8.13 (s, 1H), 8.10 (s, 1H), 8.01 (s, 1H), 7.99 (s, 1H), 8.00 (d, J = 9.0 Hz, 1H), 7.79 (d, J = 6.0 Hz, 1H), 7.70 – 7.60 (m, 4H), 7.42 – 7.15 (m, 18H), 6.84 (s, 1H), 6.71 (s, 1H), 6.65 (d, J = 6.0 Hz, 1H), 6.61 (s, 1H), 4.40 – 2.59 (m, H), 2.57 – 2.26 (m, 5H), 1.63 – 1.52 (m, 4H), 1.45 – 0.81 (d, H). 137

A.1.2 Trityl-S-$^{m}QQ_8$-PEG

1H NMR (300 MHz, CDCl3): δ 11.42 (s, 1H), 11.14 (s, 1H), 11.06 (s, 1H), 10.95 (s, 1H), 10.82 (s, 1H), 10.81 (s, 1H), 10.77 (s, 1H), 10.70 (s, 1H), 8.15 – 8.08 (m, 3H), 8.02 (s, 1H), 7.99 (s, 1H), 7.94 – 7.88 (m, 3H), 7.84 – 7.69 (m, 3H), 7.63 (d, J = 6 Hz, 1H), 7.53 (d, J = 6 Hz, 1H), 7.41 – 6.94 (m, 29H), 6.90 (s, 1H), 6.88 – 6.85 (m, 1H), 6.82 (s, 1H), 6.60 (s, 1H), 6.54 (s, 1H), 6.48 (s, 1H), 6.44 – 6.40 (m, 3H), 6.16 (s, 1H), 6.02 (s, 1H), 4.12 – 3.06 (m, H), 2.89 – 2.85 (m, H), 2.54 – 2.15 (m, H), 1.54 – 0.87 (m, H)

A.1.3 Trityl-S-$^{m}QQ_{16}$-PEG

1H NMR (300 MHz, CDCl3): δ 11.08 (s, 1H), 10.80 (s, 1H), 10.73 (s, 1H), 10.66 (s, 1H), 10.40 (s, 1H), 10.25 (s, 1H), 10.22 (s, 1H), 10.17 (s, 1H), 10.11 (s, 1H), 10.07 (s, 1H), 10.03 (s, 1H), 9.98 (s, 1H), 9.97 (s, 1H), 9.94 (s, 1H), 9.90, (s, 2H), 7.87 – 7.81 (m, 4H), 7.78 – 6.91 (m, 54H), 6.87 (d, J = 3 Hz, 1H), 6.84 – 6.81 (m, 4H), 6.79 – 6.70 (m, 9H), 6.67 – 6.64 (m, 2H), 6.34 (s, 1H), 6.35 (s, 1H), 6.27 – 6.26 (m, 2H), 6.17 (s, 1H), 6.12 (s, 1H), 5.88 (s, 1H), 5.85 (s, 1H), 5.78 (s, 1H),5.75 (s, 2H), 5.74 (s, 1H), 5.72 (s, 1H), 5.70 (s, 1H), 5.68 (s, 2H), 3.92 – 2.68 (m, H), 2.35 – 2.06 (m, 35H), 1.52 – 0.84 (m, H).

A.1.4 Trityl-S-$^{m}QQ_{32}$-PEG

1H NMR (300 MHz, CDCl3): δ 11.00 (s, 1H), 10.74 (s, 1H), 10.64 (s, 1H), 10.59 (s, 1H), 10.31 (s, 1H), 10.14 (s, 1H), 10.13 (s, 1H), 10.05 (s, 1H), 9.99 (s, 1H), 9.92 (s, 1H), 9.87 (s, 1H), 9.80 (s, 1H), 9.78 (s, 1H), 9.71 (s, 1H), 9.66 (s, 1H), 9.61 (s, 2H), 9.55 – 9.43 (m, 15H), 7.79 – 6.44 (m, 117H), 6.31 (s, 1H), 6.28 (s, 1H), 6.21 – 6.20 (m, 2H), 6.08 (s, 1H), 6.02 (s, 1H), 5. 78 (s, 1H), 5.73 (s, 1H), 5.69 (s, 1H), 5.62 (s, 1H), 5.61 (s, 1H), 5.59 (s, 2H), 5.54 (s, 1H), 5.49 – 5.37 (m, 18H), 3.87 – 1.95 (m, H), 1.27 – 0.81 (m, H).

A.2 Energy-minimized structure of 9-mer with aminomethyl group

The flexibility induced by the presence of the CH_2 in ^{m}Q is expected to create a 90° angle of the *N*-terminal part of the molecule. The foldamer would then stand perpendicular to the anchored surface for SMFS experiments.

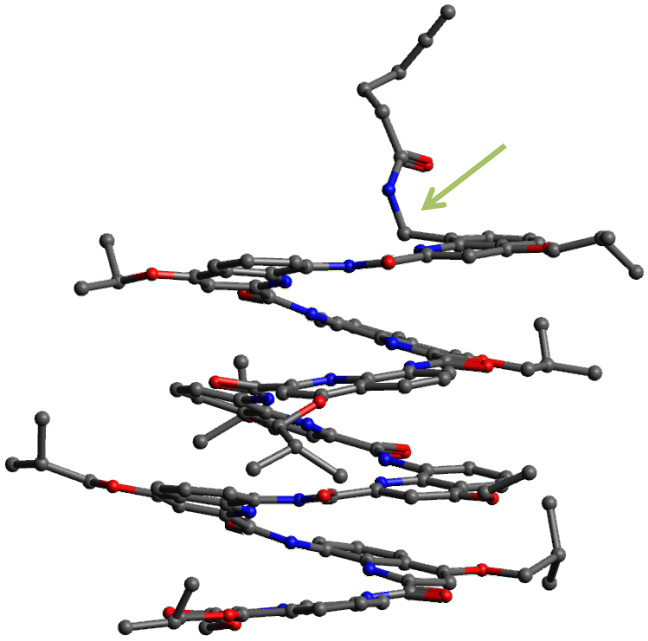

Figure S 1 Energy-minimized structure structure of a quinoline nonamer ended with an amino-methyl quinoline unit.

B. AFM-Substrates preparation

B.1 Foldamer aliquotation

To store the protected foldamers and only deprotect the requested number of foldamers prior to prepare the needed surface for AFM-SMFS experiments, we aliquoted the total quantity of foldamers in individual vials. We transferred 1 mg or 0.5 mg in separate vials through dichloromethane solution. The solutions were immediately dried up and the vials were stored in the freezer.

B.2 Deprotection of the thiol group of the foldamers

1 mg of the foldamer (trityl-S-$^{m}QQ_{n}$-PEG (n = 4, 8, 16, 32) was added into round-bottomed flask with 0.9 mL of TFA, 0.1 mL of chloroform and 0.1 ml of water. This reaction was allowed to stir for around 3 h at room temperature. The stirring bar was taken out of the flask and toluene was added. The azeotroped mixture was evaporated to remove the TFA. This operation was repeated 4 times. After dried under vacuum, the deprotected molecules were immediately used for the preparation of the functionalized surface or can be stored in the refrigerator.

B.3 Surface functionalization

The foldamers were grafted onto gold-coated silicon substrates (Au (100 nm) / Ti / Si wafer, Sigma-Aldrich) using our previously established method[3] to obtain a sparse regime of the molecule of interest. Substrates were cut (2×2 cm^2), cleaned in a 1:1:5 volume ratio of NH_4OH, H_2O_2, and H_2O solution during 15 min at 65°C, followed by UV-ozone treatment for 15 min (UV-ozone cleaner®, Model 42, Jelight Company Inc.) and finally dipped in EtOH for 5 min. Just after the cleaning procedure, they were dried by a N_2 flow and dipped for 1 h at room temperature in a solution of the foldamers ($4 \cdot 10^{-8}$ mol) and dodecyl sulfide (DDS) ($1 \cdot 10^{-7}$ mol) in dichloromethane in a closed chamber to avoid evaporation. When 2 kinds of foldamers were grafted on the same surface, half of this amount of each foldamers was added in the same solution with the DDS. The functionalized substrate was then rinsed during 10 min three times in dichloromethane and once in EtOH and finally dried with N_2 flow.

B.4 Storage conditions

After use, the surface was rinsed with EtOH and dried with N_2. The substrates can be reuse several times. The functionalization is quite stable overtime and the surfaces can be stored for several months. The main problem is the dilution by usage and accumulation of dust. When not used, the surfaces were stored in fluoroware boxes at room temperature in a dry and clean environment.

C. Cantilever calibration

The spring constant of each cantilever was calibrated by the Sader method.[4,5]

The Sader method is a direct method using the cantilever dimensions, and the resonance frequency (w_0) and quality factor (Q) obtained from the thermal spectrum. Before experiment we measured the thermal spectrum of the cantilever in air with the implemented software on PicoPlus 5500 microscope (Agilent Technologies). After the experiment, the dimensions of the cantilever were determined by scanning electron microscopy (SEM). Using an python calibration software, which implements the Sader calibration, we performed a power spectral density (PSD) analysis in order to determine Q and w_0. The cantilever spring constant can then be calculated using the following equation (for rectangular cantilevers)

$$k_c = 0.1906\, \rho\, b^2\, L\, Q\, T_i(w_0) w_0^2$$

where ρ is the density of the fluid (air or liquid), b and L are the cantilever width and length respectively, and $\Gamma_i(w_0)$ is the imaginary part of the hydrodynamic function evaluated at the resonance frequency.

The calibrated spring constant is then used during the curve analysis.

D. AFM-SMFS experiments

D.1 Instrument and Set-up

SMFS experiments were carried out with a PicoPlus 5500 microscope (Agilent Technologies) equipped with a closed-loop scanner. Gold-coated tips (OBL-10 Biolever, Bruker; nominal spring constant $k = 0.009–0.1$ N·m^{-1} and $k = 0.002$-0.02 N·m^{-1}) were calibrated before the experiment with the Sader method and used for all the force experiments.

The functionalized substrates were immobilized on a sample plate and mounted in a liquid cell, which contains the filtered solvent all along the force experiment. The surface and the scanner are than placed in a closed chamber, which was saturated with the solvent. Before starting the experiments, the cantilever was immersed during 1 h in the solvent for its equilibration, away from the surface.

D.2 Standard pulling force-distance measurements

Force measurements were performed at loading rates between 1×10^3 and 7.5×10^6 pN·s^{-1} in filtered organic solvents. The approaching velocity was kept always the same (166 nm s^{-1}). The molecules were picked up by gently pressing the AFM tip with a maximum force of 250 pN against the substrate during 0.5 sec (dwell time). For standard pulling experiments, each retraction and approaching force curve contains respectively 18000 and 2000 data points. When a molecule attaches to the tip during the approach, one can follow its stretching in the retraction curve by observing the cantilever deflection.

D.3 Pulling-relaxing force-distance measurements

For pulling-relaxing experiments, the first step consists in trapping a molecule between the tip and the substrate. The tip is therefore gently approached (max 250 pN) to the surface as for standard pulling experiment. As soon as one molecule has been caught by the tip, pulling-relaxing cycles were performed using a custom-made routine to guide the tip. The pulling is limited to a given extension or a given deflection difference, which prevents the detachment of the molecule from the tip. Reaching this fixed threshold, the tip is sent back towards the surface and records the relaxing trace. The approach is preferably limited to near the surface. To record successive curves, contact should be avoided as it could lead to the detachment of the molecule from the tip. Pulling and relaxing velocity are the same and the numbers of recorded points for both curves are also the same (10000 points). We performed force measurements at loading rates and approaching rates between 1×10^3 and 7.5×10^6 pN s^{-1} in organic solvents.

D.4 Dynamic force spectrum

To investigate the influence of the loading rate, plot we performed the pulling experiments at different velocities and we tested 2 different analyses to interpret the results.

On one side we plotted the average unfolding force values as a function of the apparent loading rate obtained by multiplying the velocity by the calibrated spring constant $lr_{app}=k_c$.velocity.

On the other side, we measured the effective loading rate on each curve by fitting with a straight line each force vs. time curve just before the unfolding of the foldamer. The slope of this fit provided the effective loading rate $lr_{eff}=\mathrm{d}f/\mathrm{d}t$ and we retrieved the effective spring constant as $lr_{eff}= k_{eff}$.velocity. We recalculated the unfolding forces for the different velocities and we plotted these effective forces as a function of the effective loading rates.

E. AFM-SMFS curves analysis

E.1 Selection and transformation

The selection of the Force-Distance curves was done manually in order to identify and categorize the different patterns. The raw 'deflection (V) *vs*. piezo-movement (nm)' curves were observed independently with a custom-built routine in IgorPro (WaveMetrics). Pulling curves exhibiting no deviation from the baseline or unspecific adhesion peak were rejected. In a first phase, all curves exhibiting other deviating signal were selected and analysed. The second step consisted in identifying the curves tracing a reproducible pattern that might be the characteristic of the unfolding of a single foldamer. To select specific curves, we listed several criteria: (i) the maximum extension should not be higher than 40 nm, which corresponds to the maximum unfolding of the foldamer and the PEG linker. (ii) The pulling curves should start with the entropic elasticity unravelling pattern of PEG. At this step, we also used the WLC fit, as a guide to select the single molecule pattern. As explained in chapter 1, the persistence length of a single PEG chain is a tabulated value. (iii) The curves should end with an elasticity overstretching of the whole molecule. (iv) In-between these two entropic elasticity behaviours, a specific and characteristic unfolding pattern should be recorded, which should be consistent with the expected stretched length.

Once these criteria were established, only the corresponding curves were transformed with a custom-built routine in IgorPro in order to obtain a force-distance curve (as explained in the introductive chapter) or 'force (pN) *vs*. time (nm)' curve. The zero-force and zero-extension were obtained by respectively fitting the baseline (by a linear horizontal fit on minimum 200 points) and the vertical contact section (after transformation, by a linear vertical fit on minimum 50 points). Therefore, the contact point (tip-substrate) corresponds to the (0,0) coordinate. During the transformation, the spring constant of the cantilever needs to be provided and the deflection sensitivity is directly calculated on each curve (inverse of the slope of contact section).

In cyclic pulling-relaxing experiments, there is not necessary a contact section nor a baseline. To determine the point of zero length and zero force in pulling-relaxing curves, an entire curve with the contact line and baseline is recorded before and after every cycle. These curves are used to determine the zero force value and the zero extension for the curves of the cycle; the stretching profiles of the successive curves are superimposed and the consistency is verified.

E.2 Data analysis

E.2.1 Measurement tools

Once reproducible curves with a specific pattern were selected and transformed, the quantitative analyses of the basic parameters were performed with IgorPro (WaveMetrics).

Several custom-built routines were available to analyse separately each type of pattern (single-peak, multi-peak, plateau) and to obtain quantitative measurements (force, length, time, ..). Basically, with the routine we can position cursors on the curves to take the desired measurements. In the Figure S **2**, pulling curves are represented with typical cursors positions for the measurement of the desired parameters.

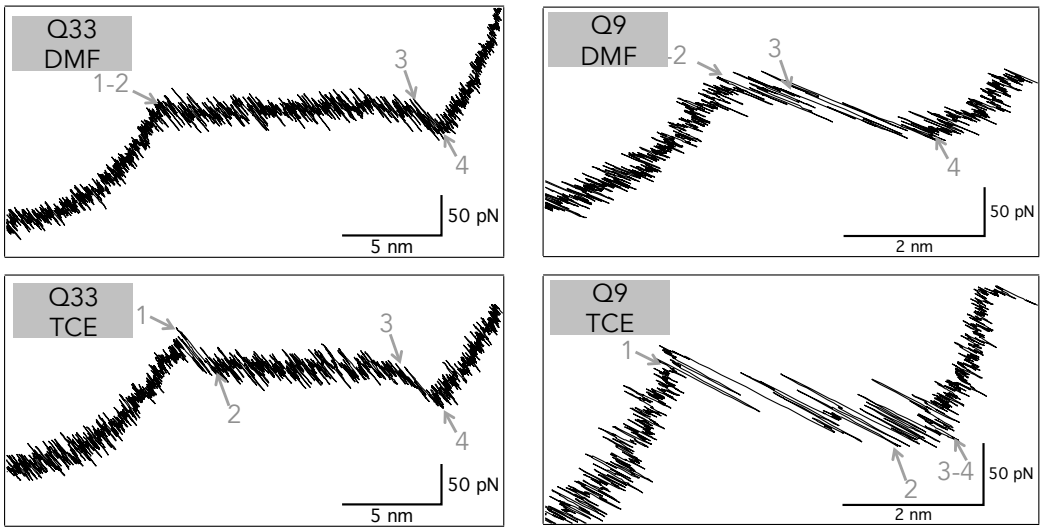

Figure S 2 Zoom in force-distance curves of 33- and 9-mer in DMF and TCE. Specific points are shown with number and referred to the cursors used to perform the quantitative measurements.

(i) Single values for probing the force at specific point in the unfolding pattern (F)

We measured the starting force of the unfolding of the foldamer (cursor #1) or the force at the end (cursor #2)

(ii) Average values between two cursors (F_{avg} , noise of the base line)

We measured the average force of the plateau (average of the point between the cursors #2 and #3) or the average force of the whole unfolding pattern (average between the point between cursor #1 and #4)

(iii) Difference between two cursors (ΔF, ΔLc, ΔL, Δt)

We measured the difference in force and in length of the starting trigger feature (*between the cursors #1 and #2) or of the ending feature (between the cursors #3 and #4), as well as the length of the plateau (between the cursors #2 and #3) and of the whole unfolding pattern (between the cursors #1 and #4).*

(iv) Slope of a linear fit (df/dt)

For the measurement of the effective loading rates to test the theory of the influence of the force transducer (PEG), we measured, at the beginning of the foldamer unfolding, the slope of a linear fit on the last 50-100 points of the force vs. time curve at the beginning of the foldamer unfolding. The slope (df/dt) represents the effective loading rate

(v) Area under a raw or fitted curve (work).

Areas under the curves are measured to estimate of the free-energy difference between the unfolded state and the folded state. Firstly the custom-built routine integrates the area under the force distance curve of the foldamer unfolding from the beginning of the unfolding (cursor #1) and the end of the unfolding (cursor #2). Secondly, a WLC function is fitted on the overstretching part of the foldamer pulling trace to measure the work accounting for the stretching of the handles (PEG). This contribution is then subtracted from the area calculated under the foldamer unfolding curve.

E.2.2 Statistical data analysis

Since molecular processes are of stochastic nature, interpretation of the observed rupture forces can be direct. Same experiments at the same pulling velocity and in the same environment lead to over a wide range forces or lengths. To determine the most probable value, the experiments need to be repeated a significantly statistical number of times. Then different statistical tools can be used to accurately interpret the data. We used different data analysis and representations to determine as precisely as possible all the parameters measured.

E.2.2.1.1 Histograms

The histograms were constructed using the IgorPro (WaveMetrics) integrated tool. The bin size was set manually. If not stated differently, the bin size is equal to 5 pN for rupture or unfolding force histograms and 0.5 nm for length histograms. The X values were always bin-centred and the Y values were normalized to probability density.

E.2.2.1.2 Statistics calculations and Gaussian fit

As our measured parameters demonstrated normal distributions, which were in good agreement with our expectation, we performed classical statistical analysis. We calculated the mean value and the standard deviation. We also fitted the histograms distributions with Gaussian functions $G(\boldsymbol{x}|\mu_i, \sigma_i)$ with mean μ_i and variance σ_i, to determine the most probable values from IgorPro. For each estimated average rupture force or length, the 95% confidence interval was computed as $\pm 1.96\sqrt{\sigma^2/(p_i N)}$ where σ^2 is the estimated variance of the i^{th} Gaussian component while $p_i N$ represents the effective size of the population.

We compared both results and they were always in good agreement.

E.2.2.1.3 Probability Density Function (PDF)

The Probability Density Function (PDF) distribution can be seen as a histogram with an infinitely small bin-size, and representing more accurately each change in the distribution. Here, we used the Kernel smoothing function (N=1000) in MatLab (MathWorks) to construct the PDF distribution directly from the raw values (force, ΔL_C, ...) and to compare with the histogram. This allows distinguishing some multi-distributions or defect in normal distribution. PDF allowed us to distinguish some outlier values. For a similar experiment type, where the day or the cantilever varied, we did observe some small second distributions. However, these PDF distributions were not reproducible from an experiment to the other, so we could discard the corresponding data.

In the literature, histograms are much more common than probability density function (PDF) distribution because they are easier to construct.

E.2.2.1.4 Multi-Gaussian analysis

When we had a doubt on the histogram distribution or when we wanted to highlight different results from different foldamers, we used the Multi-Gaussian analysis to check the contribution or the distinction of the different distributions. We fitted the data with a Gaussian mixture model (GMM) in MatLab and it gives us the mean values of each distribution as well and the width.

For a specific case (a foldamer, a solvent, a velocity) the data of a measured variable (length, force, ..) did not demonstrate reproducible multi-distribution.

E.2.3 Theoretical unfolding structures and lengths

From the X-Ray structure of a quinoline octamer, all possible bond-rotations were mechanically tested in Avogadro software. The energies were optimized (by steepest descent under the MMFF94 force field) until bond starts to rotate back to their initial position. The length of the obtained fully unfolded structures were measured and compared to the experimental value added to the folded length given by X-ray structure. The best match between the length of theoretical structure and of the experimental unfolding structure is obtained with the most extended, which is achieved through the rotation of each Cα−CO bonds of around 180°.

E.2.4 Analysis of the hopping states

The hopping events occur especially at the end of the plateau (force around 100 pN). A 33-mer was pulled at various loading rates, between 1000 $pN \cdot s^{-1}$ and 125 000 $pN \cdot s^{-1}$, and the hopping was further analysed. From the 'force vs. time curves', the total time during the fluctuations were measured between 2 cursors positioned at the beginning and at the end and the number of fluctuations were counted manually for each maximum overpassing a threshold of the average noise. The total time divided by the number of fluctuations gives the oscillation frequency. The folding time was estimated by averaging the time of the steps where the signal goes back to a partially folded state.

E.2.5 Transformation of force spectroscopy data from extension space into contour length space

Each experimental data of the Force-Distance curves were converted into contour length (L_c) values by solving the worm-like chain (WLC) equation.[6] The WLC model[7] predicts the relationship between the extension of an individual linear and flexible polymer chain and its entropic restoring force. The force required to extend a WLC with a persistence length l_p and contour length L to a distance D is given by:

$$F(D) = \frac{k_B T}{l_p}\left[\frac{D}{L} + \frac{1}{4(1-\frac{D}{L})^2} - \frac{1}{4}\right]$$

with k_B the Boltzmann constant and T the temperature. We used a l_p of 0.4 nm.

These L_c values were plotted over time. The distribution of the different L_c values gave rise to the number of intermediate partially unfolded states. Histograms are constructed with a bin size of 0.15 and automatically fitted with Peakfit (Systat Software, Inc) and multiple Gaussians.

For the cross-superposition graphs, the range representing 68% of the data of each peaks from two L_c distributions from two force-distance curves are cross-superposed to identify matching intermediate states (intersect on the diagonal). The detailed procedure is described in ref[6]. First and last possible matches are measured and used to draw subsequent rectangles. The overlapping areas of the subsequent rectangles give the possible matching L_c increments.

F. Supplementary figures

F.1 Length analysis of the distinct parts of the unfolding of a Q33 in several organic solvents

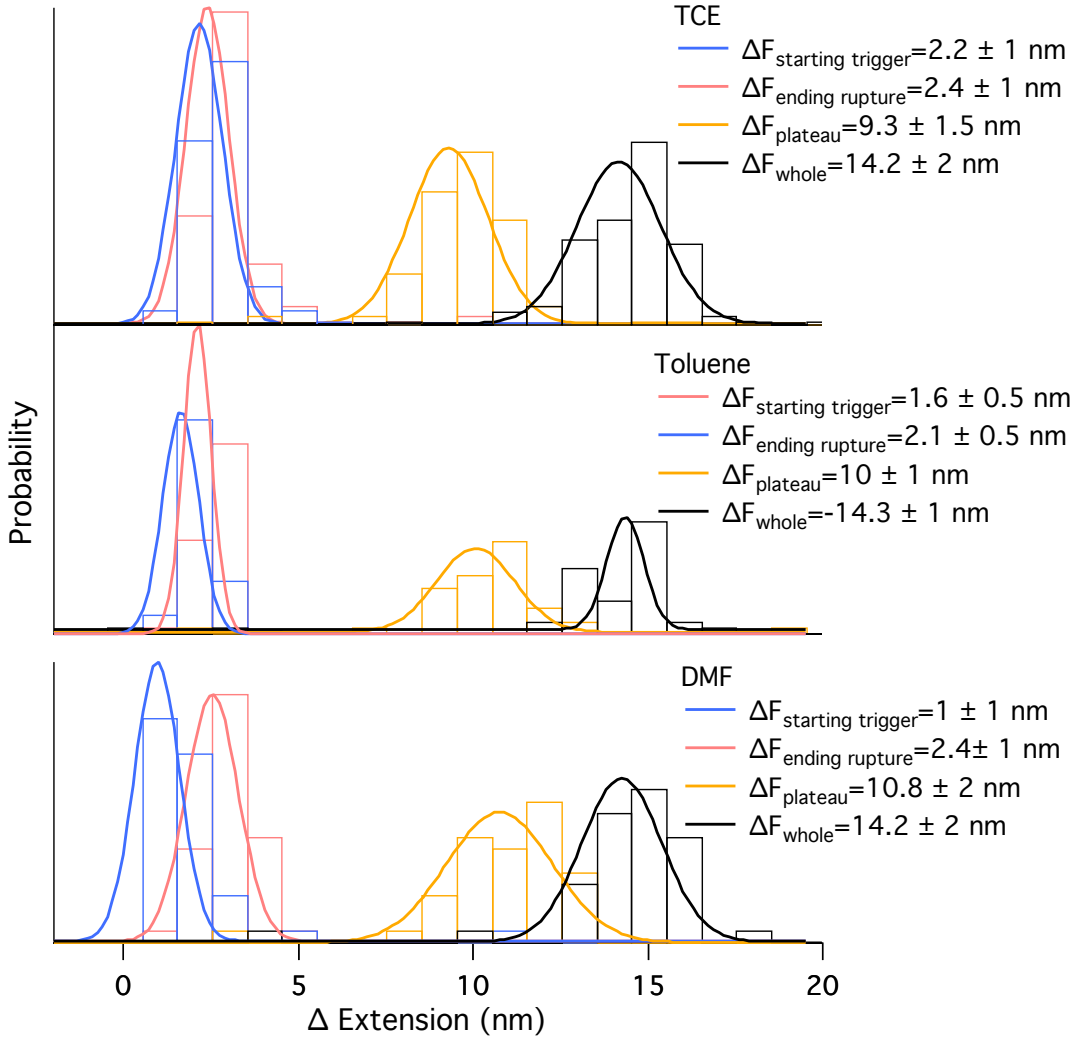

Figure S 3 Histograms of the difference of length of the different mechanical features along a pulling trace in TCE, Toluene and DMF. The colours of the distributions correspond to the different mechanical behaviours highlighted with the same colour in the force-distance curves.

F.2 Cross-superimpositions of L_c evolution of Q17and Q9

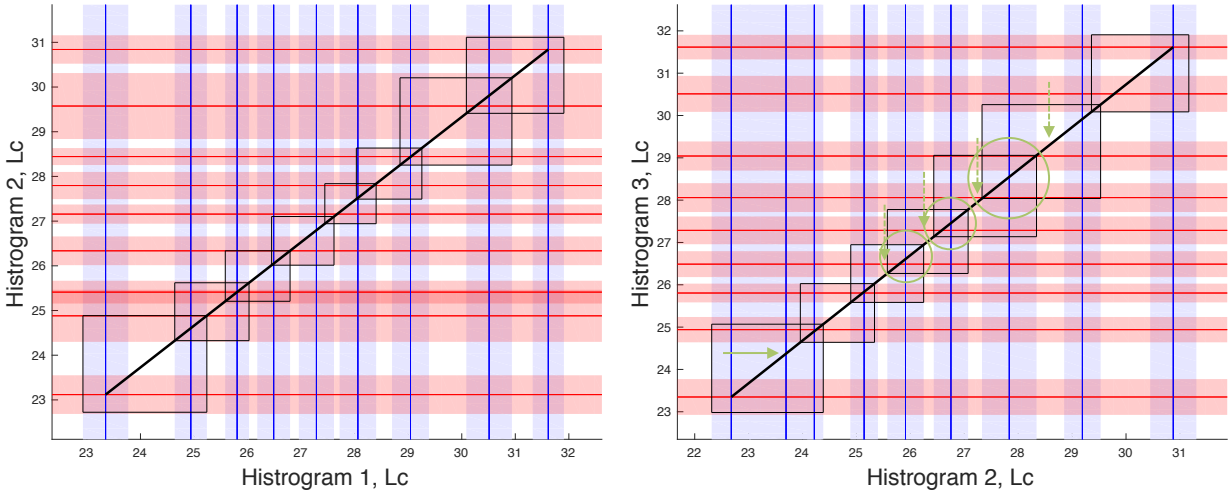

Figure S 4 Cross-superposition of 3 L_c evolution histograms (2x2) of 17-foldamers. Plain red and blue lines represent the mean L_c values of the Gaussian fits of the histograms. Transparent red and blue zones represent the band given by a standard deviation around the mean L_c of the position of the intermediate state. (Left) Diagonal rectangles are always between 2 intermediate states. (Right) We observed 3 red lines and 2 blue lines, which means that there is a missing peak that is difficult to localize because of incremental uncertainties (circles).

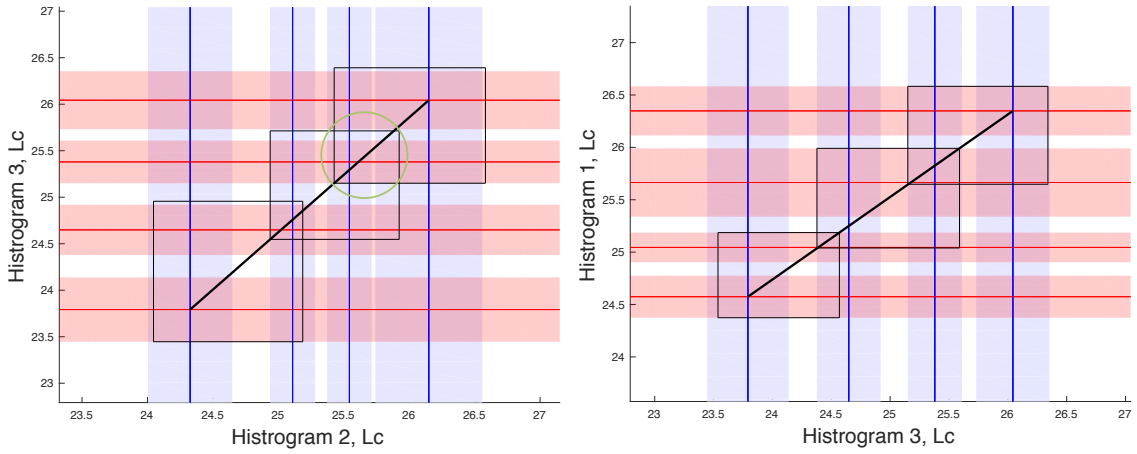

Figure S 5 Cross-superposition of 3 *Lc* evolution histograms (2x2) of 9-foldamers. Plain red and blue lines represent the mean *Lc* values of the Gaussian fits of the histograms. Transparent red and blue zones represent the band given by a standard deviation around the mean L_c of the position of the intermediate state. Both shown diagonal rectangles are always between 2 intermediate states.

F.3 Mass spectrometry analysis of final triblock Naphthyridine-constituted foldamers

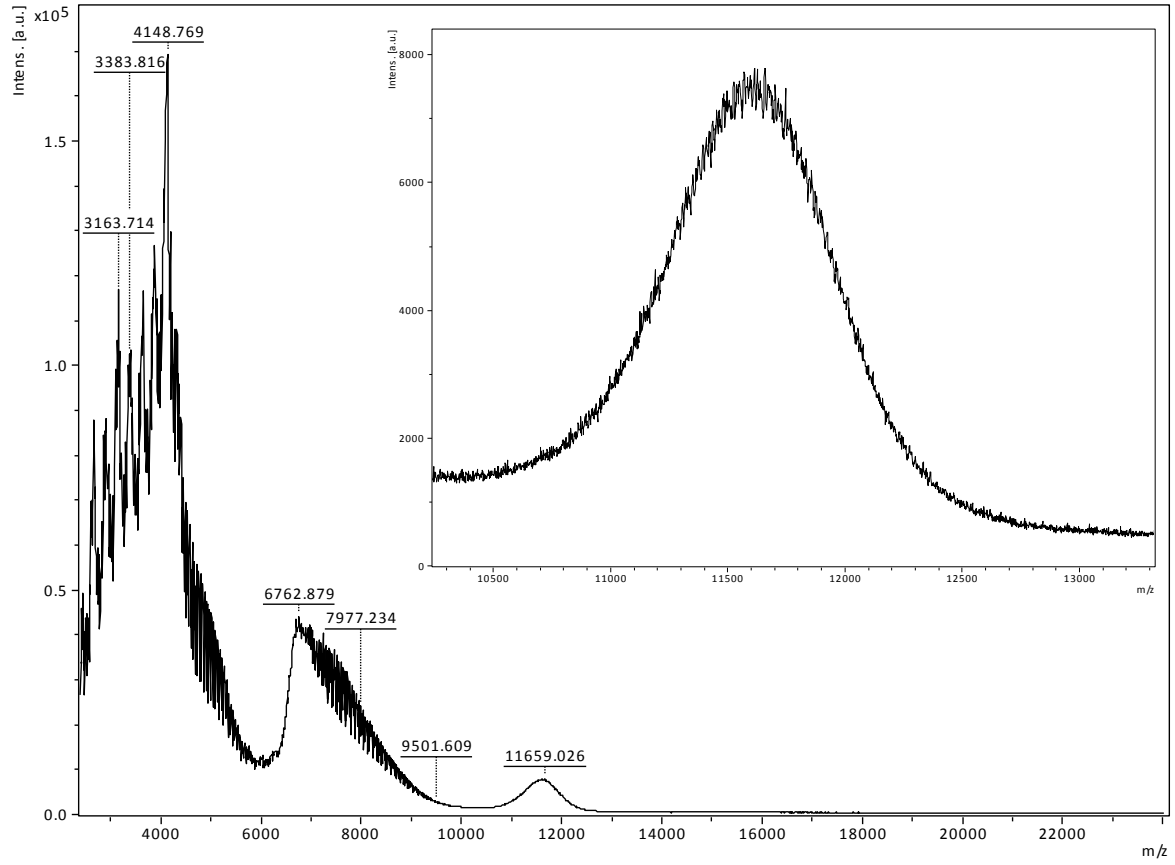

Figure S 6 MALDI spectrum on HS-$^{m}QQ_8$-N_8-$^{m}QQ_8$-PEG with DHB matrix.

G. References

(1) Li, X. Synthesis and physical properties of helical nanosized quinoline-based foldamers : structure , dynamics and photoinduced electron transport, University of Bordeaux and University of Liege, 2016.

(2) Qi, T.; Deschrijver, T.; Huc, I. *Nat. Protoc.* **2013**, *8* (4), 693.

(3) Lussis, P.; Svaldo-Lanero, T.; Bertocco, A.; Fustin, C.-A.; Leigh, D. A.; Duwez, A.-S. *Nat. Nanotechnol.* **2011**, *6* (9), 553.

(4) te Riet, J.; Katan, A. J.; Rankl, C.; Stahl, S. W.; van Buul, A. M.; Phang, I. Y.; Gomez-Casado, A.; Schön, P.; Gerritsen, J. W.; Cambi, A.; Rowan, A. E.; Vancso, G. J.; Jonkheijm, P.; Huskens, J.; Oosterkamp, T. H.; Gaub, H.; Hinterdorfer, P.; Figdor, C. G.; Speller, S. *Ultramicroscopy* **2011**, *111* (12), 1659.

(5) Sader, J. E.; Sanelli, J. A.; Adamson, B. D.; Monty, J. P.; Wei, X.; Crawford, S. A.; Friend, J. R.; Marusic, I.; Mulvaney, P.; Bieske, E. J. *Rev. Sci. Instrum.* **2012**, *83* (10), 103705.

(6) Puchner, E. M.; Franzen, G.; Gautel, M.; Gaub, H. E. *Biophys J* **2008**, *109* (50), 426.

(7) Gordon, M. *Br. Polym. J.* **1970**, *2* (5), 302.